

Searches for Neutrinos from Supernovae Using Cherenkov In-Ice Detectors

Dissertation
zur
Erlangung des Doktorgrades (Dr. rer. nat.)
der
Mathematisch-Naturwissenschaftlichen Fakultät
der
Rheinischen Friedrich-Wilhelms-Universität Bonn

von
Markus Voge
aus
Eutin

Bonn, September 2016

Dieser Forschungsbericht wurde als Dissertation von der Mathematisch-Naturwissenschaftlichen Fakultät der Universität Bonn angenommen und ist auf dem Hochschulschriftenserver der ULB Bonn http://hss.ulb.uni-bonn.de/diss_online elektronisch publiziert.

1. Gutachter: Prof. Dr. Marek Kowalski
2. Gutachter: Prof. Dr. Norbert Langer

Tag der Promotion: 10.02.2017
Erscheinungsjahr: 2017

Summary

Supernovae mark the violent death of massive stars. They are among the most energetic processes known to exist in the Universe. When a star explodes as a supernova, it can outshine its host galaxy for weeks. But still, in a core-collapse supernova, only a tiny fraction of the released energy goes into electromagnetic radiation. 99% of the supernova energy is emitted in form of neutrinos. Neutrinos may play a crucial role for the supernova to actually explode, thus enabling chemical evolution in the Universe by spreading rare elements. However, the details of the explosion process are far from understood and the neutrinos are the only information carriers leaving the interior of the star. Therefore, supernova neutrinos are indeed interesting research objects.

Besides the low-energy neutrinos emitted during the core-collapse process of the supernova, there may be neutrinos of much higher energies that are generated after the core-collapse in jets, within the envelope of the exploding star. The existence of hidden jets within supernovae can only be revealed with neutrinos. It would be important evidence for a theory: that supernovae with jets and gamma-ray bursts are similar objects, with the difference that in gamma-ray bursts, the jets are strong enough to pierce through the envelope of the star and release gamma radiation, while in the more numerous supernovae with jets, they are not. There are more scenarios that might produce high-energy supernova neutrinos, e.g. the interaction of the expelled envelope with material around the star, in so-called Type IIn supernovae. The study of neutrinos emitted by supernovae is thus scientifically very well motivated. This work covers the topic of supernova neutrino detection, both of low and high energy.

There are only about two supernova explosions per century in our Galaxy, but current neutrino detectors are limited to the detection of Galactic supernovae. Therefore, a new detector concept—located in the South Pole glacier ice—is studied, with the aim to be sensitive to extra-galactic low-energy supernova neutrino bursts. By developing and running a dedicated detector simulation, it is found in this work that a detector with 50 times the total instrumented photo-sensitive area of the existing IceCube detector would yield 11 to 44 supernova neutrino detections per decade. Several challenges are identified, most notably the development of cheap and low-noise sensors and the suppression of backgrounds.

In addition, a multi-messenger data analysis program is carried out, which registers high-energy neutrino bursts with the IceCube detector and triggers follow-up observations with optical telescopes. The neutrino burst data alone are analyzed and no significant excess of neutrino bursts is found. Therefore, it is likely that all observed neutrino bursts were produced by background fluctuations. Because additional bursts are expected to be produced by supernovae hosting jets, upper limits on the jet supernova model are derived. For model values of the jet Lorentz factor $\Gamma_{\text{jet}} = 10$ and the jet kinetic energy $E_{\text{jet}} = 3 \times 10^{51}$ erg, only about 8% of all core-collapse supernovae hosting a jet are consistent with the data, corresponding to a volumetric rate of $5.9 \times 10^{-6} \text{ Mpc}^{-3} \text{ yr}^{-1}$.

In the optical follow-up data, only one promising supernova is identified and this Type IIn supernova is extensively studied with neutrino and electromagnetic data. A causal connection between the supernova and the 1.8 seconds long neutrino burst is unlikely because of the supernova being already

more than 169 days old at the time of the neutrino burst. The combined significance of the neutrino and optical supernova detection is 2.3σ , making a coincidence between a background neutrino burst and an uncorrelated supernova plausible. Upper limits to a model of long-term neutrino emission are set. They are more than 1000 times above the predicted emission because of the long distance to the supernova.

The rest of the optical follow-up data is searched for additional supernovae as neutrino source candidates. For this, a supernova search algorithm and a Monte Carlo simulation of the supernova detection are developed. 15.0 ± 11.4 potential supernovae are identified, standing against a background expectation of $11.2^{+2.0}_{-1.7} \binom{+8.8}{-5.1}$ coincident supernova detections, with no correlation with neutrinos at all.

So far, the search for supernova neutrinos described in this work has not been fruitful. But improved technological opportunities may emerge or are already emerging: e.g. new sensor technologies for low energies and better follow-up surveys like ZTF for high energies. Therefore, a continued effort to detect supernova neutrinos has the potential to yield valuable discoveries.

Contents

1	Introduction	1
2	Particle and Astroparticle Physics	3
2.1	A Short History of Particle Physics	3
2.1.1	Discovery of Radioactive Decay	3
2.1.2	Discovery of Cosmic Rays	3
2.1.3	Discovery of Muon, Positron, and Pion	5
2.1.4	Accelerator Particle Physics	5
2.2	The Standard Model of Particle Physics	5
2.3	Neutrino Physics	8
2.3.1	Discovery of Neutrinos	8
2.3.2	Neutrino Interactions	9
2.3.3	Charged Leptons in Matter	13
2.3.4	Cherenkov Effect	15
2.3.5	Solar Neutrinos	16
2.3.6	Atmospheric Neutrinos	19
2.3.7	Neutrino Summary	20
2.4	The High-Energy Universe	21
2.4.1	Cosmic Rays	21
2.4.2	Possible Sources of Cosmic Rays	24
2.4.3	Fermi Acceleration	27
2.4.4	Multi-Messenger Astronomy	31
3	Supernovae and Gamma-Ray Bursts as Transient Neutrino Sources	35
3.1	The Evolution of Stars	35
3.2	Supernova Explosions	38
3.2.1	Supernova Spectra and Light Curves	38
3.2.2	Supernovae Type II _n	39
3.2.3	Theory of Core-Collapse Supernovae	41
3.2.4	Low-Energy Neutrinos from Core-Collapse Supernovae	42
3.2.5	Supernova 1987A	45
3.2.6	Supernova Rates	48
3.2.7	High-Energy Neutrinos from Supernovae Type II _n	49
3.2.8	High-Energy Neutrinos from Supernovae with Jets	51

3.3	Gamma-Ray Bursts	55
3.3.1	Electromagnetic GRB Emission	55
3.3.2	GRB Progenitors	55
3.3.3	GRB Neutrinos	56
4	Neutrino Detectors	59
4.1	Low-Energy Neutrino Detectors	59
4.1.1	Super-Kamiokande	59
4.1.2	Backgrounds of Low-Energy Neutrino Detectors	61
4.2	IceCube	62
4.2.1	Overview	62
4.2.2	Particle Detection	63
4.2.3	Data Acquisition (DAQ)	67
4.2.4	Event Reconstructions	68
4.2.5	Quality Parameters	78
4.2.6	Base Processing and Filtering	80
4.3	Other High-Energy Neutrino Telescopes	81
5	Search for MeV Neutrinos from Supernovae	83
5.1	Motivation	83
5.2	Detector Simulation	85
5.3	Utilized Neutrino Emission Models	88
5.4	Detector Geometry and Optimization	90
5.5	Background Studies	92
5.5.1	Sensor Noise	93
5.5.2	Muon Background	97
5.5.3	Solar Neutrino Background	98
5.5.4	Atmospheric Neutrino Background	99
5.5.5	Summary of Background Studies	101
5.6	Alternative Detector Location	101
5.7	Expected Supernova Detection Rate	103
5.8	Conclusion	105
5.8.1	Summary	105
5.8.2	Outlook	107
6	Search for High-Energy Neutrinos from Supernovae	109
6.1	Motivation	109
6.2	The Optical Follow-Up System	112
6.2.1	Overview of the System	112
6.2.2	The ROTSE Telescope Network	112
6.2.3	The Palomar Transient Factory (PTF)	113
6.2.4	The Swift Satellite	114
6.2.5	OFU Data Seasons	115
6.3	The Online Level 2 Filter of IceCube	115
6.3.1	Description of Cuts	116
6.3.2	Additional Reconstructions	119
6.3.3	Computational Constraints	120

6.3.4	Changes to the Filter	122
6.4	The OFU Filter of IceCube	125
6.5	Properties of the OFU Neutrino Sample	127
6.5.1	Rate and Purity	127
6.5.2	Angular Resolution	127
6.5.3	Angular Error Estimator	128
6.6	OFU Multiplets and Alerts	129
6.6.1	Definition of Multiplets	129
6.6.2	Definition of Alerts	129
6.6.3	Test Alerts	133
6.7	Technical Implementation of OFU	133
6.7.1	Latency of the OFU System	135
6.8	Analysis of the OFU Multiplets/Alerts	137
6.8.1	Generating Background Datasets via Scrambling	137
6.8.2	Measured and Expected Multiplets/Alerts	137
6.8.3	Upper Limits on the Choked Jet SN Model	138
6.9	Conclusion	141
6.9.1	Summary	141
6.9.2	Outlook	142
7	Coincidental Detection of Supernova PTF12csy	143
7.1	Neutrino Alert and Discovery of PTF12csy	143
7.1.1	Significance of Alert and SN Detection	145
7.2	High-Energy Follow-Up Data	149
7.2.1	Results of the Offline Analysis of Neutrino Data	149
7.2.2	X-ray Observations of PTF12csy	151
7.3	Low-Energy Follow-Up Data	152
7.3.1	Optical and UV Observations of PTF12csy	152
7.3.2	Photometry	153
7.3.3	Spectroscopy	161
7.3.4	Host Galaxy	164
7.4	Conclusion	165
7.4.1	Summary	165
7.4.2	Outlook	165
8	Analysis of the Optical Data from PTF	167
8.1	Available PTF Data	167
8.2	Data Reduction	169
8.2.1	Machine Learning	170
8.3	SN Detection Algorithm	171
8.3.1	Candidate Clustering	171
8.3.2	Cross-Check Catalogs	172
8.3.3	Light Curve Fitting	172
8.3.4	Cuts on Candidate Clusters	177
8.3.5	Manual Investigation of Clusters	178
8.4	Search Results	180
8.4.1	Comparison with Automatic Pipeline	181

8.4.2	The Case of PTF12csy	182
8.5	Monte Carlo Simulation of SN Alerts	187
8.5.1	SN Insertion	187
8.5.2	Light Curve Parametrization	189
8.5.3	Host Magnitude Determination	192
8.5.4	Limiting Magnitude Modelling	192
8.5.5	Light Curve Generation	194
8.6	Efficiency of SN Detection	194
8.7	False Positive Rate of SN Detection	197
8.8	Systematic Errors	199
8.9	Conclusion	204
8.9.1	Summary	204
8.9.2	Outlook	204
A	Cross-Sections and Effective Areas	207
A.1	Cross-section	207
A.2	Effective Volume	208
A.3	Effective Area	208
B	Some Astronomical Concepts	209
B.1	Point Spread Function and Seeing	209
B.2	Measuring Brightness in Magnitudes	209
C	Supplementary Material for Chapter 5	213
D	Derivation of the Optical Follow-Up Doublet Test Statistic	215
E	Supplementary Material for Chapter 8	219
E.1	Observability of PTF Alerts	219
E.2	Details on the PTF Data Reduction Pipeline	220
E.2.1	Data Exploration	220
E.2.2	Reference Image Construction	220
E.2.3	Image Subtraction	227
E.2.4	Source Extraction	229
E.2.5	Negative Subtractions	230
E.3	Derivation of the Host Limiting Magnitude	231
E.4	Simulation Runs	231
	Bibliography	233
	Acknowledgements	261

Introduction

This thesis covers a relatively broad range of topics, which results into a considerably large scope. While the common objectives are supernovae, i.e. stellar explosions, and in particular the detection of neutrinos emitted by supernovae, the issue is viewed from different angles. On one hand, supernovae are known to emit neutrinos of MeV energies, which is explained in Section 3.2.4. On the other hand, there might be other processes associated with supernovae, producing neutrinos in the TeV energy range, i.e. about a million times higher energy. Those processes include neutrinos from supernovae IIn, where supernova ejecta interact with the circumstellar medium, and neutrinos produced by supernovae hosting mildly relativistic jets. The respective models are introduced in Sections 3.2.7 and 3.2.8.

All of the mentioned processes have been addressed in this thesis. Chapter 5 presents simulations of a hypothetical detector for low-energy supernova neutrinos. Chapters 6 to 8 deal with high-energy supernova neutrino emission, but in Chapters 6 and 8, it is searched for neutrinos from jet supernovae, while in Chapter 7, the additional hypothesis of neutrinos from a supernova IIn is studied.

The topical broadness is accompanied by methodical diversity. In Chapter 5, a low-energy neutrino detector resembling Super-Kamiokande (see Section 4.1) is studied, while in Chapters 6 and 7, data from the high-energy neutrino observatory IceCube (see Section 4.2) are studied. Chapters 7 and 8 discuss astronomical data from optical telescopes, mainly the Palomar Transient Factory (PTF). Therefore, the thesis is based not only in the field of astroparticle physics, i.e. neutrino astronomy, but also in the field of optical astronomy, i.e. supernova research.

The thesis is structured as follows: Chapters 2 to 4 give introductions to astroparticle physics, supernova theory, and neutrino detectors, which are requirements to understand the chapters that follow. Chapters 5 to 8 present the physics analysis work and its results.

Chapter 5 discusses a possible low-energy supernova neutrino detector with the capability to extend the detection range from our own Galaxy to neighboring galaxies. The detector is simulated with different geometries and locations. Especially the backgrounds and strategies to suppress the backgrounds are investigated.

Chapter 6 presents the neutrino side of a data analysis program that combines neutrino and optical data and is targeted at jet supernovae. The neutrino event selection and its improvements with time are described. No significant neutrino signal from jet supernovae is found, instead improved upper limits on an emission model are calculated.

Chapter 7 consists of an in-depth analysis of a supernova found with the program introduced in Chapter 6. The supernova, at first a promising neutrino source candidate, is found to be very unlikely

to have produced the measured neutrinos. Besides this, upper limits to a supernova II_n emission model are calculated and analyses of the electromagnetic follow-up data are performed.

Finally, Chapter 8 covers the data reduction and subsequent statistical analysis of the entire optical follow-up data from the program in Chapter 6. A supernova search algorithm is developed and a Monte Carlo simulation is implemented to derive the efficiency of the supernova search. Several supernovae are discovered in the data and the number of supernovae expected from pure background is derived. The systematic uncertainties of the method are estimated.

Since the topics vary, it was decided not to conclude the thesis in one general chapter, as it would be either redundant or confusing. Instead, each of the Chapters 6 to 8 has its own conclusion section. Readers interested in quick access to the conclusions are pointed to Sections 5.8, 6.9, 7.4, and 8.9.

Particle and Astroparticle Physics

In order to understand the topics covered by this thesis, some background knowledge on particle and astroparticle physics is required, which is presented in this chapter.

2.1 A Short History of Particle Physics

Some would argue that the roots of particle physics as the science of the fundamental constituents of matter go back to at least ancient philosophers like the Greek Leucippus and Democritus who suggested that all matter is composed of indivisible particles called atoms [1]. However, experimentation and empirical study of the structure of matter began much later. Therefore, this journey starts in the year 1896.

2.1.1 Discovery of Radioactive Decay

The last decade of the 19th century saw a rapid succession of discoveries that led to the new field of nuclear physics. In 1896, Henri Becquerel discovered the phenomenon of spontaneous radioactivity, observing that photographic plates are blackened by uranium salt [2, 3]. Becquerel believed these new rays to be similar to X-rays, but he found that unlike X-rays, which we know today are photons and thus neutral, the uranium's rays could sometimes be deflected by electric or magnetic fields and thus some of these rays were charged [4].

Two years later, Marie and Pierre Curie started studying the radiation discovered by Becquerel and discovered other radioactive elements besides uranium [3]. Ernest Rutherford separated the radioactive phenomena into α , β , and γ radiation [3]. In 1902, together with a student, he realized that radioactivity is the spontaneous transmutation of chemical elements [3]. It was soon found that the α -particles of α -decay are helium nuclei, β -particles are either negatively charged electrons or their positive antiparticles, positrons, and γ -rays are actually high-energy photons, differing from X-rays only in the energy or wavelength that they carry.

2.1.2 Discovery of Cosmic Rays

Already in the earliest days of research on radioactivity, an instrument called the *electroscope* played a vital role. An electroscope is an instrument that measures the charge of a small body. The body loses charge if surrounded by ionized air that is electrically conductive. Radiation of sufficient energy has

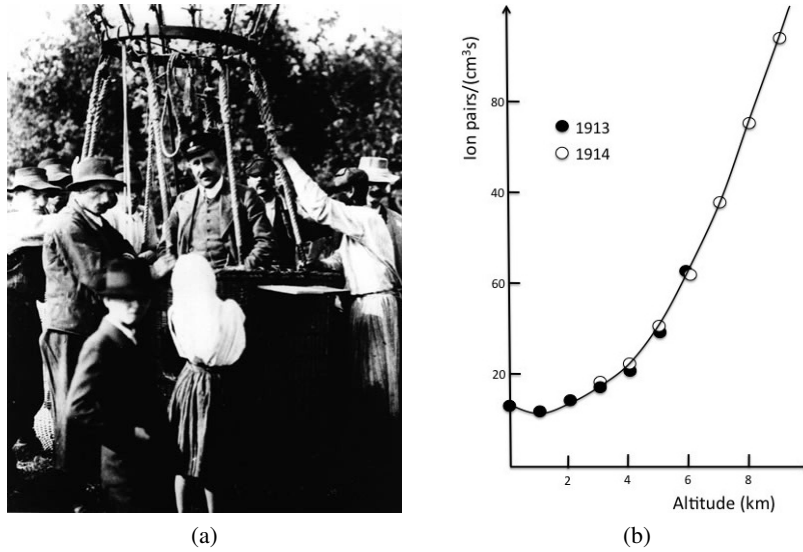


Figure 2.1: (a) Hess after his balloon flight on 7 August 1912, from [8]. (b) Ionization profile of the atmosphere measured by Kolhörster, from [8].

the property of splitting molecules of air into positive and negative components, i.e. ionizing the air by stripping off electrons from the atom. Therefore, the electroscope, by discharge, is sensitive to the presence of ionizing radiation [5].

The Curies had already used the electroscope to trace the invisible rays and identify new sources of radiation [4]. Soon researchers left their laboratories and used the electroscope to search for radioactive substances throughout nature: in the crust of the Earth, in the seas, and in the atmosphere. Surprisingly, ionizing radiation was found everywhere, and, unlike in laboratories, it was impossible to shield the electroscope from the rays, even using thick lead plates [5]. This led to the conclusion that there exists a new kind of radiation with immense penetrative power, different from the α , β , and γ -rays studied by the Curies and others.

If this radiation was caused by radioactive isotopes in the crust of the Earth, as usually assumed, then the radiation's intensity should decrease at higher altitudes due to absorption in the atmosphere. Several measurements at different altitudes were conducted, e.g. at the top and bottom of the Eiffel tower and in balloons. They indicated a slight decrease of ionization with altitude, but not as much as expected if the rays came from the Earth. So the question about the origin of this ionizing radiation remained unsolved [5]. In 1912, Victor Hess carried out seven balloon flights to heights up to 5300 m with improved experimental techniques (e.g. an improved electroscope) [6], see Figure 2.1a. He found that up to 1 km, ionization decreases. This is the component that is indeed caused by radioactive substances in the Earth. But above 1 km it increases considerably and at 5 km it is several times more intense than at ground level [7]. This result was confirmed in balloon flights up to 9200 m by German physicist Werner Kolhörster [8], see Figure 2.1b. Hess concluded that there must be a radiation penetrating the atmosphere from outer space. Thus, *cosmic rays* had been discovered. Hess also performed balloon flights at night and even during a nearly complete solar eclipse and observed no reduction in ionization, thus concluded that cosmic rays are not dominantly emitted by the sun [7].

Little was known about the nature of cosmic rays (CRs) during the next decades and many scientists, above all Millikan, believed that they were γ -rays, due to their high penetrative power [8]. In 1932 and 1933, it was repeatedly found that CR intensity depends on geomagnetic latitude and that close to

the equator, more CRs are coming from West than from East due to interaction with Earth's magnetic field [8]. This demonstrated that CRs are mostly positively charged and thus cannot be γ -rays. It took until 1941 to find that CRs mainly consist of protons [8], and still today, the composition of CRs, especially at highest energies, is a matter of active research. Also, how and where CRs are produced or accelerated to high energies remains unknown.

2.1.3 Discovery of Muon, Positron, and Pion

Until the 1950s, CRs provided a very valuable natural source of high-energy particles that were used to study fundamental particles and gave rise to the new field of particle physics. Many important discoveries were made while studying CR-induced interactions. This was enabled by new technologies such as the cloud chamber, which allowed to photograph tracks of charged particles [8]. In 1933, Carl Anderson discovered antimatter in form of the anti-electron, or *positron* [9]. Soon after, conversions of photons to electron-positron pairs were observed for the first time [8]. In 1937, Neddermeyer and Anderson discovered the elementary particle called *muon* in CRs [10], which is mainly responsible for the immense penetrative power of the radiation. Also the first meson, the charged *pion*, was discovered in CR-induced particle showers in 1947 [11].

2.1.4 Accelerator Particle Physics

After the end of World War II, technology had advanced enough to provide particle physicists with entirely new tools [8]. Charged particles, e.g. protons (hydrogen nuclei) or electrons, could be accelerated in the laboratory using new machines like the cyclotron, the synchrotron or linear accelerators. This allowed to conduct and study interactions of particles under controlled conditions [8].

The rise of particle accelerators led to a variety of new exotic particles being created and precisely studied under laboratory conditions, especially in the 1960s and 1970s. The number of discovered particles was so large that it was dubbed the “particle zoo” [8]. Scientists aimed to bring order into this zoo of particles and explain it with a simple, powerful model. A crucial improvement was the *quark model*, proposed in 1964 by Murray Gell-Mann [12] and George Zweig [13, 14]. With its help, the discovered particles could be described as combinations of relatively few fundamental particles, so-called quarks.

Two main theories of particles emerged: the electroweak theory by Glashow, Weinberg, and Salam describing the electromagnetic and weak interactions of particles [15, p. 3], and the quantum chromodynamics (QCD) describing the strong interaction. These theories were combined into what is called the “Standard Model of Particle Physics” [15, p. 67].

2.2 The Standard Model of Particle Physics

The Standard Model (SM) describes all interactions of fundamental particles except gravity, i.e. electromagnetic, weak and strong interaction, in the framework of a quantum field theory [15, p. 67]. It is a gauge theory, meaning that it is based on a local gauge invariance of the Lagrangian [15, p. 657]. The local symmetry group of the SM is $SU(3)_C \times SU(2)_L \times U(1)_Y$, where the subscripts C , L , and Y denote color (of the strong interaction), left-handed chirality, and weak hypercharge (of the electroweak interaction). The gauge group determines the interactions of particles, which are mediated by *gauge bosons*, also called vector bosons. Gauge bosons are fundamental particles of integer spin different from zero. While the $SU(3)_C$ group gives rise to eight massless gluons mediating the strong interaction,

$SU(2)_L \times U(1)_Y$ is the electroweak symmetry group, giving rise to the three massive bosons of weak interaction, W^+ , W^- , Z_0 , and the massless electromagnetic mediator, the photon γ .

The strong interaction is responsible for binding atomic nuclei: Gluon exchange creates the forces within and between nucleons. Gluons are exchanged between particles carrying a *color charge*. Unlike electromagnetic charge, there are not two kinds of colors (like + and -), but six (r , g , b , and the anti-colors \bar{r} , \bar{g} , \bar{b}). An object carrying either all three colors (rgb or $\bar{r}\bar{g}\bar{b}$) or a color and the respective anti-color (e.g. $r\bar{r}$) is color-neutral and does not participate in the strong interaction. The strong interaction has a very short range that does not go beyond the extent of atomic nuclei (~ 1 fm) [16, p. 25].

The electromagnetic interaction binds electrons to atomic nuclei as well as several atoms to molecules. Photon exchange is responsible for most physical phenomena in our daily lives, e.g. optical processes and electricity. Because the photon is massless, the range of electromagnetism is infinite, like gravity. Its strength is roughly 1/100 of the strong interaction [16, p. 25].

Finally, the weak interaction, mediated by the massive W and Z bosons, has an even shorter range than the strong interaction ($\sim 10^{-3}$ fm) and is about three orders of magnitude weaker than electromagnetism [16, p. 25]. Both properties are due to the large mass of the gauge bosons. Weak interaction is responsible for rare nuclear processes like radioactive β -decay, many particle decays and all processes involving neutrinos (s.b.). Electromagnetic and weak interaction have been successfully united into a single “electroweak theory” [16, p. 24].

There is another kind of bosons next to vector bosons: *Scalar bosons* are particles with spin 0. So far, only one scalar boson has been discovered: Evidence for the neutral Higgs boson H^0 was announced by experiments at the LHC in 2012 [17, p. 161]. In the SM, the Higgs boson, or more accurately a Higgs doublet of two scalar fields, is responsible for the spontaneous breaking of electroweak symmetry $SU(2)_L \times U(1)_Y$, which gives mass to the W and Z bosons. The particles of the Higgs field couple to matter particles (fermions), providing them with mass as well (except neutrinos) [15, pp. 83–88].

While gauge bosons mediate the forces, all matter is composed of *fermions*, which are particles of half-integer spin. Fermions are divided into two categories: quarks and leptons. *Quarks* are the building blocks of hadrons, e.g. protons and neutrons. Free quarks do not exist in nature: quarks are always confined within some hadronic particle consisting of several quarks. They are only “asymptotically free” at high momentum [16, p. 21]. There are two kinds of hadrons: *baryons* (from Greek “barys”, “heavy” [15, p. 68]) and *mesons* (from Greek “mesos”, “intermediate”). Baryons consist of three quarks (or three anti-quarks), while mesons are made out of one quark and one anti-quark. Hadrons are always color-neutral: baryons like the proton and neutron consist of three quarks carrying all three colors, mesons consist of two quarks carrying a color and the corresponding anti-color. Stable colored objects do not seem to exist in nature. Quarks and hadrons interact via all interactions.

Leptons (from Greek “leptos”, “thin” [15, p. 68]) are either charged, like the electron, or uncharged, in which case they are called *neutrinos*. Charged leptons interact via electromagnetic and weak interaction (plus gravity), while neutrinos interact only weakly (and via gravity).

Quarks and leptons are grouped into three *generations* or families, in each of which there is a particle doublet. The quarks are called up (u), down (d), charm (c), strange (s), top (t), and bottom (b) and are grouped as:

$$\begin{array}{ccc} \text{1st} & \text{2nd} & \text{3rd generation} \\ \begin{pmatrix} u \\ d \end{pmatrix} & \begin{pmatrix} c \\ s \end{pmatrix} & \begin{pmatrix} t \\ b \end{pmatrix} \end{array}.$$

The leptons are called electron (e^-), electron neutrino (ν_e), muon (μ^-), muon neutrino (ν_μ), tau (τ^-), and

	Name	Quark content	Spin [\hbar]	Charge [e]	Mass [MeV]	Lifetime
Bosons	Gluon g		1	0	0	-
	W^+, W^-		1	+1, -1	80 385	$\sim 3 \times 10^{-25}$ s
	Z^0		1	0	91 188	$\sim 3 \times 10^{-25}$ s
	Photon γ		1	0	0	Stable
	Higgs H^0		0	0	$(125.7 \pm 0.4) \times 10^3$	$\sim 1.6 \times 10^{-22}$ s
Leptons (Fermions)	Electron e^-		1/2	-1	0.511	$> 4.6 \times 10^{26}$ yr
	Muon μ^-		1/2	-1	105.7	2.2×10^{-6} s
	Tau τ^-		1/2	-1	1776.82 ± 0.16	$(290.3 \pm 0.5) \times 10^{-15}$ s
	El. neutr. ν_e		1/2	0	< 2 eV	$> 7 \times 10^9$ s (eV) $^{-1}$
	Muon neutr. ν_μ		1/2	0	< 0.190	> 15.4 s (eV) $^{-1}$
Tau neutr. ν_τ		1/2	0	< 18.2	?	
Quarks (Fermions)	Up	u	1/2	+2/3	$2.3^{+0.7}_{-0.5}$	-
	Down	d	1/2	-1/3	$4.8^{+0.5}_{-0.3}$	-
	Charm	c	1/2	+2/3	1275 ± 25	-
	Strange	s	1/2	-1/3	95 ± 5	-
	Top	t	1/2	+2/3	$(173.21 \pm 0.51 \pm 0.71) \times 10^3$	-
	Bottom	b	1/2	-1/3	4180 ± 30	-
Baryons	Proton p	uud	1/2	+1	938.272	$> 2.1 \times 10^{29}$ yr
	Neutron n	udd	1/2	0	939.565	(880.3 ± 1.1) s
	Λ^0	uds	1/2	0	1116	2.6×10^{-10} s
	$\Delta^{++}, \Delta^+, \Delta^0, \Delta^-$	uuu, uud, udd, ddd	1/2	+2, +1, 0, -1	1232	5×10^{-24} s
	Mesons	Pion π^0	$(u\bar{u} - d\bar{d})/\sqrt{2}$	1/2	0	134.98
Pion π^-, π^+		$\bar{u}d, u\bar{d}$	1/2	-1, +1	139.57	2.6×10^{-8} s
Kaon K^-, K^+		$\bar{u}s, u\bar{s}$	1/2	-1, +1	493.7	1.2×10^{-8} s
Kaon K^0, \bar{K}^0		$d\bar{s}, \bar{d}s$	1/2	0	497.7	8.9×10^{-11} s (K_S^0) 5.2×10^{-8} s (K_L^0)

Table 2.1: All elementary (above double line) and some composite particles according to the Standard Model, with values from [17, pp. 27–85] and [15, p. 69].

tau neutrino (ν_τ) and are grouped as:

$$\begin{array}{ccc}
 \text{1st} & \text{2nd} & \text{3rd generation} \\
 \begin{pmatrix} \nu_e \\ e^- \end{pmatrix} & \begin{pmatrix} \nu_\mu \\ \mu^- \end{pmatrix} & \begin{pmatrix} \nu_\tau \\ \tau^- \end{pmatrix}.
 \end{array}$$

The six types of quarks and of leptons are called *flavors*. Except for having a higher mass, the particles of the higher generations have the same properties as their relatives in the first generation. In ordinary matter, only particles from the first generation occur, e.g. a proton consists of uud , a neutron of udd , and the atomic shell consists of electrons. Hadrons containing quarks from higher generations and the charged leptons from higher generations are not stable and decay to particles from the first generation.

Table 2.1 and Figure 2.2 give an overview of all fundamental and some composite particles and their properties. In addition to the particles in Table 2.1, for each fermion there is an *anti-particle* which is an exact copy of the particle, except that the charge is inverted. For example, the anti-electron or positron e^+ has a charge of +1 e whereas the electron carries -1 e. The anti-fermions are designated with $\bar{u}, \bar{d}, \bar{c}, \bar{s}, \bar{t}, \bar{b}, e^+, \mu^+, \tau^+, \bar{\nu}_e, \bar{\nu}_\mu, \bar{\nu}_\tau$. The neutrino might be its own anti-particle, in which case it is called a Majorana particle.

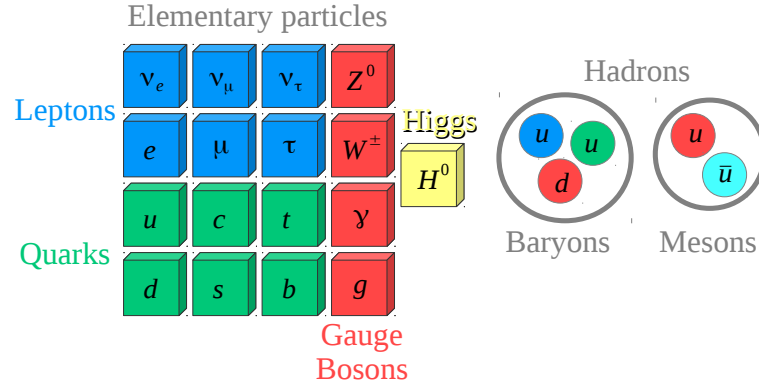


Figure 2.2: Visualization of Standard Model particles.

2.3 Neutrino Physics

2.3.1 Discovery of Neutrinos

Neutrinos were first discussed as a solution to a mystery of β -decay: β -decay is the transmutation of an atomic nucleus, either increasing its atomic number (i.e. number of protons) by one or decreasing it by one. This happens via conversion of a neutron to a proton or vice versa. If the proton number increases, then an electron is emitted (β^- decay), else a positron (β^+ decay). This is presumably a two-body decay, X and Y denoting the nuclei before and after decay:

$${}_nX \longrightarrow {}_{n+1}Y + e^-, \quad {}_nX \longrightarrow {}_{n-1}Y + e^+.$$

Consequently, with only two end products, the energy of the emitted lepton must be always the same. In order to conserve momentum, the momenta of the emerging nucleus and lepton must be back to back in the center-of-mass system and momentum and energy of the lepton are predetermined. However, measurement of the lepton energy from β -decays showed that this is not the case. Instead, the lepton energy spectrum is continuous, the energy is less than or equal to the expected energy.

The missing energy was a big mystery and appeared to contradict conservation of energy, momentum and angular momentum [15, p. 1], [16, p. 8]. Another idea was that a third invisible particle is emitted. This led Wolfgang Pauli to postulate the neutrino in 1930, as an undetected particle carrying away the missing energy. Therefore, with the neutrino, β -decay would work as follows:

$$n \longrightarrow p + e^- + \bar{\nu}_e, \quad p \longrightarrow n + e^+ + \nu_e. \quad (2.1)$$

It was clear that the neutrino interaction cross-section must be miniscule, and even Pauli himself believed that neutrinos cannot be detected [18].

In the 1950s, Frederick Reines and Clyde Cowan were determined to detect neutrinos nevertheless. They planned to exploit the inverse β -decay (IBD) reaction, the inverse of Equation 2.1:

$$p + \bar{\nu}_e \longrightarrow n + e^+ \quad (2.2)$$

where a proton and anti-neutrino convert to a neutron and a positron. Conventional β -emitters produce a much too low $\bar{\nu}_e$ flux. Therefore, their first idea included using a nuclear bomb as strongest possible neutrino source and a detector falling freely in a deep hole in order to escape the shock wave [18, fig.

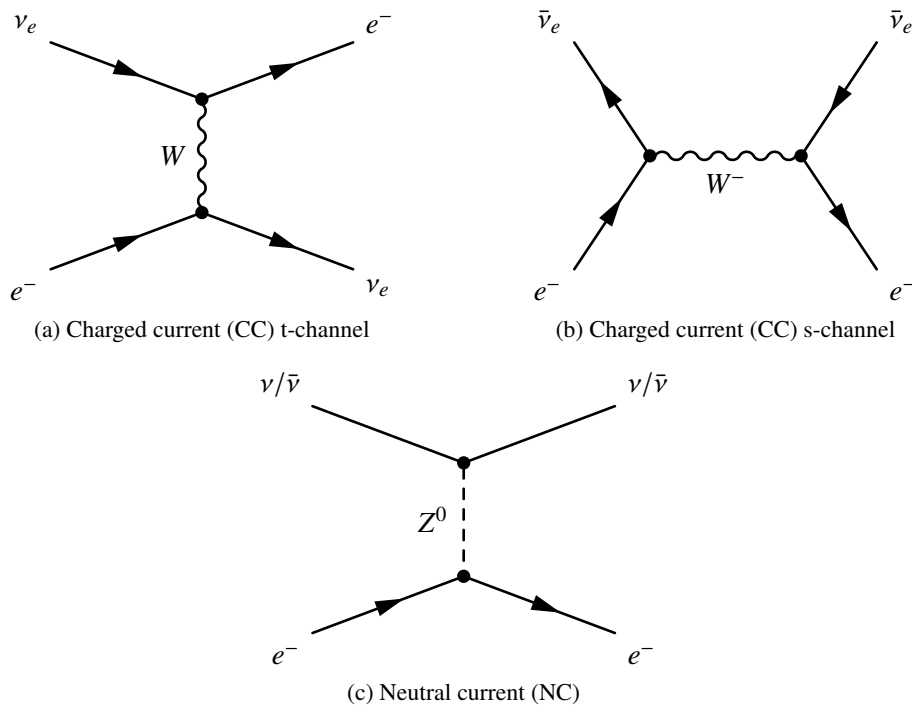


Figure 2.3: Feynman diagrams of neutrino-electron elastic scattering (ES).

1]. The advent of nuclear fission reactors allowed for a simpler experimental setup, yet with a factor of 10^4 times lower expected neutrino flux. In 1953, Cowan and Reines conducted a first experiment next to research reactors in Washington, which failed due to a high CR background.

A second experiment was conducted in 1956 at a reactor at the Savannah River Plant in Aiken, South Carolina. The improved detector made use of neutron capturing cadmium chloride dissolved in a water tank used as target material. The cadmium produces a clearer delayed signal from the neutron, following about $10\ \mu\text{s}$ after a prompt signal from the positron that annihilates with an electron. The detection of this delayed coincidence, together with a better shielding from CRs at 12 m underground, led to the first experimental observation of neutrinos. They were detected at a rate of 3.0 ± 0.2 events per hour.

After the successful first detection of neutrinos, many experiments followed, detecting not only neutrinos from nuclear reactors, but also neutrinos from the Sun, neutrinos produced by accelerator beams, neutrinos produced by CRs at the top of the atmosphere, neutrinos produced by a supernova, and most recently high-energy neutrinos from astrophysical, mostly extra-galactic, sources.

2.3.2 Neutrino Interactions

In order to build a neutrino detector, one needs to know how neutrinos interact with matter and what channels are available to observe them. Generally, cross-sections of neutrinos and therefore interaction probabilities are many orders of magnitude smaller than those of all other known matter particles. This is due to neutrinos being the only fermions that interact exclusively via the weak interaction. All other fermions interact also via the electromagnetic or strong interaction. See Appendix A.1 for an illustration of how small the neutrino cross-section is compared to other particles.

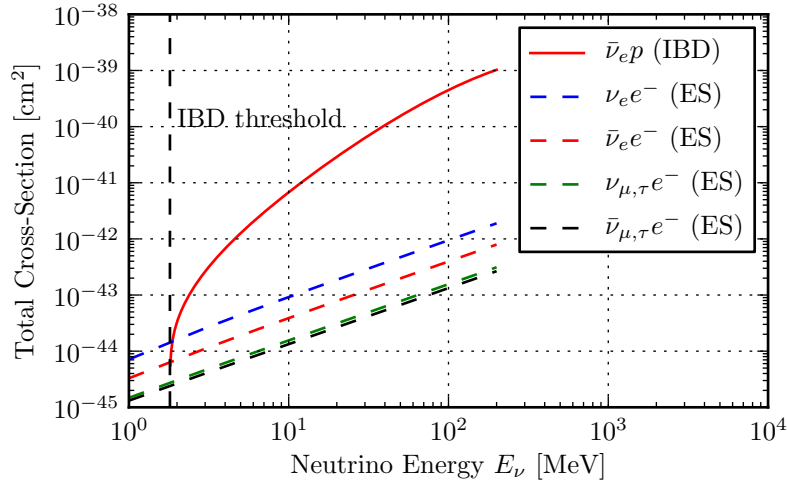


Figure 2.4: Comparison of total cross-sections for dominant low-energy neutrino interactions in water, at MeV energies.

Neutrino-Electron Elastic Scattering (ES)

The simplest neutrino interaction with matter is the reaction:

$$\nu_\alpha(\bar{\nu}_\alpha) + e^- \longrightarrow \nu_\alpha(\bar{\nu}_\alpha) + e^-, \quad (2.3)$$

which does not have a threshold energy. Therefore, neutrino-electron elastic scattering (ES) is the dominant interaction of low energy neutrinos with matter (up to the MeV range). Any neutrino flavor can participate, i.e. $\alpha = (e, \mu, \tau)$. Only ν_e and $\bar{\nu}_e$ can use the *charged current* (CC) interaction with W boson exchange, while all neutrino flavors can undergo a *neutral current* (NC) interaction with Z boson exchange [15, p. 136f], see Figure 2.3 for illustrations as Feynman diagrams. One can distinguish ES of ν_e , $\bar{\nu}_e$, $\nu_{\mu,\tau}$, and $\bar{\nu}_{\mu,\tau}$. The total cross-sections, for total squared energy $s \gg m_e$, have ratios [15, p. 139]:

$$\sigma_{\nu_e} : \sigma_{\bar{\nu}_e} : \sigma_{\nu_{\mu,\tau}} : \sigma_{\bar{\nu}_{\mu,\tau}} \simeq 1 : 0.42 : 0.16 : 0.14. \quad (2.4)$$

Figure 2.4 shows a plot of the ES total cross-sections for the different neutrino flavors.

With a lengthy calculation, one can derive that the differential cross-section depending on energy is [15, p. 139f]:

$$\frac{d\sigma}{dT_e}(E_\nu, T_e) = \frac{\sigma_0}{m_e} \left[g_1^2 + g_2^2 \left(1 - \frac{T_e}{E_\nu} \right)^2 - g_1 g_2 \frac{m_e T_e}{E_\nu^2} \right], \quad (2.5)$$

where E_ν is the total energy of the incoming neutrino, T_e is the kinetic energy of the recoil electron in the laboratory frame, and

$$\sigma_0 = \frac{2 G_F^2 m_e^2}{\pi} \simeq 88.06 \times 10^{-46} \text{ cm}^2$$

$$g_1 = \begin{cases} \frac{1}{2} + \sin^2 \theta_W \simeq 0.73 & \text{for } \nu_e \\ -\frac{1}{2} + \sin^2 \theta_W \simeq -0.27 & \text{for } \nu_{\mu,\tau} \\ \sin^2 \theta_W \simeq 0.23 & \text{for } \bar{\nu}_e \text{ and } \bar{\nu}_{\mu,\tau} \end{cases} \quad g_2 = \begin{cases} \frac{1}{2} + \sin^2 \theta_W \simeq 0.73 & \text{for } \bar{\nu}_e \\ -\frac{1}{2} + \sin^2 \theta_W \simeq -0.27 & \text{for } \bar{\nu}_{\mu,\tau} \\ \sin^2 \theta_W \simeq 0.23 & \text{for } \nu_e \text{ and } \nu_{\mu,\tau} \end{cases} .$$

Here, m_e denotes the electron mass, G_F the Fermi constant, and θ_W is the Weinberg angle or weak

mixing angle. One sees that the scale of the cross-section, governed by σ_0 , is quite small and of the order of 10^{-44} cm², or 10^{-20} barn.¹ The kinetic energy of the recoil electron is, from energy-momentum conservation:

$$T_e = \frac{2m_e E_\nu^2 \cos^2 \theta}{(m_e + E_\nu)^2 - E_\nu^2 \cos^2 \theta}, \quad (2.6)$$

where θ is the electron scattering angle. The maximal kinetic energy is, since $\cos \theta \leq 1$:

$$T_e^{\max}(E_\nu) = \frac{2E_\nu^2}{m_e + 2E_\nu}. \quad (2.7)$$

Neutrino-Electron Quasielastic Scattering (QES)

At higher energies, a new process becomes possible for muon neutrinos:

$$\nu_\mu + e^- \longrightarrow \mu^- + \nu_e. \quad (2.8)$$

This interaction is called neutrino-electron quasielastic scattering (QES) and has a threshold energy E_ν^{th} , because energy is required for the muon production [15, p. 142]. In general, when a neutrino hits a particle A to produce particles X_i :

$$\nu + A \longrightarrow \sum_i X_i,$$

then the total squared center-of-mass energy $s = (p_\nu + p_A)^2 \simeq 2E_\nu m_A + m_A^2$ (neglecting neutrino mass) must be $\geq (\sum_i m_{X_i})^2$. Thus:

$$E_\nu^{\text{th}} = \frac{(\sum_i m_{X_i})^2}{2m_A} - \frac{m_A}{2} \quad (2.9)$$

or in this case of μ production:

$$E_\nu^{\text{th}} = \frac{m_\mu^2}{2m_e} - \frac{m_e}{2} \approx 10.9 \text{ GeV}.$$

Neutrino-Nucleon Quasielastic Scattering (IBD)

Neutrinos can undergo quasielastic charged-current interactions with nucleons:

$$\begin{aligned} \nu_l + n &\longrightarrow p^+ + l^- \\ \bar{\nu}_l + p^+ &\longrightarrow n + l^+. \end{aligned}$$

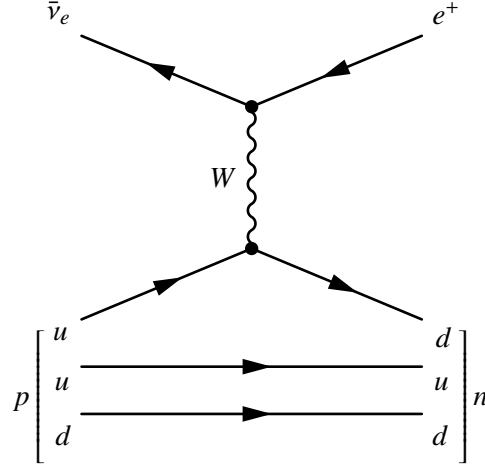
The special case of $l = e$ is also called inverse neutron decay [15, p. 160] or, in case of $\bar{\nu}_e p$, *inverse β -decay (IBD)* [19]:

$$\bar{\nu}_e + p^+ \longrightarrow e^+ + n. \quad (2.10)$$

See Figure 2.5 for a Feynman diagram of IBD. IBD is of special relevance at sub-GeV energies [19]. This is thanks to several points: its cross-section is relatively large². It is possible to reduce backgrounds by making use of the delayed coincidence between positron and neutron pulse (see Section 2.3.1), especially in scintillators. Its threshold energy—using Equation 2.9, $E_\nu^{\text{th}} = \frac{(m_n + m_e)^2}{2m_p} - \frac{m_p}{2} = 1.806 \text{ MeV}$ —

¹ 1 barn = 10^{-24} cm² = 10^{-28} m²

² Relatively large for neutrinos. It is still so small that Bethe and Peierls predicted that it will *never* be detected [18].


 Figure 2.5: Feynman diagram of inverse β -decay (IBD).

is relatively small. Cheap materials, above all water, contain free protons³ and can be used as target. The e^+ energy is strongly correlated with the $\bar{\nu}_e$ energy, permitting spectroscopy. Finally, the cross-section can be computed accurately.

There are simple approximative formulae at low ($E_\nu \approx \text{MeV}$) and high energies ($E_\nu \approx \text{GeV}$), assuming either $E_\nu \ll m_p$ or $E_\nu \gg m_n - m_p$ [19]. Alternative formulae also valid in the intermediate range have been published in [19] and make neither approximation. Their full result can be expressed very well, with $\leq 0.5\%$ difference up to 80 MeV, $\leq 1\%$ up to 160 MeV, by an empirically found formula for the total cross-section, the “Naïve+” approximation [19],

$$\sigma \approx 10^{-43} \frac{p_e}{\text{MeV}} \frac{E_e}{\text{MeV}} \left(\frac{E_\nu}{\text{MeV}} \right)^{-a+b \ln(E_\nu/\text{MeV})-c \ln^3(E_\nu/\text{MeV})} \text{cm}^2, \quad (2.11)$$

where $E_e = E_\nu - \Delta$ is the total energy of the positron, $p_e = \sqrt{E_e^2 - m_e^2}$ is the momentum of the positron. In this context, $\Delta \equiv m_n - m_p = 1.293 \text{ MeV}$ is the mass difference between proton and neutron. The values of the parameters are: $a = 0.07056$, $b = 0.02018$, $c = 0.001953$.

Figure 2.4 shows a plot of the total IBD (Equation 2.11) and ES (integral of Equation 2.5) cross-sections as function of neutrino energy E_ν . These are the most important interactions of neutrinos with water or ice, at energies in the MeV range. However, IBD, whose cross-section is ~ 100 times larger than the ES cross-section, is accessible only to $\bar{\nu}_e$.

Neutrino-Nucleon Deep Inelastic Scattering (DIS)

At high energies $E_\nu \gg m_N$, the binding energy inside atomic nuclei ($\sim \text{MeV}$) is negligible and a neutrino hitting matter interacts directly with one of the nucleons. Thus, at highest neutrino energies, neutrino interactions are dominated by so-called *deep inelastic scattering* (DIS), which is one of the processes

$$\begin{aligned} \nu_l + N &\longrightarrow l^- + X, & \bar{\nu}_l + N &\longrightarrow l^+ + X, & (CC) \\ \nu_l + N &\longrightarrow \nu_l + X, & \bar{\nu}_l + N &\longrightarrow \bar{\nu}_l + X, & (NC) \end{aligned} \quad (2.12)$$

where $N = n, p$ and X denotes any hadronic rest [15, pp. 167,175]. The two different kinds are called charged-current (CC, first line of Equation 2.12) and neutral-current (NC, second line of Equation 2.12). Figure 2.6 illustrates the DIS processes as Feynman diagrams.

³ The binding energy in the H_2O molecule ($\text{H} = p$) is of the order of eV and irrelevant at MeV energies.

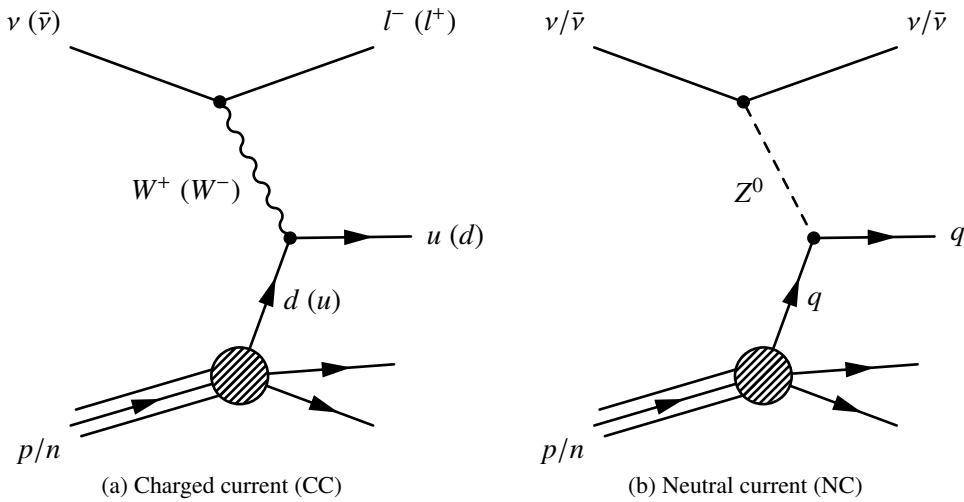


Figure 2.6: Feynman diagrams of neutrino-nucleon deep inelastic scattering (DIS).

During the process, the interacting nucleon, and thus also its host nucleus, are disrupted by the neutrino impact. This results in a hadronic particle shower, i.e. a small avalanche of hadronic particles that interact with the medium and deposit their energy by producing other particles and emitting photons. All particles eventually either decay if they are unstable (e.g. mesons) or lose most of their energy until they settle in the medium, several meters displaced from the interaction vertex.

In case of NC, this hadronic shower is everything observable from the DIS interaction. This process was first observed in 1973 by the Gargamelle experiment at CERN using $\bar{\nu}_\mu$ neutrinos. It served, together with Gargamelle observations of $\bar{\nu}_\mu + e^- \rightarrow \bar{\nu}_\mu + e^-$, as important experimental confirmation of the existence of neutral current interactions predicted by the SM [15, p. 175f.].

In case of CC, a charged lepton (e, μ, τ) is produced that can be observed as well by its interactions with the medium. The muon μ is of special importance here, because it can travel up to several km and thus enable detection of a neutrino DIS reaction far away from the DIS vertex, see Section 2.3.3.

High-energy neutrino DIS accesses large values of Q^2 , the invariant mass of the exchanged vector boson, and small values of Bjorken x , the fraction of momentum of the incoming nucleon taken by the struck quark [20]. The best experimental data giving access to the DIS cross-section therefore comes from experiments at the ep collider HERA at DESY (Hamburg), which have accessed the highest Q^2 and lowest x scales to date [20]. H1 and ZEUS have combined the data collected between 1994 and 2000 and derived parton distribution functions (PDFs) of the nucleon. Cooper-Sarkar, Mertsch, and Sarkar (CSMS) [20] utilize modern PDFs which include the combined HERA data to provide the best benchmark cross-sections for high-energy neutrino DIS. Figure 2.7 shows the CSMS cross-sections. In 2013, the Monte Carlo neutrino event generator ANIS [21], which is also used by the IceCube experiment for simulation, was updated to use the most recent DIS cross-sections by CSMS.

2.3.3 Charged Leptons in Matter

In CC neutrino interactions, e.g. IBD and DIS (see above), charged leptons are produced which can be used to indirectly detect neutrinos. Therefore, it is important to understand how charged leptons interact with matter.

At lower energies, charged leptons passing through matter lose energy dominantly by ionization and

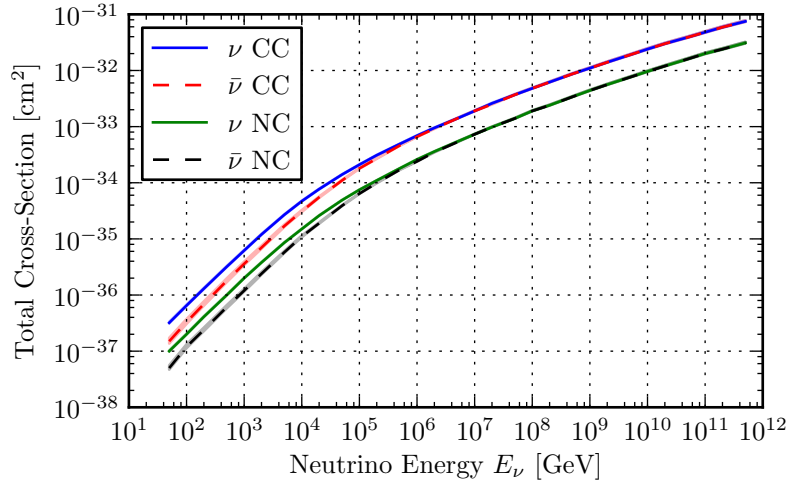


Figure 2.7: The neutrino-nucleon deep inelastic scattering (DIS) cross-section by CSMS [20], the dominant neutrino interaction at highest energies.

excitation of atoms. This is described by the *Bethe-Bloch equation* [16, p. 51], [17, p. 399],

$$\left\langle -\frac{dE}{dx} \right\rangle_{\text{ion}} = Kz^2 \frac{Z}{A} \frac{1}{\beta^2} \left[\frac{1}{2} \ln \frac{2m_e c^2 \beta^2 \gamma^2 W_{\text{max}}}{I^2} - \beta^2 - \frac{\delta(\beta\gamma)}{2} \right], \quad (2.13)$$

which yields the mean rate of energy loss in the region $0.1 \lesssim \beta\gamma \lesssim 1000$ [17, p. 399]. Here, $\beta = v/c$ is the lepton velocity and $\gamma = 1/\sqrt{1-\beta^2}$ is the lepton's Lorentz factor, i.e. $E = \gamma mc^2$. Further: $K = 4\pi N_A r_e^2 m_e c^2$, N_A is Avogadro's number, r_e the classical electron radius, z the charge number of the incident lepton, (Z, A) are the charge and mass number of the target, W_{max} is the maximum energy transfer to an electron, I the mean ionization energy of the target, and $\delta(\beta\gamma)$ a density correction.

Bethe-Bloch energy loss depends on β and on the target material alone and does not depend on the mass of the incident particle for all practical purposes [17, p. 399]. There is a broad minimum of $\langle -dE/dx \rangle$. Below the minimum energy loss increases very steeply and above the minimum it levels off on the so-called Fermi plateau [16, p. 53]. The minimum lies between $\beta\gamma = 3$ and 4 for most materials, corresponding to $E \approx 400 \text{ MeV}$ for muons and $E \approx 2 \text{ MeV}$ for electrons⁴. Particles moving in this range are called *minimum ionizing particles* or MIPs. The energy loss of a MIP in water is about $2 \text{ MeV} (\text{g/cm}^2)^{-1}$ [16, p. 53]. A low-energy lepton moving through matter is likely to be a MIP when it is detected, because it remains in the minimum ionizing region for a relatively long time, but is completely stopped and therefore not detected if its energy drops below the MIP region. Therefore (also because the primary spectrum is very steep), the flux of cosmic ray produced muons is always dominated by a large number of MIPs at low energies.

For high energies ($\gtrsim 1 \text{ TeV}$), energy loss via bremsstrahlung becomes more important than Bethe-Bloch, because it rises linearly with energy, whereas Bethe-Bloch becomes constant. Bremsstrahlung energy loss can be described by [16, p. 53], [17, p. 406]

$$\left\langle -\frac{dE}{dx} \right\rangle_{\text{brems}} \approx \frac{E}{X_0}. \quad (2.14)$$

The radiation length $X_0 \propto m^2$ depends on the mass m of the incident particle [16, pp. 53f.], [17,

⁴ It is $\beta\gamma = p/(mc) = \sqrt{E^2 - m^2 c^4}/(mc^2)$, therefore $E = mc^2 \sqrt{1 + (\beta\gamma)^2}$.

p. 404]. Electrons have a much lower radiation length than muons because of the suppression factor $(m_\mu/m_e)^2 \approx 43\,000$. This means that high-energy electrons lose their energy very quickly in matter due to bremsstrahlung. In water or ice, at TeV energies and above, electrons travel at most a few meters before they stop as their radiation length is $X_0 \approx 40$ cm in ice [17, p. 407]. High-energy muons however can travel many km and form a long track in a detector before they stop and/or decay. Moreover, high-energy electrons initiate an electromagnetic shower or cascade [17, pp. 408f.]: the electron emits a bremsstrahlung photon which generates an e^+e^- pair which in turn generate bremsstrahlung photons, and so on. This leads to a multiplication of particles, until eventually the electrons are below a critical energy for bremsstrahlung and lose energy mainly via Bethe-Bloch [17, p. 407].

In addition to bremsstrahlung, high-energy charged particles lose energy by occasional e^+e^- pair production and nuclear interactions [16, p. 54]. Both also depend, like bremsstrahlung, linearly on energy. Therefore, muon energy loss is usually described as [16, p. 54], [17, p. 408]

$$\left\langle -\frac{dE}{dx} \right\rangle_{\text{muon}} = a(E) + b(E)E, \quad (2.15)$$

where $a(E)$ denotes ionization energy losses (Bethe-Bloch), and $b(E)E$ sums up the losses due to bremsstrahlung, pair production, and nuclear interactions. Above a critical energy, ~ 1 TeV, the muon energy loss is mostly linear in energy, which allows for muon calorimetry via measurement of $\langle -dE/dx \rangle_{\text{muon}}$ [16, p. 54]. However, energy loss by $b(E)E$ generates electromagnetic or hadronic showers and is neither uniform nor continuous [17, p. 408].

Because the τ lepton is even heavier than the muon, it has low bremsstrahlung energy losses and a long radiation length as well. However, it is also much less stable than the muon and has a mean lifetime of only 290.3 fs. As a consequence, at 1 TeV of energy, the τ travels on average only about 5 cm before it decays. At 1 PeV however, an energy accessible to the neutrino observatory IceCube, it can travel about 50 m, and at higher energies respectively more (mean travel distance is linear in energy⁵).

2.3.4 Cherenkov Effect

A charged particle moving through a dielectric medium of refractive index n radiates electromagnetic radiation called *Cherenkov radiation* if its velocity $v = \beta c$ exceeds the local phase velocity of light c/n in the medium [22], [17, p. 409]. The effect is caused by polarization of the medium's atoms or molecules and can be compared to the phenomenon of a sonic boom produced by a super-sonic body [23].⁶ A sketch in Figure 2.8 illustrates this. Cherenkov radiation is negligible for energy loss,⁷ but important for particle detection [17, p. 409], because Cherenkov photons are mainly in the UV and optical range where detection media are transparent (whereas to high-energy particles and photons they are opaque).

From the geometry of super-luminal emission of radiation, Figure 2.8, the Cherenkov angle θ between

⁵ With particle velocity $\beta = v/c$, Lorentz factor $\gamma = 1/\sqrt{1-\beta^2} = E/(mc^2)$, and mean lifetime τ (at rest), the travel distance in the laboratory frame is

$$s = v\gamma\tau = \beta c\gamma\tau = c\tau\gamma\sqrt{1-1/\gamma^2} = c\tau\sqrt{\left(\frac{E}{mc^2}\right)^2 - 1}, \quad (2.16)$$

which is $s \approx c\tau E/(mc^2)$ for $E \gg mc^2$.

⁶ A charge moving below the speed of light also polarizes, but the photons emitted during relaxation of the polarized molecules cancel each other and no light is observed. Only if the polarizing particle moves above the speed of light, the radiation forms a shock front in form of a cone and is intensified similar to a super-sonic boom.

⁷ Because the energy of an optical photon is about 9 orders of magnitude lower than the energy of a GeV particle and the number of emitted Cherenkov photons is not large enough to compensate that.

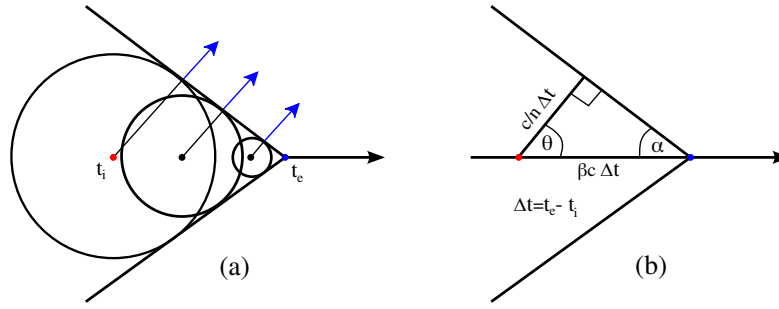


Figure 2.8: (a) A particle emitting Cherenkov radiation travels in direction of the black arrow, from the left-most red point at time t_i to the right-most blue point at time t_e . The circles indicate wave fronts of radiation at time t_e that form a shock front in form of a cone, which propagates in the direction of the blue arrows. (b) Geometry of the Cherenkov cone.

particle direction and photon direction can be calculated:

$$\cos \theta = \frac{1}{\beta n}. \quad (2.17)$$

The condition for Cherenkov emission is $\beta > 1/n$.

The number of Cherenkov photons produced per unit length x and unit wavelength λ is given by the *Frank-Tamm formula*, which can be written down in the form [17, p. 410]

$$\frac{d^2 N}{dx d\lambda} = \frac{2\pi\alpha z^2}{\lambda^2} \left(1 - \frac{1}{\beta^2 n^2(\lambda)}\right), \quad (2.18)$$

where $\alpha \approx 1/137$ is the fine structure constant, z is the charge number of the incident particle. Even though the refractive index n is a function of λ , the dominant dependence of the number spectrum is λ^{-2} , which means that the energy spectrum goes as λ^{-3} [24] (using $dE = dN hc/\lambda$ and $\alpha = e^2 c \mu_0 / (2h)$):

$$\frac{d^2 E}{dx d\lambda} = \frac{\pi e^2 z^2 c^2 \mu_0}{\lambda^3} \left(1 - \frac{1}{\beta^2 n^2(\lambda)}\right). \quad (2.19)$$

Figure 2.9 shows a plot of the Cherenkov spectrum in Equation 2.19, emitted by a particle with $z = 1$ and $\beta = 1$ in ice with refractive index $n = 1.31$. The spectrum of Cherenkov radiation is continuous and shorter wavelengths dominate.⁸ Therefore, the bulk of the Cherenkov spectrum lies in the UV and visible range. This gives Cherenkov light its typical “blue glow” color when observed with the naked eye, see Figure 2.10. Figure 2.9 also shows the spectrum after passage through South Pole ice. Due to wavelength dependent attenuation, especially at short wavelengths, the peak of the spectrum moves towards longer wavelengths after passage through the medium.

2.3.5 Solar Neutrinos

In the core of the Sun, nuclear fusion processes occur at high temperature and density. A copious number of neutrinos is produced as by-products, called solar neutrinos [15, p. 352]. The theory of stellar nucleosynthesis was first spelled out by Hans Bethe [27, 28] and others in 1939. The state-of-the-art

⁸ At low wavelengths, the refractive index becomes < 1 , so the total radiated energy, the integral of Equation 2.19 over all wavelengths with $\beta n(\lambda) > 1$, is finite. Additionally, most transparent media, for instance water/ice, are not UV-transparent.

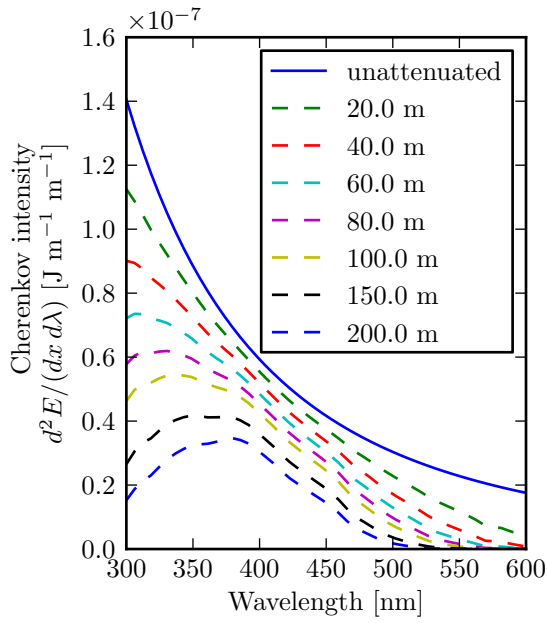


Figure 2.9: Emitted Cherenkov radiation intensity as energy per unit path length and unit wavelength, from a particle with charge $\pm 1 e$ and velocity $\beta = 1$ in a medium with refractive index $n = 1.31$ (ice). The attenuated spectrum as seen from certain distances to the source is also shown. The wavelength dependent attenuation was taken from [25, p. 84] and was measured for ice at the geographic South Pole in 1000 m depth.

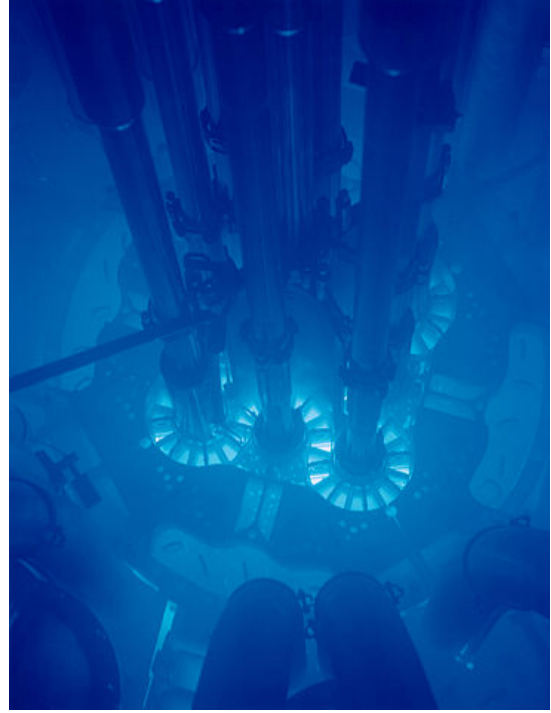


Figure 2.10: The Idaho National Laboratory's Advanced Test Reactor (ATR) core. Powered up, the fuel plates can be seen glowing bright blue. The core is submerged in water for cooling. From [26].

models of today, also including neutrino flux predictions, are called Standard Solar Models (SSMs) and were developed since the 1960s until the 2000s, most notably by John Bahcall and collaborators [29–31].

According to the models, there are two main processes of nuclear fusion inside stars: the pp -chain and the CNO-cycle [15, p. 353]. The pp -chain is basically the fusion of four protons into one α -particle (${}^4\text{He}$ -nucleus), while the CNO-cycle involves a catalytic carbon nucleus, which gains four protons and decays via two β -decays and one α -decay to its original state during one full cycle [32, p. 22]. For the Sun, the pp -chain is dominant ($\sim 99\%$ of energy production) and the CNO-cycle can be neglected ($\sim 1\%$) [32, p. 25]. The pp -chain reaction owes its name to the fusion of two protons at its beginning:



A second process follows, involving an electron (a simple crossing of pp) [32, p. 22], [15, p. 354]:



The produced deuterium ${}^2\text{H}$ forms ${}^3\text{He}$:



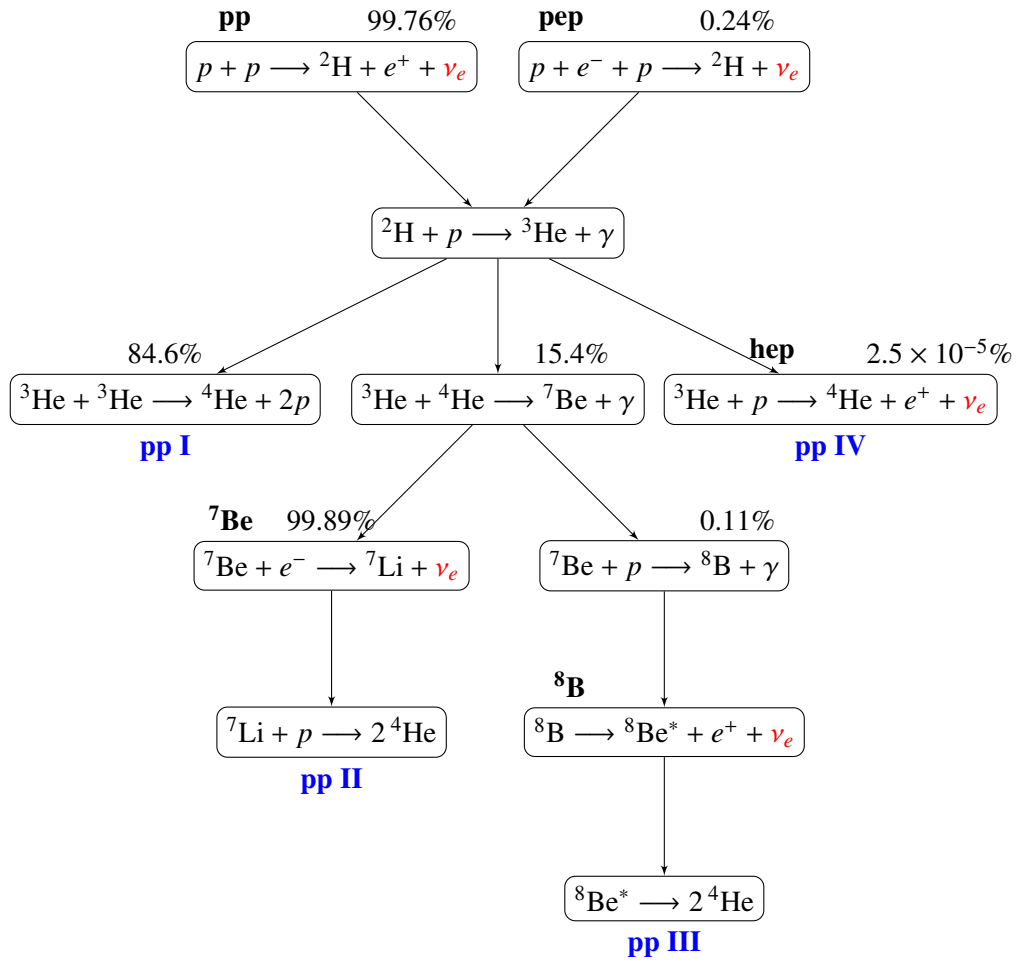


Figure 2.11: Overview of the pp -chain reactions of stellar nucleosynthesis, producing the different species of solar neutrinos (marked with red color).

From here on, there are four branches of the pp -chain: pp I, pp II, pp III, and hep (or pp IV) [32, p. 22]. Figure 2.11 gives an overview of the pp -chain processes and indicates their relative occurrence probabilities. In all of the reactions, the emitted neutrinos are marked in red color and the conventional name of the neutrino flux is written in boldface letters.

Figure 2.12 shows energy spectra of the different solar neutrino species. The largest component of the solar neutrino flux comes from the pp reaction in the very beginning of the pp chain. By numbers, about 86% of all pp chain neutrinos produced in the Sun are pp neutrinos. However, they have the lowest energies, only $E_\nu \leq 0.4$ MeV. The next higher in energy are the monoenergetic ${}^7\text{Be}$ and pep lines at about 0.4 MeV, 0.9 MeV and 1.4 MeV. About 13% of solar neutrinos are ${}^7\text{Be}$ and 0.2% are pep neutrinos. The high energy continuous spectra are from ${}^8\text{B}$ (up to ~ 16 MeV) and hep (up to ~ 19 MeV), who contribute about 0.01% and $2 \times 10^{-5}\%$ to all solar neutrinos, respectively.

For about 30 years, the neutrino fluxes predicted by the SSMs remained in conflict with solar neutrino flux measurements performed by the Homestake experiment, GALLEX, SAGE, and Kamiokande [15, pp. 366-375]. The measured fluxes were about one third or half of the predicted flux, depending on the experiment. This discrepancy between predicted and measured solar neutrino rate became known as the *solar neutrino problem* (SNP). It was finally solved by measurements done by Super-Kamiokande

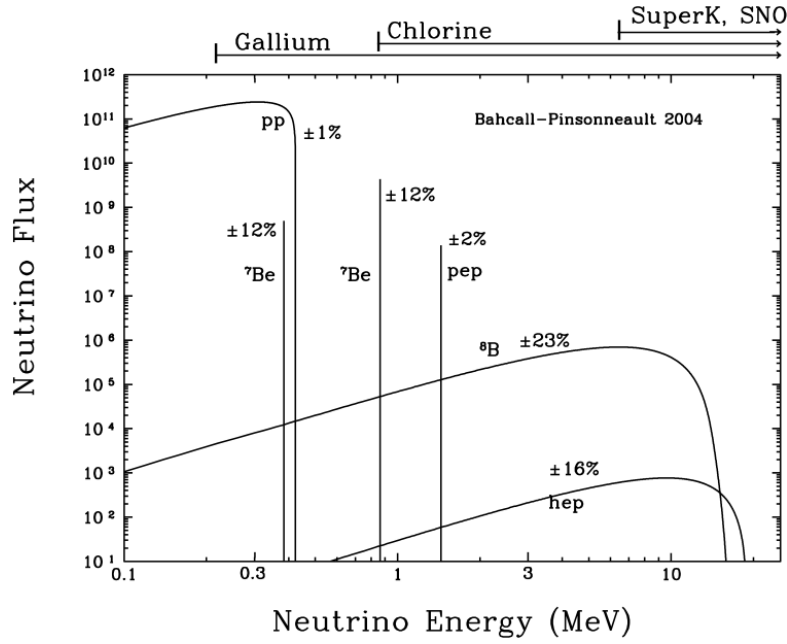


Figure 2.12: The solar neutrino energy spectra from the pp -chain, predicted by the SSM by Bahcall and Pinsonneault 2004 [31]. For continuum sources, the neutrino fluxes are given in number of neutrinos $\text{cm}^{-2} \text{s}^{-1} \text{MeV}^{-1}$ at the Earth's surface. For line sources, the units are number of neutrinos $\text{cm}^{-2} \text{s}^{-1}$. The accessibility by different detection techniques is indicated at the top. Taken from [33].

and the Sudbury Neutrino Observatory (SNO) indicating the conversion of neutrino identities during propagation, also known as *neutrino flavor oscillations* [15, pp. 377-381], [32, p. 23]. These efforts were rewarded with the Nobel prize in Physics in 2015 [34].

2.3.6 Atmospheric Neutrinos

When primary cosmic ray (CR) particles, mainly protons, hit the upper atmosphere, they interact with air nuclei to produce a shower of secondary particles. Among others, mesons are produced, mostly pions and a small number of kaons [15, p. 390]. The mesons decay according to their natural lifetime, the charged pions mostly according to:

$$\pi^{\pm} \longrightarrow \mu^{\pm} + \nu_{\mu}(\bar{\nu}_{\mu}), \quad (2.23)$$

producing muons and muon neutrinos.⁹ For a decay to happen, the meson must be undisturbed. If the meson hits another air nucleus before it decays, it initiates another particle shower and its energy is distributed among several particles. In this case, no high-energy muon and neutrino are produced. Another neutrino source is the decay of some of the muons that decay before reaching the Earth's surface:

$$\mu^{\pm} \longrightarrow \bar{\nu}_{\mu}(\nu_{\mu}) + e^{\pm} + \nu_e(\bar{\nu}_e). \quad (2.25)$$

The neutrinos produced from those decays of CR secondaries are called *atmospheric neutrinos*.

⁹ The decay

$$\pi^{\pm} \longrightarrow e^{\pm} + \nu_e(\bar{\nu}_e), \quad (2.24)$$

is strongly suppressed with branching ratio of only 0.0123% [17, p. 34] due to helicity.

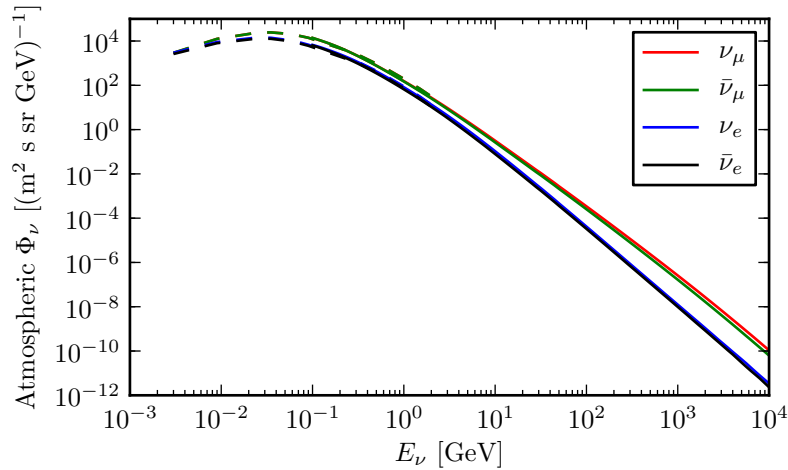


Figure 2.13: Atmospheric neutrino spectra according to [39] at low energies (dashed) and according to [40] at high energies (solid). The plotted flux was calculated for northern US at low energies and for the SNO detector location (Canada) at high energies.

Below a certain critical energy, $E_\nu \ll \sim 115 \text{ GeV} / \cos \theta$ for pions and $E_\nu \ll \sim 850 \text{ GeV} / \cos \theta$ for kaons, meson decay is more likely to occur than interaction, so that the low-energy neutrino spectrum has approximately the same power as the primary cosmic-ray spectrum [35, p. 159]. Above the critical energy, meson interactions take place and the neutrino spectrum, a power law $\propto E^{-\alpha}$, is one power steeper, i.e. it has an extra factor $1/E$ [35, p. 160].

Between a few GeV to some hundred TeV, the primary CR spectrum is approximately $\phi_{\text{CR}} \propto E^{-2.7}$ [15, p. 393]. Accordingly, the atmospheric neutrino spectrum at energies above the TeV range is roughly $\phi_\nu \propto E^{-3.7}$. Because the critical energy is higher for kaons, and because neutrinos gain a higher energy fraction in kaon decay, kaon decay becomes the dominant neutrino source for $E_\nu > 100 \text{ GeV}$ even though the kaon/pion ratio is small [35, p. 160]. At sufficiently high energies, contribution from rarer charmed mesons,¹⁰ e.g. D and Λ mesons, should become dominant [35, p. 176], [36]. This is called the *prompt component* of the atmospheric muon and neutrino flux, because of the extremely short lifetimes of the charmed particles, decaying promptly without a chance for interaction. Predictions of the crossover energy where the prompt component becomes prevalent vary by many orders of magnitude between 10 TeV and 1000 TeV [35, p. 177], [36], however the prompt flux has not been observed yet [37, 38].

Figure 2.13 shows a plot of the atmospheric neutrino spectra according to calculations detailed in [39, 40].

2.3.7 Neutrino Summary

Many natural sources of neutrinos exist. Besides the Sun producing solar neutrinos (see Section 2.3.5) and CRs producing atmospheric neutrinos (see Section 2.3.6), there are also geoneutrinos originating from nuclear decays in the Earth's crust and mantle, neutrinos emitted in a short burst during a supernova, a diffuse flux from the sum of all supernovae in the Universe called supernova relic neutrinos [41, p. 5], [42], and potentially also neutrinos from galactic and extra-galactic CR accelerators, e.g. from supernova remnants (SNRs), γ -ray bursts (GRBs), and active galactic nuclei (AGNs). The neutrinos

¹⁰ Meaning that they contain a *charm* quark.

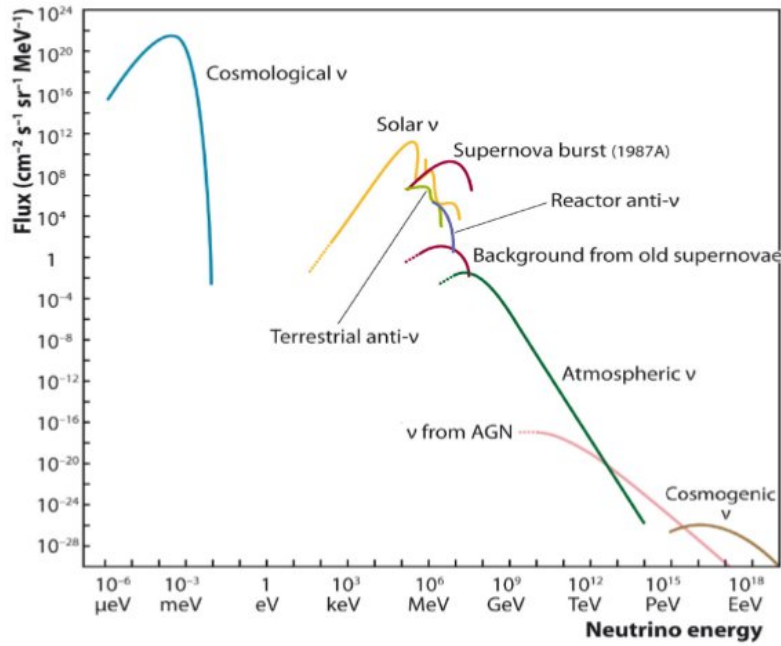


Figure 2.14: Measured and expected fluxes of natural and reactor neutrinos, taken from [43]. In the plot, geoneutrinos are called “Terrestrial” and supernova relic neutrinos are called “Background from old supernovae”.

emitted by supernovae are the focus of this thesis, therefore they are covered extensively in Chapter 3, which is dedicated to supernovae. Other neutrino fluxes, atmospheric and solar neutrinos, act merely as unwanted background to the search for supernova neutrinos.

For an overview of neutrino fluxes, Figure 2.14 shows some neutrino spectra.

2.4 The High-Energy Universe

2.4.1 Cosmic Rays

Cosmic rays (CRs) are charged particles impinging on the Earth’s atmosphere from outer space and from all directions [44, p. 5], [17, p. 378]. They are mainly protons and heavier nuclei [44, p. 15]. The energy spectrum of cosmic rays (Figure 2.15) is a nearly featureless power-law, except for the so-called “knee” and “ankle”, i.e. kinks where the power law changes its exponent such that the spectrum resembles a leg [41, p. 9]. The spectrum of CRs has been observed over eleven decades in energy from $\sim 10^9$ eV up to $\sim 10^{20}$ eV [41, p. 9].

The CR spectrum falls very steeply: The integrated flux above 10^{11} eV is higher than that above 10^{20} eV by sixteen orders of magnitude [23]. Because of the very steep spectrum, it is usually multiplied with a factor E^2 , like in Figure 2.15, in order to make its features more visible. The (differential) CR flux is: [44, p. 16], [17, p. 378]

$$\frac{d\Phi}{dE} \approx 1.8 \left(\frac{E}{1 \text{ GeV}} \right)^{-\alpha} \text{ nucleons cm}^{-2} \text{ s}^{-1} \text{ sr}^{-1} \text{ GeV}^{-1} \quad (2.26)$$

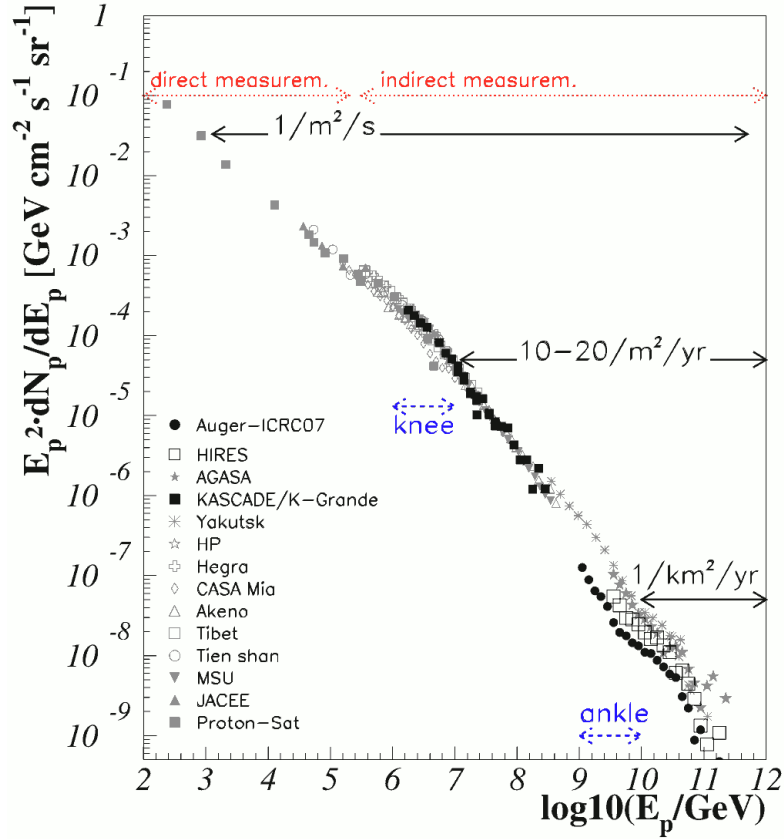


Figure 2.15: The all particle cosmic ray (CR) energy spectrum, with data points from the experiments as listed. Taken from [41, p. 11].

where E is the energy per nucleon. The exponent α is called the *spectral index* is [41, p. 10]:

$$\alpha \approx \begin{cases} 2.67 & \text{for } E < 2.5 \times 10^{15} \text{ eV} & \text{“up to knee”} \\ 3.10 & \text{for } 2.5 \times 10^{15} \text{ eV} \leq E \leq 3.2 \times 10^{18} \text{ eV} & \text{“betw. knee and ankle”} \\ 2.75 & \text{for } E > 3.2 \times 10^{18} \text{ eV} & \text{“beyond ankle”}. \end{cases} \quad (2.27)$$

The spectrum softens (steepens) at the knee around 10^{15} eV and hardens (flattens) again at the ankle around 10^{18} eV. A “second knee” between knee and ankle at around 4×10^{17} eV is discussed, which steepens the spectrum even more up to the ankle [41, p. 10].

Larmor Radius

Charged particles are confined to their host galaxy if their gyroradius is smaller than the size of the galaxy. The gyroradius or Larmor radius is the radius of a particle’s circular motion induced by movement in a magnetic field:

$$q v B_{\perp} = \frac{m v^2}{R_L} \quad \Rightarrow \quad R_L = \frac{m v}{q B_{\perp}} = \frac{p}{e Z B_{\perp}} \quad (2.28)$$

with p the momentum, Z the charge number of the particle (nucleus), and B_{\perp} the magnetic field's component perpendicular to the particle's motion.

Galactic CRs (GCRs)

GCRs are characterised by intermediate energies of few GeV up to $\sim 3 \times 10^{18}$ eV (the ankle) [41, p. 67]. Being charged, they are deflected by interstellar magnetic fields and their arrival direction is completely random. GCRs constitute the majority of cosmic rays and arrive at the Earth at a rather constant and isotropic flux which is however modulated and distorted due to the solar wind and solar magnetic field (the "heliosphere") [44, p. 16], [45, pp. 21ff.]. Above ~ 100 GeV, the Sun's influence becomes negligible [44, p. 17], but additional anisotropies are caused by deflections in the Earth's magnetic field.

Due to magnetic confinement, see Equation 2.28, low-energy CRs are confined to the Galaxy. At higher energies, when their Larmor radius approaches the size of the Galaxy, the particles should leak out of the Galaxy. This is probably one of the reasons for the steepening of the CR spectrum at the knee [44, p. 25], [41, pp. 39f.]. Another reason for the knee can be that the maximum acceleration energy of most galactic CR accelerators is reached [17, p. 383]. The flux from more powerful extra-galactic accelerators is still suppressed by the magnetic confinement. Above the ankle, the spectrum flattens, because particles from extra-galactic sources become energetic enough to reach us.

Considering the abundance and energy release of known astrophysical sources, e.g. those sources that have been observed to emit high-energy γ -rays, then one can expect that Galactic sources produce the CR spectrum up to the ankle, while extra-galactic sources contribute the flux above the ankle [41, p. 17].

This hypothesis is supported by the energy-dependent CR composition: heavy nuclei (iron) at the knee, light nuclei (proton) at the ankle. This is an indication that the maximum proton energy of most galactic CR accelerators lies around the knee. Higher charged nuclei, which are much rarer, can gain a higher energy, so that they contribute to CRs at those energies [17, p. 383].

Extra-galactic CRs (EGCRs)

EGCRs are the highest energy particles in the cosmic ray spectrum and most probably originate outside our own Galaxy. They have energies starting at the ankle around 10^{18} eV up to the highest energies ever observed (few 10^{20} eV) [44, p. 50f.]. These are also referred to as *ultra-high energy cosmic rays* (UHECR). The general understanding is that below $\sim 10^{18}$ eV, extra-galactic CRs are suppressed because of magnetic deflections that prevent them to reach our Galaxy.¹¹ The observed isotropy of the (mostly undeflected) CRs at highest energies hints towards extra-galactic sources [44, p. 27].

Above the ankle, at around 4×10^{19} eV, a flux suppression was observed by the HiRes experiment, the Pierre Auger Observatory, and the Telescope Array [17, p. 383], which supports the extra-galactic nature of UHECRs. This might signify that the maximum attainable energy of extra-galactic accelerators is reached, analogous to the knee [46]. Or it might be caused by energy losses of extra-galactic CRs due to interactions with CMB photons, i.e. the so-called Greisen-Zatsepin-Kuzmin or *GZK cut-off* [46]. In the GZK process, ultra-high energy neutrinos are created via [41, pp. 12f., 42, 106]

$$p + \gamma_{\text{CMB}} \longrightarrow \Delta^+ \longrightarrow \begin{cases} p + \pi^0 & \text{in 2/3 of cases} \\ n + \pi^+ & \text{in 1/3 of cases} \end{cases} \quad (2.29)$$

¹¹ The so-called "magnetic horizon" is the maximum distance from which we can receive CRs and becomes smaller and smaller for lower energies [44, p. 51].

where π^+ decays according to Equation 2.23 to produce neutrinos. One experiment, AGASA, did not observe a decay of the spectrum at highest energies (see the data points represented by stars in Figure 2.15) [41, p. 13]. AGASA, and other experiments, detected several events above 5×10^{19} eV, which would need to be explained by exotic phenomena, e.g. decay of extremely heavy exotic particles [41, p. 13], [47]. However, AGASA statistics were low and the systematic errors large. The GZK feature was recorded by HiRes, and subsequently confirmed by Auger and Telescope Array at higher statistics [17, p. 383]. A detection of GZK neutrinos would aid the interpretation of this feature.

2.4.2 Possible Sources of Cosmic Rays

The current understanding is that CRs below the knee are accelerated mostly at supernova remnants (SNRs) in the Galaxy, those between knee and ankle come from other Galactic sources and the highest energy CRs above the ankle are accelerated at more powerful extra-galactic sources [23], [41, pp. 17, 18, 38, 67], [44, p. 27]. The exact origin of cosmic rays, in particular above the knee, is still unknown. The power-law shape of the CR spectrum reveals that they acquire their energies via non-thermal processes, contrasting thermal black body spectra known from stars and supernovae [44, p. 16].

For UHECRs, there are two different scenarios: the *bottom-up* scenario, which assumes that the particles gain energy in an acceleration process and the *top-down* scenario, where UHECR protons are created directly at high energies as decay products of superheavy exotic particles [47], [41, p. 13]. In the top-down scenario, protons can have energies up to 10^{22} eV and the GZK cut-off can be avoided, since the protons would be produced homogeneously throughout the Universe, also near the Earth [41, p. 13]. However, the top-down scenario is not favored by the data from more recent experiments, e.g. the indication of a mixed composition (nuclei heavier than protons) at highest energies and the observation of the GZK cut-off (s.a.). Therefore, it will not be discussed here any further.

General Arguments

A few general arguments about the production of CRs can be made. One of those is *Hillas' argument* [44, p. 27]: For very high-energy particles, when the total energy $E \gg$ rest mass m , the momentum and energy are almost equal, $p \approx E$, and Equation 2.28 for the Larmor radius becomes: $R_L = E/(e Z B)$. Now, in order to efficiently accelerate particles, their Larmor radius R_L must be smaller than the accelerator radius R_s . When the Larmor radius reaches the accelerator radius, the particles are no longer magnetically confined and escape from the accelerator. Thus, the maximum energy of a particle of charge Ze from an accelerator of radius R_s is

$$E_{\max} = e Z B R_s. \quad (2.30)$$

Therefore, to reach a certain maximal energy, the source can be either small with a high magnetic field B , or large with low magnetic field B . All sources that are too small or have a too low magnetic field can be excluded. Figure 2.16 visualizes Hillas' argument as a "Hillas plot", which is a $B - R_s$ diagram in which a certain combination of Z and E_{\max} is indicated as a diagonal line. Astrophysical sources are plotted in the diagram and must lie above the line in order to accelerate particles of charge Z up to E_{\max} . Few known sources for acceleration to $E = 10^{21}$ eV are compatible with Hillas' argument [44, p. 27], which is another reason, besides the GZK cut-off, for an end to the CR spectrum at high energies.

Sometimes, general energetic arguments are made in favor of a specific class of sources. For example, assuming that a supernova (SN) emits typically $10 M_\odot = 1.99 \times 10^{31}$ kg of material at an average speed of 5×10^6 m s⁻¹, then the total released kinetic energy per SN is $1/2 m v^2 \approx 2.5 \times 10^{44}$ J =

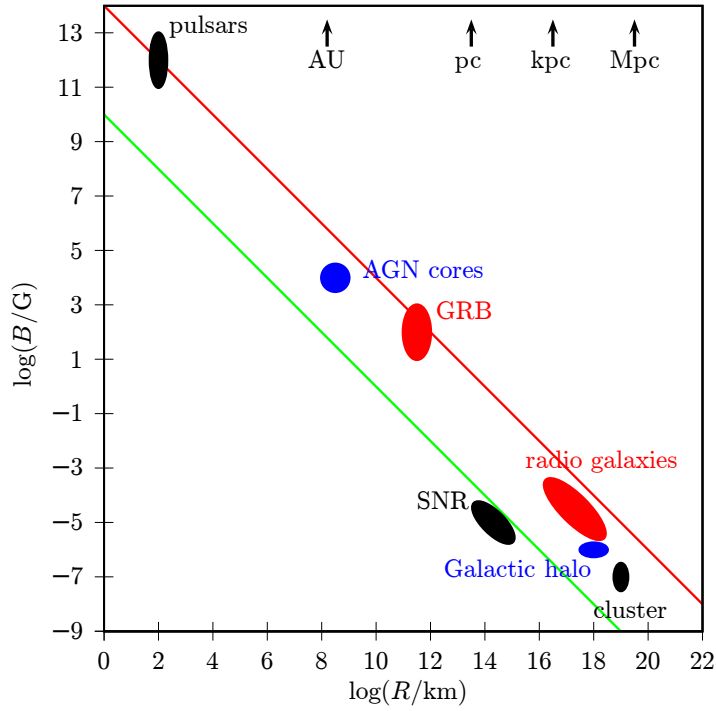


Figure 2.16: A Hillas plot: astrophysical systems are charted according to their extension (radius R) and magnetic field strength B . Sources capable of accelerating protons to $E_{\max} = 10^{21}$ eV should lie above the red line, sources above the green line can accelerate iron up to $E_{\max} = 10^{20}$ eV. Taken from [44, p. 28].

2.5×10^{51} erg.¹² Assuming a SN rate of $1/(30 \text{ yr})$ in the Milky Way, this corresponds to a “luminosity” or rather power of $L_{\text{SN}} \approx 2.6 \times 10^{42} \text{ erg s}^{-1}$. Cosmic rays are observed at an energy density of $\rho_{\text{CR}} \approx 1 \text{ eV cm}^{-3}$, thus giving a total energy of $E_{\text{CR}} \approx \rho_{\text{CR}} V_G = 6.7 \times 10^{54} \text{ erg}$ with the volume of the Galaxy $V_G \approx \pi R^2 h$, using disk radius $R = 15 \text{ kpc}$ and disk height $h = 200 \text{ pc}$. Assuming that the CRs remain inside the Galaxy for on average about $\tau_{\text{CR}} = 6 \times 10^6 \text{ yr}$, then the CR luminosity amounts to

$$L_{\text{CR}} \approx \rho_{\text{CR}} V_G / \tau_{\text{CR}} = 3.5 \times 10^{40} \text{ erg s}^{-1}. \quad (2.31)$$

Thus, if about 1% of the SN kinetic energy would be converted into accelerated particles, then it would roughly match the observed CR density, up to certain energies. Therefore, in principle, SNe or rather their remnants might be capable of producing the entire CR flux within a certain energy range [44, p. 27].

Another very basic argument is *Blandford’s argument*. If one assumes regular electromagnetic fields as acceleration mechanism, then a potential difference of $U = 10^{20} \text{ V}$ is needed to produce the highest-energy UHECRs. The energy output, or power, of such an accelerator would be $P = UI = U^2/R$. Assuming that the impedance must be $R \lesssim 1000 \Omega$ [44, p. 28], one arrives at an estimate of the CR luminosity per UHECR source:

$$L_{\text{CR}} = U^2/R \gtrsim 10^{37} \text{ W} = 10^{44} \text{ erg s}^{-1}. \quad (2.32)$$

The cosmic ray emittivity \mathcal{L} , which is the CR luminosity per unit volume, is $\mathcal{L} = L_{\text{CR}} n_s$, with source number density n_s . Since the observed UHECR emittivity is $\mathcal{L} \approx 3 \times 10^{46} \text{ erg Mpc}^{-3} \text{ yr}^{-1}$ [44, p. 28],

¹² The unit erg is frequently used in astronomy for measuring energy. It is $1 \text{ erg} \equiv 10^{-7} \text{ J}$

one can deduce for the source density: $n_s \lesssim 10^{-5} \text{ Mpc}^{-3}$. This is an interesting clue about the UHECR sources. For comparison, the most common type of active galactic nuclei (AGNs), Seyfert galaxies, has a density of $1 \times 10^{-5} \text{ Mpc}^{-3}$ to $5 \times 10^{-5} \text{ Mpc}^{-3}$ in the nearby Universe, which fits quite well [44, p. 28].

Extra-Galactic Source Candidates

As alleged extra-galactic CR production sites, with CR energies high enough to reach Earth, there are active galactic nuclei (AGNs) as persistent sources and γ -ray bursts (GRBs) as transient eruptive sources. GRBs, and the related supernovae (SNe), are discussed in Chapter 3, in the context of neutrinos produced by accelerated particles.

Active galactic nuclei (AGNs) were first discovered in the 1960s as quasi-stellar objects (QSOs) with strong radio emission that therefore could not be stars [41, p. 18]. AGNs are extremely bright cores of galaxies and are believed to be powered by a rotating supermassive black hole in the center of the galaxy. The galactic nucleus is “active” because of matter that is accreted by the black hole, forming an accretion disk which radiates strongly at optical and UV frequencies [41, p. 18], [48]. Perpendicular to the accretion disk, two relativistic jets of matter can be emitted. Along the jets there are “hot spots” that are expected to be shock environments where particles are accelerated. If hadrons are accelerated and not only leptons (electrons), then they might reach proton energies of $\sim 10^{21}$ eV [41, p. 18]. About 90% of AGNs are radio-quiet and usually located in spiral galaxies, while 10% are located in elliptical galaxies, are radio-loud and emit jets [41, p. 19]. There is a rich phenomenological AGN classification scheme, classifying AGNs according to host galaxy (=radio-loud/-quiet), luminosity, and inclination angle. Sub-classes of AGNs include quasars (very bright objects), blazars and BL Lac objects (where the jet points towards the observer), Fanoff-Riley (FR) galaxies (being looked at from the side), and Seyfert galaxies (optically relatively weak radio-quiet AGNs, where the host galaxy is clearly visible), among others [41, pp. 19f.]. AGNs with jets are prime candidates for CR production, especially for the UHECR component. γ -ray experiments have detected signals from the position of several AGNs [49] and the Auger observatory has observed a correlation of highest energy CR events with the positions of nearby AGNs [50].

Galactic Source Candidates

Galactic source candidates for the production of CRs are supernova remnants (SNRs) up to the knee, as well as X-ray binaries, in particular microquasars, and pulsars for production of CRs above 100 TeV, i.e. dominantly above the knee [41, pp. 17, 40].

Supernova remnants (SNRs) are generally believed to produce the CR spectrum up to knee energies [41, p. 38]. SNRs are created when a star explodes as a supernova. Material from the stellar envelope is ejected at high velocities and collides with the interstellar medium (ISM), which creates a shock front [41, p. 38]. The shock front can be responsible for stochastic particle acceleration, for more information see Section 2.4.3. Explaining the GCR component with SNRs works well given the available energy (s.a.). However, explaining the break in the CR spectrum at the knee is more difficult [41, pp. 39f.]. Leakage from the Milky Way starting at the knee could play a role, or perhaps different classes of SNRs with different maximum energy exist, depending on the mass loss history of the progenitor star, which determines the conditions in the shock front [41, pp. 39f.]. Accelerated CRs should create on-site pions that decay to γ -rays and could be used to confirm the CR acceleration of SNRs. However, the γ -ray spectra from accelerated electrons, radiated via bremsstrahlung and inverse Compton scattering, are difficult to distinguish from the spectra of π^0 decay [51]. The problem of distinguishing leptonic and hadronic particle acceleration could be overcome by detecting neutrinos, which are only produced

in the hadronic case. Nevertheless, recently the Fermi satellite provided direct evidence that CR protons are accelerated by SNRs by detecting the characteristic pion-decay feature in the γ -ray spectra of two SNRs [51].

During an SN explosion, the stellar core collapses under the gravitational force and is converted to neutrons almost exclusively. If the mass of the SN progenitor star was below a threshold, a neutron star forms, otherwise the neutron star collapses to a black hole [52]. *Pulsars* are fast rotating, highly magnetized neutron stars that emit electromagnetic radiation along their magnetic field axis [41, p. 40]. Since the rotational axis does not align with the magnetic field axis, the particle beam rotates and they behave like light houses: When the beam points towards Earth, a flash of radiation is seen that repeats periodically. Depending on the pulsar’s spin, its period ranges from several seconds to only milliseconds [41, p. 40]. Pulsars can host extremely high magnetic field strengths of around $B \approx 10^{12}$ G [41, p. 40].¹³ Those high magnetic fields allow for acceleration of particles to very high energies. However, pulsar spin-down luminosities of 10^{37} erg s⁻¹ are too small to contribute significantly to the CR flux below the knee. They can, however, contribute to the region between knee and ankle [41, p. 40]. Besides normal pulsars, whose most prominent example is the Crab pulsar, there are also special types of pulsars: magnetars and soft gamma repeaters (SGRs) which have even higher magnetic fields up to $B \approx 10^{15}$ G [41, p. 40].

X-ray binaries (XRBs) are binary systems consisting of a compact object, either a neutron star or a black hole, and a companion star. The companion feeds matter to the compact object and an accretion disk forms around the compact object, similar to an AGN [54]. The accretion disk heats and emits X-ray radiation [41, p. 41], [55, p. 11]. Like in AGNs, two-sided collimated jets can also be emitted perpendicular to the accretion disk, along the magnetic field axis [41, p. 41]. In this case, one speaks of a “microquasar”, i.e. a miniature version of a quasar [48]. The jet emission is not continuous, but happens in transient bursts, believed to be triggered by accretion disk instabilities when a large chunk of matter is accreted [48], [41, p. 41]. The process could be the same as in quasars, but because the system is 10^6 times smaller, it also occurs on a 10^6 times shorter time-scale [48]. During a burst event, increased X-ray emission from the accretion disk and subsequently optical to radio emission from the jet can be observed [41, p. 41], [56]. In addition to microquasars, there can be “binary pulsars”: A neutron star emits a pulsar wind that interacts periodically with the heavy companion star’s outflow, every time the pulsar orbits closest to the companion star [56]. Indeed, periodic TeV photon emission was observed from several XRB systems in the Milky Way [41, p. 41]. XRBs can cause particle acceleration up to the ankle, but like pulsars, their typical electromagnetic energy output of $\sim 10^{38}$ erg s⁻¹ is relatively small and suggests that they do not produce the bulk of CRs at lower energies. They could however contribute significantly to the total CR flux above ~ 30 TeV [41, p. 41].

2.4.3 Fermi Acceleration

Charged CR particles are usually believed to be accelerated in shock environments by a mechanism known as *1st order Fermi acceleration* at shock fronts or simply (*diffusive*) *shock acceleration* [44, pp. 32ff.], [41, p. 14], although there are alternative models, e.g. magnetic reconnection [57, 58]¹⁴. Fermi acceleration was first introduced by Enrico Fermi in 1949 [59] and 1954 [60] and refined by others in the 1970s [41, p. 14], [61].

For Fermi acceleration, an inhomogenous magnetic field is required, which is responsible for the

¹³ For comparison, the Earth’s magnetic field ranges between 0.2 G and 0.6 G [53].

¹⁴ However, the magnetic reconnection models also employ a 1st order Fermi acceleration process, but not on particles in a shock, but particles trapped within a reconnection, which is an area where two opposing magnetic field lines encounter and annihilate.

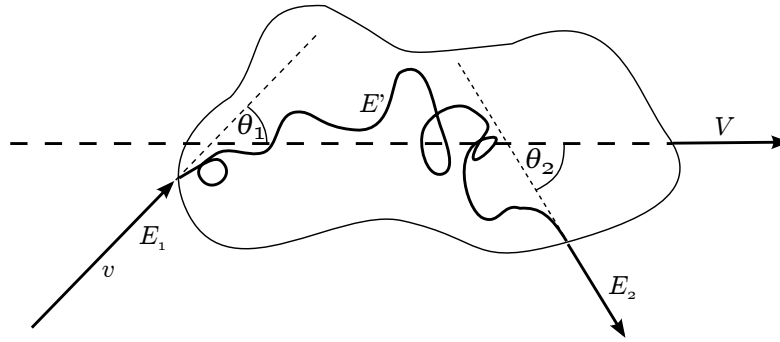


Figure 2.17: Sketch of the 2nd order Fermi acceleration of a charged particle at a cloud hosting magnetic irregularities.

acceleration [41, p. 14]. Everytime a particle crosses a magnetic irregularity, it can gain a small amount of energy. Fermi acceleration is a stochastic process: A particle undergoes a random motion, but is confined by the magnetic field. It can cross the magnetic irregularities many times. Afterwards, the particle has gained a high energy and escapes from the environment [41, p. 14].

Fermi acceleration can be regarded as the particle gaining energy from “collisions” with the magnetic irregularities [59]. If a magnetic irregularity approaches the particle, the particle gains energy. If it is receding, the particle loses energy. This is similar to a ping pong ball hitting a table tennis racket [62].¹⁵ On average, the particle gains energy, because the collision rate depends on the relative velocity, and the relative velocity is greater for head-on collisions so that head-on collisions occur more frequently [59], [62], [44, pp. 32f.]. This can be compared to driving on a motorway, where one sees much more cars going in the opposite direction than one sees cars moving in one’s own direction [64].

Fermi’s original idea was the scattering of a charged particle at irregularities of the interstellar magnetic field [59]. This can be viewed as a particle with velocity v scattering at a magnetic cloud, which moves with velocity $V \ll c$ [44, pp. 32f.]. Figure 2.17 shows an illustration. The particle enters and exits the cloud and this process is repeated many times. The average energy gain from each cloud crossing is $\langle \epsilon \rangle \propto \beta^2$. Because of the β^2 dependence, this mechanism is called *2nd order Fermi acceleration*. It is rather inefficient, because the cloud velocity $\beta = V/c$ is small, $\beta \ll 1$ [44, p. 33].

The situation changes when a planar shock front is considered instead of an irregular magnetic cloud, as depicted in Figure 2.18. A shock front (or shock wave) is created when a gas moves at a velocity greater than the speed of sound of the medium and collides with an obstacle, usually more gas, which is at or almost at rest [41, p. 14]. The phenomenon of shock waves can also be observed when an aircraft moves at supersonic speed or when a bullet or explosion is fired. The typical astrophysical example is an SNR, where the progenitor star’s atmosphere is expelled at great velocities and encounters the interstellar gas. The resulting shock front is a thin layer of disturbance, propagating at supersonic speed, with a discontinuous change of parameters like density, pressure, and temperature [44, p. 34]. The shock forms a barrier between two media having different bulk velocities [44, p. 35].

The shock front is like a permeable wall propagating with velocity v_s through a medium and disturbing it. The shock serves as separation between two reference systems that have different bulk velocities: The undisturbed medium ahead of the shock is at rest in the lab system, so $v_1 = 0$. The medium behind the shock has a velocity $v_2 < v_s$ in the same direction as v_s [44, p. 35], [61]. The geometry is not chaotic like the magnetic clouds: For a particle crossing the shock front back and forth, the medium on the other

¹⁵ This is too simplistic and only roughly correct, since the particle can also penetrate the irregularity and thus can also lose energy during an approaching collision and vice versa, see [63, p. 153].

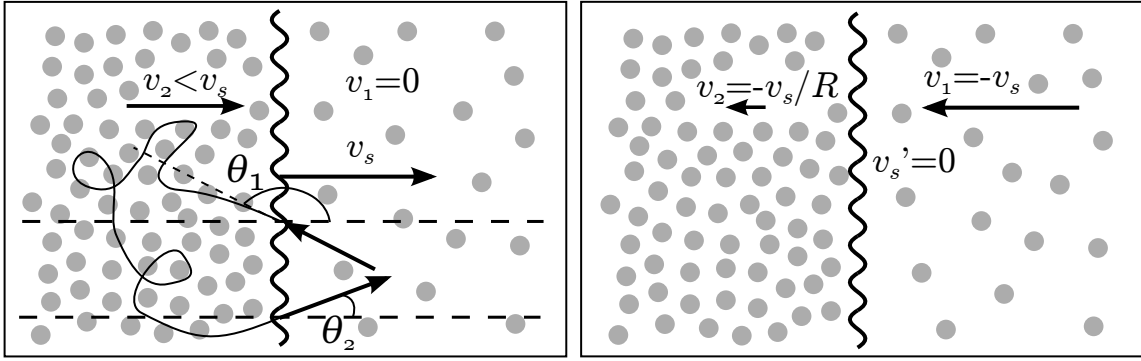


Figure 2.18: Sketch of the 1st order Fermi acceleration of a charged particle at a shock front. Left: In the laboratory frame. Right: In the shock rest frame.

side is always approaching and the collision is always head-on, so that energy is always gained on each crossing. This of course leads to a higher average energy gain [62], [63, pp. 153f.].

The treatment here is only valid for non-relativistic shocks ($v_s \ll c$), but can also be formulated for relativistic shocks [63, p. 153]. As the particle crosses the shock, one needs to Lorentz transform its initial lab system energy E_1 to E' . The particle is reflected after random scatterings, that conserve energy, and crosses the shock again. The energy E' is transformed back to the final lab system energy E_2 [44, p. 32]:

$$E' = \Gamma E_1 (1 - \beta \cos \theta_1), \quad E_2 = \Gamma E' (1 + \beta \cos \theta_2). \quad (2.33)$$

Here, $\beta = (v_2 - v_1)/c$ and $\Gamma = 1/\sqrt{1 - \beta^2}$. For the Lorentz transformations, the particle is assumed to be relativistic already, so that $E \approx pc$. The relative energy gain per cloud passage is, inserting Equation 2.33:

$$\epsilon = \frac{E_2 - E_1}{E_1} = \frac{(1 - \beta \cos \theta_1)(1 + \beta \cos \theta_2)}{1 - \beta^2} - 1. \quad (2.34)$$

To obtain the average energy gain $\langle \epsilon \rangle$ per cloud passage, one needs to determine the average scattering angles θ_1 and θ_2 , which are the angles between the vectors \vec{v} of the particle and \vec{v}_s of the shock. The angle distribution is the projection of an isotropic flux onto a plane [63, p. 152], so it is $\propto \cos \theta$, but the crossing rate is zero if the particle moves in the wrong direction. Thus, only $\cos \theta_1 < 0$ and only $\cos \theta_2 > 0$ contribute, so: [44, p. 36], [63, p. 152]

$$\langle \cos \theta_1 \rangle = \frac{\int_{-1}^0 \cos \theta_1^2 d \cos \theta_1}{\int_{-1}^0 \cos \theta_1 d \cos \theta_1} = -\frac{2}{3}, \quad \langle \cos \theta_2 \rangle = \frac{\int_0^1 \cos \theta_2^2 d \cos \theta_2}{\int_0^1 \cos \theta_2 d \cos \theta_2} = \frac{2}{3}. \quad (2.35)$$

Inserting this into Equation 2.34 yields

$$\langle \epsilon \rangle = \frac{(1 + 2/3\beta)^2}{1 - \beta^2} - 1 = \frac{1 + 4/3\beta + 4/9\beta^2}{1 - \beta^2} - 1 \approx \frac{4}{3}\beta = \frac{4}{3} \frac{v_2 - v_1}{c}. \quad (2.36)$$

Because of $\langle \epsilon \rangle \propto \beta$, this mechanism is called *1st order Fermi acceleration* and is more efficient than 2nd order Fermi acceleration. Using the equations of fluid dynamics, namely the conservation laws for mass, for momentum, and for energy, one can derive that for a stationary, steady shock, v_1 and v_2 in the

shock rest frame must satisfy: [44, pp. 34ff.], [63, p. 155]

$$R \equiv \frac{v_1}{v_2} = \frac{\kappa + 1}{\kappa - 1 + 2\kappa/M^2} \approx \frac{\kappa + 1}{\kappa - 1}. \quad (2.37)$$

Here, R is called the *compression ratio* of the shock, κ is the heat capacity ratio or adiabatic index, and M is the Mach number. The Mach number relates the shock velocity v_s to the speed of sound c_1 : $M = v_s/c_1$. For a shock to form, M must be > 1 . In Equation 2.37, we have used the strong shock limit $M^2 \gg 1$, since for typical SN shocks, $v_s \approx 10^4 \text{ km s}^{-1}$, and $c_1 \approx 10 \text{ km s}^{-1}$ [44, p. 37], [61]. For shocks created by a SN explosion, the surrounding gas will be ionized and therefore be mono-atomic [61]. For an ideal mono-atomic gas, $\kappa = 5/3$ and therefore $R = 4$ in the strong shock limit. Thus, in the shock rest frame, $v_1 = -v_s$ and $v_2 = v_1/R = -v_s/R = -v_s/4$. The velocity difference, $v_2 - v_1 = v_s(1 - 1/R)$, so it is $3/4 v_s$ for a mono-atomic strong shock.

If the relative energy gain per shock crossing is ϵ , then the particle's energy after n crossings is $E = E_0(1 + \epsilon)^n$, from which follows

$$n = \frac{\ln(E/E_0)}{\ln(1 + \epsilon)}. \quad (2.38)$$

However, n crossings are only possible if the particle did not escape from the shock front region, so with escape probability p_{esc} per crossing, the number of particles with an energy $> E$ is $N(> E) \propto (1 - p_{\text{esc}})^n$. It follows that

$$\ln N(> E) = k + \frac{\ln(E/E_0)}{\ln(1 + \epsilon)} \ln(1 - p_{\text{esc}}) \quad (2.39)$$

$$N(> E) \propto E^{-\alpha+1} \quad \text{with} \quad \alpha \equiv -\frac{\ln(1 - p_{\text{esc}})}{\ln(1 + \epsilon)} + 1 \approx \frac{p_{\text{esc}}}{\epsilon} + 1. \quad (2.40)$$

One can estimate that the escape probability is $p_{\text{esc}} = 4|v_2|/c = -4v_2/c$ [63, p. 154], [44, p. 37], so that:

$$\alpha = \frac{p_{\text{esc}}}{\epsilon} + 1 = \frac{4v_2/c}{4(v_1 - v_2)/(3c)} + 1 = \frac{3}{v_1/v_2 - 1} + 1 = \frac{3}{R - 1} + 1 = \frac{R + 2}{R - 1}. \quad (2.41)$$

For the mono-atomic strong shock case of $R = 4$, the differential spectrum is $\frac{dN}{dE} \propto E^{-\alpha}$ with $\alpha = 2$ [61], [44, p. 37], [63, p. 155].

Thus, 1st order Fermi, or shock, acceleration predicts a power-law energy spectrum, whose spectral index $\alpha = 2$ is independent of the details of the shock and is even close to the numerical value needed to explain the observed CR spectrum [63, p. 155], [44, p. 37]. This is why shock acceleration is the most widely accepted model for CR acceleration since decades. A major problem of shock acceleration is the ‘‘injection problem’’: A particle is required to already have velocities larger than thermal in order to be accelerated, because the particle must have enough energy to cross the shock front [62].

An energy spectrum $\propto E^{-2}$ is also commonly assumed for astrophysical neutrino signals, because the neutrinos produced at a CR acceleration site inherit it from the CRs. On the other hand, the spectrum could also be steepened by various effects [61], [44, p. 37].

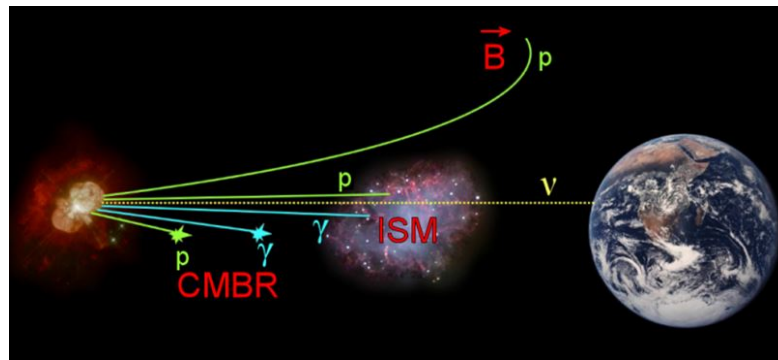


Figure 2.20: Sketch illustrating the advantages of neutrino astronomy, adopted from [67]. While protons (p) are deflected by magnetic fields (\vec{B}) and protons and photons (γ) are attenuated by cosmic microwave background radiation (CMBR) and matter of the interstellar medium (ISM), neutrinos (ν) are undisturbed on their way to the observer.

a high-energy source. For example, neutrino detection can be the tell-tale signal of a SN explosion or the acceleration of particles inside a jet. Simultaneous observations of the source with optical light can help to identify the source as a SN and provide its precise position. Optical spectra can further provide much more detailed information about the SN, e.g. the type of the SN and the conditions of the ejecta and the environment. In the case of multiple neutrino detections, the neutrino spectrum can in turn provide details about the interior of the jet where the neutrinos are produced [66], while X-rays can tell about hot gas. Combining signals from multiple messengers can also yield statistically more significant results. Even if each signal by itself is very faint and not distinguishable from noise or background, the combination of two or more signals can be. This is especially true for transient signals that only flare for a short period at a specific time.

Cosmic rays themselves, due to their charge, have randomized arrival directions because they are deflected by magnetic fields—except for extremely high energies $> 10^{19}$ eV, where statistics are limited [16, pp. 86f.]. Hence, CRs are not ideal messengers to reveal the sources of CR acceleration. Co-produced high-energy photons, i.e. γ -rays, are not deflected. However, γ -rays have a relatively large interaction cross-section and thus are easily absorbed by matter, as well as attenuated via $\gamma\gamma$ interactions with blackbody radiation, which is abundant in star forming regions [16, p. 86]. Consequently, only the surfaces of astronomical objects can be observed. Another disadvantage of γ -rays is that they can be produced by other high-energy processes that do not involve CRs, but high-energy electrons, for instance synchrotron radiation or inverse Compton scattering. In practice, distinction between γ -radiation from energetic hadrons (CRs) or leptons is difficult, since the spectral shapes can be quite similar [51].

At the highest energies, charged particles and photons have a limited free path in the Universe, because they interact with photons from the Cosmic Microwave Background (CMB) and lose their energy via the photoproduction of pions, giving rise to the GZK cutoff of CRs, and via pair production $\gamma\gamma \rightarrow e^+e^-$ [16, p. 87]. Therefore, just at the energies where the protons' directional information is conserved, the Universe becomes opaque for the protons and the observable Universe is limited. Photon-based astronomy has this fundamental limitation as well. Starting in the TeV range, only the local Universe is accessible and at 10^{15} eV, only our own Galaxy. Figure 2.19 shows the energy-dependent horizon for protons and photons.

As opposed to protons and photons, neutrinos do not have these disadvantages: They are not deflected, but also (almost) not attenuated. Neutrinos are produced only in hadronic processes, thus they are an unambiguous evidence for hadronic, i.e. CR, acceleration [65, p. 5]. Neutrinos penetrate even dense

environments and carry information directly from the place where they were created: the interior of regions where high-energy processes take place [16, p. 87], [68]. At the highest energies, neutrinos are the only particles allowing astronomy on a long distance range [44, p. 45]. Figure 2.20 illustrates the advantages of neutrinos as cosmic messengers. However, the big advantage of neutrinos, their penetrative power, is also their big disadvantage: Because of the miniscule cross-section, neutrinos are enormously difficult to detect and require huge instrumented volumes in order to be sensitive to faint signals [16, pp. 87f.]. This is why neutrinos have not been used extensively in astronomy in the past and only recently, detectors like IceCube start to observe and study astrophysical neutrinos.

Supernovae and Gamma-Ray Bursts as Transient Neutrino Sources

Since this thesis investigates neutrino signals from supernova explosions, some theoretical background on these objects is required, which is presented in this chapter.

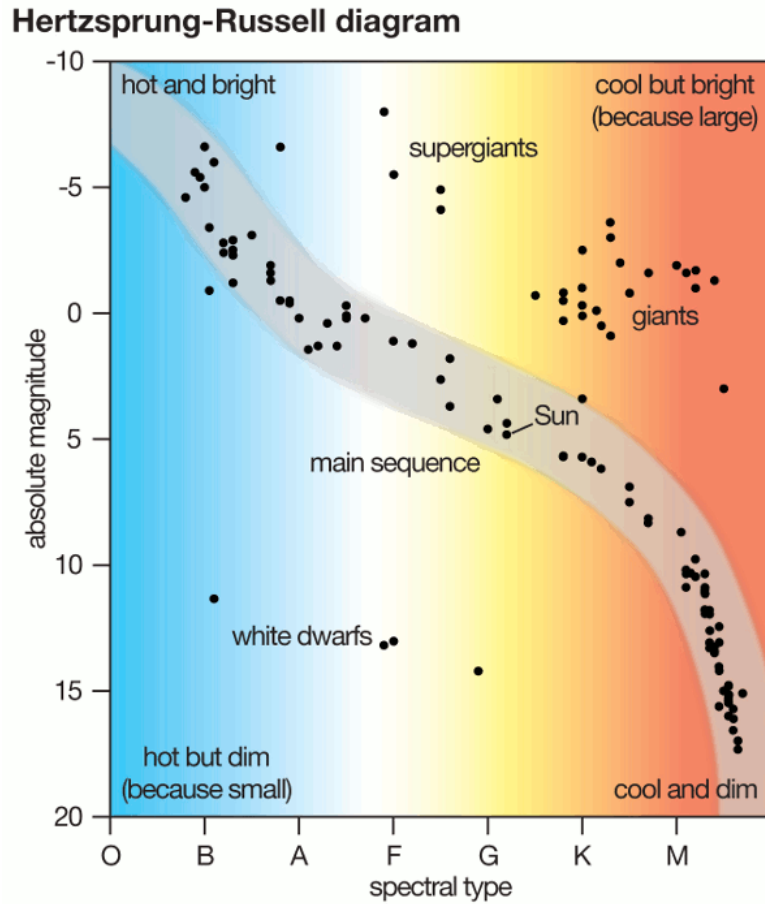
3.1 The Evolution of Stars

Stars are formed when interstellar gas, mostly hydrogen, contracts under the gravitational force [69, pp. 185–188]. The gas cloud becomes denser and hotter and starts to radiate as a *proto-star*. Eventually, the cloud's core becomes so hot that nuclear fusion processes start to combine hydrogen (H) into helium (He) nuclei, which happens at a critical temperature of 3×10^6 K [69, p. 189]. The released nuclear binding energy provides an energy source that counteracts the gravitational force of contraction via radiation pressure. The gas cloud finally stops contracting and becomes a stable star in hydrostatic equilibrium [69, pp. 188f].

Stars spend most of their lifetime on the *main sequence* (MS) of the Hertzsprung-Russell diagram (HRD), which is a scatter plot of the star's luminosity versus its surface temperature [69, pp. 190, 124]. Figure 3.1 contains a sketch illustrating an HRD. The MS is a roughly diagonal line in the HRD: Hotter stars on the HRD (having a blue color) have a higher luminosity than cooler stars (appearing with a red color). The position of a star on the MS determines not only its temperature and luminosity, but also its mass and its lifetime: Hot, blue, bright stars have higher mass and radically shorter lifetime [69, pp. 127f, 184]. The more massive a star is, the more gravitational contraction took place until the core's radiation pressure could balance contraction. Therefore, the core temperature is higher so that nuclear fusion occurs at a higher rate.

When all the H in the stellar core has been burned into He, the star leaves the MS [69, p. 190]. Deprived of an energy source, gravitational contraction of the core continues and the core is heated up. The shell surrounding the core, still containing H, is heated so much that H fusion initiates there. This creates a strong radiation pressure on the outer layers of the star. The star's radius increases enormously so that it cools down at the surface, but has increased luminosity. The star has turned into a *red giant* (upper right of the HRD). The core temperature becomes high enough for He fusion, about 10^8 K, which stabilizes the core, while shell H fusion continues [69, pp. 190–195].

If the star's mass is small, then the fusion ends with He fusion. After He fusion is finished, the core



© 2012 Encyclopædia Britannica, Inc.

Figure 3.1: Simplified sketch of a Hertzsprung-Russell diagram (HRD), which is a scatter plot of the luminosity (or absolute magnitude) versus the surface temperature (or spectral type) of stars. Smallest absolute magnitude corresponds to highest luminosity and spectral type O is hottest, M coolest. The evolution of stars can be visualized as trajectories within the HRD. From [70].

consists of mainly carbon and oxygen (C and O) and contracts and heats until it becomes a degenerate electron gas,¹ whose pressure can counteract gravity. Around the core remains a hydrogen-rich envelope and the star still appears as a red giant. Shell burning of He and H can still take place, depending on the star's mass. The outer layers expand and are completely blown away as a *planetary nebula*. The CO core remains inert and just cools down. It is called a *White Dwarf* (WD), because it is hot (white-blueish color), but very small (about the size of the Earth). As long as the WD mass stays below the Chandrasekhar mass limit of $\sim 1.4 M_{\odot}$, it is stabilized by the degenerate electron pressure, otherwise contraction continues [69, pp. 201, 203].

For a massive star of about $8 M_{\odot}$ and more [71, p. 6], [72, p. 5], the post-helium burning core can contract to become hot enough to burn C, and possibly O, Ne, Mg, and Si. In the core, where density and temperature are highest, the heaviest nuclei are fused, while there is an onion-like structure of shells

¹ A degenerate gas is an ensemble of particles in the quantum regime, so that the ensemble's state variables (pressure etc.) are governed by quantum mechanics instead of classical thermodynamics. It is the quantum analogue to the classical ideal gas.

around the core where lighter nuclei are fused.² The fusion of silicon (Si) to iron (Fe) is the ultimate end of the star's life, because ^{56}Fe is the most stable nucleus. Further fusion, creating heavier nuclei, does not release binding energy, but binding energy is required and removed from the core, which only accelerates the collapse [69, p. 174]. The Fe core is electron degenerate, but exceeding the Chandrasekhar limit [71, p. 2]. Therefore, the collapse of the core via gravitational contraction continues. Under the extreme pressure, the atomic nuclei fuse into a single giant nucleus, which is neutron degenerate and, analogous to electron degeneracy, the degenerate neutron pressure can withstand gravity, but only if the core does not surpass a mass limit. This is called the Oppenheimer-Volkoff limit of ca. $2 M_{\odot}$ to $3 M_{\odot}$, which is analogous to the Chandrasekhar limit. If the core stays below, it becomes a *neutron star* (NS), if it is above, it turns into a *black hole* (BH), a gravitational singularity [72, p. 5]. A NS is even smaller than a WD, about 10 km for a mass of $1 M_{\odot}$ [69, p. 205]. When the core of a massive star collapses, the shells around it also fall towards the center. If a NS is formed, then the shell material bounces off the rigid/incompressible core and is expelled into the outer layers of the star [69, p. 202]. This event leads to a *core-collapse supernova* (CCSN), a phenomenon that is frequently observed by astronomers. If however the core is a BH, then there can be no bounce-back, and the observational result is more speculative. Either, if the star is slowly rotating, the core-collapse might be hardly visible from outside and this is called a *failed SN* [74], [75, fig. 12]. Or, for fast rotation, this may lead to ultrabright supernovae (SNe), so-called *hypernovae*, and some gamma-ray bursts [72, p. 5], [75, fig. 12].

The bounce-back of the shell material during a CCSN is very violent, an enormous amount of gravitational energy—typically 10^{52} erg to 10^{53} erg, i.e. 10^{45} J to 10^{46} J—is released [69, p. 203], [72, p. 5], [15, p. 514]. About 99% of the total energy is released in form of neutrinos, which can escape relatively easily [72, p. 5], [71, p. 4]. Only about 1% is transferred into kinetic energy of the outer layers, but is still enough to eject the envelope with velocities between 5000 and 10 000 km s^{-1} [69, p. 203]. The star explodes and parts of its heavy-element core and of its outer shells are ejected into the interstellar medium [71, p. 2]. Most heavy elements in the Universe ($A \geq 12$) were ejected by a supernova (SN), important for the chemical evolution of galaxies, stars, planets, and life [71, p. 32], [15, p. 511].³ Only 0.01% of the released energy is electromagnetic radiation [72, p. 5]. And yet, within 20 to 30 days, the SN brightens by up to 20 magnitudes, showing luminosities of up to about $10^{10} L_{\odot}$ at peak, comparable to the luminosity of a whole galaxy [69, p. 203].

There is one SN process other than core-collapse: thermonuclear explosion, classified as SN of Type Ia. Here, a WD remnant gains mass, e.g. from a companion star in a binary star system where one star has already turned into a WD, until it reaches the Chandrasekhar mass limit. The WD starts to collapse, which initiates C and O-burning in the central degenerate C-O core. Because of the degeneracy, increased temperature does not lead to increased pressure. The result is a runaway explosion with almost the same energy output and peak luminosity each time, because the mass of the collapsing WD always equals the Chandrasekhar mass. This makes Type Ia SNe (SNe Ia) very valuable for distance measurements and cosmology [69, pp. 202f., 194].

² For example, at the end of a heavy star's life, the core contains mostly Fe, which cannot be fused with an energy release. Around the Fe core, there is a shell burning Si and other heavy elements. The next shell contains mostly O and some Ne, C, Mg, and Si. The next shell contains mostly He, and the outermost shell contains mostly H [15, fig. 15.6], [73, fig. 16].

³ For example, most iron atoms in our bodies originate from an SN [69, p. 204].

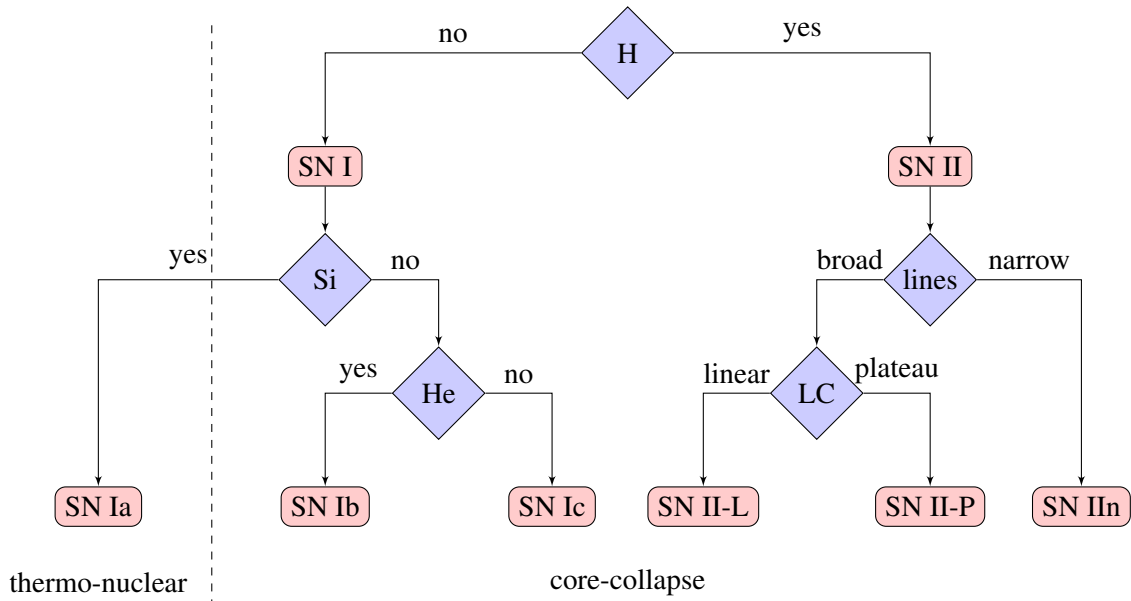


Figure 3.2: Overview of the conventional SN classification scheme.

3.2 Supernova Explosions

3.2.1 Supernova Spectra and Light Curves

SNe are classified according to properties of the spectrum, i.e. the electromagnetic emission as function of wavelength, and properties of the light curve (LC), i.e. the electromagnetic emission as function of time. Type I SNe contain no hydrogen lines in the spectrum, while Type II SN spectra have prominent hydrogen lines. SNe Ia are characterized by a Si π spectral line, while Types Ib and Ic do not have this line. SNe Ib spectra contain He I lines, while SNe Ic spectra do not [76, p. 3]. Figure 3.3 shows some example SN spectra of Types II, Ia, Ib, and Ic. Further classification within the SN II class is based mainly on the light curve. There are two main subtypes: SNe II-L (“linear”) have light curves that decay roughly linearly, resembling Type I light curves. SNe II-P (“plateau”) stay close to the maximum brightness for an extended period before decaying. Figure 3.2 visualizes the conventional classification scheme.

Concerning the physics, SNe Ia arise from the thermonuclear explosion of a WD reaching the Chandrasekhar mass, while all other types are the result of the core-collapse of a single massive star. If the SN is of Type II, then the SN progenitor star is a massive supergiant, which still had a hydrogen envelope. The WD progenitors of SNe Ia of course have no hydrogen envelope. The progenitors of Type Ib/Ic are massive supergiants, which expelled their hydrogen envelope (in the case of Ic even the helium shell below the hydrogen), e.g. Wolf-Rayet stars with extremely high stellar winds and mass loss rates [69, p. 204], [15, p. 515].

There is large variation in the class of Type II SNe, both in spectra and light curves, while the Type I light curves are broadly similar [76, pp. 3–5]. In general, most SN properties like the peak absolute magnitude vary across large ranges, with the exception of SNe Ia. This is because the exploding stars can have very different masses and radii, whereas for SNe Ia the mass and therefore the available energy is always fixed [69, p. 204], [76, p. 6].

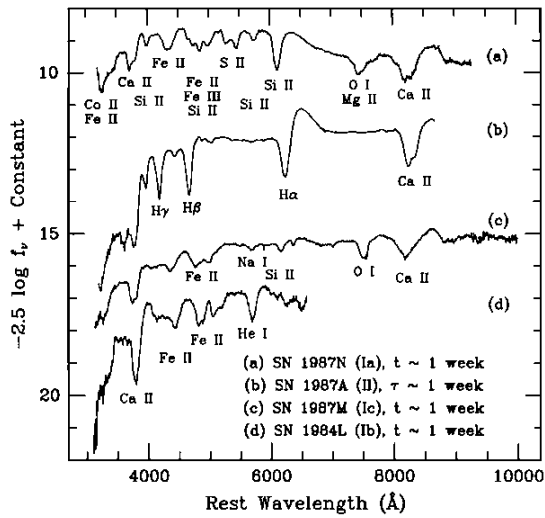


Figure 3.3: A few early-time (about 1 week after maximum brightness) SN spectra showing distinctions between the four major spectral types of SNe. From [76].

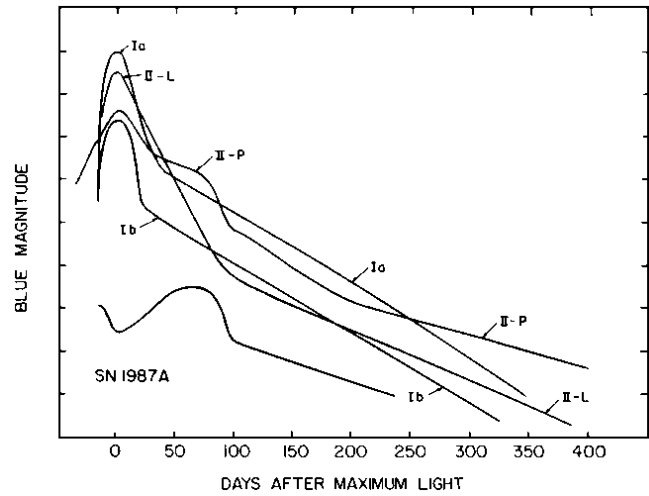


Figure 3.4: Schematic light curves for different SN types. The Ib curve also represents the Type Ic class as an average. From [76].

In a SN light curve, the initially increasing brightness is mainly due to expansion of the radiating surface, the *photosphere*, which is at the radius where the medium changes from opaque (optically thick) to transparent. At peak brightness, the optically thick envelope becomes transparent and deeper layers can shine through, the photosphere moves deeper [69, p. 204]. SNe Ia synthesize large amounts of radioactive isotopes, in particular of the nickel isotope ^{56}Ni . The prototypical SN Ia light curve is dominated by the decay chain $^{56}\text{Ni} \rightarrow ^{56}\text{Co} \rightarrow ^{56}\text{Fe}$. The released positrons and γ -rays thermalize and the energy is released as optical photons [77]. Because nickel ^{56}Ni has a shorter half-life of ~ 6 days, compared to ~ 77 days for cobalt ^{56}Co , the light curve is first dominated by a narrow luminosity peak from the quick nickel decay, building up the ^{56}Co , until the slower and dimmer cobalt to iron decay becomes visible [78]. This produces a change in the decline rate (a kink in the light curve). SN II light curves do not generally show the nickel-cobalt decay feature and have typically broader luminosity peaks, of the order of 100 days. SN luminosity decreases for about one year [15, p. 512]. At late times, more than 150 days after peak, most SN light curves resemble each other and have a decline rate close to $0.98 \text{ mag} (100.\text{d})^{-1}$ expected from cobalt decay [76, p. 7]. Some example SN light curves are displayed in Figure 3.4.

3.2.2 Supernovae Type IIn

There is an extra subclass of SNe II, which is a special case because it is not defined by the light curve behavior, but by the spectrum. This is the class of SNe Type IIn. SNe IIn are core-collapse SNe embedded in a dense circumstellar medium (CSM) that was ejected in a pre-explosion phase. Following the explosion, the SN ejecta plow through the dense CSM and collisionless shocks can form and accelerate particles, which may create high-energy neutrinos. This is comparable to a SN remnant, but on a much shorter time scale of 1 to 10 months, and is discussed in Section 3.2.7.

SNe IIn (“n” for narrow) are characterised by the presence of strong emission lines in the spectrum, most notably $\text{H}\alpha^4$, that have a narrow component sitting on a broad base. The centroid of the base is

⁴ The spectral lines of the Balmer series, the strongest optical lines of hydrogen, are denoted $\text{H}\alpha$, $\text{H}\beta$, $\text{H}\gamma$ and so forth, and

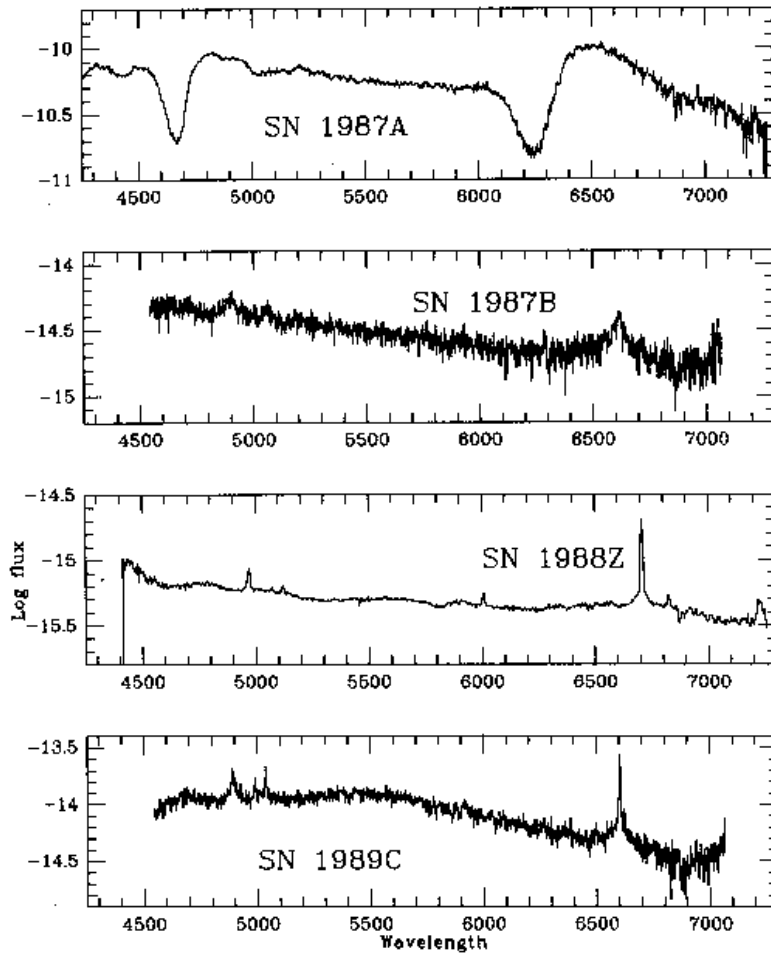


Figure 3.5: Three SN IIn spectra (the bottom three), in comparison to a SN II spectrum, which does not belong to the IIn class (SN 1987A, top). The very narrow lines, compared to the top spectrum, are apparent. From [79].

blueshifted relative to the narrow component. In addition to the strong hydrogen lines, there is continuum emission at blue wavelengths in the spectrum [76, 79]. See Figure 3.5 for plots of example spectra. The narrow line component is interpreted to originate from surrounding H II regions, and the generally slow spectral evolution implies the presence of a high-density CSM. The high-density CSM also suggests that the light curve has a plateau and that the SN stays bright for a longer time than usual [79].

Since interaction of the SN ejecta with the dense CSM can lead to the conversion of a large fraction of the ejecta's kinetic energy to radiation, SNe IIn are on average more luminous than other SNe II [80]. They generally fade quite slowly, can be visible for several years, and some belong to the most luminous SNe [76]. To give an example, SN 2006gy was at the time of discovery the most luminous SN ever recorded [81].

There is much diversity within the subclass of SNe IIn [76, 80], both spectroscopically and photometrically, which can be explained by a diversity of progenitor stars and mass loss histories prior to explosion [82]. The only property that all SNe IIn have in common is the existence of a dense CSM envelope. There are even indications of Type Ia SNe, i.e. WD explosions instead of core-collapse, embedded inside a hydrogen-rich CSM, called Type Ia SNe, which have spectra resembling Type IIn

correspond to transitions from the energy levels $n = 3$, $n = 4$, $n = 5$, and so on to the $n = 2$ level [69, p. 257].

spectra [83]. Recently, there have been observations of eruptions prior to SN IIn explosions associated with mass loss, which explain the existence of the dense CSM shells [84].

3.2.3 Theory of Core-Collapse Supernovae

Because the different classes of core-collapse supernovae (CCSNe) vary only in the properties of the star's envelope, the mechanism of the core-collapse is always the same and one theory can be applied to all CCSNe [15, p. 517]. According to models, e.g. described in [71], the process of stellar core-collapse is quite complex and physically diverse. All four known forces of nature are involved under very extreme conditions. There are several evolutionary stages of core-collapse according to [71, pp. 2–11] and [15, pp. 518–528], depicted in Figure 3.6:

1. *Initial phase of collapse, electron capture* (upper left panel of Figure 3.6): The collapse is initiated when the Fe core, which is stabilized by electron degeneracy, reaches the Chandrasekhar mass. Due to the electrons' high Fermi energy, electron capture on Fe nuclei and free protons is energetically favorable, so that neutron-rich nuclei are produced. Also, β -decay of many nuclei, and photo-disintegration of iron-group nuclei to α -particles and neutrons take place. These processes remove energy from the core and reduce the electron density and pressure. As a consequence, the collapse is accelerated. Neutrinos from the electron captures can still escape and carry away energy.
2. *Neutrino trapping* (upper right panel of Figure 3.6): The inner core density reaches $\rho_c \approx 10^{12} \text{ g cm}^{-3}$, high enough so that neutrinos can hardly escape.
3. *Bounce and shock formation* (mid-left panel of Figure 3.6): Nuclear densities are reached, $\rho_c \approx 10^{14} \text{ g cm}^{-3}$. The nuclear matter is much less compressible and has a higher pressure, so that the still collapsing outer core bounces at the nuclear matter. A shock wave moves through the outer core.
4. *Shock propagation, ν_e burst, shock stagnation* (mid-right panel of Figure 3.6): As the shock propagates through the outer core, it dissociates heavy nuclei into free protons and neutrons. On the free protons, electron capture happens at an increased rate. Most protons are transformed into neutrons and a huge number of electron neutrinos is produced via



This is called *neutronization* or *deleptonization*. The neutrinos can leave the star quickly in a short ν_e burst at shock breakout and carry away energy. The shock loses so much energy in the dissociation and deleptonization that it stalls at a radius of 100 km to 200 km and matter continues falling inward. The prompt shock is not strong enough to stop the collapse and explode the outer shells of the star.

5. *Neutrino heating, explosion* (lower left panel of Figure 3.6): A compact remnant, the proto-neutron star (PNS), forms at the center of the star by accretion of infalling material. It will evolve to a NS or a BH, depending on whether the star's initial mass lies below or above roughly $25 M_\odot$. The PNS contains a large number of trapped pair-produced neutrinos that diffuse out to a "neutrinosphere", a layer where the medium becomes transparent for neutrinos, within a fraction of a second. The neutrinos carry most the energy from the gravitational collapse and deposit a

few percent of it⁵ in the gain layer between the PNS and the stalled shock front, mainly by CC neutrino captures,



This neutrino heating increases temperature and pressure behind the shock, drives the shock outwards again and eventually leads to the SN explosion. This is called *delayed neutrino-heating mechanism*, as opposed to the *prompt mechanism* of the stalling shock.

6. *Neutrino cooling and neutrino-driven wind* (lower right panel of Figure 3.6): The hot interior of the PNS is cooled by neutrino-pair production and diffusive loss of all three lepton flavors. After several tens of seconds, the PNS becomes transparent to neutrinos and the neutrino luminosity drops significantly.

The strong neutrino heating creates a baryonic outflow from the surface of the hot neutron star, the *neutrino-driven wind*, which is in the beginning strongly heated by neutrinos and dissociated into free protons and neutrons. Simulations show that early ejecta are proton-rich and later ejecta may become neutron-rich by $\bar{\nu}_e$ absorption on free protons. This potentially leads to r-process nucleosynthesis, i.e. production of atomic nuclei by rapid neutron capture, as opposed to slow neutron capture nucleosynthesis during the lifetime of the star (s-process). The expanding matter cools and nucleons recombine to α -particles, some of which can later assemble to very heavy elements beyond iron [71, pp. 34–38], [85].

CCSN models are very complex and there are several open questions and problems with model calculations and simulations. The most severe problem is that most modeled SNe do not explode. In 1D simulations, the explosion is only successful if the neutrino luminosities are enhanced by (debated) convective processes in the PNS below the neutrinosphere, or if the SN progenitor mass was $8 M_\odot$ to $10 M_\odot$ initially [71, pp. 5f.]. 2D and 3D models show that the heated layers have very strong convection that enhances the neutrino-energy deposition. But only for a $11.2 M_\odot$ star, this led to an explosion. More massive progenitors have much higher densities that damp the shock expansion [71, p. 9]. The explosion of those stars might involve other effects of 3D hydrodynamics or of rapid rotation and magnetic fields [71, p. 1].

3.2.4 Low-Energy Neutrinos from Core-Collapse Supernovae

Because they are optically thick, CCSNe emit 99% of the released gravitational energy as neutrinos, whereas SNe Ia emit most of the released thermonuclear energy as kinetic energy of the outer shells [86]. This means that CCSNe are much more interesting for neutrino physics [15, p. 514]. The CCSN neutrinos have 10 MeV energy on average and are detectable on Earth, if the SN is not too far away [15, pp. 514, 517]. With current detectors, only SN neutrinos from within our Galaxy and the Magellanic Clouds are detectable.

During phase 1 (initial collapse, electron capture, upper left panel in Figure 3.6) and 2 (neutrino trapping in inner core, upper right panel in Figure 3.6), only ν_e neutrinos are produced from electron capture that have a non-thermal spectrum with average energy growing from 12 MeV to 16 MeV. For a total SN explosion energy of $\sim 3 \times 10^{53}$ erg, the neutrino luminosity reaches about 10^{53} erg s⁻¹, but only for less than 10 ms so that about 10^{51} erg are released before the core bounce [15, p. 521].

⁵ 10% to 20% of the radiated ν_e and $\bar{\nu}_e$ energy within a few 100 ms is sufficient, being less than 1% of the total gravitational binding energy lost in neutrinos in the entire core-collapse.

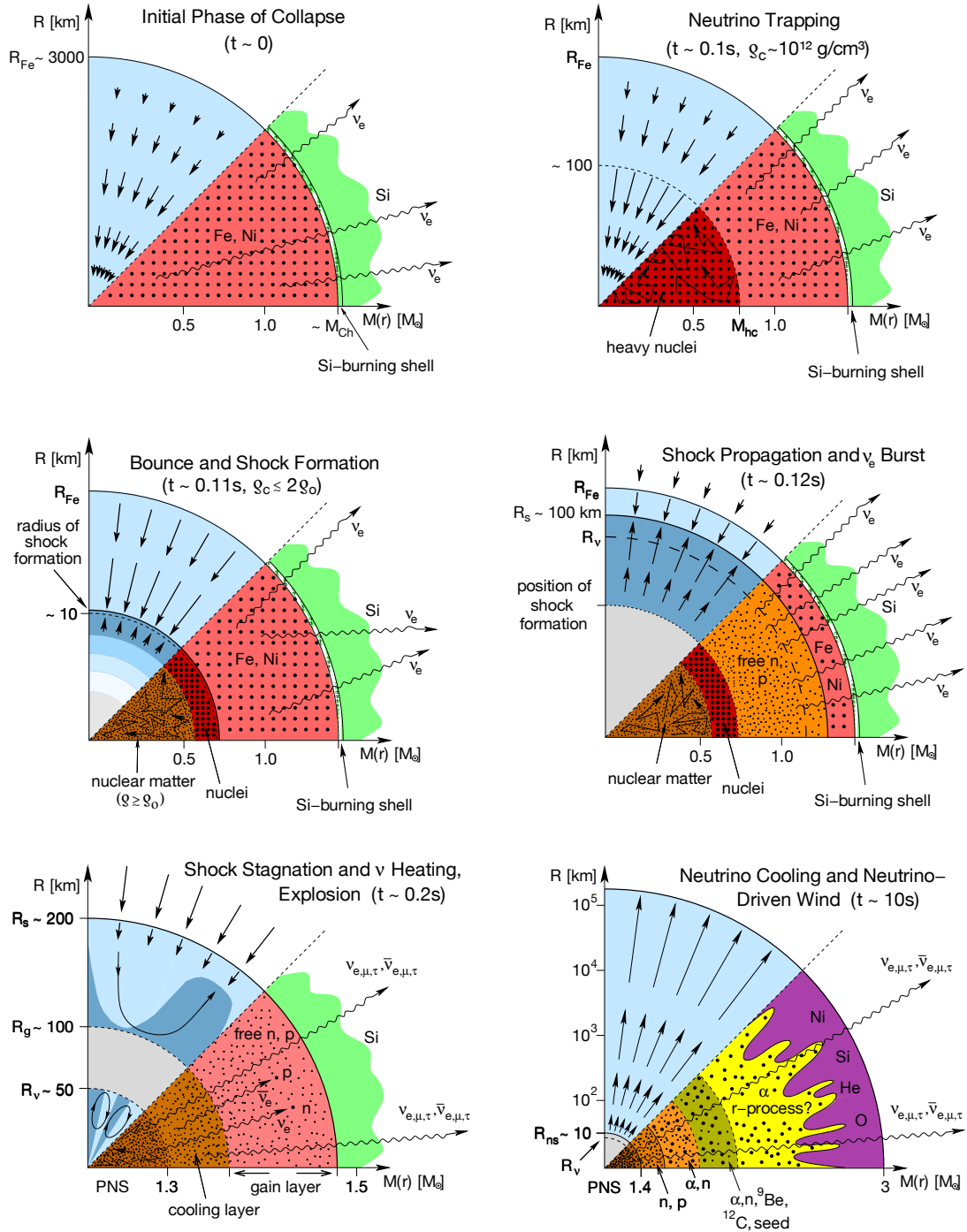


Figure 3.6: Schematic overview of the evolutionary stages of stellar core-collapse. In each panel, the upper half shows the dynamical conditions with arrows representing velocity vectors. The nuclear composition and nuclear processes are indicated in the lower half. The horizontal axis gives mass information, e.g. M_{Ch} indicates the Chandrasekhar mass. The vertical axis shows radii, e.g. R_s , R_ν , and R_{ns} are the shock radius, the neutrinosphere, and the neutron star radius. From [71, p. 3].

In phase 4 (ν_e burst, mid-right panel in Figure 3.6), the prompt *neutronization burst* is emitted. Again, purely ν_e are produced. The neutrinos pile up behind the dense, opaque shock and are finally released, at shock breakout when the shock density becomes low enough, a few milliseconds after the bounce. A few 10^{51} erg are released within a few milliseconds, which is only a small part of the total released neutrino energy. Even though the neutrino luminosity is at its maximum, the phase lasts only shortly and only the low-density periphery of the PNS is neutronized [15, p. 522].

During phase 5 and 6, the interior of the PNS has a temperature corresponding to an energy of ~ 40 MeV. Thermal neutrinos of all flavors are pair-produced inside the PNS by various processes, e.g. electron-positron annihilation:

$$e^- + e^+ \longrightarrow \nu + \bar{\nu}, \quad (3.3)$$

but also electron-nucleon bremsstrahlung, nucleon-nucleon bremsstrahlung, plasmon decay and scattering of photons on electrons. Additionally, electron neutrinos are produced by electron capture on protons ($e^- + p \rightarrow n + \nu_e$) and electron anti-neutrinos by positron capture on neutrons ($e^+ + n \rightarrow p + \bar{\nu}_e$). In the extreme high densities ($\sim 10^{14}$ g cm $^{-3}$), even neutrinos with their weak interactions are trapped. Only at a radius where the density drops to $\sim 10^{11}$ g cm $^{-3}$, the neutrino mean free path becomes larger than the core radius and they can stream out. This radius is called the *neutrinosphere*, in analogy to the photosphere. Neutrino interaction probabilities are energy and flavor dependent, so the neutrinosphere lies at a different radius for each species, between about 50 and 100 km. Each neutrinosphere produces a thermal black-body flux of neutrinos at the respective energy. Because they can interact also via the charged current, dominantly via the transformation of protons and neutrons in Equation 3.2, the neutrinosphere radius is larger for electron flavor neutrinos than for the other flavors. It is even larger for ν_e than for $\bar{\nu}_e$, because the medium is neutron-rich, so that ν_e interact more often. A smaller neutrinosphere radius is reflected in a higher average energy, because the neutrinos are in thermal equilibrium with the medium and the medium is hotter at deeper layers [15, pp. 522–525]. Figure 3.7a shows numerical simulation results of the time evolution of the neutrino emission, the “neutrino light curve”, as well as the average neutrino energy over time, for ν_e , $\bar{\nu}_e$ and the other species $\nu_x = (\nu_\mu, \nu_\tau, \bar{\nu}_\mu, \bar{\nu}_\tau)$ (which all have the same light curve and energy spectrum).

Most neutrinos emitted from the CCSN are thermal, i.e. emitted from a system in thermodynamic equilibrium. Thus, the neutrino energy spectrum should follow the theoretically expected Fermi-Dirac distribution⁶

$$\frac{dN}{dE_\nu} \propto \frac{E_\nu^2}{1 + \exp(E_\nu/T - \eta)}, \quad (3.4)$$

where E_ν is the neutrino energy, T the temperature, and η a free parameter. However, it turns out that the neutrinos are not quite thermal and different analytical forms represent the numerically derived spectra better, especially at low and high energies [88, 89]. One often used function was first given by Keil, Raffelt and Janka (KRJ) in [88, eq. 14], and refined in [90, eqs. 5.9, 5.10] and [89, eq. 6]

$$\frac{dN_\nu}{dE_\nu} = \frac{(1 + \beta)^{1+\beta} L_\nu}{\Gamma(1 + \beta) \langle E_\nu \rangle^2} \left(\frac{E_\nu}{\langle E_\nu \rangle} \right)^\beta \exp\left(-(1 + \beta) \frac{E_\nu}{\langle E_\nu \rangle} \right), \quad (3.5)$$

with $\langle E_\nu \rangle$ being the average neutrino energy, β the pinching parameter that controls the width of the spectrum, Γ the Gamma function, and L_ν representing the total energy released in a specific neutrino flavor (not the luminosity!). The three parameters $\langle E_\nu \rangle$, β , and L_ν can be obtained by fitting Equation 3.5

⁶ The Fermi-Dirac distribution describes the energy distribution of a system of fermions in thermodynamic equilibrium, in the quantum regime where the average distance between particles is close to their de Broglie wavelength. Due to the high density, this is the case here.

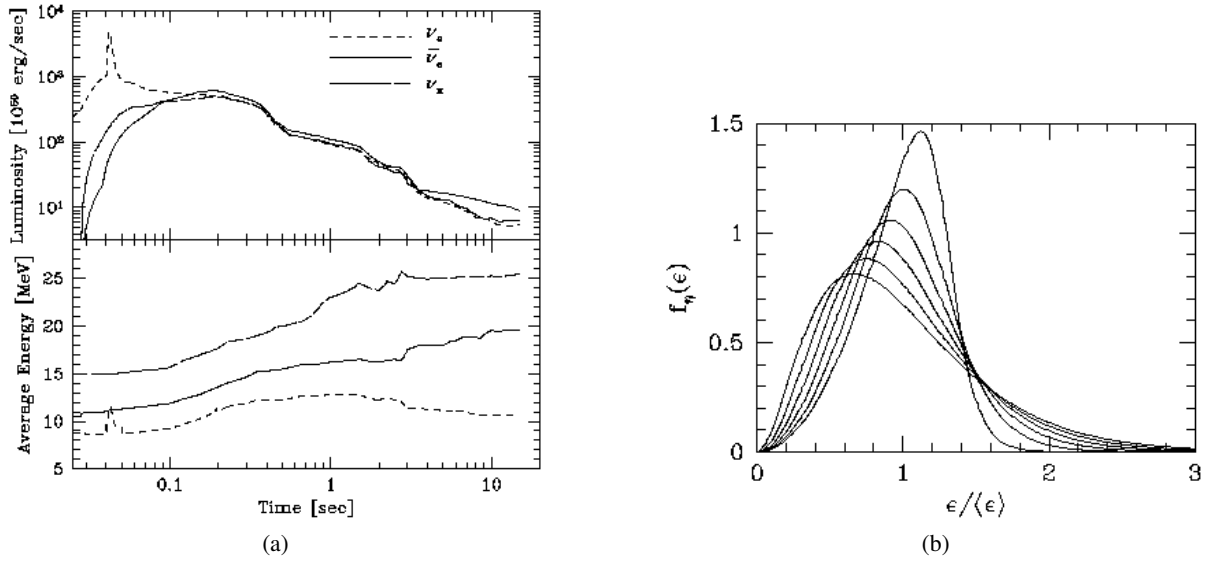


Figure 3.7: CCSN neutrino simulation results. (a) The neutrino light curve: Neutrino luminosity and average energy as function of time, obtained from numerical simulation. Time starts at the onset of the collapse. The neutronization burst is visible between 40 ms and 50 ms after collapse. The core bounce happened 3 ms to 4 ms before the neutronization burst. From [87]. (b) The analytic approximation of the neutrino energy spectrum in Equation 3.5, for different values of the pinch parameter β , as function of $E_\nu/\langle E_\nu \rangle$. From [88].

to numerical neutrino spectra, as done in [89]. The average neutrino energies are about

$$\langle E_{\nu_e} \rangle \approx 10 \text{ MeV}, \quad \langle E_{\bar{\nu}_e} \rangle \approx 15 \text{ MeV}, \quad \langle E_{\nu_x} \rangle \approx 20 \text{ MeV}, \quad (3.6)$$

but differ from model to model [15, p. 525]. Figure 3.7b shows the shape of Equation 3.5 for different values of the pinch parameter β .

The first (and so far only) observation of CCSN neutrinos happened in 1987 from SN 1987A. Because of its importance, the next section is dedicated to this detection.

3.2.5 Supernova 1987A

On 23 February 1987 at 7:35 UT, SN 1987A exploded in the Large Magellanic Cloud, a satellite galaxy of the Milky Way, at a distance of only ≈ 50 kpc from Earth [91]. It has been the only SN observed during the age of modern astronomy that occurred within either our Galaxy or one of its satellites like the Magellanic Clouds. In fact, the last recorded galactic SN before it was so-called Kepler's SN in 1604 [92], a Type Ia SN [93] which occurred in the Milky Way itself. SN 1987A was close enough that it also led to the first detection of neutrinos from outside our solar system, and it still remains the only detection of neutrinos from a SN.

SN 1987A is one of the most thoroughly studied objects outside the solar system and has been observed at all wavelengths from radio to γ -rays [91]. It was a peculiar subluminal Type II core-collapse SN [94, 95] with unusually high velocities in the spectral lines and anomalously rapid spectral and photometric evolution [91, 95], indicating that its atmosphere was more compact than expected for a usual red supergiant SN progenitor star [91]. In fact, contrary to the canonical CCSN models, 1987A's progenitor star *Sanduleak -69 202*, of which pre-explosion magnitudes, colors, and spectra exist [91], was a blue, not a red supergiant [95] with a mass of about $20 M_\odot$ [91], and there is evidence that the

progenitor was a binary system [96]. Its peculiarity might be related to its low metallicity and, being intrinsically faint ($M_V \approx -15.3$ at maximum [95]), the SN 1987A class might be rather common, however mostly going undetected except for very close explosions [95]. SN 1987A's progenitor being a compact blue supergiant, with smaller radius and higher density than red supergiants, one can understand its low luminosity, as more of the thermal energy from the shock wave is converted to kinetic energy of expanding matter before it can escape as radiation [91].

Albeit looking different on the surface, the core evolution of SN 1987A was likely very typical for core-collapse SNe [91]. Also the neutrino detection was in accordance with the canonical core-collapse models [95], in spite of the visual differences. Neutrinos from SN 1987A were detected in the water tank Cherenkov detectors Kamiokande II (KII) [97] in the Kamioka mine, Japan, and Irvine-Michigan-Brookhaven (IMB) [98] in the Morton-Thiokol salt mine near Fairport, Ohio, USA. A claimed detection in the Liquid Scintillator Detector (LSD) at Mont Blanc Neutrino Observatory is most likely spurious, due to the wrong timing of the events [91]. The Baksan liquid scintillator detector at Mount Andrychi, Russia, might have detected neutrinos from the SN, even though the published 6 events are one order of magnitude above the expectation, given the low effective volume of 280 tons [91, 99]. However, a more recent analysis properly takes into account the detector background and demonstrates consistency of 5 Baksan events with the data from the other detectors [99]. KII, with a fiducial mass of 2140 tons, detected 12 (perhaps 16) events associated with the SN, IMB 8 events with an effective mass of about 5000 tons for this search [91, 99]. The neutrino events with reconstructed electron energies between about 5 and 40 MeV occurred over an interval spanning 12 (perhaps 24) seconds and their time and energy distributions are visualized in Figure 3.8.

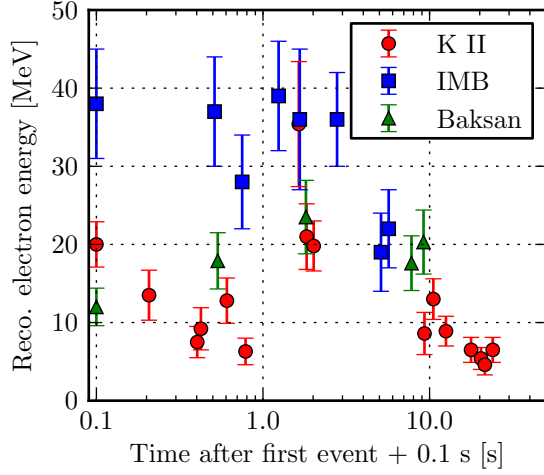
Even though only about two dozen of the estimated $\sim 10^{28}$ neutrinos that streamed through Earth were detected, they still delivered very relevant information [99, p. 1]. Comparisons of the SN 1987A neutrino signal with theoretical predictions showed that the general features of CCSN theory (see Section 3.2.3) are compatible with the observation [15, p. 533]. In particular, an extensive statistical analysis in [99], taking into account the energy-dependent efficiencies, backgrounds, and dead times of the detectors, found that there are two components in the neutrino signal:⁷ a brief (~ 1 s) soft component similar to that expected from the early phase after the core bounce, while matter is accreted onto the PNS and the shock stalls (phase 5 in Figure 3.6), and a long time scale (~ 10 s) harder component from thermal neutrino cooling of the PNS, after the shock has been revived by neutrino heating (phase 6). This indicates a *delayed* SN explosion, because in the *prompt* explosion, the shock does not come to a halt and only one component would be seen. The authors of [99] conclude that the delayed explosion models are about 100 times more probable than the prompt explosion models. The inferred average $\bar{\nu}_e$ energy, 15 MeV, also agrees well with model predictions [99], [15, p. 533]. Unfortunately, the neutrino data are too sparse to obtain more detailed information on the SN mechanism [15, p. 533], [99, p. 29].

Apart from the core-collapse itself, SN neutrinos can also help to constrain fundamental properties of neutrinos, for instance neutrino mass. With model-dependent assumptions, the strongest limit on neutrino mass from SN 1987A was [99]

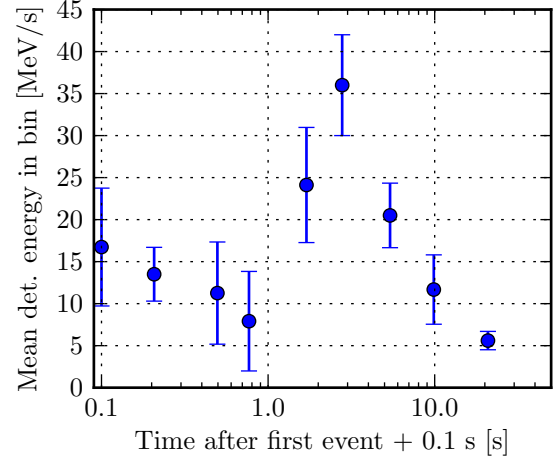
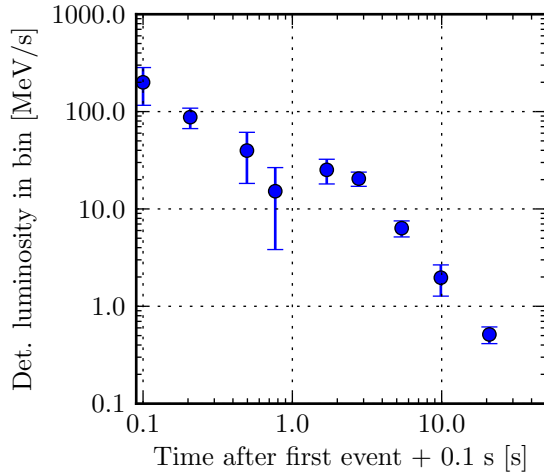
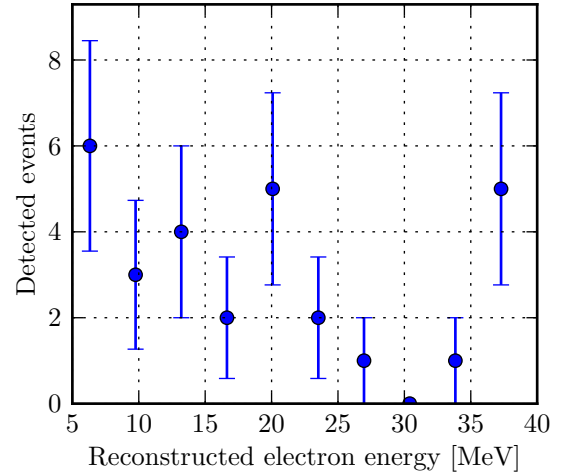
$$m_{\bar{\nu}_e} < 5.7 \text{ eV} \quad (95\% \text{ C.L.}). \quad (3.7)$$

Other physics results from the SN 1987A neutrino observation include tests of special relativity [100] and constraints on exotic particles like axions [101].

⁷ This is even visible in the much less sophisticated Figure 3.8 (b).



(a) Measured individual event energies over time.


 (b) Error weighted mean measured energy within bins of width 0.233 in $\log_{10}(t)$.

 (c) Measured luminosity (error weighted mean energy per time) within bins of width 0.233 in $\log_{10}(t)$.


(d) Distribution of reconstructed electron/positron energy.

Figure 3.8: Measured times and energies of the neutrino events attributed to SN 1987A, the so far only SN neutrinos ever observed. Panel (b) may be roughly comparable to Figure 3.7a (bottom), even though the energy-dependent detector efficiency is not taken into account so that there is a bias towards higher energy. Accordingly, panel (c) might be compared to Figure 3.7a (top) and panel (d) to Figure 3.7b, with the same caveat. Data taken from [91].

3.2.6 Supernova Rates

Even though SN explosions are rare in our Galaxy, about 1–3 CCSNe per century [102], they are not uncommon in the Universe due to its vast size. On average, there is about one CCSN somewhere in the observable Universe each second [103].

CCSNe occur at the deaths of massive stars with $8 M_{\odot}$ and more, which have very short lifetimes of only 30 Myr and less, compared to time scales of cosmological evolution on the order of Gyr.⁸ Therefore, the SN rate (the death rate of massive stars) is expected to be proportional to the star formation rate (the birth rate of stars). The star formation rate (SFR) is usually obtained by multiplying the observed galaxy luminosity with a certain calibration factor. The SFR can be converted to CCSN rate, using the mass distribution of new-born stars, the so-called initial mass function (IMF) [105].

Direct measurements of the CCSN rate in the redshift range $0 \leq z \leq 1$, using the number of observed SNe in surveys, are about a factor of two smaller than the rate that is derived from the SFR [105]. This implies that about one half of the SNe are missed because they are dim, either intrinsically or by obscuration. This has been called the “supernova rate problem” [105, 106]. Figure 3.9 shows several measurements of the SN rate and the SFR predictions. At redshift $z = 0$ (i.e. in our nearest neighborhood), the observed volumetric CCSN rate amounts to $\sim (0.71_{-0.18}^{+0.19}) 10^{-4} \text{ yr}^{-1} \text{ Mpc}^{-3}$ [105, tab. 1], based on results from the Lick Observatory Supernova Search (LOSS) [107, tab. 10]. Towards $z = 1$, the rate increases by about one order of magnitude. The observed SN rate differs from the SFR predictions by a factor ~ 2 consistently across all redshifts, from $z = 0$ to $z = 1$, for all measurements. In contrast to the general lack of SN explosions, the nearest neighborhood of the Milky Way, within a radius of ~ 10 Mpc, shows a slight overdensity of SNe, caused by a local overdensity of galaxies [108], see Figure 3.10.

Type Ia SNe occur less frequently than CCSNe, but are often over-represented in SN surveys because they are on average brighter. Their rate at $z = 0$ is estimated to be $\sim (0.30 \pm 0.06) 10^{-4} \text{ yr}^{-1} \text{ Mpc}^{-3}$ by the LOSS survey [107, tab. 10, fig. 21].

Some observational difficulties, such as dust obscuration, complicate the measurement of the SN and star formation rate. Including only data, for which dust obscuration has been taken into account, the SN rate problem is still present, but the ratio of SFR-inferred to observed SN rate has large uncertainties $\sim 1.8_{-0.6}^{+1.6}$ and is statistically consistent with no SN rate problem as well [106]. Hence, the SN rate problem is merely a hint towards a large fraction of massive stars not exploding as luminous SNe. Recent modelling of stellar rotation also suggests different luminosity calibration factors, resulting in up to $\sim 30\%$ smaller SFR estimates [109].

On the other hand, the theory of CCSNe in fact predicts the existence of intrinsically faint or completely dark SNe that arise from the collapse of an oxygen-neon-magnesium (ONeMg) instead of an iron (Fe) core (on the low mass end between 8 and $10 M_{\odot}$), and from the formation of a BH remnant in case of failed SNe (for progenitor masses $> 25 M_{\odot}$). A significant fraction of faint or dark SNe solves the SNP: The SFR-inferred to observed ratio becomes $\sim 1.1_{-0.4}^{+1.0}$ [106].

The distinction between dust obscuration and intrinsically faint SNe can be challenging using only photon observations. Neutrinos would enable an unobscured view on the SNe so that the effect of dust is excluded and the local SN rate is measured in a less biased way. Neutrino detectors also have the advantage of observing the entire sky, instead of a limited field of view. Furthermore, neutrinos are emitted from failed SNe with about the same total energy, but individual neutrinos are more energetic than those from regular SNe. Also, ONeMg SNe might be identified, because their neutrino flux and energies are diminished. Thus, neutrinos could provide a smoking gun signal of failed and/or ONeMg SNe. This can be done by detecting Supernova Relic Neutrinos (SRNs), i.e. the accumulated isotropic

⁸ For example, the travel time for light from a SN at redshift $z = 0.5$ is about 5 Gyr, so one looks back in time several Gyr already for a redshift below $z = 1$. [104, fig. 1]

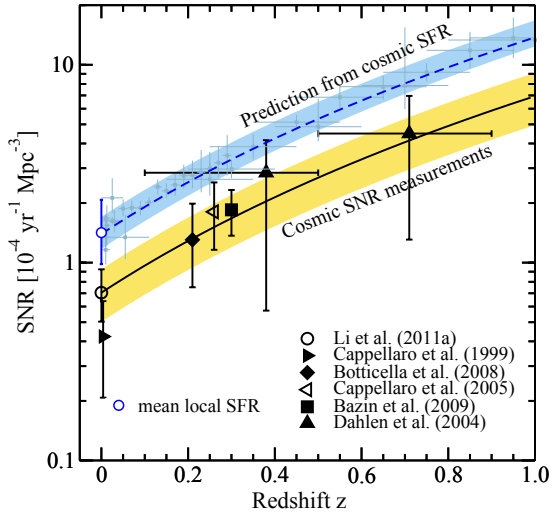


Figure 3.9: The rate of CCSNe (all types of optically luminous core-collapses, including Type II and Type Ibc) for the redshift range from 0 to 1. The lines represent fits to the SFR and SNR data. The yellow SNR band represents the uncertainty band from the LOSS measurement ([107] and called Li et al. (2011a) in the plot). Modified from [105].

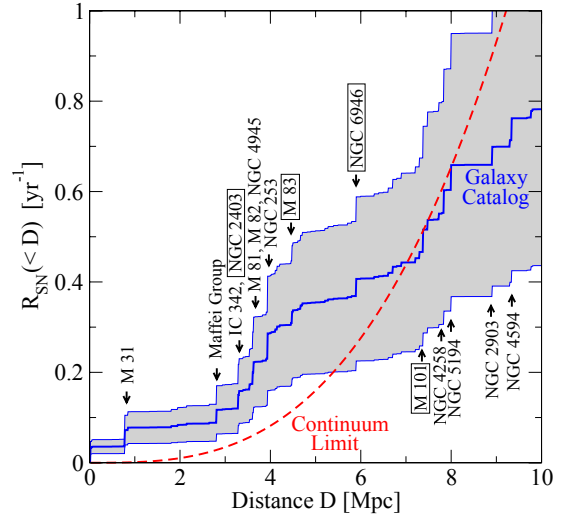


Figure 3.10: The cumulative CCSN rate as function of distance. The dashed line represents the local rate at $z = 0$ for an average volume, derived from dust-corrected SFR measurements, corresponding to a volumetric rate of about $1.6 \times 10^{-4} \text{ yr}^{-1} \text{ Mpc}^{-3}$. The stepped line (with uncertainty) is based on the SFR for individual galaxies in the particular volume around the Milky Way. Some galaxies are indicated, and those in boxes have especially high optical SN rates. Taken from [108]. In [108], it is noted that the stepped SN rate is probably underestimated by a factor of about 3, suggested by a dramatic increase of nearby SN discoveries in recent surveys.

flux from all past CCSNe. The SRN is a global average of all CCSN explosions and the detection rate and spectrum might reveal a failed and/or ONeMg SN component. This option is explored in [106]. Another option is the detection of individual SN mini-bursts of about 10 neutrinos, as explored in this work in Chapter 5. Neutrinos from individual failed SN neutrino bursts can be distinguished both by their higher average energy and by their shorter time interval ≤ 1 s, compared to ~ 10 s for regular CCSNe [106].

3.2.7 High-Energy Neutrinos from Supernovae Type IIn

Type IIn SNe presumably occur when a SN is embedded in one or more dense shells of circumstellar material (CSM), see Section 3.2.2. The collisions of the SN ejecta with the CSM shells is a potential cosmic ray (CR) accelerator, generating high-energy protons and other nuclei. If enough energy goes into CRs, then neutrinos in the TeV energy range are expected to be produced, alongside GeV–TeV γ -rays, over an interval of about 1 to 10 months. This neutrino source class emits on an intermediate time scale between short transient bursts from GRBs and jet-SNe (on the order of seconds; see Sections 3.2.8, 3.3) and long-term persistent emission from SN remnants (over hundreds or thousands of years). Compared to long GRBs (see Section 3.3), the local rate of IIn-like objects may be $\sim 10^{3-4}$ times larger, perhaps even more if there are undiscovered subluminal versions [110]. The model introduced in this section is described in the paper [110] by Murase et al.

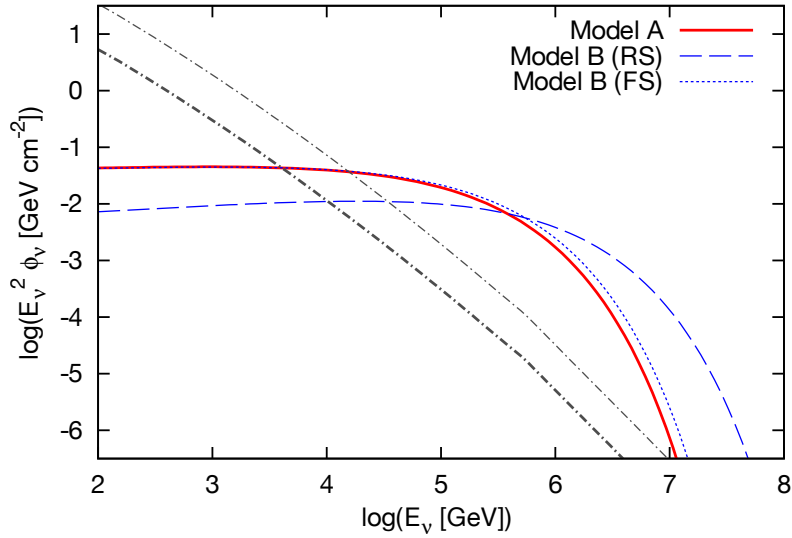


Figure 3.11: Fluences (time-integrated fluxes) of neutrinos from SNe IIn at a distance of 10 Mpc according to the model from [110]. It is assumed that 10% of the SN ejecta’s kinetic energy goes into CR acceleration, and 0.3% of the energy goes into magnetic fields. Model A emits over an interval of $\Delta t = 10^7$ s, and Model B over $\Delta t = 10^{7.8}$ s. The fluence from the background of atmospheric neutrinos within a radius of 1° is shown as black dash-dotted lines, thick for Model A, thin for Model B. This figure is fig. 1 in [110].

After the explosion of an SN IIn, the SN ejecta of mass M_{ej} crash into a CSM shell of mass M_{sh} . This collision leads to the formation of a pair of shocks: a forward and a reverse shock. The ejecta are decelerated by dissipation of kinetic energy into internal and kinetic energy of the shocked shells. If the CSM shell is massive, $M_{\text{sh}} \gtrsim M_{\text{ej}}$, then deceleration and dissipation are significant. Otherwise, the shock dynamics are still the same, but the dissipated energy is scaled down by a factor $M_{\text{sh}}/(M_{\text{sh}} + M_{\text{ej}})$. Large fractions of the kinetic energy (10%–100%) can also go into magnetic fields, and thus CRs via Fermi acceleration. If SN remnants produce the flux of Galactic CRs, then one would expect about 10% of the ejecta energy to go into CRs. Similar particle acceleration may be expected for the SN-CSM interaction of IIn SNe. If the Thomson optical depth is $\tau_T \lesssim 1 - 10$, the shocks can be *collisionless* and one may expect acceleration of CRs. Otherwise, the shock is decelerated by radiation (the shock is *radiation-mediated*) and the energy does not go into the magnetic field [110].

In the Murase et al. paper, two representative cases of CR acceleration at SN-CSM collisions are

Quantity	n_{sh}	R_{sh}	ΔR_{sh}	M_{sh}	E_{ej}	v_{ej}
Model A	10^{11} cm^{-3}	$10^{15.5} \text{ cm}$	$10^{15.5} \text{ cm}$	$1 - 30 M_\odot$	10^{51} erg	10^4 km s^{-1}
Model B	$10^{7.5} \text{ cm}^{-3}$	$10^{16.5} \text{ cm}$	$10^{16.5} \text{ cm}$	$1 - 30 M_\odot$	10^{51} erg	10^4 km s^{-1}

Quantity	E_{bol}	L_{bol}	$E_{p,r}^{\text{max}}$	$E_{p,f}^{\text{max}}$	Δt
Model A	10^{51} erg	$10^{44} \text{ erg s}^{-1}$	$3.2 \times 10^3 \text{ TeV}$	—	10^7 s
Model B	10^{50} erg	$10^{42.5} \text{ erg s}^{-1}$	$2 \times 10^4 \text{ TeV}$	$5 \times 10^3 \text{ TeV}$	$10^{7.8} \text{ s}$

Table 3.1: Parameters used for the two models in the Murase et al. [110] description of SNe IIn. See text for explanation.

considered, capable of explaining ultrabright SNe IIn: Model A and Model B, whose parameter values are listed in Table 3.1. Model A is defined by a high particle number density n_{sh} in the CSM shell and a small shell radius R_{sh} . In contrast, Model B has a lower n_{sh} and larger R_{sh} . Both models have a shell width $\Delta R_{\text{sh}} = R_{\text{sh}}$ and a very large CSM shell mass M_{sh} of several solar masses or more. Uniform SN ejecta with kinetic energy E_{ej} and high velocity v_{ej} are assumed, with a mass of up to several solar masses, but lower than the CSM mass. Model A is motivated by the observed SN 2006gy, one of the most luminous SNe ever recorded, with high photon energy E_{bol} and peak photon luminosity L_{bol} . Model B represents the dimmer, but longer lasting SN 2008iy. The forward shock (FS) of Model A is radiation-mediated, so CR acceleration can only be expected in the reverse shock (RS). In Model A, the CSM is optically thick. In the optically thin case of Model B, with a higher shell radius and lower density, CR acceleration at both shocks (FS and RS) may be considered.

The collisionless shocks accelerate charged particles to high energies via Fermi acceleration, producing a power-law distribution with spectral index of 2, see Section 2.4.3. The maximum energy E_p^{max} of the charged particles is determined by comparing the acceleration time scale to the cooling time scales and the dynamical time scale of the propagating shock. The maximum energy at the RS, $E_{p,r}^{\text{max}}$, and at the FS, $E_{p,f}^{\text{max}}$ (only for Model B), are found as given in Table 3.1. The CR spectrum is assumed to be $dN_p/dE_p \propto E_p^{-2} \exp(-E_p/E_p^{\text{max}})$, normalized by the total CR energy $E_{\text{CR}} \equiv \epsilon_{\text{CR}} E_{\text{ej}}$. Accelerated CRs are mostly confined and produce mesons via pp reactions, producing neutrinos and γ -rays. After flavor mixing, about 1/6 of the meson energy is carried by each neutrino flavor. The ν_μ fluence, i.e. the flux integrated over time, is

$$\phi_{\nu_\mu} \approx E_{\nu_\mu}^{-2} 6 \times 10^{-2} \text{ GeV cm}^{-2} \min[1, f_{pp}] \frac{\epsilon_{\text{CR}}}{0.1} \frac{E_{\text{ej}}}{10^{51} \text{ erg}} \left(\frac{d}{10 \text{ Mpc}} \right)^{-2}, \quad (3.8)$$

which agrees with numerical results of the neutrino fluence shown in Figure 3.11 (with $f_{pp} \geq 1$, $\epsilon_{\text{CR}} = 0.1$, $E_{\text{ej}} = 10^{51} \text{ erg}$, and $d = 10 \text{ Mpc}$). The new symbols in Equation 3.8 are the pp reaction efficiency f_{pp} , and the distance d to the SN. In order to detect the transient neutrino flux and separate it from the background of atmospheric neutrinos, it is important to know the position and explosion time of the SN. The neutrinos are emitted over a time scale of months to years. For Model A, a time window of $\Delta t \approx 4$ months is appropriate, while the optically thin Model B emits over a longer time $\Delta t \approx 24$ months (see Table 3.1).

The fraction of SNe with a dense and massive CSM is estimated to be a few % of all SNe so that their rate within 20 Mpc is on the order of $\sim 0.1 \text{ yr}^{-1}$. The neutrino yield expected from these SNe is not high: For a distance of 10 Mpc and plausible parameter values, the expectation for IceCube is about 2 events with energies above 4 TeV in case of Model A. In Model B, about 1 event above 20 TeV is expected from the FS, and ca. 0.2 events above 50 TeV from the RS [110].

The possibility of neutrino emission from a discovered Type IIn SN is considered in Chapter 7.

3.2.8 High-Energy Neutrinos from Supernovae with Jets

Observations of SNe, in particular of Type Ib/c, in coincidence with gamma-ray bursts (GRBs) have spawned the hypothesis of an underlying mechanism common to at least subclasses of SNe and GRBs [111]. Long GRBs (see Section 3.3) are suspected to be resulting from SN-like explosions of extremely massive stars with high angular momentum, so-called hypernovae [112]. During the explosion, an accretion disk is thought to form around the stellar core, and hot matter is released as jets streaming away perpendicular to the disk. The jets eventually pierce through the stellar envelope and produce the prompt γ -ray radiation observed from GRBs, as explained in Section 3.3.

In the context of the GRB-SN connection, models have been proposed in which some SNe host jets as well [66, 111, 113]. The difference between a jet SN and a GRB is merely the bulk Lorentz factor of the jet, while the energy carried by the jet is comparable. The SN's jet is more baryon-rich than a GRB jet and consequently has a much lower Lorentz factor of $\Gamma \approx 3$, while for GRB jets typically $\Gamma \gtrsim 100$. The lower Lorentz factor results in the jet coming to a halt in the stellar atmosphere, instead of breaking out. One also speaks of a *choked jet SN*. As a consequence, all electromagnetic radiation produced by the jet is completely absorbed and reprocessed by the star's envelope, and no GRB is observable. If however neutrinos are produced within the jets—as proposed for GRBs as well, see Section 3.3—then the neutrinos would escape from the dense environment and can be detected. SNe with mildly relativistic jets may occur in a much larger fraction of core-collapse SNe than those hosting highly relativistic jets, i.e. long GRBs [66, 111]. Detection of neutrinos from choked jet SNe would enable to probe the physical properties of the jets and would provide important insight into the connection between GRBs and SNe [66]. On the other hand, non-detection of those neutrinos can place limits on the rate of SNe hosting such jets and contribute as well to the understanding of the nature of SN explosions and the relation between SNe and GRBs.

The model of neutrino emission from soft, i.e. mildly relativistic, jets within CCSNe was first proposed by Razzaque, Mészáros, & Waxman in [111]. It was later expanded by Ando & Beacom in [66] to include the important contribution of kaons to the neutrino production. In this work, the Ando & Beacom model as presented in [66] is followed, which is explained here. The model makes assumptions on the jet dynamics: The jet kinetic energy E_{jet} is set to $E_{\text{jet},0} = 3 \times 10^{51}$ erg, which is typical for GRBs, and the jet's bulk Lorentz factor Γ to $\Gamma_0 = 3$, having an assumed opening angle of $\theta \approx \Gamma^{-1}$. Guided by knowledge from observed GRBs, the central object's variability time scale is set to 0.1 s and the jet duration to 10 s.

It is assumed that protons are accelerated at internal shocks of the jet with a spectrum $\propto E_p^{-2}$, see Section 2.4.3, normalized to the total jet energy. The maximum proton energy is found by comparing the acceleration with the energy-loss time scales. It is found that below the energy threshold for photo-pion production, i.e. $p + \gamma \rightarrow n + \pi^+$ or $p + \gamma \rightarrow p + \pi^0$, there is no energy-loss time scale shorter than the acceleration time scale. But as soon as the $p\gamma$ process becomes accessible, it prevents further acceleration, due to the very high photon density. Consequently, the maximum proton energy is determined by the $p\gamma$ threshold energy, which is given by

$$E_{p,\text{max}} = (7 \times 10^4 \text{ GeV}) \left(\frac{E_{\text{jet}}}{E_{\text{jet},0}} \right)^{-1/4} \left(\frac{\Gamma}{\Gamma_0} \right). \quad (3.9)$$

Neutrino production from the $p\gamma$ interaction is not taken into account by Ando & Beacom.

The accelerated protons produce π - and K -mesons efficiently via $p p$ interactions, and the meson multiplicity (average number of mesons produced per interaction) is 1 for pions and 0.1 for kaons. It is assumed that the mesons are produced with 20% of the parent proton's energy so that they follow the proton acceleration spectrum. The mesons eventually decay into neutrinos via $\pi^\pm, K^\pm \rightarrow \mu^\pm + \nu_\mu(\bar{\nu}_\mu)$ with branching ratios of 100% and 63%, such that the neutrino energy in the observer frame is related to the parent meson energy in the jet rest frame as:

$$E_{\nu,\pi} = \Gamma \frac{E_\pi}{4} \quad E_{\nu,K} = \Gamma \frac{E_K}{2} \quad (3.10)$$

The mesons either decay to neutrinos directly or they interact before they decay and thus lose energy, i.e. they cool. The cooling takes place either by hadronic (πp or $K p$ interactions) or by radiative (synchrotron radiation and inverse Compton scattering on thermal photons) processes. If the mesons

decay faster than they cool, then the daughter neutrinos maintain the spectrum shape of their parents (which they inherited from the protons). Otherwise, the spectrum becomes steeper. While hadronic cooling is energy independent, the radiative cooling time scale is $\propto E^{-1}$, so radiative cooling is efficient at high energies. As a consequence, there are certain energies, $E^{(1)}$ and $E^{(2)}$, that mark a break in the neutrino spectrum, as another cooling process takes over. Below $E^{(1)}$, there is no efficient cooling at work and the neutrino spectrum follows the original E^{-2} spectrum. Between energies $E^{(1)}$ and $E^{(2)}$, hadronic cooling dominates and the spectrum is suppressed by an additional factor E^{-1} . Above $E^{(2)}$, where energy-loss is dominated by radiative cooling, the neutrino spectrum is suppressed with a factor E^{-2} . The break energies $E^{(1)}$ and $E^{(2)}$ are

$$E_{\nu,\pi}^{(1)} = (30 \text{ GeV}) \left(\frac{E_{\text{jet}}}{E_{\text{jet},0}} \right)^{-1} \left(\frac{\Gamma}{\Gamma_0} \right)^5 \quad E_{\nu,K}^{(1)} = (200 \text{ GeV}) \left(\frac{E_{\text{jet}}}{E_{\text{jet},0}} \right)^{-1} \left(\frac{\Gamma}{\Gamma_0} \right)^5 \quad (3.11)$$

and

$$E_{\nu,\pi}^{(2)} = (100 \text{ GeV}) \left(\frac{\Gamma}{\Gamma_0} \right) \quad E_{\nu,K}^{(2)} = (20\,000 \text{ GeV}) \left(\frac{\Gamma}{\Gamma_0} \right). \quad (3.12)$$

Normally, $E_{\nu}^{(1)} < E_{\nu}^{(2)}$, but for certain values of Γ and E_{jet} , especially for large Γ , $E_{\nu}^{(1)}$ can be larger than $E_{\nu}^{(2)}$. In this case, the effective break energies are equal, $E_{\nu}^{(1)} = E_{\nu}^{(2)}$, i.e. there is no hadronically dominated energy regime and radiative cooling becomes dominant directly (see the two higher Γ scenarios for pions in Figure 3.12 for examples).

The break energies are higher for kaons because the kaons are heavier and the radiative cooling time scale is $\propto m^4$. Additionally, the intrinsic kaon lifetime is a factor ≈ 2 shorter than the pion lifetime, and the larger mass results in a smaller Lorentz factor, making the jet frame lifetime even shorter. The maximal neutrino energy is derived directly from the maximal proton energy in Equation 3.9, using $E_{\pi,K} = 0.2E_p$ (s.a.) and Equation 3.10:

$$E_{\nu,\pi}^{\text{max}} = (10\,500 \text{ GeV}) \left(\frac{E_{\text{jet}}}{E_{\text{jet},0}} \right)^{-1/4} \left(\frac{\Gamma}{\Gamma_0} \right)^2 \quad E_{\nu,K}^{\text{max}} = (21\,000 \text{ GeV}) \left(\frac{E_{\text{jet}}}{E_{\text{jet},0}} \right)^{-1/4} \left(\frac{\Gamma}{\Gamma_0} \right)^2. \quad (3.13)$$

The strong Γ dependence of $E_{\nu}^{(1)}$ bears the potential to extract the jet Lorentz factor Γ from a measured neutrino spectrum. Additionally, measurement of the maximal neutrino energy E_{ν}^{max} as break in the spectrum would allow to probe the maximum proton energy, i.e. the $p\gamma$ threshold, which depends on the photon density in the jet, an important parameter of the jet physics.

The neutrino fluence $F_{\nu} = dN_{\nu}/dE_{\nu}$ is normalized by its evaluation at the first break energy. It is [66]:

$$F_{\nu,\pi,0} \equiv (E_{\nu,\pi}^{(1)})^2 F_{\nu,\pi}(E_{\nu,\pi}^{(1)}) = (45 \text{ GeV cm}^{-2}) \left(\frac{E_{\text{jet}}}{E_{\text{jet},0}} \right) \left(\frac{\Gamma}{\Gamma_0} \right)^2 \left(\frac{d_L}{10 \text{ Mpc}} \right)^{-2} \quad (3.14)$$

$$F_{\nu,K,0} \equiv (E_{\nu,K}^{(1)})^2 F_{\nu,K}(E_{\nu,K}^{(1)}) = (2 \text{ GeV cm}^{-2}) \left(\frac{E_{\text{jet}}}{E_{\text{jet},0}} \right) \left(\frac{\Gamma}{\Gamma_0} \right)^2 \left(\frac{d_L}{10 \text{ Mpc}} \right)^{-2}, \quad (3.15)$$

where d_L denotes the luminosity distance to the SN. Putting all of this together, the neutrino fluence as

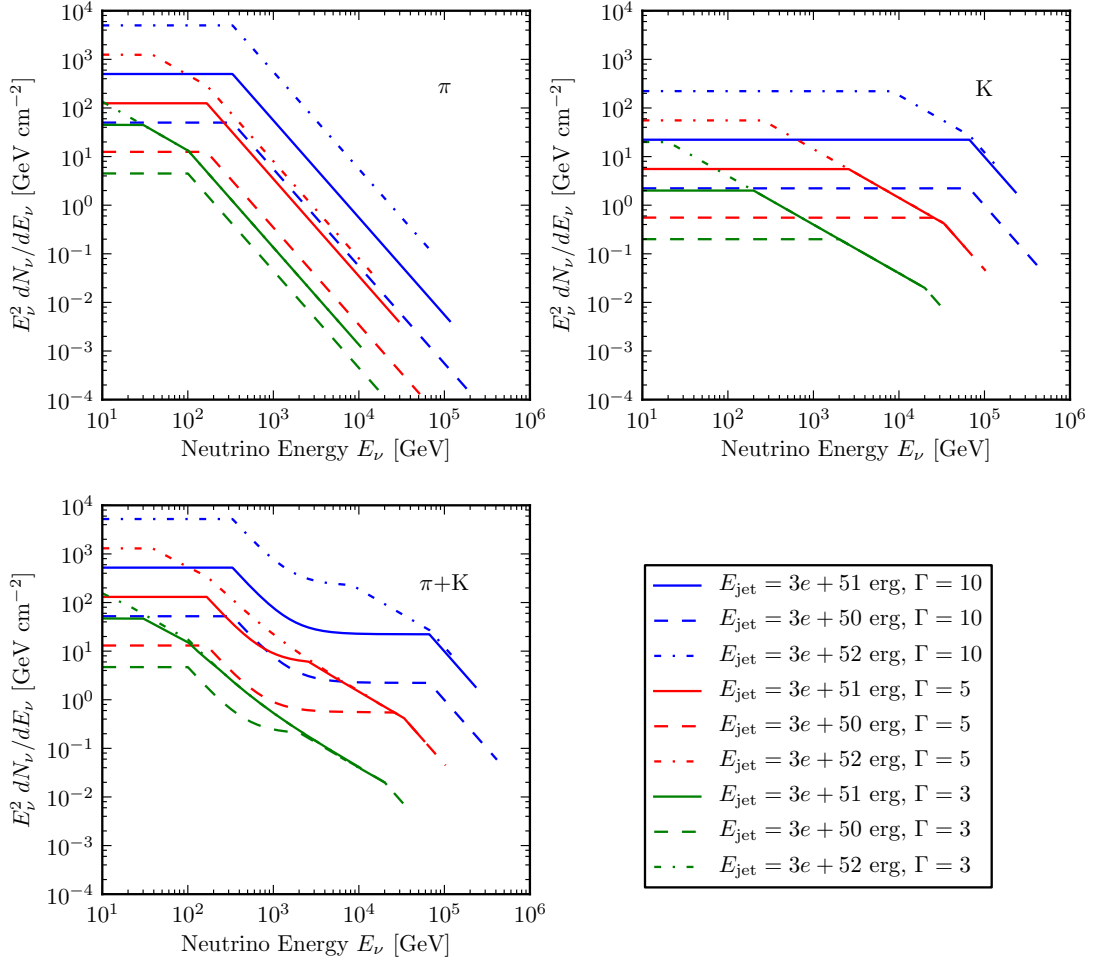


Figure 3.12: Theoretical neutrino fluence emitted from a SN at a distance of 10 Mpc hosting mildly relativistic jets, according to Ando & Beacom [66]. The contributions from pions (upper left) and kaons (upper right), as well as their sum (lower left) is plotted for different jet bulk Lorentz factors Γ and jet kinetic energies E_{jet} , as indicated in the legend (lower right).

function of energy, i.e. the energy spectrum, is the sum of the pion and kaon fluence:

$$F_\nu = \frac{dN_\nu}{dE_\nu} = \sum_{i=\pi,K} F_{\nu,i,0} \begin{cases} E_\nu^{-2}, & E_\nu < E_{\nu,i}^{(1)} \\ E_{\nu,i}^{(1)} E_\nu^{-3}, & E_{\nu,i}^{(1)} \leq E_\nu < E_{\nu,i}^{(2)} \\ E_{\nu,i}^{(1)} E_{\nu,i}^{(2)} E_\nu^{-4}, & E_{\nu,i}^{(2)} \leq E_\nu < E_{\nu,i}^{\max} \\ 0, & E_{\nu,i}^{\max} \leq E_\nu \end{cases} \quad (3.16)$$

The neutrino fluence from the Ando & Beacom model [66], according to Equation 3.16 is plotted in Figure 3.12.

The Optical Follow-Up (OFU) program of the neutrino detector IceCube (see Section 4.2) was designed specifically to target multi-messenger detections and observations of choked jet SNe. It is introduced in Chapter 6 and its results are discussed in Chapters 7 and 8.

3.3 Gamma-Ray Bursts

Gamma-ray bursts (GRBs) are extremely bright, but short flashes of electromagnetic radiation in the γ -ray band. For a period of seconds, a GRB outshines every other γ -ray source in the sky, even the Sun as closest source [112, p. 2262]. Because Earth's atmosphere is opaque to γ -rays, they remained undetected until the space age. The Vela satellites of the US Department of Defense, designed to monitor nuclear explosions, discovered GRBs in 1967. The results remained classified, because it was speculated that they are the result of an advanced extraterrestrial civilization. After realizing that the bursts are a new cosmic phenomenon, they were eventually published in 1973 [112, p. 2262].

3.3.1 Electromagnetic GRB Emission

GRBs occur at a rate of roughly a few per day [112, p. 2262]. Thanks to their brightness, GRBs can be seen from most of the observable Universe, up to very large distances of redshift $z \approx 8$ [114]. GRB spectra are non-thermal (broken power laws), peaking in the range 50–500 keV, sometimes extending to GeV energies. The γ -ray burst durations range from 10^{-3} s to 10^3 s, with a roughly bimodal distribution: there are the two classes of long GRBs (duration ≥ 2 s) and short GRBs (duration ≤ 2 s) [112, p. 2264]. The typical duration of short GRBs is 0.3 s, while long GRBs last typically 40 s [115]. Long GRBs appear to be more common than short GRBs. GRB γ -ray light curves show variability on time scales down to milliseconds [112, p. 2264].

The rapid burst of γ -rays is called the *prompt* GRB emission. It is accompanied by longer lasting *afterglow* emission, which is broad-band and detectable in X-ray, optical, infrared, and radio wavelengths [112, pp. 2265f.]. The afterglow typically lasts several hours up to several days. The afterglow light curve decays rapidly according to a power law at all wavelengths [116, pp. 13–20]. Afterglow detection is most successful in X-rays, as about 95% of GRBs detected by the NASA X-ray and UV/optical satellite Swift are detected in X-rays, while optical afterglows are detected in only about 60% of GRBs [116, p. 4].

3.3.2 GRB Progenitors

In the 1990s, it was found that GRBs are distributed isotropically and associated with host galaxies. From optical observations, redshifts could be determined, conclusively demonstrating the cosmological distance of GRBs [112, pp. 2263–5]. The vast distance however implies an enormous amount of energy

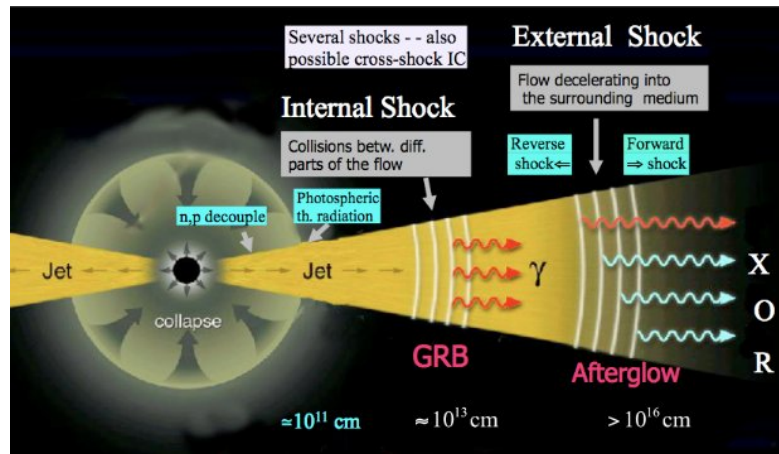


Figure 3.13: Schematic view of the GRB fireball model and the different jet emission zones with internal shock and external shock. Taken from [117].

radiated in γ -rays, which suggests that GRBs do not emit isotropically, but the emission is collimated in a beam (or jet).

Long GRBs appear to be associated with galaxies of increased star formation, while short GRBs are more often found in galaxies with old stellar population, such as elliptical galaxies [112, pp. 2299f., 2301f.]. This is an indication that long GRBs, like CCSNe, are linked with the deaths of massive stars, because massive stars evolve so quickly that their deaths happen only in regions where new stars are born. At least some long GRBs were found to be associated with Type Ib/c SNe, which strengthens this assumption [112, pp. 2267, 2301f.]. The standard picture is that long GRBs arise from the collapse of a massive star (a collapsar or hypernova) and short GRBs are the result of the merger of either a NS-NS or a NS-BH binary system. This would mean that long GRBs are related to, but much rarer than CCSNe [112, pp. 2264, 2302].

In particular, long GRBs and choked jet SNe (see Section 3.2.8) are related: Both are thought to host a jet, which is highly relativistic in case of long GRBs, but only mildly relativistic in case of choked jet SNe. Long GRB progenitors are conceived to be Wolf-Rayet stars that have lost their outer hydrogen and helium envelope [112, p. 2303], while choked jet SNe can still have those outer layers [66], which are important for efficient high-energy neutrino production.

3.3.3 GRB Neutrinos

GRBs are expected to produce neutrinos at various energies. The most successful model describing GRBs is the *fireball model*, where a fireball of hot plasma expands with relativistic velocity. The fireball is collimated along the rotational axis and jets are formed. Within the jets, there are collisions of layers and *internal shocks* are formed that accelerate particles and produce neutrinos, mainly in the PeV (10^{15} eV) energy range, emitted together with the prompt γ -rays. When the jet runs into the surrounding medium, *external shocks* can form that generate the afterglow emission and might produce afterglow neutrinos at EeV (10^{18} eV) energies. Figure 3.13 shows a sketch illustrating the fireball model.

GRBs are interesting candidates for ultrahigh-energy CR (UHECR) sources, perhaps producing CRs with energies above EeV, i.e. 10^{18} eV. The main alternative UHECR sources are active galactic nuclei (AGNs), see Section 2.4.2. Using only direct CR observations, it is difficult to distinguish between the two sources. Detection of ultrahigh-energy neutrinos may establish GRBs as the sources of UHECRs.

Current limits provided by data from the neutrino detector IceCube (see Section 4.2) place an upper limit on the flux of high-energy neutrinos associated with GRBs that is at least a factor of 3.7 below the predictions [118]. This implies either that GRBs are not the only sources of CRs with energies above 10^{18} eV or that the efficiency of neutrino production is much lower than has been predicted [118]. In either case, it means that larger instruments like an envisioned high-energy extension of IceCube [119] might be needed to detect the low flux of TeV to PeV GRB neutrinos. While GeV neutrinos from GRBs might have a higher flux, IceCube is too sparse to detect them. For those, a high-density infill, larger and denser than DeepCore (see Figure 4.6), might be necessary, like the currently planned Precision In-Ice Next Generation Upgrade (PINGU) project [120].

The X-ray Follow-Up (XFU) program of IceCube, closely related to the Optical Follow-Up (OFU) system in Section 6.2, is motivated by the potential to detect a GRB neutrino burst with IceCube and identify the subsequent X-ray afterglow. However, it has not revealed a neutrino GRB detection yet. Instead, limits on the source density and intensity can be set from the mere lack of follow-up alerts above the expected background from atmospheric neutrinos.

Neutrino Detectors

Due to their properties discussed in Section 2.3—penetrative power, non-deflection by magnetic fields and non-absorption by matter—neutrinos are interesting astronomical messengers. This motivates the pursuit of neutrino astronomy, which must still be considered to be at a pioneering stage, compared to optical astronomy, X-ray astronomy, and γ -ray astronomy. This section introduces neutrino astronomy by presenting some of its instruments, which are grand scale particle physics experiments at the same time. The Super-Kamiokande detector in Japan exemplifies a low-energy neutrino detector (but there are more, e.g. SNO and Borexino), IceCube is an example for a high-energy neutrino detector in ice, and ANTARES and KM3NeT serve as examples for high-energy neutrino detection in water. IceCube is covered in great detail, since it is the detector whose data are used in this work in Chapters 6, 7, and 8.

The chosen examples all utilize Cherenkov radiation (see Section 2.3.4) for particle detection. There are also alternative detection techniques, e.g. using liquid scintillator, which generates scintillation light when a charged particle crosses.

4.1 Low-Energy Neutrino Detectors

4.1.1 Super-Kamiokande

Super-Kamiokande is a large water Cherenkov detector located at Kamioka, Japan. It consists of a large cylindrical stainless steel tank, 39 m in diameter and 42 m in height, containing 50 ktons of purified water, buried under Mt. Ikenoyama, with an overburden of 1000 m of rock, or 2700 meter-water-equivalent (m.w.e.) [121, pp. 3f., 6f., 9]. Within the tank, there is an inner detector (ID) formed by 11 146 inward-facing 50 cm diameter photomultiplier tubes (PMTs) covering 40% of the surface area, and an outer detector (OD) with 1885 outward-facing 20 cm diameter PMTs, attached to acrylic wavelength shifting plates that improve light collection efficiency [121, p. 5]. Figure 4.1 shows a schematic view of the detector layout and a photographic picture.

Super-Kamiokande's cavity excavation started in 1991 and detector construction was completed in December 1995 [121, p. 8]. Super-Kamiokande was commissioned and data taking began in April 1996. Until July 2001, 1678 live days were recorded in a period referred to as "SK-I". During a shutdown for upgrade and maintenance, a cascade of implosions destroyed half of the detector's PMTs in November 2001 [121, p. 3]. The experiment resumed in October 2002 with half of the original ID-PMTs in a period until October 2005 called "SK-II" [123, pp. 3f.]. In July 2006, it resumed with full number

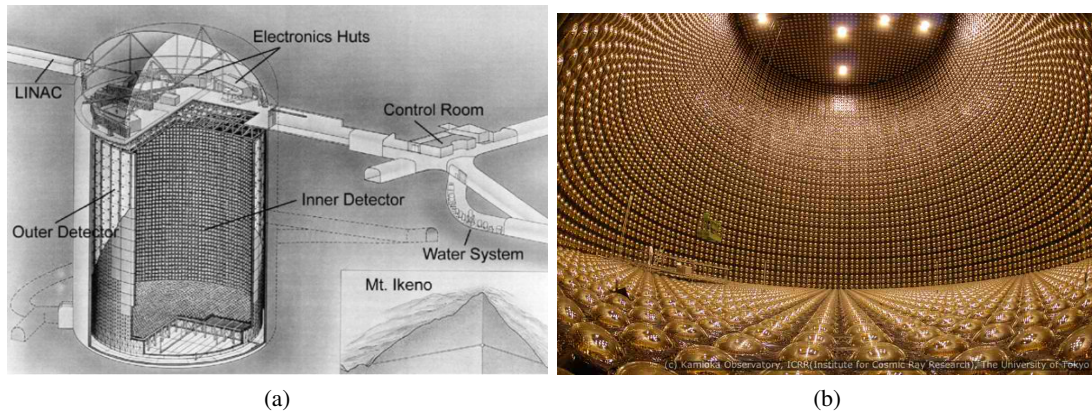


Figure 4.1: (a) A sketch of the Super-Kamiokande detector, showing the location of the PMTs on a wall that separates the cylindrical tank into the main inner and the thin outer detector. Image taken from [121, p. 8]. (b) A photograph taken inside the inner detector after completion of PMT mounting. Image taken from [122].

of PMTs under “SK-III” until an electronics upgrade in September 2008 [123, p. 4]. The period after September 2008 is called “SK-IV”, ongoing until at least February 2014 [123, p. 4].

Neutrino interactions are detected via Cherenkov light emitted by the produced charged particles. The detectable energy of events ranges from 4.5 MeV to over 1 TeV [121, p. 5]. Events entering or exiting the detector can be identified via activity in the OD. Neutrino events are classified into fully contained (FC) events, which have no hits in the OD, partially contained (PC) events with neutrino interaction in the ID and particles exiting the detector, and upward-going muon events [121, p. 5]. The latter can be assumed to be products of neutrino interactions in the rock below Super-Kamiokande. Downward-going muons from the atmosphere are observed at a rate of 2 Hz and are useful monitoring and calibration data [121, p. 5]. Super-Kamiokande’s dense instrumentation allows it to observe Cherenkov rings, created when the Cherenkov light emitted in a cone hits the surface of the cylindrical detector. From the shape of the Cherenkov ring, it is possible to identify an event as electron-like, muon-like or multi-ring [121, p. 5]. See Figure 4.2 for an example of an event display of Super-Kamiokande.

Primary scientific goals are the search for proton decay, which is a signature of Grand Unified Theories (GUTs) [125], and studies of low-energy neutrinos from the Sun, atmosphere, SNe, GRBs, and artificial neutrino beams [121, p. 3]. Some of Super-Kamiokande’s results were the first unambiguous evidence of neutrino oscillation in atmospheric neutrinos, confirmation of the solar neutrino flux deficit (solar neutrino problem, see Section 2.3.5), demonstration that solar neutrinos really come from the Sun, first measurement of the solar neutrino energy spectrum above 5 MeV, and the best lower limits on the proton lifetime [121, p. 3].

Super-Kamiokande is an important tool for SN neutrino physics. A typical core-collapse SN (CCSN) in our Galaxy would generate about 10 000 neutrino event detections in Super-Kamiokande [126], much more than the few events recorded from SN 1987A by the predecessor Kamiokande II and other small detectors (see Section 3.2.5). This high-statistics neutrino observation would be a direct observation of the stellar collapse dynamics. A detailed SN neutrino light curve would provide important insights for the understanding and modeling of core-collapse SNe [127]. Because the neutrino signal precedes the optical explosion by several hours, there is also the possibility of an early warning in order to get the best possible data coverage of a close SN [127]. Unfortunately, the SN rate in the Galaxy is quite low, only 2 to 3 per century, and Super-Kamiokande is not sensitive to SN explosions beyond our Galaxy and its satellites like the Magellanic clouds [128]. This means, the detection of at least one galactic SN within

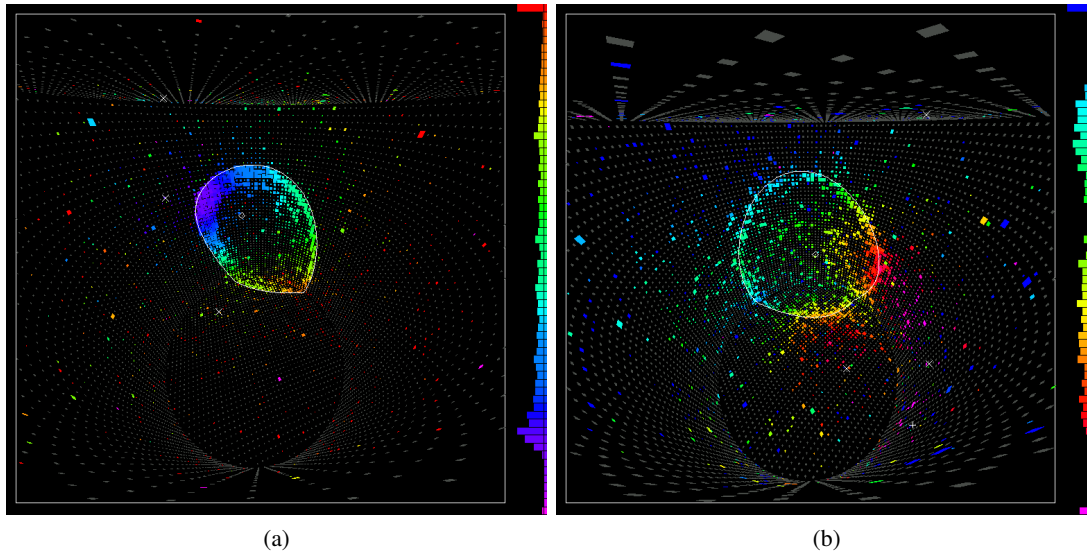


Figure 4.2: Two examples of Super-Kamiokande event displays from Monte Carlo simulation. Color corresponds to the time a PMT was hit by a Cherenkov photon (going from purple, early, to red, late). The size of a colored square corresponds to the amount of light seen by the PMT at that position [124]. Figure (a) shows a 1032 MeV muon event, where the Cherenkov ring is very clearly visible. Figure (b) is an event from a 600 MeV electron, where the ring is much fuzzier than the muon ring. This is because an electron creates an electromagnetic cascade with multiple electrons and positrons that each have a slightly different angle. Images taken from [124].

the next decades is not unlikely, but there is also a chance that no SN will be detected at all. Multiple SN detections require even more patience. The Super-Kamiokande collaboration has conducted a search for SN neutrino bursts using data from the SK-I and SK-II phases corresponding to 2589 live days. There is no evidence of a SN explosion during the data-taking period and the 90% confidence level (C.L.) upper limit on the rate of CCSN explosions out to distances of 100 kpc is 0.32 SNe yr^{-1} [126].

4.1.2 Backgrounds of Low-Energy Neutrino Detectors

Two backgrounds for low-energy neutrino detectors are discussed here, which are relevant for the detection of faint neutrino signals from extra-galactic SNe, as dealt with in Chapter 5.

Nuclear Spallation

Muons and neutrinos are the only cosmic ray-produced shower particles that can penetrate the Earth. They are the only cosmic ray (CR) particles relevant to a deep underground detector [15, p. 390]. Penetrative muons with several km long range (see Section 2.3.3), even though fewer in numbers, are a serious background for solar and atmospheric neutrino detectors. Those detectors need to be put deep underground in order to filter most of the (low-energy) muons and keep the muon passing rate at a tolerable level. Atmospheric muons passing through matter can also cause nuclear spallation, a form of nuclear transmutation or nucleosynthesis. When a high-energy particle, a primary CR particle or a muon, hits a nucleus, it can disrupt the nucleus and a large number of nuclear fragments is expelled [16, p. 330]. This leads to the creation of new, partly radioactive isotopes. For example, CR primaries create ^{14}C nuclei by spallation, a fact used for radiocarbon dating in archaeology [129].

For rare-event underground neutrino detectors, radioactive isotopes produced through atmospheric muon spallation can be a serious background at low energies because their decay mimics the rare signal [130]. The KamLAND detector studied the production of radioactive isotopes through cosmic muon spallation and found that, from the hydrogen, carbon, nitrogen, and oxygen contained in the scintillator of the detector, a multitude of radioactive isotopes can be formed, with lifetimes ranging between 10s of milliseconds up to several months [130]. Most of these isotopes, however, are primarily produced by the spallation on carbon. Only one of the 16 isotopes¹ listed in [130, Table IV] is not of carbonic origin, but created from ¹⁶O. Nevertheless, also for water Cherenkov detectors containing only oxygen, spallation is a serious background at low-energy neutrino detection. For the Super-Kamiokande detector, for instance, roughly 200 000 spallation events per year per 22.5 kton of fiducial volume have been measured (several hundred events per day) [42].

Invisible Muons

Atmospheric neutrinos at low energies can produce muons via CC interaction that lie below the energy threshold for Cherenkov radiation. For this to happen, the neutrino energy must be larger than the muon mass of 105.7 MeV, but the kinetic energy transferred to the muon must be smaller than about 58 MeV in ice, i.e. the neutrino energy must be roughly in the range between 106 MeV to 160 MeV. These muons are called *invisible muons* [42]. They can travel unseen for only ~ 1 m and decay into one electron (or positron) and two neutrinos. The electron has a distinct energy spectrum called *Michel spectrum* [42]. Because it has a much lower Cherenkov energy threshold of < 1 MeV, it is visible emitting Cherenkov radiation. The consequence is that the decay of invisible muons can mimic a rare signal, for instance the inverse β -decay process $\bar{\nu}_e + p \rightarrow n + e^+$. Thus, while decays of visible muons are easily identifiable background, invisible muons constitute a serious background for low-energy neutrino detectors, unless they can be distinguished from the signal [42, 131].

This can be achieved e.g. by making use of the Michel spectrum or via coincidence measurements. One can either identify the background by measuring γ -rays (5 MeV to 10 MeV) emitted from the nucleus that the atmospheric neutrino interacted with, one muon lifetime *before* the invisible muon event [132]. Or one identifies the signal via the neutron created in inverse β -decay [132]: The neutron is captured by another nucleus and creates a signal *after* the prompt positron signal, with characteristic delay and energy, e.g. $n + p \rightarrow d + \gamma$ ($E_\gamma = 2.2$ MeV) [42] or, if one can control the interaction medium and solve the neutron catching isotope gadolinium in water, a γ -cascade of ~ 8 MeV energy [133].

4.2 IceCube

IceCube is much larger than Super-Kamiokande and was designed for high-energy neutrino detection.

4.2.1 Overview

IceCube is located in the glacier at the geographic South Pole in the vicinity of the Amundsen-Scott station and was deployed between 2005 and 2010 [134, 135]. It encompasses an instrumented volume of 1 km^3 [135], with much sparser sensor density compared to Super-Kamiokande. Consequently, IceCube is suited for much higher energies: looking into the Northern sky (downwards, through the Earth), the detector is most sensitive from TeV to PeV energies. At higher energies, absorption in the Earth begins to attenuate the signal. Looking into the Southern sky (upwards, into the sky above the detector), the

¹ ¹⁵O is created mainly via ¹⁶O(γ, n). The other isotopes ⁸B, ¹²B, ¹³B, ⁷Be, ¹⁰Be, ¹¹Be, ⁹C, ¹⁰C, ¹¹C, ⁶He, ⁸He, ⁸Li, ⁹Li, ¹²N, and ¹³N are primarily produced in reactions on ¹²C or ¹³C.

most interesting regime for neutrino astronomy is above PeV energies, because that is where there is no background from atmospheric muons and neutrino absorption does not take place [135].

IceCube consists of 86 cables, called strings, that were melted into the ice using hot water drilling [135]. Each string is about 2.5 km long and hosts 60 spherical optical sensors, called Digital Optical Module (DOM), totalling to 5160 DOMs [134]. Each DOM consists of a 13 mm thick glass sphere vessel housing a 25 cm (10”) diameter Hamamatsu PMT sensitive to the near-UV and blue photons of Cherenkov light. In addition, a 2 kV high-voltage (HV) supply, required for the PMT, and the DOM mainboard with readout electronics are contained in the DOM. The DOM mainboard is in fact a small autonomous computer running a UNIX-like operating system [136]. Figure 4.3 shows a sketch of the DOM layout.

The in-ice array is complemented by the surface array IceTop, consisting of 324 DOMs in 162 ice tanks located at 81 stations, which is used for CR air shower detection [135, 138]. The strings are arranged in a hexagon (see Figure 4.4), with a distance of approximately 125 m between strings [139]. The DOMs on each string are located within depths of 1450 m to 2450 m [134], with a spacing of nominally 17 m [139]. There are 6 strings with high quantum efficiency (HQE) DOMs that are arranged in a 5 times denser array in the center, with shorter inter-string spacing of 42 m and inter-DOM spacing of 7 m below (for 50 DOMs) and 10 m above (for 10 DOMs) an ice region containing increased dust (so-called “dust layer”) [140], see Figure 4.6. Those denser strings, whose DOMs are concentrated in regions of very clear ice, form a sub-detector called *DeepCore*, which increases IceCube’s sensitivity for lower energy neutrinos. The neutrino energy threshold is lowered from about 100 GeV to about 10 GeV [140]. Figure 4.4 shows the location of the 86 strings and the date of completion of the different construction stages. IceCube was constructed in 7 stages, construction work taking place during the austral summers, which are labelled with the number of strings completed at the stage: IC1, IC9, IC22, IC40, IC59, IC79, and IC86 [135]. Data acquisition began already during the incomplete stages and the data sets are given the same labels.

4.2.2 Particle Detection

When a high-energy charged particle propagates through the ice, it emits Cherenkov light as detailed in Section 2.3.4. The Cherenkov photons, about 360 photons per cm [141], travel through the ice undergoing scattering and absorption. The deep ice is remarkably clear, making it very suitable for a Cherenkov detector. Figure 4.7 shows the depth-dependent effective scattering coefficient b_e and absorption coefficient a at a wavelength of 400 nm, as measured for the location of IceCube [142]. At a depth of 2.3 km, the effective scattering length² $\lambda_e = 1/b_e$ is roughly 70 m. The absorption length $\lambda_a = 1/a$, after which a photon is on average absorbed, is about 200 m, i.e. even longer. This means a single photon can travel a long distance before potentially being detected by a DOM. The deep South Pole ice is much clearer than what can be achieved in the laboratory. In fact, glacial ice is the most transparent solid known [143].

A fraction of the Cherenkov photons will eventually hit the PMTs and be recorded. A photon that hits the PMT cathode knocks out an electron, called “photoelectron” (PE), which is accelerated onto a dynode where it knocks out several more electrons, that are in turn accelerated onto the next dynode. An avalanche of electrons finally hits the anode and causes a voltage drop registered by the electronics. The final number of electrons per initial PE, the gain, is nominally 10^7 for in-ice IceCube PMTs [136]. The recorded anode voltage versus time is called waveform and contains one pulse per PE that was released

² While the geometric scattering length λ_s is the average distance between scatters, the effective scattering length λ_e is the average distance, at which a propagating photon beam is completely randomized in direction. For isotropic scattering, where the average scattering angle θ is 90° , $\langle \cos \theta \rangle = 0$, λ_e equals λ_s , but for anisotropic forward scattering as in ice or water, where $\langle \cos \theta \rangle > 0$, λ_e is significantly larger than λ_s [143].

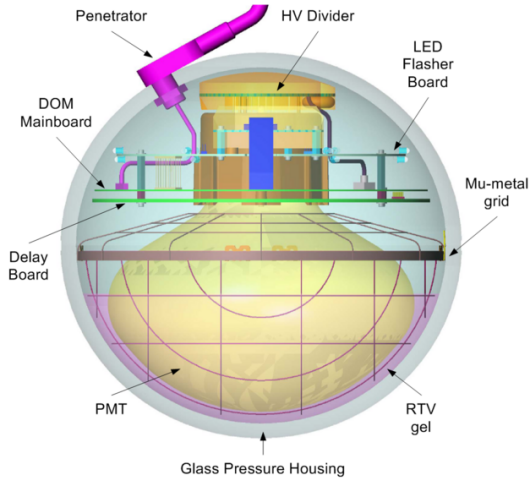


Figure 4.3: A sketch of an IceCube DOM, from [136].

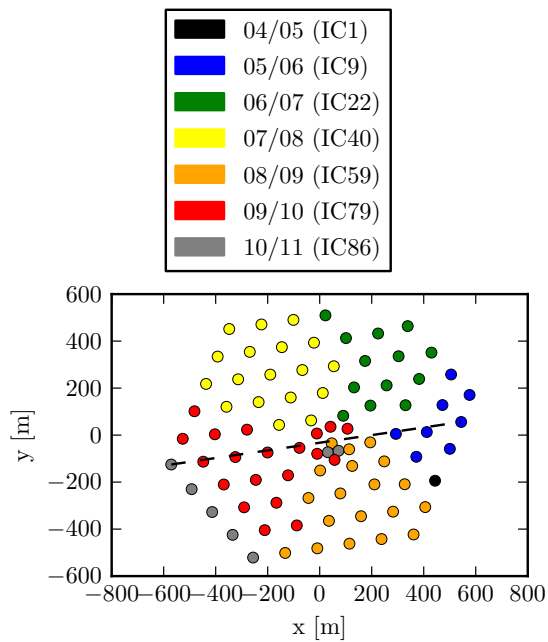


Figure 4.4: Horizontal positions of the IceCube strings. The season of deployment is indicated by the color. The dashed line is a slice along which the closest strings are plotted in Figure 4.6.

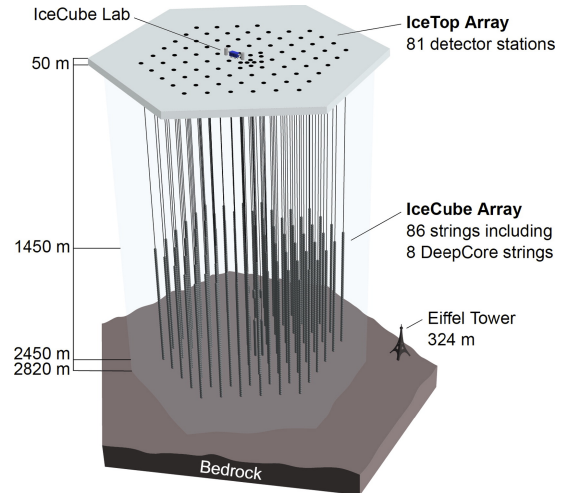


Figure 4.5: Artistic depiction of the IceCube detector array, with the Eiffel tower for comparison. The location of the ICL (IceCube Lab) near the array center on the surface can be seen. From [137].

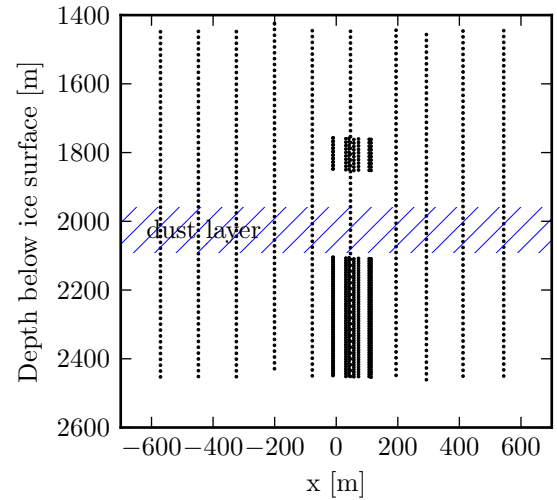


Figure 4.6: Vertical positions of the IceCube DOMs on the strings near the slice indicated in Figure 4.4. The denser DeepCore array above and below the dust layer near 2000 m depth is clearly visible.

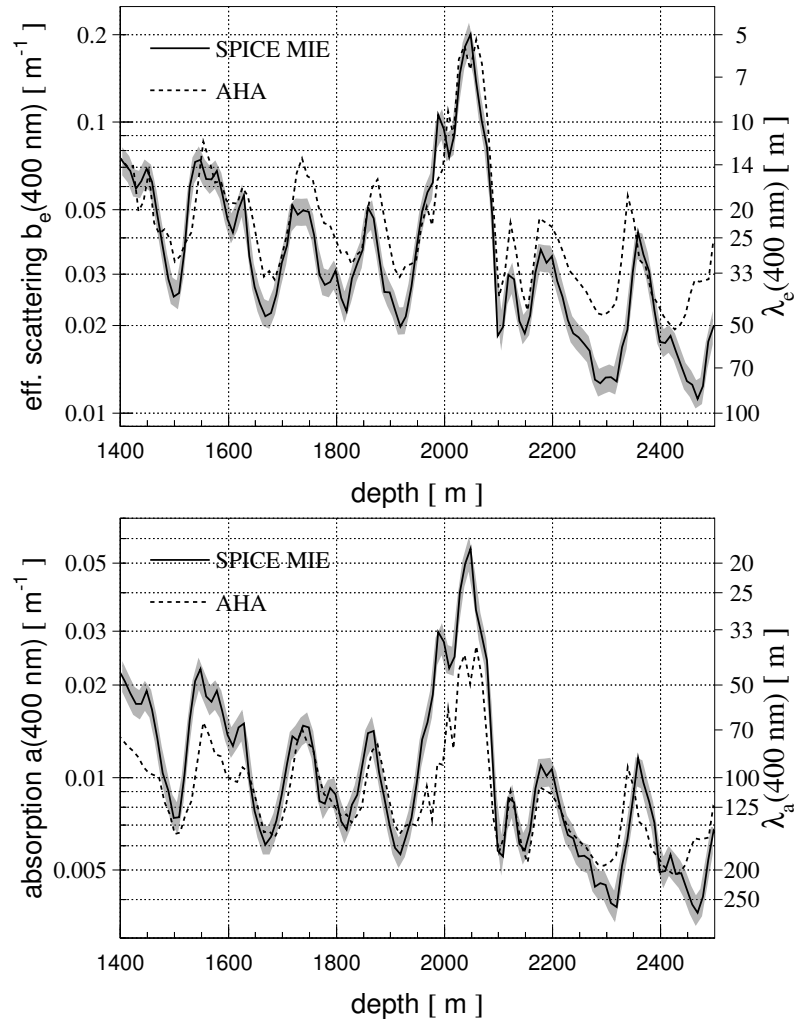


Figure 4.7: The effective scattering coefficient $b_e(400)$ and absorption coefficient $a(400)$ vs. depth, as estimated from IceCube calibration data, taken from [142, fig. 16]. The range of values allowed by estimated uncertainties is indicated with a grey band around a solid line (converged solution). Results from an updated older model (AHA) are shown with a dashed line for comparison. The axis to the right of each plot indicates the corresponding effective scattering length $1/b_e$ and absorption length $1/a$.

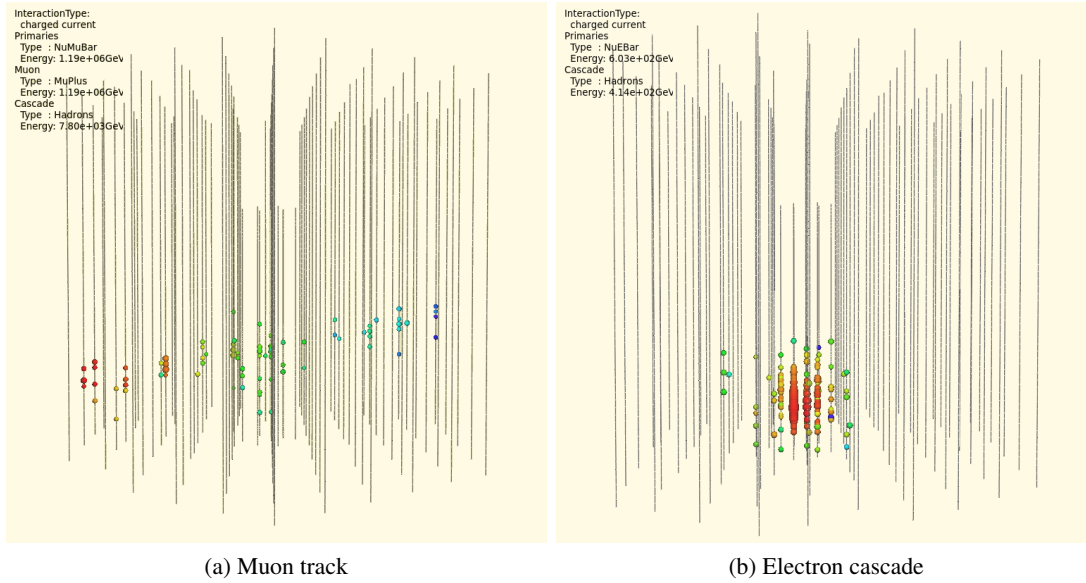


Figure 4.8: Event views of the two event signatures in IceCube: tracks and cascades. The colored spheres indicate DOMs hit by photons, where the size represents the number of photons and the color the time of the hit (time increases from red to blue). These examples are events generated via the Monte Carlo method with a full detector simulation, which is also used for physics analyses inside the collaboration.

from the cathode. From the sample of waveforms, one can extract the times and pulse heights (number of PEs). This information is used to reconstruct the event, i.e. to estimate the direction and energy of the charged particle.

There are two distinct event topologies: tracks and cascades, see Figure 4.8 for an illustration of the two event types in IceCube. Tracks are caused by muons³ traveling long distances in straight lines. On their way through the ice, they deposit part of their energy via ionization, bremsstrahlung, pair production, and nuclear interactions (see Section 2.3.3). Cherenkov light is produced along the track, which can be detected. Tracks make it easy to estimate the particle direction, due to the long lever arm, along which light is recorded, see Figure 4.8. Directional resolutions of less than 1° are achieved above 1 TeV [144]. The energy reconstruction has higher uncertainties, since only dE/dx of the muon can be measured and not the total energy E directly. Typical muon energy resolutions are about $\Delta \log_{10} E_\mu = 0.3$ for highest muon energies of ≥ 100 TeV, and worse at lower energies [145]. Cascades, on the other hand, are produced by an electromagnetic or hadronic shower of particles. The shower has an angular spread that, adding scattering of Cherenkov photons, leads to an almost spherical pattern in the detector. A cloud of photons that grows with time and has a very slight preferred direction. Cascades, if fully contained in the detector, provide a very good energy estimate, since the particle's entire energy is deposited inside the detector. Directional reconstruction is inferior to tracks and is typically accurate to 30° , but at highest energies, above 100 TeV, about 15° can be achieved using extremely time-consuming reconstructions [145, 146].

Cascades, if they are real cascades and not e.g. muon energy loss leaking into the detector, must be associated to a neutrino. They are either caused by an electron neutrino creating an electron via the CC-DIS interaction or by any flavor neutrino via the NC-DIS interaction (see Section 2.3.2). This is why a cascade analysis must apply efficient containment criteria and can then become almost background-free.

³ In principle also extremely energetic tau leptons, which are very rare and have not been observed in IceCube yet.

A muon track analysis, however, always contains the muons created by muon neutrinos via CC-DIS, as well as background muons that were produced by cosmic rays via meson decay in the atmosphere. In fact, owing to the small neutrino cross-section, for each muon neutrino event in IceCube, there are about 10^6 muon events. Consequently, since neutrinos can penetrate the Earth, but muons cannot, neutrino astronomy with muon neutrinos usually “looks downwards” and uses the Earth as a natural muon shield. Every muon track going upwards in the detector must be neutrino-induced. A cut on the zenith angle at about 90° leaves only the muon neutrino events, as well as muon events that are actually downgoing, but are mis-reconstructed as upgoing. Due to the sheer amount of muons, the mis-reconstructed muons still outnumber the neutrinos by a factor of about 20 000. Therefore, cuts on the reconstruction quality are necessary to remove the mis-reconstructions.

Because the neutrinos themselves are not observable, reconstructed quantities such as direction and energy can only be estimates on the neutrino properties. For instance, only part of the neutrino energy goes into the muon in the CC interaction. Therefore, reconstructing the muon energy only leads to a lower limit on the neutrino energy. The same is true for cascade energy reconstruction in case of NC interaction. An exception is the CC interaction of an electron neutrino, where the complete energy goes either into the electron or the hadronic cascade, both of which are contained and thus observable in the detector. The observable direction of the charged particle is also just an estimator, at best close to, but not identical to the neutrino direction. The angle between a muon neutrino and its daughter muon is a stochastic variable, but is on average small at high energies [147]

$$\theta_{\nu,\mu} \lesssim 0.7^\circ (E_\nu/\text{TeV})^{-0.7}, \quad (4.1)$$

making neutrino astronomy with muon neutrinos feasible above ~ 1 TeV.

4.2.3 Data Acquisition (DAQ)

The real-time IceCube DAQ system consists of several components. Besides the DOMs and the string cables that are deployed in the ice, they are located on the ice surface at a counting house, the IceCube Laboratory (ICL):

- The *DOMHub* is a computer that communicates with all DOM mainboards connected to one string.
- The *Master Clock* distributes high-precision UTC time signals from a GPS receiver to the DOM-Hubs, from which they become part of the physics data set.
- The *Stringhub* is a software element that converts DOM hit times to the time domain of the ICL (UTC) and sorts all hits coming from one string by time.

These components together capture the PMT signals from the DOMs to provide data about photon hits with ns precision timing [136].

In order to reduce the data volume to a manageable size, it is required to trigger the DAQ and record only relevant data. A first trigger requirement implemented in the DOM hardware is the *local coincidence* (LC) criterion. If the DOM’s PMT signal exceeds the discriminator threshold, set to the amplitude equivalent to ~ 0.25 PE, then this is called a DOM hit. Upon a hit, the DOM captures the waveform and sends a signal to its neighboring DOMs on the string. If at least one other nearest or next-to-nearest neighbor DOM has been hit within a time window of $\pm 1 \mu\text{s}$, then the LC criterion has been satisfied and the hit is tagged as an LC hit. The DOM then digitizes the waveforms and writes them to a buffer [136]. The digitized waveforms are sent to the ice surface on request. Isolated hits without LC tag contain only

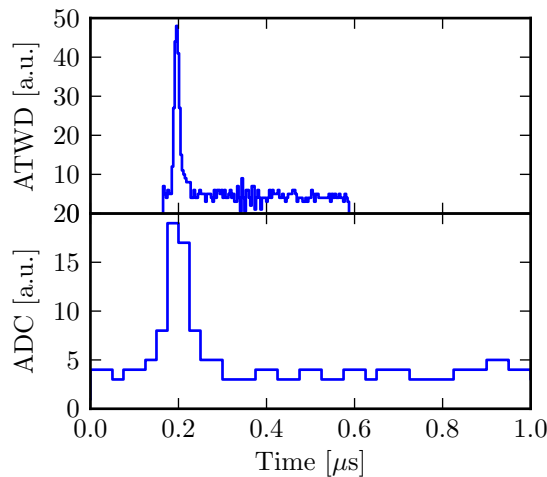


Figure 4.9: Example of an IceCube DOM’s digitized waveform (for a single PE), taken from real data, i.e. one of the very high energy starting events published in [38]. The two digitizer outputs called ATWD and ADC are plotted. The ADC waveform extends out to $6.4\ \mu\text{s}$, but is truncated at $1\ \mu\text{s}$ in the plot in order to make the ATWD waveform more visible.

a header with a timestamp and total charge, but the waveform itself is discarded [136]. Figure 4.9 shows an example of a typical digitized IceCube waveform. There are two waveform digitizers on the DOM:

- The *ATWD* (Analog Transient Waveform Digitizer): The ATWD output consists of 128 bins of $3.3\ \text{ns}$ width, covering a total of $420\ \text{ns}$ [145]. It is suited for the details of the early waveform.
- The *ADC* (Analog to Digital Converter): The ADC has 256 bins of $25\ \text{ns}$ width and thus spans a much longer time window of $6.4\ \mu\text{s}$, however it is much coarser than ATWD [136].

The actual trigger decision is made in the ICL. For muon track analyses and neutrino point source searches, a trigger called *simple multiplicity trigger* (SMT) is used. The SMT looks for a minimal number of LC hits anywhere in the detector within a time window of $5\ \mu\text{s}$. IceCube uses a setting of at least eight hits (SMT-8), so there must be at least 4 pairs of neighboring hits to trigger the detector [144], [148, p. 34]. If the trigger requirement is met, then data readout is requested from all DOMs for the time window, during which the condition is satisfied, plus extra windows $4\ \mu\text{s}$ before and $6\ \mu\text{s}$ after [148, pp. 34f.].

The data rate of the SMT-8 trigger in the completed IceCube detector varies between about 2000 and 2300 Hz, depending on the season. The rate is higher in the austral summer, because the higher air temperature leads to lower air density and correspondingly higher probability of meson decay before interacting and losing energy. More high-energy muons are created in the atmosphere above the detector, so that the trigger rate is higher.

4.2.4 Event Reconstructions

The raw data from the DOMs need to be fed into several computer algorithms in order to be reduced to a relevant sample of neutrino candidates and to extract physical parameters from these neutrino candidates, i.e. the direction and energy of the particles. This is important, because the trigger rate of ca. 2 kHz is too high to be transferred via satellite. The ICL at the South Pole hosts a data and computing center with 200 CPUs available for the purpose of real-time event reconstructions and filtering. After

extracting the waveform features, i.e. the times and charges of the individual PE pulses, several event reconstructions are done on the extracted data. These are explained in the following sections.

Waveform Feature Extraction

For the waveforms to be useful in event reconstruction, one needs to extract their features, i.e. the times, amplitudes (in units of PE), and widths of the PMT pulses. First of all, the raw waveform data need to be converted from counts to millivolts. Each PMT has its own values for gain, baseline offset, and signal transit time that are stored in a database and need to be taken into account. After this waveform calibration, the pulse information is extracted using an unfolding algorithm that treats the calibrated waveform as a linear combination of characteristic response functions to single photoelectrons [149, p. 56], [145].

Hit Cleaning

Event reconstructions can be spoiled by noise hits that are not correlated with the track. It is thus advisable to remove most of the noise hits in a process called *hit cleaning*. A first cleaning is already applied by the DOMs themselves due to the local coincidence (LC) criterion, see Section 4.2.3. However, since non-LC hits are included in the data as well, more cleaning is necessary. The simplest path would be to discard all non-LC hits, but as they have the potential to contain physics information from the particle track, more sophisticated algorithms were developed. By default, a combination of topological cleaning (SeededRT) with simple time-based cleaning (time window) is used.

SeededRT Cleaning

In the legacy of IceCube and its predecessor AMANDA, there is an algorithm called *RT cleaning* (radius-time cleaning), which is a generalization of the LC criterion of the DOMs: Every hit is checked for neighboring hits within a certain radius R and time T from the hit. Only hits with at least one neighboring hit are kept. RT cleaning is a *subtractive* hit cleaning that starts with all hits and removes certain hits.

SeededRT cleaning (SRT cleaning) is a specialization of RT cleaning, with the data as a mixture of LC and non-LC hits in mind. It is an iterative RT cleaning that starts by checking the “core” of hits. The core is defined by either the LC hits or, optionally, a reduced LC core given by the LC hits with at least two more hits in their RT range. If non-LC hits are found within R and T from a core hit, they are added to the hit selection. In the next iteration, the new hit selection is scanned and the process continues until no more hits are added to the hit selection. SRT cleaning is motivated by the idea that physics events will always have LC hits “at their core”. From this core of correlated hits, one can propagate to the periphery of the event. Noise hits that are not correlated in time and space with the event core are discarded. SRT cleaning is an *additive* hit cleaning that starts with a small number of hits and adds certain hits.

Time Window Cleaning

Time window cleaning (TWC) is a simple hit cleaning that slides a time window of configurable width over the event and searches for the window position containing the maximal number of hits. All hits falling inside the time window are kept and the rest is discarded. This enables simple removal of early or late noise hits that are not correlated with the physics event constituting the majority of hits.

It also serves as a primitive way to mitigate *coincident events*: More than one physics event occurring during one readout window is called a coincident event. Most coincident events are two or more muons streaming through the detector close after each other. When this happens, event reconstructions are

almost destined to fail because they will try to connect a track between the first and second muon. TWC is the simplest way to solve the problem of coincident events by only selecting one of the muons, the one that is brightest. This only works if the muons were separated enough in time. Coincident events occurring synchronously can only be handled by splitting the event topologically. Even though efficient algorithms for this have been developed in IceCube, they are not perfect. There is the danger of erroneously splitting a single event in two, creating a fake neutrino doublet that triggers an online follow-up alert (see Section 6.2). Therefore, such event splitting is not used in this work.⁴

Track Reconstructions

Linefit

Muon track reconstruction in IceCube needs to start with a simple and fast pattern recognition algorithm, which does not need an initial value [150]. The commonly used algorithm is known as *linefit*. Its result can be used as an initial value, also called *seed*, for more sophisticated reconstructions that would not find the solution without a good starting point.

Linefit assumes that light is propagating along a straight line (the track hypothesis) with constant velocity \vec{v} . This line is found in a least-squares optimization. The χ^2 is defined as the sum over the squared distances between each hit and the track. Let \vec{x}_i and t_i be the position and time of the i th of N_{hits} photon hits. The reconstructed muon track is characterized by a starting time t_0 , the position \vec{x}_0 of the particle at time t_0 , and by the velocity vector \vec{v} . Then:

$$\chi^2 \equiv \sum_{i=1}^{N_{\text{hits}}} \rho_i(\vec{x}_0, t_0, \vec{v})^2, \quad \rho_i(\vec{x}_0, t_0, \vec{v}) = (\vec{x}_0 + (t_i - t_0)\vec{v} - \vec{x}_i) \quad (4.2)$$

is to be minimized. This minimization can be solved analytically and therefore no iterative fit is needed [150].

While the linefit provides a quick track hypothesis, it has several limitations:

- The Cherenkov cone geometry is not taken into account.
- The ice properties, scattering and absorbing light, are not taken into account.
- It is not robust against noise hits or strongly scattered hits, because they are given a high quadratic weight and influence the fit strongly.

The first two points cannot be mitigated if the simplicity and speed of the linefit need to be retained, but the third point can be addressed. This has been done under the name *improved linefit*, which is running at the South Pole since the 2012/13 season. The improved linefit discards hits that appear to be strongly scattered. For each hit, it looks at all neighboring hits within a radius of 156 m and discards the hit if any neighboring hit has a time 778 ns earlier. As a second measure, the χ^2 function is modified into

$$\chi^2 \equiv \sum_{i=1}^{N_{\text{hits}}} \Phi(\rho_i(\vec{x}_0, t_0, \vec{v})), \quad \rho_i(\vec{x}_0, t_0, \vec{v}) = (\vec{x}_0 + (t_i - t_0)\vec{v} - \vec{x}_i), \quad (4.3)$$

⁴ In principle, this problem is of course solvable with intelligent, yet robust algorithms. The development of those has been suspended and might be a future improvement.

where the penalty function is defined as

$$\Phi(\rho) \equiv \begin{cases} \rho^2 & \text{if } \rho < \mu \\ \mu(2\rho - \mu) & \text{if } \rho \geq \mu \end{cases} \quad (4.4)$$

and μ is set to 153 m. This creates the same squared dependence for hits close to the track, but far away hits are only weighted linearly, which makes the fit more robust to noise hits. The result is a median angular resolution smaller by more than factor 2, which results in a higher probability for the subsequent fit finding the global minimum [137].

Likelihood Reconstructions

More advanced reconstructions are achieved with a likelihood-based method [150]. It employs a likelihood function that is the product of probability distribution functions (PDFs). The likelihood function describes the overall likelihood that the data are described by the model. It depends on a set of measured values $\mathbf{x} = \{x_i\}$ (the hit information extracted from the waveforms) as well as on a set of unknown parameters $\mathbf{a} = \{a_i\}$ (the track that one tries to obtain). Varying the track parameters \mathbf{a} , one can find the combination that maximizes the likelihood function $\mathcal{L}(\mathbf{x}|\mathbf{a})$ and hence provides the best agreement between data and track assumption. The track parameters are $\mathbf{a} = \vec{r}_0, t_0, \hat{v}, E_0$, an arbitrary point \vec{r}_0 on the track that the muon passes at time t_0 with energy E_0 and normalized direction \hat{v} .

The likelihood $\mathcal{L}(\mathbf{x}|\mathbf{a})$ is built up by multiplying the PDFs $p(x_i|\mathbf{a})$ for all the measured values in the set \mathbf{x} :

$$\mathcal{L}(\mathbf{x}|\mathbf{a}) = \prod_i p(x_i|\mathbf{a}) \quad (4.5)$$

The most relevant hit information is given by the hit times, so the most basic likelihood contains only time. The hit times are conveniently represented as *time residuals*

$$t_{\text{res}} \equiv t_{\text{hit}} - t_{\text{geo}}, \quad (4.6)$$

defined as the actual hit time t_{hit} relative to the expected hit time t_{geo} of an unscattered photon in the light front of the Cherenkov cone, according to the track geometry. Due to light scattering and secondary cascades along the muon track, most photon hits are expected to have positive time residuals. Negative time residuals can be caused by noise hits [150].

For numerical reasons, $-\log \mathcal{L}$ is minimized instead of \mathcal{L} being maximized. In IceCube, one can perform several iterations of a likelihood fit, each time varying the initial track hypothesis randomly, to mitigate the problem of local minima.

SPE Fit

The simplest time likelihood function is the product over p_1 , the PDF for arrival times of single photons i [150],

$$\mathcal{L}_{\text{SPE}} = \prod_{i=1}^{N_{\text{hits}}} p_1(t_{\text{res},i}|\mathbf{a}), \quad (4.7)$$

where one DOM can contribute multiple hits. Because this likelihood is the product of single photoelectron (SPE) PDFs, it is called *SPE likelihood* and is the likelihood that is maximized in course of the SPE fit. The PDF $p_1(t_{\text{res},i}|\mathbf{a})$ is obtained from the simulation of photon propagation through ice. For performance reasons, the simulation results of the time residual distributions are approximated with an

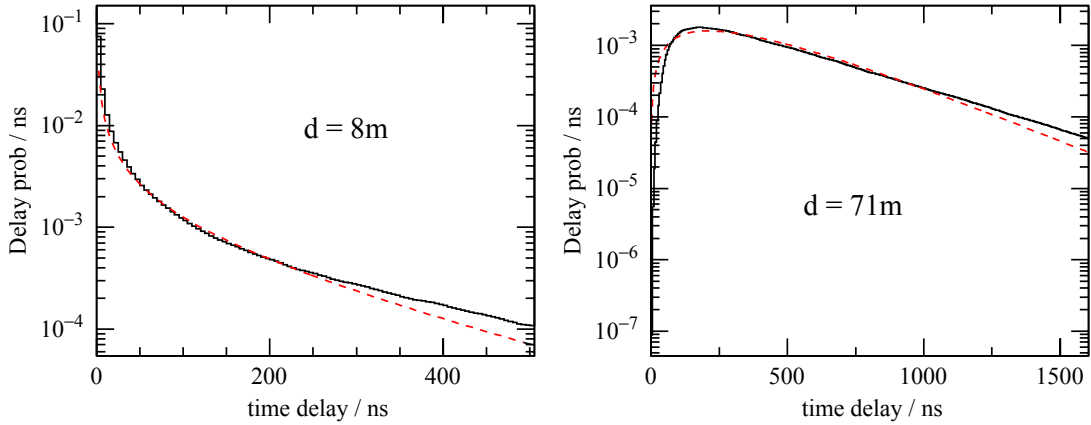


Figure 4.10: Comparison of the parametrized Pandel function (dashed curves) with a detailed photon propagation Monte Carlo simulation (black histograms) at two distances d from the muon track. From [150].

analytical function, which is called *Pandel function* and is defined as [150]

$$p_1(t_{\text{res}}|d) \equiv \frac{1}{N(d)} \frac{\tau^{-d/\lambda} t_{\text{res}}^{(d/\lambda-1)}}{\Gamma(d/\lambda)} \exp\left(-\frac{t_{\text{res}}}{\tau} - \frac{t_{\text{res}} c_{\text{ice}} + d}{\lambda_a}\right) \quad (4.8)$$

with normalization

$$N(d) \equiv e^{-d/\lambda_a} \left(1 + \frac{\tau c_{\text{ice}}}{\lambda_a}\right)^{-d/\lambda}. \quad (4.9)$$

Here, $c_{\text{ice}} = c/n$ is the speed of light in ice, λ_a the absorption length, and $\Gamma(d/\lambda)$ the Gamma function. There are two free parameters, $\lambda = 33.3$ m and $\tau = 557$ ns, which were empirically determined by Monte Carlo. The variable d is the track-DOM distance. The DOMs have an angle-dependent efficiency, which can be incorporated into Equation 4.8 by replacing d with an effective distance d_{eff} . Indeed the time residual distribution for backward illumination of the PMT is similar to a head-on illumination at a larger distance [150]. Figure 4.10 shows the shape of the Pandel function for a short and a long distance from the muon track.

The frequently used version of SPE fit in IceCube is so-called *SPE1st*. This means that only the time of the first pulse on each DOM is considered in \mathcal{L}_{SPE} . Even though this treatment is not using all available information, it was found to work better than using all the photon hit times, also known as *SPEAll*. This is presumably because the first photon hit is likely to be a nearly unscattered photon that has the strongest correlation with the particle track. The later the photon arrives, the more often it has been scattered along its path and the more ambiguous is its emission point along the track, complicating the reconstruction. Late photons do not add new information, but instead increase systematic uncertainties [151]. Another alternative version of the SPE fit is *SPEqAll*, where the charge q_i of each pulse (in number of PEs) is used as a weighting for p_1 , such that

$$\mathcal{L}_{\text{SPEqAll}} = \prod_{i=1}^{N_{\text{hits}}} p_1(t_{\text{res},i}|\mathbf{a})^{q_i}. \quad (4.10)$$

However, it is found to be inferior to SPE1st as well.

MPE Fit

In order to improve the likelihood model with respect to SPE, one can include information about the total charge, or number of PEs. For instance, one can define the arrival time distribution for the first, least scattered, photon out of N photons as the probability that any one of the N photons arrives at time t_{res} and all others arrive at some time later [150]

$$\begin{aligned} p_N^1(t_{\text{res}}) &= N p_1(t_{\text{res}}) \left(\int_{t_{\text{res}}}^{\infty} p_1(t) dt \right)^{N-1} \\ &= N p_1(t_{\text{res}}) (1 - P_1(t_{\text{res}}))^{N-1}. \end{aligned} \quad (4.11)$$

Here, $P_1(t_{\text{res}})$ is the cumulative distribution function (CDF) of the single photon PDF p_1 . The function $p_N^1(t_{\text{res}})$ is called the multi-photoelectron (MPE) PDF and provides a more realistic arrival time distribution, because the first of N photons arrives on average earlier than a single photon. The MPE PDF is used in \mathcal{L}_{MPE} :

$$\mathcal{L}_{\text{MPE}} = \prod_{i=1}^{N_{\text{Ch}}} p_{N_i}^1(t_{\text{res},i} | \mathbf{a}), \quad (4.12)$$

where every hit DOM i only contributes once, with the first hit time $t_{\text{res},i}$ and the total number of hits N_i . At low energies, where every DOM detects usually just one photon, there is no difference between the SPE and MPE PDFs. Hence, SPE and MPE perform similar below energies of 1 TeV, but above that energy, MPE outperforms SPE [152, p. 38]. It is possible to generalize MPE for all photons and define the MPE PDF for the k th out of N photons [150]. If used, this is called *MPEAll*, but as for *SPEAll*, *MPEAll* does not provide a better reconstruction result than MPE with only the first photon hit time.

For several years, the MPE fit has been the state-of-the-art muon track reconstruction for neutrino point source analyses, until it has been superseded by the more sophisticated SplineMPE fit.

SplineMPE Fit

The quality of likelihood reconstructions is only as good as the underlying PDFs that have to match the real data. The Pandel photon arrival time PDFs used for the SPE and MPE fits are analytic approximations that allow very fast computation. Even though the Pandel-based MPE reconstruction provides sufficient angular resolution for neutrino point source searches, there are some obvious disadvantages [152, p. 41]:

- The Gamma function used in the Pandel function in Equation 4.8 does not perfectly fit detailed Monte Carlo simulations, especially in the regime where $d \approx \lambda = 33.3$ m [150].
- The Pandel function does not take into account the layered structure of the South Pole ice, leading to depth-dependent scattering and absorption coefficients.
- The use of d_{eff} in Equation 4.8 to describe the angle-dependent DOM sensitivity is only an approximation used for simplicity.

One can improve the description of the photon propagation in the ice by using Monte Carlo (MC) simulation to construct the PDFs. The MC results are tabulated for all possible geometrical photon emitter and receiver configurations [152, p. 41]. Muon and photon propagation were simulated using the most detailed model of optical ice properties available and the data were stored in very fine-binned tables. The tables represent the time residual PDFs for all possible track-DOM configurations. A multi-dimensional spline surface is fitted to the tables so that only the spline parameters need to be stored

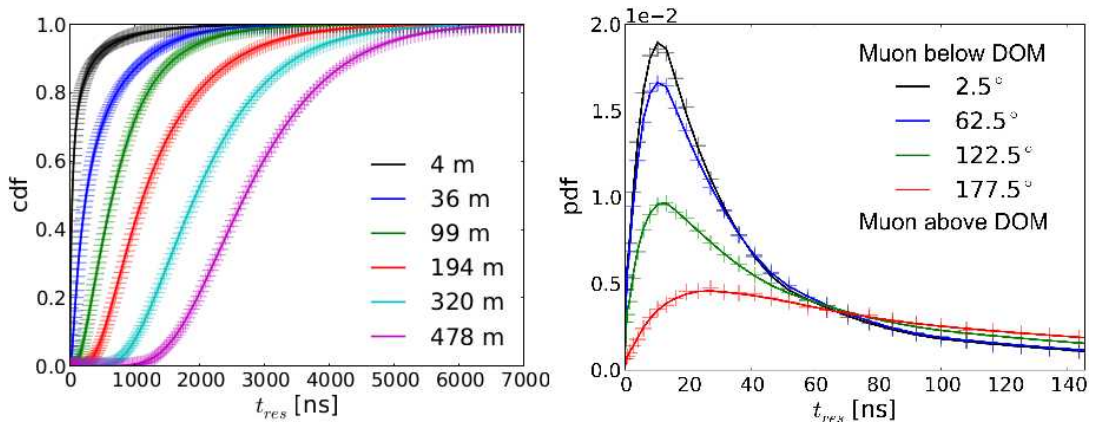


Figure 4.11: *Left*: The cumulative density functions (CDFs) of the time residual t_{res} , i.e. the integrals of the PDFs from the MC simulation, are used for the spline fitting, because they are always confined to the range between 0 and 1. They are shown in the left plot, where the crosses are the MC data points and the lines are the resulting spline fit. The plot is for certain geometrical parameters like track zenith angle and depth of the DOM, for different perpendicular distance ρ to the track as indicated. *Right*: The PDF derived from the CDF spline fit (lines) and the actual MC simulation data (crosses), for the same parameters as in the left plot, but for ρ between 23.7 m and 24.8 m and different azimuthal angle ϕ of the DOM with respect to the track, as indicated. Image taken from [152, p. 49].

instead of the full table. Splines are piecewise defined polynomial functions of certain order and the fitted spline surface is a linear combination of basic splines. The spline fitting reduces the table size from 20 GB to a little more than 200 MB so that it fits into memory. The spline fit also provides a smooth function and averages out statistical fluctuations, which facilitates the likelihood maximization. Thanks to the spline fitting, the time residual PDF can easily be convolved with a Gaussian to account for timing uncertainties, e.g. PMT jitter [152, pp. 46–48]. Figure 4.11 shows example PDFs reconstructed from the spline tables.

The likelihood fits can be carried out as before, only replacing the Pandel time arrival PDFs with the PDFs constructed from the spline fit tables. A new software module *spline-reco* was created that returns the PDF values. It can be plugged into the same reconstruction modules as used for the Pandel SPE or MPE fit. The MPE fit using the spline tables is called *SplineMPE* and provides significantly improved median angular resolution of as good as 0.4° at highest energies, compared to 0.6° achieved with Pandel-based MPE [152, pp. 38, 50].

The photon distribution tables and the spline-reco module were created by Kai Schatto using the *Photospline* [153] software module [152].

Directional Uncertainty Estimators

Paraboloid Directional Uncertainty

The estimation of the uncertainty on the reconstructed particle direction is as important as the direction itself. This is because for a point source search, where one assumes that signal neutrinos come from a single point in the sky, an event with a large reconstruction error that is reconstructed far away from the source can be correlated to the source, whereas if the error is small, it is rather unlikely that it is correlated.

The default way of estimating reconstruction uncertainty, or event-by-event *angular error*, in IceCube is called *Paraboloid fit* and involves fitting a two-dimensional paraboloid to the likelihood space around

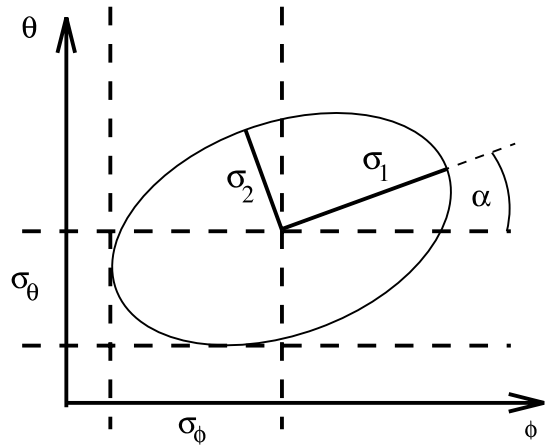


Figure 4.12: The error ellipse in θ and ϕ is either represented by σ_θ , σ_ϕ and the covariance $\text{cov}(\theta, \phi)$ or by major and minor axis σ_1 , σ_2 , and rotation angle α . From [154].

the found minimum of $-\log \mathcal{L}$, in order to determine the sharpness of the minimum [154]. A slice through the paraboloid at value

$$-\log \mathcal{L} = -\log \mathcal{L}_{\max} + \frac{1}{2} \quad (4.13)$$

provides an error ellipse and the half-axes of that ellipse, σ_1 and σ_2 (see Figure 4.12), can serve as the angular error estimator. These half-axes are conventionally circularized with the root mean square (RMS) and a single error

$$\sigma_p = \sqrt{\frac{\sigma_1^2 + \sigma_2^2}{2}} \quad (4.14)$$

is used in IceCube analyses [155].

Paraboloid fit is the de-facto standard way of estimating angular uncertainty in IceCube point source analyses. Even though it is a very robust estimator, it is computationally demanding, because it requires many likelihood function evaluations.⁵ This is especially true for complex likelihoods and events with many hits. In practice, one finds that the Paraboloid fit is relatively fast for the majority of events, but there is a long tail in the processing time distribution so that single events with many hit DOMs can take orders of magnitude more time.

Cramér-Rao Directional Uncertainty

An alternative uncertainty estimator was developed by Jan Lünemann [156, pp. 38–47]. It is based on the *Cramér-Rao bound* (CRB), also known as *information inequality*. In the scalar case of only one parameter θ , the CRB states that the variance of any unbiased estimator $\hat{\theta}$ of θ is at least as large as the inverse of the Fisher information $I(\theta)$,

$$\text{var}(\hat{\theta}) \geq \frac{1}{I(\theta)}, \quad (4.15)$$

which means that the bound can be seen as an estimator of the uncertainty. The Fisher information, for measured value x and parameter θ , is defined as expectation value of the square of the partial derivative

⁵ The likelihood function must be numerically minimized in the parameters other than (θ, ϕ) on a grid of 25 points for each iteration [156].

of the natural logarithm of the likelihood function,

$$I(\theta) = \left\langle \left(\frac{\partial}{\partial \theta} \ln \mathcal{L}(x|\theta)|_{\hat{\theta}} \right)^2 \right\rangle. \quad (4.16)$$

Under certain regularity conditions, it can be written as the second derivative,

$$I(\theta) = - \left\langle \frac{\partial^2}{\partial \theta^2} \ln \mathcal{L}(x|\theta)|_{\hat{\theta}} \right\rangle. \quad (4.17)$$

The Fisher information can thus be seen as the curvature of the log-likelihood function near the maximum residing close to the estimated value $\hat{\theta}$. A low curvature results in a large uncertainty, and a high curvature (sharp maximum) in a small uncertainty. In the multivariate case, with dataset \mathbf{x} and parameter vector $\mathbf{a} = (\theta, \phi, x, y, z)$ containing zenith angle θ , azimuth angle ϕ , and the anchor point coordinates x, y, z of the muon track, the Fisher information becomes the matrix $I(\mathbf{a})$ with elements

$$I_{mk}(\mathbf{a}) = - \left\langle \frac{\partial^2}{\partial a_k \partial a_m} \ln \mathcal{L}(\mathbf{x}|\mathbf{a})|_{\hat{\mathbf{a}}} \right\rangle. \quad (4.18)$$

The minimal covariance matrix is obtained by inverting the Fisher information matrix

$$\text{cov}(a_m, a_k) \geq \left(I(\mathbf{a})^{-1} \right)_{mk}. \quad (4.19)$$

The diagonal elements of the covariance matrix represent the minimal variance. In particular, the square root of the diagonal elements for parameters θ and ϕ (zenith and azimuth angle) can be used as estimators for the uncertainty.

In order to make the numerical implementation as fast as possible, the calculation of the Fisher matrix involving the Pandel function contained in the likelihood function has been pre-evaluated for track-DOM distances d up to 200 m in steps of 0.5 m and stored in a table. A linear interpolation between those steps is used and for distances larger than 200 m, a simple approximation is used. The inversion of the Fisher matrix I is performed via *LU* factorization. Because only simple algebraic calculations are required instead of numerical minimization, the Cramér-Rao uncertainty estimation can be several hundred times faster than the Paraboloid fit [156, pp. 41f.]

The Cramér-Rao implementation in IceCube software returns the diagonal element roots σ_θ and σ_ϕ for θ and ϕ . In order to get a circularized error on the neutrino direction, one can add the errors to the reconstructed direction $(\hat{\theta}, \hat{\phi})$ and calculate the angular distance between the two points

$$\sigma_{cr} = \angle((\hat{\theta}, \hat{\phi}), (\hat{\theta} + \sigma_\theta, \hat{\phi} + \sigma_\phi)). \quad (4.20)$$

Energy Reconstructions

Because the neutrino itself is not observable, one can at best measure the energy of the charged particle that was created by the neutrino. Due to energy loss outside of the detector, the detected particle's energy can be lower than the original neutrino energy. Thus, reconstructed energies are mostly lower limits on the neutrino energy.

In the case of a muon track, a precise measurement of the energy is only possible if the muon decays within the detector and deposits all its energy in a particle shower. However, because the muon energy loss per path length dE_μ/dx is proportional to the muon energy E_μ , see Section 2.3.3, one can roughly estimate E_μ with a measurement of dE_μ/dx . Furthermore, the expected number of detected Cherenkov

photons is directly proportional to dE_μ/dx [157]. This allows to obtain the energy once a template number of detected photons $\Lambda(\mathbf{a})$ is known for a certain known dE_μ/dx . The template $\Lambda(\mathbf{a})$ depends on the track parameters \mathbf{a} , e.g. the track angle and its path length inside the detector.

In an approximative analytic treatment, one can assume that close to the track, the photon density is $\propto 1/r$ with r being the shortest distance to the track. At large distances from the track, the photon propagation is diffusive and can be approximated with a random walk. The photon density is given by $\exp(-r/\lambda_p)/\sqrt{r}$. The *propagation length* λ_p is defined as [143]

$$\lambda_p \equiv \sqrt{\lambda_a \lambda_e / 3}, \quad (4.21)$$

where λ_a is the absorption length and λ_e the effective scattering length [143, 145]. The two distance regimes can be combined into one empirical function of the form [145]

$$\Lambda(r) = l_0 A \frac{1}{2\pi \sin \theta_c} e^{-r/\lambda_p} \frac{1}{\sqrt{\lambda_\mu r} \tanh \sqrt{r/\lambda_\mu}}, \quad (4.22)$$

with $\sqrt{\lambda_\mu} \equiv \frac{\lambda_c}{\sin \theta_c} \sqrt{\frac{2}{\pi \lambda_p}}$ and $\lambda_c \equiv \frac{\lambda_e}{3} e^{\lambda_e/\lambda_a}$,

giving the average expected number of detected photons from a template track with a certain reference muon energy E_{ref} , on a DOM at distance r from the track. Here, l_0 is the number of photons emitted per meter along the track, A is the effective photon collection area of the DOM, and θ_c is the Cherenkov angle of about 40° in ice. Because of linearity, the *light yield* λ , which is the expected average number of photons from a muon with energy E_μ , is given by

$$\lambda = \mu(E_\mu) + \rho \quad \text{with} \quad \mu(E_\mu) = E_\mu / E_{\text{ref}} \Lambda(r), \quad (4.23)$$

where ρ is the average number of noise photons. The actual number k of detected photons follows a Poisson distribution:

$$p(k|\lambda) = \frac{\lambda^k}{k!} e^{-\lambda}, \quad (4.24)$$

so that the likelihood for all DOM detections is

$$\begin{aligned} \mathcal{L}(E_\mu) &= \prod_{i=1}^{N_{\text{Ch}}} \frac{(\lambda_i(E_\mu))^{k_i}}{k_i!} e^{-(\lambda_i(E_\mu))} \\ &= \prod_{i=1}^{N_{\text{Ch}}} \frac{(\mu_i(E_\mu) + \rho)^{k_i}}{k_i!} e^{-(\mu_i(E_\mu) + \rho)}. \end{aligned} \quad (4.25)$$

This likelihood can be maximized with respect to E_μ , which is contained in $\mu_i(E_\mu) = E_\mu / E_{\text{ref}} \Lambda(r_i)$. The implementation of this likelihood maximization in IceCube is called *MuE* [152, p. 67], short for *muon energy*.

The MuE energy reconstruction has some limitations:

- It does not account for the varying optical properties in different ice layers.
- It describes a smooth, continuous photon emission and does not account for large stochastic energy losses that happen abruptly. The result is that MuE tries to match a continuous energy loss to the large stochastic losses and is biased towards higher energy.

While the first limitation is difficult to overcome in an analytic approximation, the second limitation is addressed by an improved version of MuE called *MuEx* [152, p. 67]. For MuEx, the parametrization of the expected photon density allows for upward fluctuations by convolving the likelihood function in Equation 4.25 with a probability distribution G on the light yield λ [145]

$$G(\lambda) = \frac{\text{const.}}{\lambda} \left(e^{-wy} + (y/\sigma)^2 \right)^{-1} \quad \text{with} \quad y = \ln \frac{\lambda}{\Lambda}. \quad (4.26)$$

The skewness parameter w allows for larger over-fluctuations, e.g. caused by bremsstrahlung.

The IceCube collaboration has also developed higher-quality parametrizations of the template photon density Λ , which are the tabulated results from Monte Carlo simulations of the light propagation in the ice [145]. These are superior to the analytic approximations described above, but require more computation time. The resulting tables are ca. 1 GB in size and take on order 1 μ s for a single evaluation, which is much longer than the above approximation. These parametrizations are mostly used for cascade reconstructions, where the energy measurement is more meaningful than in the case of muon tracks.

4.2.5 Quality Parameters

One can define many parameters that are useful for the separation of signal and background. For example, parameters can reflect the reconstruction quality and can help distinguish mis-reconstructed muons from neutrinos. Other possibilities are parameters that are sensitive to more specific event characteristics, e.g. parameters for the separation of cascades from tracks, or muon bundles from single muons, or even tau neutrinos from all other events. Many parameters are based on the geometry of the event.

Maximum Likelihood

The *log-likelihood* $-\log \hat{\mathcal{L}}$ of the maximized likelihood $\hat{\mathcal{L}}$ is a measure of the event's reconstruction fit quality. A small value means higher quality (higher $\hat{\mathcal{L}}$). Because the number of degrees of freedom varies from event to event, it is better to use the *reduced log-likelihood*, which is defined in analogy to the reduced χ^2 of least-squares fitting as the log-likelihood divided by the number of degrees of freedom n_{dof} . The degrees of freedom are the number of data points minus the number of free fit parameters. For SPE and MPE fit, the number of data points are the number of hit optical modules, also called N_{Ch} , number of channels. There are five free fit parameters for a track fit: the three coordinates of the track anchor point and the two angles, θ and ϕ , zenith and azimuth angle of the track. So the reduced log-likelihood is

$$\text{rlogl} \equiv \frac{-\log \hat{\mathcal{L}}}{N_{\text{Ch}} - 5}. \quad (4.27)$$

This definition is not a strict mathematical goodness-of-fit. Hence, in practice, it is often found that a different n_{dof} provides a better background-signal separation, sometimes even a non-integer n_{dof} . One can define a *modified reduced log-likelihood* like

$$\text{mrlogl}(x) \equiv \frac{-\log \hat{\mathcal{L}}}{N_{\text{Ch}} - x} \quad (4.28)$$

with a parameter x that usually takes values like 3, 3.5, 4, or 4.5.

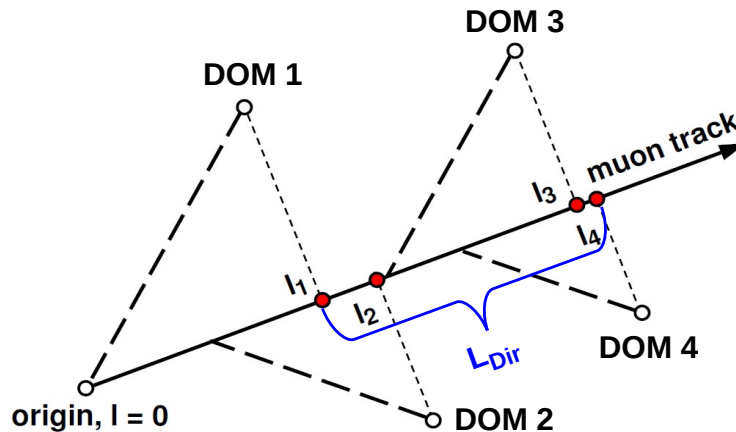


Figure 4.13: The direct hit track length L_{dir} is the portion of the track covered by direct hits projected perpendicularly onto the track. From [149, p. 59].

Direct Hits

Some quality parameters are associated with *direct hits*, i.e. relatively unscattered photons. Direct hits can be defined using the time residual t_{res} from Equation 4.6. Hits with time residual within $[-15 \text{ ns}, 75 \text{ ns}]$ are the most frequently used definition in IceCube, providing the best cut performance. The *number of direct hits*, called N_{dir} , is an important quality parameter. Another variable is the *direct hit track length* L_{dir} and is the section of the track that is covered by direct hits projected perpendicularly onto the track. This definition is illustrated in Figure 4.13.

L_{empty} and Separation

The *empty track length*, or short L_{empty} , is the longest track segment without hits within a cylinder of pre-defined radius around the track segment.

The *separation length*, or short *Separation*, is defined as the distance between the center of gravity (COG) of the first and last quartile of hits, within a specified track cylinder radius. Here, first and last quartile are defined as the first and last quarter of hit DOMs, within the cylinder, sorted by time of the first pulse. The COG is defined as the average position of the hit DOMs, weighted by the charge of the first pulse on each DOM.

Both variables are motivated by the identification of mis-reconstructions that are usually clearly visible by eye, but can be difficult to detect automatically. Coincident events, for instance, are usually reconstructed as a connection between the two muon tracks. In this case, there is a large gap in the middle of the reconstructed track, in between the two tracks. The hits are concentrated in the first and last part of the track and can those parts can have a large separation. Therefore, both a small L_{empty} and a large *Separation* are characteristic for such failed reconstructions.

Split Fits

In order to identify mis-reconstructed events, it is useful to split the event in two parts and repeat the reconstructions on both parts. There are two ways to split the event:

1. Based on hit time: the event is split into hits before and after the average pulse time.

2. Base on track geometry: the event is split into the hits on both sides of a plane perpendicular to the track that goes through the COG (defined as above).

Bayesian Fits

Because many mis-reconstructed events are actually downgoing muons that are reconstructed as upgoing, it is interesting to force any such event to be downgoing using a prior function representing our prior knowledge, like in Bayesian statistics. For this purpose, a likelihood fit is performed using a Pandel PDF multiplied with a downgoing prior function that depends only on zenith angle θ of the track hypothesis. The downgoing prior models the zenith distribution of downgoing muons and is defined as:

$$p(\theta) \equiv \begin{cases} \max(a_0 (\cos \theta)^{a_1} e^{-a_2/\cos \theta}, p_{\min}) & \text{if } \cos \theta \geq 0 \\ 10^{-v+s \cos \theta} & \text{if } \cos \theta < 0 \end{cases} \quad (4.29)$$

The function's form and parameters were found empirically using downgoing muon data. The parameter values are: $a_0 = 2.50 \times 10^{-7}$, $a_1 = 1.68$, $a_2 = 0.78$, $p_{\min} = 1.38 \times 10^{-87}$, $v = 200$, $s = 1000$. In the downgoing region, $\cos \theta \geq 0$, the prior becomes very small at the horizon ($\cos \theta \rightarrow 0$), down to p_{\min} . In the upgoing region, $\cos \theta > 0$, a penalty is applied and the prior is even smaller, $p \leq 10^{-200}$. The penalty has a slope so that it becomes $p = 10^{-1200}$ at $\cos \theta = -1$. This causes the minimizer to “roll back” towards the allowed downgoing region.

Thanks to the penalty term, the prior constrains the zenith angle to the downgoing range. Doing a likelihood maximization with this prior PDF returns the best-fitting downgoing track. The maximized log-likelihood value of the Bayesian fit can be compared to the unconstrained maximized log-likelihood. An upgoing track forced to be downgoing should have a much worse likelihood. However, for mis-reconstructed downgoing tracks, the difference between the fits with and without prior should be smaller.

4.2.6 Base Processing and Filtering

In the IceCube Lab, basic data processing, event reconstruction, and filtering happens in real-time to enable transmission of a relevant subset of the data via satellite. The available bandwidth is limited to 100 GB/day, so that the full trigger rate of several kHz cannot be sent via satellite.

The general purpose processing is called *Base Processing* and includes calibration and feature extraction of the data, as well as basic reconstructions used for various filters. Every working group in the IceCube collaboration can define and install its own filter that selects a subsample of all triggered events. For point source analyses using muon tracks, the relevant filter is called *Muon Filter*. Other filters exist in parallel, selecting different subsamples, e.g. the *Cascade Filter* selecting cascade-like events or a filter selecting candidates for extremely high-energy (EHE) events. One event can be tagged by several filters. Every event having any filter tag is transferred via NASA's Tracking and Data Relay Satellite System (TDRSS) [158, 159], which is also used by low-earth orbiting spacecraft like the Swift X-ray satellite [160], the Hubble Space Telescope, and the International Space Station [161].

The individual steps of the base processing, as far as the muon track channel is concerned, are (omitting some of the technical details):

1. Data from DOMs that are known to be faulty are removed.
2. The waveforms are calibrated and the pulse information is extracted.
3. *SeededRT cleaning* (see Section 4.2.4) is performed on the IceCube pulses, with $R = 150$ m, $T = 1000$ ns, and the reduced LC core setting.

Search for MeV Neutrinos from Supernovae

This chapter is based on a paper written mainly by the author of this thesis, with help from Sebastian Böser, Lukas Schulte, and Marek Kowalski, building on previous work by Nora Linn Strotjohann. The paper was published in the journal *Astroparticle Physics* [141]. The parts contributed by others were either removed or reformulated. It is indicated where work of others has been used.

5.1 Motivation

Section 3.2.5 explained that in 1987, a core-collapse supernova (SN) exploded in the vicinity of our Galaxy. Until today, SN 1987A has been the only event with a successful SN neutrino detection. Even though the number of detected neutrinos was quite small, i.e. ~ 20 [91], it had a large impact on both astrophysics and particle physics and led to many publications. The SN neutrinos allowed to observationally test models of the core-collapse [99], to set constraints on neutrino properties like mass [99], to test special relativity [100], and constrain the existence of exotic particles, for instance axions [101].

Given today's detectors, an SN in our Galaxy would result in $\sim 10^4$ neutrino events detected individually in Super-Kamiokande [126, 168] and other large low-energy neutrino detectors, as well as up to millions of neutrinos detected through an increase in noise rate in IceCube [169]. This would enable an immense scientific harvest, as explained in [168, 170], ranging from core-collapse physics via neutrino mixing parameters and neutrino mass hierarchy to exotic particle physics (e.g. exclusion of axions, right-handed neutrinos, and Kaluza-Klein particles), as well as providing a valuable early warning for observations of photons that are expected to arrive hours later. However, with an expected rate of only 1–3 Galactic SNe per century [102], the chance for a detection during the lifetime of the experiments is not overwhelmingly high. In the fortunate case of an SN detection, the uniqueness of the progenitor system will make it difficult to distinguish effects of astrophysical diversity from effects due to particle physics (e.g. neutrino oscillations), because both will impact the light curve and energy spectra.

As pointed out in [108] and [171], the situation will change drastically once neutrino detectors reach the sensitivity threshold to detect “mini-bursts” of neutrinos from SNe in neighboring galaxies. Not bound to our own Galaxy, the rate of SN detections can be increased by enlarging the detector. As will be shown in Section 5.7, an effective volume of ~ 10 Mtons is sufficient to detect SNe at a rate of ~ 1 to 4 per year—albeit most of them with less than ten individual neutrino events. Despite the low number of detected neutrinos, these routine observations would provide a wealth of information and allow entirely new studies [171]. Here are some of the scientific benefits of a large SN neutrino detector:

1. Determination of the core-collapse SN (CCSN) rate in our local Universe in a novel and less biased way. There is an apparent mismatch in rates: only about half the rate of SNe expected from the star formation rate is detected by optical surveys, see Section 3.2.6. A direct measurement would help solve the riddle of missing SNe.
2. Test of models predicting non-standard CCSN neutrino bursts, e.g. *failed* (i.e. optically unobservable) SNe or SNe from a collapsing ONeMg instead of an iron core (see Sections 3.1 and 3.2.6). In failed SNe, a black hole (BH) is formed directly, swallowing the electromagnetic radiation before it can escape. Neutrinos, however, can escape, and the expected neutrino burst from such an event is both more luminous and hotter [172]. Average neutrino energies can be roughly twice as high as in the case of the collapse to a neutron star (NS), opening the opportunity to identify the collapse to a BH.
3. Identification of questionable optical SN candidates, e.g. luminous blue variables [173], as “SN impostors” by the non-detection of neutrinos [171].
4. Triggering early optical, UV, and X-ray observations, possible because the neutrinos arrive several hours before the electromagnetic signal. Observation of the very first electromagnetic radiation from an SN, the shock breakout, is very important to constrain the nature of an SN and its progenitor. Very early data are hard to obtain without an early warning. So far, observations shortly after shock breakout exist for few (~10) SNe, including SN 1987A and SN 2008D, which exploded serendipitously while Swift was taking data of another SN in the same galaxy [174]. Even without directional information from the neutrinos, the follow-up could focus on the observation of nearest galaxies, from which a neutrino detection would be most likely.
5. Improving the significance of very weak high-energy neutrino or gravitational wave signals. The precise explosion time information from the MeV neutrino signal can be important in multi-messenger analyses [108, 171].
6. Measurement of the average SN neutrino luminosity and energy spectrum by combining the data from many mini-bursts. CCSN explosions are not understood yet and there is significant variance in e.g. the predicted mean neutrino energy [89]. A measurement of the neutrino luminosity and energy spectrum would provide valuable input to these models. It is also essential for predicting the redshifted spectrum of the Supernova Relic Neutrinos (SRNs), the diffuse isotropic flux from all past CCSNe [108, 171].
7. Measurement of the diffuse background from SRNs itself [89, 106].

The closest SN explosions, occurring at a lower rate, would provide a higher number of SN neutrinos. With higher statistics, an even broader physics program could be accessed:

1. Determination of the SN neutrino luminosity and energy spectrum on a per burst basis, revealing different classes of CCSN explosions.
2. Setting neutrino mass limits. From the observation of the arrival times of the neutrinos from SN 1987A, a limit in the eV range has been set on the effective mass of the anti-electron neutrino [175]. By observing neutrinos from a more distant SN, more stringent limits could be set.
3. By its impact on the predicted flux, the neutrino mass hierarchy can be addressed as well, provided a sufficient number of neutrinos is observed [169].

Motivated by this scientific potential, several megaton scale neutrino detectors are currently planned (e.g. Deep-TITAND [171], Hyper-Kamiokande [176, 177] and UNO [178]). Those are either water Cherenkov detectors located in mines or marine detectors, similar to ANTARES [162].

In this chapter, the potential of a ~ 10 Mton detector in the Antarctic ice shield is explored. In the existing IceCube detector, optimized for TeV–PeV energies [135], SN neutrino bursts are typically searched for by looking for a collective enhancement of photomultiplier noise rates [169]. This method only works for Galactic SNe where the number of interacting neutrinos is large enough. More distant SNe will not provide enough neutrinos, so that the few individual neutrino events must be observed directly. Due to the long sensor distance and consequently high energy threshold of IceCube, attempting to detect individual neutrino events significantly reduces the effective mass and hence distance at which SNe can be detected [179]. A dedicated effort is now under way to reduce the energy threshold to a few GeV in the PINGU (Precision IceCube Next-Generation Upgrade) project [120], with one of its goals being the determination of the neutrino mass hierarchy through the Mikheyev-Smirnov-Wolfenstein (MSW) effect [180]. The objective of this chapter is to go much further than PINGU, identifying what would be needed to lower the energy threshold down to ~ 10 MeV energies in order to reliably detect single SN neutrino interactions. The challenge is to reduce the energy threshold by three orders of magnitude while controlling the background at a level required for the detection of rare SN explosions.

While the focus of this chapter are SN neutrinos, it should be noted that such a detector will very likely provide much more physics potential. Some possibilities might be: a much increased precision of solar neutrino measurements, as well as an unprecedented sensitivity at the GeV scale, allowing atmospheric neutrino oscillation studies and sensitivity to other astrophysical phenomena such as collisional heating in GRBs [181, 182]. Another, possibly more ambitious, prospect is the search for proton decay.

5.2 Detector Simulation

MeV neutrinos can best be detected via inverse β -decay (IBD, see Section 2.3.2),

$$\bar{\nu}_e + p \rightarrow e^+ + n, \quad (5.1)$$

that requires a threshold energy of $E_\nu > 1.806$ MeV. To compute the positron energy, the approximation

$$E_{\text{pos}} = E_\nu - \Delta, \quad \Delta \equiv m_n - m_p = 1.293 \text{ MeV}, \quad (5.2)$$

is used, with mass difference Δ between proton and neutron, neglecting the small recoil energy of the neutron.¹ The IBD signature in a Cherenkov detector comes from the positron, which is emitting Cherenkov photons.

The ultimate question to be answered here is how many SN detections a possible detector can deliver. This problem can be decomposed into the following components:

- *Effective volume* V_{eff} or *effective mass* M_{eff} : The two quantities, related with each other by the medium's mass density,² are defined by the geometrical volume that the detector would have if it was able to detect 100% of the interactions (here the positron signature) occurring inside its volume.

¹ Due to momentum conservation, the momentum of the neutron p_n will be at most of the same order as the neutrino momentum $p_\nu \approx E_\nu \approx 10$ MeV. Thus, the recoil energy $p_n^2/(2m_n)$ is negligible, because of the high neutron mass, $m_n \approx 1000$ MeV [15, p. 525].

² For the mass density of the South Pole ice, an ice density of $\rho_0 = 0.9167 \text{ g cm}^{-3}$ [183] under normal conditions is used. With an assumed pressure of $p = 300 \text{ bar} = 3 \times 10^{-2} \text{ GPa}$ and a Young's modulus $Y = 7.8 \text{ GPa}$ of the ice [184], the glacier

- *Interaction cross-section σ* : the effective area that a target particle (here a hydrogen atom, i.e. proton) has with respect to the interaction with an incoming particle (here neutrino). Figuratively, if the neutrino passes through the area σ , then the interaction takes place, otherwise not. Thus, σ is related to the interaction probability of a stream of neutrinos. The approximation for the energy dependence of the IBD cross-section from Equation 2.11 is used.
- *Effective area A_{eff}* : the detector's effective area is the effective area of all target particles combined. It is therefore the product of number of target particles (equivalent to effective mass) and σ . In other terms, A_{eff} is the geometrical area that the detector would have if 100% of the neutrinos streaming through this area would be detected.
- *Neutrino flux or spectrum ϕ_ν* : The predicted energy-dependent number of neutrinos hitting the detector per unit area and time. This is determined by the SN neutrino emission models (see Section 5.3).
- *Event rate R* : The detected rate of neutrino events is the product of the neutrino flux and the effective area.

From the average event rate R , one gets the average detected number of events, which is used to calculate the detection probability of a certain model SN at a certain distance. Combining this with the expected SN explosion rate, one obtains the number of SN detections.

Effective volume/mass is the central quantity describing the performance of a neutrino detector. The main task of the detector simulation is to obtain V_{eff} . For a real detector, V_{eff} is the geometrical volume multiplied with the detector's efficiency. During the Monte Carlo (MC) simulation of the detector, N_{sim} events are generated inside a certain simulation volume V_{sim} and the number of detected events, N_{det} , is counted. The effective volume V_{eff} is then defined as

$$V_{\text{eff}} \equiv V_{\text{sim}} \frac{N_{\text{det}}}{N_{\text{sim}}}. \quad (5.4)$$

The effective mass or volume depends on the properties of the detector (e.g. size and detection efficiency) and the properties of the detected positron (e.g. energy, direction, or interaction vertex position), but not on the neutrino or positron spectrum. For the purpose of this chapter, the effective mass is averaged over all vertex positions and directions and depends only on the positron energy E_e . In principle, any positron spectrum can be used to simulate the energy-dependent $M_{\text{eff}}(E_e)$. Two methods are employed in this work:

1. Injection of positrons according to the spectrum predicted by an SN neutrino emission model, see Section 5.3. This results directly in the *average effective mass* $\overline{M}_{\text{eff}}$, which depends on the simulated spectrum.
2. Injection of positrons with a flat (uniform) spectrum within a certain energy range. Thus, $M_{\text{eff}}(E_e)$ is filled with equal statistics in each energy bin, but the simulation tends to take more time, because high-energy events, rare in many real spectra, need more processing time.

density is

$$\rho_{\text{ice}} \approx \frac{\rho_0}{\left(1 - \frac{\rho}{\gamma}\right)^3} \approx 0.9274 \text{ g cm}^{-3}, \quad (5.3)$$

and this is employed for conversion of effective volume to effective mass.

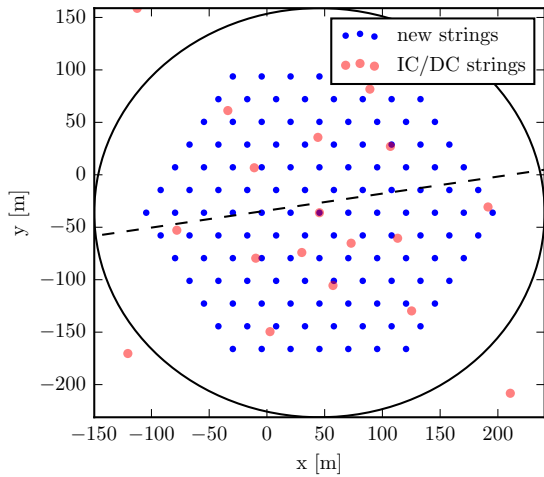


Figure 5.1: The string positions of the hypothetical detector viewed from above, with inter-string distance (string spacing) of 25 m. The black circle indicates the boundary of the cylindrical simulation volume, positions of existing IceCube/DeepCore strings are plotted for comparison.

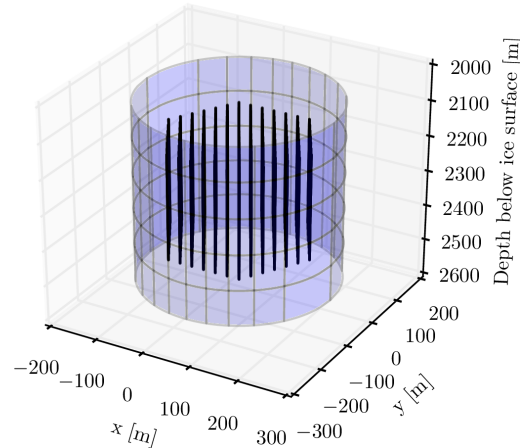


Figure 5.2: The layout of the hypothetical detector with inter-string spacing of 25 m. The enclosing cylindrical simulation volume is indicated as well.

For the detector optimization in Section 5.4, method 1 is used, with 10 000 events simulated for each detector configuration. Once the optimal geometry has been found, method 2 is used only for the optimal detector configuration, with higher statistics of 240 000 events. See Appendix A for more information on the definition of cross-section, effective volume and effective area, and the connection between the quantities.

For an accurate simulation of the photon propagation in the glacial ice, the *PHOTONICS software package* [185–187] is used, a Monte Carlo photon tracking code, which calculates photon flux and time distributions for a light source emitting in a heterogeneous medium. It was created by the IceCube collaboration and the specific photon tracking results for the ice at the IceCube location are stored in binary tables available within the collaboration. They include the full depth-dependence of the scattering and absorption properties of the ice [142, 143]. For this detector simulation, spline parameterizations of the photonics tables were used, similar to those used by the SplineMPE fit introduced in Section 4.2.4.

Each MC event is simulated by generating an interaction vertex homogeneously within and beyond the detector volume. The simulation volume is a cylinder enclosing the hexagonal detector, with radius 30% larger than the largest extent of the detector and height extending 100 m above and below the detector, see Figures 5.1 and 5.2. The positron’s direction is chosen randomly and isotropically as well. The positron energy is sampled according to either a flat spectrum (uniform distribution) or one of the energy spectra shown in Figure 5.6. Using the PHOTONICS code, first the average number of detected photons is calculated for each sensor, given the neutrino vertex, positron direction and energy, and sensor position. The actual number of detected photons is drawn from a Poisson distribution and then the photon hit times are sampled for each of these photons from the respective arrival time distributions provided by PHOTONICS. Finally, trigger and filter algorithms can be applied on the event’s data to decide whether the event is detected or not.

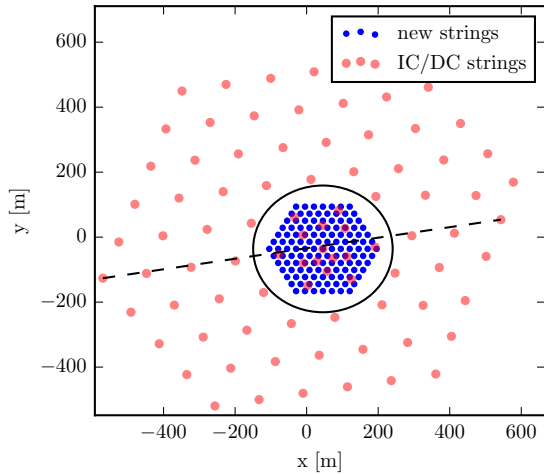


Figure 5.3: A zoomed out version of Figure 5.1. The dashed line indicates the position of a vertical slice through the detectors, with the strings closest to it plotted in Figure 5.4.

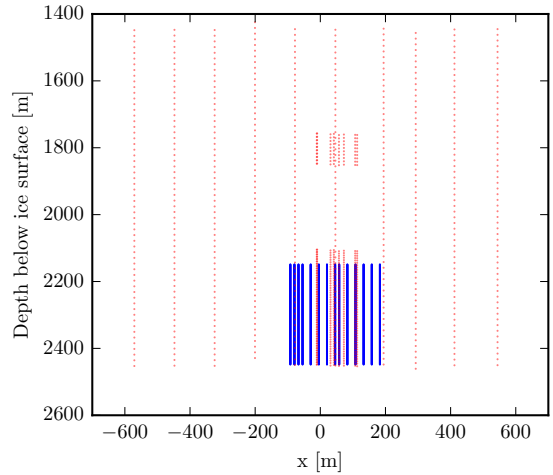


Figure 5.4: The x-z projection of strings closest to a vertical slice through the IceCube/DeepCore detector and the new hypothetical detector (indicated in Figure 5.3). The legend of Figure 5.3 applies.

5.3 Utilized Neutrino Emission Models

As detailed in Section 3.2.4, a CCSN produces neutrinos of all flavors, over a characteristic interval of about 10 s (see Figure 5.5 and Figure 3.7a). The details of the neutrino spectrum and light curve, the average neutrino energies, and the neutrino flavor ratios are controversial and differ from model to model [89]. A large variety of neutrino emission models exists (e.g. [188–191]), but for the sake of simplicity, this study restricts itself to three benchmark models to assess the performance of a hypothetical neutrino detector. Those are the model of the Lawrence Livermore (LL) group [87], the Thompson, Burrows, and Pinto (TBP) model [192], and a model for neutrino emission from a failed SN [172].

The LL model [87], also shown in Figure 3.7a, is one of the few hydrodynamic SN models leading to an explosion. It calculates the neutrino spectrum during the entire burst, over ~ 15 s. However, it was criticized because many relevant processes were not considered [89, p. 7]. A refined simulation by TBP [192] includes all the relevant neutrino processes, such as nucleon-nucleon bremsstrahlung and neutrino-electron scattering, but it does not lead to an explosion, and the simulation was stopped at 0.25 s after core bounce. Because there was no explosion in the TBP simulation, the total released neutrino energy is unknown. In [89], it was simply assumed to be the same as in the LL simulation, and the same assumption is used here.

Alternative models predicting low-energy neutrinos include *failed SNe*, in which stars heavier than $\sim 25 M_{\odot}$ form black holes. Current understanding is that those very massive stars can explode in a powerful hypernova or GRB in the case of a rotating core and sufficient magnetic field strength [106]. In the opposite case, it is assumed that no major outburst can occur because the ejecta fall back onto the central black hole [106]. The event would be very faint or even dark in optical emission, while as bright or even more luminous in neutrinos than ordinary SNe [193, 194]. The resulting neutrinos have average energies of $\langle E \rangle \approx 20 - 24$ MeV and are emitted over a shorter period of 1 s or less [172].

In the Monte Carlo detector simulation, Equation 3.5 for the released neutrino energy spectrum dN_{ν}/dE_{ν} is used to represent the LL and TBP model SNe. Equation 3.5 was fitted to the numerical neutrino spectra from LL and TBP by [89] to obtain values for the three parameters $\langle E_{\nu} \rangle$, β , and L_{ν} . The values obtained by [89] and used in this work are summarized in Table 5.1. dN_{ν}/dE_{ν} is converted to

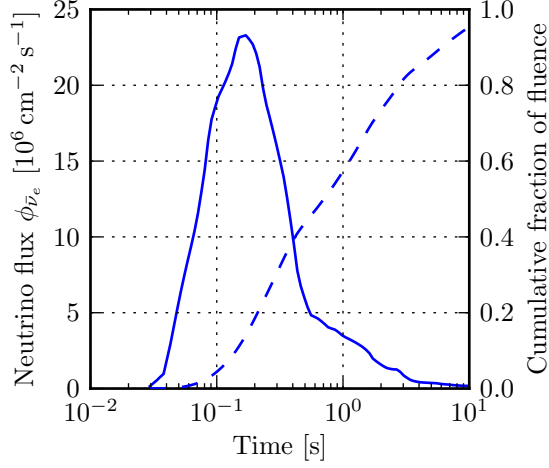


Figure 5.5: Time evolution of the $\bar{\nu}_e$ flux for an SN at 1 Mpc, according to the Lawrence Livermore model [87]. The solid line represents the differential flux and the dashed line the cumulative flux (normalized to one).

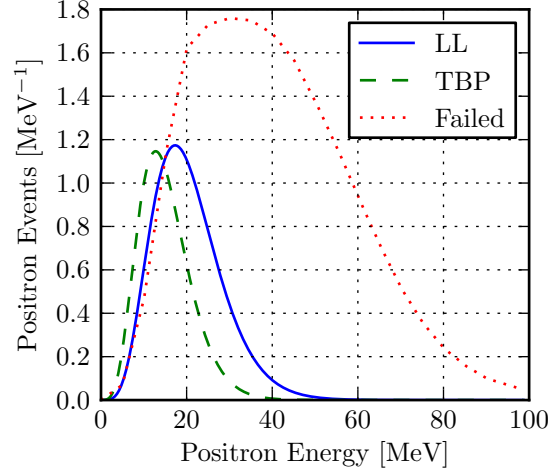


Figure 5.6: Positron spectra for the Lawrence Livermore (LL) [87], Thompson, Burrows, Pinto (TBP) [192] and a failed SN model [172] for an SN at 1 Mpc and an effective detector volume of 1 Mton at all positron energies.

	Mass [M_{\odot}]	$\langle E_{\bar{\nu}_e} \rangle$ [MeV]	$\beta_{\bar{\nu}_e}$	$L_{\bar{\nu}_e}$ [erg]
LL SN	20	15.4	3.8	4.9×10^{52}
TBP SN	11 and 15	11.4	3.7	(4.9×10^{52})
Failed SN	25 – 40	20 – 24	—	$\sim 1 \times 10^{53}$

Table 5.1: Parameters of the Lawrence Livermore (LL) model [89], the Thompson, Burrows, Pinto (TBP) model [89] and the failed SN model [172] for the neutrino spectrum of a CCSN. The table presents the stellar mass of the progenitor star, as well as the values to be inserted into Equation 3.5: the average neutrino energy $\langle E_{\bar{\nu}_e} \rangle$, the pinch parameter $\beta_{\bar{\nu}_e}$, and the energy released in anti-electron neutrinos $L_{\bar{\nu}_e}$. The TBP model does not lead to an explosion, i.e. the simulation does not yield a neutrino energy release. The energy release from the LL model is assumed and used. Note that for failed SNe, Equation 3.5 is not valid, instead the positron spectrum given in [172] is used.

fluence Φ_ν at distance d ,

$$\Phi_\nu(d) = \frac{dN_\nu}{dE_\nu} \frac{1}{4\pi d^2} = \frac{(1+\beta)^{1+\beta} L_\nu}{\Gamma(1+\beta) \langle E_\nu \rangle^2} \left(\frac{E_\nu}{\langle E_\nu \rangle} \right)^\beta \exp\left(- (1+\beta) \frac{E_\nu}{\langle E_\nu \rangle}\right) \frac{1}{4\pi d^2}. \quad (5.5)$$

The fluence Φ_ν is multiplied with the effective area A_{eff} . The result yields the positron spectrum plotted in Figure 5.6, for which a constant effective mass of 1 Mton, independent of positron energy, is used. For the detector simulation of LL or TBP, the product of the fluence Φ_ν and the IBD cross-section serves as an unnormalized version of the positron spectrum before detection, which is used to sample random energies from.³ For the failed SN model, the IBD positron spectrum given in [172] is used directly for the plot in Figure 5.6. Since the cross-section rises with energy, the positron spectrum in the detector is harder than the incident neutrino spectrum. Neutrino oscillations, which harden the spectrum further, are taken into account only for the failed SN model [172].

For a typical positron energy of 20 MeV, the corresponding track length is ~ 10 cm in ice, resulting in ~ 3600 Cherenkov photons (300 nm to 600 nm) [169, p. 6]. Since the light yield scales linearly with the positron track length, and hence with the positron energy, the average amount of light produced per neutrino is model dependent.

5.4 Detector Geometry and Optimization

In order to optimize the detector geometry, the effective mass is calculated as function of the spacing between strings (the horizontal inter-string distance), while all other aspects of the detector are kept constant. The detector is optimized using only the LL neutrino spectrum, which is in between the low-energy TBP and high-energy failed SN models (see Section 5.3). In the first iteration, only a very simplistic trigger requirement is used: A minimum number of five photo-sensors must be hit by photons. This trigger threshold is chosen to allow for a reconstruction of the vertex position and positron direction, which correspond to five degrees of freedom. More sophisticated trigger and filter methods are introduced in Section 5.5.

The detector shall be capable of detecting MeV neutrinos with high statistics, hence it must be very densely instrumented. On the other hand, the effective mass shall be high enough to detect at least about one CCSN per year. Figure 5.7 displays the SN detection range—defined as the distance at which 50% of SNe are detected—of a neutrino detector as function of its effective mass. With an expected CCSN explosion rate of about 1 to 2 within a radius of ~ 8 Mpc (see Figure 5.16), the detector's range should be at least 8 Mpc. Figure 5.7 thus implies that an effective mass of about 10 Mton or more is adequate. Consequently, a large number of vertical strings is necessary. Here, 127 strings are used after a first attempt with 61 strings yielded too low effective volumes. The strings are arranged in a filled hexagon, similar to IceCube (see Figures 5.1, 5.2, 5.3, 5.4). They are chosen to be equipped with optical sensors along a section of 300 m. For the vertical position of the sensors, the ice layer between 2150 m and 2450 m below the surface is chosen, where the DeepCore array is already located. At this depth, air bubbles have fully degenerated due to the high ambient pressure and only a small dust concentration was measured [142, 143]. Accordingly, the ice in these depths has the longest effective scattering lengths of $\lambda_e \approx 25$ m to 90 m and absorption lengths of $\lambda_a \approx 90$ m to 250 m at 400 nm wavelength [142, 143]. These excellent optical properties—surpassing what can be achieved under laboratory conditions—allow for an efficient photon detection as well as precise reconstruction of the event position and direction.

³ Multiplying with a certain number of target particles would yield the normalized pre-detection spectrum for a volume containing that number of particles, but the normalization is not important for drawing random values from a distribution.

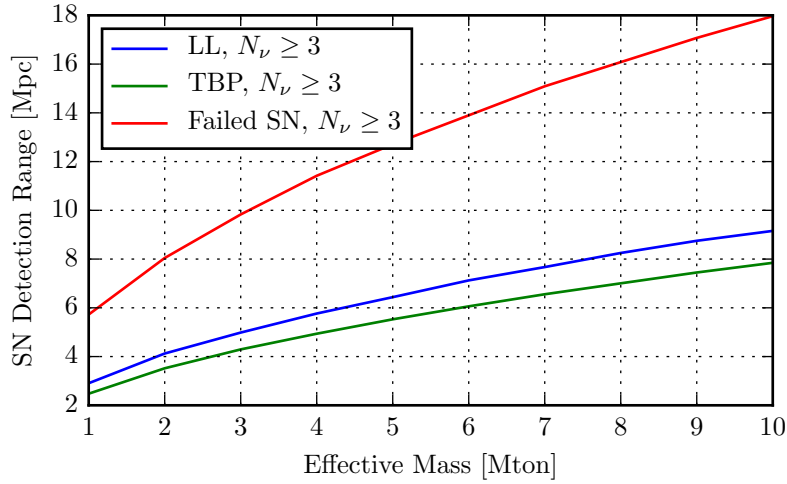


Figure 5.7: SN detection range—i.e. the distance, at which the SN detection probability is 50%—versus the effective mass of a neutrino detector. The effective mass is assumed constant at all energies and is multiplied with cross-section and neutrino fluence to obtain the average number of detected events. The range is found as the distance where the cumulative Poisson probability to detect at least three neutrinos becomes 50%. Three neutrinos are considered the minimum number of SN neutrinos required to claim an SN detection.

IceCube employs photo-sensors, so-called digital optical modules (DOMs) [136], each including a 10” Hamamatsu PMT integrated into a pressure-resistant glass sphere that also includes the electronics for HV generation and in situ digitization of the PMT signal (see also Section 4.2). The dark noise rate of individual DOMs averages around 500 Hz [169]. IceCube DOMs have a non-trivial directional sensitivity [195], which is incorporated into the PHOTONICS simulation package [185] and hence included in the simulation. Both regular efficiency and high quantum efficiency (HQE) PMTs are deployed in IceCube. From laboratory measurements, an effective area⁴ of 19.4 (26.3) cm² was obtained for an IceCube DOM equipped with a regular (HQE) PMT.

Due to the relatively low energy of SN neutrinos and the correspondingly small light yield, a high density of photo-sensitive area is required to achieve an acceptable detection efficiency. It is found that even for the closest possible vertical spacing of one HQE optical module per meter on the 300 m long strings and the closest possible horizontal string spacing of 10 m, the effective mass for neutrino detection falls short of the 10 Mton target (see Figure 5.8). For that reason, the strings are simulated with one photo-detector per meter (i.e. 300 sensors on each string), but each sensor having an effective area equivalent to ~ 5.4 HQE IceCube optical modules (the average number of detected photons returned by PHOTONICS is scaled up by that factor). The use of significantly larger photocathode area may be very challenging and is in particular limited by the achievable drill hole diameter. However, ongoing R&D for new optical modules with larger effective area, lower cost, and less noise, based on wavelength-shifting material, shows promising first results [196, 197].

Closer horizontal string spacing compared to the ~ 125 m of IceCube is desirable for a very low energy threshold in the MeV energy range. This spacing is varied between 10 m and 40 m to maximize the effective detector volume. As the string distance increases, the geometrical detector volume increases, but the fraction of detected neutrino events with at least five hit sensors decreases. The simulation results are shown as solid lines in Figure 5.8. The maximum effective volume is found to be ~ 18 Mton for a string spacing around 30 m for a LL neutrino spectrum, which is used as benchmark model in this

⁴ Averaged over all incident angles and wavelengths, assuming isotropic emission with a Cherenkov spectrum $\propto \lambda^{-2}$.

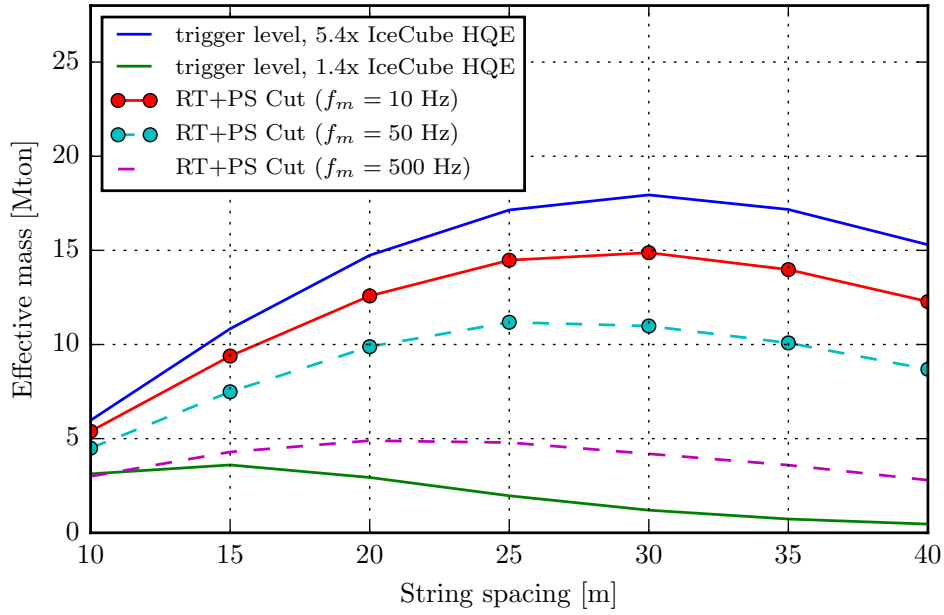


Figure 5.8: Effective mass at trigger level with one optical module per string meter having 1.4 (lower solid) and 5.4 times (upper solid) the effective area of IceCube HQE DOMs. This indicates that the highest sensor density possible with conventional technology—i.e. one HQE DOM per string meter—will result in even lower effective mass than the simulation result with 1.4 HQE DOMs. Thus, higher sensor effective area is needed to reach the goal of ~ 10 Mton. The effective mass after applying radius-time (RT) cleaning and phase space (PS) cuts (see Section 5.5.1) is shown for different module noise rates (solid with bullets, dashed with bullets, dashed). The noise cleaning is done such that a noise trigger rate of about 1 mHz remains, a dead time of 0.16% due to atmospheric muons is included.

simulation.

5.5 Background Studies

Up to this point, only the most basic trigger requirement was applied: The number of sensors hit by photons is required to be at least five for each neutrino event. In this section, the dominant sources of background are discussed and how they can be controlled by imposing additional constraints on the distribution of photon hits. Contributions from random noise, atmospheric neutrinos, atmospheric muons, and solar neutrinos are considered.

Neutrinos from SNe come in bursts. To be distinguished from uncorrelated uniform background or noise triggers, an SN will need to produce a certain number, or multiplicity, of neutrino triggers within a given time window. One can claim an SN detection if a certain number of trigger events N_ν occur within a time window of $\Delta t_{\text{SN}} \approx 1 - 10$ s (see Figure 5.5). Under the constraint of a limited rate of false SN detections, N_ν and Δt_{SN} determine the maximally allowed background or noise trigger rate f_{noise} .

To calculate the acceptable f_{noise} , one can imagine each noise event to open a window of length Δt_{SN} , in which on average $\mu = f_{\text{noise}} \Delta t_{\text{SN}}$ events occur. If $N_\nu - 1$ or more events fall into the window in addition to the event that opened the window, they will produce a false SN detection. Accordingly, the average number of false SN detections per year is the average number of background or noise events per year times the Poisson probability $P_{\geq N_\nu - 1}$ for $N_\nu - 1$ or more additional events occurring in one window. It is $P_{\geq N_\nu - 1} = 1 - P_{\text{cum}}(N_\nu - 2 | \mu)$, with cumulative Poisson probability $P_{\text{cum}}(n | \mu) = P_{\leq n} \equiv \sum_{k=0}^{k=n} P_k$,

N_ν	Δt_{SN} [s]	f_{noise} [mHz]	N_ν	Δt_{SN} [s]	f_{noise} [mHz]
3	10	0.86	3	1	3.99
4	10	3.74	4	1	20.96
5	10	9.61	5	1	60.32

Table 5.2: Maximally allowed noise and/or background trigger rate f_{noise} for an average of 1 false SN detection per year, consisting of N_ν events falling into a time window of Δt_{SN} .

defined as sum over the Poisson probabilities $P_k \equiv \frac{\mu^k}{k!} e^{-\mu}$. Also, $P_{\geq N_\nu-1}$ is almost equal to the Poisson probability $P_{N_\nu-1}$ for exactly $N_\nu - 1$ events, because the Poisson mean $\mu = f_{\text{noise}} \Delta t_{\text{SN}} \ll 1$. So, for the number of false SN detections N_{SN} as function of f_{noise} , N_ν , and Δt_{SN} , one can either write

$$\frac{N_{\text{SN}}}{1 \text{ yr}} = f_{\text{noise}} P_{\geq N_\nu-1} = f_{\text{noise}} (1 - P_{\text{cum}}(N_\nu - 2 | f_{\text{noise}} \Delta t_{\text{SN}})), \quad (5.6)$$

or, approximating,

$$\begin{aligned} \frac{N_{\text{SN}}}{1 \text{ yr}} &= f_{\text{noise}} P_{\geq N_\nu-1} \approx f_{\text{noise}} P_{N_\nu-1} \\ &= f_{\text{noise}} \frac{(f_{\text{noise}} \Delta t_{\text{SN}})^{N_\nu-1}}{(N_\nu - 1)!} e^{-f_{\text{noise}} \Delta t_{\text{SN}}} \\ &\approx f_{\text{noise}}^{N_\nu} \frac{\Delta t_{\text{SN}}^{N_\nu-1}}{(N_\nu - 1)!}. \end{aligned} \quad (5.7)$$

From either equation follows the maximally allowed f_{noise} for a certain N_{SN} . If one limits the false SN detection rate to about $N_{\text{SN}} = 1$ per year, comparable to the expected signal SN detection rate, one gets the maximally allowed noise rates shown in Table 5.2. For example, one can accept at most ≈ 0.9 mHz of background or noise trigger rate if one wants to detect SNe with three neutrino events within 10 s. In the following estimates, the rounded value of 1 mHz will be used as tolerable upper limit on the noise and background rates.

5.5.1 Sensor Noise

Since the Antarctic ice shield is a very low-radioactivity environment, the main sources of random noise are introduced by the photo-sensors themselves: radioactive isotopes, mainly contained in the DOM's glass vessel, and thermal noise in the electronics. For the IceCube modules, this results in a dark count rate of ~ 500 Hz [169]. It is known that some fraction of the noise is not purely random [169], but correlated in time, however this is neglected here for the sake of simplicity.

As mentioned above, the detector presented here will not be feasible using IceCube modules. New photo-sensor technologies (e.g. based on wavelength-shifters as light collectors) are currently discussed for deployment in future extensions to IceCube [196], that might offer increased effective photo-sensitive area in combination with a significantly reduced noise rate. These technologies are still in the design phase, so the achievable noise rate is not known yet. Dark noise rates of 500 Hz, 50 Hz, and 10 Hz are used as template values in absence of solid numbers.

As shown in Table 5.2, the rate f_{noise} of background or noise neutrino triggers has to stay below ≈ 1 mHz if only one false three-neutrino SN burst detection is tolerated per year. Now, the trigger rate caused by random noise is calculated, depending on the total number of modules in the detector N_{tot} .

the random noise hit rate per module f_m , the number of hit modules n_{trig} that is required for a neutrino event to trigger and the trigger time window t_{trig} . Assuming that one module has registered a random noise hit and opened the trigger window, the probability P_m for any module to also see at least one noise hit during this time window t_{trig} is complementary to the Poisson probability P_0 to register no hit,

$$P_m = 1 - P_0 = 1 - e^{-f_m t_{\text{trig}}}. \quad (5.8)$$

The probability for a noise trigger P_{noise} is the probability that at least $n_{\text{trig}} - 1$ more modules also encounter a noise hit in the time window. Using the binomial distribution, again via the complementary probability of registering $n_{\text{trig}} - 2$ noise hits or less,

$$P_{\text{noise}} = 1 - B_{\text{cum}}(n_{\text{trig}} - 2 | N_{\text{tot}}, P_m), \quad (5.9)$$

where $B_{\text{cum}}(m | n, p) \equiv \sum_{k=0}^m \binom{n}{k} p^k (1-p)^{n-k}$ is the cumulative binomial probability for up to m successes out of n tries with probability p . Ignoring the effect of overlapping trigger windows, the rate of noise triggers in the detector is then

$$f_{\text{noise}} = N_{\text{tot}} f_m P_{\text{noise}}. \quad (5.10)$$

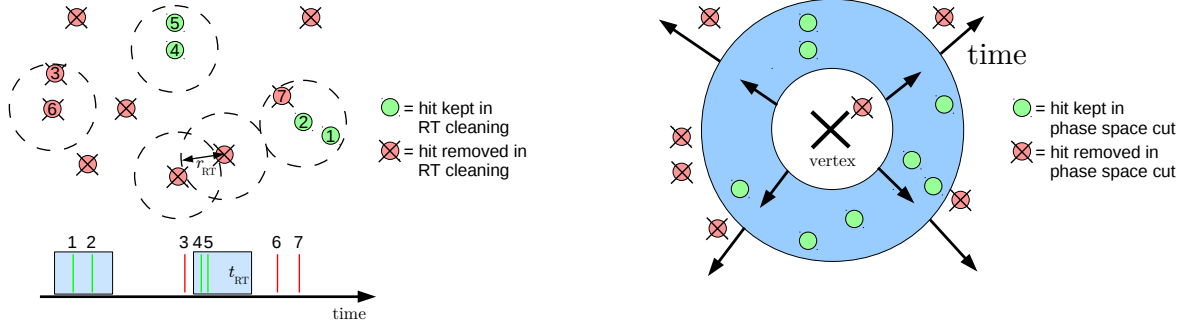
Using generic values for the dark count rate $f_m = 500$ Hz, $N_{\text{tot}} = 38\,100$ for a detector with 127 strings and 300 modules per string, and requiring $n_{\text{trig}} = 5$ hits in $t_{\text{trig}} = 1000$ ns, the rate of false SN events is $f_{\text{noise}} = 19$ MHz,⁵ i.e. 10 orders of magnitude above the allowed value from Table 5.2. Even assuming a module dark noise rate as low as $f_m = 10$ Hz, still $f_{\text{noise}} = 247$ Hz, well in excess of what can be tolerated. This clearly shows that it is necessary to apply intelligent trigger algorithms that take advantage of the non-uniform distribution of photons from neutrino interaction and thus limit the number of modules considered by the trigger. In the following, two strategies that reject events induced by sensor noise are presented.

Local Coincidence Radius-Time (RT) Cleaning

Noise hits are distributed uniformly across the detector, while signal hits follow a certain topology: A positron from IBD produces Cherenkov light along its few cm long track. Compared to the string and module spacing, one can consider the positron to be a point source of light that is scattered in the ice. These events are thus characterized by photon hits spreading roughly spherically from the vertex, with a preferred direction due to the Cherenkov cone.

This topology of signal hits can be exploited. As demonstrated for IceCube, requiring a local coincidence between photon hits is a very efficient way to reduce the effect of random noise [198]. A hit is required to be accompanied by at least another hit within a certain radius r_{RT} and time window t_{RT} in order to fulfill the local coincidence criterion. Figure 5.9a shows an illustration of this radius-time (RT) requirement. The local coincidence cleaning is found to indeed reduce the noise trigger rate, while keeping most of the signal events. The parameters t_{RT} and r_{RT} are optimized for the maximum effective mass at each string spacing d_{str} .

⁵ In fact, with a trigger window of 1000 ns, only 10^6 disjoint trigger intervals fit into one second instead of 19×10^6 , so the detector would in principle be noise-triggered continuously. In addition, this is the saturated regime, where $P_{\text{noise}} = 1$, so $f_{\text{noise}} = N_{\text{tot}} f_m$, and every noise hit also leads to a noise trigger.



(a) RT cleaning. Dashed circles indicate the radius r_{RT} , blue boxes the time window t_{RT} of the local coincidence cleaning.

(b) PS cut. The blue region marks the expanding spherical shell (at a certain point in time) used in the phase space cut.

Figure 5.9: Illustration of the local coincidence (RT) cleaning and the phase space (PS) cut. Each colored sphere corresponds to a hit optical module.

Phase Space (PS) Cut

The local coincidence cleaning selects hits that are likely causally connected, i.e. close to each other in time and space. However, this does not take into account the global pattern of signal hits in the detector. As photons propagate away from the vertex, the photon distribution can be roughly modeled as an expanding spherical shell. The rate of noise events can be significantly reduced by defining a so-called *fiducial detector volume* (the spherical shell) and accepting only hits within this volume for the trigger, see Figure 5.9b.

This fiducial volume is defined with respect to the time and position of the neutrino vertex, where the positron is produced. Since the vertex is not known a priori, a χ^2 -minimization of the residual time, i.e. the photon propagation time minus the expected photon propagation time for straight travel from the vertex—implemented by Sebastian Böser—was performed to reconstruct the vertex position. Using this simple method, a positional resolution of ~ 15 m can be achieved. To incorporate this limited knowledge of the vertex position, a random Gaussian smearing with 10 m standard deviation in each spatial coordinate is applied to the true vertex position of the simulated events, corresponding to $\sim \sqrt{3} 10$ m = 17.3 m spatial resolution. The interaction time is smeared with a Gaussian of 100 ns width, since a median first hit time of ~ 92 ns after interaction implies that a resolution $\lesssim 100$ ns can be achieved.⁶ Figure 5.10 shows an example distribution of hits in the two-dimensional phase space (PS) given by the distance Δr between the hit module and the reconstructed vertex and the time Δt between the hit and the reconstructed neutrino interaction. For every detector configuration, the 0.1th and 99.9th percentile of the distance are calculated at each time (orange lines in Figure 5.10, red line is the median) and represent the inner and outer radius of the fiducial volume, r_{\min} and r_{\max} . The resulting spherical shell expands with time and contains $\approx 99.8\%$ of the signal hits. Only hits falling within this fiducial phase space are considered for the trigger. Since all photons are eventually absorbed, the fiducial volume is cut at time t_{\max} , which is a new parameter to be optimized. As the phase space volume (i.e. the number of sensors contributing to the trigger) quickly increases with t_{\max} , the noise trigger rate f_{noise} rapidly rises with t_{\max} as well. Figure 5.11 shows how steeply the noise trigger rate f_{noise} is rising with t_{\max} . The value of t_{\max} is chosen so that it limits the noise trigger rate, calculated from the phase space volume, to

⁶ The time resolution $\sigma_t = \sigma_r/c_{\text{ice}} \approx 70$ ns, derived from the spatial resolution $\sigma_r = 15$ m (with $c_{\text{ice}} \approx 0.22$ m ns⁻¹), is similar.

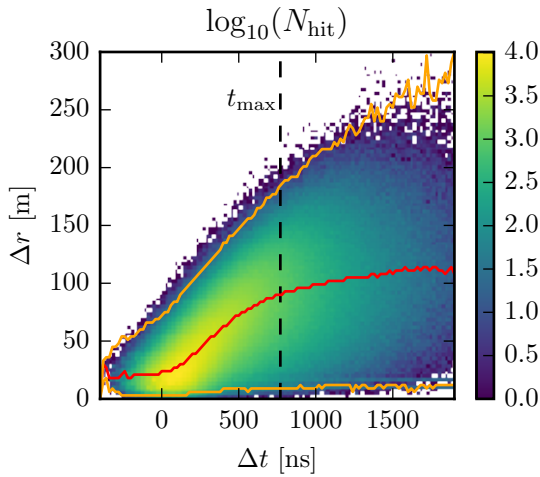


Figure 5.10: Distribution of signal hits from 240 000 simulated events in the detector with 25 m string spacing, after applying the optimal RT cleaning for 50 Hz module noise rate, listed in Table 5.3. Plotted is the spatial distance Δr to the vertex position vs. time difference Δt between the hit and the neutrino interaction.

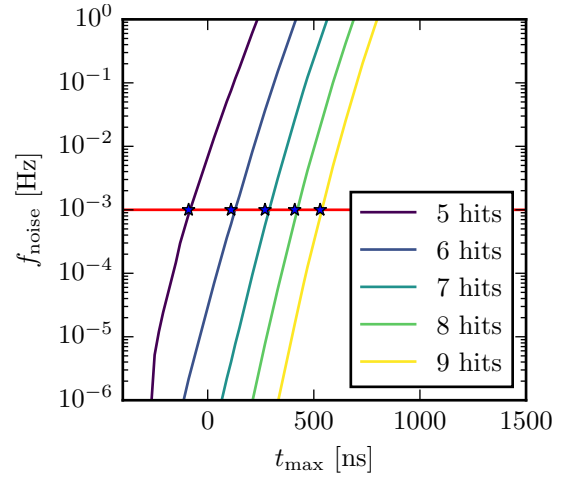


Figure 5.11: Noise trigger rate f_{noise} of the detector with 25 m string spacing, for a module noise rate of $f_m = 50$ Hz, as function of phase space cut time t_{max} , for different values of n_{trig} . Note the extremely steep rise of the curve that spans 6 orders of magnitude in noise rate within only few hundreds of nanoseconds. This plot was made without applying the RT cleaning, which would flatten the curves and move them to the right.

$f_{\text{noise}} \leq 1$ mHz for a given sensor noise rate f_m . The derivation of f_{noise} is given in Appendix C.

Under the constraint of $f_{\text{noise}} \leq 1$ mHz, the number of hits n_{trig} required to form a trigger, the string spacing d_{str} of the detector, the cleaning radius and time (r_{RT} and t_{RT}), and t_{max} are optimized simultaneously in order to maximize the effective mass for SN signal neutrinos of the LL spectrum. Due to the high dimensionality, this is a difficult optimization problem. The parameter values, for which simulation is performed, have to be chosen very carefully, because it is computationally not possible to investigate the full parameter space with high resolution.

Result of Noise Cleaning

Figure 5.8 shows the resulting optimized effective mass after applying the two noise cuts, Table 5.3 lists the optimal parameters, for module noise rates of $f_m = 10$ Hz, 50 Hz, 500 Hz. While this method reduces the trigger efficiency for neutrino interaction by up to a factor of 3.7,⁷ at the same time the noise trigger rate is reduced by many orders of magnitude. For the module dark noise rate of 500 Hz, as provided by IceCube DOMs, the effective mass of this detector configuration falls short of the initial target of 10 Mton. In order to retain 10 Mton, reducing the sensor noise rate to $\lesssim 50$ Hz per meter instrumented string (~ 350 mHz per cm^2 effective photo-sensitive area) is desirable. Another benefit of lower sensor noise is the larger optimal string spacing, resulting in a detector that is less sensitive to low-energy background events from solar neutrinos (see Section 5.5.3).

While more advanced algorithms considering the full event topology would still allow for a moderate increase of the effective mass, this study demonstrates the importance of both large photo-sensitive area and at the same time low noise optical sensors, posing a technological challenge. Correlated noise that

⁷ For 500 Hz, M_{eff} drops from 18 Mton to 4.9 Mton.

	f_m	[Hz]	10	50	500
optimized parameters	d_{str}	[m]	30	25	20
	n_{trig}		5	5	5
	r_{RT}	[m]	110	70	25
	t_{RT}	[ns]	1150	380	130
	t_{max}	[ns]	1630	770	390
prop- erties	f_{noise}	[Hz]	6.2×10^3	$(1.3 \times 10^6)^a$	$(1.9 \times 10^7)^a$
	$f_{\text{noise}}^{\text{cut}}$	[Hz]	10^{-3}	10^{-3}	10^{-3}
	M_{eff}	[Mton]	14.9	11.2	4.9

^a The detector is continuously noise triggered.

Table 5.3: Optimal parameters for string spacing (d_{str}), required hit multiplicity (n_{trig}), RT cleaning radius (r_{RT}) and time (t_{RT}) as well as maximum hit time window (t_{max}), together with resulting effective mass M_{eff} as function of module noise rate f_m . The parameters are chosen such that RT cleaning and phase space cut limit the rate of noise triggers f_{noise} down to $f_{\text{noise}}^{\text{cut}} = 1$ mHz. For the uncut noise trigger rates f_{noise} (see Equation 5.10), a trigger window of $t_{\text{trig}} = 2500$ ns was chosen, which contains about 98% of signal hits and would yield about the maximum trigger level effective mass of 18 Mton.

is not treated here will be more difficult to reject and provides additional motivation to achieve low dark noise rates in future photo-sensor R&D. In the following, a module noise rate of 10 Hz is assumed.

5.5.2 Muon Background

Muons crossing the detector or passing nearby are easily separable from the SN neutrino signal via the huge amount of Cherenkov light produced by the extended track. An additional outer layer of photo-sensitive modules, naturally provided by IceCube, will ensure that even muons passing by at large distances or stopping just above the detector can be identified as such and be vetoed.

For a conservative first estimate of the dead time⁸ caused by atmospheric muons, all muons reaching the top of the detector are assumed to be energetic enough to cross it. From [36, fig. 15], one obtains a muon flux of $\Phi_{\mu} \approx 8 \times 10^{-8} \text{ cm}^{-2} \text{ s}^{-1} \text{ sr}^{-1}$ for the top of the detector at 2150 m depth, giving a muon passing rate of about

$$R_{\mu} = \Phi_{\mu} (300 \text{ m})^2 \pi \approx 230 \text{ Hz} \quad (5.11)$$

using a detector cross-sectional area of $(300 \text{ m})^2$ and an effective solid angle of π that accounts for the lower flux from angles closer to horizon where the ice shield is thicker. A muon traveling through the entire detector has a track length of ~ 300 m and emits about $N_0 \approx 10^7$ Cherenkov photons on its path (360 photons per cm). As a worst case, it is assumed that all photons are trapped within the detector volume by scattering. This is used to compute how long the photons will at most remain detectable within the detector before they are absorbed. The number of photons after a path $x = ct/n_{\text{ice}}$ is given by:

$$N_{\gamma} = N_0 e^{-\frac{x}{\lambda_a}}, \quad (5.12)$$

with $t_{\text{abs}} = n_{\text{ice}} \lambda_a / c \lesssim 0.45 \times 10^{-6} \text{ s}$, for an absorption length of $\lambda_a \lesssim 100 \text{ m}$ and a refractive index of

⁸ The time span, in which the detector is unable to take data.

$n_{\text{ice}} = 1.356$. After a time

$$t = t_{\text{abs}} \ln \frac{N_0}{N_\gamma} \approx 7 \mu\text{s} \quad (5.13)$$

the number of unabsorbed photons in the detector due to a crossing muon has fallen below $N_\gamma = 1$, which is well below the trigger threshold. Therefore, it is conservatively assumed that each passing muon illuminates the detector for a time interval of $7 \mu\text{s}$ which can be considered as dead time for SN neutrino detection, corresponding to a fraction of $R_\mu \cdot 7 \mu\text{s} = 0.16\%$ of detector operation time.

An alternative detector (see Section 5.6) located at a shallow depth of 750 m to 1050 m would experience a muon flux of $\Phi_\mu \approx 2 \times 10^{-6} \text{ cm}^{-2} \text{ s}^{-1} \text{ sr}^{-1}$ at the top [36, fig. 15] and thus a much higher muon passing rate of over 5000 Hz. Because of the long absorption length of ~ 350 m, photons remain in the shallow ice detector for $\sim 25 \mu\text{s}$, causing an effective dead time of $\sim 15\%$.

Passing muons are easily identified because of the dense instrumentation and can be rejected applying a veto. However, muons also produce *spallation* products via fragmentation of ^{16}O nuclei and capture of the generated neutrons [128]. The decay of these numerous products can mimic low-energy neutrino events and is a serious background. Super-Kamiokande has demonstrated [128, 131] that a cut on a likelihood function including the spatial and temporal distance from the passing muon as well as the energy loss of the muon can be used to efficiently remove spallation events. However, this results in an additional 20% effective dead time for Super-Kamiokande while raising the threshold for neutrino detection to ~ 15 MeV. As not all of the spallation and neutron capture cross-sections are known and their calculation goes beyond the scope of this work, this background cannot be quantified here. Yet, it shall be noted that Super-Kamiokande is located at a depth of 2700 meters-water-equivalent [121], comparable to the deep location considered here, and the passing muons should be reconstructed with similar quality, indicating that performance factors may be similar. A demonstration that this background can be controlled is left for future studies.

5.5.3 Solar Neutrino Background

Put aside the cosmic neutrino background—which is too low in energy to be detectable—the dominant flux of neutrinos at Earth comes from the Sun, where neutrinos are abundantly produced in several different fusion cycles, see Section 2.3.5. As only ν_e and no $\bar{\nu}_e$ are generated in the Sun, solar neutrinos cannot undergo IBD. The dominant interaction for solar neutrinos is elastic scattering on electrons (ES). Charged current interactions on ^{18}O , ^{17}O , and deuterium⁹ occur at about two orders of magnitude lower rate [199] and are ignored here. Furthermore, only ^8B neutrinos need to be considered, since all other solar neutrino fluxes are too low in energy to be detectable in the detector configuration or well below the ^8B flux in magnitude [33, 200], see Figure 2.12.

To calculate the interaction rate, the analytical expression for the neutrino-electron elastic scattering (ES) differential cross-section given in Equation 2.5 is used and multiplied with the energy-dependent effective mass of the detector given in Figure 5.12b to obtain the effective area plotted in Figure 5.12c. The shape of the ^8B neutrino spectrum is taken from [201] and normalized to a total flux of $\Phi(^8\text{B}) = 5 \times 10^6 \text{ cm}^{-2} \text{ s}^{-1}$ [202], with components $\Phi_{\nu_e}(^8\text{B}) = 1.7 \times 10^6 \text{ cm}^{-2} \text{ s}^{-1}$ and $\Phi_{\nu_{\mu,\tau}}(^8\text{B}) = 3.3 \times 10^6 \text{ cm}^{-2} \text{ s}^{-1}$ [203], which are results of measurements by SNO and are consistent with those expected for neutrino oscillations. Multiplying the effective area and the fluxes, one arrives at an approximate solar neutrino event rate of 42 mHz at trigger level. Additional application of local coincidence cleaning and the phase space cut (see Section 5.5.1) reduces this rate to 23 mHz, still significantly higher than the maximum allowed rate of random background events $f_{\text{noise}}^{\text{BG}} = 1 \text{ mHz}$.

⁹ The reaction is $\nu_e + n \rightarrow p + e^-$, analogous to IBD.

Configuration	Solar ν_e	Atm. $\nu_e + \bar{\nu}_e$	LL $\bar{\nu}_e$
5 hits, no cleaning	0.42	0.005	3.94
5 hits, RT+PS	0.23	0.004	3.12
6 hits, RT+PS	0.13	0.004	2.56
7 hits, RT+PS	0.08	0.004	2.04

Table 5.4: Average number of events per 10 s from solar and atmospheric neutrino background (up to 100 MeV) as well as the SN neutrino signal for a LL SN in 10 Mpc distance for different numbers of hit modules and without and with noise cleaning (RT+PS) applied.

The bulk of solar neutrinos is less energetic than the bulk of SN neutrinos (see Figure 5.12a). Changing the trigger requirement from 5 hits to 7 hits increases the energy threshold and thus reduces the expected event rate of solar neutrinos by a factor of three, while reducing the signal efficiency for SN neutrinos from the LL model by only about 30%, see Table 5.4.

Alternatively, a cut on the event direction is possible. The electron emerging from the ES roughly keeps the direction of the incident neutrino, while the IBD effectively randomizes the positron direction. For a sufficiently densely instrumented array such as Super-Kamiokande, an angular resolution of about $\pm 30^\circ$ at $E_e = 10$ MeV is feasible [131, 199]. Assuming a one-sigma (68% of the events) angular cone of this size to reject neutrinos from the direction of the Sun, a solid angle of $\Omega_{\text{cut}} = 2\pi(1 - \cos(30^\circ))$, or 6.7% of the sky, is cut away. This cut is used (instead of a cut on number of hits) to discriminate the solar neutrino rate to $f_\odot = (1 - 0.68)^3 23 \text{ mHz} \approx 0.75 \text{ mHz}$, while retaining $(1 - \Omega_{\text{cut}}/(4\pi))^3 \approx 81\%$ of the SN events. While this is already more efficient than a cut on the number of hits, the most powerful rejection will be achieved using a likelihood method that incorporates both the direction and energy for each event within the time window. A more detailed discussion is left out here, but a full event reconstruction, including the lepton direction, is identified as a requirement to reduce the high rate of solar neutrinos.

5.5.4 Atmospheric Neutrino Background

Cosmic rays colliding with the Earth’s atmosphere produce ν_e and $\bar{\nu}_e$ in similar abundance and a ν_μ and $\bar{\nu}_\mu$ flux roughly twice as high, see Figure 2.13. The dominant component are the electron anti-neutrinos, interacting via IBD with a cross-section two orders of magnitude higher than the ES of electron neutrinos [131], see also Figure 2.4. The atmospheric neutrino flux calculations from [39], the ES cross-section from Equation 2.5, and the cross-section for IBD from Equation 2.11 are used. They are multiplied and integrated from 3 MeV to 100 MeV. The result is an expected trigger level event rate (triggering on 5 hit sensors) of 0.5 mHz for IBD from $\bar{\nu}_e$ and 0.007 mHz for ES from all species ν_e , $\bar{\nu}_e$, ν_μ , and $\bar{\nu}_\mu$. The ES component is therefore negligible. The resulting spectrum, shown in Figure 5.12d, peaks well above the peak of SN interactions, allowing to further discriminate these events.

Another component of the background are *invisible muons* that are produced in the interactions of low-energy atmospheric muon neutrinos, see Section 4.1.2. The muons themselves are below the threshold for Cherenkov light emission and thus invisible. They can only travel few tens of centimeters and then decay to electrons which—due to their lower mass—can have a velocity above the Cherenkov threshold and become visible. These *Michel electrons* have been measured by Super-Kamiokande [131, 204] and amount to ~ 90 events per year in their effective volume of 22.5 ktons. At the peak energy of the Michel electron spectrum, 40 MeV, the effective mass of the detector simulated in this work is roughly 1000 times larger (see Figure 5.12b), so one can expect about 100 000 events per year, or a rate of

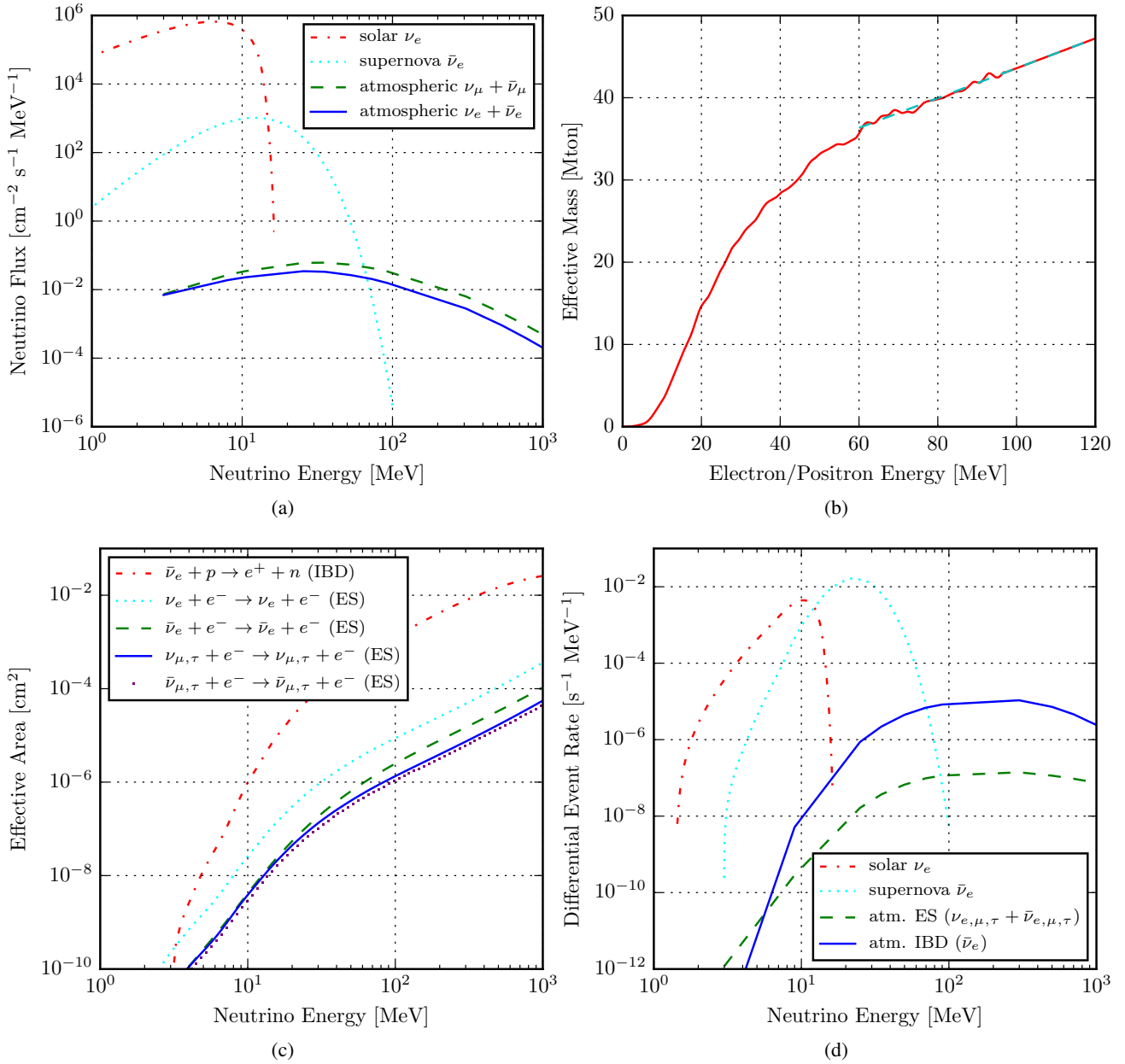


Figure 5.12: (a) The flux for solar [199, 201] and atmospheric [39] neutrinos as function of energy. The SN neutrino flux on Earth according to the LL model [87] is shown as well, normalized to a luminosity of $4.9 \times 10^{51} \text{ erg s}^{-1}$ in $\bar{\nu}_e$ for an SN distance of 10 Mpc (average flux for a burst duration of 10 s). (b) Effective detector mass as function of e^\pm energy, triggering on 5 hit modules, after applying noise cleaning down to $f_{\text{noise}}^{\text{cut}} = 1 \text{ mHz}$ for 10 Hz module noise. Above 100 MeV, a linear extrapolation (dashed) is used. (c) The effective area of the same detector for elastic scattering (ES) and inverse β -decay (IBD), not including cuts to reject solar neutrinos. (d) Event rate per MeV as function of neutrino energy for solar, atmospheric, and SN neutrino fluxes from (a), with effective areas from (c).

≈ 3 mHz. While already small compared to the background of solar neutrinos, further reduction can be achieved by using the surrounding IceCube detector to veto accompanying atmospheric muons from the same air shower that are above the Cherenkov threshold. Additionally, Michel electrons have slightly higher energies than standard CCSN neutrinos. Note that only invisible muons from muon neutrinos and not the atmospheric muons themselves can penetrate the detector and produce Michel electrons since, once below the Cherenkov threshold, the muons will decay within ~ 1 m.

5.5.5 Summary of Background Studies

The high sensor multiplicity requires intelligent trigger and selection algorithms to cope with the backgrounds arising from sensor noise, atmospheric muons, and solar, as well as atmospheric neutrinos. Despite making use of the event topology, the suppression of noise to a sufficiently low level will be a major challenge and requires future improvements in sensor development. Vetoing of atmospheric neutrinos and muons will result in some detector downtime. In particular, the discrimination of spallation products from muons passing the ice may pose a significant challenge and still has to be demonstrated. The dominant source of neutrino background stems from solar ^8B neutrinos, that need to be suppressed by reconstructing their direction and/or increasing the energy threshold.

5.6 Alternative Detector Location

An interesting alternative location for a Cherenkov detector in the South Pole ice is at a depth of 750 m to 1050 m, where the IceCube predecessor AMANDA-A is located. It is known from measurements that at this depth the absorption length is exceptionally long with up to $\lambda_a \approx 350$ m [25, figs. 3.3, 3.5]. However, the presence of air bubbles results in a very short effective scattering length of only $\lambda_e \approx 0.3$ m [25, fig. 3.2]. This results in an effective propagation length of $\lambda_p = \sqrt{\lambda_e \lambda_a / 3} \approx 6$ m, after which the photon flux has on average dropped by a factor e^{-1} [205]. The photons cannot travel long distances and are hence confined to a small volume for a rather long time of $\lambda_a/c \approx 1$ μs on average, before finally being absorbed. The result is a diffuse “photon cloud” within a small volume. This leads to a high detection probability, given the light is emitted in the vicinity of a photo-sensor, since it is likely that sooner or later the scattered photon hits the photo-sensitive area by chance. The achievable effective mass is significantly higher than in the deep ice.

Such a detector—using the same detector layout as in the deep ice—is simulated using an analytic description of the photon propagation as a random walk, because the photons are very strongly scattered, diffused, and randomized. In this model, the light intensity of N_γ photons, emitted from a point-like source, at a distance r from the source is [25, eq. 3.7]

$$I(r) = \frac{3N_\gamma}{16\pi\lambda_e r} \exp\left(-\frac{r}{\lambda_p}\right), \quad \text{where } \lambda_p = \sqrt{\frac{\lambda_e \lambda_a}{3}}. \quad (5.14)$$

An average Cherenkov photon emission N_γ of 183 photons per MeV positron energy above the Cherenkov threshold energy $E_{\text{th}} = m_e c^2 / \sqrt{1 - 1/n_{\text{ice}}^2} = 0.756$ MeV is assumed [206]. The intensity $I(r)$ is to be multiplied with the sensor effective area to obtain the average number of detected photo-electrons (PEs). The actual number of PEs is drawn using a Poisson distribution with this average. The time distribution of the PEs at distance r is given by [25, eqs. 3.1, 3.8]

$$\frac{dn}{dt}(r, t) \propto \left(\frac{1}{\lambda_e t}\right)^{1.5} \exp\left(-\frac{3r^2}{4c_{\text{ice}}\lambda_e t}\right) \exp\left(-\frac{c_{\text{ice}} t}{\lambda_a}\right), \quad (5.15)$$

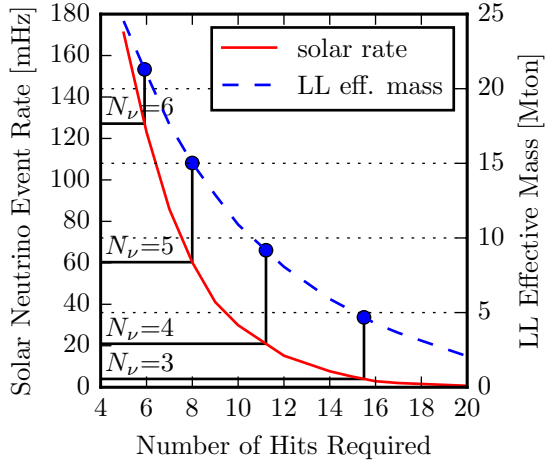


Figure 5.13: The solar neutrino event rate in the shallow ice detector (from neutrino-electron elastic scattering), together with the effective mass for SN neutrino events (LL model), as a function of the number of module hits required to trigger an event (which is a proxy of event energy). Horizontal lines indicate tolerable noise rates for a 1 second time window during which at least N_ν events shall lead to an SN detection (from Table 5.2). The vertical lines point to the corresponding effective mass.

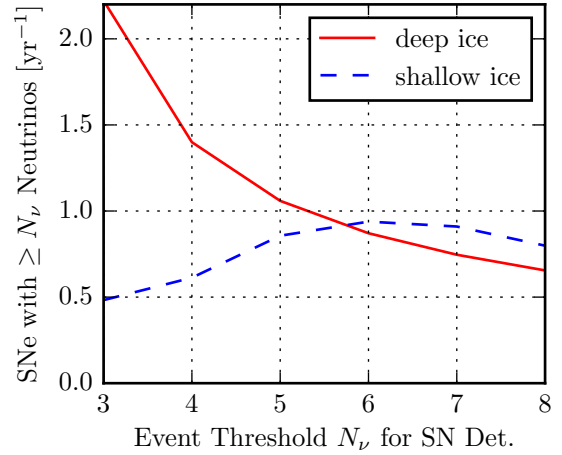


Figure 5.14: Number of SN detections per year as function of the neutrino multiplicity threshold N_ν that must fall within the time window Δt_{SN} to claim an SN detection. For deep ice, $\Delta t_{\text{SN}} = 10$ s and the same cuts are used for every N_ν . But in the shallow ice, $\Delta t_{\text{SN}} = 1$ s, and the cut on the number of hits is relaxed for higher N_ν , as shown in Figure 5.13.

where $c_{\text{ice}} = c/n_{\text{ice}} \approx 0.221 \text{ m ns}^{-1}$. This function is used as probability distribution to draw a detection time for each PE. The depth-dependent effective scattering and absorption length, λ_e and λ_a , are taken from figs. 3.2 and 3.5 in [25], using appropriate functions that fit the data, found by Nora Linn Strotjohann [207]. Because of on-going R&D on cylindrical-shaped sensors, and due to simplicity, the optical modules are modeled as perfectly efficient cylinders, where every photon hitting the cylinder mantle would be detected. The cylinders have 1.82 cm diameter and 1 m length, so that the effective area is comparable to what is used in the deep ice, i.e. 5.4 HQE IceCube DOMs per meter.

Sensor noise is less of a problem in the shallow ice, since the Cherenkov photons from neutrino events are very localized. Because the volume and number of modules to consider for signal hits is $\propto r^3$, the PS cut is very efficient and results in much lower noise trigger rates without cutting away much of the signal. Even very small noise trigger rates such as 0.1 mHz can be realized without significant loss in effective mass (less than 5% loss). After applying optimized module noise cuts to reduce the noise rate to 0.1 mHz, one obtains ~ 25 Mton effective mass, when triggering on 5 hit modules—including the higher dead time induced by atmospheric muons, conservatively estimated to 15% as explained in Section 5.5.2.

The main drawback of the shallow, diffusive ice is the lack of directional reconstruction of events. Due to the strong scattering, any information on the direction of the charged particle is lost. Among other things, this makes it impossible to veto elastic scattering events from solar neutrinos by their direction. The shallow ice detector is also more sensitive at low energies, resulting in a generally much higher solar neutrino detection rate. A cut on the number of detected photons to increase the energy threshold is the only option to suppress the solar neutrino background. But due to the large overlap of the energy spectra of solar neutrinos and SN neutrinos (see Figure 5.12), one significantly loses detection efficiency.

Figure 5.13 shows the solar neutrino event rate and the effective mass for SN neutrinos (LL spectrum) as function of the number of hit modules required for the event trigger. Horizontal lines show the levels of solar event rate that can at most be tolerated, with the SN search window reduced from 10 seconds to 1 second (thus missing about 40% of the SN neutrino events, according to Figure 5.5). For a number of neutrino events $N_\nu \geq 3$ per SN detection, a solar rate of ≈ 4 mHz can be allowed (see Table 5.2). One would have to select events with at least 16 hit modules and the effective mass drops to about 4.3 Mtons.

Raising the neutrino event threshold N_ν relaxes the requirement on the solar rate—i.e. the cut on the hit modules—yielding a higher effective mass, but at the same time reducing the number of detected SNe. Optimizing for the highest SN detection rate, the best results for the shallow ice are found at $N_\nu \geq 6$ (see Figure 5.14) with a cut on at least 6 hit modules in an SN search window of $\Delta t_{\text{SN}} = 1$ s at an effective mass of about 21 Mton (see Figure 5.13). However, only about 60% of the SN neutrino events arrive within $\Delta t_{\text{SN}} = 1$ s, (see Figure 5.5), adding a factor of about $0.6^6 \approx 5\%$ to the SN detection rate. In contrast, in the deep ice, the optimum with effective mass of 12.1 Mton lies at $N_\nu \geq 3$, with a SN search window of $\Delta t_{\text{SN}} = 10$ s, so a collection efficiency of 95%, yielding only a correction factor $0.95^3 \approx 86\%$. The achieved SN detection rates are compared in Table 5.6, revealing that the shallow ice is inferior to the deep ice, yielding a lower total SN detection rate. However, at neutrino event multiplicity $N_\nu \geq 6$ and more, the shallow ice detector actually delivers slightly more SN detections than the deep ice detector.

While the shallow ice detector performs well as a mere photon counting experiment, there are other physics cases such as proton decay that rely on directional information and cannot be pursued in the shallow ice. Moreover, the detector in the shallow ice will suffer from additional backgrounds as well, above all atmospheric muons (much higher muon passing rate and longer dead time) and muon-induced spallation events that might become unmanageable at the low depth. Also, IceCube cannot be used as a veto in the shallow ice. Therefore, a detector located in the shallow, diffusive ice is strongly disfavored.

5.7 Expected Supernova Detection Rate

Knowing the detector effective area as a function of neutrino energy (Figure 5.12c), one can proceed to calculate the sensitivity to an SN neutrino burst with a given spectrum. The probability to detect an SN is calculated from Poisson statistics. An SN is considered as detected if at least three neutrino events trigger the detector within 10 s, which is the threshold that can be used if all background event rates are controlled to within 1 mHz. Figure 5.15 shows the SN detection probability as function of the distance to the SN using the three considered SN models, with cuts applied against 10 Hz dark noise of the modules and against solar neutrinos, including a dead time of 0.16% due to atmospheric muons and 95% of SN neutrinos falling into the 10 s window (see Section 5.5 and Figure 5.5). The distance up to which ≥ 3 neutrinos will be detected with a probability of $\geq 50\%$ is 6.6 Mpc for the TBP model, 9.6 Mpc for the LL model and 25.6 Mpc for the failed SN model, respectively.

With these probabilities at hand, the rate of expected SN detections can be computed, given the CCSN rate in the local environment. The determination of the local CCSN rate is based on work by Nora Linn Strotjohann for her Bachelor thesis [207]. The Gravitational Wave Galaxy Catalog (GWGC)—a catalog of nearby galaxies and their blue luminosity—is used that extends out to 100 Mpc distance [209]. The GWGC lists the galaxies' distance, morphological type code, and absolute blue magnitude (among other quantities) [209]. Following [208], it is assumed that the blue luminosity of a galaxy is proportional to the star formation rate and hence also to the SN rate. The conversion factors from blue luminosity to SN rate depend on the galaxy type and are obtained from SN observations (see Table 5.5). They are given in “SN units” SNu , $1 \text{ SNu} \equiv 1 \text{ SN} (100 \text{ yr})^{-1} (10^{10} L_\odot^B)^{-1}$, where L_\odot^B is the blue solar luminosity,

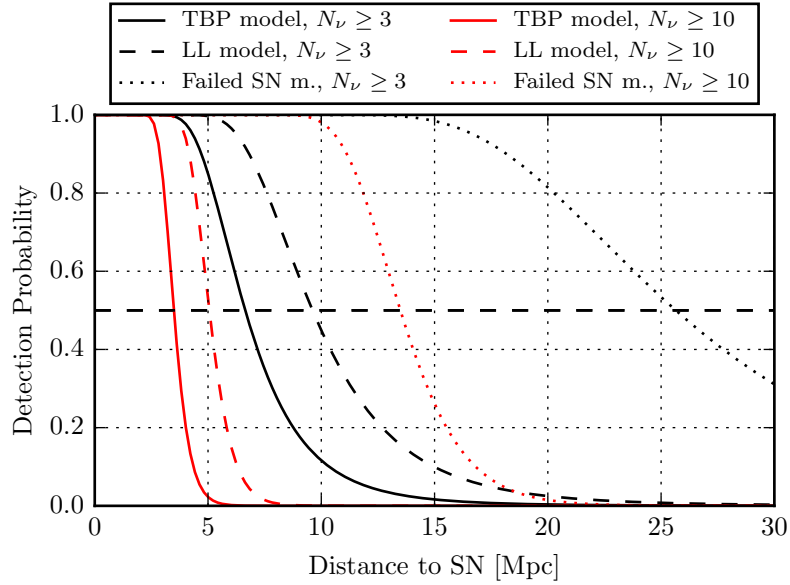


Figure 5.15: SN detection probability for the simulated detector after application of the cuts described in Section 5.5. The results for the TBP model, the LL model, and a failed SN model (compare Table 5.1) for the detection of at least either 3 or 10 neutrino events from the SN are shown.

Galaxy	Type	SN Rate [SNu]
Elliptical	E-S0	< 0.05
Spiral-like	S0a-Sb	0.89 ± 0.34
Spiral	Sbc-Sd	1.68 ± 0.60
Others	Sm, Irr., Pec.	1.46 ± 0.71

Table 5.5: The expected rates of CCSNe for different galaxy types in SN units ($1 \text{ SNu} = 1 \text{ SN} (100 \text{ yr})^{-1} (10^{10} L_B)^{-1}$). Values from [208, tab. 4], scaled by 1.68 (see text).

i.e. luminosity in the B filter. In order to apply the conversion factors to the galaxy catalog, the galaxies' absolute blue magnitude M_B is converted to blue luminosity relative to the Sun, L_B/L_\odot^B , using an absolute blue magnitude $M_\odot^B = 5.48$ mag of the Sun [210, tab. 2.1],

$$\frac{L_B}{L_\odot^B} = 10^{(M_\odot^B - M_B)/2.5}. \quad (5.16)$$

Nora Linn Strotjohann has found that these conversion factors lead to a total SN rate that is lower by a factor 1.68 [207], compared to the total SN rate using conversion factors derived from a more recent and more sophisticated study of a comprehensive compilation of local SNe, performed by the Lick Observatory Supernova Search (LOSS) [107]. This additional scale factor is included in the rate estimate to ensure consistency with currently available data. The result is a CCSN rate of about 1.5 per year within 10 Mpc. Elliptical galaxies of type E and S0 are ignored, since they contribute almost nothing to the CCSN rate. For a number of galaxies, the catalog leaves the morphological type unspecified. Those galaxies are excluded from the rate determination, however including them as the type of highest SN rate only increases the total SN rate by about 9%. For a small fraction of galaxies, the catalog contains no absolute blue magnitude, and those galaxies are excluded as well.

The initial mass function (IMF) is the distribution of stellar masses at birth time. A theoretical prediction of the SN rate based on the cosmic star formation rate and the IMF [105] is a factor two higher than the SN rate obtained from direct SN observations (see also Section 3.2.6). One explanation might be that there is observational bias to miss many faint SNe. Another possibility is a significant contribution of failed SNe that cannot be detected optically, but still emit neutrinos [105]. Scaling the prediction from blue luminosity by a factor of two, yielding about 3 SNe per year within 10 Mpc, this discrepancy is taken into account. In addition, it also leads to better agreement with the locally strongly enhanced observed rate of nearby SNe, which is rather $\sim 1.8 - 2.5$ SNe per year within 10 Mpc [109, fig. 5]. The rate estimates based on blue luminosity and those scaled to the star formation rate—both shown in Figure 5.16—are regarded as lower and upper limit, respectively.

Table 5.6 gives a summary of expected SN detections per decade in different neutrino event multiplicity bins. The total resulting number of SN detections with the cuts described in Section 5.5 ranges from 22 to 44 per decade for the LL model and about half of that for the TBP model. For failed SNe, the assumption that SNe collapse to a black hole at a rate of 10% of the regular CCSN rate is made. Yet, due to a more energetic neutrino spectrum, failed SNe are detected with a higher efficiency, resulting in 20 to 41 failed SN observations per decade, comparable to the number of detections from the LL model. Altogether, one can expect to observe at least one SN per year on average, perhaps up to 5 or more. The rate of SNe producing strong bursts of ten or more neutrinos is between 0.2 and 0.5 per year without failed SNe, or up to almost 1 event per year if failed SNe are included. Note that while for a neutrino multiplicity of three, the event is as likely to be from an SN as from detector noise or solar background, a single event with a multiplicity of four (five) already constitutes an SN signal of $\sim 2\sigma$ ($\sim 4\sigma$). Yet, the true power of the approach lies in the combination with follow-up missions that can detect the same SN in the optical or X-ray regime.

5.8 Conclusion

5.8.1 Summary

A 10 Mton-scale neutrino detector is required in order to be sensitive to CCSN neutrinos from beyond the Large Magellanic Cloud. Being sensitive to CCSNe in neighboring galaxies would yield a detection

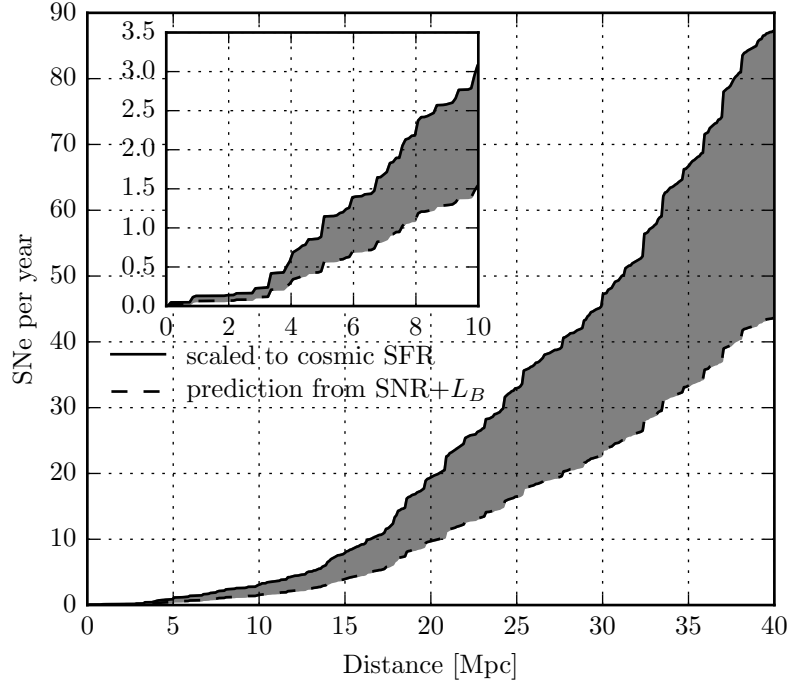


Figure 5.16: The cumulative expected SN rate: lower curve (dashed) according to observed SN rate and blue luminosity [208], normalized to the results of [107], upper curve (solid) scaled by a factor 2 to match expectations from the cosmic star formation rate [105]. The galaxy distribution and their blue luminosity values are taken from [209].

	N_ν	CCSNe (LL)		CCSNe (TBP)	Failed SNe
		deep	shallow	deep	deep
L_B	≥ 3	22.2	9.4	10.5	20.3
	≥ 4	14.0	9.4	7.2	14.4
	≥ 5	10.6	9.4	5.6	10.5
	≥ 6	8.7	9.4	4.5	7.9
	≥ 7	7.5	8.1	3.8	6.1
	≥ 10	5.3	5.8	2.3	3.4
SFR	≥ 3	44.4	18.8	20.9	40.7
	≥ 10	10.7	11.5	4.6	6.8

Table 5.6: Expected number of SN detections within one decade based on SN rates computed from the blue luminosity L_B of galaxies [107, 208] (first 6 rows). The last two rows are for a prediction scaled to match the star formation rate (SFR) [105] (see Figure 5.16). Failed SNe are assumed to occur at a fraction of 10% of all CCSNe. For the LL model, values for the simulated shallow ice detector (see Section 5.6) are listed as well.

rate of up to several SNe per year. In this chapter, an implementation of such a detector in the very clear Antarctic ice at around 2300 m depth below surface is explored, where photons can travel with very little scattering. A central result is that a 10 Mton detector with sensitivity to 10 MeV neutrinos would require a 127-string installation with about 50 times the total photocathode area used in IceCube.

A particular contribution of this work is the thorough study of different sources of background for a low-energy neutrino detector in the ice, and of the methods to suppress the backgrounds. Sensor noise is identified as a serious background source, however it can be removed using causality cuts if it is not larger than 50 Hz per sensor. The main background remaining after the noise reduction is due to solar ^8B neutrinos. They can be identified via lower photon multiplicity or—if one manages to reconstruct their direction—by their angular proximity to the Sun. Atmospheric muons will provide exceedingly bright events in such a dense installation, resulting in a small downtime. More challenging is the rejection of Michel electron events, yet with the IceCube detector fully surrounding the array, their identification will be straight forward and only a modest performance reduction is expected from their rejection.

Using a catalog of nearby galaxies, the rate of detectable SN neutrino bursts is computed. Depending on the assumed SN rate and explosion model, one can expect to observe between 11 and 44 SNe per decade in neutrinos (not counting the failed SNe). Failed SNe, where the star collapses to a black hole, may produce more than 20 detectable bursts per decade. Such an SN can be indirectly identified by the absence of an optical counterpart¹⁰, or more directly, by observing neutrinos of higher energies. The limited energy resolution of the detector ($\approx 30\%$ per neutrino event) should be sufficient to estimate the effective temperature of the neutrino emission and hence the nature of the burst.

A neutrino detector as described in this chapter will not only yield a precise measurement of the local SN rate with the ability to uncover failed SNe. A few of the SNe will be closer, perhaps even Galactic, and hence yield a much higher number of coincident neutrinos, allowing to infer details about the explosion or even the neutrino mass hierarchy [211, 212]. It is pointed out that the low energy threshold and very large effective mass make such a detector potentially interesting for a number of other physics phenomena, including e.g. proton decay studies and solar neutrino analysis.

5.8.2 Outlook

While a possible route towards the desired goal—routine observation of SNe in neutrinos—has been demonstrated, some very optimistic assumptions have been made along the way. Many problems still have to be solved.

In particular, the demand for new and cheaper technology is pointed out, motivating dedicated R&D for photo-sensors with large effective photo-cathode area, but at the same time very low self-noise. Work in this direction has already been initiated and is embedded into the IceCube low-energy extension project PINGU (see [120], section 14). Efforts include the use of wavelength-shifters [196] and of multiple small PMTs within a single module, similar to the KM3NeT optical modules [213].

The study of muon induced nuclear spallation events as background source has not been done in this work. They may represent a serious background, because they are very hard to distinguish from the SN neutrino signal. The conventional way to suppress spallation events is using temporal and spatial correlations with the originating muon, resulting in additional dead time [128, 131]. More detailed studies including an accurate description of the nuclear processes as well as full event reconstruction are required, which are both beyond the scope of this thesis. These could be the next steps following this work.

¹⁰ With the risk of confusing it with a regular, dust obscured SN

Search for High-Energy Neutrinos from Supernovae

6.1 Motivation

The quest to identify the sources of high-energy cosmic rays (CRs) goes back into the early 1910s when Viktor Hess and fellow scientists discovered and observed the ionizing radiation for the first time. Yet, more than 100 years later, it is not completely understood where and how CRs are produced. As pointed out in Section 2.4.4, neutrinos could play a vital role in this endeavour, since they are very likely co-produced with charged CRs and due to both their neutrality (they travel on straight paths, pointing back to their sources) and their penetrative power (they are not absorbed by dust or dense environments).

A big step forward in neutrino astronomy was the detection of an isotropic astrophysical neutrino flux in the 100 TeV to PeV energy range, published by the IceCube collaboration in 2013 [38, 146]. This analysis, named High-Energy Starting Events (HESE), aims at events with a very high amount of deposited charge that start within the detector.¹ Events with interaction vertex inside of the detector are very likely neutrino events, since muons can only very rarely sneak in without leaving a trace in the outer detector layers. This way, bundles of several muons that look like a single very energetic muon are effectively suppressed. Because of the high charge requirement, the neutrinos necessarily have very high energies. This results in a high probability to find astrophysical neutrinos, i.e. neutrinos from beyond the Earth's atmosphere, since the atmospheric neutrino spectrum is very steep ($\propto E^{-3.7}$) compared to expected astrophysical neutrino spectra ($\propto E^{-2}$ to $\propto E^{-3}$). Thus, the number of expected background events above a certain charge threshold is relatively small (e.g. $10.6_{-3.6}^{+5.0}$ events above 6000 photoelectrons in two years of HESE data, $15.0_{-5.8}^{+10.1}$ in three years), while the number of detected events is significantly larger (e.g. 28 in two, 37 in three years).

So far, there is no indication for any neutrino point source (PS) in the measured astrophysical neutrino flux. The data are consistent with isotropy and there is no significant excess of neutrino events from the southern sky, where most of the Galactic plane is located. This isotropy implies a dominantly extragalactic origin of the neutrino flux and suggests numerous sources that cannot be resolved yet, each source contributing only a single neutrino to the small HESE sample. It may take many years of more data acquisition until the strongest neutrino PS becomes visible within the ensemble of point sources, for which at least two well-resolved neutrinos from the same source are required. And even after the

¹ The outer detector layers are used as a veto.

establishment of a PS in the astrophysical neutrino flux: Due to the limited resolution of the neutrino direction— 0.1° to 1.0° for tracks or 10° to 30° for cascades—there may be a multitude of astrophysical sources that have to be considered as the origin of the neutrino emission.

In this chapter, a different, complementary approach to neutrino astronomy is presented. This analysis is characterized by three different concepts: it is *time-dependent*, *multi-messenger* and *online*. I will explain those three concepts and their advantages and disadvantages in the following:

1. **Time-dependent vs. time-integrated:** A time-dependent neutrino PS analysis searches for a time-variable or *transient* emission, whereas time-integrated analyses assume that the source emission is constant. Due to the smaller amount of background during a short emission time-window, a weaker neutrino fluence is required for a discovery in time-dependent searches, i.e. the signal-to-noise ratio is better. However, one has to assume a transient nature of at least some sources. To constant sources, time-dependent searches are generally less sensitive than time-integrated searches.
2. **Multi-messenger vs. neutrino-only:** Multi-messenger analyses combine different astrophysical observation channels in order to gain more physical insight into a source and/or to increase the statistical significance of a coincidence that would not be significant in each of the channels by itself. Typical channels to combine neutrino data with are photon data, e.g. optical, X-ray or γ -ray observations. Gravitational waves, neutrons or extremely high-energy (and thus undeflected) charged CRs are other examples. Compared to neutrino-only analyses, multi-messenger analyses tend to be more complex and rely on the assumption that the source is detectable with multiple messengers.
3. **Online vs. offline:** In IceCube, the terms online and offline distinguish between data analyses that are executed immediately after data acquisition (DAQ) at the South Pole in near-real time and those that are performed at research institutes in the North after a significant amount of time has passed. Offline analyses have the advantage of having access to almost unlimited CPU resources so that computationally demanding reconstructions can be performed. Additionally, detector monitoring information, e.g. on mis-behaving or non-functional DOMs, becomes available within days or weeks after the DAQ and is available only to offline analyses, improving the reconstruction quality if correctly taken into account. Offline analyses are traditionally performed after a full year of new data has been acquired.

In contrast, online analyses are restricted to less sophisticated reconstructions, but have the advantage of a very low latency of on average 3 minutes in case of the analysis presented here. This short latency enables to trigger follow-up observations with other telescopes. The telescopes observe the neutrino arrival direction, aiming for the detection of a transient electromagnetic counterpart, which might be fading within minutes or hours. Telescopes have limited fields of view (FoV) and duty cycles (fraction of time during which observations can take place) and cannot continuously monitor 2π of the sky, i.e. the entire northern sky, like IceCube does. Therefore, active follow-up triggered by an online IceCube neutrino analysis has the potential to obtain a more complete dataset. Fast transients can be observed that might otherwise be missed. A potential source can be observed even if it lies in a part of the sky that is rarely or never surveyed, due to the limited observation time available to busy observatories.

In summary, the advantages of a time-dependent multi-wavelength online neutrino analysis are: increased signal-to-noise ratio, increased significance, more physical insight, and a more complete multi-wavelength dataset. In addition, in the light of the discovered astrophysical neutrino flux, this kind of

analysis bears the potential to reveal neutrino point sources as contributors to this flux on a much shorter time scale than with the HESE analysis. The reason is that thanks to the increased signal-to-noise ratio of transient sources, the event selection criteria can be relaxed. Instead of only about 15 events per year, one may tolerate about 100 000 events, which are dominantly background. This does not pose a problem, because a transient burst of neutrinos is unlikely to arise from the uniform background. The tolerant event selection results in a much higher number of astrophysical events in the sample. For example, using Monte Carlo (MC) simulation, the optical follow-up IC86–3 sample (see Section 6.2, in particular Section 6.2.5) is estimated to contain about 600 astrophysical ν_μ events, adopting the all-flavor spectrum of $\Phi_\nu = 6.7 \times 10^{-18} \text{ GeV}^{-1} \text{ s}^{-1} \text{ sr}^{-1} \text{ cm}^{-2} (E/100 \text{ TeV})^{-2.5}$ [214]—obtained from a global analysis combining several IceCube datasets—and assuming a flavor ratio of 1:1:1 (thus a factor 1/3). The higher event number increases the chances of a transient PS detection.

More importantly, if a simultaneous detection of a transient source in neutrinos and photons would be accomplished, then it might not only be the first significant detection of a high-energy neutrino PS, but at the same time the *identification* of the source would be achieved because of the unambiguous angular resolution of the photon data. As discussed above, the relatively poor resolution of the neutrino direction would allow for several source scenarios. Time-dependent, multi-wavelength, and ideally online neutrino analyses have the potential to be the quickest, maybe even the only, route towards neutrino point source detection and identification. The more numerous and faint the individual neutrino sources are, the more attractive this type of analysis becomes.

Of course, this analysis strategy only pays off if a sizable fraction of the neutrino sources is transient, and if the transient sources flare simultaneously in neutrinos and photons. Prime candidates for transient high-energy neutrino emission are cataclysmic events such as long duration GRBs [41, 112, 215] and choked jet SNe [66, 111], as introduced in Sec. 3.3 and 3.2.8. Those two source classes are related: Both are thought to host a jet. The choked jet is more baryon-rich and has a much lower Lorentz factor $\Gamma \approx 3$ (mildly relativistic) than the GRB jet with $\Gamma \gtrsim 100$ (highly relativistic). The mildly relativistic jet cannot penetrate the stellar envelope and remains optically thick, making it invisible in γ -rays. The produced neutrinos at TeV energies can escape nevertheless and might trigger the discovery of a SN in the follow-up channels. Mildly relativistic jets may occur in a much larger fraction of core-collapse SNe than highly relativistic jets, i.e. GRBs [66, 111].

Both jet SN and long GRB sources are expected to emit a short, about 10 s long burst of neutrinos [66] either 10 s to 100 s before or at the time of the γ -ray burst [112], setting the natural time scale of the neutrino search. After recording the neutrino burst, follow-up observations can be used to identify the counterpart of the transient neutrino source. The γ -ray burst itself usually fades too rapidly to schedule electromagnetic follow-up observations, since 95% of GRBs have a duration of less than ~ 150 s [216]. However, there are good detection prospects using the GRB afterglow, in optical or in X-ray data. Still, a fast response within minutes to hours is required for this. A choked jet SN is found by detecting a SN light curve in the follow-up images, slowly rising and then declining within weeks after the neutrino burst. Following this scientific motivation, an online neutrino analysis was installed at IceCube in 2008, see the following Section 6.2.

Detection of neutrinos from GRBs and choked jet SNe would be remarkable discoveries. If the correlation with an optical SN is shown, then it would be a strong evidence for the presence of a mildly relativistic jet with significant kinetic energy [66]. It would also be the first identification of an extragalactic neutrino source. Data from many SNe/GRBs would yield the distribution of the jet Lorentz factor, providing important insight into the SN-GRB connection [66]. The non-detection of those neutrinos is interesting as well, as one can place limits on the rate of SNe hosting jets. This can contribute to the understanding of the nature of SN explosions in general and the relation between SNe and GRBs.

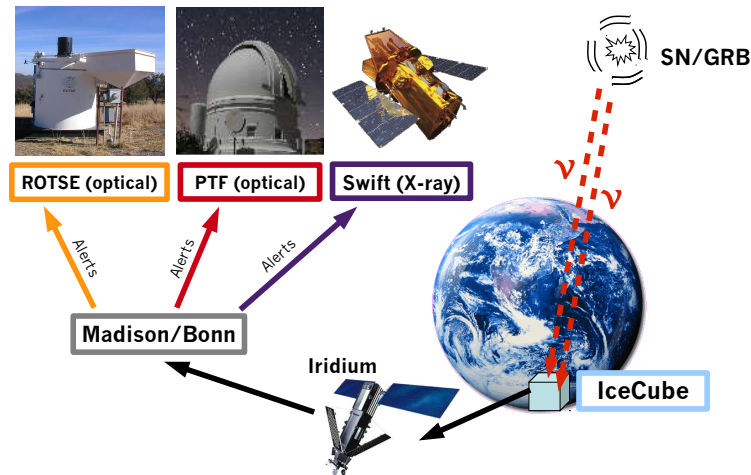


Figure 6.1: Overview of the components of IceCube’s optical follow-up (OFU) and X-ray follow-up (XFU) system: A neutrino burst emitted by a transient source such as a SN or GRB creates a multiplet detection in IceCube. A message is sent via Iridium satellites and a server issues alerts, which are distributed to follow-up instruments.

6.2 The Optical Follow-Up System

6.2.1 Overview of the System

In late 2008, an online neutrino event selection was set up at IceCube, targeted at the detection of muon neutrino bursts from transient neutrino point sources. The analysis is running in real-time within the limited computing resources at the South Pole, capable of quickly reconstructing and filtering the neutrino candidates. After passing certain requirements at the IceCube site, a message is sent via satellite to a dedicated server in the Northern hemisphere, which checks the alert conditions and if required issues follow-up triggers (alerts) that are sent to the follow-up instruments within a latency of only a few minutes [217, p. 40], [218, 219]. The system, called optical follow-up (OFU) or X-ray follow-up (XFU) depending on follow-up wavelength, is visualized in Figure 6.1. The follow-up programs are also called Neutrino triggered Target of Opportunity (NToO). After introducing the follow-up instruments of OFU/XFU in the rest of this section, the details of the neutrino data processing and the resulting data sample are given in Sections 6.3, 6.4, and 6.5. The neutrino multiplets and alerts measured by the system are discussed in Section 6.6. The IceCube neutrino detector itself has already been introduced in Section 4.2.

The OFU and XFU real-time follow-up programs encompass three follow-up instruments: the Robotic Optical Transient Search Experiment (ROTSE) [220], the Palomar Transient Factory (PTF) [221, 222] and the Swift satellite [160]. In addition, IceCube also maintains a real-time γ -ray follow-up (GFU) program, using a separate neutrino filter and alert algorithm, which is targeting slower transients (time scale of weeks), e.g. flaring Active Galactic Nuclei (AGNs). GFU is sending alerts to the γ -ray telescopes MAGIC and VERITAS and is not discussed here [217, p. 16].

6.2.2 The ROTSE Telescope Network

ROTSE [220] was a network of four optical telescopes with 0.45 m aperture and $1.85^\circ \times 1.85^\circ$ FoV, located in Australia, Texas, Namibia and Turkey. Figure 6.2 shows a photograph of one of the identical telescopes. It was a completely automatic and autonomous system that could receive alerts, perform

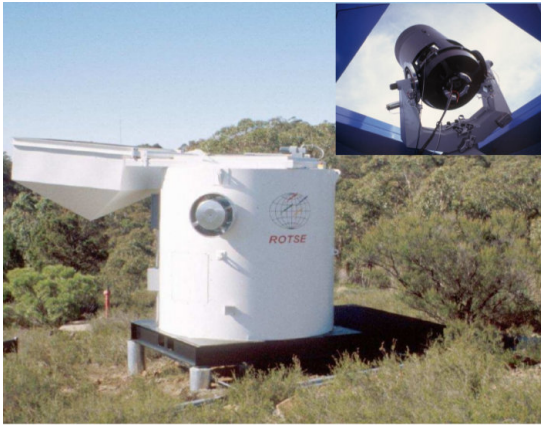


Figure 6.2: Photograph of the ROTSE-III telescope enclosure at the Siding Springs Observatory near Coonabarabran, Australia, with the hatch cover fully open. A top-right inset shows the telescope itself. Image taken from [149, p. 92].

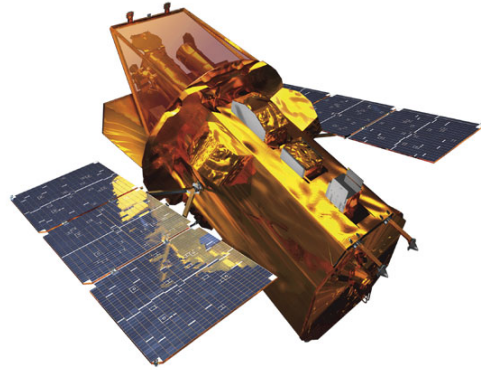


Figure 6.3: Rendering of the NASA Swift Gamma-Ray Burst mission spacecraft, boarding three instruments, mainly used for observing γ -ray bursts. Image taken from [223].

observations and process the data without requiring human interaction. The limiting magnitude of $\sim 16 - 18.5$ mag was however insufficient to discover faint or far SNe. For instance, for a very bright SN with -20 mag absolute magnitude, the detection radius is about 160 Mpc to 500 Mpc, while a faint SN with -14 mag is only visible within a radius of about 10 Mpc to 30 Mpc.

ROTSE was the first OFU follow-up instrument and initiated the program. Since December 2008 (first alert sent 2008-12-18), IceCube has been sending ~ 25 alerts per year to ROTSE. The first 116 alerts (with a background expectation of 104.7 ± 10.2 alerts), sent until 2013-01-30, were followed up with a median latency of 27.2 hours between the neutrino alert and start of the first follow-up observation. Since late 2012, only the two northern hemisphere telescopes continued operation,² and ROTSE did not accept alerts anymore after 2015-11-19. The last alert sending attempt happened on 2016-02-11 and on 2016-02-19, alert forwarding to ROTSE was turned off.

The ROTSE data from 2008-12 until 2009-12 were searched for SN counterparts. No SN was found in the follow-up data and upper limits on the fraction of SNe hosting mildly relativistic choked jets were set. The results were published in [218], more details can be found in [149].

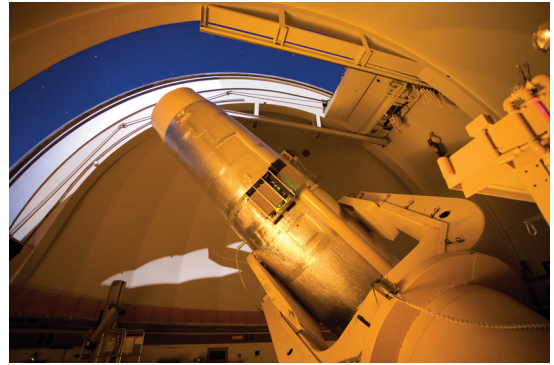
6.2.3 The Palomar Transient Factory (PTF)

PTF [221, 222] is a survey based at the Palomar Observatory in San Diego County, California, USA, at an altitude of about 1700 m [224]. It utilizes the 1.2 m (48-inch) Schmidt telescope (see Figure 6.4) on Palomar Mountain, named Samuel Oschin telescope. It is abbreviated P48 in the following chapters. The P48 is equipped with two filters: Mould R and SDSS g , see Figure 7.9 for a plot of the filter transmission curves. The focal plane spans $3.4^\circ \times 2.2^\circ$ and is equipped with a mosaic of 12 CCDs, of which 11 are operational, with total FoV of 7.26 ($^\circ$)². See Figure 7.2 for a plot of the PTF FoV with the CCD positions. The typical R -band limiting magnitude of PTF during dark time is about 21 mag. All the PTF data are reduced using the Lawrence Berkeley National Laboratory (LBNL) real-time pipeline responsible for transient identification and the Infrared Processing and Analysis Center (IPAC) pipeline at Caltech, described in [225]. The image photometric calibration is described in [226]. PTF pursues a

² The last alert was successfully sent to one of the southern hemisphere telescopes on 2012-09-17.



(a) The Palomar 48-inch telescope dome in a long exposure photograph, with the night sky above.



(b) The Palomar 48-inch Schmidt telescope itself, inside the dome.

Figure 6.4: Images of the Palomar 48-inch telescope, taken from [227], credit: Palomar Observatory/California Institute of Technology.

number of science goals, most notably the discovery and observation of SNe. Several other telescopes at Palomar Mountain and at other locations can be used for photometric and spectroscopic follow-up observation. IceCube has been sending ~ 9 alerts per year to PTF, since August 2010 (first alert sent 2010–08–16). The PTF alerts are a subset of the ROTSE alerts, see Section 6.6 for details. The first 23 alerts (with a background expectation of 18.8 ± 4.3 alerts), sent until 2013–02–13, were followed up with a median latency of 34.9 hours between the neutrino alert and start of the first follow-up observation.

An exceptional supernova found in the PTF follow-up data is discussed in Chapter 7. The general analysis of the PTF data and the search for SNe are described in Chapter 8.

6.2.4 The Swift Satellite

Swift [160] is a satellite operated by NASA (see Figure 6.3) that boards three science instruments: a 170 nm to 600 nm ultraviolet/optical telescope (UVOT), a 0.3 keV to 10 keV X-ray telescope (XRT), and a 15 keV to 150 keV hard X-ray Burst Alert Telescope (BAT). Swift’s main goal is the discovery and study of GRBs, of which it detects about 100 per year [228] (about one third of all GRBs)³. IceCube’s X-ray follow-up program triggers Swift’s XRT, which can provide valuable information by observing a GRB afterglow in X-rays. The XRT has a FoV of only 0.4° in diameter, whereas the median error radius of the neutrino direction is typically $\sim 0.5 - 1^\circ$. For an increased probability to find a neutrino counterpart, Swift performs seven pointings for each IceCube follow-up, resulting in an effective FoV of about 1° in diameter, which covers on average roughly 40% of the IceCube error circle. Since XRT and UVOT point in the same direction, XRT X-ray observations also lead to ultraviolet and optical UVOT data, which may be analyzed as well. IceCube has been sending ~ 6 alerts per year to Swift, since February 2011. The Swift alerts are a subset of the ROTSE alerts, with an overlap of Swift and PTF alerts,⁴ see Section 6.6 for details. The first 18 alerts (with a background expectation of 17.9 ± 4.2 alerts), sent until 2014–02–26, were followed up with a median latency of 1.9 hours between the neutrino alert and start of the first follow-up observation [229]. The follow-up scheduling is not fully automatic and includes human supervision.

The analysis of the Swift data from the XFU is not part of this thesis and is presented elsewhere.

³ <http://gcn.gsfc.nasa.gov/> and <http://grbweb.icecube.wisc.edu>

⁴ Of the first 18 Swift alerts, 14 were also PTF alerts. Of the first 23 PTF alerts, 11 were also Swift alerts.

Season	Start Date	Stop Date	Start MJD	Stop MJD	First run	Last run	Livetime [d]
IC40	2008-12-18	2009-05-20	54818	54971	112211	113821	121.9
IC59	2009-05-20	2010-05-31	54971	55347	113823	115968	320.3
IC79	2010-05-31	2011-05-13	55347	55694	115973	118173	275.5
IC86-1	2011-09-16	2012-05-15	55820	56062	118691	120155	220.1
IC86-2	2012-05-15	2013-02-01	56062	56324	120157	121787	240.8
IC86-2 BDT	2013-02-01	2013-05-02	56324	56414	121788	122275	72.2
IC86-3	2013-05-02	2014-05-06	56414	56783	122278	124701	353.7

Table 6.1: Characteristics of the OFU neutrino sample data seasons. The livetime values for IC40 and IC59, since not part of this analysis, were adopted from [149, p. 85f].

6.2.5 OFU Data Seasons

The OFU neutrino data are divided into data acquisition (DAQ) seasons that are labeled with the prefix “IC” for IceCube and the number of IceCube strings present during the season. Table 6.1 lists the DAQ seasons and their properties: The calendaric start and end time, the start and end in modified Julian date (MJD), the start and end run number,⁵ and the livetime, i.e. the summed amount of time, in which the detector was taking data. Starting with “IC86-1”, the complete detector configuration was in operation and a counting number is appended to the label. Due to a special change of the event selection within the season, IC86-2 is divided into two parts: The part before introduction of a boosted decision tree (BDT) is simply called “IC86-2”, the post-BDT part is called “IC86-2 BDT” (see Section 6.4).

In the following sections 6.3, 6.4, 6.5, and 6.6, the details of the neutrino part of the multi-messenger OFU program are presented. Optical data are analyzed and discussed in Chapters 7 and 8.

6.3 The Online Level 2 Filter of IceCube

The background of cosmic-ray induced muons from the atmosphere above the detector amounts to $\sim 10^6$ muon events per neutrino event. Finding the neutrino events in this vast amount of background is a challenging task. For a successful online follow-up analysis, it must be conducted in near real-time. This and the following section are dedicated to this online event selection.

As detailed in Section 4.2.6, a base processing and filtering of the IceCube data is performed centrally at the South Pole. This first crude reconstruction and data reduction is used collaboration-wide. The main purpose is to reduce the amount of triggered data to a level, which allows the transmission to northern institutes via satellite, where data analysis continues. The emphasis therefore does not lie on efficient suppression of background and only very loose quality cuts are applied. Several different filters exist, most notably the Muon Filter selecting muon tracks and the CascadeFilter selecting cascades. Because they are the first filters applied after the trigger, they are also referred to as *Level 1*.

For a data analysis running online, in real-time, the base processing is not sufficient. Therefore, the *Online Level 2 Filter (Online L2)* was introduced, specifically designed for the needs of the OFU, XFU, and GFU follow-up programs. Like the base processing, it processes data in real-time at the South Pole. It serves two main purposes:

1. Reduce the data rate to a level, at which computationally more demanding reconstructions can

⁵ IceCube data are divided into segments of eight hour runs.

be applied,⁶ with cutting away as little neutrino signal as possible. Thus, Online L2 serves as an intermediate level between Level 1 and neutrino level.

2. Provide the more elaborate and demanding reconstructions needed for efficient neutrino event selection.

The Online L2 filter takes all events from the Level 1 Muon Filter as input, since it focuses exclusively on muon tracks. It applies cuts to the Muon Filter stream, performs additional reconstructions, and passes the output stream on. The event rate of $\sim 30 - 40$ Hz of the Muon Filter is reduced to $\sim 5 - 6$ Hz. Any online muon neutrino analysis can pick up the generic Online L2 stream and use it to create a specialized neutrino sample, focusing e.g. on low or high energies, upgoing or downgoing tracks. Notably, the OFU/XFU filter (see Section 6.4) and the GFU filter use the Online L2 as input. As a readily available sample, it has also been used as starting point for other near real-time analyses like a Crab flare analysis [230], or in offline GRB analyses [231].

6.3.1 Description of Cuts

For the IC86–2 season, the Online L2 filter has been redesigned by the author of this thesis, building on work done by Robert Franke, Anna Franckowiak, and others. The at the time best available track reconstruction, the MPE fit (see Section 4.2.4), previously performed after cutting to Online L2 level, was moved before the Online L2 cuts and thus applied to all input Muon Filter events. As a result, many previously mis-reconstructed upgoing events were correctly identified as downgoing muons with the MPE fit. Figure 6.5 visualizes this effect. Because of this and the better quality of the MPE-based cut variables, the signal efficiency of the Online L2 filter, i.e. the fraction of signal events passing the cuts, could be increased. The cuts were re-optimized. However, the main cut logic was not changed, since improvements could not be identified while investigating alternative cut logics involving new cut variables like L_{empty} and *Separation* (see Section 4.2.5 for definitions).

In the IC86–2 Online L2 filter, a two-iteration SPE fit (SPE1st Pandel PDF), seeded with the Muon Filter single-iteration SPE fit, and an MPE fit, seeded with the two-iteration SPE fit, are applied to all the Muon Filter events *prior to* the Online L2 event selection. Based on the shape of the zenith angle θ distribution of events (Figure 6.5), four regions of the sky were identified, which have distinct event rates and backgrounds,

A: $180^\circ \geq \theta_{\text{MPE}} \geq 115^\circ$ (upgoing, vertical)

B: $115^\circ > \theta_{\text{MPE}} \geq 82^\circ$ (upgoing, horizontal)

C: $82^\circ > \theta_{\text{MPE}} \geq 66^\circ$ (downgoing, horizontal)

D: $66^\circ > \theta_{\text{MPE}} \geq 0^\circ$ (downgoing, vertical),

where θ_{MPE} denotes the zenith angle given by the MPE fit. Studies showed that the two upgoing regions A and B behave so similarly that the gain of separately optimized cuts is negligible and it was decided to merge region A and B to one region AB. Performing parameter space grid scans, the optimal cuts were found as follows:

⁶ In offline processing (*Offline Level 2*), similar more demanding reconstructions are performed on all Level 1 events, since computing resources are not as scarce as at the South Pole.

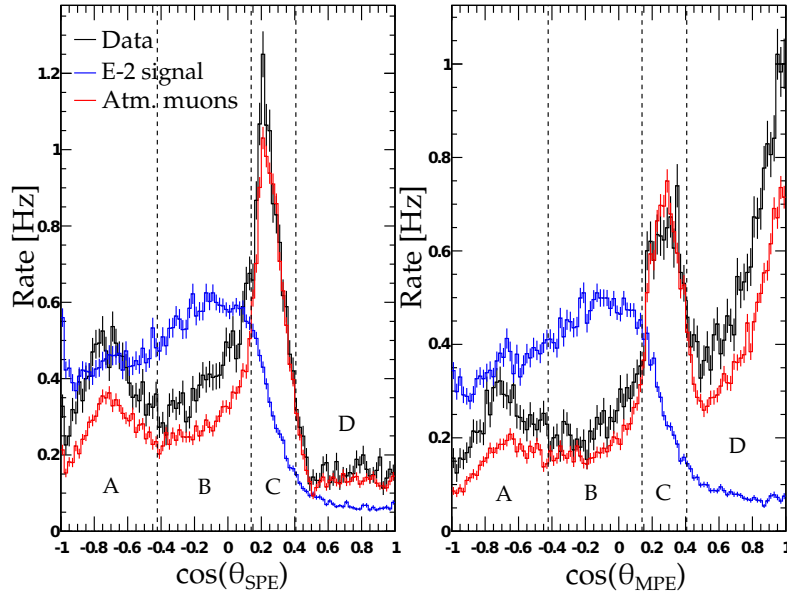


Figure 6.5: Zenith angle distribution at Muon Filter level for the one-iteration SPE reconstruction of the Muon Filter (left, up to season IC86–2 the most accurate reconstruction available before Online L2 cuts) and the MPE reconstruction (right, available since IC86–2). Zenith angle regions A, B, C, and D are divided by dashed lines. Shown are experimental data (black), MC simulated muon neutrino signal at arbitrary normalization (blue, weighted with E^{-2} energy spectrum), and MC simulated atmospheric muon background from cosmic ray air showers (red, should ideally describe data, because background-dominated at this level).

The event lies in region AB ($\theta_{\text{MPE}} \geq 82^\circ$) AND (

$$\left(\frac{L_{\text{dir}}^{\text{MPE}}}{160}\right)^2 + \left(\frac{N_{\text{dir}}^{\text{MPE}}}{9}\right)^2 \geq 1 \quad \text{OR} \quad \text{mrlog}_{\text{SPE}}(4.5) \leq 8.3 \quad \text{OR} \quad \log_{10}(q_{\text{tot}}) \geq 2.7$$

) OR the event lies in region C ($82^\circ > \theta_{\text{MPE}} \geq 66^\circ$) AND (

$$\text{mrlog}_{\text{SPE}}(4.5) \leq 8.3 \quad \text{AND} \quad \log_{10}(q_{\text{tot}}) \geq (3.3 \cos(\theta_{\text{MPE}}) + 1.13)$$

) OR the event lies in region D ($\theta_{\text{MPE}} < 66^\circ$) AND (

$$\text{mrlog}_{\text{SPE}}(4.5) \leq 10.5 \quad \text{AND} \quad ($$

$$\cos(\theta_{\text{MPE}}) \leq 0.5 \quad \text{AND} \quad \log_{10}(q_{\text{tot}}) \geq (3.3 \cos(\theta_{\text{MPE}}) + 1.18))$$

$$\text{OR} \quad (\cos(\theta_{\text{MPE}}) > 0.5 \quad \text{AND} \quad \log_{10}(q_{\text{tot}}) \geq (0.6 \cos(\theta_{\text{MPE}}) + 2.53))$$

)
).

The background in the upgoing part of the sky (region AB) is due to atmospheric downgoing muons mis-reconstructed as upgoing particles, i.e. the reconstruction quality can be used as a discriminator. The cut is a logical OR on track reconstruction quality variables, combined with an OR selecting high energy events regardless of the reconstruction quality. Consequently, the signal efficiency for well-reconstructed events—most interesting for point source searches—is high, while the large background of mis-reconstructed downgoing atmospheric muons is suppressed. One of the quality variables is the *direct ellipse*, which is a combination of the number of direct hits N_{dir} and their projection on the fitted track, direct length L_{dir} . See Section 4.2.5 for definitions of N_{dir} and L_{dir} . They are combined in a way that the cut describes an ellipse in the L_{dir} versus N_{dir} plane, see Figure 6.6. The other quality variable is

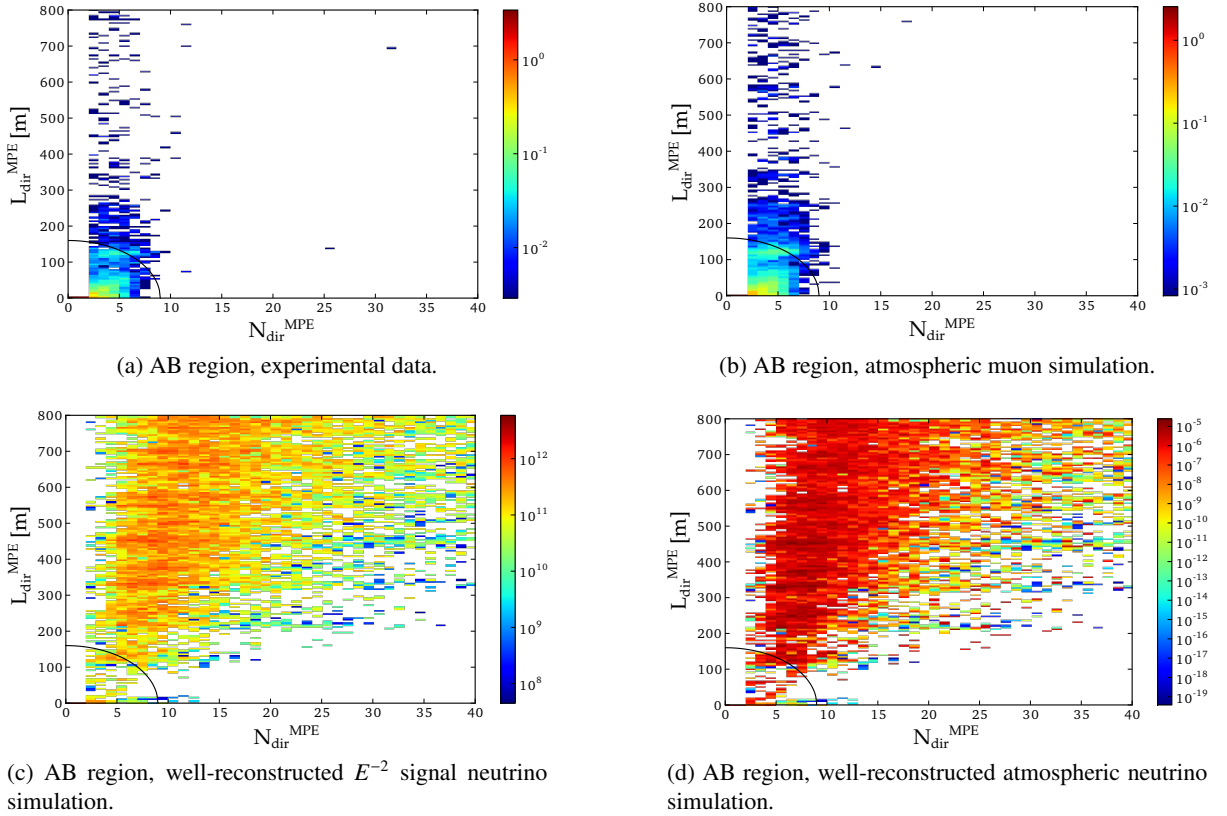


Figure 6.6: Direct length L_{dir} versus number of direct hits N_{dir} , calculated with respect to the MPE fit. The direct ellipse cut is indicated by a black curve: events below are discarded. It is evident that most data and atmospheric muon events lie within the ellipse, while most well-reconstructed neutrino events (MPE fit within 3° from the true direction) lie outside.

$\text{mrlogl}_{\text{SPE}}(x)$, which is a modified version of the reduced likelihood of the fit (again see Section 4.2.5). The parameter x is set to 4.5 for the Online L2 filter, providing best efficiency in all zenith regions. The $\text{mrlogl}_{\text{SPE}}(x)$ uses the likelihood of the Muon Filter SPE fit, not of the MPE fit, because it yields better efficiencies. Energy proxy is the total charge q_{tot} deposited in all DOMs, measured in photo-electrons (PE).

In the upgoing AB region, signal efficiency lies above 99% for well-reconstructed events, which are defined as events having an MPE reconstruction within 3° from the Monte Carlo truth. The passing rate is about ~ 2 Hz.

In the downgoing regions C and D, the background consists of well-reconstructed downgoing atmospheric muons, i.e. fit failures cannot be used to reject background. Therefore, it is more difficult to distinguish signal neutrino events from atmospheric muon events. Because the atmospheric background has a softer energy spectrum compared to the expected signal, a possibility is to cut on the energy and select only high-energy events. However, this drastically reduces the signal efficiency, especially for soft spectra, and explains why point source analyses are generally more sensitive to sources in the sky below the neutrino detector. The Muon Filter uses a zenith-dependent cut on q_{tot} and it was found that tightening the same cut is a very powerful way to reduce the background, see Figure 6.7. A logical AND combination with $\text{mrlogl}_{\text{SPE}}(x)$ was found to yield the highest signal efficiency. The direct ellipse has

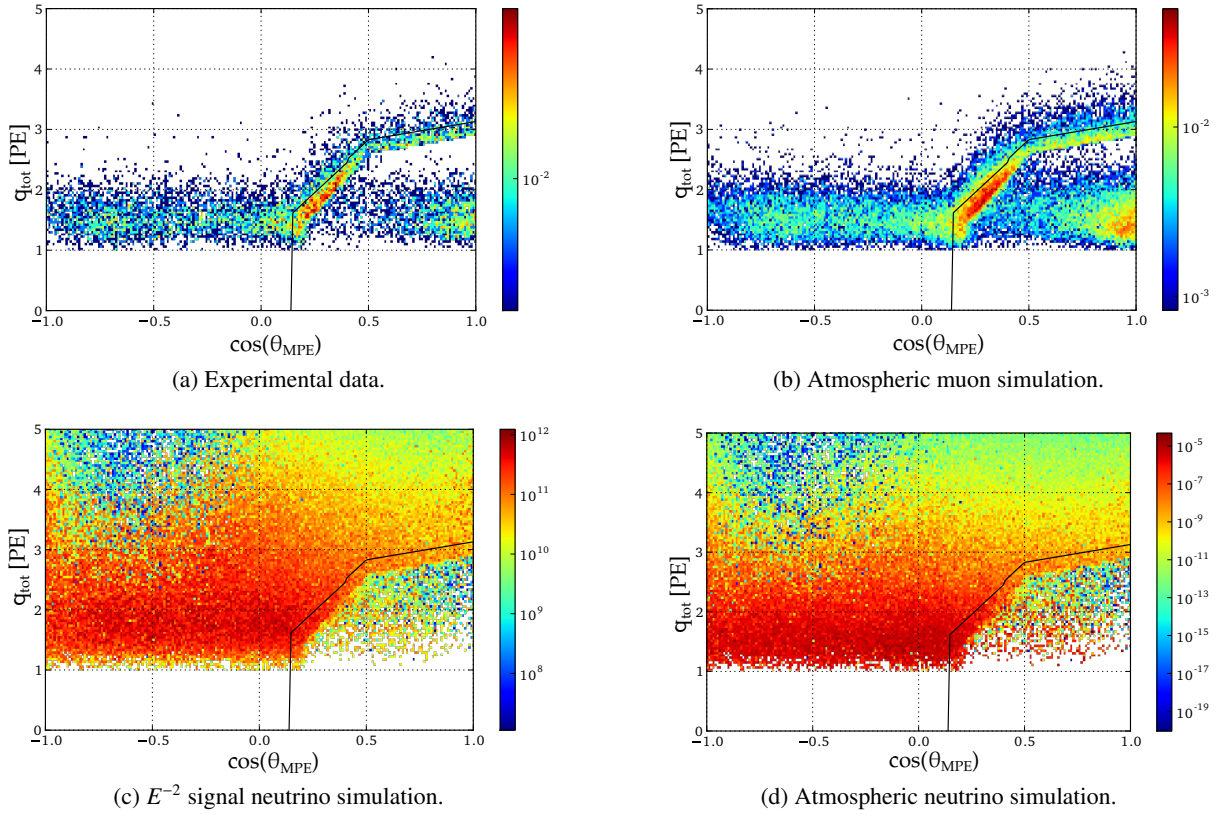


Figure 6.7: Total charge q_{tot} versus MPE fit zenith angle θ_{MPE} . A zenith-dependent cut on q_{tot} was done before by the Muon Filter and the Online L2 filter does likewise, but harder. The higher cut threshold is indicated as black line, events below the line are discarded. Note that there are events within the Muon Filter cut region, because the Muon Filter relies on the SPE fit.

basically no power to separate between signal and background.

The efficiency for well-reconstructed events in regions C and D is about 79% for an E^{-2} spectrum and 45% for an E^{-3} spectrum. The passing rate is ~ 3 Hz. The passing rates of the filter are also tabulated in Table 6.2. Table 6.3 displays the filter efficiency values and the efficiency versus energy for the different zenith regions is plotted in Figure 6.8.

6.3.2 Additional Reconstructions

For events passing the Online L2 filter, additional reconstructions and calculations are performed (see Sections 4.2.4 and 4.2.5 for details):

- A *Bayesian fit* for all upgoing events (defined as $\theta_{\text{MPE}} > 80^\circ$).
- *Split fits*: A chain of improved linefit (replacing the old linefit since IC86–2) and two-iteration SPE fit on both halves of the event pulses split once in time and once in space (with MPE as track hypothesis).
- (added for IC86–2) Bayesian fits on the split events if the unsplit event is upgoing.
- Energy reconstruction MuE based on the MPE fit.

Region	Exp. Data [Hz] (% of Muon Filter)
AB (upgoing)	1.99 (14.5)
C (downgoing horizontal)	1.49 (19.1)
D (downgoing vertical)	1.43 (12.3)
Full Sky	4.91 (14.8)

Table 6.2: Event passing rates of the Online L2 filter, determined with experimental data. The bracketed numbers are the percentage with respect to the Muon Filter rate.

Region	E^{-1} (well-reco.)	E^{-2} (well-reco.)	E^{-3} (well-reco.)
IC86–2 AB (upgoing)	90.24 (99.38)	89.17 (99.24)	81.91 (98.60)
IC86–2 CD (downgoing)	91.48 (98.82)	65.91 (78.93)	18.79 (45.44)
IC86–1 upgoing	90.87 (99.38)	84.91 (98.28)	76.57 (96.63)
IC86–1 downgoing	94.32 (98.62)	63.59 (68.27)	27.00 (29.40)

Table 6.3: Signal efficiency of the Online L2 filter with respect to the Muon Filter in percentage. The IC86–2 filter was designed as part of this thesis. For comparison, also the previous season’s values (IC86–1) are shown. In parenthesis is the efficiency for well-reconstructed events, which are defined as events with MPE fit less than 3° from the true direction.

- (added for IC86–2) Improved energy reconstruction *MuEx*, which allows for upward fluctuations in the expected photon density, for the MPE fit.
- The very fast *Cramér-Rao fit* for angular error estimation is done on the two-iteration SPE fit and the MPE fit.
- (added for IC86–3) The much slower *Paraboloid fit* for angular error estimation is done on the MPE fit, but only for upgoing events due to computational constraints (see below).
- (added for IC86–4) Improved track reconstruction *SplineMPE fit* and a corresponding Cramér-Rao fit.
- (added in IC86–2) The direct variables N_{dir} , L_{dir} , etc. are calculated for the Muon Filter SPE fit, the two-iteration SPE fit, and the MPE fit.
- (added for IC86–2) q_{tot} is calculated and stored.
- (added for IC86–2) L_{empty} and *Separation* are calculated and stored, both use the MPE fit.

The addition of reconstructions makes the OnlineL2 sample more attractive for analyzers since it provides more and higher quality variables, which can be used to select a neutrino sample, e.g. using a machine learning algorithm.

6.3.3 Computational Constraints

The computing environment at the South Pole has limited resources. Yet, it must handle the rate of data coming in from the detector in real-time. Because events need to be sorted chronologically in the output data stream (e.g. to look for bursts of neutrinos), one cannot afford single events with excessively long

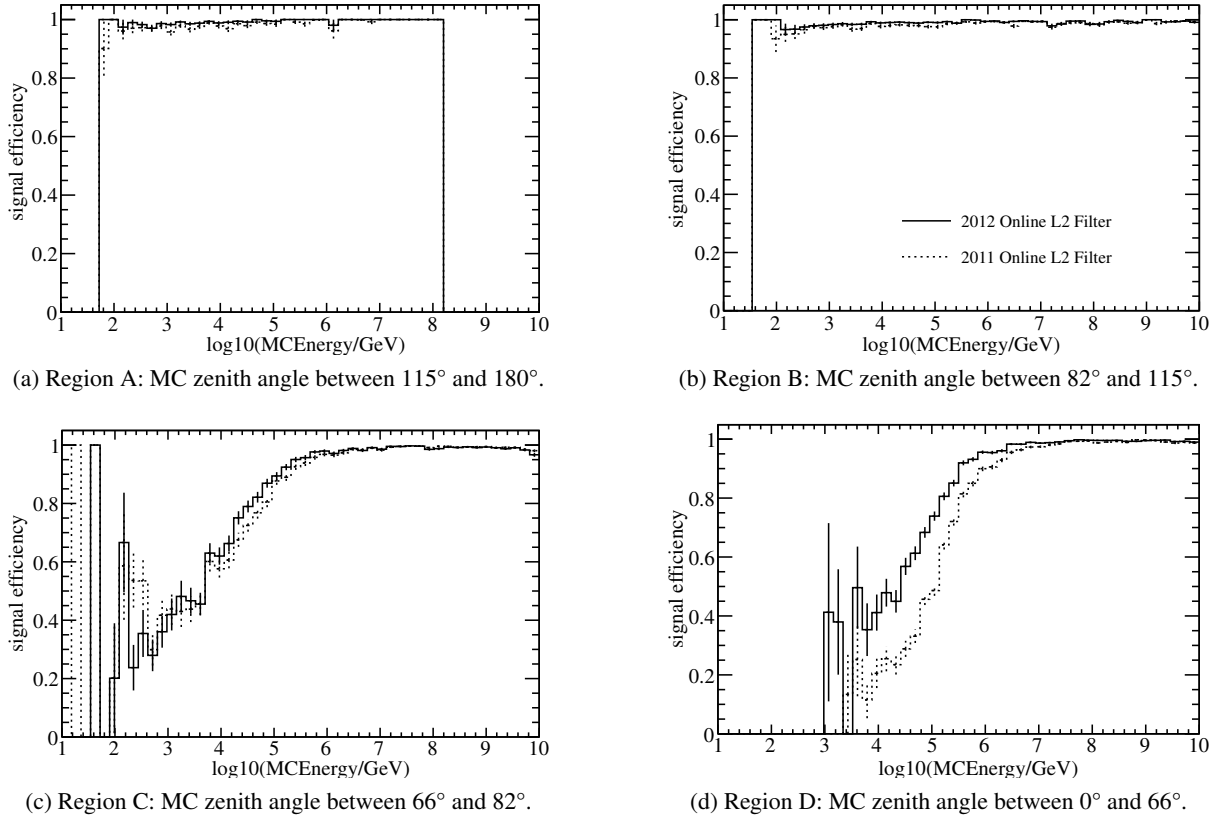


Figure 6.8: Efficiency of the Online L2 filter with respect to the Muon Filter as function of true MC simulation neutrino energy for well-reconstructed events (MPE fit within 3° from the true direction) in zenith regions A, B, C and D. The dashed line shows the efficiency of the previous season's Online L2 filter cuts for comparison. Efficiency is either comparable or higher than the previous filter's efficiency.

processing times. If a fraction of events is processed too slowly and if the fraction is too high, then the entire processing chain will have to wait for these events to finish. The result is that the processing lags behind the incoming data, even though an average event is processed quicker than required to handle the data rate. Therefore, not the average processing time of a reconstruction is critical, but rather the tails of the processing time distribution or, for instance, the 99th percentile. Because a lag of the processing will increase over time, this situation must be avoided. Thus, the processing time distribution of the Online L2 filter must be examined before it goes online.

During the Online L2 test processing, the processing time spent by each reconstruction is stored so that the processing time distribution can be plotted. As an example, Figure 6.9 shows processing time distributions from the work on the IC86–3 version of the OnlineL2 filter. Additional reconstructions that slightly change the slope of the distribution (as the SplineMPE fit applied to all Online L2 events) are much more manageable than reconstructions that add a bump to the distribution at high processing time (as the Paraboloid fit and an alternative angular error estimator applied to all events). In the example, this means that SplineMPE can be applied to all Online L2 events, but the Paraboloid fit can only be applied to upgoing events.

The reason is that upgoing events have a smaller average number of hit DOMs because they consist

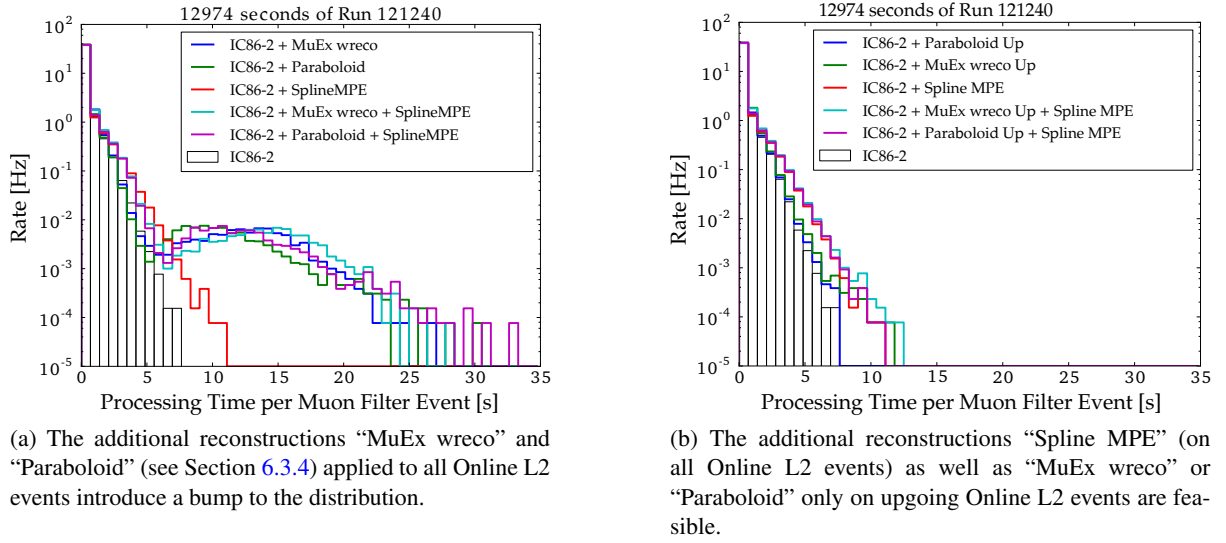


Figure 6.9: Distribution of the OnlineL2 filter processing time per event at Muon Filter level. Status quo (black bars) is the time required by the previous season’s filter (from IC86–2). These measurements were done on a cluster of working nodes with 2.67 GHz Intel Xeon CPUs.

of single neutrinos,⁷ whereas downgoing events are dominated by *muon bundles*—multiple low-energy muons that produce many hits in the detector and look like one very energetic muon, therefore passing the energy cuts. Processing time usually depends on the number of hit DOMs because algorithms often involve looping over the hit DOMs.

6.3.4 Changes to the Filter

The filter described so far is the post IC86–2 version that was created by the thesis author. For completeness, the cuts used in the previous seasons are listed here as well. They were developed by Robert Franke, Anna Franckowiak, and others. The first two OFU seasons, IC40 and IC59 (see Table 6.1 for a seasons overview), are documented in Anna Franckowiak’s PhD thesis [149].

In IC79, only upgoing events were processed by the Online L2 filter and the cuts were (variables are based on the one-iteration SPE fit of the Muon Filter):

$$\begin{aligned} &\text{The event is upgoing } (\theta_{\text{SPE}} \geq 80^\circ) \quad \text{AND} \quad \text{mrlogl}_{\text{SPE}}(2) \leq 8.2 \quad \text{AND} \quad (\\ &\quad \text{mrlogl}_{\text{SPE}}(2) \leq 7.38 \quad \text{OR} \quad N_{\text{dir}}^{\text{SPE}} \geq 5 \quad \text{OR} \quad N_{\text{Ch}} \geq 80 \\ &), \end{aligned}$$

where N_{Ch} is the number of hit optical modules.

In IC86–1, the cuts were (variables still based on the one-iteration SPE fit of the Muon Filter):

$$\begin{aligned} &\text{The event is upgoing } (\theta_{\text{SPE}} \geq 80^\circ) \quad \text{AND} \quad (\\ &\quad \left(\frac{L_{\text{dir}}^{\text{SPE}}}{180} \right)^2 + \left(\frac{N_{\text{dir}}^{\text{SPE}}}{10} \right)^2 \geq 1 \quad \text{OR} \quad \text{mrlogl}_{\text{SPE}}(2) \leq 7.3 \quad \text{OR} \quad N_{\text{Ch}} > 70 \\ &) \quad \text{OR} \quad \text{the event is downgoing horizontal } (75^\circ \leq \theta_{\text{SPE}} < 80^\circ) \quad \text{AND} \quad (\end{aligned}$$

⁷ Or mis-reconstructed muons *looking like* a single upgoing neutrino.

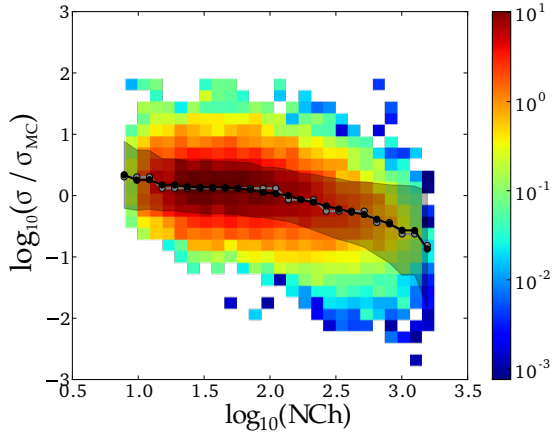


Figure 6.10: Distribution of directional uncertainty pull, i.e. estimated error over true error, for the Cramér-Rao fit, as function of the number of hit modules N_{Ch} . The average and median are indicated as black and gray lines, the RMS as shaded region around the average. The plot was made with MC simulation of muon neutrino signal (E^{-2} spectrum), for Online L2 events reconstructed within 10° from the true direction.

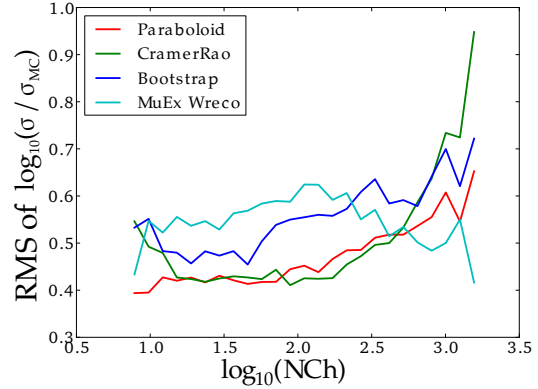


Figure 6.11: The root-mean-square (RMS) of the pull for the four compared angular uncertainty estimators, as function of number of hit modules N_{Ch} . This corresponds to the width of the shaded area in Figure 6.10. The plot was made with MC simulation of muon neutrino signal (E^{-2} spectrum), for Online L2 events reconstructed within 10° from the true direction.

$$\begin{aligned} & \text{rlogl} < 7.3 \quad \text{OR} \quad \log_{10}(q_{\text{tot}}) > 1.95 \\ &) \quad \text{OR} \quad \text{the event is downgoing vertical } (\theta_{\text{SPE}} < 75^\circ) \quad \text{AND} \quad (\\ & \log_{10}(q_{\text{tot}}) > 3.3 - 1.3 \left(\frac{\theta_{\text{SPE}}}{1.309} \right)^6 \\ &), \end{aligned}$$

where $\text{rlogl} = \text{mrlogl}(5)$ is the reduced log-likelihood of the Muon Filter SPE fit.

Since IC86–2, the Online L2 filter cuts have not changed, except for the addition of a logical OR on high total charge events for regions C and D, added for the IC86–3 season. In region AB, the OR condition was already applied before. This is to ensure that high-energy events are not lost, even if the track reconstruction is of bad quality in a detector saturated with light. In regions C and D, the q_{tot} threshold was chosen in order to limit the passing rate increase to less than 0.2 Hz. It was found at $\log_{10}(q_{\text{tot}}) = 2.5$ in region C and at $\log_{10}(q_{\text{tot}}) = 3$ in region D. As a consequence, the signal efficiency has increased by 0.6% in region C and by 2.4% in region D for an E^{-2} weighted muon neutrino signal (2.0% and 4.5% for E^{-3} , 0.5% and 0.8% for E^{-1}).

Additional reconstructions added to the Online L2 filter are described in the following sections.

Improved Angular Error Estimator

The estimation of the uncertainty of a track reconstruction is very important for neutrino point source analyses, see Section 4.2.4, p. 74. Therefore, alternatives for the quick, but inferior, approximative Cramér-Rao fit (see p. 75) were examined for the Online L2 filter. The algorithms under study, implemented in internal IceCube collaboration code, were the previously used Cramér-Rao fit, the Paraboloid fit (see p. 4.2.4), the gulliver-bootstrap fit (called Bootstrap later on), and MuEx wreco. Bootstrap tries

to estimate the directional uncertainty by choosing random subsamples of the event’s pulses⁸ and running a track reconstruction on each subsample. The resulting variance from several such subsample fits is used to compute an estimate of the angular error. MuEx wreco is part of the MuEx module that can also reconstruct energy. It uses a similar bootstrapping method, however does not use the standard IceCube likelihood fit implementation, but an alternative fit that takes into account the ice properties.

The angular error codes were compared in terms of quality and processing time. For comparison of the uncertainty estimation quality, the quantity *pull* was used, defined as estimated error σ over real error σ_{MC} , i.e. the deviation of the reconstruction from the true Monte Carlo direction. A pull larger than one means the error is overestimated, a pull smaller than one means it is underestimated. Figure 6.10 shows an example pull distribution as function of the energy proxy N_{Ch} . While the error estimator can be corrected such that its mean (or median) lies at a pull of one, it is not possible to reduce the spread of the pull distribution. Therefore, an accurate error estimator is characterized by a small pull distribution spread. In Figure 6.11, the root-mean-square (RMS) is used to quantify the spread of the pull distribution. It was found that Cramér-Rao performs well at low N_{Ch} , comparable to Paraboloid, but at high N_{Ch} (high energies), its RMS value is steeply rising. MuEx wreco performs best at high energies, followed by Paraboloid.

The processing time required by Paraboloid and MuEx wreco was also studied and the results are shown in Figure 6.9. Both fits require similar processing time and introduce a long tail to the processing time distribution, if applied to all events. The reason is a strong rise of the processing time with the number of hit modules N_{Ch} . Because high N_{Ch} events are common in downgoing events, caused by bundles of multiple atmospheric muons from the same air shower, there is a significant fraction of very high N_{Ch} events in the downgoing regime, compared to relatively low N_{Ch} events in the upgoing regime. This leads to the bump vanishing and processing becoming feasible, if the fit is only applied to upgoing events.

Therefore, starting with IC86–3, the Paraboloid fit was added for all upgoing events passing the Online L2 filter, meaning $\theta_{MPE} \geq 80^\circ$. In spite of the slightly better MuEx wreco performance, it was decided to use Paraboloid, because it is well established, known to be stable, and widely used for almost all point source analyses in IceCube. There was some interest within the collaboration to add Paraboloid to the Online L2, whereas there was no experience yet with the performance of MuEx wreco.

Improved Track Reconstruction

For offline neutrino point source analyses, an improved track reconstruction was developed that is called *SplineMPE*, see Section 4.2.4, p. 73. It makes use of spline fit tables describing the optical properties of the glacier ice, in which the IceCube detector is embedded. Promising a median angular resolution improved by about 30%, from $\sim 0.7^\circ$ to $\sim 0.5^\circ$, it was investigated if the reconstruction can also be run online. There are several configuration options for the SplineMPE fit affecting both the accuracy and the processing time. In particular, there are two default settings called “fast” and “slow”. Because of the processing constraints at the South Pole, and because other studies showed the accuracy improvement of the slow setting to be only $\sim 0.02^\circ$, only the fast configuration was studied, comparing the performance of different settings.

It was found that the angular resolution is indeed improved from $\sim 0.7^\circ$ to $\sim 0.5^\circ$ at high energies around 1 PeV, see Figure 6.12. While it does increase the average processing time, it does not introduce tails to the processing time distribution, but only changes its slope, even when run on all Online L2 events (see Figure 6.13). Therefore, after the SplineMPE code passed a code review and was adapted

⁸ This process is called bootstrapping in statistical analysis.

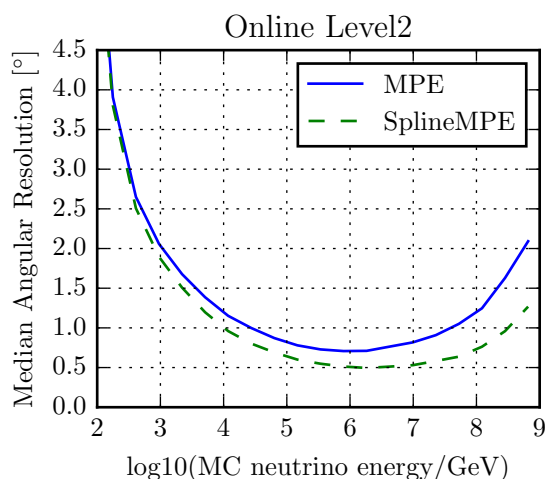


Figure 6.12: Comparison of the median angular resolution for the MPE fit and the improved SplineMPE fit on Online Level 2. 50% of events are reconstructed with true error σ_{MC} below the plotted value. At highest energies, the angular resolution worsens because a large fraction of events shines inside the detector from far outside and is thus hardly reconstructable.

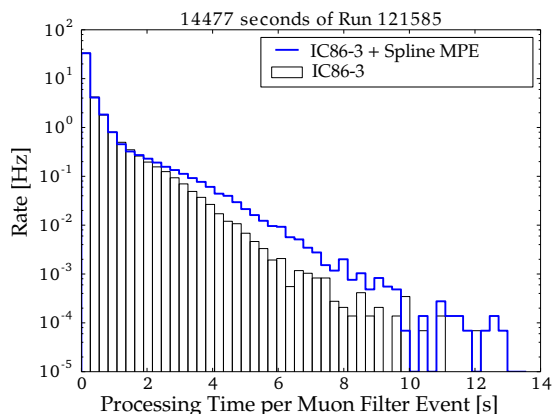


Figure 6.13: Distribution of processing time per event, without and with the SplineMPE fit applied to all events passing the Online L2 filter cuts.

to the IceCube coding standards, it could be run at South Pole and was added to the Online L2 filter for the IC86–4 season.

6.4 The OFU Filter of IceCube

The purpose of the OFU filter is to reduce the Online L2 event stream to a sample consisting mainly of neutrinos. The OFU filter sample can subsequently be searched for short bursts of neutrinos, i.e. two or more neutrinos within a short interval and with a small angular separation. For this purpose, the background event rate has to be reduced from about 2 Hz to about 3 mHz by the OFU filter. The OFU filter considers only the northern sky, i.e. upgoing muon tracks ($\theta > 90^\circ$) passing the Online L2 filter, in order to use the efficient muon shield provided by the Earth and to be sensitive also to soft spectra, e.g. from choked jet SNe.

Until the IC86-2 season (see Table 6.1 for a seasons overview), the OFU filter event selection was based on simple rectangular cuts instead of a more sophisticated machine learning algorithm. The cuts were developed by Anna Franckowiak and Andreas Homeier.

During the IC86–2 season, making use of the increased number of variables provided by the new Online L2 filter, a new OFU filter was developed by Andreas Homeier, which consists of a *boosted decision tree (BDT)* [232, pp. 103–110]. The OFU event selection was switched to the new BDT filter on 2013-02-01, during the IC86–2 DAQ season, and has not changed since.

A BDT is a machine learning method involving a decision tree: a tree of consecutive yes/no decisions, where each decision is called a node. In analogy to a tree, the first node is called the root, the final nodes are called leaves. At each node, the variable providing the best signal/background separation is used for the yes/no decision. At the leaf nodes, the outcome of the yes/no decision decides about each event being signal or background, depending on the class of the majority of training events ending up there.

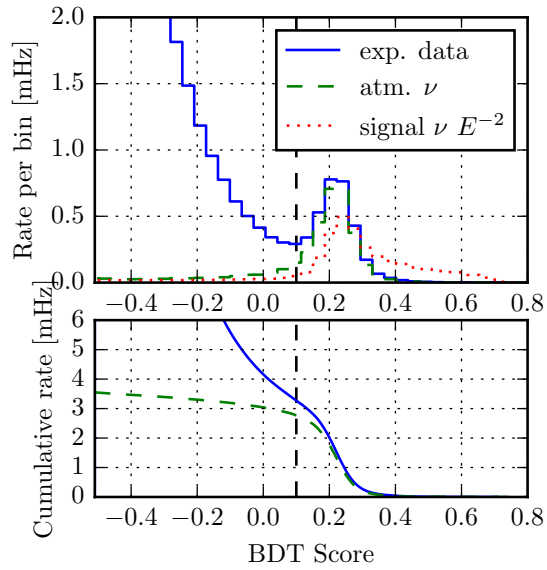


Figure 6.14: Distribution of the OFU filter BDT score value for experimental data, simulated atmospheric neutrinos, and simulated signal neutrinos with an energy spectrum proportional to E^{-2} . The cut value is shown as dashed line (events below are discarded). The passing rate as function of BDT cut value is plotted in the lower panel.

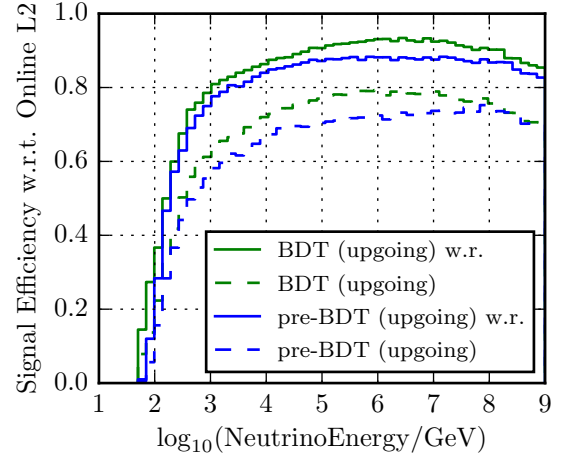


Figure 6.15: Signal efficiency, i.e. fraction of contained signal neutrino events, of the OFU filter as function of neutrino energy with respect to the upgoing Online L2 filter. The efficiency of the BDT-based and the previous filter is plotted, for all events and well-reconstructed (w.r.) events, meaning reconstructed within 3° from the true direction.

The effect of such a decision tree is to divide the phase space of n input variables into n -dimensional cubes (hypercubes) that are classified as either signal or background. Compared to conventional rectangular cuts that select only one region per variable and thus only a single hypercube, the decision tree selects many small hypercubes and the phase space division can be very granular. This leads to a better separation of signal and background.

The decision tree is grown with the use of a training sample, where the nature of each event (signal or background) is known. Because decision trees are not stable with respect to fluctuations in the training sample, they often lead to over-specialization for the specific training sample, called *overtraining*. To avoid this, the decision tree is *boosted*, which means that several other trees are derived by using reweighted versions of the same training sample. For example, events that were misclassified in the original tree are given a higher weight. A forest of decision trees is formed and the final classification is a combination of the individual tree classifications. This leads to a much more stable classifier.

One can optimize the BDT for a hard or a soft signal spectrum by adjusting the signal weighting. Because the OFU filter shall be sensitive to both hard spectra like E^{-2} , e.g. from GRBs, and soft spectra like E^{-3} , e.g. from choked jet SNe, the signal in the training sample is weighted with neither of the two, but with a normalized combination of an E^{-1} , E^{-2} , and E^{-3} weight:

$$w_i = \frac{\frac{w_i^{E^{-1}}}{\sum_j w_j^{E^{-1}}} + \frac{w_i^{E^{-2}}}{\sum_j w_j^{E^{-2}}} + \frac{w_i^{E^{-3}}}{\sum_j w_j^{E^{-3}}}}{\sum_j w_j} \quad (6.1)$$

This weighting yields a very balanced BDT with high signal efficiency for soft and hard spectra.

The output of the BDT classifier is a single number for each event, the BDT score. It lies between

-1 and +1, where background events tend to have BDT scores close to -1 and signal events close to +1. The BDT score can be used as a single simple value to cut on. To achieve a data rate of about 3 mHz, the BDT score cut was set at ≥ 0.1 . Figure 6.14 shows a distribution of the BDT score distribution for background and signal. Below the cut value of 0.1, experimental data is dominated by background from atmospheric muons that are mis-reconstructed as upgoing. Above 0.1, data consist of mostly atmospheric neutrinos, with only a small fraction of muons. For Figure 6.14, neutrino MC simulation has been weighted to an atmospheric neutrino spectrum taken from Honda et al. (2007) [233], with a prompt charm component from Enberg et al. (2008) [234]. The efficiency of the new OFU BDT filter compared to that of the previous rectangular cuts is plotted in Figure 6.15.

6.5 Properties of the OFU Neutrino Sample

For the sake of simplicity, only the BDT OFU filter event sample is discussed here.

6.5.1 Rate and Purity

Using neutrino Monte Carlo simulation weighted to an atmospheric neutrino spectrum, the passing rate of the OFU BDT sample for atmospheric neutrinos is estimated to be

$$R_{\nu,\text{atm}} = (2.77 \pm 0.24(\text{syst}) \pm 0.02(\text{stat})) \text{ mHz}. \quad (6.2)$$

For this estimate, the neutrino simulation is weighted to the conventional flux from Honda et al. (2007) [233], with a prompt flux from Enberg et al. (2008) [234]. The systematic uncertainty is estimated from the difference observed when weighting to the conventional flux from Barr et al. (2004) [235] and the prompt flux from the Bugaev et al. (1998) model RQPM, where both alternative models change the rate in the same direction.

The experimental data rate of the OFU BDT sample is

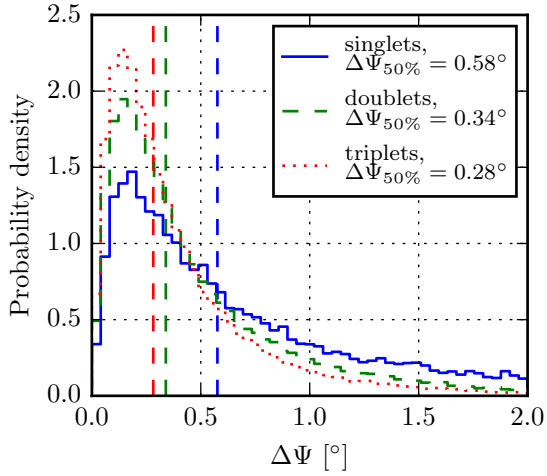
$$R_{\nu,\text{data}} = (3.33 \pm 0.02) \text{ mHz} \quad (\text{IC86-2 BDT}) \quad (6.3)$$

$$R_{\nu,\text{data}} = (3.27 \pm 0.01) \text{ mHz} \quad (\text{IC86-3}). \quad (6.4)$$

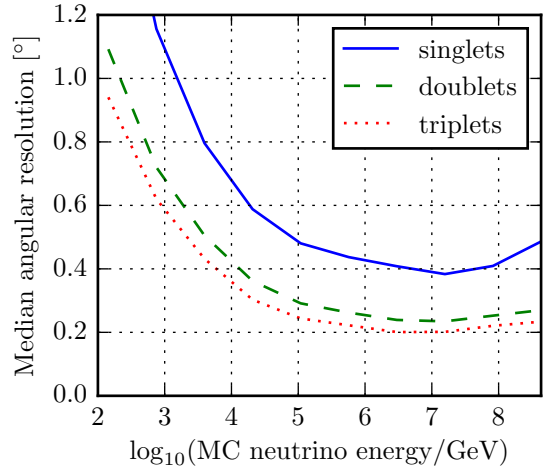
The average rate weighted with the livetime is (3.28 ± 0.01) mHz. Hence, the purity of the sample, i.e. the fraction of contained neutrino events, lies between about 80% and 90%. The contamination with background events from atmospheric muons is roughly between 0.3 mHz and 0.8 mHz. Estimating this background directly from atmospheric muon simulation is challenging, because it is a tiny fraction of the trigger rate of 2 kHz, which means that a very large number of events has to be generated to obtain even poor statistics of OFU filter events.

6.5.2 Angular Resolution

Thanks to the selection of high quality events, mostly neutrinos, the directional reconstruction at OFU filter level is on average better than at Online L2. Figures 6.16a and 6.16b show the point spread function (PSF) and the median angular resolution for single OFU filter events and for small bursts of neutrinos, called multiplets (introduced in Section 6.6). The PSF (Figure 6.16a) is the probability density function of the angle between the true and the reconstructed direction. The median of the one-dimensional PSF is the median angular resolution (plotted in Figure 6.16b). A two-dimensional version of the PSF in terms of angular coordinates, right ascension and declination, is plotted in Figure 6.17. For neutrino multiplets,



(a) The point spread function (PSF), i.e. the probability distribution of the angle $\Delta\Psi$ between the reconstructed and the true direction, for an E^{-2} neutrino spectrum. The median (also plotted in Figure 6.16b) is indicated with a dashed line of corresponding color.



(b) The median angular resolution, i.e. 50% of the multiplets have a reconstruction closer to the truth. Note that for this plot, all events were sampled within the respective energy bin for demonstration purposes. Receiving a multiplet with multiple high energy events is unrealistic with naturally occurring soft energy spectra.

Figure 6.16: Quality of the directional reconstruction of BDT OFU filter singlets (single events) and of the average direction of doublets (two events) and triplets (three events). The multiplets are defined in Section 6.6. These plots are for the MPE fit.

e.g. doublets (two events) or triplets (three events), the individual directions are averaged assuming that all neutrinos originate from the same point source. This dramatically increases the angular resolution. For example, at the energy of highest reconstruction quality, receiving three neutrinos from the same source would reduce the median error on the source position from 0.4° to 0.2° .

6.5.3 Angular Error Estimator

For the correct interpretation of the observed neutrino events, an accurate error on the reconstructed direction is as important as the reconstruction result itself, see Sections 4.2.4 and 6.3.4. It is available on an event-by-event basis from error estimator algorithms. The algorithm used by the OFU, because of its fast execution time and thus availability at South Pole processing, is the *Cramér-Rao* fit (see p. 75). Because angular error estimators generally deviate from the actual error, they must be *calibrated* using neutrino MC simulation, where the true error is known. To measure the deviation, the *pull* is defined as ratio between reconstructed and true error. The pull often depends on energy, e.g. at low energies the error is overestimated (pull larger than one), while at high energies it is underestimated (pull smaller than one). Therefore, it makes sense to parametrize the error calibration as function of an energy proxy. One way to calibrate is to calculate the median pull in each energy proxy bin and fit a function f_c , e.g. a polynomial, to the medians. By division of the reconstructed error by the evaluated correction function f_c , the error is corrected to a median pull of one, i.e. the error will be over- and underestimated at equal frequency. Figure 6.18 shows example plots of the uncalibrated and calibrated Cramér-Rao error at OFU level.

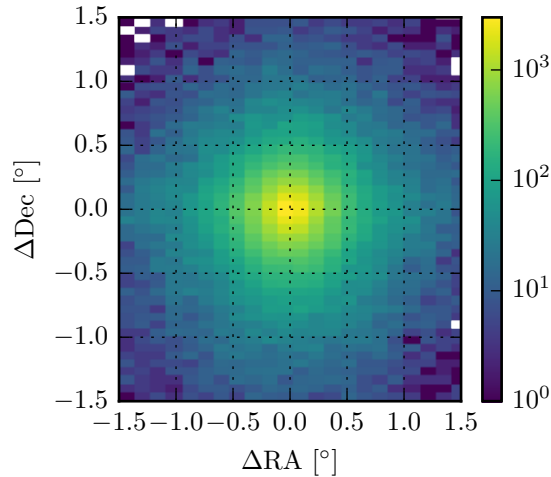


Figure 6.17: Two-dimensional histogram of the point spread function (PSF) of neutrino doublets in the OFU sample, created by a simulated neutrino point source with an E^{-2} spectrum. Each bin shows the relative frequency of the displacement of the average doublet direction relative to the source.

6.6 OFU Multiplets and Alerts

6.6.1 Definition of Multiplets

In order to suppress the background of atmospheric neutrinos, the OFU program selects neutrino multiplets. A multiplet is defined as two or more neutrinos arriving with an angular separation $\Delta\Psi$ of less than 3.5° and with a temporal separation ΔT of less than 100 s. Each new arriving neutrino event is compared to all previous events within the 100 s window (all events from the last 100 s are stored in a buffer). All events in the 100 s window, which are less than 3.5° apart from the new event, form a multiplet together with the new event itself. In the context of OFU, single events are called *singlets*, multiplets consisting of two events *doublets*, multiplets with three events *triplets*, and so on.

6.6.2 Definition of Alerts

Based on criteria that changed over time, certain neutrino multiplets were forwarded to the various follow-up instruments. In the beginning of the OFU program, in seasons IC40 and IC59 (see Table 6.1 for a seasons overview), each measured multiplet was forwarded to the ROTSE telescope network.

In IC79, each multiplet was forwarded to ROTSE, but only subsets of doublets were forwarded to PTF (since 2010-07-21) and Swift (since 2011-02-08). The selection of PTF and Swift doublet alerts happened via cuts similar to the OFU filter cuts in IC79. The cuts had to be fulfilled by both events in the doublet in order to be a PTF/Swift alert.

The OFU Test Statistic λ

With the start of the OFU IC86-1 season, on 2011-09-16, a new and more flexible alert classification criterion was introduced. It is based on the analytic approximative maximization of a likelihood ratio, for the special case of a neutrino doublet with rich signal content, and is derived in Appendix D. The result of this calculation is called the *OFU test statistic* λ , providing a single parameter for the selection

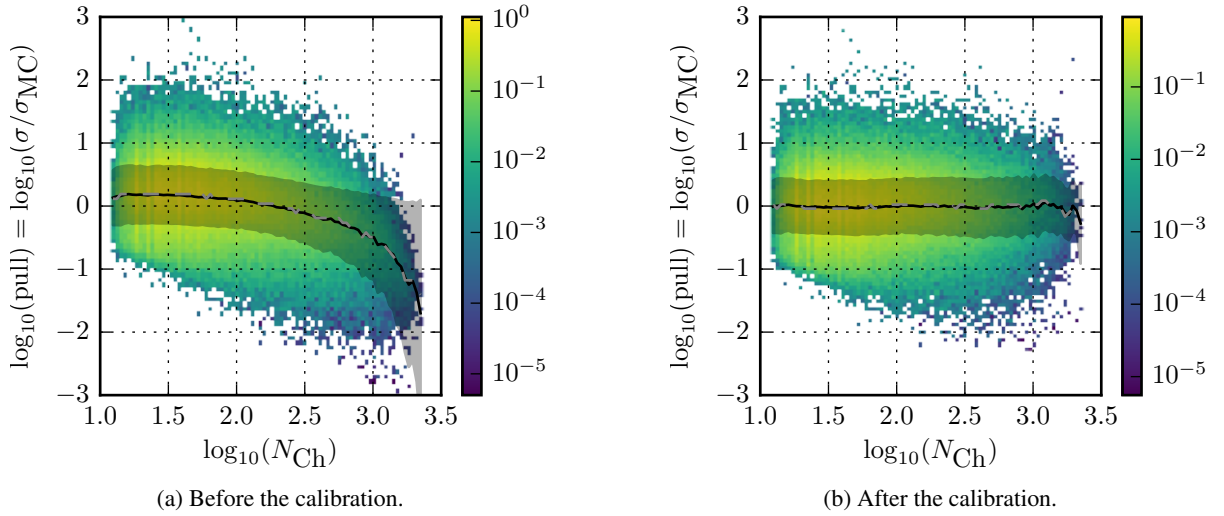


Figure 6.18: Histogram of the logarithm of the Cramér-Rao pull versus the logarithm of the number of hit modules. The solid black line indicates the average, the dashed gray line the median of the distribution in the pull dimension.

of the most significant alerts,

$$\begin{aligned}
 \lambda &= \frac{\Delta\Psi^2}{\sigma_q^2} + 2 \ln(2\pi\sigma_q^2) && \text{(space)} \\
 &- 2 \ln\left(1 - \exp\left(-\frac{\theta_A^2}{2\sigma_w^2}\right)\right) && \text{(telescope)} \\
 &+ 2 \ln\left(\frac{\Delta T}{100 \text{ s}}\right). && \text{(time)}
 \end{aligned} \tag{6.5}$$

Here, the time between the neutrinos in the doublet is denoted as ΔT , their angular separation as $\Delta\Psi$. The quantities σ_q and σ_w are defined by

$$\sigma_q^2 = \sigma_1^2 + \sigma_2^2 \quad \text{and} \quad \sigma_w^2 = \left(1/\sigma_1^2 + 1/\sigma_2^2\right)^{-1} \tag{6.6}$$

and depend on the event-by-event directional uncertainties σ_1 and σ_2 of the two neutrino events, typically $\sim 1^\circ$. For σ_1 and σ_2 , the calibrated *Cramér-Rao* angular uncertainty (see Sections 4.2.4 and 6.5.3) is inserted. The angle θ_A corresponds to the circularized angular radius of the field of view (FoV) of the follow-up telescope. It is set to $\theta_A = 0.9^\circ$ for the ROTSE test statistic λ_{ROTSE} , motivated by the $1.85^\circ \times 1.85^\circ$ FoV of ROTSE. It was decided to use λ_{ROTSE} also for PTF, since its FoV ($\sim 2.2^\circ \times 3.4^\circ$) does not deviate strongly from ROTSE's. For Swift, which has a significantly smaller FoV of about 1° in diameter, a different value of $\theta_A = 0.5^\circ$ is in use for the test statistic λ_{Swift} . Figure 6.19 holds a plot of the distributions of λ_{ROTSE} and λ_{Swift} for background doublets.

The properties of σ_w are such that it is less than or equal to the smallest single event error: $\sigma_w \leq \min(\sigma_i)$, while σ_q is equal to or greater than the largest error: $\sigma_q \geq \max(\sigma_i)$. The error σ_w is also the error on the alert's average direction, see Equation 6.11.

The test statistic λ consists of three terms: the space term, the telescope term, and the time term (see Equation 6.5). The space term is small for alerts, which have small angular separation $\Delta\Psi$ relative to

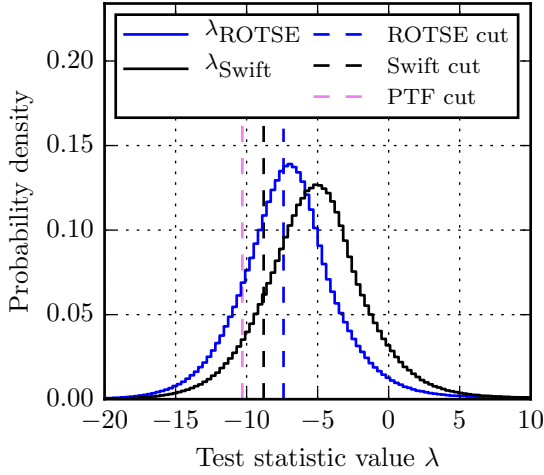


Figure 6.19: Comparison of the background probability density function (PDF) for the OFU test statistic λ_{ROTSE} (defined for the ROTSE/PTF FoV) and for the OFU test statistic λ_{Swift} (defined for the Swift FoV). This plot is for background doublets. The PTF cut is on λ_{ROTSE} , the others on the corresponding λ . The simulated season is IC86-1.

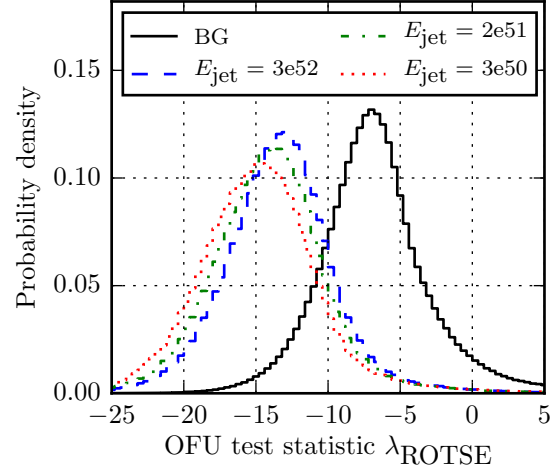


Figure 6.20: Probability density function (PDF) for the OFU test statistic λ_{ROTSE} , defined for the ROTSE/PTF FoV, for doublets generated by background (solid, black) and by signal flux from the choked jet SN model (Section 3.2.8), with different jet energies E_{jet} . The simulated season is IC86-1.

the reconstruction error σ_q , given σ_q is not too large (ensured by the \ln term). The telescope term is small for doublets whose average direction is likely to lie inside the FoV of the follow-up instrument, i.e. whose average direction error σ_w is small compared to the follow-up FoV radius θ_A . Finally, the time term is small for neutrinos arriving shortly after each other, which is unlikely in case of a uniform background. Overall, λ is smaller for more signal-like alerts that are well-reconstructed, close in space, close in time, and with a source likely to lie inside the follow-up FoV.

Thus, λ is a useful parameter to separate signal and background doublets. Figure 6.19 shows the background distributions of λ_{ROTSE} and λ_{Swift} , Figure 6.20 shows distributions of λ_{ROTSE} for both background (mostly atmospheric neutrinos) and signal neutrinos. The background distribution was obtained by scrambling experimental data (see Section 6.8.1), then scanning the scrambled data for doublets. The signal distributions were generated by injecting MC simulation events according to the signal spectrum and then scanning for doublets. The signal spectrum is taken from the choked jet SN model (Section 3.2.8), with a jet Lorentz factor $\Gamma = 5$ and different jet energies E_{jet} . The smaller E_{jet} , the harder the neutrino spectrum (c.f. Equations 3.11 and 3.13), and thus the doublets become more signal-like, i.e. λ tends towards smaller values.

For each follow-up instrument, a specific cut on λ is applied in order to send the most significant alerts at the tolerated rate, which is determined via integration of the background distribution. Those cut values changed over time as well. In the DAQ seasons IC86-1 and IC86-2 (pre-BDT), the λ cut values were:

$$\begin{aligned}
 \text{ROTSE: } & \lambda_{\text{ROTSE}} < -7.4 \\
 \text{PTF: } & \lambda_{\text{ROTSE}} < -10.3 \\
 \text{Swift: } & \lambda_{\text{Swift}} < -8.8.
 \end{aligned} \tag{6.7}$$

After the introduction of the BDT filter, the λ cut values had to be adjusted and for seasons IC86–2 BDT and IC86–3, the values

$$\begin{aligned} \text{ROTSE: } \lambda_{\text{ROTSE}} &< -8.58 \\ \text{PTF: } \lambda_{\text{ROTSE}} &< -11.07 \\ \text{Swift: } \lambda_{\text{Swift}} &< -9.41 \end{aligned} \quad (6.8)$$

were in use. The OFU test statistic λ is only defined for doublets. Multiplets of multiplicity higher than two are passed directly to all follow-up instruments. Since the expected background rate is low (~ 0.03 per year, see Table 6.4), each observation of a triplet or higher order multiplet is of high significance.

Veto Criteria

For the higher quality follow-up instruments PTF and Swift, there are veto criteria that aim to prevent the issue of alerts that can not be followed up or will result in low quality data. For PTF alerts, the Galactic plane is excluded from the follow-up, because the large number of stars in the Galactic plane, some of them variable in brightness, leads to very low chances of identifying a SN. The number of potential SN candidates would be too high, making it impossible to find real SNe with a reasonable amount of effort. Thus, a PTF alert is not sent if the error weighted average alert direction is closer than 10° to the Galactic plane. For Swift as a space-based X-ray telescope, the Galactic plane is not an issue, because the density of X-ray sources is much lower. However, observations cannot be carried out if the alert is too close to the Sun or the Moon.⁹ Therefore, in seasons IC79, IC86–1, and IC86–2 (pre-BDT), alerts were not sent if the average direction was closer than 40° to the Sun or closer than 15° to the Moon. For seasons IC86–2 BDT and IC86–3, this was increased to 44° (Sun) and 20° (Moon).

The Average Alert Direction

The average direction $\langle \hat{r} \rangle$ of an alert is a weighted arithmetic mean, weighting the individual reconstructed neutrino directions \hat{r}_i with their inverse squared error, given by the event-by-event directional uncertainty σ_i (Cramér-Rao),

$$\langle \hat{r} \rangle = \frac{\sum_i \hat{r}_i w_i}{\sum_i w_i} = \frac{\sum_i \hat{r}_i / \sigma_i^2}{\sum_i 1 / \sigma_i^2}, \quad w_i \equiv \frac{1}{\sigma_i^2}. \quad (6.9)$$

The error on this average alert direction can be derived by applying Gaussian error propagation:

$$\sigma_{\langle \hat{r} \rangle} = \sqrt{\sum_i \left(\frac{\partial \langle \hat{r} \rangle}{\partial \hat{r}_i} \right)^2 \sigma_i^2} = \sqrt{\sum_i \left(\frac{1 / \sigma_i^2}{\sum_j 1 / \sigma_j^2} \right)^2 \sigma_i^2} = \frac{\sqrt{\sum_i 1 / \sigma_i^2}}{\sum_i 1 / \sigma_i^2} = \frac{1}{\sqrt{\sum_i 1 / \sigma_i^2}}. \quad (6.10)$$

In the usual case of only two neutrinos (a doublet), the error $\sigma_{\langle \hat{r} \rangle}$ becomes σ_w , which is also used in the test statistic λ (see Equation 6.6), with σ_w defined via

$$\frac{1}{\sigma_w^2} = \frac{1}{\sigma_1^2} + \frac{1}{\sigma_2^2}. \quad (6.11)$$

⁹ Of course, also PTF cannot observe sources close to the Sun or the Moon, but because the targeted SNe do not fade as rapidly as GRBs targeted by Swift, it might be possible to observe a few weeks or months later.

For the average direction and σ_w , it is assumed that the neutrinos were emitted by a single point source, i.e. that the intrinsic variance of the source direction is zero. Because each event adds information on the common source position, the properties of σ_w are such that it is less than or equal to the smallest single event error: $\sigma_w \leq \min(\sigma_i)$. This can lead to a relatively small average error for individual events with small errors.

6.6.3 Test Alerts

In addition to the multiplets and alerts used for physics analysis, the data stream is continually searched for *test alerts*, which have negligible physical importance, but are an important tool to monitor if the system is working properly. They can be regarded as the *heart beat* of OFU. Test alerts arise from *test singlets*, which pass cuts on the Online L2 sample that are looser than the OFU filter cuts (e.g. a cut on the BDT score > -0.51 instead of > 0.1 is used to select test singlets). The test singlet level at a rate of about 40 mHz (about one event every 25 seconds) is therefore an intermediate step between the 2 Hz of the Online Level 2 and the 3 mHz of the OFU filter level (about one event every 5 – 6 minutes). The last 100 s of test alert singlets are searched for multiplets not within 3.5° from the last arriving event, but within a concentric ring (called *annulus*) between 3.5° and 7.5° . The test singlet cuts and the annulus radii are chosen such that a test alert rate of roughly one every 15 minutes is achieved. This rate is low enough not to overload the alert transmission system, but high enough to notice when the system is not operational and test alerts are missing, see Sections 6.7.1 and 6.8.1.

6.7 Technical Implementation of OFU

Up to the Online L2 filter, the data processing for the follow-up system is done centrally on a cluster of worker nodes at the South Pole. They are located in the IceCube Lab (ICL), which serves as IceCube’s counting house, i.e. computing center for DAQ and data processing and filtering (PnF). After the Online L2, the OFU filter is run on a single dedicated server in the ICL, which is fed a data stream containing the Online L2 events. The OFU filter is applied and the remaining events are searched for multiplets (see Section 6.6), i.e. short neutrino bursts. If a multiplet or test multiplet is found, then an alert message is written to disk containing condensed information about the multiplet, such as the event separation in time and space, the average direction, N_{Ch} , N_{dir} , L_{dir} , etc. The message is written in the *JSON (JavaScript Object Notation)*¹⁰ format, a human-readable, open-standard, language-independent format for data interchange, widely used in web development. The JSON syntax resembles that of Python’s *dictionaries* and *lists*—or rather JavaScript’s *objects* and *arrays*—meaning it is a collection of name-value pairs, where each value can be a string, a number, a boolean, an array holding several items, or another collection of name-value pairs. An example of an OFU multiplet alert message is listed in Figure 6.21.

When a new multiplet alert message appears on disk on the ICL server, a sender daemon written in Python notices it and sends the JSON message to the northern hemisphere via the *ITS (IceCube Teleport System)* [236], see Figure 6.1. The ITS utilizes the Short Burst Data (SBD) service via the commercial Iridium satellite constellation, a system of 66 satellites operated by Iridium Communications Inc.¹¹ Because of the large number of Iridium satellites, there are always satellites above the South Pole and a connection is guaranteed. The drawback is that the bandwidth is quite low and only a certain number

¹⁰ <http://json.org/>, <https://tools.ietf.org/html/rfc7159>

¹¹ <https://www.iridium.com/company/companyprofile>, <https://www.iridium.com/services/details/iridium-sbd>

```

{
  "vars": {
    "deltaPsi": 1.320873042545713,
    "deltaT": 1.785199165344238,
    "ra": 104.4909495584437,
    "dec": 17.23273890258817,
    "dirError": 0.7464879606811304,
    "runID": 119892,
    "eventIDs": [ 33784460, 33789493 ],
    "NCh": [ 17, 21 ],
    "NDir": [ 9, 11 ],
    "LDir": [ 526.8565749102511, 402.5149455436219 ],
    "logl": [ 99.21752433022802, 121.7891100979322 ],
    "MuE": [ 1155.214642550579, 3344.873964220008 ],
    "eventRAs": [ 1.83534238144073, 1.816947033746402 ],
    "eventDecs": [ 0.3101862342716899, 0.2952476765947076 ],
  },
  "likelihood_params": {
    "Swift_llh": -16.548934491770552,
    "ROTSE_llh": -18.089820299488686
  },
  "detectortime": "2012-03-30T01:06:58.414810886Z",
  "debug": {
    "NTestAlerts": 0,
    "NAlerts": 1,
    "sendTm": "2012-03-30T01:09:42.Z+0000"
  },
}

```

Figure 6.21: Example OFU multiplet alert JSON message. Curly braces signify the beginning and end of a name-value pair collection (dictionary, map, or object). Square brackets signify the beginning and end of a list or array of items.

of ASCII characters can be transmitted, comparable to an SMS text message. In contrast, the high bandwidth TDRSS connection used to transfer the full IceCube data can transmit about 100 GB/day of binary data, but because the satellites are not always above the horizon at the South Pole, one has to live with delays of about 12 to 24 hours.

Communication with ITS occurs via XML-RPC [237], a system for remote procedure calls (RPC) using XML (Extensible Markup Language) to write the procedure calls and the HTTP protocol for transportation. RPC enables computer programs to communicate with each other via a network. It is possible to execute code (i.e. call a function or procedure) running on a different computer. In the case of OFU, the sender daemon on the ICL server is running an XML-RPC server, which communicates via ITS with another XML-RPC server run by a receiver daemon (also written in Python) on a dedicated server in Madison, Wisconsin, USA. The function argument of the procedure call is simply the JSON message string. The receiving daemon receives the JSON message, writes it to its own disk, extracts the multiplet information and determines if the physics alert criteria are met (in particular, it calculates the OFU test statistic λ , see Section 6.6.2). If so, then an alert is sent out to the respective follow-up instrument by the receiving daemon. This is done via email in case of PTF and Swift, while the ROTSE telescopes were contacted directly via a socket connection implemented in C. An additional alert file is also written to disk by the receiver daemon to document the alert.

6.7.1 Latency of the OFU System

Because the goal of the OFU and XFU is to provide quick follow-up data to neutrino events, it is important that there is a low latency, i.e. delay time between the neutrinos and the follow-up. This is especially important for observations of GRB afterglows that are fading fast within few hours (see Section 3.3), not so much for detection of SNe that are bright within weeks after explosion (see Section 3.2).

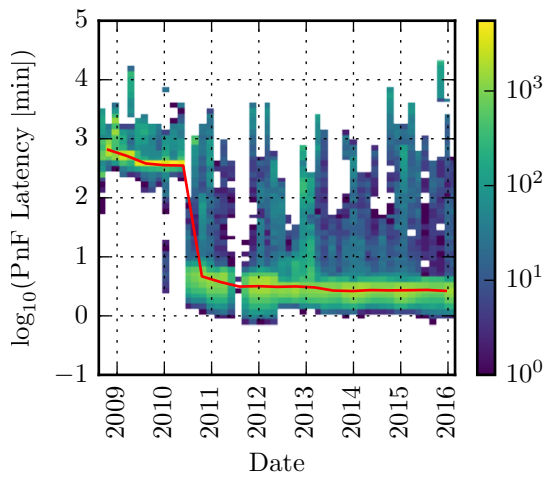
There are different systems involved that add to the total latency, see Section 6.7. At the beginning, the processing and filtering of the IceCube data (PnF) has to take place, leading to a delay, which is defined here as *PnF latency*. Then, the alert is transmitted via satellite over the IceCube teleport system (ITS), causing a second latency, defined here as *ITS latency*. Finally, the Madison-based server has to receive the message, do calculations, and send out alerts to the follow-up instruments. Depending on the observation schedule and the conditions for observation, some time passes until the first follow-up data is taken. The time between the neutrino alert and the first follow-up data is defined as the *full latency* of the OFU/XFU.

Several time stamps allow to measure the latencies. In the JSON alert message, the field `detectorTime` contains the time when the first event of the multiplet started in the IceCube detector, defining the time of the neutrino multiplet. The `sendTm` is the time when data processing is finished and the JSON message is handed over to the ITS by the Python daemon. The time when the receiving daemon in Madison receives the JSON message is not documented, but since it writes a copy of the JSON message to disk, the UNIX file modification time stamp `mtime` can be used to estimate that time. The `mtime` is preserved for alerts since 2009-08-28 and it is called here the `recvTime`. The difference between `detectorTime` and `sendTm` is the PnF latency, while the difference between `sendTm` and `recvTime` is the ITS latency.

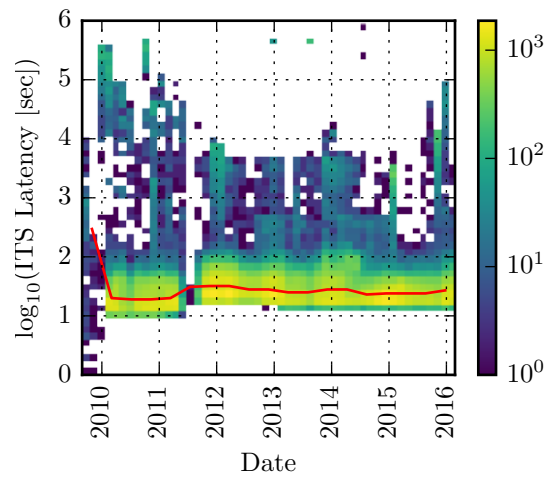
Thanks to their higher rate, the test alerts (see Section 6.6.3) are ideal for studying the PnF and ITS latency. Plots of both latencies as function of time can be found in Figure 6.22. There was a significant drop in the median PnF latency from about 5 to 10 hours to only about 2 to 5 minutes, which happened in mid-2010 with the transition from the IC59 to the IC79 season, because of a change of the PnF processing. Note that without this change, GRB follow-up observations would not be possible. The median ITS latency, on the other hand, was constantly as low as about 20 to 30 seconds, confirming that ITS is a suitable communication medium for real-time messages.

For the full latencies, the data of the follow-up instruments must be investigated as well. For ROTSE, the observation date from the FITS file [238] header of the first observation was compared with the `detectorTime` of the alert. This was done for the first 116 alerts sent in the seasons IC40, IC59, IC79, IC86-1, and IC86-2 (pre-BDT). The resulting latency is plotted in Figure 6.23a, the median value was 27.2 hours. For PTF, the date of the earliest observation of the field(s) after the alert was extracted from the PTF database at the National Energy Research Scientific Computing Center (NERSC) and again compared with the neutrino alert time. This was done for the first 23 alerts sent in seasons IC79, IC86-1, and IC86-2 (pre-BDT). The resulting latency is plotted in Figure 6.23b, the median value was 34.9 hours. For Swift, the latencies were taken from Evans et al. (2015) [229] and are plotted in Figure 6.23c for the first 18 alerts sent during IC79, IC86-1, IC86-2, IC86-2 BDT, and IC86-3. The median latency was 1.9 hours.

Optical telescopes naturally have longer latencies because they depend on external conditions to allow observations, e.g. a dark night sky and good weather conditions. In case of Swift, as a space-based instrument designed for rapid follow-up with minimal slew time, the latency is much lower, which is also required for GRB afterglow observation.

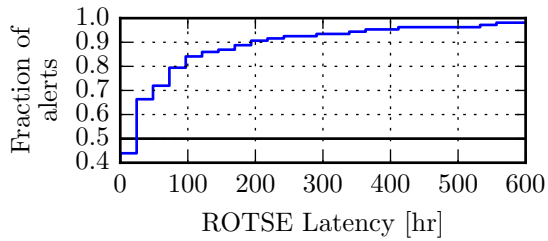


(a) IceCube processing and filtering (PnF) latency.

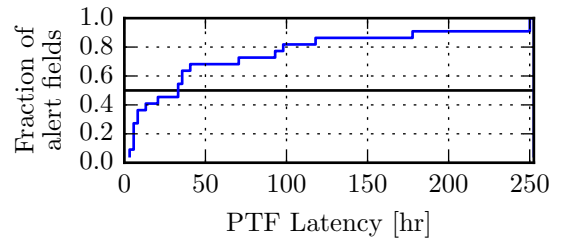


(b) IceCube Teleport System (ITS) latency. The overall median ITS latency is 25 sec.

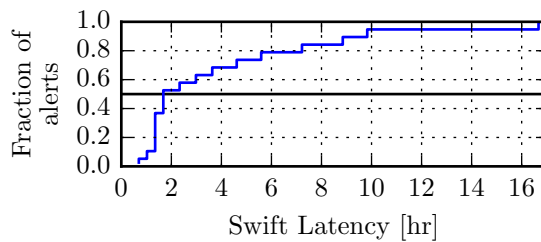
Figure 6.22: Histogram of the latency caused (a) by the IceCube processing and filtering and (b) by the alert message transmission as function of time (calendar year).



(a) ROTSE follow-up latency. The overall median latency is 27.2 h.



(b) PTF follow-up latency. The overall median latency is 34.9 h.



(c) Swift follow-up latency. The overall median latency is 1.9 h.

Figure 6.23: Histogram of the full latency of the follow-up programs, from time of the neutrino alert to time of first observation.

6.8 Analysis of the OFU Multiplets/Alerts

6.8.1 Generating Background Datasets via Scrambling

To estimate the number of alerts and multiplets as well as the OFU test statistic λ distribution arising from pure background, it is necessary to generate random background datasets. Because using Monte Carlo (MC) simulation would lead to large systematic uncertainties on the derived quantities, it is better to use a data-driven approach: By randomizing the experimental data, a process called *scrambling*, random background datasets can be generated. This is a viable solution because the data are dominated by background. Possible contained signals are very weak and the signal events constitute a negligible fraction of all events ($N_{\text{sig}} \ll N$).

For this work, the scrambling has been done by randomly permuting (shuffling) the event times, such that each event is assigned a different time, but the rest of the event attributes remains unchanged. Then, for each event, equatorial coordinates, i.e. right ascension and declination, are calculated from the local detector coordinates, i.e. zenith and azimuth angle, using the new time. By doing so, all detector effects are entirely preserved. For example, the distribution of the azimuth angle, which has more events at angles where detector strings are aligned, and the zenith angle distribution, which depends on both the detector and physical effects like Earth-absorption, remain unchanged. Also the time distribution, which is affected by seasonal variation, is kept, because all event times are still present, only belonging to events that have different coordinates. This means that on the other hand, all potential correlations between the events in time and space, e.g. a signal-like clustering of events at a certain point in the sky, are destroyed.

Before one can start the scrambling, one needs a full experimental dataset corresponding to the uptime of the OFU program. For this purpose, events tagged as test singlets were extracted from the offline experimental data in the IceCube data warehouse for the seasons IC79, IC86–1, IC86–2, IC86–2 BDT and IC86–3. Parts of the data must be excluded from the analysis. In case of problems with the detector, a run is marked as *bad run* by the IceCube collaboration in a list to be used by offline data analyzers. The list is read in and singlets from those runs are excluded from the scrambling. Furthermore, at some times the IceCube DAQ had no problems, but the online system of the OFU was not operational. Those parts of the data must be excluded as well. The test alerts (see Section 6.6.3) are used as a tool to determine the times when the OFU was not operational. The time difference Δt between adjacent test alerts is histogrammed, see Figure 6.24. For normal operation, the test alert rate is stable and the distribution is an exponential distribution.¹² If there were problems leading to missing test alerts, then this is visible as tails that don't follow the exponential. By investigating the Δt distribution, a cut was placed at $\Delta t = 6500$ s (1 hour 48 minutes). If the Δt between two test alerts was larger, then the interval in between is considered to be OFU downtime and data from that interval are excluded from the scrambling.

6.8.2 Measured and Expected Multiplets/Alerts

Since the initiation of the OFU program in 2008, many neutrino multiplets have been measured and alerts sent to follow-up instruments. Table 6.4 lists the measured and expected numbers of doublets, triplets, and quadruplets. Additionally, the numbers of follow-up alerts sent to ROTSE, PTF, and Swift are listed, together with the expected numbers in case of pure background. The numbers are grouped by

¹² Or, more specifically, it is an Erlang distribution with shape $k = 1$, which is the distribution of the waiting time between two occurrences of independent events that occur at a constant average rate. The Erlang distribution with $k = 1$ simplifies to the exponential distribution.

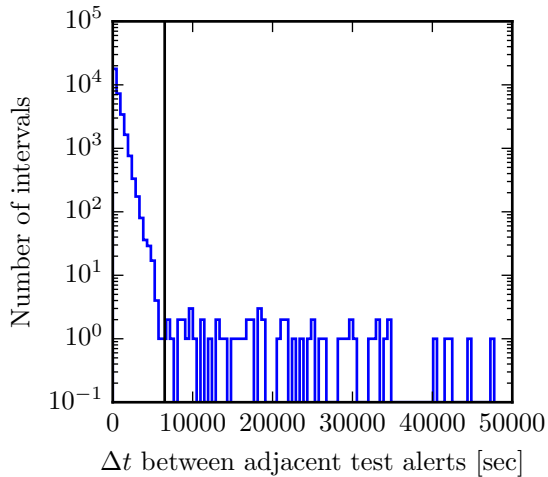


Figure 6.24: Histogram of the time difference Δt between test alerts from the OFU system, for season IC86-1, with the cut value as vertical line.

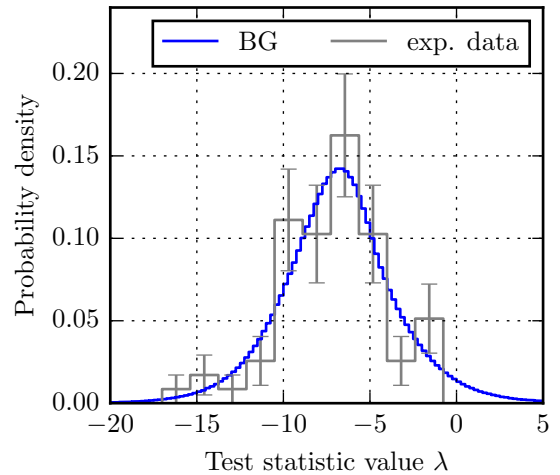


Figure 6.25: Background distribution of the OFU test statistic λ derived from scrambling of experimental data (blue) and for comparison the measured distribution of λ (gray). This is for the IC86-3 DAQ season.

OFU DAQ seasons. See Table 6.1 for the definition and properties of the DAQ seasons. All expectations were derived from 100 000 scramblings of experimental data as explained in Section 6.8.1, for each season separately.

The multiplet and alert numbers in Table 6.4 do not show the presence of a signal on top of the background. All numbers are consistent with the background expectation within 1σ , except for the doublets in IC40 (2.2σ overfluctuation), the PTF alerts in IC79 (1.4σ), the ROTSE alerts in IC86-1 (1.8σ), and the Swift alerts in IC86-2 BDT (2σ). From the absence of more alerts, especially the absence of triplets and higher order multiplets, one can derive generic upper limits to transient sources that emit neutrinos within 100 s. This is being worked on by Andreas Homeier and Nora Linn Strotjohann. However, there seems to be a general tendency towards slight overfluctuation. For all seasons added up, the overfluctuation is on the level of 1.4σ for doublets, 1.2σ for ROTSE alerts, and 1σ for PTF alerts, while for Swift alerts, there is no overfluctuation. This allows for a small signal component where the individual sources are faint (either intrinsically faint or far away), producing mostly single neutrinos, at most few doublets, and no triplets.

6.8.3 Upper Limits on the Choked Jet SN Model

The experimental results of the Optical Follow-Up (OFU) program do not indicate transient neutrino sources that emit 100 s long bursts. The data can be used to set limits on the choked jet SN model introduced in Section 3.2.8. For this purpose, a meta-analysis is performed, combining data from several seasons. The seasons IC79, IC86-1, and IC86-2 are used within the PTF alert submission periods,¹³ matching the analysis period of the optical PTF data, as covered in Chapter 8. A meta-analysis test

¹³ This means: The IC79 season since 2010-07-21, the full IC86-1 season, the IC86-2 season until the end of 2012 (with iPTF beginning in 2013). See Chapter 8.

Multiplets:			
Season	Doublets	Triplets	Quadruplets
IC40 (08/09)	15 (8.6 ± 2.9)	0 (0.003 ± 0.055)	0 ($< 1 \times 10^{-5}$)
IC59 (09/10)	29 (26.0 ± 5.1)	0 (0.008 ± 0.089)	0 ($< 1 \times 10^{-5}$)
IC79 (10/11)	20 (27.1 ± 5.2)	0 (0.008 ± 0.089)	0 ($< 1 \times 10^{-5}$)
IC86–1 (11/12)	49 (44.0 ± 6.7)	0 (0.018 ± 0.134)	0 ($< 1 \times 10^{-5}$)
IC86–2 (12/13)	55 (50.0 ± 7.1)	0 (0.022 ± 0.149)	0 ($< 1 \times 10^{-5}$)
IC86–2 BDT (13)	18 (14.2 ± 3.8)	0 (0.006 ± 0.077)	0 ($< 1 \times 10^{-5}$)
IC86–3 (13/14)	72 (66.8 ± 8.2)	0 (0.025 ± 0.160)	0 ($< 1 \times 10^{-5}$)
Sum	258 (236.7 ± 15.4)	0 (0.09 ± 0.30)	0 ($< 7 \times 10^{-5}$)

Alerts:			
Season	ROTSE	PTF	Swift
IC40 (08/09)	15 (8.6 ± 2.9)	—	—
IC59 (09/10)	29 (26.0 ± 5.1)	—	—
IC79 (10/11)	20 (27.1 ± 5.2)	10 (6.4 ± 2.5)	1 (1.0 ± 1.0)
IC86–1 (11/12)	28 (19.8 ± 4.5)	8 (5.7 ± 2.4)	6 (5.2 ± 2.3)
IC86–2 (12/13)	24 (23.2 ± 4.8)	5 (6.7 ± 2.6)	4 (6.1 ± 2.5)
IC86–2 BDT (13)	4 (3.8 ± 2.0)	2 (1.1 ± 1.0)	3 (1.0 ± 1.0)
IC86–3 (13/14)	21 (18.5 ± 4.3)	5 (5.3 ± 2.3)	4 (4.7 ± 2.2)
Sum	141 (127.0 ± 11.3)	30 (25.2 ± 5.0)	18 (17.9 ± 4.2)

Table 6.4: Number of multiplets and alerts measured and (in parentheses) expected from background alone. The IceCube season is indicated, with the calendar year(s) in brackets. The expectations were derived from 100 000 scramblings per season.

statistic TS is defined as follows, building on the test statistic used in [149],

$$TS \equiv \prod_{\text{season}} \left(\prod_{k=2}^{\infty} P_{\nu}(N_k^{\text{season}}, \mu_k^{\text{season}}) \right)^{N_2^{\text{season}}} \sqrt{\prod_{i=1}^{N_2^{\text{season}}} P_{\lambda,i}^{\text{season}}}. \quad (6.12)$$

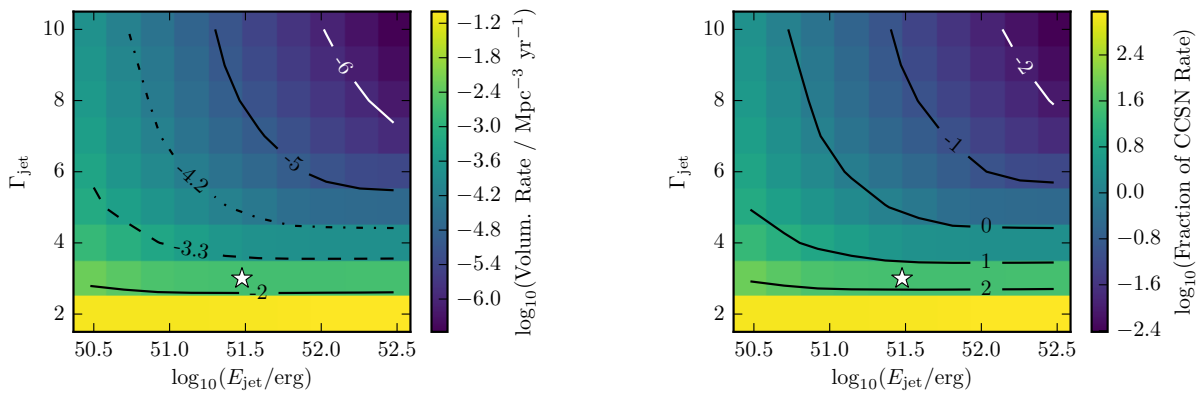
In this equation, N_k^{season} and μ_k^{season} are the measured and expected number of multiplets with multiplicity k in a specific DAQ season. The probability to obtain at least N_k^{season} multiplets is given by $P_{\nu}(N_k^{\text{season}}, \mu_k^{\text{season}}) = 1 - \text{CDF}(N_k^{\text{season}} - 1, \mu_k^{\text{season}})$ —the inverse of the Poissonian cumulative density function CDF. Another component of the test statistic are the p-values $P_{\lambda,i}^{\text{season}}$ of the measured neutrino doublets, which are obtained for each observed doublet test statistic λ_i via integration of the distribution of λ (see Section 6.6.2). Because at this point the number of doublets N_2^{season} shall not play a role, the product of the p-values is “normalized” by taking the N_2^{season} th root, i.e. instead of the product, the geometric mean of the p-values is used. This is to prevent that many mediocre p-values are more significant than few extraordinary ones.

The expectation values μ_k^{season} and the distributions of $P_{\lambda}^{\text{season}}$ are obtained from simulation of the IceCube neutrino detector. Background is simulated via scrambling of experimental data (see Section 6.8.1). Signal, which is added to the background, is simulated using Monte Carlo simulation of the IceCube detector’s response to a signal neutrino flux. Pseudo-experiments of pure background and background with added signal are simulated by drawing random numbers from the Poisson distribution of μ_k^{season} and from the distribution of $P_{\lambda}^{\text{season}}$. Each time, TS is evaluated and the value is filled into a distribution. The experimental observation of the N_k^{season} and $P_{\lambda}^{\text{season}}$ values yields a value of $\log_{10}(TS_{\text{obs}}) = -4.74$, which—integrating the background TS distribution—corresponds to a p-value of 1.9%, or 2.1 σ significance (one-sided Gaussian).

The choked jet SN model is evaluated for combinations of the jet’s bulk Lorentz factor Γ_{jet} and the jet kinetic energy E_{jet} . The parameters Γ_{jet} and E_{jet} determine the strength of the neutrino burst from a single SN. At each parameter setting, pseudo-experiments are carried out for a range of the assumed volumetric source rate ρ , i.e. number of SNe per volume and time in the nearby Universe that host a choked jet producing neutrino bursts of such strength. With the generated TS distributions of background and signal, an upper limit is derived for each $(\Gamma_{\text{jet}}, E_{\text{jet}})$ setting, in terms of ρ . The Neyman description of limits (see [239], reprinted in [240]) is followed. The limits are calculated at 90% confidence level, i.e. the upper limit is the value of ρ , which is found to provide a TS value smaller (meaning more signal-like) than $\log_{10}(TS_{\text{obs}}) = -4.74$ in 90% of simulated experiments.

The obtained upper limits on the choked jet SN model are plotted in Figure 6.26, as function of the two model parameters Γ_{jet} and E_{jet} . In Figure 6.26a, they are given in terms of the volumetric rate ρ of the source SNe, in units of $\text{Mpc}^{-3} \text{yr}^{-1}$. Two measurements of the volumetric CCSN rate are shown: the observed local CCSN rate of $\rho = 5.3 \times 10^{-4} \text{Mpc}^{-3} \text{yr}^{-1}$ ($\log_{10} \rho = -3.3$) within 10 Mpc and 10 years by Kistler et al. [171] (dashed line). And the local CCSN rate of $\rho = 0.705 \times 10^{-4} \text{Mpc}^{-3} \text{yr}^{-1}$ ($\log_{10} \rho = -4.2$) derived for the local Universe from a SN survey by Li et al. [107] (dash-dotted line). In Figure 6.26b, the upper limits are plotted relative to the survey CCSN rate of Li et al. [107]. In both plots, the default parameter setting from the Ando & Beacom model [66], $(\Gamma_{\text{jet}} = 3, E_{\text{jet}} = 3 \times 10^{51} \text{erg})$, are marked with a star.

The derived upper limits are an improvement compared to previous upper limits set in [149, 218] with the IC40 and IC59 season data of the OFU program, and in [241] with a dedicated low-energy event selection of IceCube and DeepCore data from the IC86-2 season (2012–05–15 until 2013–04–30). However, as a caveat, it must be noted that the effect of systematic uncertainties on the IceCube data is not included in the limits presented here, which would lead to slightly weaker limits.



(a) Upper limits in terms of absolute rate, in units of $\text{Mpc}^{-3} \text{yr}^{-1}$. Estimates of the full CCSN rate are plotted with a dashed [171] and dash-dotted line [107].

(b) Upper limits in terms of relative rate, relative to the CCSN rate estimate given in [107].

Figure 6.26: Upper limits on the rate of CCSNe hosting choked jets, derived from the non-observation of 100 s long neutrino bursts with the IceCube Optical Follow-Up program. Γ_{jet} and E_{jet} are parameters of the model in [66], with defaults marked with a star.

Still, the limits are not strong enough to constrain the Ando & Beacom choked jet SN model with its default parameter setting. Only parts of the parameter space with higher values of Γ_{jet} , resulting in stronger bursts, can be constrained. For instance, for the setting $\Gamma_{\text{jet}} = 10$, $E_{\text{jet}} = 3 \times 10^{51}$ erg ($\log_{10}(E_{\text{jet}}/\text{erg}) = 51.5$), only about 8% of all Li et al. CCSNe hosting a jet are consistent with the OFU data (this corresponds to a volumetric rate of $5.9 \times 10^{-6} \text{Mpc}^{-3} \text{yr}^{-1}$), while at $\Gamma_{\text{jet}} = 9$, $E_{\text{jet}} = 1.8 \times 10^{52}$ erg ($\log_{10}(E_{\text{jet}}/\text{erg}) = 52.3$), only about 1% ($7.4 \times 10^{-7} \text{Mpc}^{-3} \text{yr}^{-1}$).

6.9 Conclusion

6.9.1 Summary

IceCube’s optical follow-up (OFU) program is a multi-messenger search for transient neutrino sources. It consists of a neutrino event selection running online, in near real-time, at the South Pole. The stream of events is searched for multiplets within a time window of 100 s. In the case of a significant neutrino multiplet, automated alerts are sent to follow-up instruments, which subsequently observe the sky near the reconstructed event direction using visible light. The program was installed at IceCube in 2008 [149].

Part of the work for this thesis is the design of an improved Online Level 2 filter (see Section 6.3), which provides the data analysis base for the OFU filter. Many reconstructions and variables have been added to the Online Level 2, making it more useful for neutrino point source analyses and comparable to more sophisticated offline event samples, which are widely used in IceCube. However, compared to the offline samples, the Online Level 2 is already calculated *in situ* in near real-time, with only few minutes of latency, while the others need to be calculated days or weeks after DAQ in off-site computing centers. This has made the Online Level 2 attractive for some point source analyses, especially transient searches like GRB analyses. In addition, the efficiency of the Online Level 2 filter for selecting signal neutrinos has been improved, especially for downgoing events.

In this thesis, it is also worked on the analysis of the OFU multiplet data. In particular, a new

scrambling code has been written, with help from Andreas Homeier (see Section 6.8.1 for information on the scrambling). The new scrambling framework allows to consistently simulate the background for the various OFU seasons in a common format, independent from the variations of the OFU data and IceCube data formats. The OFU seasons up to the IC86–3 season (2013/14) are analyzed, using the scrambling for data-driven background estimation. There is no significant indication of a transient neutrino signal in the OFU data, however there is a slight overfluctuation on the 1σ level.

Due to the non-observation of signal, upper limits on the Ando & Beacom choked jet SN model [66] (see Section 3.2.8) are derived in Section 6.8.3. A new multi-season test statistic is defined, with the novelty of including the information provided by the doublet test statistic λ . The p-value from the experimental data inserted into the test statistic amounts to 1.9%, or 2.1σ significance. The upper limits on the choked jet SN model are stronger than previous limits, but not constraining for default parameter values of bulk jet Lorentz factor $\Gamma_{\text{jet}} = 3$ and jet kinetic energy $E_{\text{jet}} = 3 \times 10^{51}$ erg. However, for the parameter space at large Γ_{jet} , a large fraction of CCSNe hosting a jet can be excluded. For example, for $\Gamma_{\text{jet}} = 10$, $E_{\text{jet}} = 3 \times 10^{51}$ erg, only about 8% of all CCSNe hosting a jet are consistent with the OFU data, while at $\Gamma_{\text{jet}} = 9$, $E_{\text{jet}} = 1.8 \times 10^{52}$ erg, only about 1%.

6.9.2 Outlook

The simplest improvement of the work presented here is to analyze more of the OFU data to derive stronger upper limits. Only three OFU seasons have been used in order to match the analysis of the optical data in Chapter 8. However, more data are available and can be combined to provide stronger limits.

The systematic errors on the IceCube neutrino Monte Carlo simulation are not included in the upper limits calculated here. There are several sources of error on the IceCube neutrino Monte Carlo simulation. For example, if the DOM efficiency is over- or underestimated, then this will lead to a wrong detector response to a neutrino signal, resulting in either too many or too few events. Similar effects can arise from a wrong understanding of the South Pole ice or the neutrino cross-section. These uncertainties on the simulation can be estimated and included in the limit calculation to get a more robust result, which would be an obvious improvement over the work presented here.

Improvements on the optical follow-up (OFU) program itself can be envisioned as well. For example, the potential of the neutrino doublets to detect point source signals could be improved by using a more accurate directional reconstruction and/or by using a more accurate estimate of the reconstruction error. They would improve the separation power of the doublet test statistic λ . Both has been worked on as part of this thesis, because the SplineMPE reconstruction and the Paraboloid error estimator have been implemented into the Online Level 2 filter (see Section 6.3). The obvious next step is to make use of these improvements in the OFU program.

Coincidental Detection of Supernova PTF12csy

This chapter is based on a paper written by the author of this thesis and published in the *Astrophysical Journal* [242].

7.1 Neutrino Alert and Discovery of PTF12csy

IceCube’s optical follow-up (OFU) program is introduced in Chapter 6. It is an automated search for multiplets of neutrinos that are close in time and space. The most significant multiplets create alerts that have been sent to optical telescopes, ROTSE and PTF, and to the X-ray satellite Swift. On 2012 March 30 (MJD 56 016), the most significant alert since initiation of the OFU program was recorded and sent to ROTSE and PTF simultaneously. Its significance is $\sim 2.7\sigma$, converting the cumulative distribution function (CDF) value of the OFU test statistic λ (see Equation 6.5) to single-sided Gaussian std. deviations. The significance is also above the threshold for Swift ($\sim 1\sigma$), however the alerts’s distance to the moon was 13.5° at the time, within Swift’s moon proximity constraint,¹ which delayed the Swift observations by three weeks. The two neutrino events causing the alert happened on 2012 March 30 at 01:06:58 UTC (MJD 56 016.046 505) and 1.79 seconds later, with a directional separation of 1.32° . The combined average neutrino direction is at right ascension $6^{\text{h}}57^{\text{m}}45^{\text{s}}$ (104.4°) and declination $17^\circ 11' 24''$ (17.2°) in J2000, with an error radius of $\sigma_w = 0.54^\circ$. The average direction is a weighted arithmetic mean, weighting the individual directions with their inverse squared error, given by the event-by-event directional uncertainty, see Equation 6.9. The error σ_w on the average direction is defined in Equation 6.11. For the averaging, it is assumed that the two neutrino events were emitted by a point source at a single fixed position, see Section 6.6.2 for the caveat. A variance of the individual true neutrino directions does not need to be taken into account, since the assumed intrinsic variance is zero in case of a point source. This leads to a relatively small error on the average direction.

The main event properties are summarized in Table 7.1: the occurrence time on 2012 March 30, the reconstructed muon energy proxy \hat{E}_μ (from the code *MuE*, see Section 4.2.4, page 76), and the estimated directional error σ_i (from *Cramér-Rao*, see Section 4.2.4, page 75). The quantity \hat{E}_μ is a fit parameter and serves as a proxy for the muon energy, however it is not an estimator of the true muon energy. The energy E_ν of the neutrino that produced the muon is not directly observable, since only the muon crossing the detector is accessible. However, using Monte Carlo (MC) simulated neutrino events, one can use the muon energy proxy \hat{E}_μ to compare with MC events having a similar \hat{E}_μ value.

¹ Swift is unable to observe sources closer than 15° to the moon.

Time (UTC)	σ_i [°]	\hat{E}_μ [GeV]	E_ν (Atm.) [TeV]	E_ν (E^{-3}) [TeV]	E_ν (E^{-2}) [TeV]
01:06:58.415	0.96	1155	$0.5^{+2.9}_{-0.4}$	$0.7^{+5.6}_{-0.5}$	$5.4^{+290}_{-5.0}$
01:07:00.200	0.66	3345	$0.9^{+6.7}_{-0.7}$	$1.5^{+14.8}_{-1.3}$	$15.7^{+611}_{-14.5}$

Table 7.1: Properties of the neutrino alert events. \hat{E}_μ is only a proxy correlated with muon energy, but not an estimator of the true muon energy. E_ν is median neutrino energy with 90% C.L. error interval.

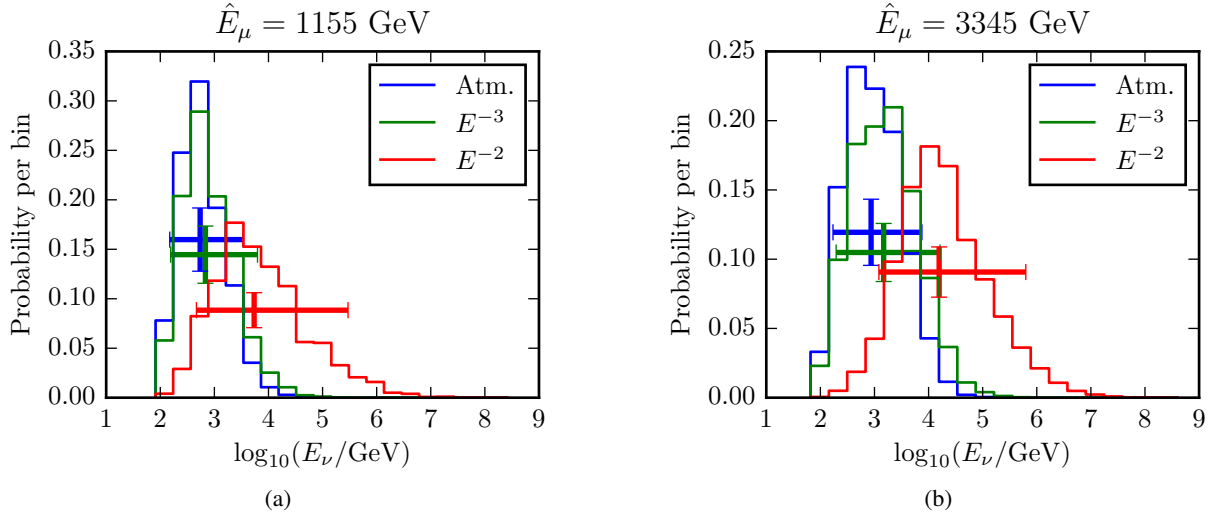


Figure 7.1: Probability distribution function (PDF) for the true neutrino energy E_ν for event 1 (a) and 2 (b), derived from Monte Carlo simulation by selecting events with similar muon energy proxy \hat{E}_μ . The simulated events are weighted according to the indicated energy spectrum. Vertical bars mark the position of the distribution’s median, horizontal bars indicate the 90% confidence interval.

From those MC events, a distribution of the true muon energy E_ν can be derived, which depends on the assumed underlying neutrino energy spectrum. E_ν probability density functions (PDFs) are filled with true energy values of MC events that have the reconstructed muon energy proxy \hat{E}_μ not more than 10% and the reconstructed zenith angle $\cos(\theta)$ not more than 0.1 away from the observed values of the two alert events. The PDFs for the two neutrino events are plotted in Figure 7.1. The median and the central 90% C.L. interval are calculated from the E_ν PDFs. The results are listed in Table 7.1, where the assumed neutrino spectrum is given in parentheses. Note that the energy PDFs are asymmetric, especially for harder spectra, like E^{-2} , leading to very asymmetric confidence intervals as well.

Follow-up observations at the direction of the neutrino alert were performed with multiple instruments (see Section 7.3.1). In the PTF images, a core-collapse supernova (SN), named *PTF12csy*, was discovered at right ascension $6^{\text{h}}58^{\text{m}}32^{\text{s}}744$ ($104.636\,43^\circ$) and declination $17^\circ15'44.37''$ ($17.262\,33^\circ$) in the J2000 system, only 0.2° away from the average neutrino direction, see Figures 7.2 and 7.3. The SN was a promising candidate for the source of the neutrinos, but a search of the Pan-STARRS1 archive (see Section 7.3.1) revealed that it was already at least 169 observer frame days old, i.e. 158 days in host galaxy rest frame, at the time of the neutrino alert. Therefore, it is highly unlikely that the neutrinos were produced by a jet at the SN site, as this is expected to happen immediately after core-collapse in the choked jet scenario (see Section 3.2.8).

However, steady neutrino emission on a time scale of several months is a possibility and explored in Section 7.2.1.

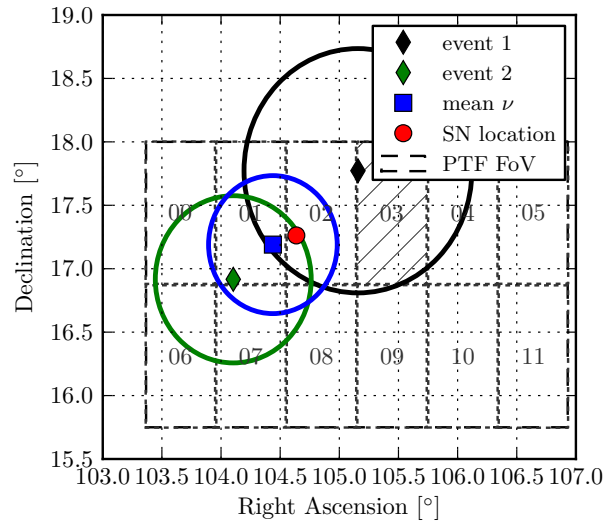


Figure 7.2: Map of the sky with the two neutrino event directions, the average neutrino direction, and the location of SN PTF12csy. Estimated reconstruction errors are indicated with circles, the PTF FoV is shown as dashed box. The positions of the PTF survey camera CCD chips are plotted with dotted lines and the chip number is printed on each chip's field (see [221]). Note that chip 03 is not operational and thus hatched in the plot.

7.1.1 Significance of Alert and SN Detection

Neutrino Alert Probability

The value of the OFU test statistic λ (see Equation 6.5) for the neutrino doublet amounts to -18.1 . The test statistic λ is smaller for more signal-like alerts that are well-reconstructed, close in space, close in time, and with a source likely to lie inside the follow-up FoV. Figure 7.4 shows a distribution of λ from alerts generated by background events, mostly atmospheric neutrinos. The background distribution of λ is constructed from experimental data, containing mostly atmospheric neutrinos, via scrambling of the event times, see Section 6.8.1. That way, all detector effects are entirely preserved, yet all potential correlations between the events in time and space, and thus a potential signal, are destroyed.

The false alarm rate (FAR) for an alert with $\lambda \leq -18.1$ is 0.226 yr^{-1} , calculated via integration of the λ distribution below -18.1 (see Figure 7.4). Considering the OFU live time of 220.1 days in the data acquisition season of the alert, September 2011 to May 2012, yields $N(\lambda < -18.1) = 0.136$ false alerts. Hence, the probability, or p-value, for one or more alerts at least as signal-like to happen by chance in this period is $1 - P_{\text{Poisson}}(0; N(\lambda < -18.1)) \approx 12.7\%$. The OFU system had already been sending alerts to PTF for ~ 460 days at the time of the alert. Scaling up the number of expected alerts with $\lambda \leq -18.1$, one derives a probability of $\sim 24\%$ during 460 days.

SN Detection Probability

The estimated explosion time of SN PTF12csy does not fall within the *a priori* defined time window for a neutrino-SN coincidence of $\mathcal{O}(1 \text{ day})$.² It is thus not considered an *a priori* detection of the follow-up program. Despite this fact, for illustrative purposes, the *a posteriori* probability is calculated that a random core-collapse SN (CCSN) of any type, at any stage after explosion, is found coincidentally

² Anna Franckowiak defined a time window $\Delta T_{\text{SN}} = 5 \text{ d}$ for a coincidence between neutrino signal and SN explosion in her PhD thesis [149, p. 115].

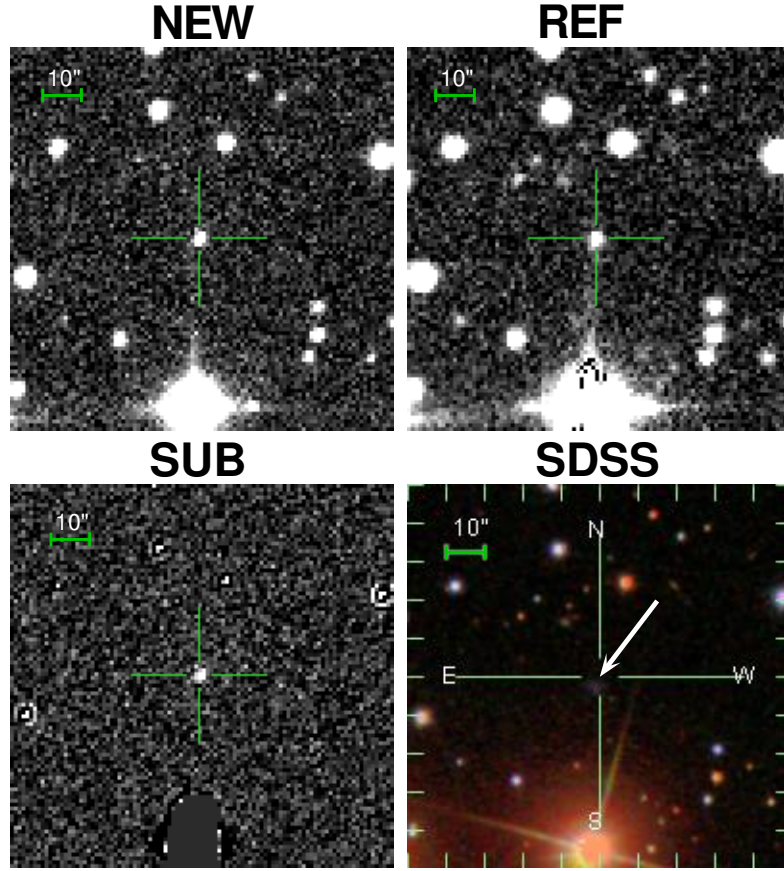


Figure 7.3: New image, reference image and post-subtraction image of the PTF discovery of PTF12csy from 2012 April 09, with the location of PTF12csy in the center. This image shows only a small fraction of the PTF FoV. The image from the Sloan Digital Sky Survey (SDSS-III) DR12 [243–246] is shown for reference, showing a faint host galaxy to the south of the SN.

within the error radius of this neutrino doublet and within the luminosity distance of PTF12csy, i.e. 300 Mpc. The number of such random SN detections is

$$\begin{aligned}
 \bar{N}_{\text{det}} &= \frac{\Omega_s}{4\pi} \int_0^{300 \text{ Mpc}} \frac{dN_{\text{SN}}}{dt dV} \Delta\bar{t}(m_{\text{lim}}, \hat{M}, r) dV = \frac{\Omega_s}{4\pi} \int_0^{300 \text{ Mpc}} \frac{dN_{\text{SN}}}{dt dV} \Delta\bar{t}(m_{\text{lim}}, \hat{M}, r) 4\pi r^2 dr \\
 &= \Omega_s \int_0^{300 \text{ Mpc}} \frac{dN_{\text{SN}}}{dt dV} \Delta\bar{t}(m_{\text{lim}}, \hat{M}, r) r^2 dr
 \end{aligned} \tag{7.1}$$

where Ω_s is the solid angle of the doublet error circle (blue circle in Figure 7.2)—which is ~ 0.93 ($^\circ$)²— $dN_{\text{SN}}/(dt dV)$ is the volumetric SN rate and $\Delta\bar{t}$ is the average control time, defined in Equation 7.5 below. For the volumetric SN rate, the results of Li et al. (2011) [107] are used, which depend on the SN type: SNe Ia have a rate of $0.301 \times 10^{-4} \text{ Mpc}^{-3} \text{ yr}^{-1}$, SNe Ibc have $0.258 \times 10^{-4} \text{ Mpc}^{-3} \text{ yr}^{-1}$, and SNe II $0.447 \times 10^{-4} \text{ Mpc}^{-3} \text{ yr}^{-1}$ [107, tab. 10] (SNe Ia are not considered here, since they are usually not considered to produce high-energy neutrinos and thus a SN Ia would not have enjoyed the same amount of attention).

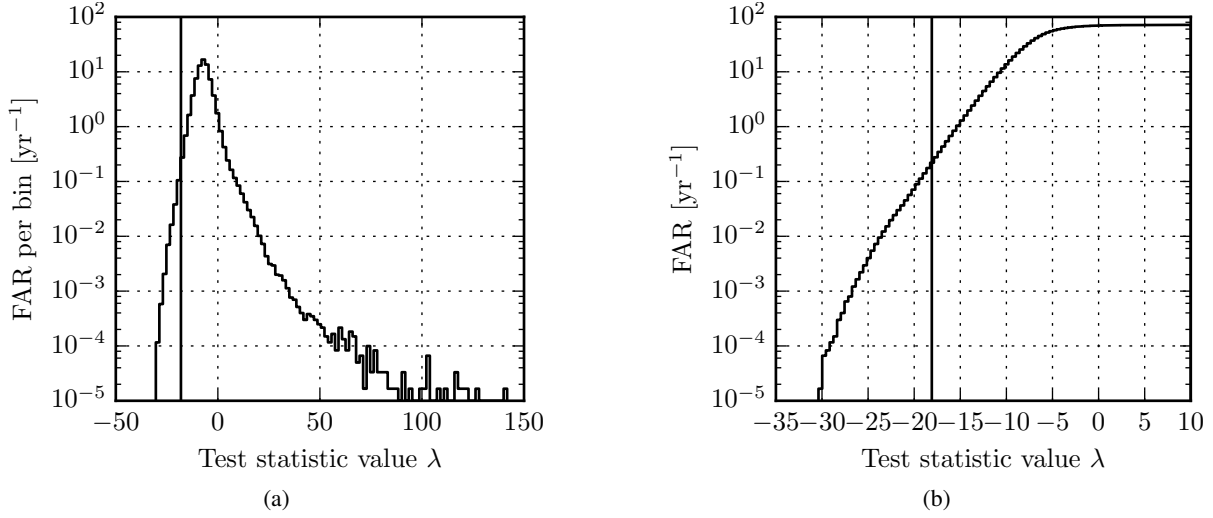


Figure 7.4: (a) Distribution of the test statistic λ (see Equation 6.5) for random coincidence doublets. (b) Cumulative version of (a). Distribution generated by permuting the ≈ 8 months of experimental data, mostly atmospheric neutrinos, 10 000 times (see text). The found value of $\lambda = -18.1$ for the reported alert from 2012 March 30 is indicated as vertical line. Signal-like doublets tend to smaller values. The distribution (a) is scaled to represent the false alarm rate (FAR), i.e. each bin contains the expected number of alerts per year from background. Integrating the histogram in (a) from the λ -value to the left yields the FAR plotted in (b).

Limiting Magnitude and Detection Efficiency

The limiting magnitude m_{lim} is the highest magnitude (faintest object) that a telescope is able to detect. This magnitude depends on many parameters, such as the photometric conditions of the night (sky background brightness, clouds, atmospheric seeing, etc.), the zenith angle of the object, or the integration time. If m_{lim} was constant all the time, then the detection efficiency ϵ_{det} would be a step function,

$$\epsilon_{\text{det}}(m) = \theta(m) = \begin{cases} 1 & \text{if } m \leq m_{\text{lim}} \\ 0 & \text{if } m > m_{\text{lim}} \end{cases}. \quad (7.2)$$

For a description closer to reality, the detection efficiency is modeled as a step function with the step at the average limiting magnitude m_{lim} , which is smeared with a Gaussian function that has a width σ ,

$$\begin{aligned} \epsilon_{\text{det}}(m) &= \int_{-\infty}^{\infty} \theta(m') \frac{1}{\sqrt{2\pi}\sigma} e^{-(m'-m)^2/(2\sigma^2)} dm' = \int_{-\infty}^{m_{\text{lim}}} \frac{1}{\sqrt{2\pi}\sigma} e^{-(m'-m)^2/(2\sigma^2)} dm' \\ &= \frac{1}{2} \operatorname{erf}\left(\frac{1}{\sqrt{2}} \frac{m_{\text{lim}} - m}{\sigma}\right) + \frac{1}{2}. \end{aligned} \quad (7.3)$$

The detection efficiency is plotted in Figure 7.5 and is 50% at the average m_{lim} , consistent with the definition of limiting magnitude in [247]. For PTF, an average $m_{\text{lim}} = 20.6$ mag with Gaussian width of $\sigma = 0.4$ mag is assumed, matching the values³ presented in [221, p. 1400] for the Mould-*R* band, the dominantly used P48 survey filter.

³ Median of 20.6 mag, 25th percentile of 20.8 mag, 75th percentile of 20.3 mag.

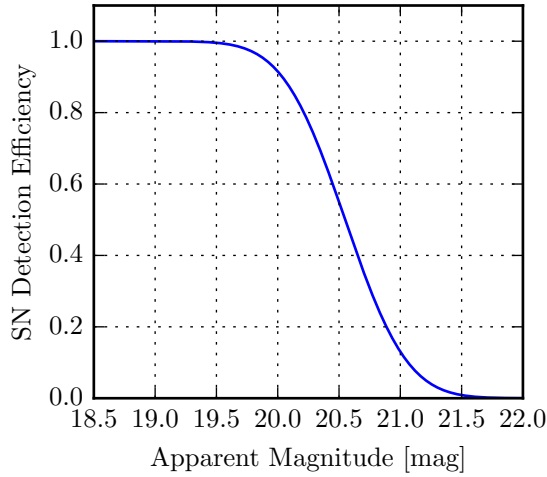


Figure 7.5: PTF’s SN detection efficiency modeled as smeared step function (Equation 7.3). A limiting magnitude of (20.6 ± 0.4) mag is assumed.

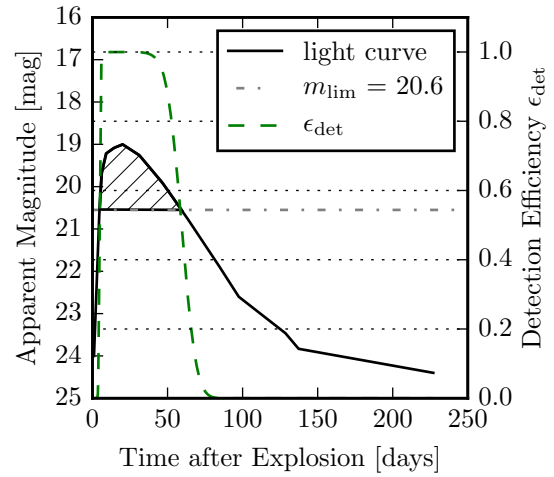


Figure 7.6: The template light curve is shown as solid line for an apparent peak magnitude of 19 mag, hatched where it is brighter than the average limiting magnitude of 20.6 mag, plotted as horizontal dash-dotted line. The detection efficiency (Figure 7.5), evaluated for the current light curve magnitude, is plotted as green dashed curve. Detection efficiency is 50% where the light curve crosses the limiting magnitude. The integral of the green dashed curve yields the control time.

The Control Time

The control time Δt^4 is the effective time window, during which a particular SN is detectable, i.e. roughly speaking brighter than the limiting magnitude of the telescope. It is the integral of the detection efficiency ϵ_{det} over time, where ϵ_{det} is evaluated for the magnitude of the light curve $m(t|\hat{M}, r)$ at time t (see Figure 7.6),

$$\Delta t(\hat{M}, r) = \int_0^{\infty} \epsilon_{\text{det}}(m(t|\hat{M}, r)) dt. \quad (7.4)$$

The control time depends on the absolute peak magnitude \hat{M} , the distance r to the SN, and the shape of the SN light curve $m(t|\hat{M}, r)$. The light curve used here is a SN II_n template light curve obtained from Peter Nugent’s SN template web page,⁵ see Figure 7.6 for a plot.

If one knows the absolute peak magnitude distribution of CCSNe, called the *luminosity function (LF)* in the literature [249], one can use it to calculate a weighted average of the control time. Li et al. (2011) [249] have collected a volume-limited sample of 175 SNe and constrained the peak magnitudes of the SNe. They derived the observed fractions of different SN types and computed the LFs $dN_{\text{SN}}/d\hat{M}$ from this. The average absolute peak magnitudes are $\langle \hat{M} \rangle = -18.5$ mag (with a 1σ dispersion of 0.76 mag), $\langle \hat{M} \rangle = -16.1$ mag ($\sigma = 1.24$ mag), and $\langle \hat{M} \rangle = -16.1$ mag ($\sigma = 1.37$ mag) for the SNe Ia, Ibc and II, respectively [249]. The LFs have been corrected for Galactic, but not for host galaxy extinction. They are plotted in Figure 8.21 (left column) for the SN types Ia, Ibc, and II. Using the LF $dN_{\text{SN}}/d\hat{M}$,

⁴ First introduced by Swiss astronomer Fritz Zwicky [248] for the calculation of SN rates. See also [247] for definition and application of the control time in an astronomical SN survey.

⁵ https://c3.lbl.gov/nugent/nugent_templates.html

the average control time becomes

$$\Delta\bar{t}(r) = \int_{-\infty}^{\infty} \Delta t(\hat{M}, r) \frac{dN_{\text{SN}}}{d\hat{M}} d\hat{M}, \quad (7.5)$$

where the LF is normalized to 1, i.e. $\int_{-\infty}^{\infty} dN_{\text{SN}}/d\hat{M} d\hat{M} = 1$. Because the LF depends on the SN type, one $\Delta\bar{t}$ is calculated for each of the two core-collapse types Ibc and II, and combined with the respective volumetric CCSN rate for that type.

The Result

The resulting expectation value for coincidental SN detections is $\bar{N}_{\text{det}} \approx 0.007 \text{ (II)} + 0.004 \text{ (Ibc)} = 0.011$, which results in a Poisson probability of $\sim 1.1\%$ to detect any CCSN (one or more) by chance within 300 Mpc, within the neutrino alert's error radius. Fisher's method [250–253] for combining p-values from statistically independent hypothesis tests is used to obtain a p-value for the occurrence of both the neutrino doublet and the SN detection. In Fisher's method, N p-values p_i (null hypothesis probabilities from hypothesis tests) enter a single test statistic ξ ,

$$\xi \equiv -2 \sum_{i=1}^N \ln p_i, \quad \text{for } N = 2: \quad \xi = -2(\ln p_1 + \ln p_2). \quad (7.6)$$

The test statistic ξ is distributed according to the χ^2 -distribution with $k = 2N$ degrees of freedom, from which the p-value for the combined test can be derived as

$$p = 1 - \text{CDF}_{\chi^2}(\xi, k), \quad (7.7)$$

where CDF_{χ^2} is the cumulative distribution function (CDF) of the χ^2 -distribution. Figure 7.7 illustrates Fisher's method for two p-values p_1 and p_2 , showing the value of the combined p-value p in the p_1 - p_2 -plane. Combining the CCSN detection probability of 1.1% with the probability of 12.7% for the neutrino alert, Fisher's method delivers a combined p-value of 1.0%, corresponding to a significance of 2.3σ (single-sided Gaussian). For the total live time of 460 days, the combined p-value is 1.8%, which corresponds to a 2.1σ significance. This means, even ignoring the *a posteriori* nature of the p-value, a chance coincidence of the neutrino doublet and the SN detection cannot be ruled out and thus the SN detection is considered coincidental.

The following Section 7.2 reports about the available high-energy follow-up data. Limits on a possible long-term neutrino emission from PTF12csy are set using one year of IceCube data. Limits on the X-ray flux are obtained using the Swift satellite. Section 7.3 deals with the analysis of the low-energy optical and UV data.

7.2 High-Energy Follow-Up Data

7.2.1 Results of the Offline Analysis of Neutrino Data

Type II_n SNe, such as PTF12csy, are a promising class of high-energy transients (see 3.2.7). The expected duration of neutrino emission from SNe II_n is 1 to 10 months, hence it is extremely unlikely that two neutrinos arrive within less than 2 s, so late after the SN explosion. However, to test the possibility of a long-term emission, a search for neutrinos from PTF12csy within a search window of

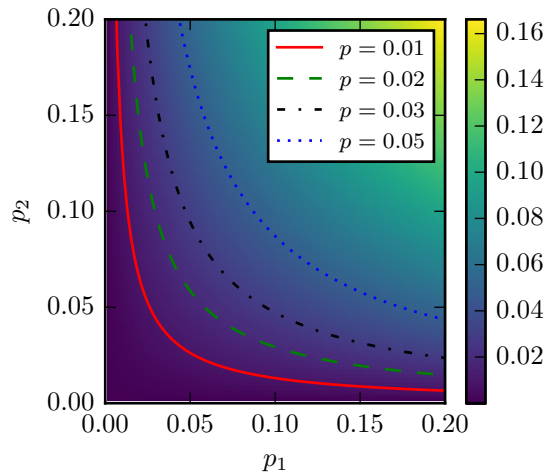


Figure 7.7: Illustration of Fisher’s method: The color scale indicates the combined Fisher p-value p for two individual p-values p_1 and p_2 . Contour lines at some constant colors, i.e. values of p , are plotted.

roughly one year has been conducted. The results are reported in this section. For details, see [242, sec. 4.1] and [254].

After the core-collapse of a SN IIn, the SN ejecta are crashing into massive circumstellar medium (CSM) shells and a pair of shocks is travelling outwards: a forward shock (FS) and a reverse shock (RS). As detailed in Section 3.2.7, cosmic rays (CRs) might be accelerated and multi-TeV neutrinos produced, potentially detectable with IceCube. In [255, sec. 3.8], Nora Linn Strotjohann estimated the neutrino signal from SN PTF12csy in IceCube to be on average only 0.07 IceCube neutrino events, even for an optimistic choice of model parameters.

Despite the low expectation for the neutrino fluence, about one year of IceCube data are analyzed for a long-term emission. The neutrino emission models A and B—shown in fig. 1 of [110] and Figure 3.11—are tested. They are two representative cases of CR accelerating scenarios (see Section 3.2.7): Model A corresponds to a CSM shell with a high density at a small radius, while Model B is the opposite with lower density and larger radius. Model A is close to a scenario explaining superluminous SNe IIn such as SN 2006gy, while Model B is a good description for dimmer, but longer lasting SNe like SN 2008iy. Both models have a neutrino energy spectrum close to E^{-2} , with a cut-off energy around 70 TeV for Model A, around 84 TeV for the forward shock (FS) in Model B, and around 275 TeV for the reverse shock (RS) in Model B. In Model A, only the reverse shock is of importance for CR acceleration.

About one year of IceCube data are analyzed: the entire IceCube 86 strings data acquisition season 2011/12, from 2011 May 13 to 2012 May 15. The long search window is motivated by the large uncertainty on the explosion date (between 2011 March 21 and 2011 October 13), as well as the long duration of neutrino emission for some scenarios, like ~ 700 days for Model B in [110].

The result of the analysis is that no sign of signal contribution is visible in the neutrino event sample, for both models A and B. 90% C.L. Neyman upper limits (see [239], reprinted in [240]) are set on the tested neutrino fluence models, which amount to ~ 1500 and ~ 1300 times the fluences given for model A and B above, respectively. These limits are much higher than the fluence prediction because of IceCube being insensitive to SNe IIn at such large distances. Figure 7.8 shows a plot of the tested neutrino fluence and the limits set using 1 yr of IceCube data.

This null result and IceCube’s lacking sensitivity to the SN further support the conclusion that the SN detection is coincidental.

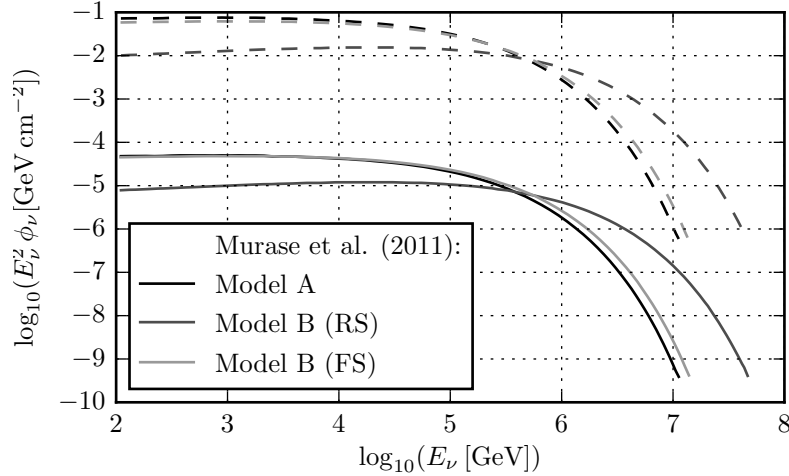


Figure 7.8: The neutrino fluence at Earth from PTF12csy (solid lines) and derived upper limits set by IceCube (dashed lines, corresponding gray scales) as function of energy for the tested models A, B reverse shock (RS), and B forward shock (FS) from [110].

Nevertheless, it is interesting to roughly estimate the hypothetical emitted neutrino fluence: Taking the median neutrino energies of the two alert neutrinos from Table 7.1 and looking up the effective areas for the OFU neutrino sample at the respective energies, one can derive a hypothetical neutrino fluence of $3.2 \times 10^{-4} \text{ erg cm}^{-2}$ for a source spectrum $\propto E^{-2}$ ($E_\nu = 5.4 \text{ TeV}, 15.7 \text{ TeV}$), or $10.8 \times 10^{-4} \text{ erg cm}^{-2}$ for a source spectrum $\propto E^{-3}$ ($E_\nu = 0.7 \text{ TeV}, 1.5 \text{ TeV}$). Assuming that this neutrino fluence was emitted by the SN, this would imply a radiated neutrino energy of $\sim 3.4 \times 10^{51} \text{ erg}$ or $\sim 1.2 \times 10^{52} \text{ erg}$ using the luminosity distance of $\sim 300 \text{ Mpc}$, corresponding to about 15 or about 50 times the radiated electromagnetic energy of $E_{\text{bol}} = 2.1 \times 10^{50} \text{ erg}$ (see Section 7.3.2). This is higher than what can be expected, since with reasonable assumptions that the explosion energy $E_{\text{ej}} \leq 10E_{\text{bol}}$ [256, 257] and a fraction $\epsilon_{\text{CR}} \leq 0.1$ of it going into CRs [110], the energy in neutrinos should be on the same order or less than E_{bol} . Thus, also with a simple energetic argument, isotropic neutrino emission from PTF12csy causing the neutrino alert is implausible, especially on a time scale of seconds. However, a beamed emission from a jet with a small opening angle of $< 30^\circ$ would in principle be possible.

7.2.2 X-ray Observations of PTF12csy

The Swift satellite observed the supernova four times, on 2012 April 20 (MJD 56 037) and around 2012 November 15 (MJD 56 246) (see Table 7.2). Source detection was performed by Phil Evans using the software developed for the 1SXPS catalog [258] on each of the four observations, and on a summed image made by combining all the datasets. No counterpart to PTF12csy was detected. Evans generated upper limits for each of these images, following [258]. A $28''$ radius circle centered on the optical position of PTF12csy was used to measure the detected X-ray counts c at this location, and the expected number of background counts c_{bg} , predicted by the background map created in the source detection process. Then, Evans used the Bayesian method of [259] to calculate the 3σ upper limit c_{UL} on the X-ray count rate of PTF12csy, using the XRT exposure map to correct for any flux losses due to bad pixels on the XRT detector, and the finite size of the circular region.

The upper limit count rate is converted to unabsorbed flux Φ_{UL} using the HEASARC Tool

Time [MJD]	Exposure [ks]	c	c_{bg}	c_{UL}	Φ_{UL}
56 037.15	4.9	1	1.47	1.3	4.6
56 245.29	2.0	1	0.62	2.1	7.4
56 246.04	1.2	2	0.44	9.8	30.0
56 247.62	5.0	2	1.35	2.1	7.4
Sum	13.0	6	3.71	1.3	4.6

Table 7.2: Swift XRT observations of PTF12csy. Energy range: 0.2 keV to 10 keV. c : measured counts within a 28'' aperture. c_{bg} : expected background counts within the same aperture. c_{UL} : 3σ upper limit on the X-ray count rate in 10^{-3} s^{-1} . Φ_{UL} : upper limit on the unabsorbed source flux in $10^{-14} \text{ erg cm}^{-2} \text{ s}^{-1}$.

WebPIMMS,⁶ assuming a black body model with $T = 0.6 \text{ keV}$ as in [260], a Galactic hydrogen column density of $1.31 \times 10^{21} \text{ cm}^{-2}$ [261],⁷ and a redshift of $z = 0.0684$. The result is a 0.2 keV to 10 keV X-ray flux $< 4.6 \times 10^{-14} \text{ erg cm}^{-2} \text{ s}^{-1}$ for the most constraining upper limits, corresponding to a 0.2 keV to 10 keV X-ray luminosity of $L_X < 5.2 \times 10^{41} \text{ erg s}^{-1}$ with a luminosity distance of about 308 Mpc. Using a power-law $\propto E^{-2}$ instead of a black body as an alternative X-ray emission model, the unabsorbed flux upper limit becomes $< 7.4 \times 10^{-14} \text{ erg cm}^{-2} \text{ s}^{-1}$, and hence, $L_X < 8.4 \times 10^{41} \text{ erg s}^{-1}$.

Comparing with other SNe IIn, e.g. SN 2008iy [260], which had a measured X-ray luminosity of $L_X = (2.4 \pm 0.8) \times 10^{41} \text{ erg s}^{-1}$, or SN 2010jl [262] with $L_X \approx 1.5 \times 10^{41} \text{ erg s}^{-1}$, one cannot exclude X-ray emission from PTF12csy with the measured upper limit. However, [263] suggest that L_X be about 10^{-4} of the bolometric luminosity at the time of the shock breakout. With the estimated bolometric luminosity from Section 7.3.2 around the time of the first Swift observations, this implies $L_X \approx 6.4 \times 10^{38} \text{ erg s}^{-1}$, well below these X-ray limits.

7.3 Low-Energy Follow-Up Data

The measurement of an astronomical object's brightness, or more precisely its intensity (photon energy per time and area) is called photometry. It is usually measured in magnitudes (see Appendix B.2) by integrating the spectral intensity over a certain wavelength range using a filter, which has a wavelength-dependent transmission and thus selects only the photon flux from a certain part of the spectrum. Meanwhile, the measurement of an object's photon energy distribution, resulting in a spectrum, is called spectroscopy. After an overview of the available data and the observational instruments in Section 7.3.1, the analysis of the photometric data from SN PTF12csy is explained in Section 7.3.2, followed by the spectroscopic analysis in Section 7.3.3, and a closer look at the galaxy hosting the SN in Section 7.3.4.

7.3.1 Optical and UV Observations of PTF12csy

During the follow-up program of the neutrino alert, the first observations were done on 2012 April 03, 05, 07 and 09 (MJD 56 020 to 56 026) by PTF with the Palomar Samuel Oschin 48-inch telescope (P48) [221], which is a wide-field Schmidt telescope. The images (see Figure 7.3) revealed a so far undiscovered supernova, named *PTF12csy*,⁸ at a magnitude of ~ 18.6 in the Mould R -band, at right ascension 104.63643° and declination 17.26233° . More photometric observations were carried out,

⁶ <https://heasarc.gsfc.nasa.gov/Tools/w3pimms.html>

⁷ <http://www.swift.ac.uk/analysis/nhtot/index.php>

⁸ The PTF collaboration names all the discovered sources with the letters "PTF", followed by the year of discovery, followed by an incremental alphabetical string as a counter ID within each year, ordered like a, b, c, ..., z, aa, ab, and so on.

with the P48 and the Palomar 60-inch (P60) telescopes [221] at the Palomar Observatory in California, and the Faulkes Telescope North (FTN) [264] at Haleakala on Maui, Hawaii. Spectroscopy was taken as well, with the Gemini North Multi-Object Spectrograph (GMOS) [265] on the 8 m Gemini North telescope (Mauna Kea, Hawaii) on 2012 April 17 (MJD 56 034) and with the Low-Resolution Imaging Spectrometer (LRIS) [266] on the 10 m Keck I telescope (Kamuela, Hawaii) on 2013 February 09 (MJD 56 332), enabling the identification of the SN as a Type II_n SN with narrow emission lines. The spectra are available from WISEREP⁹ [267].

P48 data were extracted by Yi Cao using an aperture photometry pipeline, and calibrated with 21 close-by SDSS stars [243–246], selected by the author of this thesis. The faint host galaxy was subtracted and the upper limits are at the 5σ level. P48 magnitudes are in the PTF natural AB magnitude system, which is similar, but not identical to the SDSS system (see Equation B.4 in Appendix B.2). The difference is given by a color term, which is ignored in this work, except for the conversion of Mould R to SDSS r , explained in Section 7.3.2. The P60 photometry was generated by Mansi Kasliwal, tied to the same 21 SDSS calibration stars. Note that there might be host galaxy contamination in the late-epoch P60 photometry. The FTN data were processed by an automatic pipeline, without host subtraction, and agree very well with the host-subtracted P60 data taken in the same night.

The Pan-STARRS1 (PS1) telescope is not part of the real-time triggering and response system, but its wide-field coverage provides a useful archive to search retrospectively for detections. PS1 is a 1.8 m telescope located at Haleakala on Maui in the Hawaiian islands, equipped with a 3.3° FOV and a 1.4 gigapixel camera [268]. In the course of its 3π steradian survey, the telescope observes each part of the sky typically 8 to 10 times per year [269]. PS1 first detected PTF12csy on MJD 55 847.582 and archived it as object *PSO J104.6365+17.2622*. This corresponds to the first known detection of the SN. The magnitudes in all PS1 images were obtained by members of the Pan-STARRS1 Science Consortium, with PSF fitting within the Pan-STARRS Image Processing Pipeline [270]. They are calibrated to typically seven local SDSS DR8 field stars. The magnitudes are in the natural PS1 AB system as defined in [271], which is similar to, but not exactly the same as SDSS AB magnitudes. Particularly the g -band can differ.

The Swift UVOT data were analyzed by Nora Linn Strotjohann using the publicly available Swift analysis tools [272].¹⁰ Details are given in [255].

ROTSE’s limiting magnitude of about 16 – 17 mag prevented a detection of the SN in ROTSE follow-up observations.

7.3.2 Photometry

Photometric Corrections

For the plots discussed in the following sections, several corrections are applied to the photometry. It is corrected for Galactic extinction using $R_V = A_V/E(B - V) = 3.1$, $E(B - V) = 0.071$ and $A_V = 0.219$ following Schlegel et al. (1998) [273].¹¹ The extinction coefficient is converted to the filters’ effective wavelengths using the algorithm from Cardelli et al. (1989) [274],¹² i.e. 0.35 mag for u , 0.30 mag for B , 0.26 mag for g , 0.19 mag for r , 0.11 mag for z . The extinction within the host galaxy could not be determined. Data for the Na I D line is missing in the Gemini North spectrum and there is no absorption feature visible in the Keck spectrum. Therefore, it is assumed that the host extinction is negligible. This

⁹ <http://wiserep.weizmann.ac.il>

¹⁰ See <http://www.swift.ac.uk/analysis/uvot/> for instructions

¹¹ Obtained via the NASA/IPAC Infrared Science Archive <http://irsa.ipac.caltech.edu/applications/DUST/>.

¹² Via <http://dogwood.physics.mcmaster.ca/Acurve.html>.

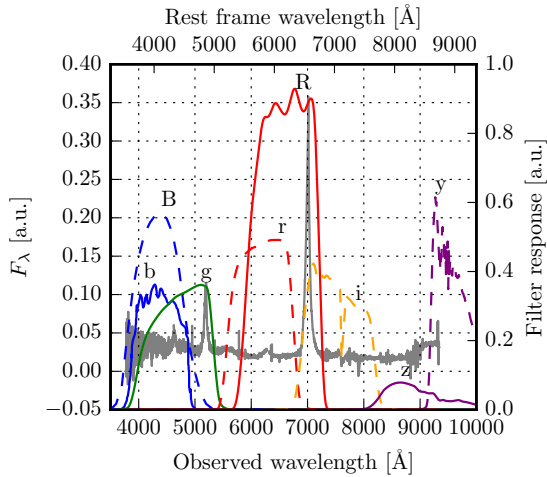


Figure 7.9: *Background, gray, left axis*: Gemini North spectrum from 2012 April 17 (MJD 56 034). *Foreground, multiple colors, right axis*: The filter response functions of the applied photometric filters, defined as filter transmission or effective area. Note that the absolute normalization is arbitrary and only the shape of the curves is relevant. The $H\alpha$ line contributes to the P48 R -band filter and the P60 i -band filter, but not to the P60 r -band filter. When converting the P48 r -band magnitude to SDSS r , this has to be considered, since the formulae in [226] are only valid for star-like black body spectra, which do not have strong emission lines like the $H\alpha$ line in PTF12csy’s spectrum.

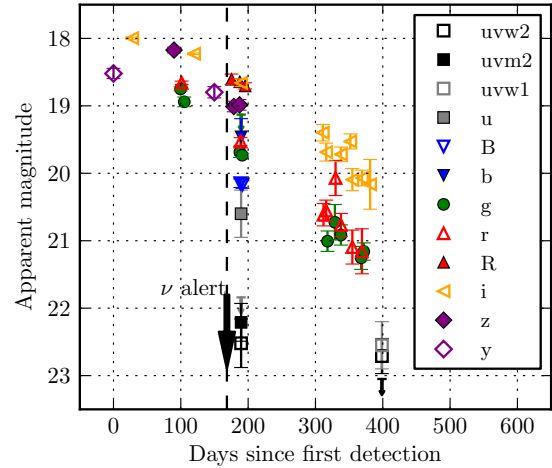


Figure 7.10: PTF12csy photometry in apparent magnitudes without applying corrections. The photometry is averaged over intervals of 10 days. The data originate from the following telescopes: $uvw2$, $uvm2$, $uvw1$, u , b : UVOT; B : P60; g : P60, PS1, FTN; r : P60, PS1, FTN; R : P48; i : P60, PS1, FTN; z : P60, PS1; y : PS1.

is consistent with the analysis of SN 2008iy, which occurred in a similar host galaxy [260].

In Figure 7.9, the Gemini North spectrum is overlaid with the applied photometric filters. The strong Balmer lines contribute differently to the various filters. For the construction of the spectral energy distribution from photometry (see Section 7.3.2), the black body continuum is approximated by removing the contribution of the strongest emission lines, $H\alpha$ and $H\beta$, from the photometry. For this, the Gemini North spectrum and the filter curves are used. For Figures 7.11 and 7.12, the P48 Mould R magnitudes are converted to SDSS r by subtracting the $H\alpha$ contribution (as above), applying the formulae in [226] valid for black body spectra, and then re-adding the $H\alpha$ contribution to the r -band. After conversion, the P48 R magnitudes are consistent with the P60 SDSS r magnitudes.

The Swift UVOT data contain host contamination. Since no GALEX data from a pre- or post-SN epoch were available for the host galaxy¹³, no host subtraction could be done in the UV filters of UVOT. For the u , b and v filters, the host is subtracted by interpolating the host magnitudes from the SDSS DR10 data¹⁴ to the effective wavelengths of the UVOT filters.

The Light Curves

The earliest detection of PTF12csy was in the Pan-STARRS1 y -band on 2011 October 13 (MJD 55 847.582), 169 days prior to the neutrino alert in observer frame, corresponding to 158 days in

¹³ See <http://galex.stsci.edu/GalexView/>

¹⁴ <http://skyserver.sdss3.org/public/en/tools/chart/navi.aspx>

host galaxy rest frame using $z = 0.0684$ (see Section 7.3.3). The latest non-detection, again in Pan-STARRS1, was on 2011 March 21 (MJD 55 641.3) in a 30 s z -band frame, 206 days before the first detection (193 days in rest frame). Hence, the explosion time is not well constrained and can be any-time between MJD 55 641.3 and MJD 55 847.6. Hereafter, the y -band detection at MJD 55 847.582 is referred to as the first detection. It is used as day 0 for the light curve.

The uncorrected SN light curves with the data available through the IceCube optical follow-up program are displayed in Figure 7.10, including photometry acquired with the Swift UVOT filters $uvw2$, $uvm2$, $uvw1$, u and b ; the Johnson B filter on P60; the SDSS filters g , r , i with data from P60, PS1, and FTN; the SDSS z filter on P60; Mould R filter on P48; and Pan-STARRS y filter on PS1. The entire uncorrected photometry in apparent magnitudes, as seen in Figure 7.10, is also available in Table 7.3. The light curves are averaged within intervals of 10 days width, for each filter and telescope separately. Note that, in contrast to most of the other photometry, no host subtraction has been performed for the Swift UVOT magnitudes presented in Figure 7.10 and Table 7.3.

Figure 7.11 shows the light curve of selected filters in absolute magnitudes, after the photometric corrections. Light curves of other exceptional Type II SNe are overlaid for comparison: SN 2006gy and SN 2010jl. SN 2006gy [81, 275] was at the time of discovery the most luminous SN ever recorded, with total radiated energy of 10^{51} erg and peak visual magnitude of about -22. The progenitor star of SN2006gy was likely a very massive star, similar to η Carinae, with multiple mass ejection episodes. The enormous luminosity was powered by the interaction between the ejecta and these massive shells [276, 277]. SN2006gy's light curve in Figure 7.11 is relative to the estimated explosion date. A distance modulus of $\mu = 34.5$ and an extinction of $A_R = 1.68$ mag are applied to the data from [81, 278, 279]. At late epochs, the SN's luminosity is comparable to PTF12csy and the decline rate is also similar.¹⁵ SN 2010jl [280, 281] is an SN IIn, which bears the closest spectroscopic similarities with PTF12csy (see Section 7.3.3). It shows signs of collisionless shocks in an optically thick CSM, hinting towards potential high-energy neutrino production [282]. SN 2010jl's phase in Figure 7.11 is relative to the time of the V -band maximum and a distance modulus of $\mu = 33.43$ is applied. Note that the SN 2010jl light curve is not extinction corrected. The light curve evolution is similar, however flatter than PTF12csy's g -band light curve (g is closest to the V -band). The brightness is comparable to PTF12csy.

The brightest observed absolute magnitudes from SN PTF12csy, after application of photometric corrections (see Section 7.3.2) and conversion to absolute magnitudes with a distance modulus of $\mu = 37.443$ ($z = 0.0684$) are $M_g \approx -19.0$ mag, $M_r \approx -19.0$ mag, $M_i \approx -19.6$ mag, $M_z \approx -19.4$ mag, and $M_y \approx -19.0$ mag, assuming standard cosmology with Hubble parameter $H_0 = 70$ km s⁻¹ Mpc⁻¹, matter density $\Omega_m = 0.3$, and dark energy density $\Omega_\Lambda = 0.7$. While these are lower limits to the peak magnitude due to the sparse sampling, these absolute magnitudes are relatively modest compared to the most luminous SNe IIn, e.g. SN 2006gy ($M_R = -22$ mag) [278] or SN 2008fz ($M_V = -22.3$ mag) [283]. They are however comparable to the SNe IIn 2008iy ($M_r \approx -19.1$ mag) [260], 1988Z ($M_R \lesssim -18.9$ mag) [284], and SN 2010jl ($M_R \lesssim -20.0$ mag) [281].

Decline Rates and Energy Source

The light curves of PTF12csy indicate a plateau within ~ 100 days after first detection, and a slow fading afterwards. The corrected absolute magnitude light curves have been fitted to obtain the linear decline rates in different photometric filters, during different epochs, see Figure 7.12 and Table 7.4. For some epochs and filters, especially g and r , the decline rates are close to 0.98 mag (100days)⁻¹, the decline

¹⁵ Note that the light curve is interpolated and smoothed and that after 217 d, only two data points are available at 394 d and 824 d, giving the wrong impression of linear declines.

7 Coincidental Detection of Supernova PTF12csy

MJD Date	Rest frame days	Mag	Abs. mag	Lim. mag	Filter	Tel.
55 273.219	-537.589	—	—	21.11	<i>g</i>	P48
55 294.162	-517.987	—	—	20.62	<i>R</i>	P48
55 431.514	-389.429	—	—	18.99	<i>R</i>	P48
55 477.402	-346.478	—	—	20.67	<i>R</i>	P48
55 596.889	-234.642	—	—	18.90	<i>g</i>	P48
55 641.304	-193.071	—	—	21.40	<i>z</i>	PS1
55 847.588	0.005	18.52 ± 0.08	-18.92	—	<i>y</i>	PS1
55 875.515	26.145	18.00 ± 0.02	-19.45	—	<i>i</i>	PS1
55 937.502	84.163	18.17 ± 0.04	-19.27	—	<i>z</i>	PS1
55 948.816	94.752	18.82 ± 0.05	-18.62	—	<i>g</i>	PS1
55 948.841	94.776	18.66 ± 0.02	-18.79	—	<i>r</i>	PS1
55 957.475	102.858	19.00 ± 0.02	-18.44	—	<i>g</i>	PS1
55 967.269	112.024	18.23 ± 0.01	-19.22	—	<i>i</i>	PS1
55 997.366	140.194	18.80 ± 0.08	-18.64	—	<i>y</i>	PS1
56 022.981	164.169	18.61 ± 0.08	-18.84	18.23	<i>R</i>	P48
56 026.246	167.225	19.01 ± 0.08	-18.43	—	<i>z</i>	PS1
56 034.841	175.270	19.47 ± 0.04	-17.98	—	<i>r</i>	P60
56 034.844	175.273	18.99 ± 0.08	-18.46	—	<i>z</i>	P60
56 035.177	175.584	18.64 ± 0.04	-18.80	—	<i>R</i>	P48
56 035.922	176.281	18.68 ± 0.03	-18.76	—	<i>i</i>	P60
56 035.925	176.284	20.15 ± 0.06	-17.30	—	<i>B</i>	P60
56 035.928	176.287	19.69 ± 0.05	-17.75	—	<i>g</i>	P60
56 036.581	176.899	18.66 ± 0.04	-18.78	20.97	<i>i</i>	FTN
56 036.585	176.902	19.54 ± 0.06	-17.90	21.12	<i>r</i>	FTN
56 036.590	176.906	19.73 ± 0.07	-17.72	21.23	<i>g</i>	FTN
56 037.150	177.431	—	—	19.13	<i>v</i>	UVOT
56 037.150	177.431	20.60 ± 0.35	-16.84	20.79	<i>u</i>	UVOT
56 037.150	177.431	22.21 ± 0.28	-15.23	22.76	<i>uwm2</i>	UVOT
56 037.150	177.431	22.52 ± 0.36	-14.92	22.71	<i>uww2</i>	UVOT
56 037.150	177.431	—	—	21.84	<i>uww1</i>	UVOT
56 037.150	177.431	19.46 ± 0.27	-17.98	19.95	<i>b</i>	UVOT
56 039.175	179.326	18.74 ± 0.03	-18.70	—	<i>i</i>	P60
56 039.177	179.328	19.55 ± 0.04	-17.89	—	<i>r</i>	P60
56 039.178	179.329	20.17 ± 0.06	-17.28	—	<i>B</i>	P60
56 039.181	179.332	19.73 ± 0.04	-17.71	—	<i>g</i>	P60
56 040.285	180.365	18.60 ± 0.07	-18.85	20.98	<i>i</i>	FTN
56 043.178	183.073	18.70 ± 0.05	-18.74	—	<i>R</i>	P48
56 158.504	291.015	19.40 ± 0.12	-18.05	—	<i>i</i>	P60
56 161.496	293.815	20.58 ± 0.12	-16.86	—	<i>r</i>	P60
56 163.490	295.682	19.69 ± 0.13	-17.76	—	<i>i</i>	P60
56 165.486	297.550	21.01 ± 0.15	-16.44	—	<i>g</i>	P60
56 176.465	307.826	20.73 ± 0.26	-16.72	—	<i>g</i>	P60
56 177.453	308.751	20.07 ± 0.26	-17.37	—	<i>r</i>	P60
56 185.431	316.218	19.72 ± 0.11	-17.73	—	<i>i</i>	P60
56 185.432	316.219	20.77 ± 0.17	-16.68	—	<i>r</i>	P60
56 185.436	316.223	20.92 ± 0.15	-16.53	—	<i>g</i>	P60
56 200.887	330.685	19.81 ± 0.30	-17.63	—	<i>i</i>	P60
56 202.385	332.086	21.09 ± 0.25	-16.35	—	<i>r</i>	P60
56 215.381	344.250	21.23 ± 0.39	-16.21	—	<i>r</i>	P60
56 215.429	344.295	20.11 ± 0.10	-17.33	—	<i>i</i>	P60
56 215.435	344.301	21.25 ± 0.17	-16.19	—	<i>g</i>	P60
56 219.344	347.960	21.16 ± 0.13	-16.28	—	<i>g</i>	P60
56 219.837	348.421	20.97 ± 0.13	-16.47	—	<i>r</i>	P60
56 224.988	353.242	20.01 ± 0.17	-17.44	—	<i>i</i>	P60
56 229.808	357.754	20.20 ± 0.45	-17.24	—	<i>i</i>	P60
56 246.320	373.208	22.71 ± 0.26	-14.73	23.34	<i>uww2</i>	UVOT
56 246.320	373.208	22.55 ± 0.35	-14.89	22.79	<i>uww1</i>	UVOT
56 246.320	373.208	—	—	23.05	<i>uwm2</i>	UVOT

Table 7.3: Photometric observations of PTF12csy from the IceCube follow-up program. The rest frame days are relative to the first detection on MJD 55 847.582. Each filter is averaged within 10-day intervals. No correction for extinction is applied.

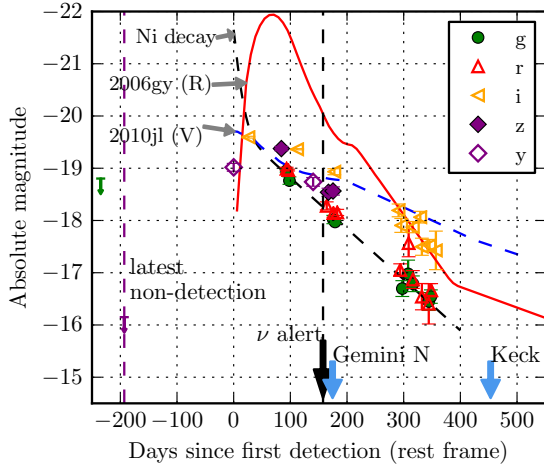


Figure 7.11: PTF12csy photometry (symbols) in absolute magnitudes, with correction for Galactic extinction, and conversion of P48 Mould R magnitudes to SDSS r magnitudes (see Section 7.3.2). The data originate from the following telescopes: g : P48, P60, PS1, FTN; r : P48, P60, PS1, FTN; i : P60, PS1, FTN; z : P60, PS1; y : PS1. The photometry is averaged over intervals of 10 days. Other absolute SN II light curves (lines) and a theoretical light curve from radioactive decay of nickel (black dashed line) are added for comparison. The comparison light curves are partly not extinction corrected and have different reference dates (see text).

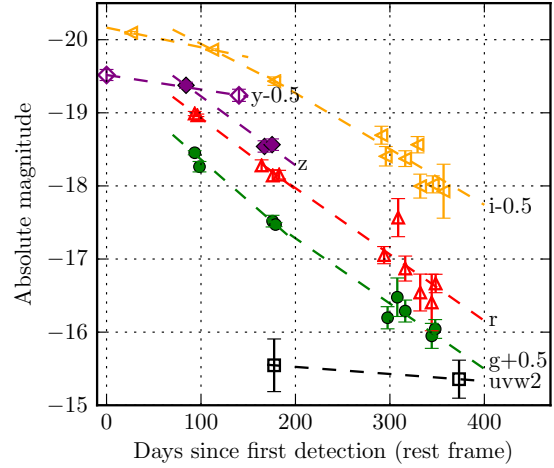


Figure 7.12: Light curves of several filters with the fitted linear declines. See Table 7.4 for the numerical values of the found decline rates. To improve visibility, values have been added to some filters' magnitudes as indicated (e.g. $g + 0.5$).

rate expected for radioactive ^{56}Co decay [260], while in general decline rates are slower, indicating that at least part of the radiated energy is powered by interaction of the SN ejecta with a dense CSM [260].

Additionally, radioactive decay of ^{56}Co at a still relatively high absolute magnitude of about -19 mag implies preceding ^{56}Ni decay with an extremely bright peak, which is not observed, although the data are quite sparse (see Section 3.2.1). Assuming that the luminosity is generated by the radioactive decay chain $^{56}\text{Ni} \rightarrow ^{56}\text{Co} \rightarrow ^{56}\text{Fe}$ alone, one can estimate the mass of ^{56}Ni necessary for the observed luminosity. The nickel decay law is

$$N_{\text{Ni}}(t) = N_{0,\text{Ni}} e^{-\kappa_{\text{Ni}} t}, \quad (7.8)$$

where $\kappa_{\text{Ni}} = \ln 2/t_{1/2,\text{Ni}}$ is the decay constant and $t_{1/2,\text{Ni}}$ is the ^{56}Ni half-life. For the subsequent ^{56}Co decay, the decay law is [285, p. 27]

$$N_{\text{Co}}(t) = \frac{\kappa_{\text{Ni}}}{\kappa_{\text{Co}} - \kappa_{\text{Ni}}} N_{0,\text{Ni}} (\exp(-\kappa_{\text{Ni}} t) - \exp(-\kappa_{\text{Co}} t)) \quad (7.9)$$

With the decay laws, the energy release per time, per initial nickel nucleus, can be calculated as sum of the energy released in both decays: $\epsilon = \epsilon_{\text{Ni}} + \epsilon_{\text{Co}}$. The nickel mass leading to a certain luminosity $L(t)$, at time t after the nickel production, is given by

$$M_{\text{Ni}} = \frac{L(t)}{\epsilon} \frac{M_{\text{mol}}^{\text{Ni}}}{N_A}, \quad (7.10)$$

Filter	0 d to 150 d	70 d to 200 d	170 d to 400 d
<i>uww2</i>	—	—	0.097 ± 0.227
<i>g</i>	—	1.127 ± 0.044	0.893 ± 0.051
<i>r</i>	—	0.974 ± 0.053	0.907 ± 0.059
<i>i</i>	0.269 ± 0.024	0.656 ± 0.089	0.764 ± 0.052
<i>z</i>	—	0.943 ± 0.079	—
<i>y</i>	0.199 ± 0.080	—	—

Table 7.4: Decline rates of the PTF12csy light curve. Units: mag (100 d)⁻¹. Indicated periods in rest frame days relative to first detection at MJD 55 847.582).

with molar mass of nickel $M_{\text{mol}}^{\text{Ni}} = 55.942 \text{ g}$ [286, p. 1618], and Avogadro’s constant $N_A = 6.022 \times 10^{23}$ particles per mole. The half-lives $t_{1/2, \text{Ni}} = 6.075 \text{ d}$, $t_{1/2, \text{Co}} = 77.236 \text{ d}$ [287]¹⁶ and the average thermal decay energies $\Delta E_{\text{Ni}} = 1.72 \text{ MeV}$, $\Delta E_{\text{Co}} = 3.64 \text{ MeV}$ [285, p. 27] are used. With Equation 7.10, it is estimated that $M_{\text{Ni}} \gtrsim 3.4 \times 10^{33} \text{ g} \approx 1.7 M_{\odot}$ would be required to provide the bolometric luminosity of $L = 9.7 \times 10^{42} \text{ erg s}^{-1}$ at $t = 100 \text{ d}$ in rest frame (see Section 7.3.2). A lower limit is set on the ⁵⁶Ni mass because it is assumed that the SN explosion and thus generation of ⁵⁶Ni happened at the latest possible time, directly before the first detection. Figure 7.11 shows the corresponding theoretical light curve resulting from the radioactive decay of nickel and cobalt (black dashed line). Adopting an earlier explosion time results in an even larger ⁵⁶Ni mass. This is much more than the usual amount of ⁵⁶Ni of $<0.5 M_{\odot}$, often $<0.1 M_{\odot}$ (see e.g. [288], also [257]). However, extremely superluminous SNe might have ⁵⁶Ni masses of that order of magnitude [289].

It is noted that in addition to the ⁵⁶Ni mass and luminosity arguments, the spectrum showing intermediate width Balmer lines and a continuum appears inconsistent with radioactive decay as well (see Figure 7.17).

Fitting an Interaction Model

Here it is assumed that the light curve is powered by conversion of the ejecta’s kinetic energy to luminosity through interaction of the ejecta with the CSM. Following Ofek et al. (2014) [262] (see also [263]), the light curve is modeled in form of the bolometric luminosity L as a power-law of the form

$$L(t) = L_0 (t - t_0)^{\alpha}. \quad (7.11)$$

See also the very similar calculation in [290], which is a generalization of [291] and considers an optically thin CSM, and [292], which covers an optically thick CSM.

After shock breakout, there is a phase of power-law decline of the luminosity, with a power-law index of typically $\alpha \approx -0.3$. This lasts until the shock runs over a CSM mass equivalent to the ejecta mass and the shock enters a new phase of either conservation of energy if the density is low enough and the gas cannot cool quickly (the Sedov-Taylor phase), or conservation of momentum if the gas radiates its energy via fast cooling (the snow-plow phase). During the late stage, the light curve will decline more steeply, in both cases [262].

It is tried to fit the interaction model from [262] to the PTF12csy light curve data with the least-squares method. The fit is performed within the range of 93 to 200 rest frame days, starting at the first *r*-band detection. The *r*-band light curve is used, scaled with the bolometric luminosity from Section 7.3.2. It is found that the power-law index α needs to be significantly steeper than -0.3 in order to describe the

¹⁶ Accessible via <http://www.nndc.bnl.gov/ensdf/>.

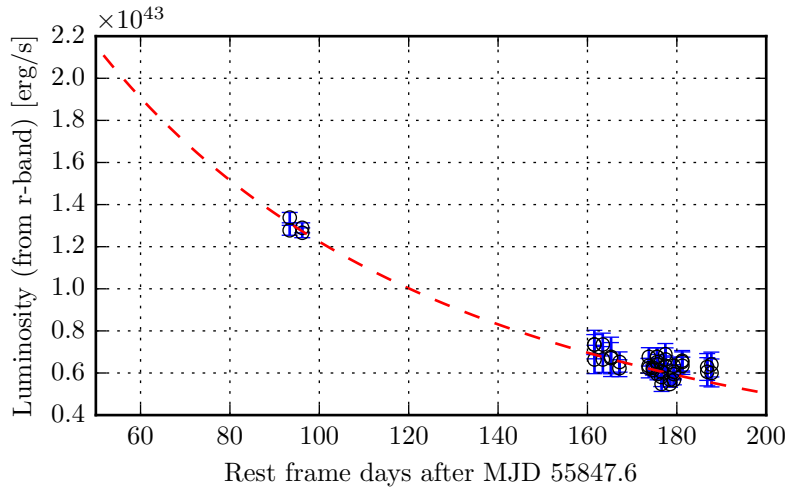


Figure 7.13: The light curve fit: photometric data (open circles) from the r -band, converted from magnitudes to luminosity using the found luminosity of $6.4 \times 10^{42} \text{ erg s}^{-1}$ at rest frame day 177 from Section 7.3.2. The best fit function of the Ofek et al. (2014) [262] interaction model is shown (red dashed line).

data. It lies in the range of -3 to -1.2 , using the constraint on the explosion time (see Section 7.3.2) as boundaries for the temporal zero point t_0 of the power-law (the explosion time). The best fit is found at $\alpha = -3.0$, with the explosion time $t_0 = -193 \text{ d}$ at the lowest allowed value—the date of the last non-detection—and the luminosity normalization $L_0 = 3.5 \times 10^{50} \text{ erg s}^{-1}$. See Figures 7.13, 7.14, 7.15 for plots of the light curve fit and the χ^2 . The minimal χ^2 is -51.0 , with a number of degrees of freedom of 39, so reduced χ^2 of $51/39 = 1.3$.

A power-law index α of -3 suggests a very steep CSM density profile $\propto r^{-5}$ (see [262, eq. 12]), compared to the profile $\propto r^{-2}$ resulting from a wind with steady mass loss. However, the self-similar solutions of the hydrodynamical equations [293] that are used in [262, eq. 12] are invalid if the CSM density profile is steeper than r^{-3} . Nevertheless, as discussed for the late-time light curve in [262, sec. 5.2], probably the profile is steeper than r^{-3} .

This allows for several possible explanations:

1. Already between rest frame days 93 and 200, the SN was in the late, e.g. snow-plow, phase. This is consistent with SN 2010jl, where the late-time light curve also shows a power-law index $\alpha \approx -3$ [262, sec. 5.2]. Assuming that the break in the light curve between power-law phase and late phase occurred just before the first r -band detection at day 93, and comparing with SN 2010jl [262], then this means that the SN was likely already a few hundred days old, and the r -band maximum was about 1 to 1.25 mag brighter than the observed one (see [262, fig. 1]), consistent with SN 2010jl’s r -band maximum. It follows that the power-law phase ended ≤ 286 rest frame days after explosion, from which one can derive a swept CSM mass of $\lesssim 12 M_{\odot}$, using [262, eq. 22] and adopting the standard values given for SN 2010jl.
2. The SN is powered by ejecta-CSM interaction, but its light curve is declining steeper than a $t^{-0.3}$ power-law. This is possible, e.g. if spherical symmetry, assumed in [262], is broken, if the optical depth is lower than in SN 2010jl—leading to a lower efficiency and faster decline—or if the CSM density profile falls steeper than r^{-2} (s.a.).
3. The SN is not powered by interaction, but by radioactive decay, leading to an exponential light curve decline. However, this appears unlikely, as noted above in Section 7.3.2.

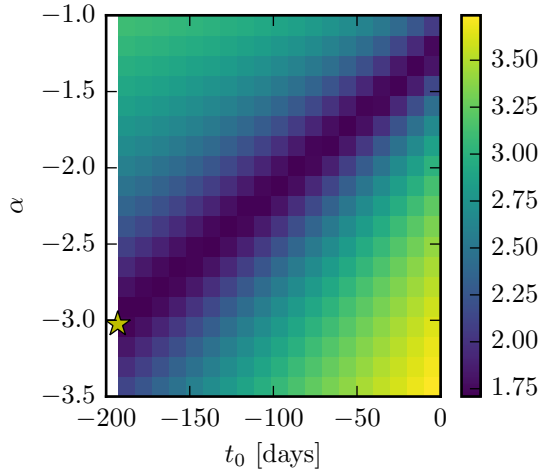


Figure 7.14: Landscape of $\log_{10}(\chi^2)$ values of the least-squares fit, as function of the fit parameters power-law index α and explosion time t_0 . The third fit parameter, luminosity normalization L_0 , is varied at each point to find the minimal χ^2 , with the global best fit value of $3.5 \times 10^{50} \text{ erg s}^{-1}$ as initial value. The global best fit is indicated with a star symbol.

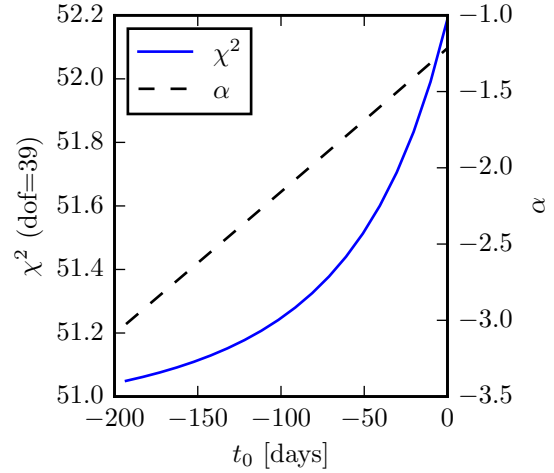


Figure 7.15: The χ^2 value of the light curve fit (solid curve, left axis), as function of the explosion time t_0 . For each value of t_0 , the other parameters α and L_0 have been varied to find the best fit (minimum of χ^2) and the best fit value of the power-law index α is plotted (dashed curve, right axis).

Spectral Energy Distribution (SED)

Since the spectra are only roughly calibrated, the spectral energy distribution (SED) is approximated from photometric data. For the highest spectral range and number of observations, a window of 10 observer frame days around day 189, from day 184 to 194, is used to select data (day 172.2 to day 181.6 in rest frame). Photometric corrections are applied, e.g. $H\alpha$ and $H\beta$ removed (see Section 7.3.2). The data are plotted in Figure 7.16 as function of the filters' effective wavelengths. A black body spectrum is assumed to describe the SED and is fitted to the data. For each filter, a model data point corresponding to the black body spectrum is calculated via integration of the black body spectrum multiplied with the filter response function, following the SDSS definition of AB magnitude in [294, eq. 7] (see Equation B.5 in Appendix B.2). A χ^2 least-squares fit minimizes the difference between the model data and the measured data.

The fit results in a reduced $\chi^2/n_{\text{dof}} = 7.9/5 = 1.6$ and delivers estimates for both the rest frame temperature T and the absolute bolometric luminosity L_{bol} of the photosphere emitting the black body radiation: $T = (7160 \pm 270) \text{ K}$ and $L_{\text{bol}} = (5.53 \pm 1.18) \times 10^{42} \text{ erg s}^{-1}$, where the errors correspond to 1σ . Applying the Stefan-Boltzmann law, one can calculate the radius R_{phot} of the black body photosphere from the bolometric luminosity L_{bol} and black body temperature T . It is estimated to be $R_{\text{phot}} = (1.7 \pm 0.1) \times 10^{15} \text{ cm}$.

Finally, to obtain an estimate on the total radiated energy, the lines' contributions to the luminosity have to be added to the continuum luminosity. Using the Gemini North spectrum, the contribution of the $H\alpha$ and $H\beta$ line to the total luminosity is computed and added to the continuum luminosity from the black body fit. This results in an estimated total radiated luminosity of $(6.4 \pm 1.2) \times 10^{42} \text{ erg s}^{-1}$ at day 189 in the observer frame, i.e. day 177 in the rest frame.

The fitted shape of the i -band light curve is used (see Section 7.3.2, Figure 7.12, Table 7.4) to extrapolate this value. A total radiated luminosity of $\approx 9.7 \times 10^{42} \text{ erg s}^{-1}$ is found at 100 d (rest frame),

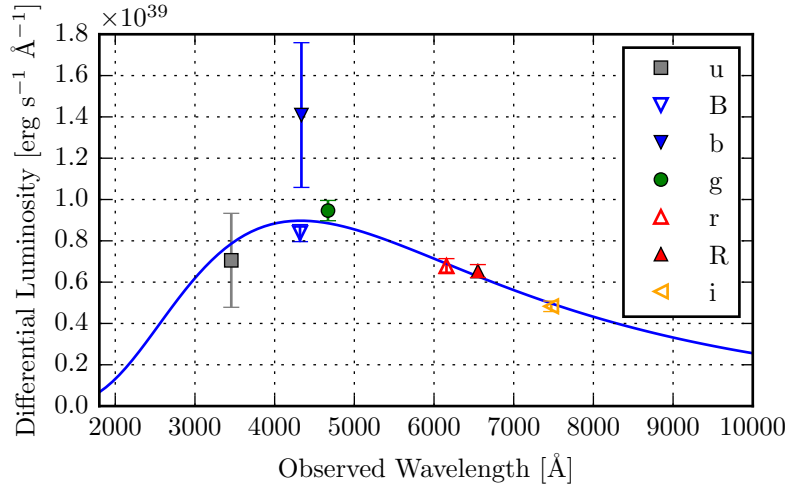


Figure 7.16: SED of PTF12csy using photometry from 10 days around day 189 (observer frame) after the first detection. The fitted rest frame temperature is $T = (7160 \pm 270)$ K and the fitted bolometric luminosity $(5.53 \pm 1.18) \times 10^{42}$ erg s^{-1} .

as used in Section 7.3.2, and a total energy of $E_{\text{bol}} = 2.1 \times 10^{50}$ erg radiated within 400 rest frame days after first detection, comparable to SN 2008iy, which had $\sim 2 \times 10^{50}$ erg [260] and SN 2010jl with 4.3×10^{50} erg [281]. This is a lower limit on the total radiated energy, since photometric data between explosion and first detection are missing and no extrapolation before the first detection is done. Additionally, as discussed below, a possible contribution of X-ray and γ -ray emission to the total radiated energy is neglected, since it is not included in the black body spectrum based on the UV and optical data.

It is recommended to treat these results with caution, since [262] pointed out that at late times the fraction of energy released from SNe IIn in X-rays can increase, causing the optical spectrum to deviate from a black body, as fewer photons are available in the optical. This can lead to an underestimation of the photospheric radius. In this context, the estimates of R_{phot} , L_{bol} , and E_{bol} must be treated as lower limits. Unfortunately, the X-ray flux from PTF12csy was not detected (see Section 7.2.2), so its contribution to the radiated energy is unknown.

7.3.3 Spectroscopy

Two spectra were acquired (Table 7.5, Figure 7.17). They are dominated by narrow emission lines, characteristic for Type IIn SNe, with a very weak blue continuum emission, which indicates the old age of the SN. No continuum is visible in the late spectrum. The SN emission lines are primarily hydrogen, the Balmer series is visible from $H\alpha$ up to $H\epsilon$. The oxygen lines $O\text{ I } \lambda\lambda 7772, 7774, 7775, 8447$, $O\text{ II } \lambda 3727$ with $\text{FWHM} \approx 500 \text{ km s}^{-1}$, and $O\text{ III } \lambda\lambda 4364, 4960, 5008$ with $\text{FWHM} \approx 350 \text{ km s}^{-1}$ are very narrow and were most likely produced by circumstellar gas released by the progenitor prior to explosion and then photoionized by UV radiation [76]. Other lines that could be identified are $\text{He I } \lambda\lambda 4472, 5876, 7065, 3965, 4922, 5048$, $\text{N II } \lambda\lambda 5755, 6550, 6585$, $\text{Ne III } \lambda\lambda 3869, 3968$, and $\text{S II } \lambda 6716$.

Figure 7.18 shows a close-up on the $H\alpha$ line from both spectra, plotted vs. Doppler velocity relative to the rest frame line center. For the conversion of wavelength λ to Doppler velocity v , the relativistic Doppler effect is used. In the early spectrum, the $H\alpha$ line peaks at the line center and the line is composed of a narrow, intermediate and broad component with FWHM of $\sim 400 \text{ km s}^{-1}$, $\sim 2000 \text{ km s}^{-1}$, and $\sim 5000 \text{ km s}^{-1}$ respectively, found by fitting a superposition of three Gaussian functions to the $H\alpha$

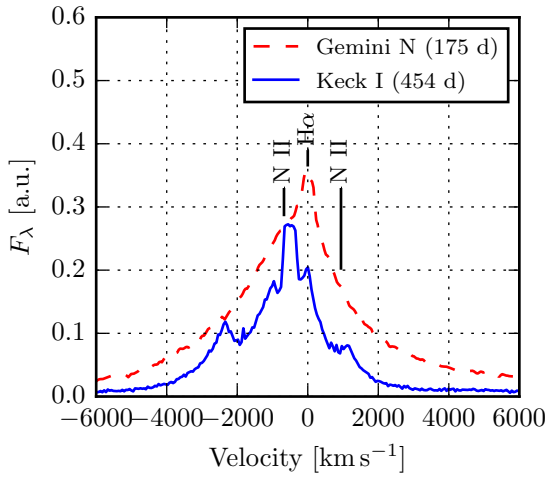


Figure 7.18: Comparison of the $H\alpha$ line in both spectra. The x-axis shows the Doppler velocity relative to the line center at 6564.61 \AA , assuming a redshift of 0.0684. The structure of the $H\alpha$ line is complex. The early spectrum shows a narrow, intermediate, and broad component, while the late spectrum's $H\alpha$ is very irregular and perhaps convolved with other spectral lines, e.g. $N \text{ II}$.

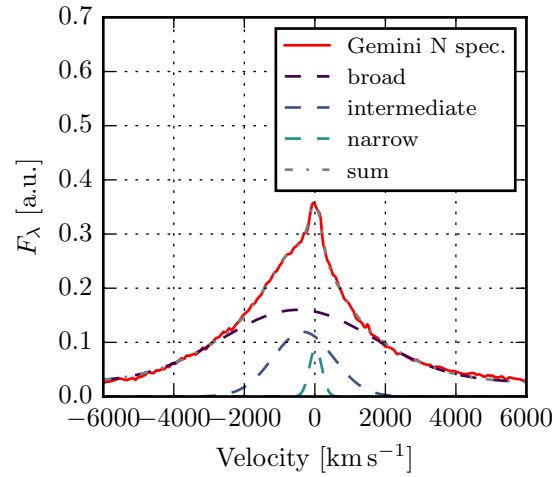


Figure 7.19: Close-up of the $H\alpha$ line of the earlier Gemini N spectrum (solid line), with the fitted narrow, intermediate, and broad Gaussian components (dashed lines) and the sum of the three components (dash-dotted line), which fits the spectrum very closely.

idence for a wavelength dependence of the blueshift. Therefore, the authors conclude that the origin of the blueshifts is most likely the rapid formation of large dust grains, confirming [295] and having implications on the origin of dust in galaxies.

Alternatively, [297] explain the line blueshift in SN 2010jl with a bulk velocity of the emitting gas towards the observer. This is more consistent with observations if the spectral lines are symmetric about a center and if there is no wavelength dependence of the blueshift. The bulk velocity is believed to be the result of radiative acceleration of the gas by flux from the SN. Presumably, there are also other possible explanations for the blueshift, e.g. the geometry or density structure of the CSM. In case of SN PTF12csy, spectral line blueshift is only clearly visible in the $H\alpha$ line, prohibiting the interpretation of the blueshift in favor of any scenario.

The late spectrum's $H\alpha$ line has a much more complicated structure than the early spectrum's. It does not peak at zero velocity anymore, but the peak is blueshifted and there are many sub-peaks. Again, the blueshift might be connected to dust formation or radiative gas acceleration, but other reasons are conceivable as well. At least part of the late $H\alpha$ line's complex appearance might be due to superposition of other spectral lines, e.g. $N \text{ II}$. Apart from that, it is an indication of an inhomogeneous, maybe clumpy, CSM structure, and perhaps asymmetric SN explosion.

The spectra have been compared to template spectra from the Padova-Asiago Supernova Archive (ASA) [298] using the online tool GELATO¹⁷. The algorithm [298] divides a spectrum into 11 relevant bins and averages within the bins to classify and compare with the archived spectra. The PTF12csy spectra have been de-reddened with $E(B - V) = 0.1$ and compared to only Type II SNe. GELATO returned the best 30 matching spectra together with their phases, ordered by quality of fit. The results are listed in Table 7.6. For both the Gemini North spectrum taken at 175 d and the Keck I spectrum from 454 d, the majority of best matching template spectra come from SN 2010jl. The mean phase of

¹⁷ <https://gelato.tng.iac.es>

Spectrum	SN Name	Type	Best QoF	N_{spec}
Gemini N	2010jl	IIn	4.89	20
	1995G	IIn	3.07	3
	1988Z	IIn	2.81	1
	2008es	IIL	2.72	1
	2005gj	IIn	2.72	1
	1988S	IIn	2.65	4
Keck I	2010jl	IIn	7.91	24
	1988Z	IIn	4.00	3
	PTF11kx	IIn-IaCSM	3.16	2
	1987A	II-peculiar	2.94	1

Table 7.6: Results of the GELATO spectral comparison. N_{spec} : Number of spectra among best 30 fits. QoF : quality of fit, as defined in [298], inversely proportional to average deviation between spectrum and template spectrum.

the matching spectra is significantly higher for the Keck I spectrum: (378 ± 102) d, versus (154 ± 21) d for the Gemini N spectrum. However, the reference dates for the spectra are mostly the discovery date, only rarely date of maximum light or explosion date.

7.3.4 Host Galaxy

The galaxy hosting PTF12csy is a faint dwarf galaxy designated SDSS J065832.82+171541.6¹⁸, barely visible in the SDSS DR12 images. Since the galaxy has no catalogued redshift, it is extracted from the spectra. The Keck I spectrum is used due to higher resolution and less SN contribution. Gaussians are fit to the very narrow (FWHM ≈ 5 nm) lines O II at $\lambda = 3727.09$ Å and O III at $\lambda = 4960.30, 5008.24$ Å, resulting in an averaged redshift of 0.0684 ± 0.0001 . This redshift corresponds to a luminosity distance of ~ 300 Mpc, assuming standard cosmology with Hubble parameter $H_0 = 70$ km s⁻¹ Mpc⁻¹, matter density $\Omega_m = 0.3$, and dark energy density $\Omega_\Lambda = 0.7$.

Adopting the luminosity distance from above, the host galaxy has absolute magnitudes of $M_g \approx -16.2$ mag, $M_r \approx -16.6$ mag and $M_i \approx -16.7$ mag¹⁸ (corrected for Galactic extinction). This is slightly fainter than the Small Magellanic Cloud at $M_V = -16.9$ mag [260]. Using the luminosity-metallicity relation from eq. 1 in [299], a metallicity of $12 + \log O/H \approx 8$ is found, indicating that the host galaxy is quite metal-poor. The host galaxy is similar to 2008iy’s dwarf host galaxy ($M_r \approx -13.7$ mag) [260], but brighter and probably less metal-poor.

Overluminous SNe IIn, such as PTF12csy, have been preferentially found to occur in subluminous, low-metallicity dwarf galaxies [260, 280], such as the host of PTF12csy. This is a trend, which is also observed for long GRBs [280]. Statistics are still low and [260] cautioned that there could be some selection bias due to intrinsically bright SNe in faint host galaxies being more easily discovered during surveys doing aperture photometry. However, new surveys performing image subtraction and observing large untargeted fields, e.g. PTF and Pan-STARRS, provide increasing evidence for this trend, as most of the discovered bright objects would have been luminous enough to be detected in bright galaxies and in searches that are targeted to bright galaxies [280]. PTF12csy, probably discovered by coincidence in an unbiased way, confirms this emerging trend as well, suggesting that there is a physical reason

¹⁸ <http://skyserver.sdss.org/dr12/en/tools/explore/summary.aspx?id=0x112d1f06c01f0a28>

connected to the host metallicity.

The SDSS DR12¹⁸ has the host galaxy’s catalogued center position of right ascension 104.636 78° and declination 17.261 58°, about 3'' away from the SN position at right ascension 104.636 43° and declination 17.262 33° (see also Figure 7.3). With an apparent radius of about 2.5'', corresponding to ~3.5 kpc, this is quite far from the center of the galaxy, i.e. about 4 kpc off-center. Hence, one can assume that the SN occurred in the periphery of the host galaxy, in a local environment that might be different from the center or the average within the galaxy.

7.4 Conclusion

7.4.1 Summary

The highest significance alert from the IceCube Optical Follow-Up program led to the coincidental discovery of an interesting and unusual Type IIn SN, *PTF12csy*, which was already at least 169 days old. The combined *a posteriori* significance of the neutrino doublet alert and the coincident detection of any core-collapse SN within the error radius of the neutrino events (0.54°) and within the luminosity distance of the SN (300 Mpc) is 2.3σ , for the time interval of the IceCube data acquisition season 2011/12.

PTF12csy is rare and unusual: With absolute peak magnitudes of $M_r < -19$, perhaps about -20, it belongs to the most luminous SNe. The SN is most likely powered by interaction of the ejecta with a dense circumstellar medium (CSM). The spectrum indicates a complicated structure of the CSM. Its host galaxy is a faint and metal-poor dwarf galaxy, confirming an observed trend for luminous SNe IIn. *PTF12csy* is similar in photometry and spectroscopy to other rare luminous SNe IIn, e.g. SNe 2008iy and 2010jl. The total radiated energy is 2×10^{50} erg within the first 400 rest frame days after detection.

Given the ejecta-CSM interaction, high-energy (HE) cosmic ray production and neutrino emission may be expected on a time scale of 1 months to 10 months, according to [110] and [300], see Section 3.2.7. However, the SN is too far away for IceCube to detect this emission. A complementary neutrino analysis performed offline, using one year of IceCube data, which cover most of the optical SN fluence, did not reveal a signal-like accumulation of neutrino events from the SN’s position, leading to a very high upper limit of more than 1000 times the tested model fluence, owing to the large distance.

Due to the long delay of several months between explosion date and neutrinos, the doublet of neutrinos within less than two seconds cannot be explained by the formation of a jet shortly after core-collapse according to the choked jet model introduced in Section 3.2.8. Nor can it be explained by the expected HE neutrino production from ejecta-CSM interaction of SNe IIn (s.a.). The only reasonable explanation is that the SN detection was coincidental and the neutrino doublet was produced by uncorrelated background events of atmospheric neutrinos and/or mis-reconstructed atmospheric muons.¹⁹

7.4.2 Outlook

As an alternative, non-standard interpretation, it is conceivable that the SN first produced a supramassive neutron star (NS), i.e. a NS with mass above the Oppenheimer-Volkoff limit of ca. $2 M_\odot$ to $3 M_\odot$ (see Section 3.1), which is stabilized by its high spin, but slows down due to magnetic braking. After a certain amount of time, the NS becomes so slow that it collapses to a black hole. Such a model, called “blitzar”, was introduced to explain the phenomenon of Fast Radio Bursts (FRBs) [301]. FRBs,

¹⁹ With a small statistical chance on the order of a few percent that one of the neutrinos is part of the measured diffuse astrophysical flux, see [146].

discovered in 2007 [302], consist of a bright, highly dispersed millisecond radio pulse that is not associated with a known pulsar or gamma-ray burst and does not repeat. The high dispersion suggests that the sources are at cosmological distances, which implies an extremely high radio luminosity [301]. In such a delayed collapse, a jet could form that produces HE neutrinos, leading to a neutrino burst such as the observed neutrino doublet. However, [301] speak of delay times between a few hundred and a few thousand years, even millions of years, instead of few hundred days. Besides, the theoretical details of this model, especially the neutrino production, have not been worked out yet, so this interpretation remains speculative.

The coincidental detection of a Type II_n SN following an IceCube neutrino alert demonstrates the capability of the follow-up system to reveal transient HE neutrino sources. An advantage of the follow-up paradigm is the prompt availability of multi-messenger information for the identification of the source, as well as the mere statistical significance of a coincidence between a neutrino burst and an electromagnetic transient detection. In this case, the significance is very low due to the delay of several months between explosion and neutrinos. However, this coincidence motivates the continuation of the follow-up program, as well as further stacked neutrino analyses of Type II_n SNe.

Analysis of the Optical Data from PTF

In this work, the first 23 IceCube neutrino doublet alerts that have been forwarded to PTF between August 2010 and December 2012 are analyzed. The selection of analyzed alerts follows a change in the PTF DAQ system from the PTF to the iPTF (intermediate Palomar Transient Factory) program, which sets a natural delimiter for the optical data analysis.

8.1 Available PTF Data

Table 8.1 gives an overview of the first 23 IceCube neutrino alerts sent to PTF, see Section 6.2.3 for PTF and 6.6 for the IceCube alerts. Each alert comprises one or several PTF fields that follow-up observations were requested for. The fields are determined by the Madison-based alert server that also sends the alert to PTF (see Section 6.7), based on the fields that are touched by the alert’s error circle. Note that three alerts with IDs 1, 10, and 11 were omitted from the analysis due to erroneous neutrino data. Another alert on 2011–02–25 (IC79 DAQ season) was missed due to a glitch on the dedicated alert server located in Madison. The observability of the sky at the neutrino alert direction from the Palomar Observatory is indicated in Table 8.1, classified as *good*, *medium*, *bad*, or *none*. It represents the impression of the information visualized in Figures E.1 to E.5, which are explained in detail in Appendix E.1. For the PTF data analysis, images taken within 100 days after the neutrino alert are considered. The number of those *new exposures* from within 100 days is indicated in the table for filters *R* and *g* that are in use at the PTF 48-inch telescope (P48). The number of *reference exposures* selected for image subtraction is denoted as well. A reference image is constructed from the reference exposures and subtracted from the new images. Sources brighter than the reference are extracted, so that a SN increasing in brightness becomes visible. See Appendix E.2 for information on the selection of reference images and the data reduction process.

In parentheses, one can find the date of the reference image closest to day 10 after the neutrino alert—thought of as hypothetical maximum light time of a SN exploding at the time of the neutrino alert—in days after the alert. The values for the new and reference exposures refer to CCD 08, one of 12 CCDs covering the P48 field of view (see Figure 7.2), because it is most representative for the majority of CCDs. The values can be slightly different for other CCDs, especially in case of reference exposures, on which selection cuts are applied, see Section 8.2. Only if for some CCDs, no references are available at all or if they were taken shortly after the neutrino alert, it is marked with a footnote.

If the number of reference images is zero, it is marked with *blue color*. No image subtraction and

ID	Alert time (UTC)	Observability	PTF field ID	New exp.		Ref. exp.	
				R	g	$R (\Delta t)$	$g (\Delta t)$
2	2010-08-16 00:07:07	good	{ 2914 3019	8	0	6 (520)	—
3	2010-11-24 21:06:06	medium	4564	6	1	7 (509)	0
4	2010-12-17 13:23:30	medium	{ 3529 3428	3	0	7 (-49)	—
				3	0	7 (-119)	—
5	2010-12-31 01:25:09	good	{ 3923 3828	2	6	7 (343)	7 (1097) ^a
				4	7	7 (-48)	4 (1095) ^b
6	2011-01-25 15:21:09	good	{ 2963 2964	10	0	7 (778)	—
				7	0	7 (336)	—
7	2011-03-03 16:01:27	bad	{ 2820 2925	0	6	—	0
				0	6	—	0 ^c
8	2011-03-26 21:53:41	none	{ 3338 3339	0	0	—	—
				0	0	—	—
9	2011-05-01 15:57:25	medium	3004	0	50	—	3 (4.8) ^d
12	2011-10-24 02:41:11	bad	5023	0	0	—	—
13	2011-12-28 04:01:50	medium	2982	122	0	6 (803)	—
14	2012-01-17 22:01:34	good	3562	16	0	7 (-277)	—
15	2012-02-08 00:14:29	medium	3123	0	0	—	—
16	2012-02-16 06:42:26	bad	{ 2888 2889	0	0	—	—
				0	0	—	—
17	2012-03-03 16:47:21	medium	2820	1	0	7 (-410)	—
18	2012-03-30 01:06:58	good	3455	29	0	7 (730)	—
19	2012-04-25 19:34:56	none	2805	0	0	—	—
20	2012-06-09 00:29:56	good	{ 4785 4717	23	0	7 (-10.6)	—
				24	0	7 (-688)	—
21	2012-09-17 18:08:03	good	2924	40	23	4 (-754) ^e	7 (794)
22	2012-10-23 04:46:15	good	{ 3006 3111	18	0	7 (-782)	—
				45	0	7 (-792)	—
23	2012-12-21 02:17:24	good	3074	2	0	7 (-1015)	—

^a for CCD 00: 3 (2.2); for CCD 07: 0

^b for CCD 00: 3 (2.2); for CCD 07: 0

^c only for CCD 04: 7 (1358)

^d Four CCDs have one, one CCD two ref. exp. taken at $\Delta t = 30$ d.

^e for CCD 01: 7 (1.7); for CCD 11: 7 (1.8)

Table 8.1: The first 23 IceCube neutrino doublet alerts (excluding 1, 10, and 11), sent to PTF between August 2010 and December 2012. The column “New exp.” lists the number of exposures taken within 100 days after the alert, in the R and g filter. The column “Ref. exp.” lists the number of reference exposures available (ideally 7) and Δt is the reference exposure time which is closest to a hypothetical SN maximum 10 days after the neutrino alert, in days after the neutrino alert time. Comments on the observability of the alert position are also included. Note that the numbers refer to CCD 08 of the P48 camera and can be slightly different for the other CCDs.

data analysis can be done in this case. Only for three alerts, this is the case in the g -band, because g observations are less common and reference images are harder to obtain. If at least one of the reference images was taken shortly after the neutrino alert, it is marked with *red color*. This means that there might be contamination from SN light in the reference image, if the SN exploded at the time of the neutrino alert and had a fast rise in brightness. This is the case mainly for one alert, ID 9, where it was decided to use potentially contaminated exposures as references because no other references were available, but there was a large number of new images (50) spread over a large interval of about 90 days. The possible SN contamination is taken care of in the data reduction by doing also negative subtractions, allowing negative changes in brightness (source dimmer than in reference image), so that a fading SN present in the reference image would be visible as well, see Appendix E.2.5.

8.2 Data Reduction

In order to find transient sources in the PTF images, one has to look for changes with respect to a reference image. This is done via *image subtraction*, i.e. the reference image is subtracted from the new (follow-up) image, so that only magnitude differences between the reference and the new image remain. This technique is also known as difference imaging. A high-quality reference image from a long exposure time under good photometric conditions, i.e. small atmospheric seeing and high limiting magnitude, is required (see Addendices B.1 and B.2). It is constructed from several individual exposures that are combined into a single, very deep image. If a reference image could be constructed at the time of the alert, then an automatic pipeline and SN search was running, see Section 8.4.1. However, for 38% of the follow-up fields, this was not the case, so that an independent data reduction pipeline was used, which is described here.

The data reduction occurs in several steps:

1. A reference image is constructed from individual exposures by *co-addition*.
2. The reference image is *subtracted* from the new exposures.
3. In the subtraction image, sources are identified and their properties are *extracted*.

The results are stored in a PostgreSQL¹ database that can be queried to further analyze the extracted sources, called *candidates* because they are potential SNe.

The pipeline that was used for data reduction was provided by Peter Nugent of PTF. It is a collection of bash UNIX shell scripts, invoking several executables that are partly available on the web as free software, partly developed in-house by PTF. In particular, three central pieces of software are used in conjunction to create reference images and to perform image subtraction. These are called SExtractor [303, 304],² SCAMP [305, 306],³ and SWarp [307, 308]⁴ and were written by Emmanuel Bertin. The pipeline and the software components are described in more detail in Appendix E.2. In short, the pipeline works as follows: SExtractor (short for Source Extractor) scans an image for sources and builds a catalog of all found astronomical objects, see Appendix E.2.4 for details. The catalog contains astrometric⁵ and photometric⁶ information on the sources, however the astrometry and photometry are

¹ <http://www.postgresql.org/>

² <http://www.astromatic.net/software/sextractor>

³ <http://www.astromatic.net/software/scamp>

⁴ <http://www.astromatic.net/software/swarp>

⁵ Astrometry is a term for the measurement of the position of astronomical sources, i.e. their coordinates.

⁶ Photometry is a term for the measurement of the brightness of astronomical sources, see Appendix B.2.

not well calibrated. Therefore, SCAMP (Software for Calibrating AstroMetry and Photometry) can be executed on the SExtractor output to derive precise astrometry and photometry, relative to a well calibrated astronomical reference catalog, usually accessed online from a public web server. SWarp is an image stacking tool that reads the SCAMP output. It is capable of background subtraction, resampling and co-addition. SWarp performs the reference image construction, using the output of SCAMP that builds on the SExtractor data, see Appendix E.2.2 for details. The image subtraction (Appendix E.2.3) is done by a software called HOTPANTS [309], after SCAMP and SWarp have provided astrometric alignment of the reference and the new image. The resulting difference image is scanned with SExtractor and the source candidates and their astrometric and photometric properties are extracted.

8.2.1 Machine Learning

On a subtraction image, typically many fake source candidates appear, caused by noise and artifacts. In fact, in PTF, only about 1 in 1000 candidate objects are astrophysically real, i.e. due to a magnitude change beyond the Earth’s atmosphere. Subtraction artifacts or *mis-subtractions* can arise e.g. from imperfect alignment of the two images, edge effects on one or both images, incorrect PSF convolution, CCD array defects, or cosmic ray muons passing through the CCD during exposure [310]. Other spurious sources can be produced by moving light sources passing through the image during exposure, e.g. anthropogenic satellites or minor planets, i.e. rocks moving through the solar system in the vicinity of the Earth. Those sources can be easily discriminated by requiring a source candidate to appear on several exposures in the same and different nights. For the trickier mis-subtractions, quality cuts must be introduced.

For this purpose, a machine learning classification algorithm, called *realbogus* and explained in [310], is applied to each subtraction source candidate, in order to provide a statistical statement about whether a candidate is astrophysically “real” or spuriously “bogus”. The *realbogus* algorithm is a random forest classifier [311], i.e. a collection of decision trees constructed by randomly choosing subsets of the data and of the feature variables (see also Section 6.4). The random forest was trained by PTF members using data that has been classified as real or bogus by twelve human experts. The software providing the machine learning is the *Weka Data Mining Software* [312, 313] implemented in the Java programming language. The machine learning classifier is fed 28 candidate variables from the SExtractor output. See [310, tab. 1] for a complete list of variables.

The output of the algorithm, the machine learning *realbogus* score called *ml* from now on, is a single number between 0 and 1. The higher *ml*, the more likely the candidate is real and not bogus. The score value *ml* is a convenient quality parameter, in which the discriminative power of all input variables is condensed, also taking into account correlations that are difficult to assess using rectangular cuts. The score can be used in a single simple cut. Figure 8.1 shows the normalized distribution of the *ml* score for experimental data (dominated by background, e.g. mis-subtractions) and simulated SN candidates, which were created uniformly across all magnitudes by Chris Frohmaier of the PTF collaboration. From the plot, a cut value of about 0.2 seems intuitive. However, a large number of simulated SNe—especially SNe on bright and therefore close host galaxies, see Figure 8.2—exhibit small *ml* values. As suggested in [310, p. 1185] and by Peter Nugent of the PTF collaboration, it is recommended to use a rather conservative cut value of $ml \geq 0.07$ and perform other selections on groups of associated candidates.

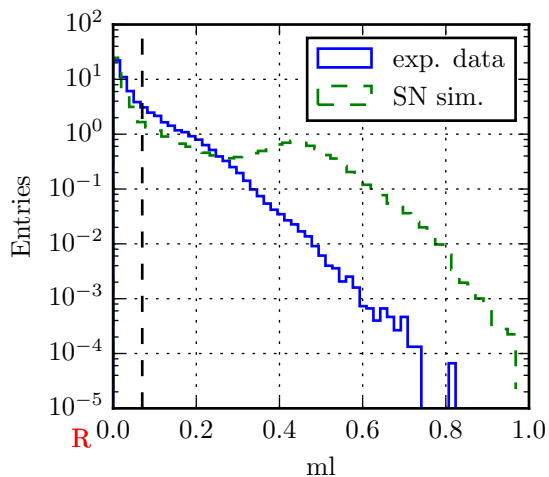


Figure 8.1: Normalized distributions of the realbogus score ml , for experimental data (dominated by background by a factor ~ 1000) and simulated SNe. The cut value at 0.07 is indicated with a vertical dashed line. All candidates were measured with the R filter.

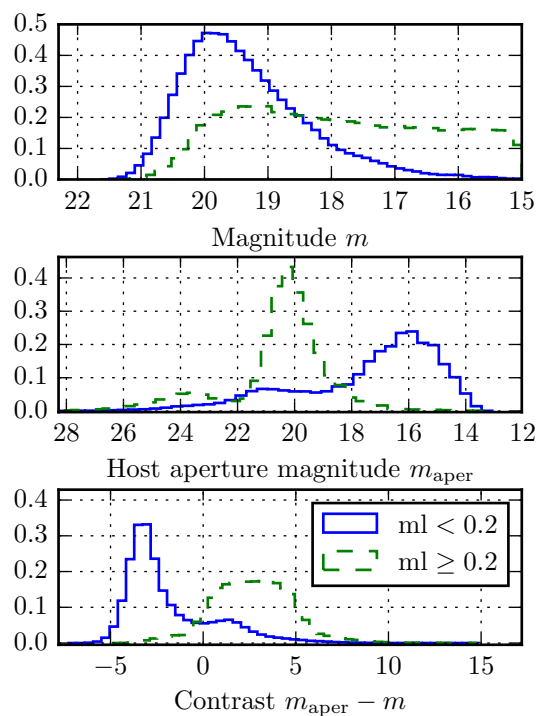


Figure 8.2: Normalized distributions of the candidate magnitude m , the host galaxy aperture magnitude m_{aper} at the candidate position, and the contrast $m_{\text{aper}} - m$, i.e. the magnitude difference between host and candidate. The distributions are plotted for simulated SN candidates, R filter, having ml score below and above 0.2. Candidates with low ml are slightly fainter (higher m), but more pronounced is the host being brighter (lower m_{aper}) and therefore the contrast being smaller.

8.3 SN Detection Algorithm

8.3.1 Candidate Clustering

The image subtraction delivers a total number of 3 054 386 source candidates—1 733 032 positive, 1 321 354 negative—all stored in the analysis DB. Each candidate has an associated position and time of detection. In order to identify SNe, one has to correlate the candidates in space and time. Therefore, candidates are first grouped into spatial *clusters* of candidates. A candidate cluster contains all the candidates whose positions on the sky are so close that they can be considered to belong to the same object. For this purpose, it is looped over all candidates in the DB. For each candidate, neighboring candidates that lie within a radius of $3''$ are selected and merged with the candidate into a single cluster. The radius of $3''$ takes into account the typical seeing conditions determining the size of the point spread function (PSF) of the telescope, i.e. the typical angular distance that two objects must have to be distinguished as separate objects, see Appendix B.1. If a neighboring candidate already belonged to another cluster, the clusters are merged into a single cluster. The clustering delivers in total 208 505 clusters containing two or more candidate detections, from all of the 29 analyzed follow-up fields from 20 follow-up alerts.

The clusters are then analyzed further, e.g. they are cross-checked with catalogs and their light curve is investigated, in order to identify potential SNe and dismiss noise or background clusters.

8.3.2 Cross-Check Catalogs

For each of the clusters, catalogs of astronomical objects are queried for all objects located within 5'' from the average cluster position. The information about these objects is stored in the candidate DB as well. The catalogs used in this analysis are:

1. **SDSS:** The Sloan Digital Sky Survey (SDSS) [243, 244, 246, 314] is a wide-field survey carried out from 2000 to 2014 with a 2.5 m diameter telescope located at the Apache Point Observatory, New Mexico, USA. SDSS uses the SDSS filters u , g , r , i , z in mostly the visible spectrum, with central wavelengths that cover the range of 3500 – 9300 Å. SDSS is a vast source of information about in total ~470 million astronomical objects, of which ~260 million are classified as stars and ~210 million as galaxies [315]. It also contains 5.3 million spectra. However, it does not cover the full sky, but only roughly 1/3 of it. The SDSS relational database can be accessed online via HTTP/GET requests using SQL (Structured Query Language) queries, a common way to interact with relational databases.
2. **2MASS:** The 2-Micron Sky Survey [316] is an infrared survey covering 99.998 % of the sky, with data collected between 1997 and 2001 with two dedicated 1.3 m diameter telescopes located at Mount Hopkins, Arizona, and Cerro Tololo, Chile. The filters are in the near infrared and are called J (1.25 μm), H (1.65 μm), and K_s (2.16 μm). The 2MASS catalog contains 471 million extracted point sources (which can be stars or unresolved galaxies) and 1.6 million extended sources, i.e. galaxies. Similar to SDSS, the 2MASS catalog, hosted at the IPAC, can be queried online via HTTP/GET requests. 2MASS does not provide as much detail as SDSS, but covers the full sky.
3. **AGN catalogs:** The MPA Garching Active Galactic Nuclei (AGN) Catalogue [317, 318] was downloaded from [318] and loaded into the analysis DB. It is based on the SDSS Data Release 4 and contains 88 178 emission line galaxies that are classified as AGN as described in [317]. Another AGN catalog stored on the PTF DB server was copied to the analysis DB as well. It was also constructed from SDSS data, but contains only 5553 entries, of which 640 are also contained in the MPA Garching catalog.

8.3.3 Light Curve Fitting

For the selection of potential SN clusters, the photometric data or light curve (LC), i.e. the magnitude as function of time, is checked for consistency with a SN light curve. For this purpose, two functions are fit to the photometry: a model SN light curve and a flat, i.e. constant, function. This is motivated by the observation that most noise clusters have a light curve consisting of fluctuations around a constant magnitude, without any evolution. The ratio of the goodness of the two fits yields the *goodness ratio* g . Here, the reduced χ^2 , χ^2/n_{dof} , is used as goodness of fit, with the number of degrees of freedom n_{dof} (equaling the number of data points minus the number of fit parameters) and

$$\chi^2 \equiv \sum_i \frac{(x_i - x_{\text{model},i})^2}{\sigma_i^2} \quad (8.1)$$

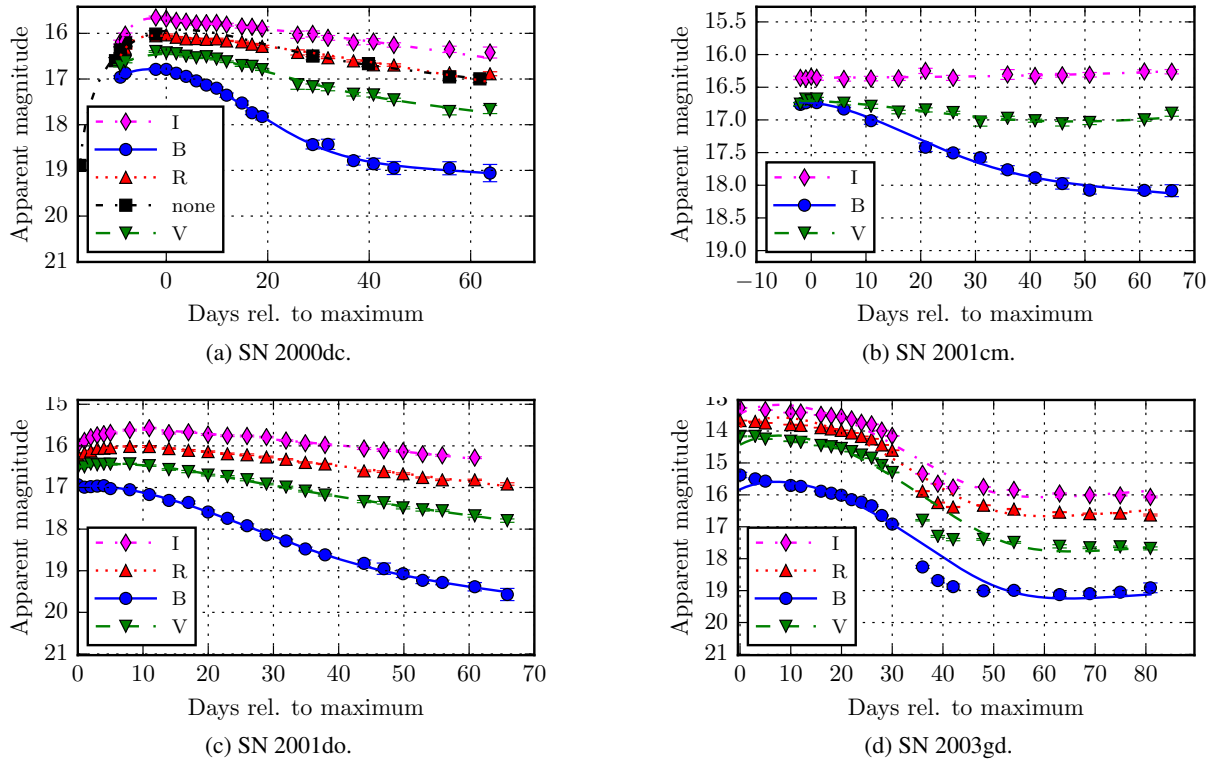


Figure 8.3: Example LCs of CCSNe in the SNDB [320] (all type II), with the LC fit applied. The filter names are printed in the legend. The black squares (filter “none”) indicate unfiltered photometry.

where x_i and σ_i are the LC magnitude and its error and $x_{\text{model},i}$ is the magnitude value of the best fit model. Then, g is defined as

$$g = \frac{\chi_{\text{flat}}^2 / n_{\text{dof}}^{\text{flat}}}{\chi_{\text{SN}}^2 / n_{\text{dof}}^{\text{SN}}}. \quad (8.2)$$

The goodness ratio g is larger for LCs that are inconsistent with a flat function (flat reduced $\chi^2 \gg 1$), but consistent with a SN LC (SN reduced $\chi^2 \approx 1$). For LCs that are also consistent with a flat function, g is close to or smaller than unity (flat reduced $\chi^2 \approx 1$, SN reduced $\chi^2 \geq 1$). This means that either the cluster is not an SN or the data are too noisy to identify it as an SN. The goodness ratio g is used as a cut parameter later on. The method was developed by the thesis author without knowledge of Taylor et al. (2014) [319], where a very similar method is used and a *flatness score* is defined as $\chi_{\text{SN}}^2 / (\chi_{\text{SN}}^2 + \chi_{\text{flat}}^2)$.

The SN model LC for the fitting is adopted from a paper by Cowen, Franckowiak & Kowalski (2009) [321] who used models by Waxman et al. [322] and Arnett [78] to fit early CCSN light curves. The model LC is expressed in terms of bolometric luminosity L (total radiated energy per time in units

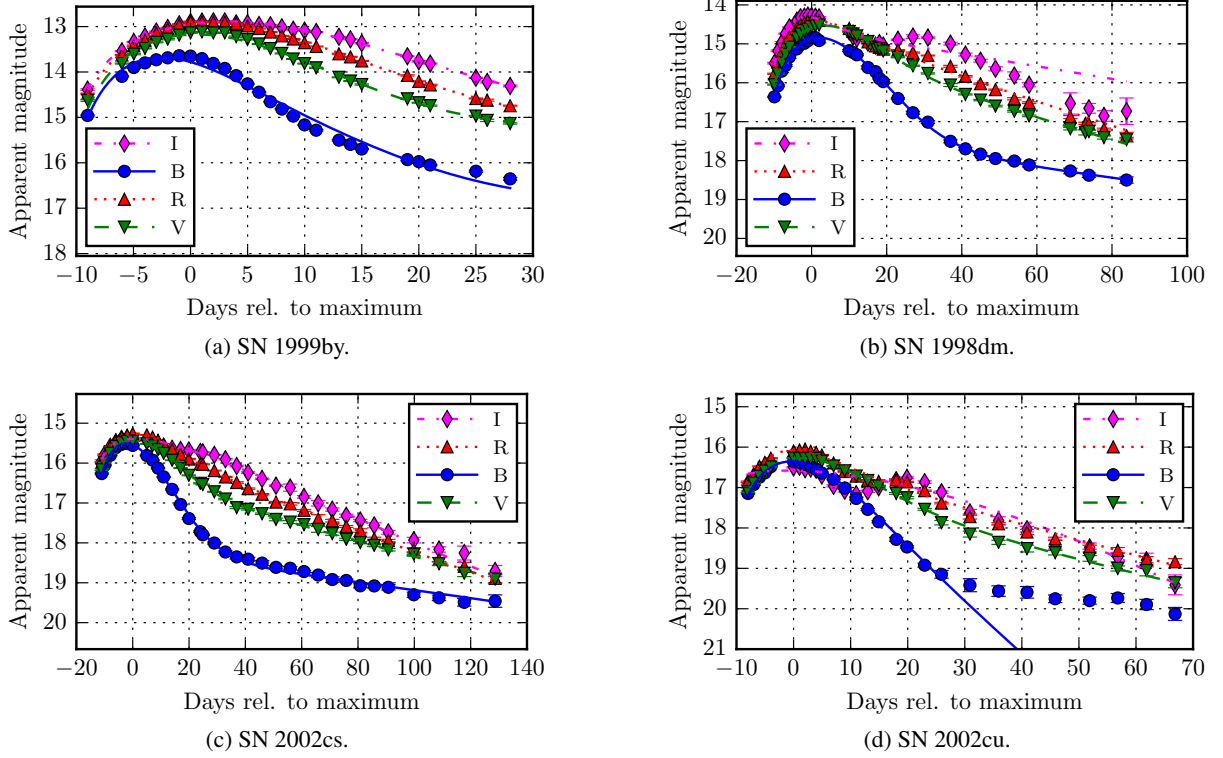


Figure 8.4: Example LCs of SNe Ia in the SNDB [320], with the LC fit applied. The filter names are printed in the legend.

of erg s^{-1}) as function of time t as

$$L(t) = L_{\text{sbo}}(t) + L_{\text{exp}}(t) \quad (8.3)$$

$$L_{\text{sbo}}(t) = \frac{L_0}{\exp(a_2(t - t_0)^{0.5}) - 1} (t - t_0)^{1.6} \quad (8.4)$$

$$L_{\text{exp}}(t) = \epsilon_{\text{Ni}} M_{\text{Ni}} \exp\left(-\frac{(t - t_0)^2}{\tau_m^2}\right) \int_0^{(t-t_0)/\tau_m} \exp\left(z^2 - z \frac{\tau_m}{\tau_{\text{Ni}}}\right) 2z dz \quad (8.5)$$

and consists of the shock breakout component $L_{\text{sbo}}(t)$ from Waxman et al. [322] and the expansion phase component $L_{\text{exp}}(t)$ from Arnett [78]. The LC approximation during the shock breakout phase comes from the assumption of a black body radiating at a fixed wavelength. The relations of SN radius $R \propto \delta_t^{0.8}$ and temperature $T \propto \delta_t^{-0.5}$ from [322] with $\delta_t = (t - t_0)$ lead to Equation 8.4, with L_0 (related with R), a_2 (related with T) and explosion time t_0 as free parameters. The LC approximation during expansion phase is based on the assumptions of homologous expansion, radiation pressure dominance, and the presence of the decaying radioactive isotope ^{56}Ni in the ejected matter, which is assumed to be the sole energy source. The parameter $\epsilon_{\text{Ni}} = 3.9 \times 10^{10} \text{ erg s}^{-1} \text{ g}^{-1}$ (adopted from [285]) is the radiative energy released per decaying unit mass of ^{56}Ni and $\tau_{\text{Ni}} = 8.8 \text{ d}$ [285] is the mean lifetime of ^{56}Ni and is related with half-life $t_{1/2}$ via $\tau_{\text{Ni}} = t_{1/2} / \ln(2)$. The nickel mass M_{Ni} , the time scale τ_m of the LC, and the explosion time t_0 are free parameters.

In order to be fitted to the experimental data, the luminosity L_0 and nickel mass M_{Ni} are replaced by

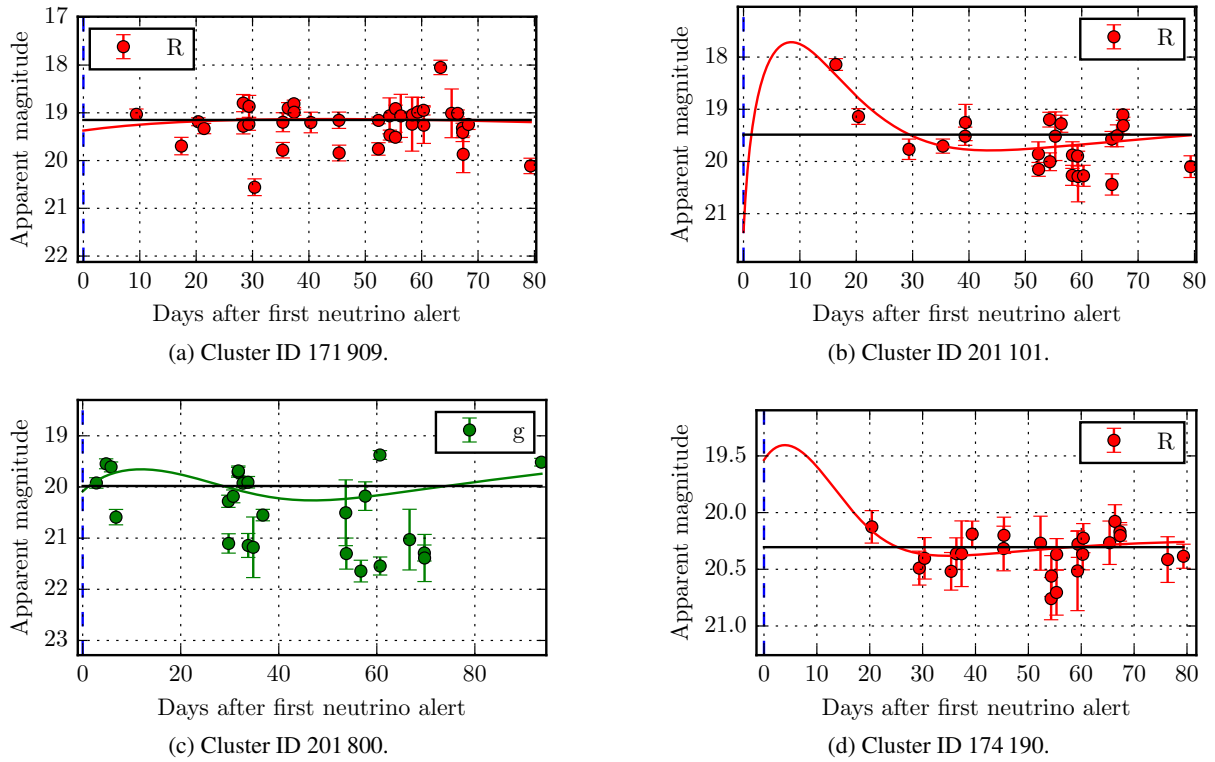


Figure 8.5: Some typical background LCs of clusters of sources in the PTF optical data.

the normalization parameters a_1 and a_3 and the model SN LC is converted into magnitudes. The model LC has in total five parameters ($a_1, a_2, a_3, \tau_m, t_0$) that are allowed to vary freely during the fit. The method of least squares is used, i.e. the squared difference between data and model points, as defined in Equation 8.1, is minimized while varying the parameters of the model. The same is done for the flat fit. Before the fit is applied, the LC is averaged within bins of 0.1 days (2.4 hours) width. This is justified by the fact that SNe evolve on much longer timescales and the LC fit function is unable to describe such rapid fluctuations.

To assess if the LC fitting works, the UC Berkeley SNDB [320], a database of real SN LCs assembled by the Alexei Filippenko group at UC Berkeley, was downloaded.⁷ The data were mostly collected at the Lick and Keck observatories with the Johnson-Cousins $BVRI$ filters [323]. The SNDB contains 2147 core-collapse SNe (CCSNe, i.e. SN Types Ib, Ic, Ib/c, II) and 3015 SNe Type Ia. However, only a small fraction of the SNe have associated photometry: 33 CCSNe and 167 Ia SNe. Each of these SNe has photometry in multiple filters, resulting in 144 CCSN and 668 SN Ia light curves. By studying CCSN LCs, suitable initial values of the LC fit were derived. The LC fit performs well on most LCs from the SNDB. Figures 8.3, 8.4, and 8.5 show example LC fit results.

Most CCSN LCs are fitted with satisfying accuracy, like the examples in the left column of Figure 8.3. Plateau SNe, which feature a flat LC part followed by a sudden drop, are not described by the LC model. Hence, the fit result is of limited accuracy, as seen in Figure 8.3d. However, the sudden drop causes the flat fit to perform weaker. Consequently, the goodness ratio g is relatively high even if the SN LC fit

⁷ From <http://hercules.berkeley.edu/database/phpMyAdmin/>. Access date was 2015-02-06, the site has since moved to <http://heracles.astro.berkeley.edu/sndb/> and the public interface has been changed from phpMyAdmin to a self-written web application.

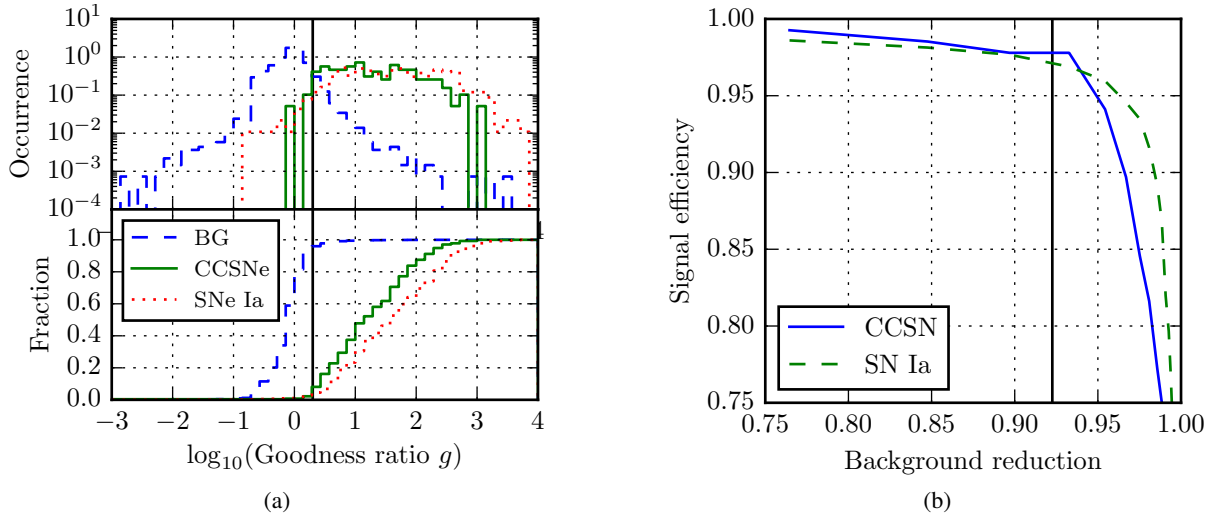


Figure 8.6: (a) Histogram of the goodness ratio g derived from fits to the LC, for dominantly background LCs and real SN LCs from CCSNe and SNe Ia. The position of the chosen cut value of $g \geq 2$ is indicated with a black vertical line. (b) The receiver operating characteristic (ROC) curve, i.e. the fraction of signal retained by the cut on g versus the fraction of eliminated background. The ROC curve is constructed by evaluating the signal and background efficiency for various values of the g cut. The background reduction achieved by the chosen cut value of $g \geq 2$ is indicated with a black vertical line.

has large deviations. More problematic are plateau SNe, for which only data from within the plateau are available, e.g. the I filter LC in Figure 8.3b. These are hard to identify as a SN—especially if the magnitude error is large and thus data quality too low—since they do not present enough photometric evolution and could be a constant source as well. A better LC model would not help in this case.

SNe of Type Ia can be fitted with the LC model as well, even though they are not a target of this study because they are not expected to emit a high-energy neutrino flux. The fit works especially well for the bulge of an early SN Ia LC, see left column of Figure 8.4. Some LCs have a double-peak structure, on which the fit fails, see Figure 8.4b. There can also be problems with a flattening of the LC after the bulge, see Figure 8.4d. But as for CCSNe, even for these failing fits, in most cases g is significantly larger than 1.

In Figure 8.5, a few typical background LCs are plotted with the result of the LC fit as a curve and the result of the flat fit as a horizontal line. It is clear that there is no evolution in the LCs (except maybe Figure 8.5b), but just random fluctuations around a certain average level. Therefore, the goodness ratio g is often close to 1 or below.

Figure 8.6 shows the performance of the goodness ratio g as a cut parameter to separate real SN LCs from background LCs. Because of the low signal to background ratio of $\sim 1 : 1000$ [310] in the sources extracted from the PTF data, a subsample of 10 000 source clusters of the total 208 505 clusters is used as background LCs in Figure 8.6. The signal LCs for CCSNe and SNe Ia are the 144 non-Ia and 668 Ia LCs from the SNDB. A clear separation of signal and background is provided by g . A cut of $g \geq 2$ was chosen for this study, indicated as black vertical line in Figure 8.6. It cuts away $\sim 92\%$ of the background clusters, while only 2.2% of CCSNe and 2.8% of SNe Ia are lost.

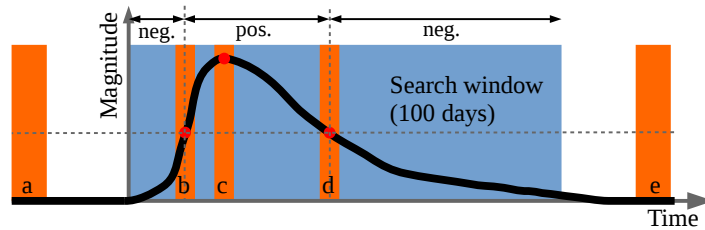


Figure 8.7: A hypothetical SN light curve (LC) and illustration of reference image contamination with background light. If the reference images (whose time of exposure is indicated with an orange box) were taken either long before or after the SN explosion (case labelled a or e), then the SN LC is always positive. In case c, reference taken at maximum, the LC is always negative. In the general case of contamination, case b or d, the LC should be first negative, then positive, then negative—as indicated with arrows and labels at the top.

8.3.4 Cuts on Candidate Clusters

There are various sources of background or noise clusters that need to be filtered out for finding SNe. Those bogus clusters can be the result of mis-subtractions, as discussed above, a minor planet, e.g. an asteroid, stars of varying magnitude, so-called *variable stars* or short VarStars in the following, or *active galactic nuclei* (AGNs) that sometimes pass into a flaring state of increased brightness. In order to discriminate these bogus clusters from SNe, a series of cuts is applied to the clusters, chosen after discussions with Peter Nugent of the PTF collaboration:

1. **Cluster size:** The cluster is required to contain at least 5 candidates with a good subtraction quality, i.e. a ml score value of 0.07 or more (see Section 8.2.1). This is to reject minor planets that are only present (at the same position) during one night and mis-subtractions that are of poor quality. It also ensures that there are enough data points to fit the light curve and interpret it.
2. **Negative subtractions:** If more than 1 candidate in the cluster comes from a negative subtraction, then the cluster is rejected. This cut is motivated by a study by Peter Nugent (Frohmaier et al. in preparation) on the first 1200 SNe found by PTF. Transient sources that flare, e.g. VarStars and AGNs, go up and down in brightness on a short time scale and thus appear as both a positive and a negative source. However, this is not the case for SNe. For the images whose reference image might contain SN light contamination⁸ (see Section 8.1, Table 8.1), the algorithm is more complicated, see Figure 8.7. For these, three cases are accepted, designed to select rising and declining SN light curves: (1) cluster entirely positive (tolerating 1 negative candidate), i.e. case a/e in Figure 8.7; (2) cluster entirely negative (tolerating 1 positive candidate), i.e. case c in Figure 8.7; (3) cluster first negative (tolerating 1 positive), then positive (tolerating 1 negative), then negative (tolerating 1 positive candidate), i.e. case b/d Figure 8.7. Other (random) patterns of negative and positive subtractions are rejected.
3. **Catalog veto 1:** If a star from one of the catalogs has good photometry and is located within 5'' of the average cluster position, then the cluster is rejected because it is very likely to be a VarStar. Likewise, if a cataloged AGN is within 5'' from the cluster, it is rejected as being very likely an AGN flare.

⁸ Namely: PTF field 2924, CCD 01, filter R; 2924, 11, R; 3004, all CCDs, g; 3828, 00, g; 3923, 00, g.

Cut Level	0	1	2	3	4	5	6
Cut Name	Initial	Cluster size	Neg. sub.	Catalog veto 1	Interval	Catalog veto 2	LC fits
Clusters	208 505	36 354	12 397	5407	5292	5036	790 (378)
Cut strength	-	83%	66%	56%	2%	5%	84% (92%)

Table 8.2: Overview of the SN detection algorithm cut procedure with the number of clusters (SN candidates) remaining after each cut and the cut strength, i.e. the fraction of clusters removed by the cut.

4. **Time interval:** The cluster is required to span a time interval of at least 2 days. This is again to reject minor planets, but also because a shorter interval does not allow to see a rise or decay of a SN light curve.
5. **Catalog veto 2/magnitude change:** The cluster is rejected if both of the two following conditions are true:
 - **Catalog veto 2:** Any cataloged object is located within 1'' from the cluster's average position.
 - **Magnitude change:** The cluster encompasses a change in magnitude of less than 0.5 (in any direction) between the minimal and the maximal magnitude.

The motivation of this cut is that a cluster located very close to a galactic center is very likely the result of bad subtractions or of some variability in the galactic nucleus. The second criterion of magnitude change weakens the first criterion so that a SN with a rising or declining light curve is not missed, even if it happens to be very close to the galaxy's center.

6. **LC goodness ratio:** As detailed in Section 8.3.3, The ratio g of the reduced χ^2 of the two LC fits—the SN LC and the constant LC—is required to be at least 2. Therefore, noise clusters that are on average constant are rejected, while objects with a SN-like development in the LC are preferred. As a side effect, plateau-like SN LCs with no apparent evolution can be rejected as well. If the fit fails, then the cluster is kept for manual investigation as a safety precaution.

After applying the six cuts to the 208 505 initial clusters, 790 potential SN clusters remain for the more detailed manual analysis, see following Section. Details on the cut procedure can be found in Table 8.2. The strongest cuts, meaning that they remove the highest fraction of clusters, are the cut on the cluster size and on the LC goodness ratio (on the LC fits). The numbers in bracket for the goodness ratio cut are the values obtained when fit failures are not accepted. Almost all of the fit failures are bogus clusters with just enough detections to pass the other cuts, but less than 5 after LC binning. Yet, it was decided to spend the extra effort and also investigate those clusters (more than 50% of all) further. In retrospect, one can say that 14 of 30 potential SNe and one of two unambiguous SNe would have been missed if failed fits were rejected (see Section 8.4).

8.3.5 Manual Investigation of Clusters

The remaining 790 potential SNe must be investigated manually by eye. The cuts explained in the previous section served only to reduce the SN candidate clusters to a number that is manageable by a human scanner. In spite of the efforts to automatically remove background sources—such as mis-subtractions, minor planets, and VarStars—the final decision on the nature of a source is very subtle and is hard to automate completely.

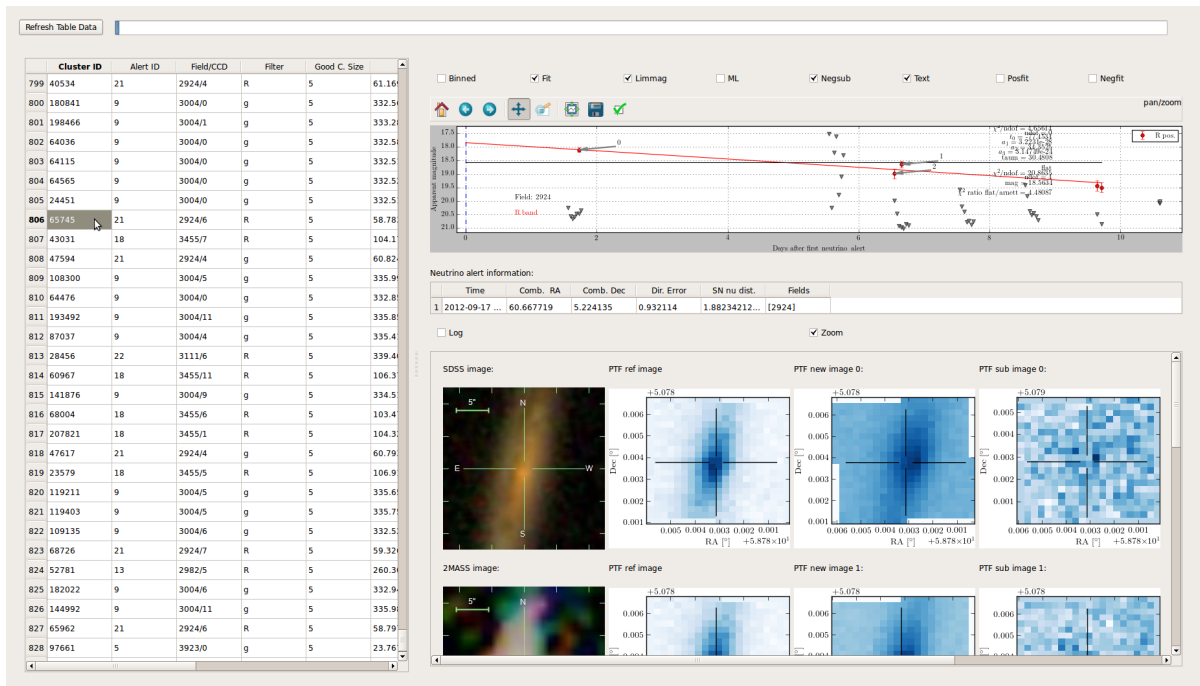


Figure 8.8: Screenshot of the Python Qt4 application written to facilitate the SN analysis.

Some intuition and experience is required for a successful source classification and there is an element of subjectivity and potential bias in the manual investigation that cannot be avoided completely. Probably the best approach is to employ several human scanners to average out subjectivity and get a majority vote. However, these human resources were not available and only the thesis author himself scanned the data.

For the purpose of manual checking, a small application was written by the thesis author, see the screenshot in Figure 8.8. It displays all relevant information about the clusters in a table in the left panel. Upon clicking on a table row, the right panel displays the light curve, information on the neutrino alert, and zoomable cutouts of the CCD images (new, reference, and subtraction) along with cutout images from the SDSS and 2MASS catalogs.

After closer looks at the data and comparison with known SNe, known stars and known galaxies, the following criteria were defined in order to get more uniform classifications and reduce bias as much as possible:

1. **Subtraction images:** Are the subtractions bogus? A clean subtraction of a source is characterized by a more or less circular bright spot on top of a constant background. For most bogus sources, there is no real source visible in the subtraction images, only random noise, leading to random detections. Reasons for this include irregularities at the CCD edge, fringe patterns,⁹ or star spikes.¹⁰ The cluster is then classified as *artifact*. Table 8.8 shows an example of an artifact.
2. **Host:** Is the host a star? If it looks like the source sits on top of a stellar source (one that is not in the catalogs, so it was not vetoed), then it is unlikely to be a SN and is discarded as

⁹ Fringe patterns are caused by interference of the light with internal reflections at thin layers of the CCD [149, p. 97].

¹⁰ Bright stars in astronomical images are characterized by cross-shaped spikes extending far out. These are of course no physical structures in space, but are caused by diffraction of light in the telescope, e.g. at the mount of the secondary mirror [69, p. 55].

VarStar. The distinction between a star and a small, perhaps unresolved, galaxy can be difficult, if not impossible. If SDSS data are available, it is easier to distinguish (but then, stars are usually already excluded by the SDSS catalog veto). Using only PTF and 2MASS data, mis-classification is expected to be more common.

3. **Proximity to center:** Is the source close to the center of the object visible in the reference image? Then, it is possible that the source is an *AGN*, but it can be a *SN* as well.
4. **LC shape:** Are there big jumps in magnitude over a very short period of time (e.g. much less than a day) that are not consistent with the magnitude errors? Such strong short-time variability is not expected from a *SN*. Also, if the source gets dimmer (like a fading *SN*), but then rebrightens, it is unlikely (even though not impossible) that the source is a *SN*.
5. **Non-detections:** Are there exposures, which have good limiting magnitude, but there are no source detections—in spite of detections before and/or after? If so, then this source cannot be a *SN*, since a *SN* does not fluctuate enough to suddenly disappear (and reappear). This criterion easily reveals the majority of clusters as bogus and is probably most easily exploited in an automatic algorithm. However, one has to be careful not to discard a *SN* with non-detections before or late after explosion. Also, if the source is close to the detection limit, it can happen that there are some non-detections, in spite of the average limiting magnitude suggesting detectability. Common sense must be applied considering the difference between limiting magnitude and magnitude and the number of allegedly missing detections. Therefore, it was decided not to introduce an automated cut on non-detections.

These criteria are exclusive: If one or more are true (except for (3), center proximity), then it is unlikely that the cluster is a *SN*.

Section 8.4 presents the results of the search for SNe in the neutrino follow-up images. For an interpretation of the result, it is of importance to estimate the background expectation. That means, one needs to know the frequency of SNe found in random coincidence with a neutrino alert. The efficiency of the PTF data reduction and the *SN* detection algorithm presented in this section is a crucial ingredient for that. It was estimated with a Monte Carlo (MC) simulation that is covered in Section 8.5.

8.4 Search Results

The data from the PTF neutrino follow-up were reduced, as explained in Section 8.2, and analyzed for SNe, as explained in Section 8.3. In particular, Section 8.3.4 explained what automatic cuts were applied to the light curve (LC) data. In Section 8.3.5, criteria for the manual classification of remaining *SN* candidates, based on the CCD and catalog images and LC data, were defined. These exclusive criteria are (1) subtraction images look bad, (2) host seems to be a star, (3) proximity to center, (4) LC suggests flaring variability, (5) too many non-detections.

For the most *optimistic SN selection*, the decision hierarchy is as follows: If (1) is true, then the cluster is classified as *artifact*. If (2) is true, then it is classified as *VarStar*. If (3) is true and one of (4) and (5), then it is classified as *AGN*. If (3) is false and one of (4) and (5) is true, then it is classified as *artifact*. If neither is true, then the *SN* nature cannot be excluded and the source is classified as *SN*.

Sometimes, the quality of the subtractions is questionable, even though the CCD images look good enough to not qualify them as bad. This was marked with a dedicated comment, e.g. if there appears another bright source next to the *SN* candidate or if the reference image might be spoiled. A more *cautious SN selection* removes the candidates that have such a comment.

	No. of Artifacts	No. of VarStars	No. of AGNs	No. of SNe
optimistic	717	16	27	30
cautious	734	15	19	22
pessimistic	717	16	51	6
cautious pessimistic	734	15	39	2

Table 8.3: Resulting numbers of found objects depending on the qualitative level of confidence, as defined in the text.

Most potential SNe are close to the center of a small, probably very distant, host galaxy. Unfortunately, without spectroscopic information it is very difficult, if not impossible, to reliably differentiate between a SN on a small host, an AGN flare, and a VarStar. Therefore, it is possible that some or all of the SN candidates close to the center of the host are either an AGN or a VarStar. A *pessimistic SN selection* uses the decision from the optimistic selection, but classifies all clusters as AGN where the center proximity criterion (3) is true.

A fourth, *cautious pessimistic SN selection* is as the pessimistic selection from above, but also classifies the questionable cases from the cautious SN selection as artifacts. Table 8.3 presents the resulting number of artifacts, VarStars, AGNs, and SNe for the four different qualitatively defined levels of confidence: optimistic, cautious, pessimistic, and cautious pessimistic. The number of found SNe varies from 30 for the optimistic to only two for the cautious pessimistic selection, where the SN is clearly visible in the new images on top of the disk of the host galaxy (see Tables 8.5 and 8.6). The arithmetic mean of the four selections is 15.0 ± 11.4 SNe and may serve as the best possible estimator for the number of SNe in the PTF follow-up data.

The two unambiguous SNe from the cautious pessimistic selection are presented in Tables 8.5 and 8.6, which shows information about the alert, the SN position, cutouts of the PTF CCD images, the catalog images from SDSS and 2MASS and the light curve averaged over 0.1 days bins. The same information is given in Table 8.7 for a likely SN from the optimistic/cautious sample, which might be an AGN as well. Finally, Table 8.8 shows a typical case of an artifact cluster without evidence for an SN (without light curve binning).

8.4.1 Comparison with Automatic Pipeline

In addition to the SN search performed for this thesis, there exists an automatic pipeline at PTF for the routine discovery of transient objects [225]. The original plan of the optical follow-up program with PTF was to make use of this automated pipeline for the rapid identification of a potential neutrino counterpart and the possibility to react, e.g. by requesting spectra for interesting SN candidates.

The problem of this approach was that the automatic pipeline was available only for a subset of the neutrino alerts. Because the automatic pipeline requires a reference image to be available, it cannot be executed if there is none. For the alerts analyzed in this work (see Section 8.1), for 11 of the 29 follow-up fields, no reference image was available at the time of the alert, because PTF had never taken an image of the field before. This means that for 38% of the fields, the automatic pipeline could not run and the follow-up data was not analyzed for potential SN counterparts to the neutrino burst. This circumstance motivated the use and development of an independent pipeline and SN search as explained in Sections 8.2, and 8.3. For the independent pipeline, new observations late after the neutrino alerts were scheduled in order to produce the missing reference images.

The results of the automatic pipeline are compared to the results of this work using a list of all

PTF name	SN type	Cluster ID	Found?	Comment
10ysx	II	89 903	No	Is within 1'' from a catalog source and varies less than 0.5 mag.
10abhm	Ia	125 275	Yes	See Table 8.6.
11bnf	Ia	165 658	No	Has 2 negative subtractions.
12csy	IIn	10 344	No	Did not pass goodness ratio cut, see Section 8.4.2.
12fjx	Ia	147 520	Yes	See Table 8.5.

Table 8.4: The five SNe found in the follow-up fields by the automatic PTF pipeline. The PTF-internal name is given, as well as the cluster ID assigned in the independent offline pipeline described in the thesis. It is indicated if the SN was detected in the independent pipeline and, if not, why it was not detected. The two detected SNe can be investigated in the table given in the comment.

automatically identified PTF transients and the PTF web interface providing more information. Of all identified transients in any of the follow-up fields, only five transients were classified as SNe by PTF and have at least one detection in the 100 day window after the neutrino alert. They are listed in Table 8.4. Two SNe were also found in the independent pipeline and are shown in Tables 8.5 and 8.6. Three SNe were not detected: one because it did not pass catalog veto 2, one because it had two negative subtractions, and one because it did not pass the goodness ratio cut. All of these failure reasons are likely if the SNe are of old age, which they were. Three SNe are SNe Ia, thus they are no likely high-energy neutrino sources. Only 12csy (IIn) and 12fjx (Ia) were first detected in the 100 day window after the neutrino alert, whereas the others exploded before the neutrino alert and had already been detected before. So, 12csy is the only promising SN detection from the automatic PTF pipeline, which is why it was the only source that further follow-up and spectral observations were requested for. Chapter 7 is dedicated to (PTF)12csy. The reason it went undetected in the independent pipeline and SN search algorithm is explained in the next section.

8.4.2 The Case of PTF12csy

The most promising optical follow-up SN detection from the automatic PTF pipeline is PTF12csy, which is extensively covered in Chapter 7. Curiously, it was not detected by the independent pipeline and SN detection algorithm developed in this chapter. The reason is that the light curve of 12csy (see Figure 8.9) is so flat that the goodness ratio g , while larger than 1, has a value of 1.49 and is thus below the cut value of 2. As mentioned above, the goodness ratio cut is developed for early SN light curves that rise or decline significantly. Because the SN is very old, at least about 160 days, the light curve decays rather slowly. In this particular case, more follow-up data, e.g. from the P60 telescope, exist for a much larger time range, see Figure 7.10. If these data would have been included in the LC fit, it would have been clearly identified as a SN, despite of its old age. However, over the rather short range of about 30 days in the P48 PTF survey data, there is no significant evolution.

In a more a posteriori approach, one could have chosen the goodness ratio cut such that 12csy is included in the sample, i.e. 1.49 or lower. If one would have done so, then the number of SN candidates to manually investigate would have grown from 790 to at least 1022. If rejecting LC fit failures, at least 610 candidates would have remained for manual investigation.

Cluster ID	PTF alert	Alert date (UTC)	Field/CCD	RA [°]	Dec [°]	GCS
147 520	20	2012-06-09 00:29:56	4717/11	241.07076	47.30266	20

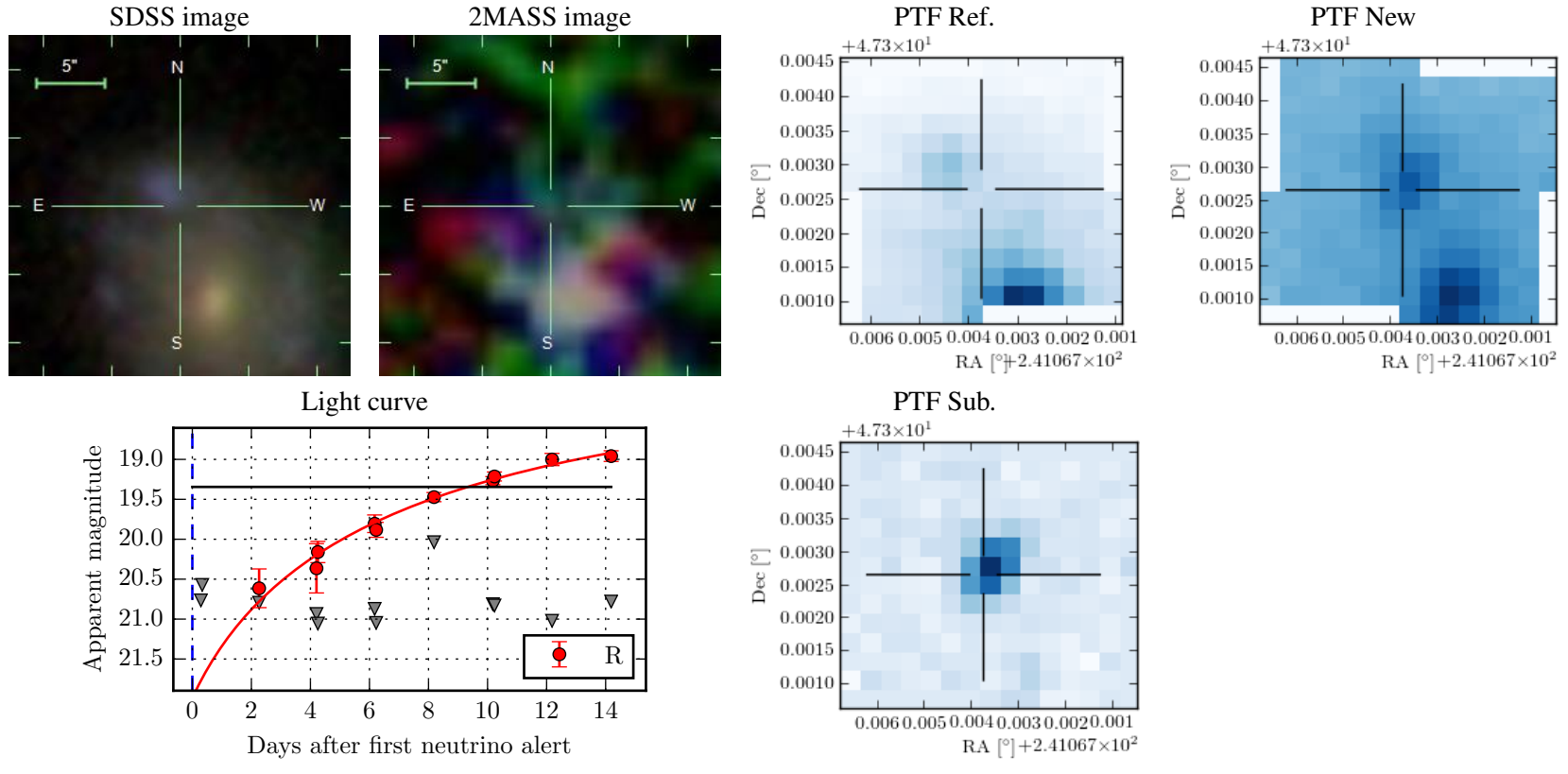


Table 8.5: One of the two unambiguous SNe found in the PTF follow-up data. GCS is the *good cluster size*, i.e. the number of exposures in the cluster, which have a machine learning score of 0.07 or more (see Section 8.2.1). Limiting magnitude is visualized by grey triangles.

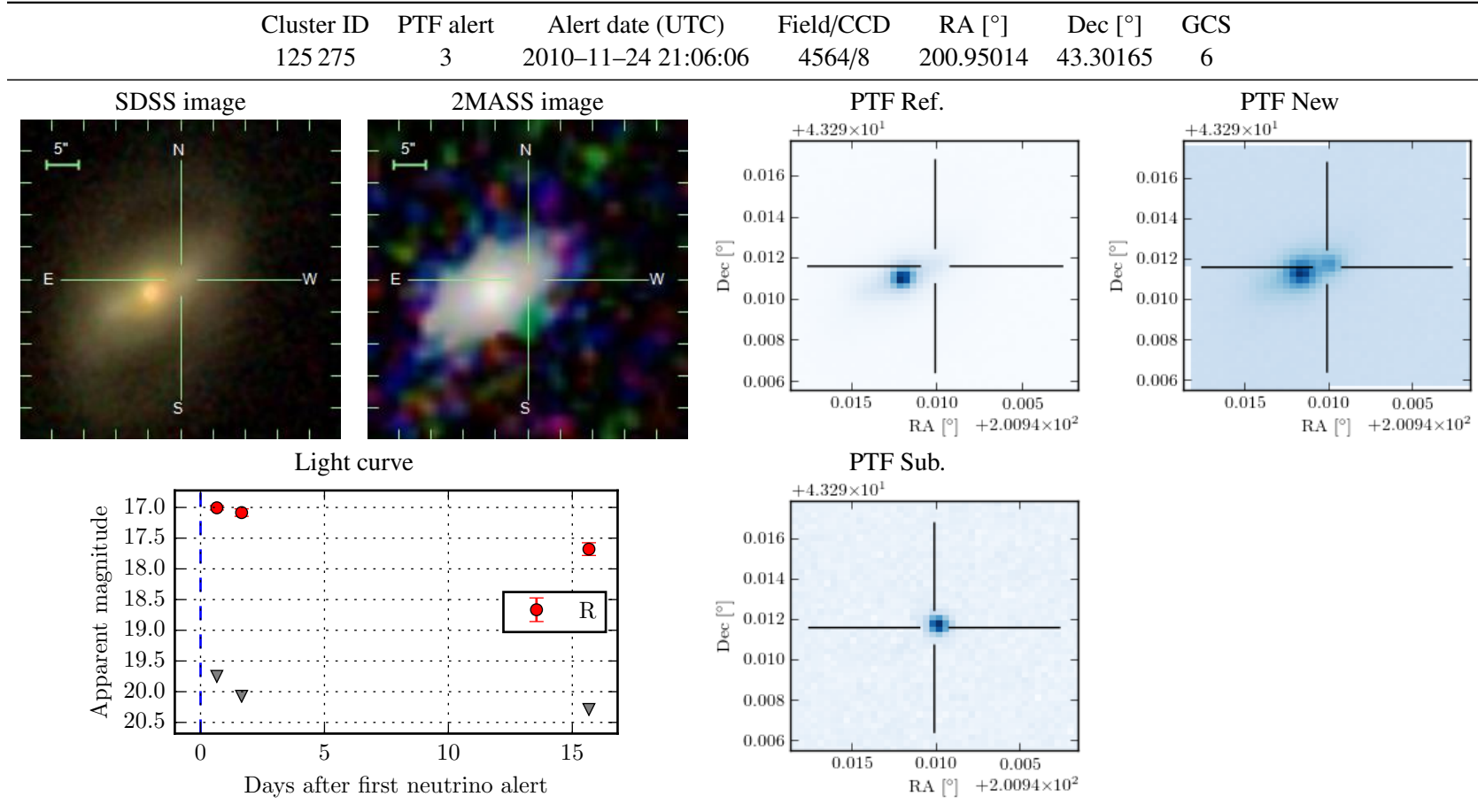


Table 8.6: One of the two unambiguous SNe found in the PTF follow-up data. GCS is the *good cluster size*, i.e. the number of exposures in the cluster, which have a machine learning score of 0.07 or more (see Section 8.2.1). Limiting magnitude is visualized by grey triangles.

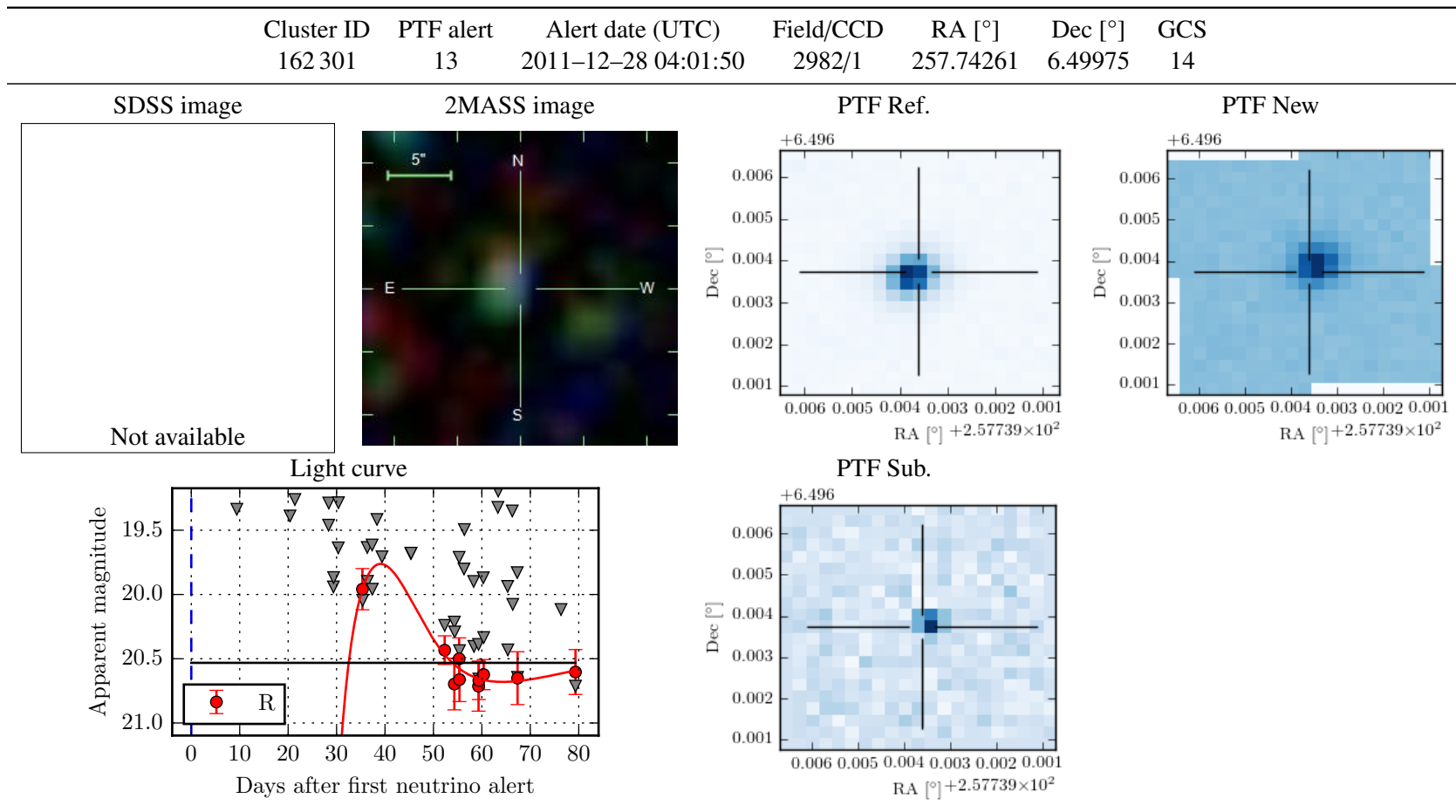


Table 8.7: An example for a likely SN, which might also be an AGN flare or VarStar. GCS is the *good cluster size*, i.e. the number of exposures in the cluster, which have a machine learning score of 0.07 or more (see Section 8.2.1). Limiting magnitude is visualized by grey triangles.

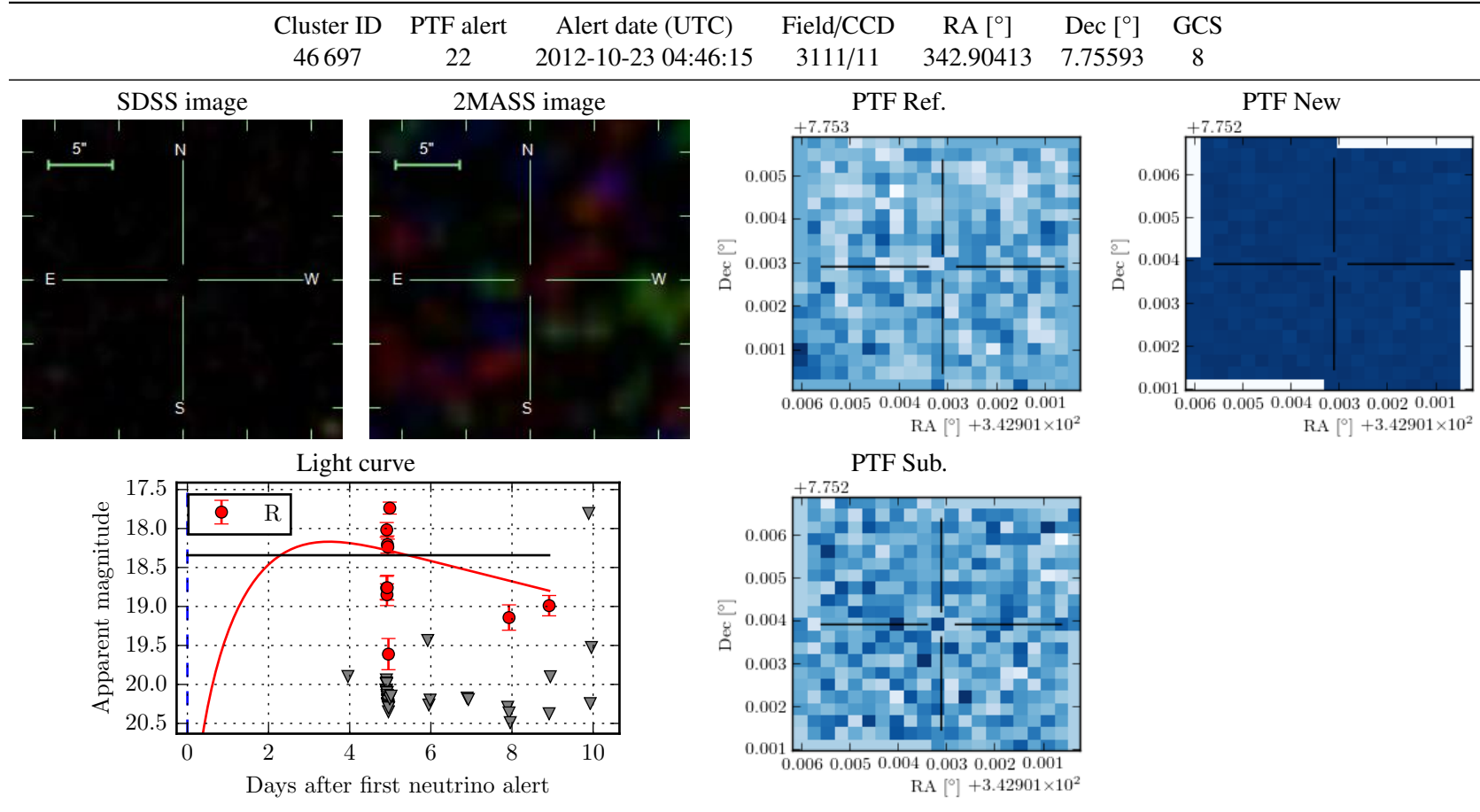


Table 8.8: An example for an artifact in the SN search, close to the CCD edge. No host is visible in the reference, and no source in the subtraction or new image. In addition, there is very strong short-time variation and detections are missing for exposures with good limiting magnitude. GCS is the *good cluster size*, i.e. the number of exposures in the cluster, which have a machine learning score of 0.07 or more (see Section 8.2.1). Limiting magnitude is visualized by grey triangles.

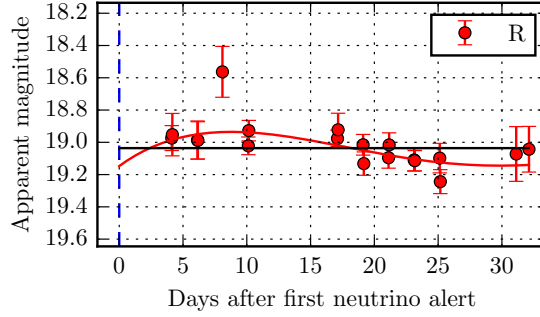


Figure 8.9: The light curve of the SN IIn PTF12csy, as seen by the SN detection algorithm, with the LC fit applied to the P48 PTF survey data. The goodness ratio g between a constant function and an LC function is only 1.49 because the light curve is almost constant.

8.5 Monte Carlo Simulation of SN Alerts

In order to estimate how many SNe one expects to find serendipitously, with no causal connection to a neutrino multiplet, a Monte Carlo simulation is performed to determine the efficiency of the SN detection algorithm introduced in the previous Section 8.3. Therefore, pseudo SNe are generated that have properties close to real optical observations of SNe. The same cuts from Section 8.3.4 that are applied to real data are applied to the pseudo SNe as well. The fraction of pseudo SNe passing the cuts is a proxy for the SN detection efficiency.

8.5.1 SN Insertion

During a simulation run, one random SN at a time is inserted into each of the analyzed OFU alerts. First, the luminosity distance d_L to the SN must be specified. A random host galaxy absolute magnitude M_G is drawn, according to the luminosity weighted distribution of galaxy absolute magnitudes, obtained from [324, fig. 8]. The magnitude is converted to apparent magnitude m_G with d_L , using Equation B.9, which is then a host galaxy magnitude representative for this SN distance.

The SN is put randomly into the active field of view of the P48 follow-up telescope by choosing one of the alert's follow-up fields, then choosing one CCD, and putting the SN onto the contained SDSS galaxy closest in magnitude to the drawn magnitude m_G . The SN is placed onto the host galaxy (see below), the background brightness at the SN position is calculated and the LC properties are simulated accordingly, see Section 8.5.5. If there are no SDSS data for the PTF fields, then the SN is placed uniformly inside a random CCD and average photometric conditions are used for the LC generation.

The SN is placed randomly on top of the galaxy according to the galaxy's light intensity profile that was fitted by SDSS. Two different elliptical profiles are fitted to each galaxy in SDSS, for each of the five SDSS filters u, g, r, i, z [314]:¹¹ An *exponential* profile, where the light intensity drops radially according to

$$\Phi(r) = I_0 e^{-1.68 r/r_e}, \quad (8.6)$$

and a *de Vaucouleurs* profile, where radial intensity is described by

$$\Phi(r) = I_0 e^{-7.67 (r/r_e)^{1/4}}, \quad (8.7)$$

r is the distance of a certain point to the galaxy center and r_e is the effective radius of the galaxy, which

¹¹ See also <http://www.sdss.org/dr12/algorithms/magnitudes/> for explanation.

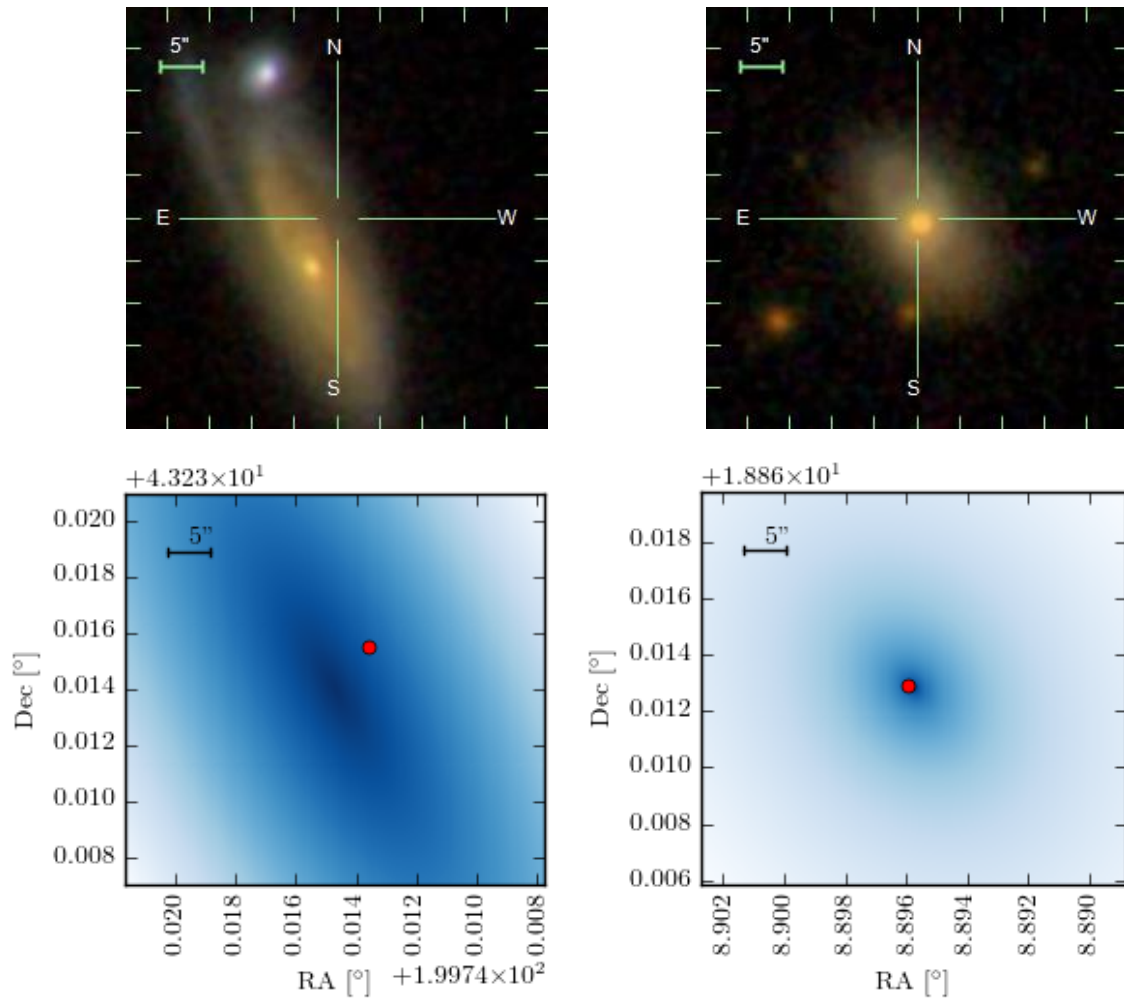


Figure 8.10: Example of a random SN insertion into a galaxy with exponential profile (left column) and de Vaucouleurs profile (right column). The upper row shows the SDSS catalog image with the position of the SN insertion at the center. The lower row shows the description of the galaxy's light intensity distribution in the SDSS catalog, obtained by a fit to the data. The distribution is used as PDF to draw random SN coordinates. The exemplary drawn SN coordinates are indicated with a red dot.

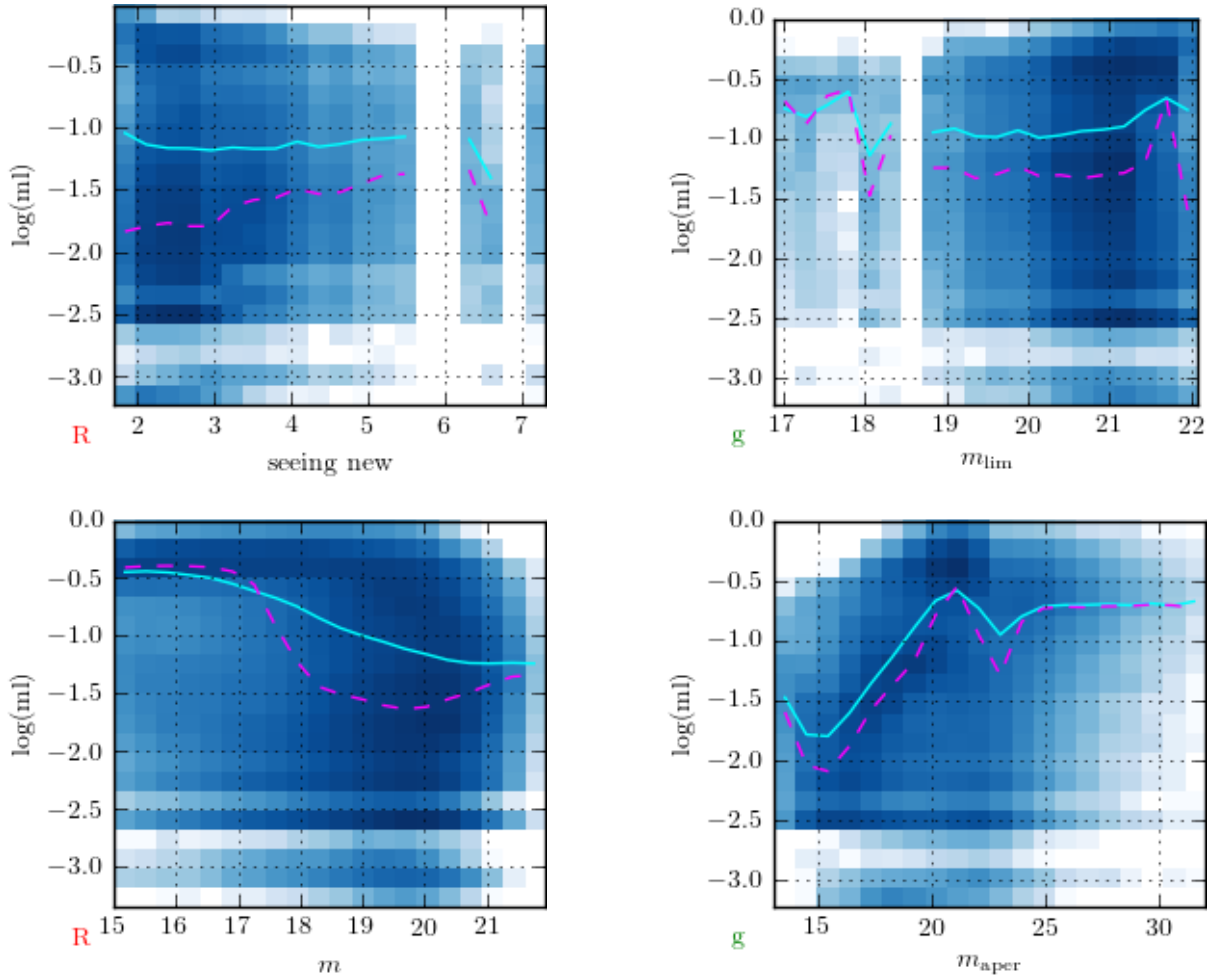


Figure 8.11: Histograms of the machine learning score ml versus various parameters. It is strongly correlated only with the SN magnitude m and host magnitude m_{aper} (bottom row). The mean along the y-axis is shown as solid cyan line, the median as dashed pink line.

contains 50% of the total flux. The two models describe the majority of galactic light distributions well. The fitted galaxy profile with the highest log-likelihood value is used: either exponential or de Vaucouleurs, from either the r or i band (in which the $\text{H}\alpha$ line at 656 nm from the Balmer series of hydrogen falls, which is a tracer for the SN rate). The galaxy profile is treated as a 2D probability distribution and the simulated SN position is drawn randomly according to this distribution. Figure 8.10 illustrates the shape of the galaxy profiles and example SN insertions.

8.5.2 Light Curve Parametrization

After the SN has been inserted, a random light curve (LC) is generated with a Monte Carlo (MC) method. For realistic LC simulation, the photometric properties are drawn randomly from suitable parameter distributions. The parameter distributions were constructed from simulated fake SNe created by Chris Frohmaier, a member of the PTF collaboration. The fake SN candidates were created by applying image subtraction (see Section 8.2) on synthetic point sources that were injected into PTF images onto

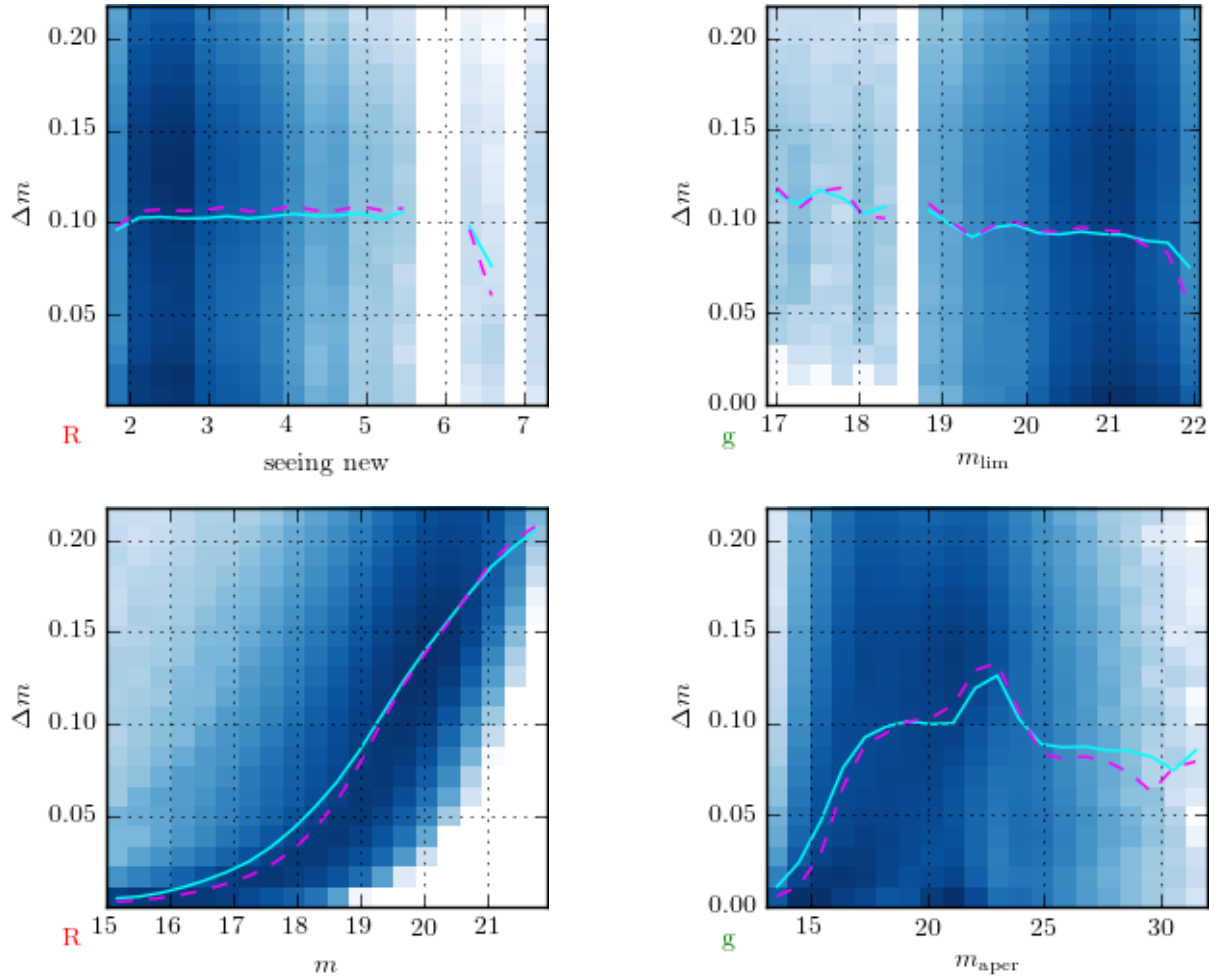


Figure 8.12: Histograms of the magnitude error Δm versus various parameters. It is strongly correlated only with the SN magnitude m and host magnitude m_{aper} (bottom row). The mean along the y-axis is shown as solid cyan line, the median as dashed pink line.

host galaxies, uniformly across a broad magnitude range. The total dataset contains 30 029 920 fake SN candidates, about 10 times the amount of experimental PTF data in this analysis.

The parameters of interest for the LC construction are:

- The machine learning classifier ml that represents the quality of the photometry from the difference imaging.
- The error on the magnitude Δm that represents the photometric accuracy.
- The limiting magnitude m_{lim} that determines whether a point in the light curve is detected or not.

The limiting magnitude is calculated analytically, as explained in Section 8.5.4. The other two parameters, ml and Δm , must be described as function of the most important parameters that they depend on. Parameters that potentially correlate with the photometric quality are:

- The seeing (see Appendix B.1).

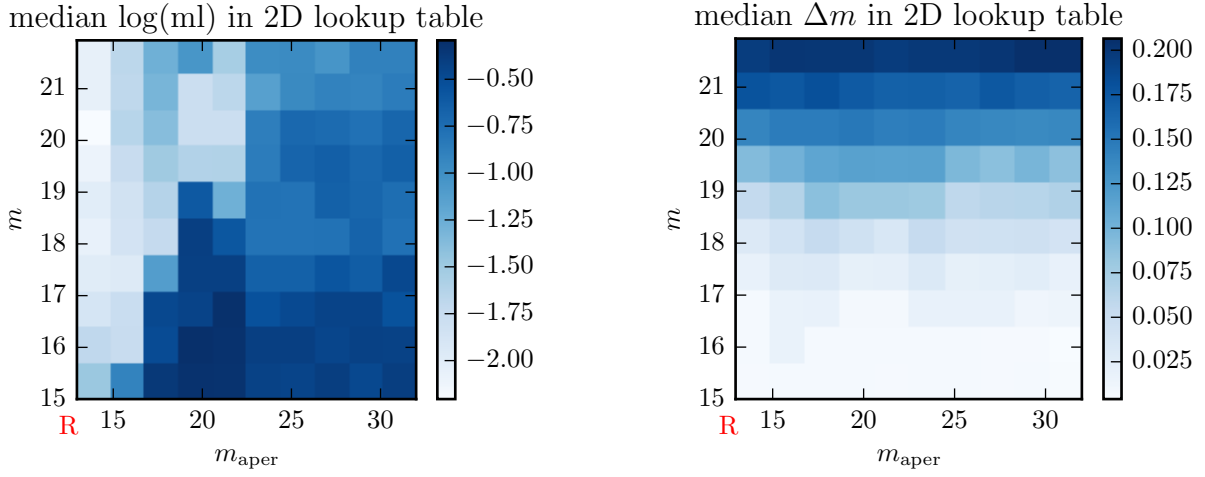


Figure 8.13: Median value of \log_{10} of the machine learning score ml (left) and of the magnitude error Δm (right) in the bins of the two-dimensional lookup table. Bright SNe (small m) on dark host galaxies (large m_{aper}) tend to have higher ml value (better photometric quality). Bright SNe also have lower magnitude error, independent of m_{aper} .

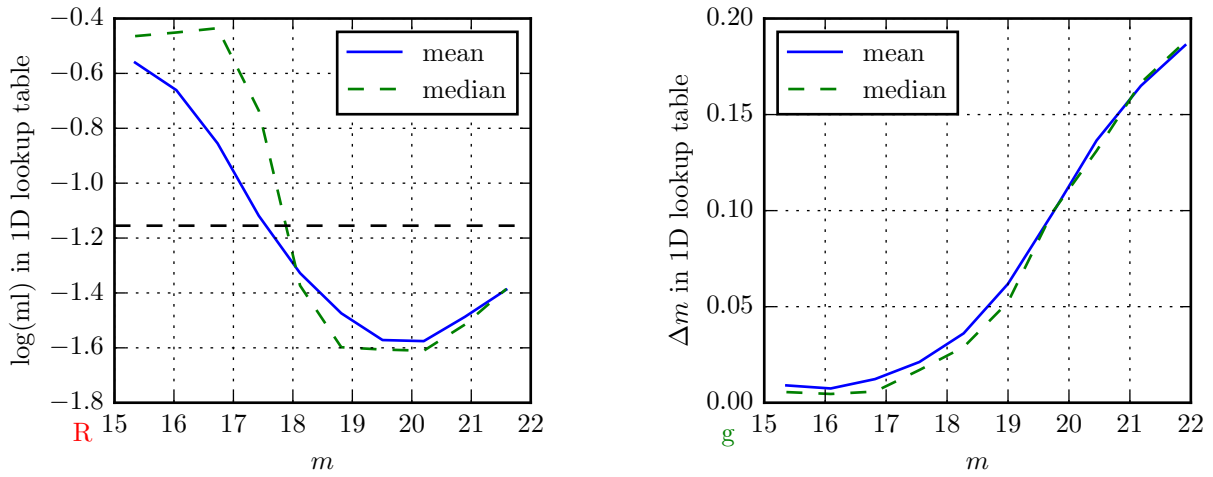


Figure 8.14: Median and average value of \log_{10} of the machine learning score ml (left) and of the magnitude error Δm (right) in the bins of the one-dimensional lookup table. Bright SNe (small m) tend to have higher ml value (better photometric quality) and lower magnitude error Δm . The ml cut value of 0.07 is indicated (left) with a dashed line.

- The limiting magnitude m_{lim} .
- The median sky brightness per pixel, m_{sky} .
- The median RMS of the sky brightness per pixel, m_{sig} .
- The SN magnitude m .
- The host galaxy aperture magnitude m_{aper} .

Plotting m_{lim} and Δm against all the listed parameters revealed that the dependence on most parameters is rather weak or not existent, see Figures 8.11 and 8.12. It was therefore decided to neglect all parameters except m and m_{aper} , on which m_{lim} and Δm depend most strongly.

In 10 bins of m and m_{aper} , 2D histograms of m_{lim} versus Δm were created. They are histogrammed together in order to correctly describe correlations between m_{lim} and Δm . The 2D histograms are stored in a two-dimensional lookup table for the LC generation. Figure 8.13 attempts to visualize the lookup table by plotting the median value of m_{lim} and Δm (instead of the 2D histograms) for each bin of m and m_{aper} . If during the SN insertion (Section 8.5.1) no SDSS host galaxy could be found, then only the SN magnitude m is known and no host galaxy magnitude m_{aper} can be determined (see Section 8.5.3 for m_{aper} determination). Thus, a one-dimensional lookup table with 2D histograms for 10 bins of m was created as well. Similar to Figure 8.13, Figure 8.14 plots the median value of m_{lim} and Δm from the one-dimensional lookup table as function of m .

8.5.3 Host Magnitude Determination

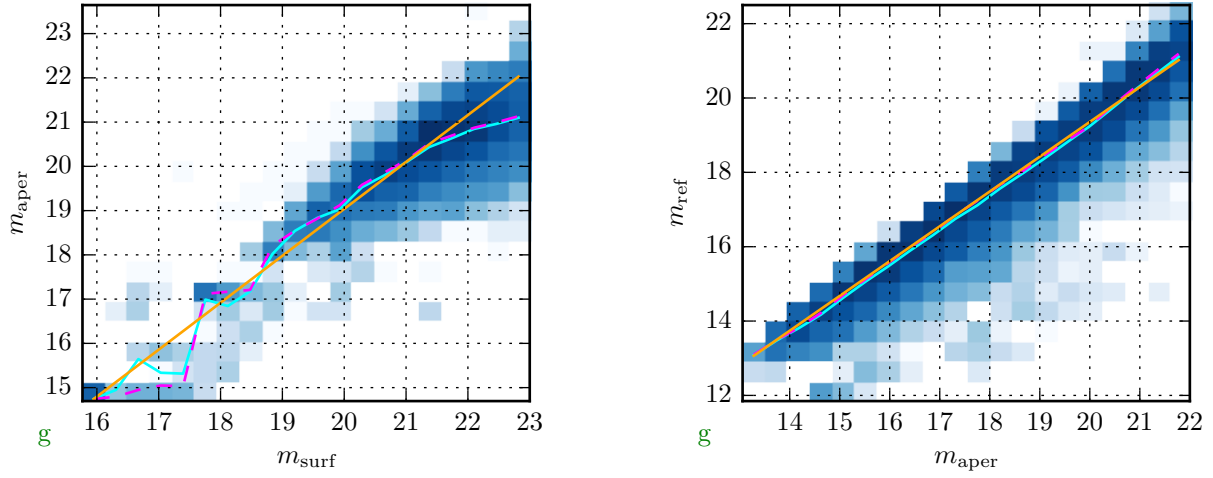
The photometric parameters depend strongly on the host galaxy aperture magnitude m_{aper} , see Section 8.5.2. It was measured for every source candidate extracted from the PTF data. The problem is that during the MC simulation, the SNe are inserted onto random SDSS galaxies, for which the PTF aperture magnitude is a priori unknown. To solve this problem, a quantity called the SDSS surface magnitude m_{surf} was calculated for a selection of 415 215 of the fake SN candidates. The surface magnitude is a synthetic magnitude created by integrating the SDSS galaxy's light intensity distribution $\Phi(r)$ (Equation 8.6 or 8.7), multiplied with a Gaussian PSF centered on the SN, whose FWHM equals the seeing. This is to emulate real photometry that reflects the photometric conditions, see Appendix B.1. A larger seeing results in a higher m_{surf} because a larger area of the galaxy's surface is probed by the photometry.

Figure 8.15a shows a plot of m_{aper} versus m_{surf} for the fake candidates that m_{surf} was calculated for. There is a clear correlation, proving that the method works, and a line was fitted to the median m_{aper} values. The fit result serves as a conversion formula to obtain m_{aper} from m_{surf} during simulation.

8.5.4 Limiting Magnitude Modelling

The *limiting magnitude* in astronomy is the apparent magnitude of the faintest object that can still be detected. It can be defined in several ways, e.g. as the magnitude of isolated stars, at which 50% of the stars are detected, i.e. the detection efficiency being 50% [247, p. 1435]. An alternative formulation, used by PTF [221], is to set the limiting magnitude at the magnitude of the faintest object that can be detected with a certain significance, e.g. 5σ .

The conventional definition of the limiting magnitude refers to the detection of isolated stars. However, when a source sits on top of a bright background, such as an SN on top of a host galaxy, the limiting magnitude tends to be smaller (worse) due to the reduced signal-to-noise ratio or contrast. To take this effect into account in the simulation, a simple approximative model is used to derive the host



(a) PTF aperture magnitude m_{aper} versus SDSS surface magnitude m_{surf} for identical spots of SN host galaxies.

(b) PTF PSF magnitude m_{ref} of the closest object in the reference image versus PTF aperture magnitude m_{aper} .

Figure 8.15: Correlations between different magnitude definitions, found empirically with simulated fake SN data provided by PTF collaboration member Chris Frohmaier. The mean along the y-axis is shown as solid cyan line, the median as dashed pink line. The solid orange line is the result from a linear least-squares fit. The plots are for the g -band, those for the R -band look very similar.

limiting magnitude $m_{\text{lim}}^{\text{host}}$ from the isolated limiting magnitude $m_{\text{lim}}^{\text{iso}}$, the host's surface magnitude m_{host} , and the sky background m_{sky} :

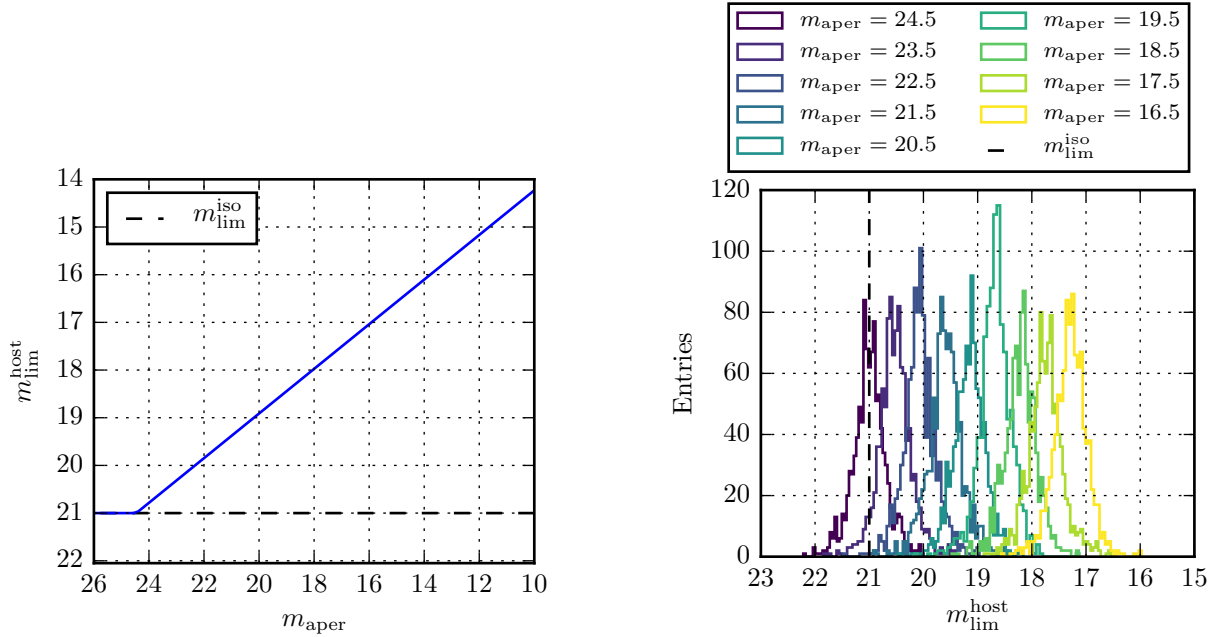
$$m_{\text{lim}}^{\text{host}} = m_{\text{lim}}^{\text{iso}} - \left(\frac{m_{\text{sky}} - m_{\text{host}}}{2} \right). \quad (8.8)$$

The derivation of this equation can be looked up in Appendix E.3.

If the host galaxy's surface magnitude m_{host} is only as bright as the sky background m_{sky} (the largest possible magnitude that can be measured), then the isolated limiting magnitude $m_{\text{lim}}^{\text{iso}}$ is recovered. But for a brighter host environment with $m_{\text{host}} < m_{\text{sky}}$, the host limiting magnitude $m_{\text{lim}}^{\text{host}}$ becomes smaller and thus worse.

During the MC simulation, m_{host} is derived from the SDSS catalog information: The aperture photometry magnitude m_{aper} , determined as explained in Section 8.5.3, is converted to point-spread-function (PSF) photometry magnitude (called m_{ref} in Figure 8.15b) via another correlation shown in Figure 8.15b. This conversion is done to be able to compare m_{host} with the limiting magnitude $m_{\text{lim}}^{\text{iso}}$, which was measured for the PSF photometry of isolated stars. The sky magnitude m_{sky} is derived from information provided by the PTF pipeline: from the parameter `medsky`, the median sky brightness, that can be different in every exposure. The resulting limiting magnitude $m_{\text{lim}}^{\text{host}}$ is visualized in Figure 8.16 as function of host magnitude m_{aper} for $m_{\text{lim}}^{\text{iso}} = 21$ mag.

The calculated limiting magnitude $m_{\text{lim}}^{\text{host}}$ only corresponds to the average limiting magnitude for sources on a host galaxy, like $m_{\text{lim}}^{\text{iso}}$ is the average limiting magnitude for isolated sources. To account for limiting magnitude variations, the positive tail of the $m - m_{\text{lim}}^{\text{iso}}$ distribution (where the magnitude seems to defy the limiting magnitude) was plotted and mirrored at 0 to create the histogram shown in Figure 8.17. The histogram is used as PDF for the m_{lim} variation Δm_{lim} . In the MC simulation, a random Δm_{lim} is drawn and added to $m_{\text{lim}}^{\text{iso}}$, which is then converted to $m_{\text{lim}}^{\text{host}}$ for the actual limiting magnitude that determines whether the source is detected or not.



(a) The linear relation between $m_{\text{lim}}^{\text{host}}$ and host magnitude m_{aper} (correlated with m_{host}), see Equation 8.8. The host limiting magnitude $m_{\text{lim}}^{\text{host}}$ reaches $m_{\text{lim}}^{\text{iso}}$ for $m_{\text{host}} \geq m_{\text{sky}}$.

(b) MC simulated limiting magnitude distributions for different host galaxy aperture magnitudes m_{aper} , for an isolated limiting magnitude of $m_{\text{lim}}^{\text{iso}} = 21$ mag.

Figure 8.16: Visualization of the effect of the host limiting magnitude $m_{\text{lim}}^{\text{host}}$ modeling on the conventional isolated average limiting magnitude $m_{\text{lim}}^{\text{iso}}$, set to 21 mag for the plots.

8.5.5 Light Curve Generation

After a SN has been randomly inserted (see Section 8.5.1), a random light curve (LC) is generated. The LC generation happens according to a randomly chosen set of LC parameters obtained by fits to LCs in the SNDB (see Section 8.3.3). The *Milky Way extinction* at the SN position is queried from the NASA/IPAC Infrared Science Archive¹² and taken into account. The results from Schlegel et al. (1998) [273] and the algorithm determined by Cardelli, Clayton, and Mathis (1989) [274] are adopted. The host magnitude m_{aper} (see Section 8.5.3) and the host limiting magnitude $m_{\text{lim}}^{\text{host}}$ (see Section 8.5.4) are determined and taken into account. Random values for m_l and Δm are drawn (see Section 8.5.2) and applied.

The result is a synthetic SN light curve that takes into account the quantity and quality of the actual PTF follow-up data. The LC function is fitted to the synthetic LC (see Section 8.3.3), the same cuts as for experimental data (described in Section 8.3.4) are applied to the LC and the outcome is stored. Figure 8.18 shows examples of simulated SN LCs. Details of how the simulation runs are carried out are given in Appendix E.4.

8.6 Efficiency of SN Detection

The results of the signal CCSN simulation runs can be used to verify if the SN detection algorithm is performing well. If the method works, then under optimal circumstances, i.e. sufficient available data

¹² At <http://irsa.ipac.caltech.edu/applications/DUST/>. The HTTP interface is used for scripted access.

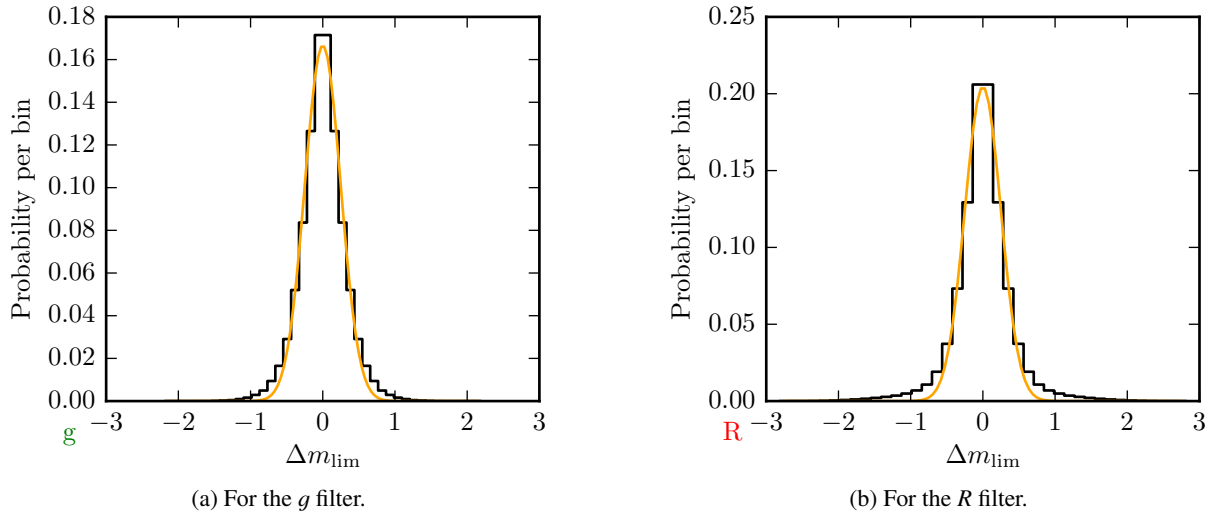


Figure 8.17: The Δm_{lim} distribution obtained by mirroring the positive tail of $m - m_{\text{lim}}$. It resembles a Gaussian function (fitted curve), but has fatter tails.

and a bright SN explosion, the detection probability should reach almost 100%.

That this is the case can be seen in Figure 8.19. For all plots except Figure 8.19e, undetectable cases with no or too few exposures (less than 5) have been removed from the sample in order to show the performance of the detection algorithm for available data. Figure 8.19a shows the SN detection probability as function of apparent peak magnitude m_{peak} for all SNe with at least 5 exposures. For the brightest SNe, below $m_{\text{peak}} \approx 13$ mag, it reaches about 85%. The reason that it does not get closer to 100% is that a large fraction of SNe with at least 5 exposures do not have significantly more exposures. This leads to about 15% of them failing one of the LC cuts (see Section 8.3.4). In Figure 8.19c, the fractions of the different outcomes of the simulation are plotted as function of m_{peak} . One can see that the main mode of failure is a failing cut on the good cluster size (*GCS cut* in the legend of Figure 8.19), i.e. even though ≥ 5 exposures are available, it happens that less than 5 have a ml score above 0.07. The second most frequent failure is the cut on the minimum time interval, which can be unfulfilled when not enough data are available. Looking only at SNe that have at least 10 exposures, the detection probability rises to 95%, as shown in Figure 8.19b. Figure 8.19d reveals that the minimum interval cut failures vanish and the GCS cut failures are cut in half, constituting the remaining 5%.

Looking at Figures 8.19c and 8.19d, one sees that towards higher peak magnitude, i.e. darker LC, the fraction of SNe failing the GCS cut rises strongly up to $m_{\text{peak}} \approx 20$ mag. This is caused by the optical quality getting worse (and thus ml score getting smaller, see Figures 8.13 and 8.14), but also by a rising fraction of exposures not being detected because the limiting magnitude is reached. Eventually, above 20 mag, the LC becomes too dark and there is a steep rise of the cases where no exposures are detected at all, until at about 23 mag this is the only outcome. Causes of failed SN detection that were excluded, except for Figure 8.19e, are:

- a star or AGN is too close to the randomly inserted SN (fraction of about 3%),
- no data at all are available, i.e. unsuccessful follow-up, which can happen e.g. when the target is behind the Sun, see Figures E.1–E.5 (fraction of about 30%),
- less than 5 exposures were taken (fraction of about 15%).

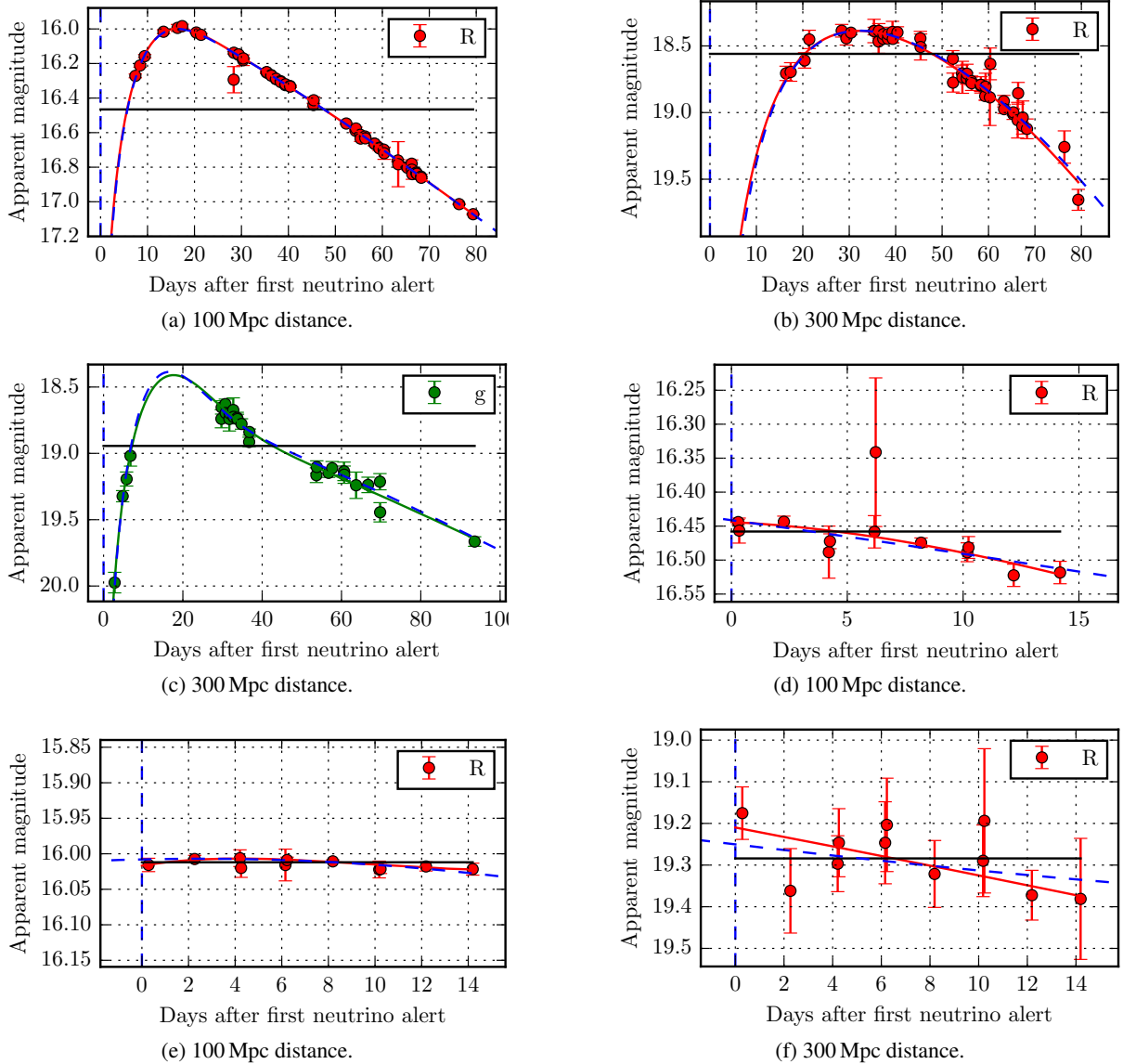


Figure 8.18: Examples of simulated SN light curves with the LC fit applied to them (solid curve) and the underlying true LC (dashed curve). The flat function fit is shown as solid horizontal line. For most LCs, especially when the explosion time is close to the neutrino alert time, as in (a)–(c), the fit performs well and the goodness ratio is well above the cut value of 2. If the SN is old, with explosion time well before the neutrino alert as in (d)–(f), then there can be little evolution in the LC. In some cases, as in (d), the goodness ratio is still above 2, but there are cases where it is not, such as (e) and (f). This happens more frequently when the data are sparse or the magnitude errors large.

If not excluded, these extra failure modes reduce the SN detection probability to only 45% (see Figure 8.19e). While important for a realistic simulation of the false positive rate, see following Section, these failures are not relevant to assess the detection algorithm performance.

Another interesting plot is the SN detection probability as function of contrast, shown in Figure 8.20. The contrast here is defined as magnitude difference between the brightest SN detection and the underlying host galaxy. Higher contrast means that the SN tends to outshine the galaxy. This leads to a higher signal to noise ratio, better limiting magnitude, and better photometric properties, so that the SN is easier to detect. Figure 8.20 verifies that the detection probability strongly depends on contrast, being almost 100% at highest contrast. At a contrast of 0 mag, i.e. the SN is at most as bright as the surrounding environment of the host galaxy, the detection probability is only 45%. It is zero for contrasts of < -5 mag.

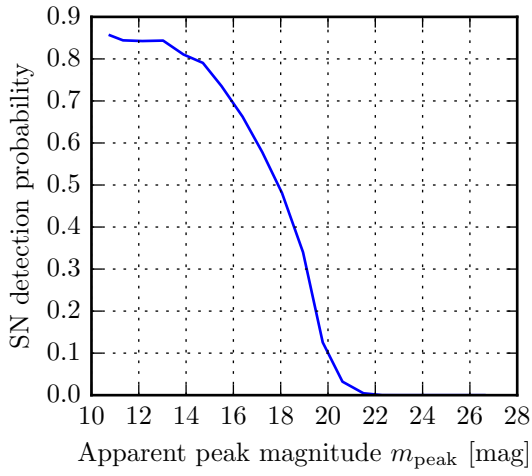
8.7 False Positive Rate of SN Detection

For the interpretation of the SN search result, it is important to know the background expectation. How many by chance coincident SN detections are expected to happen, without any correlation between the neutrino burst and the SN?

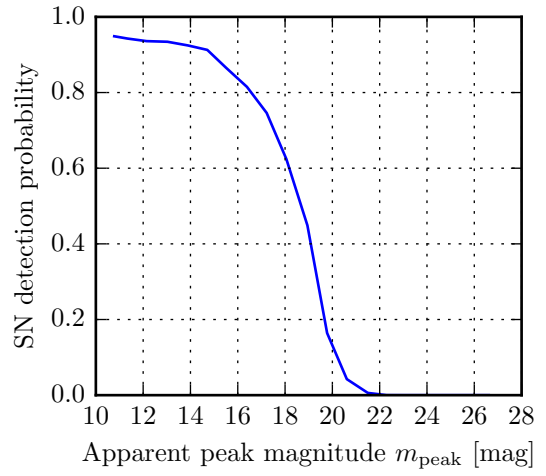
To answer this question, the SN detection probability for background SNe (meaning with random explosion time within a 300 d window) is averaged in each distance bin over all simulated peak magnitudes to yield the detection probability as function of luminosity distance to the SN. The average is a weighted arithmetic mean, using the SN *luminosity function* (LF) as weight. The LF is the probability distribution for the SN peak absolute magnitude. That is, the detection probabilities of peak magnitudes that occur more frequently are given a higher weight in the averaging. The LFs are taken from Li et al. (2011a) [249]. They are uncorrected for host galaxy extinction so that the effect is included in the calculation. The LFs are divided into the three SN classes SNe Ia, SNe Ibc, and SNe II, and are plotted in the left column of Figure 8.21. They span a range from -13 mag (dimmiest) to -20 mag (brightest). While the distributions for Type Ibc and Type II are similar, with a large spread around -16 mag, the Type Ia distribution has a lower spread and is concentrated at much brighter magnitudes around -18 mag to -19 mag. For the calculation, a smooth distribution is required, so that a kernel density estimation (KDE) is performed, plotted as blue curve in the left column of Figure 8.21. KDE is a technique to estimate the smooth probability density function of sparse data [325].

The simulation result of the CCSN background SNe is averaged with the Type Ibc and the Type II LF, the SN Ia background SN simulation is combined using the Type Ia LF. The resulting SN detection probabilities $P_{\text{det}}(d_L)$ as function of luminosity distance d_L are plotted in the right column of Figure 8.21. A function describing $P_{\text{det}}(d_L)$ well, derived from the Poissonian CDF, is fitted to the SN detection probability sample points (dashed curves in Figure 8.21 right). This function can be integrated to yield the expected number of background SN detections.

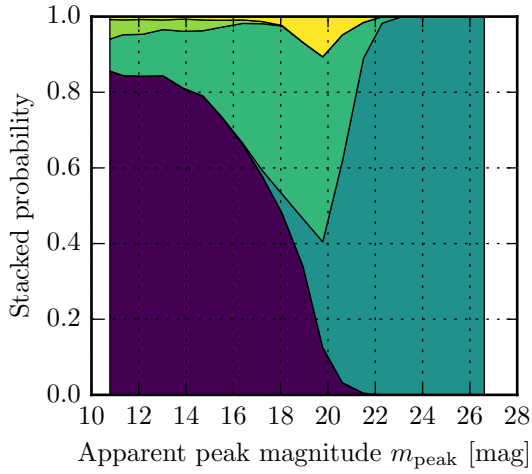
The explosion time window for the background SNe was $[-200 \text{ d}, \dots, 100 \text{ d}]$ in the simulation. Since the detection probability at -200 days is not zero, a correction must be done to mitigate that. The detection probability, averaged over all distances and peak magnitudes, is plotted as function of the explosion time, see Figure 8.22. A linear function is fitted to the left tail of the distribution. The extra contribution from the extrapolation gives a correction factor: about 15% for SNe II, about 16% for SNe Ibc, and about 3% for SNe Ia.



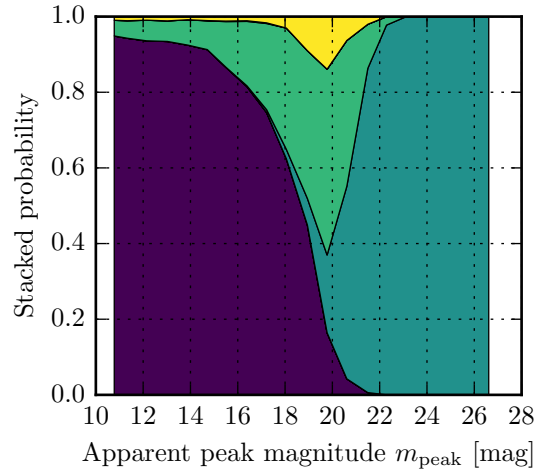
(a) At least 5 exposures (all in principle detectable SNe).



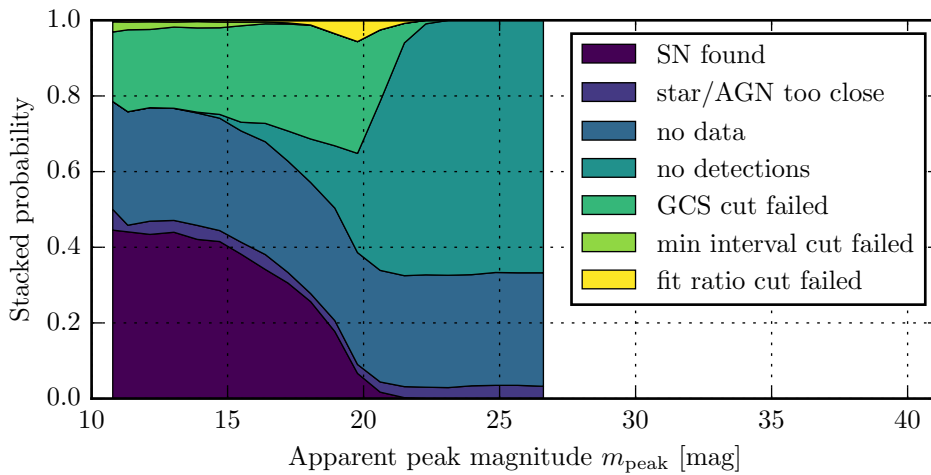
(b) At least 10 exposures.



(c) At least 5 exposures (all in principle detectable SNe).



(d) At least 10 exposures.



(e) All simulated SNe.

Figure 8.19: Plots of the SN detection and failure probabilities of simulated signal CCSNe (explosion time coincides with neutrino alert) as function of apparent peak magnitude m_{peak} . (a)–(b) SN detection probability. (c)–(d) Stacked plot of the probability of all occurring outcomes: The diameter of the bands represents their probability.

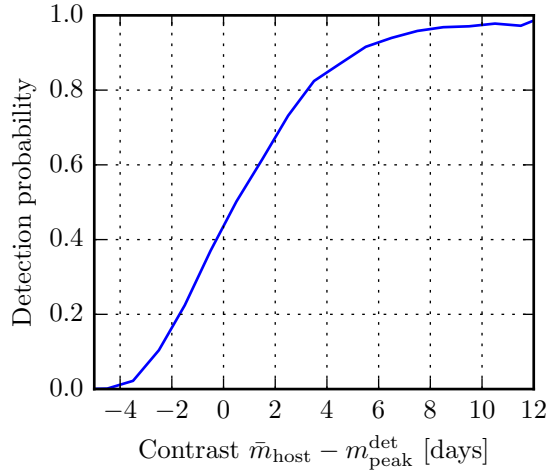


Figure 8.20: SN detection probability for signal CCSNe as function of the contrast, i.e. difference between the average host magnitude \bar{m}_{host} and the detected peak SN magnitude $m_{\text{peak}}^{\text{det}}$. Positive contrast means that the SN at peak is brighter than the host. Cases where less than 5 exposures are available have been excluded from the plot.

The estimated number of coincidental SN detections for all analyzed follow-up alerts is

$$N_{\text{SN,BG}} = N_{\text{fields}} \frac{\Omega_{\text{FoV}}}{4\pi} \Delta t \frac{dN_{\text{SN}}}{dV dt} \int_0^{\infty} P_{\text{det}}(d_L) 4\pi d_L^2 dd_L. \quad (8.9)$$

The total exposed solid angle of the follow-up program is the number of fields N_{fields} that follow-up images were requested for, multiplied with the light-sensitive solid angle of one PTF field, Ω_{FoV} . In this work, a total of 20 alerts are analyzed that consist of 29 PTF fields (each field can occur more than once). One PTF field has a light-sensitive area of about $\Omega_{\text{FoV}} \approx 7.26 (\text{°})^2$ [221]. The time window Δt is the window, in which SNe are searched for. Since there is no restriction on the SN explosion time, $\Delta t = 300$ d, i.e. the length of the complete simulation time window going from -200 d to 100 d relative to the neutrino alert time. An important external ingredient is the assumed volumetric SN explosion rate $dN_{\text{SN}}/(dV dt)$. It is taken from Li et al. (2011b) [107, tab. 10], which presents results from the Lick Observatory Supernova Search (LOSS). See also Section 3.2.6. The adopted values are listed in Table 8.9, along with the results of the calculation using Equation 8.9.

The statistical errors on the expected number of background SN detections were derived by adding/subtracting the one std. deviation error to/from the volumetric SN rate and, in addition, adding/subtracting the one std. deviation error to/from all SN detection probability sample points before doing the $P_{\text{det}}(d_L)$ fit. The derivation of the systematic errors is covered in Section 8.8.

8.8 Systematic Errors

As the main sources of systematic uncertainty on the estimated number of detected background SNe (see Section 8.7), there have been identified:

Uncertainties propagated from external input needed for the calculation:

- **Rate:** Uncertainty on the volumetric SN explosion rate. The volumetric SN rate is taken from [107] and displayed in Table 8.9 with the systematic uncertainty on the value. The SN rate with added/subtracted error can be inserted in the calculation to directly yield an upper/lower bound.

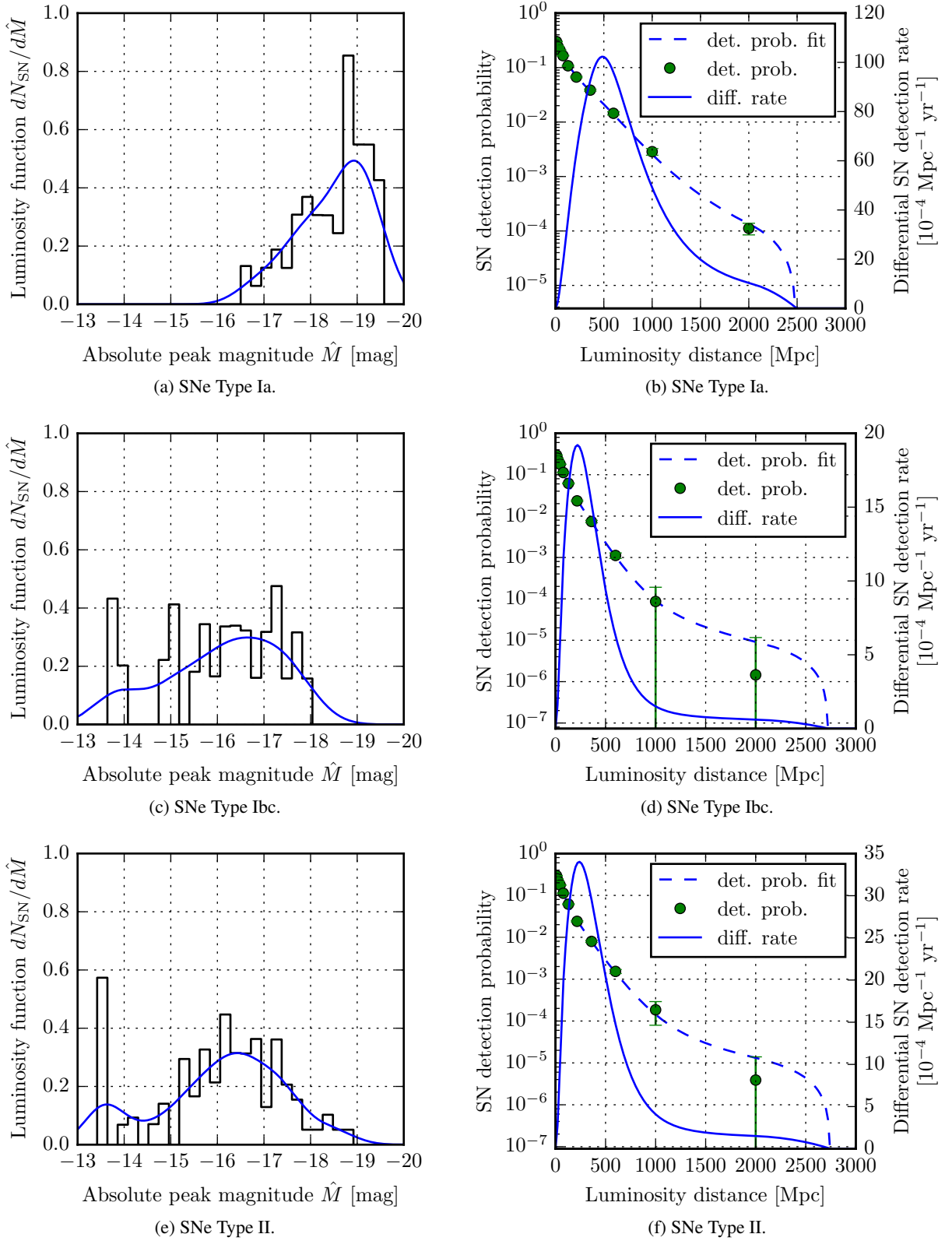


Figure 8.21: Left column (a, c, e): SN luminosity functions from Li et al. (2011a) [249], i.e. the SN absolute peak magnitude frequency distributions for the SN classes Type Ia, Ibc, and II. Right column (b, d, f): SN detection probabilities as function of luminosity distance, for SNe of Types Ia, Ibc, and II.

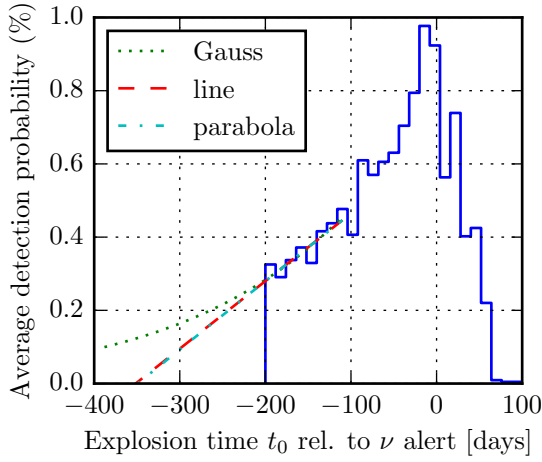


Figure 8.22: SN detection probability as function of SN explosion time relative to the neutrino alert time. The histogram is extrapolated before -200 days using different functions. The difference between the linear and parabolic fit is negligible, so that the lower bound is very close to the nominal value.

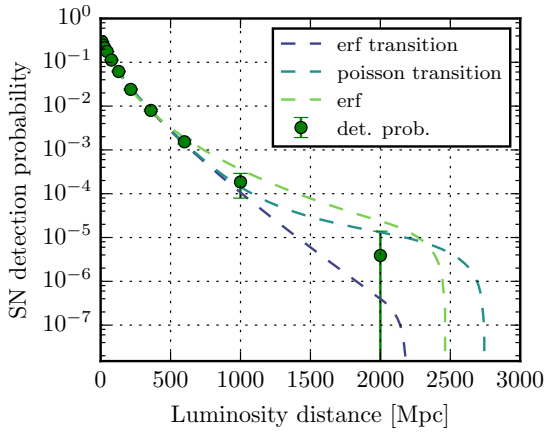


Figure 8.23: Different options for fitting the simulated SN detection probability as function of distance: smooth transition between two error functions (erf), smooth transition between two Poissonian CDFs, and a single error function.

Type	Volumetric SN rate $\frac{dN_{\text{SN}}}{dV dt}$ [10^{-4} SNe Mpc $^{-3}$ yr $^{-1}$]	Calculated $N_{\text{SN,BG}}$
Ia	$0.301^{+0.038}_{-0.037} \left(\begin{smallmatrix} +0.049 \\ -0.049 \end{smallmatrix} \right)$	$8.2^{+1.8}_{-1.6} \left(\begin{smallmatrix} +8.4 \\ -5.0 \end{smallmatrix} \right)$
Ibc	$0.258^{+0.044}_{-0.042} \left(\begin{smallmatrix} +0.058 \\ -0.058 \end{smallmatrix} \right)$	$1.0^{+0.4}_{-0.3} \left(\begin{smallmatrix} +1.2 \\ -0.5 \end{smallmatrix} \right)$
II	$0.447^{+0.068}_{-0.068} \left(\begin{smallmatrix} +0.131 \\ -0.111 \end{smallmatrix} \right)$	$2.0^{+0.7}_{-0.5} \left(\begin{smallmatrix} +2.5 \\ -1.0 \end{smallmatrix} \right)$
Sum	$1.006^{+0.089}_{-0.088} \left(\begin{smallmatrix} +0.151 \\ -0.134 \end{smallmatrix} \right)$	$11.2^{+2.0}_{-1.7} \left(\begin{smallmatrix} +8.8 \\ -5.1 \end{smallmatrix} \right)$

Table 8.9: The assumed volumetric SN explosion rate, i.e. rate per volume, from [107], and the calculated number of expected background SN detections $N_{\text{SN,BG}}$ in the analyzed PTF follow-up program. Uncertainties are separated into statistical and systematic (in parentheses).

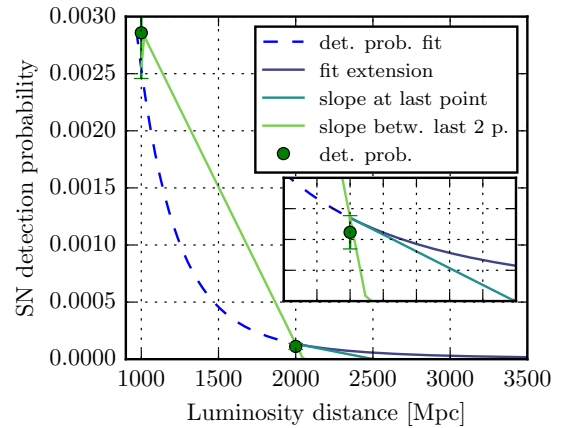


Figure 8.24: Different options for extrapolating the simulated SN detection probability beyond the simulated range: with the fit function (darkest curve), a line with the slope at the last simulation point (medium colored curve), or a line with the slope between the last two simulation points (lightest curve). An infill shows a zoomed version.

- **LF:** Uncertainty on the SN luminosity functions, taken from [249]. The 1σ error is added/subtracted to every SN's magnitude to obtain alternative LFs. In the calculation of the average detection probability versus distance (see Section 8.7), the alternative LFs are used to derive an upper/lower bound on the detection rate from the LF uncertainty.

Uncertainties arising internally in the MC simulation and subsequent calculation of the background SN detection rate:

- **LM:** Uncertainty on the limiting magnitude m_{lim} of the PTF P48 telescope. A simplified model of m_{lim} has been used (see Section 8.5.4), based on the average limiting magnitude measured by the PTF pipeline for the entire image. The width of the m_{lim} variation plot in Figure 8.17, about ± 0.5 mag, is used as systematic uncertainty on m_{lim} . In the calculation, the variation of the limiting magnitude is implemented as variation (in the opposite direction) of the SN peak magnitude for the detection probability lookup, and an upper/lower bound on the detection rate is derived. This approach neglects other correlated effects of modifying the SN magnitude (e.g. different photometric quality), but eliminates the need to resimulate.
- **LC:** Uncertainty on the shape of the SN light curves. It is not known if the selected template LCs from the SNDB (see Section 8.3.3) are representative. To assess the impact of the LC shape, the simulated LCs are split into two subgroups: flat and steep, depending on the average decline rate being smaller or larger than the median. The SN detection probability and the detection rate are recalculated for the two subgroups to yield an upper and lower bound.
- t_0 **Extrapol.:** Uncertainty on the extrapolation of the SN detection probability before explosion time t_0 of -200 days. Different functions can be used to fit and extrapolate, yielding different correction factors (see Section 8.7). A linear function is used by default, an upper and lower bound are derived from fitting a Gaussian and a parabola, see Figure 8.22.
- d **Interpol.:** Uncertainty on the interpolation of the detection probability as function of distance d , see Section 8.7 and Figure 8.21. Different functions can be used for the interpolation. A good fit was achieved using an empirically found function consisting of two piecewise defined Poissonian CDFs, which are joined by a smooth transition. This was used for the nominal result. An alternative—adopted from [319, eq. 3]—is the description of the detection probability as function of magnitude with the error function,¹³ where the distance is converted to magnitude using Equation B.9. A third option is the smooth transition between two piecewise defined error functions, which yields a fit that is almost as good as the Poissonian CDF transition. The alternative fits provide the upper and lower bound. See Figure 8.23 for a plot of the three alternative fits.
- d **Extrapol.:** The fit function for the detection probability versus distance approaches zero very slowly, with a convex curvature. This can lead to a large contribution at very large distances. While detection probability is relatively low, the contribution is high because of the large observed volume. However, it is questionable if SN detections beyond several Gpc (e.g. at $d \gtrsim 3$ Gpc, where redshift $z \gtrsim 0.5$) are feasible in reality. Simulating the detection probability at very large distances is challenging, because the probability is so low that a very large number of SNe must be simulated before even a low number gets detected. A more realistic description of the detection probability might be a drop to zero at a certain large distance.

Therefore, the detection probability is extrapolated beyond the last simulated point (at 2 Gpc) with a linear function of the same slope as the fit function at the last point. This yields the nominal

¹³ Result of the convolution of the normal distribution and a step function.

Uncertainty	$N_{\text{SN,BG}}$ for SNe Ia	$N_{\text{SN,BG}}$ for SNe Ibc	$N_{\text{SN,BG}}$ for SNe II
Rate	$8.2 \begin{pmatrix} +1.3 \\ -1.3 \end{pmatrix}$	$1.0 \begin{pmatrix} +0.2 \\ -0.2 \end{pmatrix}$	$2.0 \begin{pmatrix} +0.6 \\ -0.5 \end{pmatrix}$
LF	$8.2 \begin{pmatrix} +2.1 \\ -1.4 \end{pmatrix}$	$1.0 \begin{pmatrix} +0.5 \\ -0.3 \end{pmatrix}$	$2.0 \begin{pmatrix} +0.7 \\ -0.5 \end{pmatrix}$
LM	$8.2 \begin{pmatrix} +7.4 \\ -4.1 \end{pmatrix}$	$1.0 \begin{pmatrix} +0.9 \\ -0.3 \end{pmatrix}$	$2.0 \begin{pmatrix} +1.9 \\ -0.6 \end{pmatrix}$
LC	$8.2 \begin{pmatrix} +1.6 \\ -1.2 \end{pmatrix}$	$1.0 \begin{pmatrix} +0.2 \\ -0.0 \end{pmatrix}$	$2.0 \begin{pmatrix} +0.5 \\ -0.1 \end{pmatrix}$
t_0 Extrapol.	$8.2 \begin{pmatrix} +0.3 \\ -0.0 \end{pmatrix}$	$1.0 \begin{pmatrix} +0.2 \\ -0.0 \end{pmatrix}$	$2.0 \begin{pmatrix} +0.3 \\ -0.0 \end{pmatrix}$
d Interpol.	$8.2 \begin{pmatrix} +0.5 \\ -0.2 \end{pmatrix}$	$1.0 \begin{pmatrix} +0.3 \\ -0.1 \end{pmatrix}$	$2.0 \begin{pmatrix} +0.6 \\ -0.2 \end{pmatrix}$
d Extrapol.	$8.2 \begin{pmatrix} +1.9 \\ -0.2 \end{pmatrix}$	$1.0 \begin{pmatrix} +0.3 \\ -0.0 \end{pmatrix}$	$2.0 \begin{pmatrix} +1.0 \\ -0.1 \end{pmatrix}$
Human	$8.2 \begin{pmatrix} +1.6 \\ -1.6 \end{pmatrix}$	$1.0 \begin{pmatrix} +0.2 \\ -0.2 \end{pmatrix}$	$2.0 \begin{pmatrix} +0.4 \\ -0.4 \end{pmatrix}$
Quadrature sum	$8.2 \begin{pmatrix} +8.4 \\ -5.0 \end{pmatrix}$	$1.0 \begin{pmatrix} +1.2 \\ -0.5 \end{pmatrix}$	$2.0 \begin{pmatrix} +2.5 \\ -1.0 \end{pmatrix}$

Table 8.10: Nominal expectation values for number of background SN detections with systematic errors in parentheses, for various sources of systematic uncertainty (see text). The total systematic errors, obtained by adding the individual errors in quadrature (i.e. the root of the sum of squares), are given in the bottom row.

result. An upper bound comes from the continuation of the fit function beyond the simulation points. A lower bound is found by using a linear function of the slope between the last two simulated points. See Figure 8.24 for a plot showing the different extrapolations.

- **Human:** The final SN selection was done manually by a human scanner (the thesis author), which is not included in the MC simulation. Any simulated SN that would be part of the manual investigation sample is assumed to be selected as a SN with 100% efficiency. To assess the actual human SN selection efficiency with a blind test is difficult and time consuming. It could not be done because of a lack of data (FITS images of simulated SNe). Therefore, the error introduced by the human scanning is estimated $\pm 20\%$ as an educated guess. It goes in both directions because there is not only the possibility of missing SNe, but also of mis-identifying other sources as SNe.

Each uncertainty is investigated independently, upper and lower bounds are calculated to derive confidence intervals. The resulting individual systematic errors are listed in Table 8.10, identified by the boldface acronyms given above. The largest sources of uncertainty are the limiting magnitude (LM) and the luminosity function (LF). The uncertainties are added in quadrature¹⁴ for the total systematic errors:

$$\begin{aligned}
 \text{Type Ia: } N_{\text{SN,BG}} &= 8.2 \begin{pmatrix} +8.4 \\ -5.0 \end{pmatrix} \\
 \text{Type Ibc: } N_{\text{SN,BG}} &= 1.0 \begin{pmatrix} +1.2 \\ -0.5 \end{pmatrix} \\
 \text{Type II: } N_{\text{SN,BG}} &= 2.0 \begin{pmatrix} +2.5 \\ -1.0 \end{pmatrix} \\
 \text{all SNe (sum): } N_{\text{SN,BG}} &= 11.2 \begin{pmatrix} +8.8 \\ -5.1 \end{pmatrix}.
 \end{aligned} \tag{8.10}$$

¹⁴ Meaning to take the square root of the sum of squares.

8.9 Conclusion

8.9.1 Summary

The analysis discussed in this chapter was performed to search for optical SN signatures in PTF images taken as follow-up to IceCube neutrino alerts. The 20 analyzed neutrino alerts were recorded between August 2010 and December 2012 and triggered optical follow-up in 29 PTF fields. If some of the neutrino alerts were caused by SN explosions, then one might find optical SN counterparts in the follow-up images acquired after the neutrino alerts. Because the PTF fields are large (7.3 ($^{\circ}$)²) and the images relatively deep, it is not unlikely to detect SNe by chance.

The data reduction applied to the PTF images involves reference image construction and image subtraction. It delivers ca. 3 million source candidates that are spatially analyzed inside a PostgreSQL analysis database and grouped into ca. 200 000 clusters of nearby source detections. A SN detection algorithm was developed. In particular, an automated lookup in the astronomical catalogs SDSS and 2MASS was implemented for cross-checks. A central part of the SN detection algorithm was newly developed and involves the fitting of the SN light curve with analytical functions and using the ratio of the goodness-of-fit as selection parameter. The remaining 790 SN candidates were manually investigated and classified using self-developed rules and a dedicated GUI application.

A Monte Carlo simulation of the SN search was developed completely from scratch. This was motivated by two objectives: (1) To compare the number of found SNe with the expected number of background SNe found by chance coincidence. (2) To assess that the method works, i.e. the efficiency of the SN selection is as high as expected. The simulation uses the following technique: Using meta-data about fake SNe inserted into real images, multi-dimensional distributions were constructed of the parameters required to describe a SN in the analysis. When a SN is simulated, random values are drawn from the distributions according to the optical quality parameters of the real images. In particular, after selecting a SN host galaxy of appropriate brightness, the SN is inserted randomly on top of the galaxy. The local background brightness from the host galaxy, which serves as an important quality parameter, is calculated from SDSS data. An analytic limiting magnitude model has been developed that depends on the local background brightness. Finally, quite some effort has been invested to estimate the systematic uncertainties on the SN detection expectation.

The SN search led to 15.0 ± 11.4 SN detections, with the most pessimistic/optimistic selections ranging between only 2 and 30 SNe. Without available spectra, it is not possible for most SN candidates to unambiguously classify them. The number of detected SNe can be compared to the expected number of random background SN detections, which was determined with the dedicated Monte Carlo simulation. The result is a background expectation of $11.2^{+2.0}_{-1.7} \binom{+8.8}{-5.1}$ SN detections. The number of found and expected SNe lie close to each other, without an indication of signal SNe creating neutrino bursts in IceCube.

8.9.2 Outlook

The uncertainties on both the number of found and the number of expected SNe are very large, which is unfortunate because it limits the power of the analysis to distinguish the signal from the null hypothesis. Therefore, the most valuable outcome of the analysis might not be the result itself, but the experience gained along the way. Some weaknesses and possibilities for improvement, as perceived by the thesis author, are summarized below:

1. The SN search could be further automated by excluding clusters that have many non-detection images inspite of good image quality. However, some caution is advised (see Section 8.3.5).

2. The light curve (LC) fitting applied in the SN search, while performing well in most cases, has problems describing some SN light curves, especially plateau SNe. In [249], LC template functions are derived by averaging over many LCs. Separate templates for all SN classes are compiled, therefore also plateau SNe (type II-P) are described well. It could be checked if those template functions perform better than the LC function used in this analysis. The SN rates from [107] were derived with the same template functions from [249] and are already used in this analysis.
3. The systematic uncertainty on the manual SN selection could be estimated by doing a (double) blind test. Ideally, the manual SN selection should be done by several human scanners, in order to average out individual biases and to be able to better assess the biases. See e.g. [310] for a detailed description on how to achieve this.
4. In the simulation, a more detailed modeling of the limiting magnitude (e.g. as function of the host galaxy brightness) could be done, e.g. based on empirical data.
5. Instead of the method used here—sampling random numbers from probability distributions created with fake SN insertion meta-data—it would be more accurate to directly perform the insertion of fake SNe into the actual images that are analyzed, running an identical data reduction pipeline. This was not done because of a lack of time and knowledge.
6. It would be beneficial to have access to more astronomical catalog data, e.g. the NASA/IPAC Extragalactic Database (NED)¹⁵ or the Set of Identifications, Measurements, and Bibliography for Astronomical Data (SIMBAD)¹⁶. The SDSS catalog has the highest quality, but is only available for parts of the sky. Of particular interest is a more complete star catalog, as it would help to remove bogus SN candidates produced by variable stars.

Improvements of the analysis should aim at reducing the large systematic errors. One of the most important enhancements would be the establishment of a rapid and robust data analysis of the follow-up data. If potential SN candidates are discovered early on, within few weeks after the neutrino alert, then it is possible to acquire spectral data, which would eliminate ambiguity about the nature of the sources. This would enable to reduce the systematic error on the experimental number of found SNe to almost zero. In the presented analysis, this was not possible, mainly because for many alerts no reference images were available. With the successor of the PTF survey, the *Zwicky Transient Facility* (ZTF)¹⁷ [326, 327] about to start in 2017, this will be very easy to achieve. ZTF will employ a camera with a field of view of 47° ²—more than six times more than the 7.3° ² of PTF—large enough to scan the entire visible sky every few days, yielding “over 300 visits each year over the entire Northern” sky. All fields will have reference images for immediate data reduction and no transient will be missed. It is therefore strongly advised to repeat this analysis with ZTF.

Also on the simulation side, systematic uncertainties should be reduced as much as possible. The largest uncertainty comes from the assumed error on the limiting magnitude (LM) modeling. Fortunately, this error can be reduced with a more sophisticated LM modeling—as suggested in point 4 above—and might be eliminated altogether by performing actual image subtraction and data reduction—as suggested in point 5. Other large errors, the uncertainty on the light curve (LC) and the human error, can be addressed by more careful treatment as suggested in points 2 and 3. On the other hand, some systematic errors are external and outside of the experimenter’s control, namely the error on the volumetric SN rate and the error on the luminosity functions (LF). Finally, assessment of the error on the

¹⁵ <http://ned.ipac.caltech.edu/>

¹⁶ <http://simbad.u-strasbg.fr/simbad/>

¹⁷ <http://www.ptf.caltech.edu/ztf>

extrapolation of the detection probability (*d* Extrapol.) is challenging because of the extensive computation required to estimate the small detection probability at large distances (see Section 8.8, the point on *d* Extrapol.). However, it is in principle possible to develop an improved simulation strategy for large distances, e.g. only simulating a subset of all SNe that has a higher chance of detection and taking the subset nature into account.

Beyond merely repeating the analysis with improved infrastructure, the next step would be to use the experimental results to place limits on neutrino emission models, e.g. the choked jet SN model introduced in Section 3.2.8. A meta-analysis method, combining both the neutrino and optical data analysis results from all seasons, was developed by the thesis author, but later discarded, because the analysis of optical PTF data turned out to be complicated and uncertainties so high that the limits would not be very meaningful. Upper limits using IceCube neutrino data alone have been derived and are discussed in Section 6.8.3.

Cross-Sections and Effective Areas

A.1 Cross-section

In particle physics, the *interaction cross-section* or simply *cross-section* can be defined as an effective cross-sectional area, such that if an incident particle hits this area, the interaction takes place. For an incident beam of point-like particles, for instance neutrinos, that means that the neutrinos “see” a cross-section σ for each target particle, for instance an atomic nucleus. A neutrino beam consisting of N neutrinos spread across the area A and passing a path length dx in the target medium, will be attenuated by the dN_t target particles, contained in the target volume $dV = A dx$, according to:

$$dN = -N \frac{dN_t \sigma}{A} = -N \frac{dN_t \sigma}{A dx} dx = -N \frac{dN_t}{dV} \sigma dx = -N n_t \sigma dx, \quad (\text{A.1})$$

with target particle number density $n_t = dN_t/dV$. This leads to the typical differential equation for attenuation $dN/dx = -N n_t \sigma$, which is easily solved to

$$N(x) = N_0 e^{-n_t \sigma x} = N_0 e^{-x/\lambda}. \quad (\text{A.2})$$

Here, one can define an *attenuation length*

$$\lambda \equiv \frac{1}{n_t \sigma} = \frac{1}{\frac{N_{\text{nucl}} N_A}{V_{\text{mol}}} \sigma} = \frac{M_{\text{mol}}}{N_{\text{nucl}} N_A \rho \sigma} \approx \frac{1 \text{ g}}{N_A \rho \sigma}. \quad (\text{A.3})$$

It is the path length, after which the incident beam has been attenuated to $1/e$ of its original strength. For nuclei in ordinary matter, $n_t = N_{\text{nucl}} N_A / V_{\text{mol}}$, with N_{nucl} the number of nuclei per molecule, Avogadro’s number N_A the number of molecules in one mole, and V_{mol} the molar volume. One can also interpret the ratio of remaining to incident number of particles $N(x)/N_0$ as the inverse of the *interaction probability* $P(x) = 1 - N(x)/N_0 = 1 - \exp(-x/\lambda) = 1 - \exp(-n_t \sigma x)$ for a passage through a path length x of target material. In general, the cross-section σ , and thus the interaction probability, depends on parameters of the particles, e.g. energy.

As an example that illustrates how faint neutrino interactions are, consider the passage of neutrinos through a solid massive material such as lead. Lead has a density of $\rho = 11.35 \text{ g/cm}^3$. For an electron neutrino at 10 MeV energy, the dominant interaction is elastic scattering on electrons (see Section 2.3.2) with a cross-section of $\sim 1 \times 10^{-43} \text{ cm}^2$. One has to consider that the neutrinos do not interact with nuclei

as targets, but with electrons, so the target number density is roughly half the nucleon number density. The resulting attenuation length is $\lambda \approx 2.9 \times 10^{18}$ cm, which corresponds to about 0.9 pc or 3.1 light-years, comparable to the distance to the closest neighbor stars. For comparison, consider the radiation length X_0 that corresponds to the path after which a high-energy electron's energy has dropped to $1/e$ by bremsstrahlung and corresponds to $7/9$ of a high-energy photon's mean free path for pair production [17, p. 404]. For high-energy photons or electrons ($E \gtrsim 10$ MeV) in lead, X_0 is only 0.6 cm [17, p. 116], which is more than 18 orders of magnitude smaller than the attenuation length of neutrinos.

For high energy neutrinos, the cross-section becomes much higher. For example, for neutrinos at 1 TeV, the dominant CC DIS cross-section (see Section 2.3.2) is $\sim 6.2 \times 10^{-36}$ cm². This translates into an attenuation length of “only” 2.4×10^{10} cm in lead, so ca. 240 000 km, about 62% of the distance between Earth and Moon. For higher energies, the cross-section rises further, so that for neutrino energies above 1 PeV, the Earth is not transparent anymore and neutrino astronomy using the Earth as a muon shield becomes difficult.

A.2 Effective Volume

Effective volume is a useful detector parameter, which is defined as the geometrical volume that a perfectly efficient detector would have. Assuming that every single interaction occurring inside a certain volume would be detected with 100% efficiency (and 0% outside), then that volume would be the effective volume.

When performing detector simulation, there is a simple relation for the effective volume: It is the fraction of detected events times the volume in which interactions were simulated,

$$V_{\text{eff}} = \frac{N_{\text{det}}}{N_{\text{sim}}} V_{\text{sim}}. \quad (\text{A.4})$$

This effective volume is the effective volume for the observed interaction, e.g. if neutrino interactions producing leptons are observed, then it is the effective volume with respect to the produced leptons. The effective mass generally depends on the energy and can also depend on the direction of the detected particle.

A.3 Effective Area

While the effective volume is a useful quantity describing the detection of secondary particles in the detector, the effective area is a quantity describing the detector response to an incident flux of primary particles, for instance neutrinos. Analogue to the effective volume, the effective area is the geometrical area of a hypothetical detector with 100% efficiency. To calculate the effective area A_{eff} from the effective volume V_{eff} , one simply needs to consider the cross-section of the observed neutrino interaction. Each target particle in the effective volume contributes its cross-section σ to the effective area A_{eff} , so that

$$A_{\text{eff}} = \sigma N_A \frac{V_{\text{eff}}}{V_{\text{mol}}} N_{\text{nucl}}, \quad (\text{A.5})$$

where $N_A V_{\text{eff}}/V_{\text{mol}}$ gives the number of target molecules in the effective volume and N_{nucl} is the number of target particles (e.g. nuclei) per molecule. Multiplying A_{eff} with a neutrino flux (number of neutrinos per time and area) directly yields the event rate in the detector.

Some Astronomical Concepts

B.1 Point Spread Function and Seeing

The *point spread function (PSF)* describes the response of a telescope to a point source of radiation. It can be seen as the spatial distribution of the measured light intensity for an unresolved point source. In theory, a perfect lense with circular aperture (light collecting opening) would create a diffraction pattern known as an *Airy disk* [69, p. 54f.]. An Airy disk pattern contains of a bright blob (the disk) in the center and several concentric rings (the higher order interference maxima) around it. It can usually be approximated by a Gaussian profile, ignoring the outer rings,

$$I(x, y) = I_0 \exp\left(-\frac{x^2 + y^2}{2\sigma^2}\right), \quad (\text{B.1})$$

with intensity I_0 at the center, spatial coordinates x and y (either angle coordinate or pixel coordinate on camera chip), and Gaussian width σ corresponding to one standard deviation. The width σ is inversely proportional to the aperture diameter of the telescope.

Only for space-based telescopes outside the Earth's atmosphere, the PSF corresponds to the theoretical Airy disk. For ground-based optical telescopes, the PSF is dominated by *atmospheric seeing* [69, p. 49 f.]. Seeing is caused by turbulent mixing of the atmosphere due to small fluctuations of density and temperature. The result is a time and space-dependent refractive index, which causes a point source, e.g. a star, to dance rapidly around its average position, on the time scale of about 0.01 s. For an image sensor, typically integrating for seconds, minutes, or longer, the resulting image is a blurred blob. The PSF width is given practically only by the seeing and the Airy disk can be ignored. Seeing is usually measured as FWHM (full width at half maximum) of the PSF. Using a Gaussian profile again, the seeing FWHM s and the Gaussian width σ are connected by

$$s = 2\sqrt{2\ln 2}\sigma. \quad (\text{B.2})$$

B.2 Measuring Brightness in Magnitudes

The measurement of an astronomical object's brightness is called *photometry* and it is often measured in *magnitudes*. The unit magnitude for brightness was introduced in antiquity as a rather subjective measure of a star's brightness. Stars were categorized into six classes, according to their apparent angular

size (since brighter stars appear larger, even though being point sources due to their large distance), with the brightest stars being in the first and the faintest in the sixth class [69, p. 30].

The human brain processes sensations logarithmically, meaning that if a signal strength is increased by a certain factor, then this is perceived as increase by a certain difference. This realization gave rise to the modern quantitative definition of magnitude as logarithmic scale for an object's radiation intensity (transmitted power per unit area), measured at a specific wavelength or in the passband of a specific filter. The simplest way to determine the magnitude m from an object's intensity I is relative to a reference object with known magnitude m_{ref} and measured intensity I_{ref} via [69, p. 30]

$$m - m_{\text{ref}} \equiv -2.5 \log_{10} \left(\frac{I}{I_{\text{ref}}} \right),$$

$$\frac{I}{I_{\text{ref}}} = 10^{-0.4(m - m_{\text{ref}})}.$$
(B.3)

This equation defines the magnitude scale as a relative one. The factor -2.5 ensures that the ancient magnitude scale more or less matches the modern definition. A difference of one magnitude in apparent brightness corresponds to a difference of factor $10^{0.4} \approx 2.512$ in physical intensity. Stars whose intensity differs by a factor 100 differ by exactly 5 magnitudes, or 5 mag, in brightness. The minus sign in Equation B.3 leads to brighter stars being assigned a smaller magnitude value, which is counter-intuitive.

Since the above definition of magnitude is only relative, one needs to agree on a reference point in order to derive magnitude values on an absolute scale. The choice of reference point is arbitrary and different photometric magnitude systems exist, based on different choices. One often used system is the *Vega magnitude* system, in which the star Vega (or α Lyrae, so the brightest star in the constellation Lyra) is defined to have a brightness of 0 mag in all filters [69, p. 31]. Another system is the *AB magnitude* system, which does not rely on a natural astronomical object that may be subject to change (such as Vega), but instead is defined in terms of an artificial source having a certain absolute physical flux per unit frequency. The *monochromatic AB magnitude*, as used by the Sloan Digital Sky Survey (SDSS), was defined by Oke & Gunn (1983) [328] and is given in [294, eq. 1],

$$m_{\text{AB}} = -2.5 \log_{10} f_{\nu} - 48.6,$$
(B.4)

where f_{ν} is the flux per unit frequency measured in cgs units, i.e. $\text{ergs s}^{-1} \text{cm}^{-2} \text{Hz}^{-1}$. The zero point of this system, where $m_{\text{AB}} = 0$ mag lies at a flux of $f_{\nu} = 3631$ Jy, in the unit Jansky (Jy) and $1 \text{ Jy} = 10^{-26} \text{ W m}^{-2} \text{ Hz}^{-1} = 10^{-23} \text{ erg s}^{-1} \text{ cm}^{-2} \text{ Hz}^{-1}$. The monochromatic AB magnitude is handy for quick conversions of magnitudes to fluxes, if the exact normalization is unimportant. In addition to monochromatic magnitude, the SDSS photometric system defines a *broadband AB magnitude* as [294, eq. 7]

$$m = -2.5 \log_{10} \left(\frac{\int d(\log_{10} \nu) f_{\nu} S_{\nu}}{\int d(\log_{10} \nu) S_{\nu}} \right) - 48.6,$$
(B.5)

where f_{ν} is the energy flux per unit frequency incident on the atmosphere and S_{ν} is the response function of the telescope system at frequency ν , including atmospheric transmission, telescope transmission, filter transmission, and quantum efficiency of the light sensor, i.e. S_{ν} is the detection probability for an incident photon at ν . This broadband definition of AB magnitude can in principle reproduce the measured magnitudes exactly, given that the source's spectrum and the system response is known perfectly.

Many astronomical surveys, such as PTF 6.2.3, use a different definition of magnitude that depends on a so-called *zero point (ZP)*. For this ZP magnitude system, the flux f is not measured in physical units, but in counts measured by the CCD (charge-coupled device) image sensor of the telescope camera. The

ZP is the magnitude that a flux producing 1 count would have, so

$$m = \text{ZP} - 2.5 \log_{10} \left(\frac{f}{1 \text{ count}} \right). \quad (\text{B.6})$$

This definition is very convenient, allowing for easy conversion from the CCD output to magnitude and vice-versa.

In astronomy, one distinguishes between apparent and absolute magnitudes. *Absolute magnitude* is defined as the magnitude of an object measured at a fixed distance of 10 pc. Thus, absolute magnitude corresponds to the intrinsic radiated luminosity of a source, independent of its distance to the observer. To distinguish it from absolute magnitude, the magnitude measured at Earth is called *apparent magnitude*. It is straight forward to convert absolute magnitude M and apparent magnitude m back and forth using the general magnitude definition from above. When I is the intensity measured at Earth for apparent magnitude m , I_0 the intensity measured at 10 pc from the source for absolute magnitude M , L the luminosity of the source, and d_L the luminosity distance to the source, then

$$\mu \equiv m - M = -2.5 \log_{10} \frac{I}{I_0} = -2.5 \log_{10} \frac{L/(4\pi d_L^2)}{L/(4\pi (10 \text{ pc})^2)} = \quad (\text{B.7})$$

$$= -2.5 \log_{10} \left(\frac{10 \text{ pc}}{d_L} \right)^2 = -5 \log_{10} \frac{10 \text{ pc}}{d_L} = 5 \log_{10} \frac{d_L}{10 \text{ pc}} = \quad (\text{B.8})$$

$$= 5 \left(\log_{10} \frac{d_L}{1 \text{ pc}} - 1 \right). \quad (\text{B.9})$$

The difference μ between apparent and absolute magnitude is also called the *distance modulus*.

Supplementary Material for Chapter 5

For the noise cleaning with the phase space cut (Section 5.5.1), the noise trigger rate f_{noise} as function of the cut value t_{max} must be known. To obtain f_{noise} , the phase space volume,

$$V_{\text{PS}}(t_{\text{max}}) \equiv \int_{t_{\text{min}}}^{t_{\text{max}}} V(\Delta t) d\Delta t = \int_{t_{\text{min}}}^{t_{\text{max}}} \frac{4}{3}\pi \left((r_{\text{max}}(\Delta t))^3 - (r_{\text{min}}(\Delta t))^3 \right) d\Delta t, \quad (\text{C.1})$$

is calculated via integration of the fiducial volume of spherical shells up to t_{max} .¹ The average number of noise hits within the phase space volume V_{PS} is the product of V_{PS} , the density of instrumented modules per unit volume, ρ_m , and the module noise hit rate f_m ,

$$\lambda(t_{\text{max}}) = V_{\text{PS}}(t_{\text{max}}) \rho_m f_m. \quad (\text{C.2})$$

Then, the noise trigger rate is the Poisson probability to have n_{trig} or more noise hits within the phase space volume V_{PS} , multiplied with the “number of phase space volumes” within the detector per time, so the geometrical detector volume V_{det} over V_{PS} ,

$$f_{\text{noise}} = \left(1 - P_{\text{cum}}(n_{\text{trig}} - 1 | \lambda) \right) \frac{V_{\text{det}}}{V_{\text{PS}}}. \quad (\text{C.3})$$

A plot of f_{noise} according to Equation C.3 is shown in Figure 5.11.

If the PS cut is combined with RT cleaning, it is more complicated to calculate f_{noise} : The noise hit rate of each sensor module is effectively reduced thanks to the local coincidence criterion of the RT cleaning. The probability for at least one noise hit on any single module during the RT time window is

$$P_{m,\text{RT}} = 1 - e^{-f_m t_{\text{RT}}}. \quad (\text{C.4})$$

This means that the probability for no noise hit on n modules is $(1 - P_{m,\text{RT}})^n$. The number of modules contained in the RT volume is

$$n_{m,\text{RT}} \approx \rho_m \frac{4}{3} \pi r_{\text{RT}}^3. \quad (\text{C.5})$$

¹ t_{min} is a rather technical parameter set to -500 ns, which is lower than the lowest occurring values of Δt .

So, the probability for at least one noise hit that is RT-correlated with a certain module is

$$P_{\text{RT}} \approx 1 - (1 - P_{m,\text{RT}})^{n_{m,\text{RT}}}. \quad (\text{C.6})$$

Because the RT cleaning removes all hits that are not RT-correlated, the module noise rate f_m is reduced to an effective noise rate $f'_m = f_m P_{\text{RT}}$. Substituting f_m with f'_m , Equations C.2 and C.3 still hold.

Derivation of the Optical Follow-Up Doublet Test Statistic

The optical follow-up (OFU) program detects multiplets of neutrinos that are less than 100 s apart in time and less than 3.5° apart in space. Any triplet or higher order multiplet occurs so rarely from background (at a rate of ~ 0.03 per year) that a detection is fairly significant on its own. However, in the case of neutrino doublets, random background detections occur frequently (on the order of ~ 50 per year). It is desirable to use as much information as possible in order to separate background and signal doublets and thus increase the discovery potential and sensitivity.

One route to achieve this goal is to employ the Neyman-Pearson lemma [329] from statistical hypothesis testing, which states that the ratio of the likelihoods L for the null hypothesis H_0 (background doublet) and the alternative hypothesis H_1 (signal doublet):

$$\lambda(x) = \frac{\mathcal{L}(x|H_0)}{\mathcal{L}(x|H_1)} \quad (\text{D.1})$$

serves as the most powerful test statistic. Most powerful means that at a given level of significance, the probability to detect a deviation from H_0 (the sensitivity) is maximized. The likelihood-ratio test is the foundation for most neutrino point source searches in IceCube and its application for neutrino astronomy is discussed in depth in [330] and [331]. The likelihood \mathcal{L} can depend on many observables and thus make full use of the information that is contained in the neutrino detections. As opposed to a binary true-false decision in case of the simplistic multiplet selection criteria (either the neutrinos are close or not), the likelihoods and the derived test statistic λ are continuous variables and provide a much more powerful discrimination between signal and background. While the binary test does not distinguish between neutrinos barely fulfilling the selection criteria and neutrinos that are e.g. extremely close in time, the λ test handles all situations in a statistically correct way and can also use other information.

This is why a likelihood-ratio test was chosen for the optical and X-ray follow-up programs. A neutrino doublet test statistic was derived by mostly Miles Smith and Andreas Homeier for the application in the X-ray follow-up (XFU). The driving motivation was that Swift's observation schedule did not allow to respond to many follow-up alerts, as was the case for follow-up with ROTSE. The test statistic is used to select only the neutrino doublets with the highest probability of being signal, which are the ones most worthy to follow up. The derivation of this test statistic has not been part of this thesis' work, but since it is widely used in the OFU program discussed in Chapter 6, its derivation is presented here.

Following [331], one first defines the logarithmic likelihood ratio,

$$D = 2 \ln \left(\frac{\mathcal{L}(n_s, x_s)}{\mathcal{L}(n_s = 0)} \right) = 2 \ln \left(\frac{\prod_{k=1}^N \left(\frac{n_s}{N} S_k + \frac{N-n_s}{N} B_k \right)}{\prod_{k=1}^N B_k} \right), \quad (\text{D.2})$$

where S_k and B_k are the signal and background probability of the k th event, n_s is the signalness of the sample, correlated with the number of signal events, and N is the total number of events. For the special case of a doublet with two signal neutrinos, we set $n_s = N = 2$, and the expression simplifies to

$$D = 2 \ln \left(\frac{\prod_{k=1}^2 S_k}{\prod_{k=1}^2 B_k} \right) = 2 \left(\ln \left(\sum_{k=1}^2 S_k \right) - \ln \left(\sum_{k=1}^2 B_k \right) \right) = 2 \sum_{k=1}^2 (\ln(S_k) - \ln(B_k)) = 2 \sum_{k=1}^2 \ln(S_k/B_k). \quad (\text{D.3})$$

The signal probability S_k for the k th event depends on the angle $\Delta\Psi_k$ between the event's direction and the assumed source, and the directional error σ_k , while the background probability B_k is constant and normalized to 1 over the entire analyzed solid angle Ω and analyzed livetime T ,

$$S_k = \frac{1}{2\pi\sigma_k^2} \exp\left(\frac{-\Delta\Psi_k^2}{2\sigma_k^2}\right) \cdot \frac{1}{\tau} \text{box}(t_k|t_0, t_0 + \tau), \quad B_k = \frac{1}{\Omega T}. \quad (\text{D.4})$$

S_k consists of a Gaussian space term and a boxcar time term: The function $\text{box}(x|a, b)$ is a boxcar function, which is 1 if x is between a and b and 0 otherwise. With S_k and B_k ,

$$D = 2 \sum_{k=1}^2 \left[\ln((2\pi\sigma_k^2)^{-1}) - \frac{\Delta\Psi_k^2}{2\sigma_k^2} \right] + 2 \sum_{k=1}^2 \left[\ln\left(\frac{T}{\tau} \text{box}(t_k|t_0, t_0 + \tau)\right) \right] + 2 \sum_{k=1}^2 \ln(\Omega), \quad (\text{D.5})$$

where the last term with $\ln(\Omega)$ is a constant offset that is dropped hereafter. In order to stay finite, the boxcar function must enclose both event times t_1 and t_2 , i.e. $t_0 \leq t_1$ and $\tau \geq t_2 - t_0$.

For small angles $\Delta\Psi_k$, one can approximate $\Delta\Psi_k^2 \approx 2(1 - \cos \Delta\Psi_k) = 2(1 - \hat{r}_s \cdot \hat{r}_k)$ with the dot product between the unit vectors \hat{r}_s (direction of source) and \hat{r}_k (direction of neutrino event). Then:

$$\begin{aligned} D &= -2 \left(\ln((2\pi\sigma_1\sigma_2)^2) + \frac{1 - \hat{r}_s \cdot \hat{r}_1}{\sigma_1^2} + \frac{1 - \hat{r}_s \cdot \hat{r}_2}{\sigma_2^2} \right) + 2 \ln\left(\frac{T}{\tau}\right) \Big|_{t_0 \leq t_1, \tau \geq t_2 - t_0} \\ &= -2 \left(\ln((2\pi\sigma_1\sigma_2)^2) + \frac{1}{\sigma_1^2} + \frac{1}{\sigma_2^2} - \hat{r}_s \cdot \left(\sum_{k=1}^2 \frac{\hat{r}_k}{\sigma_k^2} \right) + \ln\left(\frac{\tau}{T}\right) \Big|_{t_0 \leq t_1, \tau \geq t_2 - t_0} \right) \\ &= -2 \left(\ln((2\pi\sigma_1\sigma_2)^2) + \frac{1}{\sigma_1^2} + \frac{1}{\sigma_2^2} - \hat{r}_s \cdot \langle \hat{r} \rangle \left| \sum_{k=1}^2 \frac{\hat{r}_k}{\sigma_k^2} \right| + \ln\left(\frac{\tau}{T}\right) \Big|_{t_0 \leq t_1, \tau \geq t_2 - t_0} \right), \end{aligned} \quad (\text{D.6})$$

where the average event direction,

$$\langle \hat{r} \rangle \equiv \frac{\sum_{k=1}^2 \frac{\hat{r}_k}{\sigma_k^2}}{\left| \left(\sum_{k=1}^2 \frac{\hat{r}_k}{\sigma_k^2} \right) \right|} \quad (\text{D.7})$$

has been used. The norm of the average direction,

$$\begin{aligned} \left| \sum_{k=1}^2 \frac{\hat{r}_k}{\sigma_k^2} \right| &= \sqrt{\left(\frac{\hat{r}_1}{\sigma_1^2} + \frac{\hat{r}_2}{\sigma_2^2} \right)^2} = \sqrt{\frac{1}{\sigma_1^4} + \frac{1}{\sigma_2^4} + 2 \frac{\hat{r}_1 \hat{r}_2}{\sigma_1^2 \sigma_2^2}} \\ &= \sqrt{\frac{1}{\sigma_1^4} + \frac{1}{\sigma_2^4} + 2 \frac{1}{\sigma_1^2 \sigma_2^2} - 2 \frac{1}{\sigma_1^2 \sigma_2^2} + 2 \frac{\hat{r}_1 \hat{r}_2}{\sigma_1^2 \sigma_2^2}} = \sqrt{\left(\frac{1}{\sigma_1^2} + \frac{1}{\sigma_2^2} \right)^2 - 2 \frac{1}{\sigma_1^2 \sigma_2^2} + 2 \frac{\hat{r}_1 \hat{r}_2}{\sigma_1^2 \sigma_2^2}}. \end{aligned} \quad (\text{D.8})$$

We define:

$$\begin{aligned} \frac{1}{\sigma_w^2} &\equiv \frac{1}{\sigma_1^2} + \frac{1}{\sigma_2^2}, & \sigma_q^2 &\equiv \sigma_1^2 + \sigma_2^2 & \Rightarrow \sigma_w^2 \sigma_q^2 &= \sigma_1^2 \sigma_2^2, \\ \hat{r}_1 \hat{r}_2 &= \cos \Delta\Psi, & \hat{r}_s \langle \hat{r} \rangle &= \cos \theta, \end{aligned} \quad (\text{D.9})$$

with the angle $\Delta\Psi$ between the two events of the doublet and the angle θ between the average event direction and the assumed source direction. With that:

$$D = -2 \left(\ln \left((2\pi \sigma_w \sigma_q)^2 \right) + \frac{1}{\sigma_w^2} \left(1 - \cos \theta \sqrt{1 - 2 \frac{\sigma_w^2}{\sigma_q^2} (1 - \cos \Delta\Psi)} \right) + \ln \frac{\tau}{T} \Big|_{t_0 \leq t_1, \tau \geq t_2 - t_0} \right). \quad (\text{D.10})$$

Approximating for small x ,

$$\sqrt{1-x} \approx 1 - \frac{x}{2}, \quad \cos x \approx 1 - \frac{x^2}{2}, \quad (\text{D.11})$$

$$\begin{aligned} \frac{D}{-2} &\approx \ln \left((2\pi \sigma_w \sigma_q)^2 \right) + \frac{1}{\sigma_w^2} \left[1 - \left(1 - \frac{\theta^2}{2} \right) \left(1 - \frac{\sigma_w^2}{\sigma_q^2} \left(1 - \frac{\Delta\Psi^2}{2} \right) \right) \right] + \ln \frac{\tau}{T} \Big|_{t_0 \leq t_1, \tau \geq t_2 - t_0} \\ &\approx \ln \left((2\pi \sigma_w \sigma_q)^2 \right) + \left(\frac{\theta^2}{2\sigma_w^2} + \frac{\Delta\Psi^2}{2\sigma_q^2} \right) + \ln \frac{\tau}{T} \Big|_{t_0 \leq t_1, \tau \geq t_2 - t_0} \\ &= \frac{\theta^2}{2\sigma_w^2} + \ln(2\pi \sigma_w^2) + K_\Psi + K_\tau, \end{aligned} \quad (\text{D.12})$$

where a term containing $\theta^2 \Delta\Psi^2$ has been omitted in the small angle approximation, and the constants

$$K_\Psi \equiv \frac{\Delta\Psi^2}{2\sigma_q^2} + \ln(2\pi \sigma_q^2), \quad K_\tau \equiv \ln \frac{\tau}{T} \Big|_{t_0 \leq t_1, \tau \geq t_2 - t_0} \quad (\text{D.13})$$

have been introduced. D is maximized, i.e. $D/2$ minimized, at $\theta = 0$, where the source position estimator equals the average neutrino event direction. However, this is not what we are interested in, for we want to maximize the probability to find the source in the field of view (FoV) of the follow-up telescope. This probability is roughly the integral of the likelihood (interpreted as probability density) $\mathcal{L}(n_s = N, \theta)$ over the FoV, which corresponds to the integral of $\exp(D/2) = \mathcal{L}(n_s = N, \theta) / \mathcal{L}(n_s = 0)$,

$\mathcal{L}(n_s = 0)$ being constant.

$$\begin{aligned}
 \int_{\Omega_{\text{FoV}}} e^{D/2} d\Omega &= \int_{\phi} \int_{\theta} e^{-\frac{\theta^2}{2\sigma_w^2}} \frac{1}{2\pi\sigma_w^2} e^{-K\Psi} e^{-K\tau} \sin\theta d\theta d\phi \\
 &\approx 2\pi \int_{\theta} e^{-\frac{\theta^2}{2\sigma_w^2}} \frac{1}{2\pi\sigma_w^2} e^{-K\Psi} e^{-K\tau} \theta d\theta = \int_{\theta} \frac{\theta}{\sigma_w^2} e^{-\frac{\theta^2}{2\sigma_w^2}} e^{-K\Psi} e^{-K\tau} d\theta \quad (\text{D.14}) \\
 &= \left[-e^{-\frac{\theta^2}{2\sigma_w^2}} \right]_0^{\theta_A} e^{-K\Psi} e^{-K\tau} = \left(1 - e^{-\frac{\theta_A^2}{2\sigma_w^2}} \right) e^{-K\Psi} \frac{T}{\tau} \Big|_{t_0 \leq t_1, \tau \geq t_2 - t_0}.
 \end{aligned}$$

The angle θ_A is the half-opening angle of the FoV cone, i.e. the radius of the FoV. This integration represents a marginalization with respect to the variable θ , i.e. the θ dependency was removed via integration. The only remaining variable is τ , the width of the time window. The expression is maximized for τ as small as possible, however comprising both doublet events, i.e. $t_0 = t_1, \tau = t_2 - t_1 \equiv \Delta t$, so τ is simply the time difference Δt between the two doublet events. Finally, we define the test statistic λ as:

$$\lambda \equiv -2 \ln \left(\int e^{D/2} d\Omega \right) = \frac{\Delta\Psi^2}{\sigma_q^2} + 2 \ln(2\pi\sigma_q^2) - 2 \ln \left(1 - e^{-\frac{\theta_A^2}{2\sigma_w^2}} \right) + 2 \ln \frac{\Delta t}{T}. \quad (\text{D.15})$$

See Section 6.6.2 for the application of λ for the optical follow-up doublets. The total analyzed livetime, i.e. the longest possible time window τ , is $T = 100$ s in this case.

Supplementary Material for Chapter 8

E.1 Observability of PTF Alerts

Not all of the alerts that were forwarded to PTF could be followed up successfully. There can be various reasons why PTF was unable to take follow-up exposures. Those reasons include the sheer visibility of the field: It must be above the horizon during the night and not too close to the Moon. Other possible reasons are bad weather during potential observation times, maintenance of the telescope, malfunction of the telescope equipment, or conflicting observation schedules.

Figures E.1 to E.5 show information on the observability of the follow-up fields during the first 28 days after the alert. Nights, which are defined as the Sun’s elevation being more than 15° below the horizon, are indicated as grey shades.

The alert’s visibility according to its ephemeris, i.e. its position in the sky for a certain location on Earth—Palomar Mountain—at a certain time, is plotted as a black line. Visibility is defined as the inverse of the airmass and depends on the elevation above the horizon. Airmass, in turn, is defined as the optical path length through Earth’s atmosphere, relative to the shortest optical path length at sea level, i.e. at the zenith. That means, the visibility is 1 if the observed source is at the zenith and goes to 0 as the source approaches the horizon.¹ For the airmass $a(h)$ as function of the elevation angle h above the horizon, the following analytic form from [332] is used, which was derived as an approximation to tabulated values:

$$a(h) = \frac{1}{\sin h + 0.50572 (h + 6.07995^\circ)^{-1.6364}}. \quad (\text{E.1})$$

Visibility is $1/a(h)$, unless the Moon is closer than 20° , elevation $h < 5^\circ$ or the Sun’s elevation is $> -15^\circ$, in which cases it is set to 0.

In addition to the visibility and night periods as grey shades, Figures E.1 to E.5 visualize the distance to the Moon as blue and to the Sun as green shades. The shades’ color intensity is maximal if the distance is 0° and fades linearly to 0 at a distance of 15° for the Moon, 40° for the Sun.

Meteorological data is visualized as a pale red line in the plots. It represents the approximate weather situation, i.e. the sky transparency, in the vicinity of Palomar Mountain. The line is at a value of 1 for a clear sky, at 0 for an overcast sky, and otherwise in between. The underlying data were taken from hourly METAR weather reports [333, 334] that are measured at every commercial airport and

¹ Palomar Observatory is at an altitude of about 1700 m [224], so that the actual airmass is < 1 at the zenith. This is not taken into account here and the computed airmass/visibility corresponds to sea level.

used for aviation. The METAR reports are publicly available² and there are several publicly accessible databases that archive METAR reports. From one of those databases,³ data were automatically retrieved and parsed using a script. The METAR data was queried for the station at Ramona Airport, the airport closest to Palomar Mountain, which is about 35 km south of Palomar Observatory and at a lower altitude of about 430 m [335] instead of 1700 m [224], so that the sky transparency obtained in this way can only serve as a rough estimate of the meteorological conditions at Palomar Observatory.

Most cases of missing or sparse follow-up data can be explained by investigating the observability plotted in Figures E.1 to E.5. However, for some alerts, e.g. PTF alerts 15, 17, and 23, the observability does not explain why observations were not carried out. It might have been due to technical maintenance of the telescope, or for organizational reasons. In case of PTF alert 23, the reason is simply the transition from PTF to iPTF: The first two exposures were taken on 2012–12–21 and went into the PTF database, which is analyzed here. In February 2013, 44 more exposures within the 100 d window were carried out, but because of the transition to iPTF on 2013–01–01, they are contained in the iPTF database and not part of this analysis.

E.2 Details on the PTF Data Reduction Pipeline

E.2.1 Data Exploration

The data taken with the P48 telescope are gathered on storage servers at the National Energy Research Scientific Computing Center (NERSC)⁴, with meta-data about the photometry put into a PostgreSQL database at NERSC. For each alert and observation field, the PTF photometry database at NERSC was queried to obtain lists of suitable reference exposures, as well as of all available new exposures taken during the first 100 days following each alert date. Because part of the original data files—images stored in the FITS format [238]—had already been erased from the file servers, they had to be pulled back from a tape archive with a command-line tool interfacing a tape robot.

Reference exposures were selected from periods either before, shortly after or well after the neutrino alert. Here, shortly after means up to about 3 days after the alert,⁵ so that a SN exploding at the time of the neutrino alert is either not visible yet or its light is still negligible compared to maximum light. Well after means: usually several hundred, but at least 100 days after the neutrino alert, to make sure that a SN has already faded enough for a significant difference in magnitude between the reference and the new exposures. Besides the time criterion, at least 3, preferably 7, exposures with limiting magnitude of >19.5 mag, preferably >20.0 mag, and with seeing of $<3.5''$, preferably $<3''$, were selected to construct the reference image for each field. If not enough high quality reference exposures could be found, new observations of the field were scheduled (if possible) in order to produce suitable references.

E.2.2 Reference Image Construction

The central software pieces used to create one deep reference image from several reference exposures are SExtractor, SCAMP, and SWarp. Due to the complexity, a flow chart of the reference image construction process was created that can be viewed in Figure E.6.

² For example at <http://aviationweather.gov/dataserver> for every METAR issued during the last three days, or <http://www.nws.noaa.gov/tg/datahelp.php> for the most recent METAR.

³ <http://mesonet.agron.iastate.edu/cgi-bin/request/asos.py>

⁴ <http://www.nersc.gov/>

⁵ With an exception for PTF alert 9, which has most reference exposures from 5 days, some from 30 days after the alert. Without this exception, analysis of PTF alert 9 would have been impossible.

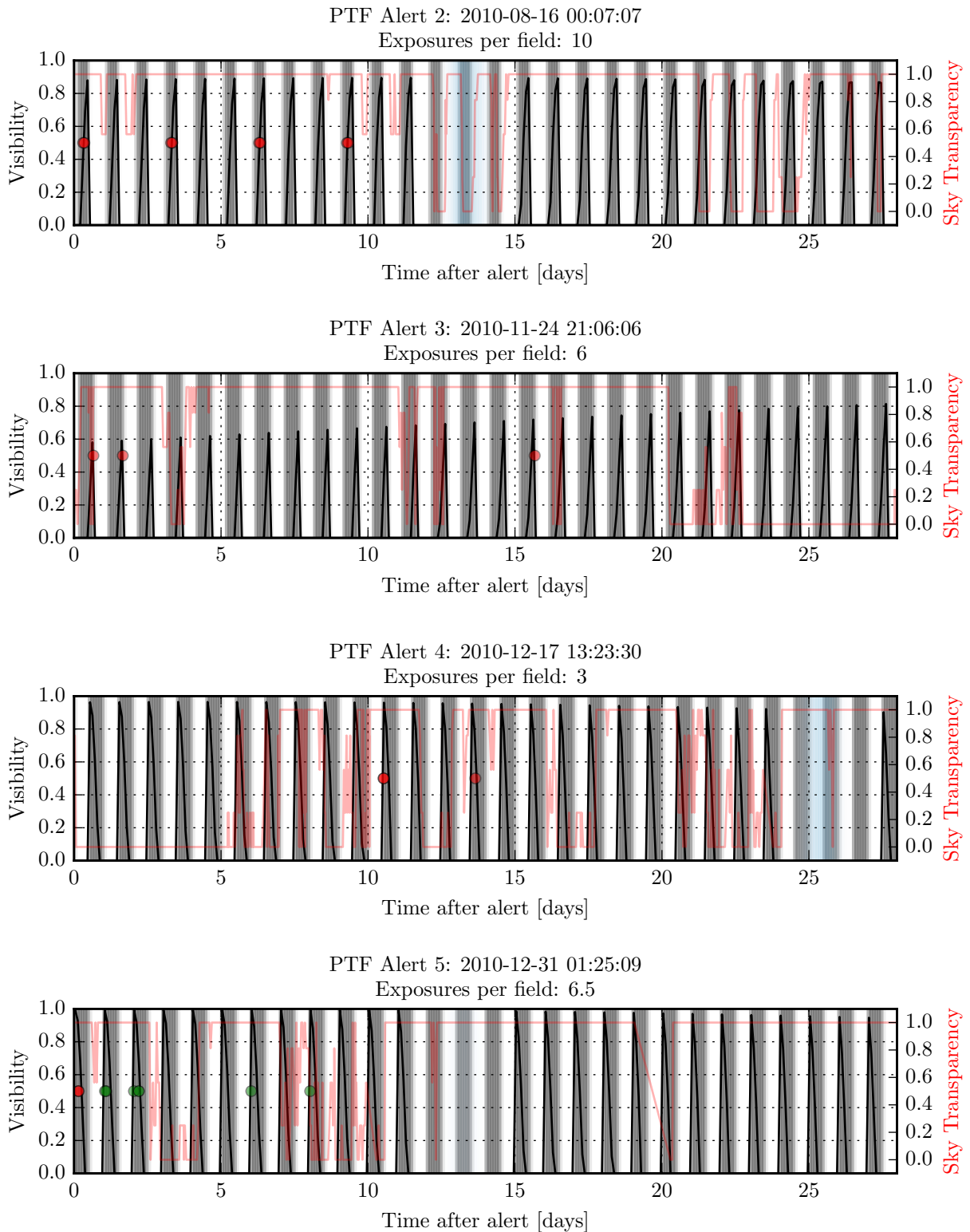


Figure E.1: Observability of the neutrino alert direction, given ephemerical and meteorological constraints. The black line shows the theoretical visibility of the object, in terms of airmass, distance to the Moon and altitude of the Sun. The pale red line represents the local weather situation. It is at 1 for a clear sky, at 0 for an overcast sky, otherwise in between. Blue and green shades depict the distance to Moon and Sun. Times of P48 exposures taken with the *R* and *g* filter are shown as red and green dots in the center of the image.

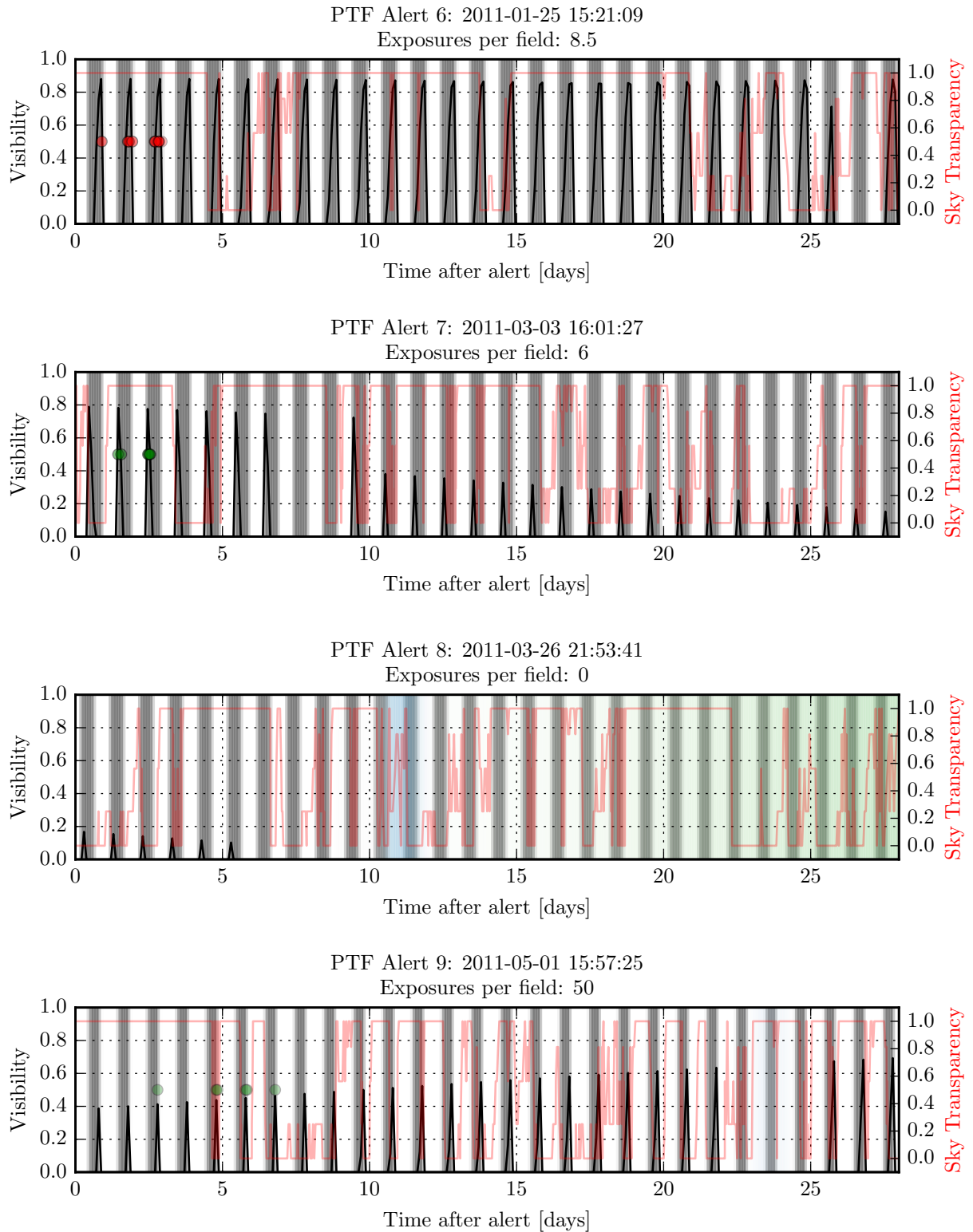


Figure E.2: See Figure E.1.

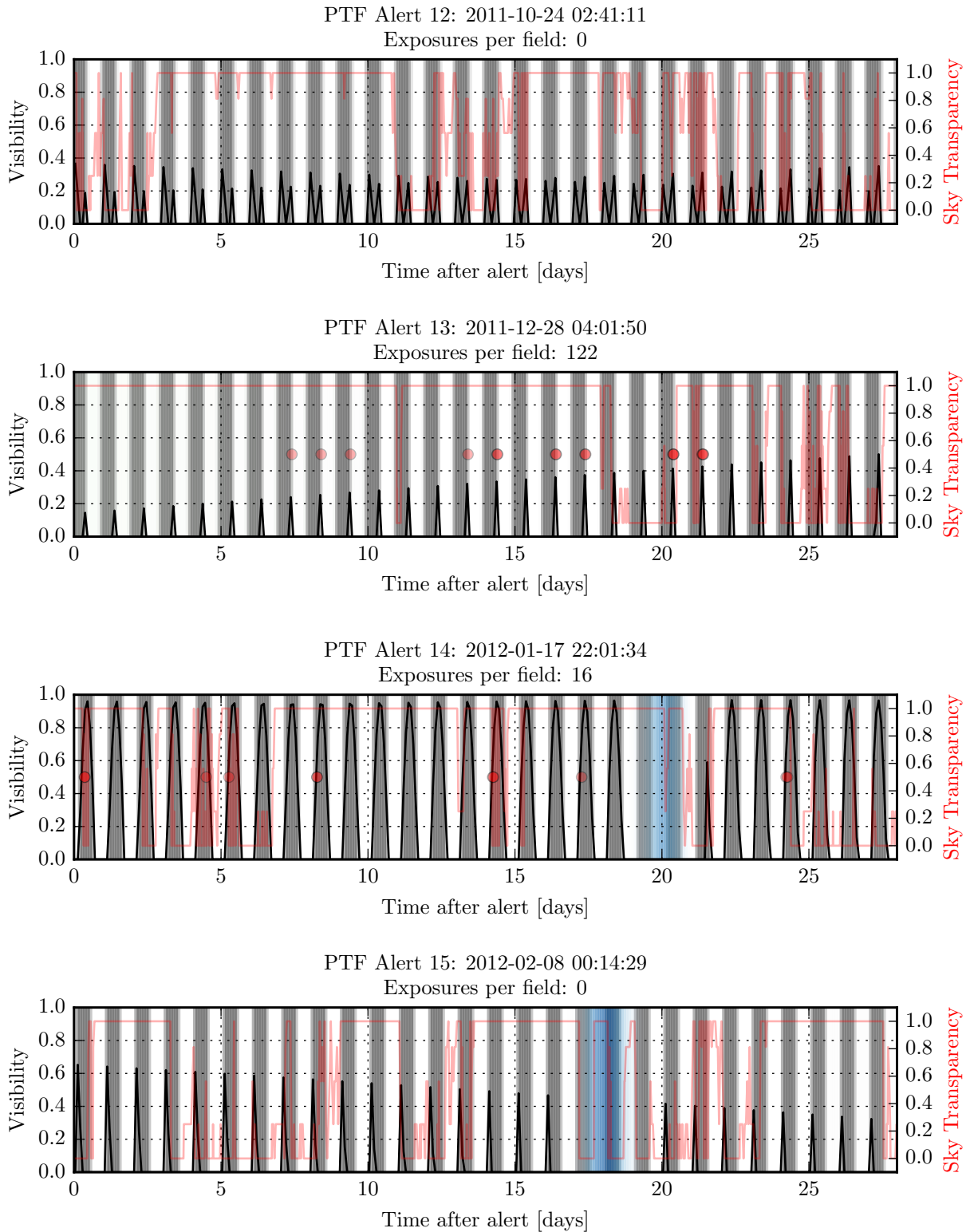


Figure E.3: See Figure E.1.

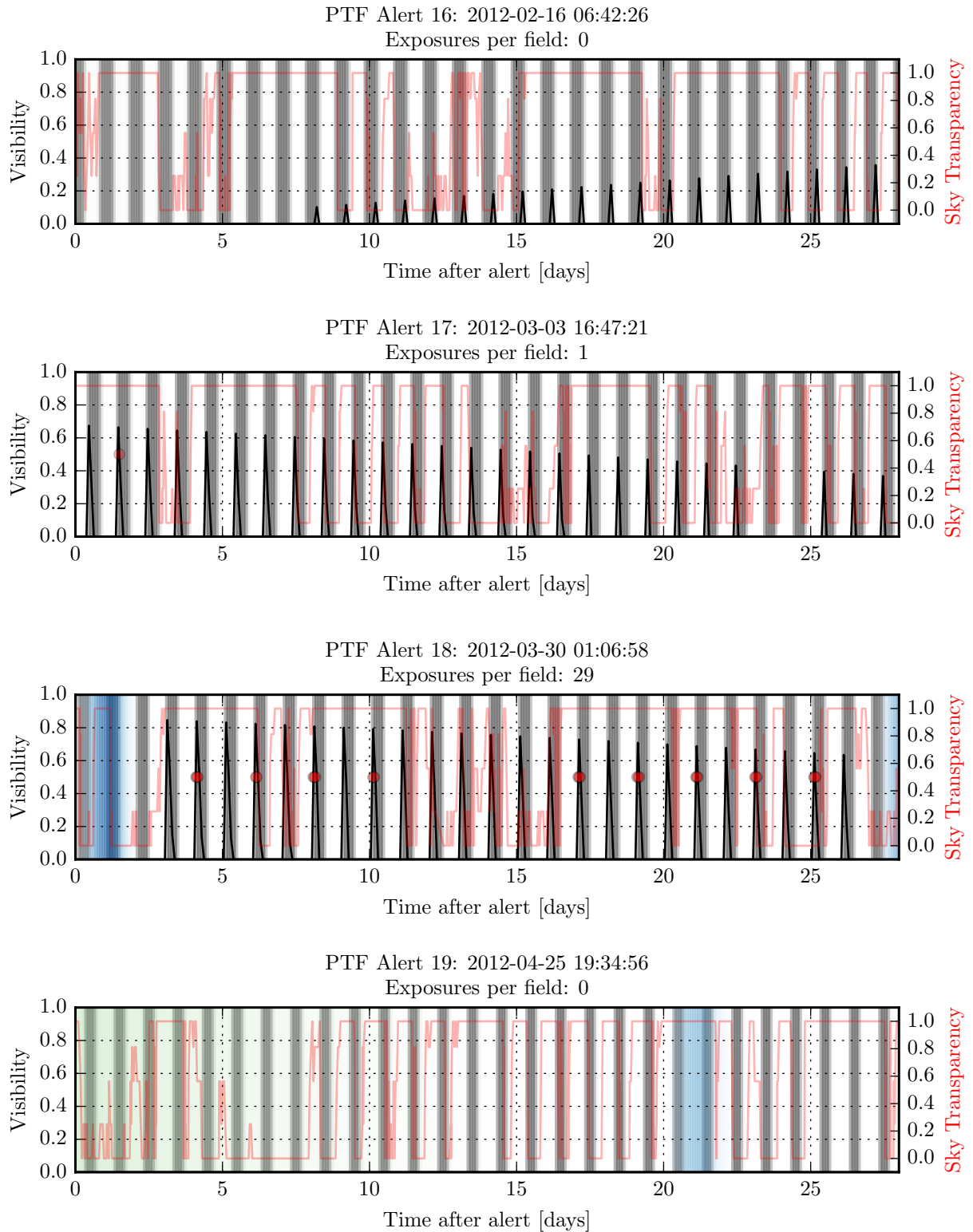


Figure E.4: See Figure E.1.

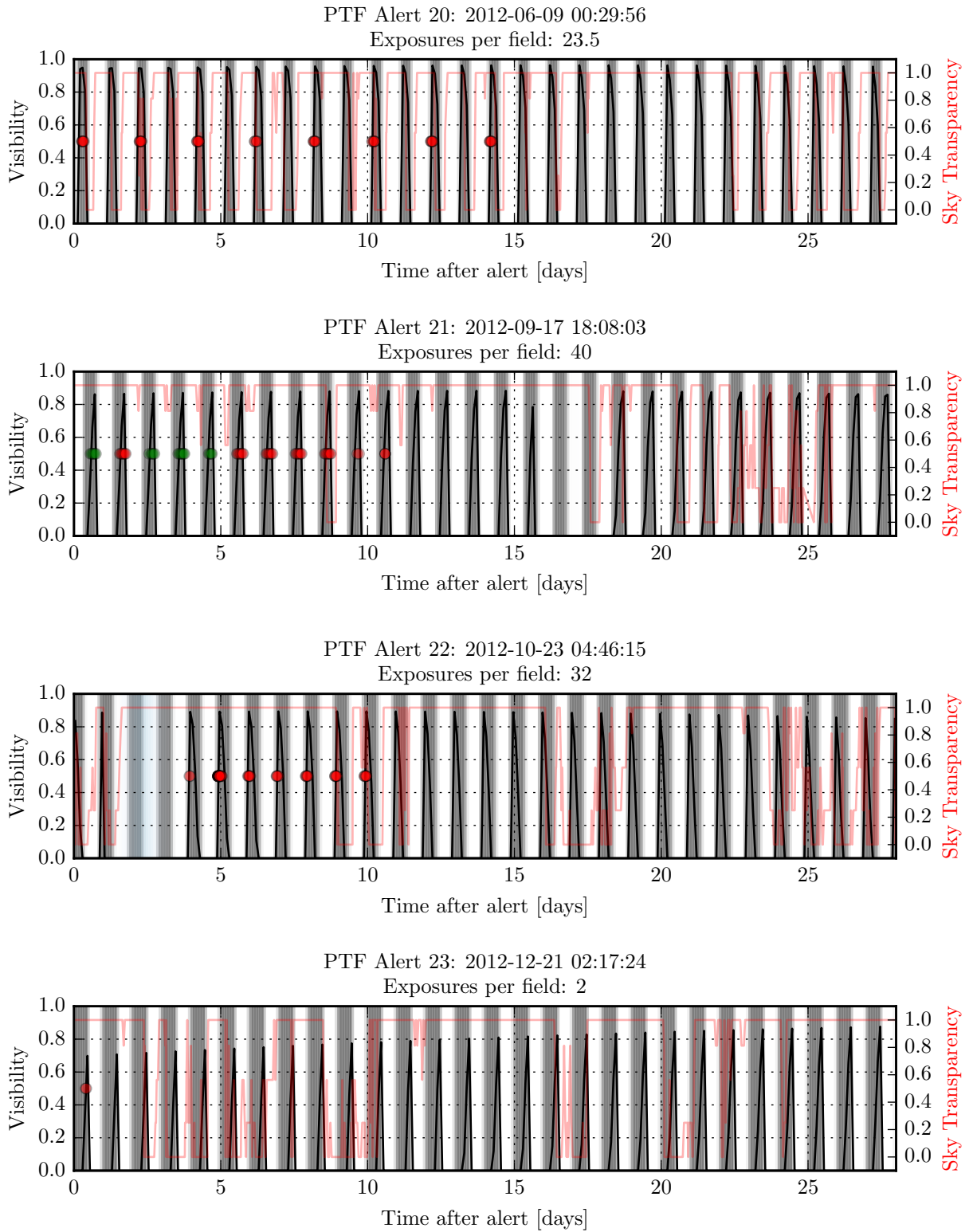


Figure E.5: See Figure E.1.

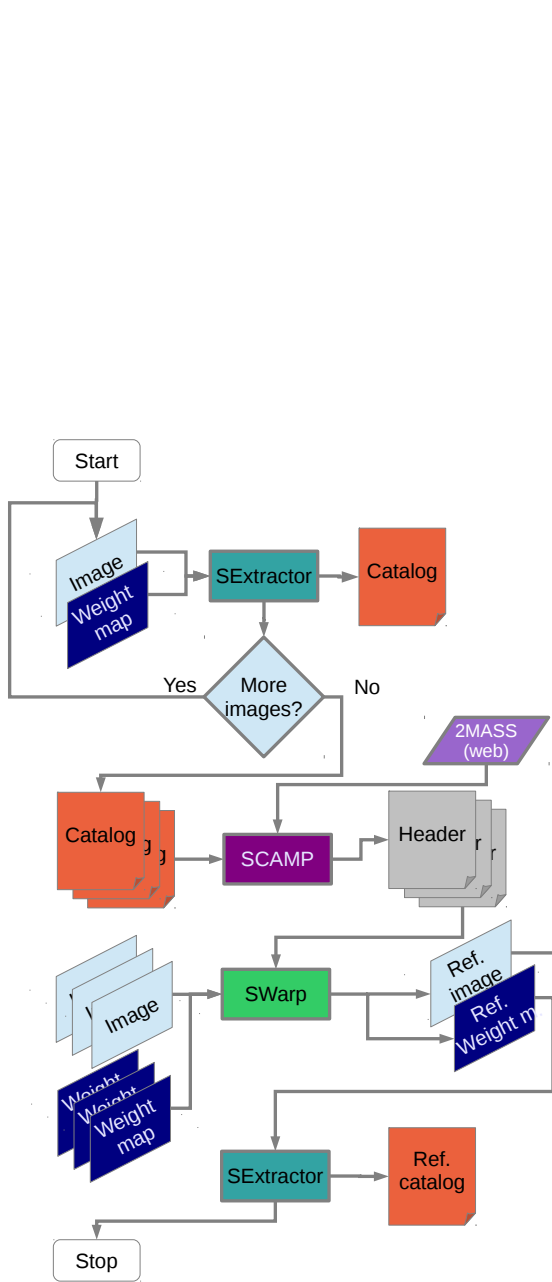


Figure E.6: Flow chart of the reference image construction process. See text for explanations.

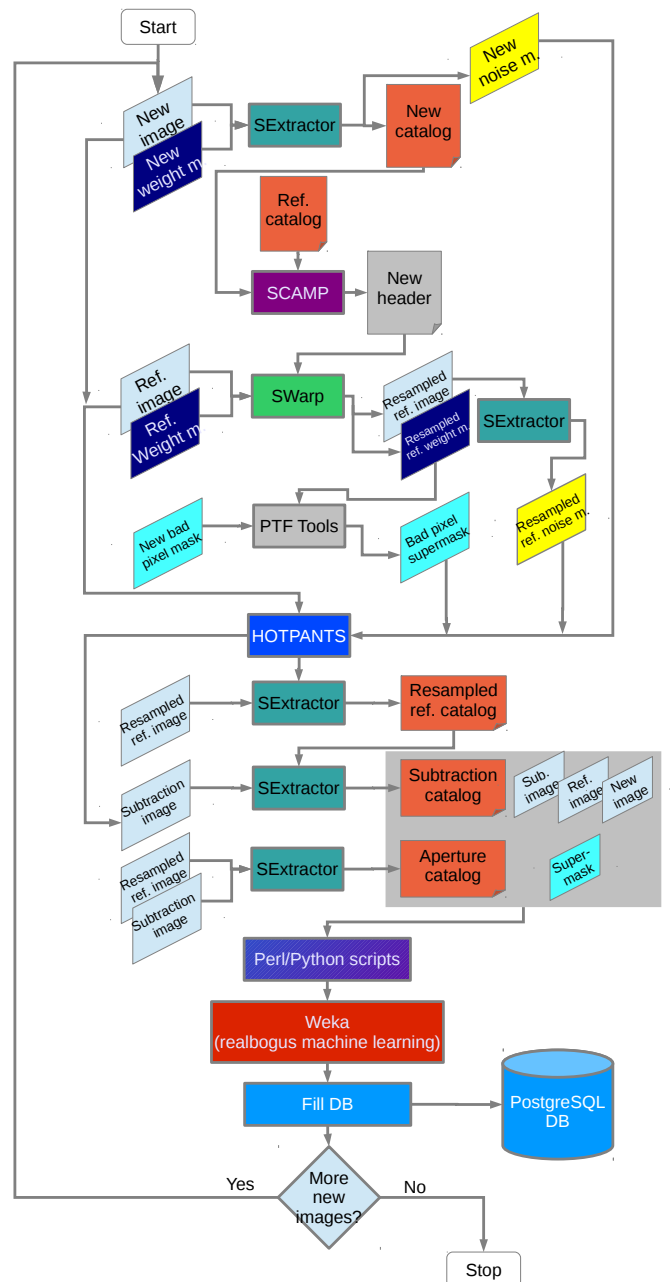


Figure E.7: Flow chart of the image subtraction and the source extraction process. Some of the details are not mentioned in the text for brevity, e.g. the bad pixel masks (to exclude e.g. saturated pixels from subtraction) created with PTF-internal tools.

First, `SExtractor` is executed on each of the reference exposures that are to be combined. `SExtractor` scans the image for astronomical objects and builds a catalog of objects with astrometric⁶ and photometric⁷ measurements for all found sources in each reference exposure.

In the next step, `SCAMP` [306] is run on the `SExtractor` catalog files of all exposures, which derives a full, improved, robust astrometric and photometric calibration, relative to a well calibrated astronomical reference catalog, so that accurate and consistent coordinates are available for the images.

Afterwards, reading in the `SCAMP` output and the original reference exposure FITS files, `SWarp` performs the actual co-addition, or image stacking. It subtracts background, resamples the input FITS images, combines them into a composite frame, and saves the resulting FITS image to disk [308]. The background subtraction needs to be done because backgrounds are subject to change from image to image, resulting in artifacts in the composite image if not subtracted. Before the co-addition, the images have to be aligned, i.e. they have to be resampled by `SWarp`. Resampling is the projection of a grid of pixels to another grid. The output frame is scanned pixel-per-pixel and each pixel center is converted to a position in the input frame. For this position, an interpolated value is calculated from the neighboring input frame pixels [308]. Several interpolation methods are available. The one used here is the Lanczos4 interpolation, defined as

$$h(x, y) = \prod_{i=i_x-3}^{i_x+4} \prod_{j=j_y-3}^{j_y+4} f_{ij} \operatorname{sinc}(i - i_x) \operatorname{sinc}\left(\frac{i - i_x}{4}\right) \operatorname{sinc}(j - j_y) \operatorname{sinc}\left(\frac{j - j_y}{4}\right), \quad (\text{E.2})$$

where i_x and j_y are the floor integer values of the continuous pixel coordinates x and y , f_{ij} is the value of the pixel with index (i, j) , and $\operatorname{sinc}(x) \equiv \sin(\pi x)/(\pi x)$. The Lanczos4 function is thus a sort of weighted average over a region of $(2 \cdot 4)^2 = 64$ pixels. The Lanczos4 function provides the best resampling for correctly sampled data, i.e. when the FWHM (full width at half maximum) of the point spread function (PSF, see Appendix B.1) is about 3 pixels [308], which is the case for PTF images. After the resampling, the images can be co-added pixel per pixel. This is done by taking the median of all pixel values.

After the `SWarp` co-addition, `SExtractor` is run again on the deep reference image, creating a catalog of the contained objects.

E.2.3 Image Subtraction

Also for the image subtraction, the central software pieces are `SExtractor`, `SCAMP`, and `SWarp`, accompanied by a program called `HOTPANTS` that does the actual subtraction. The deep reference image (see Appendix E.2.2) is subtracted from all new images that were taken within 100 days after the neutrinos. This is done in order to find sources that have changed in brightness, either increased or decreased, and are thus potential SNe. Due to the complexity, a flow chart of the image subtraction process was created. It is visible in the upper half of Figure E.7 (up to `HOTPANTS`). The flow chart provides a few details left out in the text, e.g. weight maps, noise maps, and bad pixel masks used to exclude saturated pixels from the subtraction.

The subtraction is run on each of the new images separately. First, `SExtractor` is executed. It builds a catalog of objects for all found sources in the image. Then, `SCAMP` is run on the `SExtractor` catalog files of the new image, which derives a full, improved, robust astrometric and photometric calibration, relative to the astrometry catalog of the reference image. Thus, the coordinates of objects in the new image are consistent with the coordinates in the reference image.

⁶ Astrometry is a term for the measurement of the position of astronomical sources, i.e. their coordinates.

⁷ Photometry is a term for the measurement of the brightness of astronomical sources, see Section B.2.

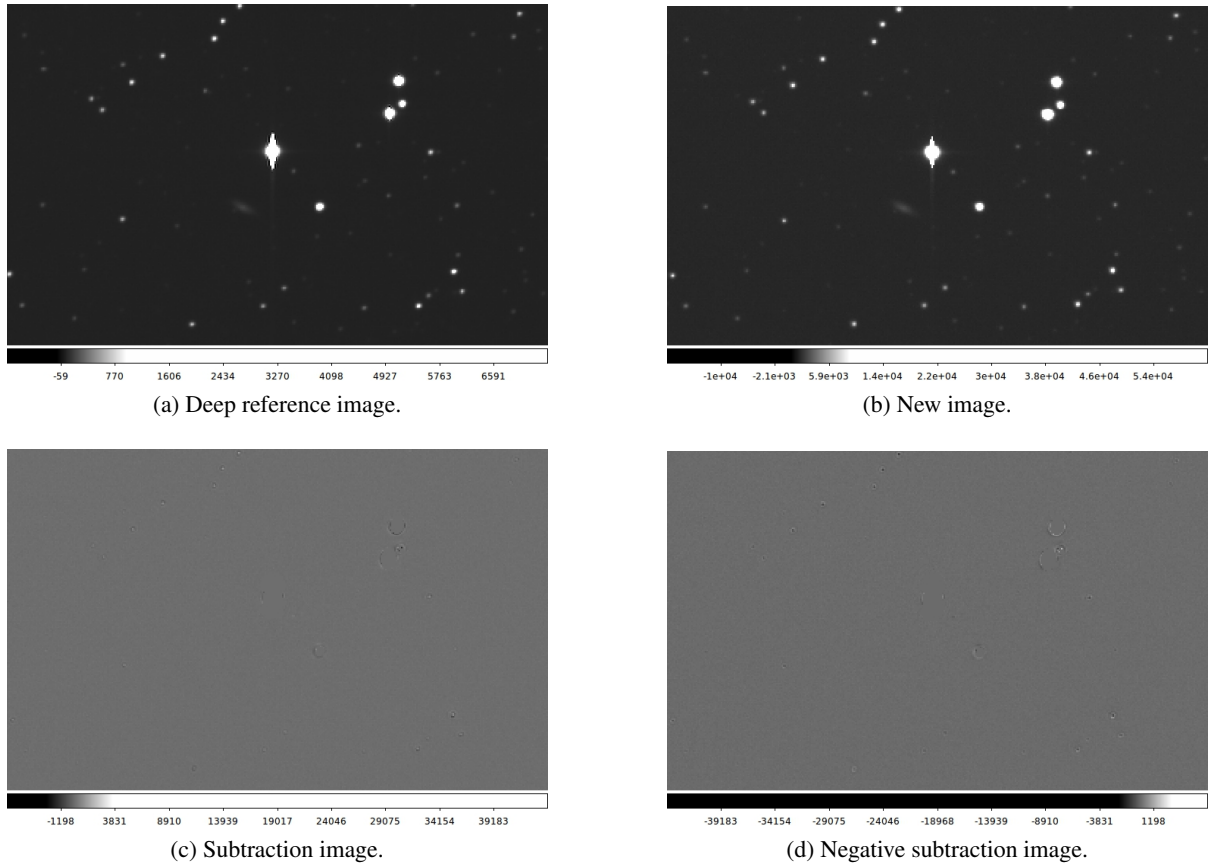


Figure E.8: Example of a successful image subtraction. These are portions of images from PTF field 2982, CCD 00, R filter. The reference image is a composite of six 60 s exposures, while the new image is one 60 s long exposure. Looking closely, one can notice a slight rotation of the reference relative to the new image. This is not a problem thanks to the resampling of the reference image before subtraction. In the subtracted image, some mostly negative contour lines remain, but there are no sources left.

Afterwards, SWarp is executed on the reference image, using the SCAMP astrometric solution of the new image, provided as a header file. No background subtraction and no co-addition is done (only one image is provided), but SWarp performs a *resampling of the reference image* and saves the resulting FITS image to disk. The resampling, done according to Equation E.2, is important to align the reference image with the new image. In the resampled reference image, each pixel should correspond to the same pixel in the new image.

Finally, the reference image can be subtracted from the new image. It is done by another software called HOTPANTS (High Order Transform of PSF ANd Template Subtraction), written by Andrew Becker [309]. After the *astrometric alignment* has been completed by SCAMP and SWarp, HOTPANTS takes care of the *photometric alignment*. It is a robust implementation of an algorithm from Alard (2000) [336] for image subtraction using a position-dependent kernel. Image subtraction cannot be simply done pixel-by-pixel. The new and the reference image were usually taken under different photometric conditions, e.g. with different air transparency, atmospheric seeing, and/or exposure time. This leads to the two images having different PSFs, which must be accounted for in the subtraction. If this is not done, artificial sources will pop up if the new image has a broader PSF. To avoid this, the reference

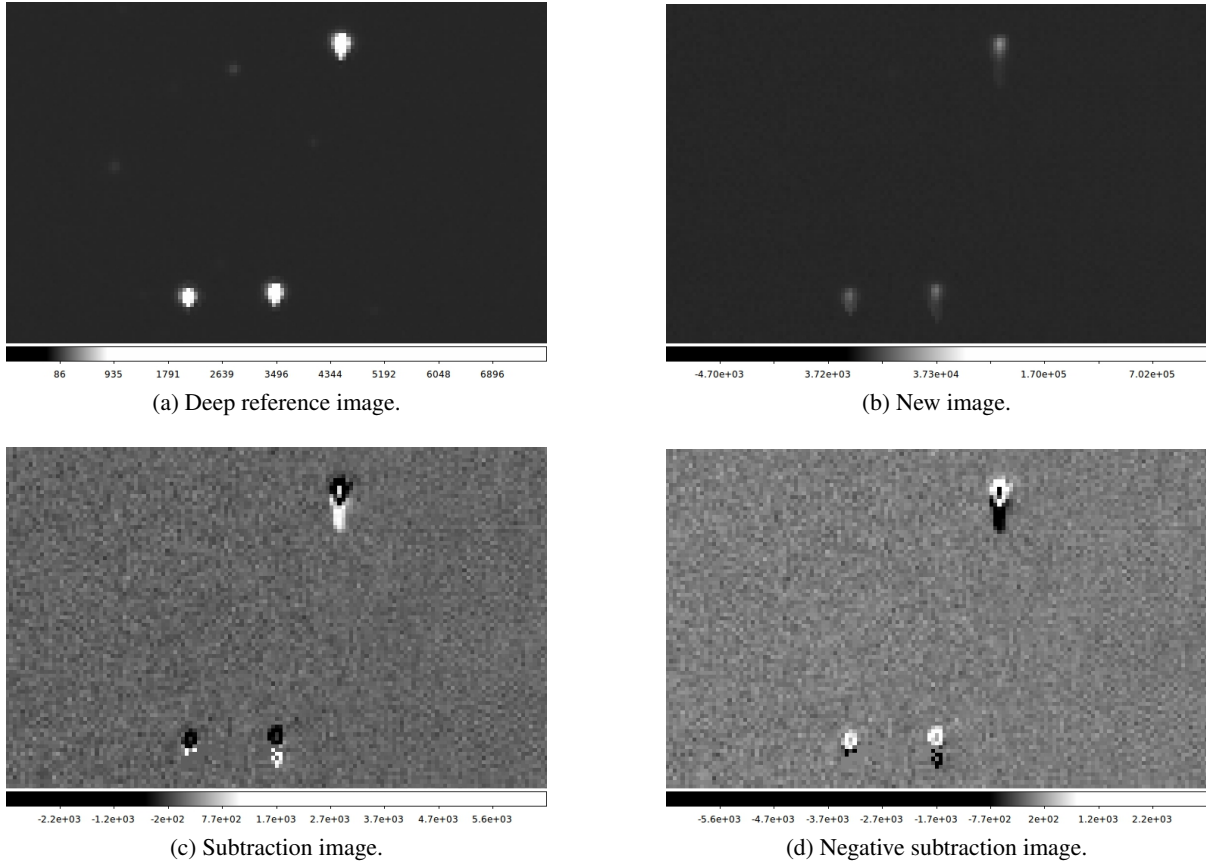


Figure E.9: Example of failed image subtraction, or mis-subtraction. These are portions of images from PTF field 2820, CCD 00, R filter. The reference image is a composite of seven 60 s exposures, while the new image is one 60 s long exposure. The mis-subtraction candidates contain both positive and negative pixels, a sign of subtraction artifacts. This is probably caused by distortion close to the CCD edge.

image R is convolved with a kernel K to match the PSF of the new image I . The goal is then to find the kernel K that minimizes

$$\sum_i ([R \otimes K](x_i, y_i) - I(x_i, y_i))^2 \quad (\text{E.3})$$

across a certain range of the coordinates x and y [336]. In practice, HOTPANTS divides the image into several regions, for which separate kernels are fitted. In each region, several small sub-regions are determined that center on an individual astronomical object and are used to find the kernel [309]. The output from the HOTPANTS run is the subtraction image, or difference image.

See Figures E.8 and E.9 for examples of successful and unsuccessful image subtraction.

E.2.4 Source Extraction

After the image subtraction, the resulting difference images are scanned for source candidates using the source extraction software **SExtractor**. It identifies astronomical sources (stars and galaxies) and determines their properties: photometric source properties, e.g. the magnitude, and geometrical properties such as the FWHM (full width at half-maximum) and ellipticity of the source profile.

SExtractor performs the following working steps [304, 337]: First, it measures the level of the

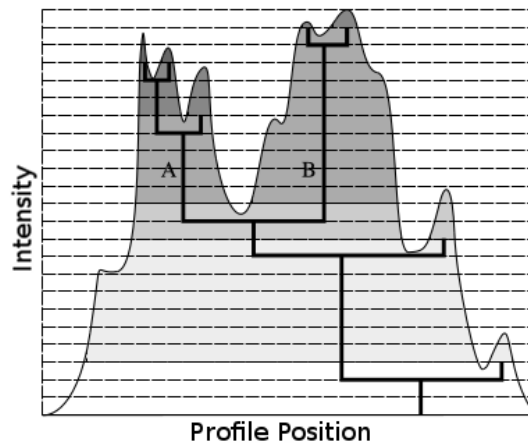


Figure E.10: Sketch illustrating the deblending done by SExtractor (taken from [304]). It is implemented with a threshold that starts at the maximum intensity and is sequentially lowered. At each threshold level, the intensity of separate sub-objects surpassing it is determined and the sub-objects are kept if their above-threshold intensity (indicated by shaded areas) relative to the total intensity is large enough. In this case, two peaks A and B are the resulting sub-objects.

sky background region-wise with an averaging technique that crops outliers. A *background map* is constructed and *subtracted* from the image. The image is then *filtered* (convolved with a specified kernel) to mitigate noise contamination. Objects are found by identifying connected groups of pixels brighter than a certain *threshold*. Then, the objects are *deblended*, meaning that objects are broken into separate sub-objects. If the intensity profile has two (or more) peaks with a valley in between, then the object is broken up if there are at least two disjunct peaks that each have an integrated intensity larger than a certain fraction of the total intensity. See Figure E.10 for an illustration. SExtractor then measures the objects' shapes and positions, i.e. the astrometry. A cleaning is done and then the photometry is performed, i.e. the objects' brightness measured. Afterwards, the objects are classified as stars or galaxies using a neural network. Finally, the catalog with the object, i.e. source candidate, data is written out.

After the source extraction, the machine learning classification algorithm *realbogus* (see Section 8.2.1) is executed. A Python script executes the machine learning code and puts all meta-data about the subtraction, the candidates, and the result of the *realbogus* algorithm into a PostgreSQL database (DB), which is used for the subsequent data analysis. The source extraction and machine learning process is visualized in the lower half of the flow chart in Figure E.7 (after HOTPANTS).

E.2.5 Negative Subtractions

In order to tolerate a potential contamination of the reference image with SN light, also negative subtractions are performed. Instead of subtracting the reference image R from the new image I , i.e. $I - R$, one does $R - I$. Doing so, negative changes in flux with respect to the reference image (source brighter in R than in I) will appear as positive sources in the subtraction image.⁸ Because $R - I = -(I - R)$, the subtraction does not have to be repeated, but the subtraction image from the normal subtraction can simply be multiplied with -1 . Afterwards, SExtractor is executed again to extract the sources from the negative subtraction image.

⁸ SExtractor only extracts sources that are positive relative to the sky background.

Again, a Python script executes the realbogus machine learning code and puts all meta-data about the negative subtraction, the negative candidates, and the result of the realbogus algorithm into the PostgreSQL analysis DB.

E.3 Derivation of the Host Limiting Magnitude

In the Poissonian regime, the significance s of a photometric detection with a CCD, in terms of number of standard deviations σ , is approximately given by the number of signal counts N_{sig} over the square root of the number of background counts N_{bg} ,

$$s = \frac{N_{\text{sig}}}{\sqrt{N_{\text{bg}}}} = \frac{F_{\text{sig}}}{\sqrt{F_{\text{bg}}}}, \quad (\text{E.4})$$

with signal and background flux F_{sig} and F_{bg} . Hence, for limiting magnitude defined via the signal-to-noise ratio significance $s = \text{const}$, the limiting flux F_{lim} is

$$F_{\text{lim}} = F_{\text{sig}}(s) \propto \sqrt{F_{\text{bg}}}. \quad (\text{E.5})$$

Thus, the limiting flux $F_{\text{lim}}^{\text{host}}$ for a source sitting on a host galaxy providing the background flux $F_{\text{bg}} \approx F_{\text{host}}$,⁹ relative to the limiting flux $F_{\text{lim}}^{\text{iso}}$ of an isolated source on top of the sky background flux $F_{\text{bg}} \approx F_{\text{sky}}$, is

$$\frac{F_{\text{lim}}^{\text{host}}}{F_{\text{lim}}^{\text{iso}}} = \sqrt{\frac{F_{\text{host}}}{F_{\text{sky}}}} = \sqrt{\frac{F_{\text{host}}/F_{\text{test}}}{F_{\text{sky}}/F_{\text{test}}}} = \frac{10^{0.2(m_{\text{test}}-m_{\text{host}})}}{10^{0.2(m_{\text{test}}-m_{\text{sky}})}} = 10^{0.2(m_{\text{sky}}-m_{\text{host}})}, \quad (\text{E.6})$$

where the general definition of magnitude from Equation B.3 was used to convert from fluxes F to magnitudes m . Using Equation B.3 again, it follows that the limiting magnitude $m_{\text{lim}}^{\text{host}}$ for objects sitting on a host is

$$m_{\text{lim}}^{\text{host}} = m_{\text{lim}}^{\text{iso}} - 2.5 \log_{10} \left(\frac{F_{\text{lim}}^{\text{host}}}{F_{\text{lim}}^{\text{iso}}} \right) = m_{\text{lim}}^{\text{iso}} - 2.5 \log_{10} \left(10^{0.2(m_{\text{sky}}-m_{\text{host}})} \right) = m_{\text{lim}}^{\text{iso}} - \left(\frac{m_{\text{sky}} - m_{\text{host}}}{2} \right). \quad (\text{E.7})$$

E.4 Simulation Runs

One simulation run comprises 10 SN insertions for each of the 20 analyzed alerts. For each inserted SN, 20 random light curves are generated¹⁰. This results in a total number of 4000¹¹ simulated SNe, spread equally across the insertion positions and the alert fields in order to obtain an average outcome of the conducted PTF follow-up program.

One simulation run is performed for each luminosity distance d and each absolute SN peak magnitude M_{peak} . From d and M_{peak} follows the apparent peak magnitude m_{peak} of the SNe. The distance d is sampled at 10 bins spanning logarithmically the range from 10 to 1000 Mpc, plus one extra bin at 2000 Mpc. The peak magnitude M_{peak} is sampled at 10 bins spanning linearly the range from -20 mag to -13 mag. This means 110 simulation runs comprising 800 000 SNe were performed for each class of SNe. Three SN classes have been simulated: signal CCSNe, background CCSNe, and background

⁹ Other components of the background flux, e.g. dark noise, are neglected in this estimation.

¹⁰ Except for 2000 Mpc distance, where 200 LCs are generated to get enough statistics.

¹¹ For 2000 Mpc distance 40 000 SNe.

SNe Ia. The only difference between signal and background is the distribution of the explosion time t_0 : For signal, it is drawn uniformly from within ± 500 seconds of the neutrino alert time.¹² For background, it is drawn uniformly from within -200 and 100 days relative to the neutrino alert time. A relatively large time window is used, because a background SN with any explosion time might show up in the data.

The SDSS query for suitable galaxies within the CCD (see Section 8.5.1) is slow, up to about 20 to 30 seconds per query and more, probably due to the large CCD size. For this reason, only one full simulation run including SDSS queries was done and the results were stored. The interesting quantities to derive from the SN insertion are the background brightness, i.e. the host galaxy aperture magnitude m_{aper} , and the Milky Way extinction A_V at the SN position. Therefore, pairs of m_{aper} and A_V are stored for each simulated distance, from which values are randomly drawn in the subsequent simulations. This speeds up one simulation run from about 2.5 days to few hours.

¹² Motivated by the assumed intrinsic time delay between SN explosion and neutrino burst, taken from [216].

Bibliography

- [1] A. Melsen, *From atomos to atom: the history of the concept atom*, Mineola, N.Y: Dover Publications, 2004, ISBN: 0486495841 (cit. on p. 3).
- [2] H. Becquerel, “Sur les radiations émises par phosphorescence,” *Comptes Rendus* 122 (Feb. 1896) 420–421, URL: <http://gallica.bnf.fr/ark:/12148/bpt6k30780/f422.chemindefer> (cit. on p. 3).
- [3] “This month in physics history March 1, 1896 Henri Becquerel discovers radioactivity,” *APS News* 17.10 (Mar. 2008), URL: <http://www.aps.org/publications/apsnews/200803/physicshistory.cfm> (cit. on p. 3).
- [4] *Nobel Prize in Physics 1903 - Presentation Speech*, 2014, URL: http://www.nobelprize.org/nobel_prizes/physics/laureates/1903/press.html (visited on 06/24/2015) (cit. on pp. 3, 4).
- [5] *Nobel Prize in Physics 1936 - Presentation Speech*, 2014, URL: http://www.nobelprize.org/nobel_prizes/physics/laureates/1936/press.html (visited on 06/23/2015) (cit. on p. 4).
- [6] V. Hess, “Observations in low level radiation during seven free balloon flights,” *Physikalische Zeitschrift* 13 (1912) 1084–1091 (cit. on p. 4).
- [7] *Victor F. Hess - Nobel Lecture: Unsolved Problems in Physics: Tasks for the Immediate Future in Cosmic Ray Studies*, 2014, URL: http://www.nobelprize.org/nobel_prizes/physics/laureates/1936/hess-lecture.html (visited on 06/24/2015) (cit. on p. 4).
- [8] A. De Angelis, “Spontaneous ionization to subatomic physics: Victor Hess to Peter Higgs,” *Nuclear Physics B Proceedings Supplements* 243 (Oct. 2013) 3–11, doi: [10.1016/j.nuclphysbps.2013.09.008](https://doi.org/10.1016/j.nuclphysbps.2013.09.008) (cit. on pp. 4, 5).
- [9] C. D. Anderson, “The Positive Electron,” *Physical Review* 43 (Mar. 1933) 491–494, doi: [10.1103/PhysRev.43.491](https://doi.org/10.1103/PhysRev.43.491) (cit. on p. 5).
- [10] S. H. Neddermeyer and C. D. Anderson, “Note on the Nature of Cosmic-Ray Particles,” *Physical Review* 51 (May 1937) 884–886, doi: [10.1103/PhysRev.51.884](https://doi.org/10.1103/PhysRev.51.884) (cit. on p. 5).
- [11] C. M. G. Lattes et al., “Processes Involving Charged Mesons,” *Nature* 159 (May 1947) 694–697, doi: [10.1038/159694a0](https://doi.org/10.1038/159694a0) (cit. on p. 5).

- [12] M. Gell-Mann, “A schematic model of baryons and mesons,” *Physics Letters* 8 (Feb. 1964) 214–215, doi: [10.1016/S0031-9163\(64\)92001-3](https://doi.org/10.1016/S0031-9163(64)92001-3) (cit. on p. 5).
- [13] G. Zweig, *An SU(3) Model for Strong Interaction Symmetry and its Breaking*, Jan. 1964, URL: <http://cds.cern.ch/record/352337/files/CERN-TH-401.pdf> (cit. on p. 5).
- [14] G. Zweig, *An SU(3) Model for Strong Interaction Symmetry and its Breaking: II*, Feb. 1964, URL: <http://lib-www.lanl.gov/la-pubs/00323548.pdf> (cit. on p. 5).
- [15] C. Giunti and C. Kim, *Fundamentals of neutrino physics and astrophysics*, Oxford University Press, 2007, ISBN: 9780198508717 (cit. on pp. 5–8, 10–13, 16–20, 37–39, 41, 42, 44–46, 61, 85).
- [16] C. Grupen, *Astroparticle physics*, Berlin New York: Springer, 2005, ISBN: 3540253122 (cit. on pp. 6, 8, 14, 15, 32, 33, 61).
- [17] K. A. Olive and Particle Data Group, “Review of Particle Physics,” *Chinese Physics C* 38.9, 090001 (Aug. 2014) 090001, doi: [10.1088/1674-1137/38/9/090001](https://doi.org/10.1088/1674-1137/38/9/090001), arXiv: [1412.1408](https://arxiv.org/abs/1412.1408), URL: <http://pdg.lbl.gov> (cit. on pp. 6, 7, 14–16, 19, 21, 23, 24, 208).
- [18] *Frederick Reines - Nobel Lecture: The Neutrino: From Poltergeist to Particle*, 2014, URL: http://www.nobelprize.org/nobel_prizes/physics/laureates/1995/reines-lecture.html (visited on 06/29/2015) (cit. on pp. 8, 11).
- [19] A. Strumia and F. Vissani, “Precise quasielastic neutrino/nucleon cross-section,” *Physics Letters B* 564 (July 2003) 42–54, doi: [10.1016/S0370-2693\(03\)00616-6](https://doi.org/10.1016/S0370-2693(03)00616-6), eprint: [astro-ph/0302055](https://arxiv.org/abs/hep-ph/0302055) (cit. on pp. 11, 12).
- [20] A. Cooper-Sarkar, P. Mertsch, and S. Sarkar, “The high energy neutrino cross-section in the Standard Model and its uncertainty,” *Journal of High Energy Physics* 8, 42 (Aug. 2011) 42, doi: [10.1007/JHEP08\(2011\)042](https://doi.org/10.1007/JHEP08(2011)042), arXiv: [1106.3723](https://arxiv.org/abs/1106.3723) [hep-ph] (cit. on pp. 13, 14).
- [21] A. Gazizov and M. Kowalski, “ANIS: High energy neutrino generator for neutrino telescopes,” *Computer Physics Communications* 172 (Nov. 2005) 203–213, doi: [10.1016/j.cpc.2005.03.113](https://doi.org/10.1016/j.cpc.2005.03.113), eprint: [astro-ph/0406439](https://arxiv.org/abs/astro-ph/0406439) (cit. on p. 13).
- [22] P. A. Čerenkov, “Visible Radiation Produced by Electrons Moving in a Medium with Velocities Exceeding that of Light,” *Physical Review* 52 (Aug. 1937) 378–379, doi: [10.1103/PhysRev.52.378](https://doi.org/10.1103/PhysRev.52.378) (cit. on p. 15).
- [23] T. Stanev, *High energy cosmic rays*, 2004 (cit. on pp. 15, 21, 24).
- [24] G. B. Collins and V. G. Reiling, “Čerenkov Radiation,” *Physical Review* 54 (Oct. 1938) 499–503, doi: [10.1103/PhysRev.54.499](https://doi.org/10.1103/PhysRev.54.499) (cit. on p. 16).
- [25] R. A. Porrata, “The Energy Spectrum of Pointlike Events in AMANDA-A,” PhD thesis: University of California, 1997, ISBN: 978-0-591-60345-3, URL: <http://search.proquest.com/docview/304329359> (cit. on pp. 17, 101, 102).
- [26] Argonne National Laboratory, *Advanced Test Reactor*, File: Advanced Test Reactor.jpg, [Creative Commons Attribution](https://creativecommons.org/licenses/by/4.0/), 2009, URL: https://en.wikipedia.org/wiki/File:Advanced_Test_Reactor.jpg (visited on 07/09/2015) (cit. on p. 17).

- [27] H. A. Bethe, “Energy Production in Stars,” *Physical Review* 55 (Jan. 1939) 103–103, doi: [10.1103/PhysRev.55.103](https://doi.org/10.1103/PhysRev.55.103) (cit. on p. 16).
- [28] H. A. Bethe, “Energy Production in Stars,” *Physical Review* 55 (Mar. 1939) 434–456, doi: [10.1103/PhysRev.55.434](https://doi.org/10.1103/PhysRev.55.434) (cit. on p. 16).
- [29] J. N. Bahcall et al., “Solar Neutrino Flux.,” *ApJ* 137 (Jan. 1963) 344–346, doi: [10.1086/147513](https://doi.org/10.1086/147513) (cit. on p. 17).
- [30] J. N. Bahcall, M. H. Pinsonneault, and S. Basu, “Solar Models: Current Epoch and Time Dependences, Neutrinos, and Helioseismological Properties,” *ApJ* 555 (July 2001) 990–1012, doi: [10.1086/321493](https://doi.org/10.1086/321493), eprint: [astro-ph/0010346](https://arxiv.org/abs/astro-ph/0010346) (cit. on p. 17).
- [31] J. N. Bahcall and M. H. Pinsonneault, “What Do We (Not) Know Theoretically about Solar Neutrino Fluxes?” *Physical Review Letters* 92.12, 121301 (Mar. 2004) 121301, doi: [10.1103/PhysRevLett.92.121301](https://doi.org/10.1103/PhysRevLett.92.121301), eprint: [astro-ph/0402114](https://arxiv.org/abs/astro-ph/0402114) (cit. on pp. 17, 19).
- [32] W. C. Haxton, R. G. Hamish Robertson, and A. M. Serenelli, “Solar Neutrinos: Status and Prospects,” *ARA&A* 51 (Aug. 2013) 21–61, doi: [10.1146/annurev-astro-081811-125539](https://doi.org/10.1146/annurev-astro-081811-125539), arXiv: [1208.5723](https://arxiv.org/abs/1208.5723) [[astro-ph.SR](https://arxiv.org/abs/astro-ph.SR)] (cit. on pp. 17–19).
- [33] J. N. Bahcall and C. Peña-Garay, “Solar models and solar neutrino oscillations,” *New Journal of Physics* 6 (June 2004) 63, doi: [10.1088/1367-2630/6/1/063](https://doi.org/10.1088/1367-2630/6/1/063), eprint: [hep-ph/0404061](https://arxiv.org/abs/hep-ph/0404061) (cit. on pp. 19, 98).
- [34] *The Nobel Prize in Physics 2015*, 2015, URL: http://www.nobelprize.org/nobel_prizes/physics/laureates/2015/ (visited on 11/25/2015) (cit. on p. 19).
- [35] T. K. Gaisser and M. Honda, “Flux of atmospheric neutrinos,” *Annual Review of Nuclear and Particle Science* 52 (2002) 153–199, doi: [10.1146/annurev.nucl.52.050102.090645](https://doi.org/10.1146/annurev.nucl.52.050102.090645), eprint: [hep-ph/0203272](https://arxiv.org/abs/hep-ph/0203272) (cit. on p. 20).
- [36] E. V. Bugaev et al., “Atmospheric muon flux at sea level, underground, and underwater,” *Phys. Rev. D* 58.5, 054001 (Sept. 1998) 054001, doi: [10.1103/PhysRevD.58.054001](https://doi.org/10.1103/PhysRevD.58.054001), eprint: [hep-ph/9803488](https://arxiv.org/abs/hep-ph/9803488) (cit. on pp. 20, 97, 98).
- [37] R. Abbasi et al., “Measurement of the atmospheric neutrino energy spectrum from 100 GeV to 400 TeV with IceCube,” *Phys. Rev. D* 83.1, 012001 (Jan. 2011) 012001, doi: [10.1103/PhysRevD.83.012001](https://doi.org/10.1103/PhysRevD.83.012001), arXiv: [1010.3980](https://arxiv.org/abs/1010.3980) [[astro-ph.HE](https://arxiv.org/abs/astro-ph.HE)] (cit. on p. 20).
- [38] IceCube Collaboration, “Evidence for High-Energy Extraterrestrial Neutrinos at the IceCube Detector,” *Science* 342, 1242856 (Nov. 2013) 1, doi: [10.1126/science.1242856](https://doi.org/10.1126/science.1242856), arXiv: [1311.5238](https://arxiv.org/abs/1311.5238) [[astro-ph.HE](https://arxiv.org/abs/astro-ph.HE)] (cit. on pp. 20, 68, 109).
- [39] T. K. Gaisser, T. Stanev, and G. Barr, “Cosmic-ray neutrinos in the atmosphere,” *Phys. Rev. D* 38 (July 1988) 85–95, doi: [10.1103/PhysRevD.38.85](https://doi.org/10.1103/PhysRevD.38.85) (cit. on pp. 20, 99, 100).
- [40] M. Honda et al., “Improvement of low energy atmospheric neutrino flux calculation using the JAM nuclear interaction model,” *Phys. Rev. D* 83.12, 123001 (June 2011) 123001, doi: [10.1103/PhysRevD.83.123001](https://doi.org/10.1103/PhysRevD.83.123001), arXiv: [1102.2688](https://arxiv.org/abs/1102.2688) [[astro-ph.HE](https://arxiv.org/abs/astro-ph.HE)] (cit. on p. 20).

- [41] J. K. Becker, “High-energy neutrinos in the context of multimessenger astrophysics,” *Phys. Rep.* 458 (Mar. 2008) 173–246, doi: [10.1016/j.physrep.2007.10.006](https://doi.org/10.1016/j.physrep.2007.10.006), arXiv: [0710.1557](https://arxiv.org/abs/0710.1557) (cit. on pp. 20–24, 26–28, 31, 111).
- [42] S. Ando, K. Sato, and T. Totani, “Detectability of the supernova relic neutrinos and neutrino oscillation,” *Astroparticle Physics* 18 (Jan. 2003) 307–318, doi: [10.1016/S0927-6505\(02\)00152-4](https://doi.org/10.1016/S0927-6505(02)00152-4), eprint: [astro-ph/0202450](https://arxiv.org/abs/hep-ph/0202450) (cit. on pp. 20, 62).
- [43] C. Spiering, “Towards high-energy neutrino astronomy. A historical review,” *European Physical Journal H* 37 (Aug. 2012) 515–565, doi: [10.1140/epjh/e2012-30014-2](https://doi.org/10.1140/epjh/e2012-30014-2), arXiv: [1207.4952](https://arxiv.org/abs/1207.4952) [[astro-ph.IM](https://arxiv.org/abs/1207.4952)] (cit. on p. 21).
- [44] M. Kachelriess, “Lecture notes on high energy cosmic rays,” *ArXiv e-prints* (Jan. 2008), arXiv: [0801.4376](https://arxiv.org/abs/0801.4376) (cit. on pp. 21, 23–30, 33).
- [45] I. G. Usoskin, “A History of Solar Activity over Millennia,” *Living Reviews in Solar Physics* 10 (Mar. 2013) 1, doi: [10.12942/lrsp-2013-1](https://doi.org/10.12942/lrsp-2013-1) (cit. on p. 23).
- [46] J. Abraham et al., “Measurement of the energy spectrum of cosmic rays above 10^{18} eV using the Pierre Auger Observatory,” *Physics Letters B* 685 (Mar. 2010) 239–246, doi: [10.1016/j.physletb.2010.02.013](https://doi.org/10.1016/j.physletb.2010.02.013), arXiv: [1002.1975](https://arxiv.org/abs/1002.1975) [[astro-ph.HE](https://arxiv.org/abs/1002.1975)] (cit. on p. 23).
- [47] G. Sigl et al., “Probing grand unified theories with cosmic-ray, gamma-ray, and neutrino astrophysics,” *Phys. Rev. D* 59.4, 043504 (Feb. 1999) 043504, doi: [10.1103/PhysRevD.59.043504](https://doi.org/10.1103/PhysRevD.59.043504), eprint: [hep-ph/9809242](https://arxiv.org/abs/hep-ph/9809242) (cit. on p. 24).
- [48] I. F. Mirabel and L. F. Rodríguez, “Microquasars in our Galaxy,” *Nature* 392 (Apr. 1998) 673–676, doi: [10.1038/33603](https://doi.org/10.1038/33603) (cit. on pp. 26, 27).
- [49] A. Lemièrè, “AGN Observations with H.E.S.S.,” *High Energy Gamma-Ray Astronomy*, ed. by F. A. Aharonian, H. J. Völk, and D. Horns, vol. 745, American Institute of Physics Conference Series, Feb. 2005 443–448, doi: [10.1063/1.1878443](https://doi.org/10.1063/1.1878443) (cit. on p. 26).
- [50] Pierre Auger Collaboration et al., “Correlation of the Highest-Energy Cosmic Rays with Nearby Extragalactic Objects,” *Science* 318 (Nov. 2007) 938–, doi: [10.1126/science.1151124](https://doi.org/10.1126/science.1151124), arXiv: [0711.2256](https://arxiv.org/abs/0711.2256) (cit. on p. 26).
- [51] M. Ackermann et al., “Detection of the Characteristic Pion-Decay Signature in Supernova Remnants,” *Science* 339 (Feb. 2013) 807–811, doi: [10.1126/science.1231160](https://doi.org/10.1126/science.1231160), arXiv: [1302.3307](https://arxiv.org/abs/1302.3307) [[astro-ph.HE](https://arxiv.org/abs/1302.3307)] (cit. on pp. 26, 27, 32).
- [52] A. Heger et al., “How Massive Single Stars End Their Life,” *ApJ* 591 (July 2003) 288–300, doi: [10.1086/375341](https://doi.org/10.1086/375341), eprint: [astro-ph/0212469](https://arxiv.org/abs/astro-ph/0212469) (cit. on p. 27).
- [53] C. C. Finlay et al., “International Geomagnetic Reference Field: the eleventh generation,” *Geophysical Journal International* 183 (Dec. 2010) 1216–1230, doi: [10.1111/j.1365-246X.2010.04804.x](https://doi.org/10.1111/j.1365-246X.2010.04804.x) (cit. on p. 27).

- [54] R. Fender, “Relativistic Outflows from X-ray Binaries (‘Microquasars’),” *Relativistic Flows in Astrophysics*, ed. by A. W. Guthmann et al., vol. 589, Lecture Notes in Physics, Berlin Springer Verlag, 2002 101, eprint: [astro-ph/0109502](#) (cit. on p. 27).
- [55] R. A. Remillard and J. E. McClintock, “X-Ray Properties of Black-Hole Binaries,” *ARA&A* 44 (Sept. 2006) 49–92, doi: [10.1146/annurev.astro.44.051905.092532](#), eprint: [astro-ph/0606352](#) (cit. on p. 27).
- [56] I. F. Mirabel, “Microquasars,” *Comptes Rendus Physique* 8 (Jan. 2007) 7–15, doi: [10.1016/j.crhy.2006.12.001](#) (cit. on p. 27).
- [57] E. M. de Gouveia dal Pino and A. Lazarian, “Production of the large scale superluminal ejections of the microquasar GRS 1915+105 by violent magnetic reconnection,” *A&A* 441 (Oct. 2005) 845–853, doi: [10.1051/0004-6361:20042590](#) (cit. on p. 27).
- [58] B. Khiali, E. M. de Gouveia Dal Pino, and M. V. del Valle, “A magnetic reconnection model for explaining the multiwavelength emission of the microquasars Cyg X-1 and Cyg X-3,” *MNRAS* 449 (May 2015) 34–48, doi: [10.1093/mnras/stv248](#), arXiv: [1406.5664](#) [[astro-ph.HE](#)] (cit. on p. 27).
- [59] E. Fermi, “On the Origin of the Cosmic Radiation,” *Physical Review* 75 (Apr. 1949) 1169–1174, doi: [10.1103/PhysRev.75.1169](#) (cit. on pp. 27, 28).
- [60] E. Fermi, “Galactic Magnetic Fields and the Origin of Cosmic Radiation.,” *ApJ* 119 (Jan. 1954) 1, doi: [10.1086/145789](#) (cit. on p. 27).
- [61] R. J. Protheroe, “Acceleration and interaction of ultra high energy cosmic rays,” *Topics in Cosmic-Ray Astrophysics*, ed. by M. A. Duvernois, 1999 247, eprint: [astro-ph/9812055](#) (cit. on pp. 27, 28, 30).
- [62] F. M. Rieger, V. Bosch-Ramon, and P. Duffy, “Fermi acceleration in astrophysical jets,” *Ap&SS* 309 (June 2007) 119–125, doi: [10.1007/s10509-007-9466-z](#), eprint: [astro-ph/0610141](#) (cit. on pp. 28–30).
- [63] T. K. Gaisser, *Cosmic rays and particle physics*, 1990 (cit. on pp. 28–30).
- [64] D. Dolgopyat, “Fermi Acceleration,” Winter Meeting of Canadian Mathematical Society, 2006, URL: <http://www.math.umd.edu/~dolgop/FA.pdf> (visited on 08/11/2015) (cit. on p. 28).
- [65] K. D. Hoffman, “High energy neutrino telescopes,” *New Journal of Physics* 11.5, 055006 (May 2009) 055006, doi: [10.1088/1367-2630/11/5/055006](#), arXiv: [0812.3809](#) (cit. on pp. 31, 32).
- [66] S. Ando and J. F. Beacom, “Revealing the Supernova Gamma-Ray Burst Connection with TeV Neutrinos,” *Physical Review Letters* 95.6, 061103 (Aug. 2005) 061103, doi: [10.1103/PhysRevLett.95.061103](#), eprint: [astro-ph/0502521](#) (cit. on pp. 32, 52–56, 111, 140–142).
- [67] Leung Center for Cosmology and Particle Astrophysics, *Experiment –I. Ultra High Energy Neutrinos and Cosmic Rays*, National Taiwan University, Sept. 2015, URL: <http://lecospa.ntu.edu.tw/experiment-2/experiment-i-ultra-high-energy-neutrinos-and-cosmic-rays/> (cit. on p. 32).

- [68] P. O. Hulth, “Ultra High Energy Neutrino Telescopes,” *International Journal of Modern Physics A* 21 (2006) 1914–1924, doi: [10.1142/S0217751X06032861](https://doi.org/10.1142/S0217751X06032861) (cit. on p. 33).
- [69] A. Weigert, H. J. Wendker, and L. Wisotzki, *Astronomie und Astrophysik: Ein Grundkurs*, Weinheim: Wiley-VCH, 2005, ISBN: 3527403582 (cit. on pp. 35–40, 179, 209, 210).
- [70] Britannica Online for Kids, *Hertzprung-Russell diagram*, Dec. 12, 2015, URL: <http://kids.britannica.com/comptons/art-149080> (cit. on p. 36).
- [71] H.-T. Janka et al., “Theory of core-collapse supernovae,” *Phys. Rep.* 442 (Apr. 2007) 38–74, doi: [10.1016/j.physrep.2007.02.002](https://doi.org/10.1016/j.physrep.2007.02.002), eprint: [astro-ph/0612072](https://arxiv.org/abs/astro-ph/0612072) (cit. on pp. 36, 37, 41–43).
- [72] A. Y Potekhin, “The physics of neutron stars,” *Physics Uspekhi* 53 (Dec. 2010) 1235–1256, doi: [10.3367/UFNe.0180.201012c.1279](https://doi.org/10.3367/UFNe.0180.201012c.1279), arXiv: [1102.5735](https://arxiv.org/abs/1102.5735) [[astro-ph](https://arxiv.org/abs/astro-ph).SR] (cit. on pp. 36, 37).
- [73] S. M. Bilenky et al., “Absolute values of neutrino masses: status and prospects,” *Phys. Rep.* 379 (May 2003) 69–148, doi: [10.1016/S0370-1573\(03\)00102-9](https://doi.org/10.1016/S0370-1573(03)00102-9), eprint: [hep-ph/0211462](https://arxiv.org/abs/hep-ph/0211462) (cit. on p. 37).
- [74] J. R. Gerke, C. S. Kochanek, and K. Z. Stanek, “The search for failed supernovae with the Large Binocular Telescope: first candidates,” *MNRAS* 450 (July 2015) 3289–3305, doi: [10.1093/mnras/stv776](https://doi.org/10.1093/mnras/stv776), arXiv: [1411.1761](https://arxiv.org/abs/1411.1761) [[astro-ph](https://arxiv.org/abs/astro-ph).SR] (cit. on p. 37).
- [75] S. J. Smartt, “Progenitors of Core-Collapse Supernovae,” *ARA&A* 47 (Sept. 2009) 63–106, doi: [10.1146/annurev-astro-082708-101737](https://doi.org/10.1146/annurev-astro-082708-101737), arXiv: [0908.0700](https://arxiv.org/abs/0908.0700) [[astro-ph](https://arxiv.org/abs/astro-ph).SR] (cit. on p. 37).
- [76] A. V. Filippenko, “Optical Spectra of Supernovae,” *ARA&A* 35 (1997) 309–355, doi: [10.1146/annurev.astro.35.1.309](https://doi.org/10.1146/annurev.astro.35.1.309) (cit. on pp. 38–40, 161, 162).
- [77] P. A. Mazzali et al., “Can Differences in the Nickel Abundance in Chandrasekhar-Mass Models Explain the Relation between the Brightness and Decline Rate of Normal Type IA Supernovae?” *ApJ* 547 (Feb. 2001) 988–994, doi: [10.1086/318428](https://doi.org/10.1086/318428), eprint: [astro-ph/0009490](https://arxiv.org/abs/astro-ph/0009490) (cit. on p. 39).
- [78] W. D. Arnett, “Type I supernovae. I - Analytic solutions for the early part of the light curve,” *ApJ* 253 (Feb. 1982) 785–797, doi: [10.1086/159681](https://doi.org/10.1086/159681) (cit. on pp. 39, 173, 174).
- [79] E. M. Schlegel, “A new subclass of Type II supernovae?” *MNRAS* 244 (May 1990) 269–271 (cit. on p. 40).
- [80] D. Richardson et al., “A Comparative Study of the Absolute Magnitude Distributions of Supernovae,” *AJ* 123 (Feb. 2002) 745–752, doi: [10.1086/338318](https://doi.org/10.1086/338318), eprint: [astro-ph/0112051](https://arxiv.org/abs/astro-ph/0112051) (cit. on p. 40).
- [81] N. Smith et al., “SN 2006gy: Discovery of the Most Luminous Supernova Ever Recorded, Powered by the Death of an Extremely Massive Star like η Carinae,” *ApJ* 666 (Sept. 2007) 1116–1128, doi: [10.1086/519949](https://doi.org/10.1086/519949), eprint: [astro-ph/0612617](https://arxiv.org/abs/astro-ph/0612617) (cit. on pp. 40, 155).

- [82] T. J. Moriya and N. Tominaga,
“Diversity of Luminous Supernovae from Non-steady Mass Loss,”
ApJ 747, 118 (Mar. 2012) 118, doi: [10.1088/0004-637X/747/2/118](https://doi.org/10.1088/0004-637X/747/2/118),
arXiv: [1110.3807](https://arxiv.org/abs/1110.3807) [[astro-ph.HE](#)] (cit. on p. 40).
- [83] J. Deng et al., “Subaru Spectroscopy of the Interacting Type Ia Supernova SN 2002ic:
Evidence of a Hydrogen-rich, Asymmetric Circumstellar Medium,”
ApJ 605 (Apr. 2004) L37–L40, doi: [10.1086/420698](https://doi.org/10.1086/420698), eprint: [astro-ph/0311590](https://arxiv.org/abs/astro-ph/0311590)
(cit. on p. 41).
- [84] E. O. Ofek et al., “Precursors Prior to Type IIn Supernova Explosions are Common: Precursor
Rates, Properties, and Correlations,” *ApJ* 789, 104 (July 2014) 104,
doi: [10.1088/0004-637X/789/2/104](https://doi.org/10.1088/0004-637X/789/2/104), arXiv: [1401.5468](https://arxiv.org/abs/1401.5468) [[astro-ph.HE](#)] (cit. on p. 41).
- [85] S. Woosley and T. Janka, “The physics of core-collapse supernovae,”
Nature Physics 1 (Dec. 2005) 147–154, doi: [10.1038/nphys172](https://doi.org/10.1038/nphys172), eprint: [astro-ph/0601261](https://arxiv.org/abs/astro-ph/0601261)
(cit. on p. 42).
- [86] D. A. Howell et al.,
“The type Ia supernova SNLS-03D3bb from a super-Chandrasekhar-mass white dwarf star,”
Nature 443 (Sept. 2006) 308–311, doi: [10.1038/nature05103](https://doi.org/10.1038/nature05103), eprint: [astro-ph/0609616](https://arxiv.org/abs/astro-ph/0609616)
(cit. on p. 42).
- [87] T. Totani et al., “Future Detection of Supernova Neutrino Burst and Explosion Mechanism,”
ApJ 496 (Mar. 1998) 216–225, doi: [10.1086/305364](https://doi.org/10.1086/305364), eprint: [astro-ph/9710203](https://arxiv.org/abs/astro-ph/9710203)
(cit. on pp. 45, 88, 89, 100).
- [88] M. T. Keil, G. G. Raffelt, and H.-T. Janka,
“Monte Carlo Study of Supernova Neutrino Spectra Formation,”
ApJ 590 (June 2003) 971–991, doi: [10.1086/375130](https://doi.org/10.1086/375130), eprint: [astro-ph/0208035](https://arxiv.org/abs/astro-ph/0208035)
(cit. on pp. 44, 45).
- [89] S. Ando and K. Sato, “Relic neutrino background from cosmological supernovae,”
New Journal of Physics 6 (Nov. 2004) 170, doi: [10.1088/1367-2630/6/1/170](https://doi.org/10.1088/1367-2630/6/1/170),
eprint: [astro-ph/0410061](https://arxiv.org/abs/astro-ph/0410061) (cit. on pp. 44, 45, 84, 88, 89).
- [90] M. T. Keil, “Supernova Neutrino Spectra and Applications to Flavor Oscillations,”
ArXiv Astrophysics e-prints (Aug. 2003), eprint: [astro-ph/0308228](https://arxiv.org/abs/astro-ph/0308228) (cit. on p. 44).
- [91] W. D. Arnett et al., “Supernova 1987A,” *ARA&A* 27 (1989) 629–700,
doi: [10.1146/annurev.aa.27.090189.003213](https://doi.org/10.1146/annurev.aa.27.090189.003213) (cit. on pp. 45–47, 83).
- [92] D. A. Green and F. R. Stephenson, “Historical Supernovae,”
Supernovae and Gamma-Ray Bursters, ed. by K. Weiler, vol. 598,
Lecture Notes in Physics, Berlin Springer Verlag, 2003 7–19, eprint: [astro-ph/0301603](https://arxiv.org/abs/astro-ph/0301603)
(cit. on p. 45).
- [93] S. P. Reynolds et al., “A Deep Chandra Observation of Kepler’s Supernova Remnant: A Type
Ia Event with Circumstellar Interaction,” *ApJ* 668 (Oct. 2007) L135–L138,
doi: [10.1086/522830](https://doi.org/10.1086/522830), arXiv: [0708.3858](https://arxiv.org/abs/0708.3858) (cit. on p. 45).

- [94] J. D. Lyman, D. Bersier, and P. A. James, “Bolometric corrections for optical light curves of core-collapse supernovae,” *Monthly Notices of the Royal Astronomical Society* 437.4 (2014) 3848–3862, doi: [10.1093/mnras/stt2187](https://doi.org/10.1093/mnras/stt2187), eprint: <http://mnras.oxfordjournals.org/content/437/4/3848.full.pdf+html>, URL: <http://mnras.oxfordjournals.org/content/437/4/3848.abstract> (cit. on p. 45).
- [95] L. Da Silva, “The classification of supernovae,” English, *Astrophysics and Space Science* 202.2 (1993) 215–236, ISSN: 0004-640X, doi: [10.1007/BF00626878](https://doi.org/10.1007/BF00626878), URL: <http://dx.doi.org/10.1007/BF00626878> (cit. on pp. 45, 46).
- [96] P. Podsiadlowski, “The progenitor of SN 1987 A,” *PASP* 104 (Sept. 1992) 717–729, doi: [10.1086/133043](https://doi.org/10.1086/133043) (cit. on p. 46).
- [97] K. Hirata et al., “Observation of a neutrino burst from the supernova SN1987A,” *Physical Review Letters* 58 (Apr. 1987) 1490–1493, doi: [10.1103/PhysRevLett.58.1490](https://doi.org/10.1103/PhysRevLett.58.1490) (cit. on p. 46).
- [98] R. M. Bionta et al., “Observation of a neutrino burst in coincidence with supernova 1987A in the Large Magellanic Cloud,” *Physical Review Letters* 58 (Apr. 1987) 1494–1496, doi: [10.1103/PhysRevLett.58.1494](https://doi.org/10.1103/PhysRevLett.58.1494) (cit. on p. 46).
- [99] T. J. Loredo and D. Q. Lamb, “Bayesian analysis of neutrinos observed from supernova SN 1987A,” *Phys. Rev. D* 65.6, 063002 (Mar. 2002) 063002, doi: [10.1103/PhysRevD.65.063002](https://doi.org/10.1103/PhysRevD.65.063002), eprint: [astro-ph/0107260](https://arxiv.org/abs/astro-ph/0107260) (cit. on pp. 46, 83).
- [100] M. J. Longo, “Tests of relativity from SN1987A,” *Phys. Rev. D* 36 (Nov. 1987) 3276–3277, doi: [10.1103/PhysRevD.36.3276](https://doi.org/10.1103/PhysRevD.36.3276) (cit. on pp. 46, 83).
- [101] G. G. Raffelt, “Astrophysical axion bounds: an update,” *Beyond the Desert 1997: Accelerator and Non-Accelerator Approaches*, ed. by H. V. Klapdor-Lleingrothaus and H. Päs, 1998 808, eprint: [astro-ph/9707268](https://arxiv.org/abs/astro-ph/9707268) (cit. on pp. 46, 83).
- [102] R. Diehl et al., “Radioactive ^{26}Al from massive stars in the Galaxy,” *Nature* 439 (Jan. 2006) 45–47, doi: [10.1038/nature04364](https://doi.org/10.1038/nature04364), eprint: [astro-ph/0601015](https://arxiv.org/abs/astro-ph/0601015) (cit. on pp. 48, 83).
- [103] Kamioka Observatory and ICRR (Institute for Cosmic Ray Research), *Search for Supernova Relic Neutrinos*, The University of Tokyo, June 8, 2015, URL: <http://www-sk.icrr.u-tokyo.ac.jp/sk/physics/srn-e.html> (cit. on p. 48).
- [104] L. E. Strigari et al., “The concordance cosmic star formation rate: implications from and for the supernova neutrino and gamma ray backgrounds,” *J. Cosmology Astropart. Phys.* 4, 017 (Apr. 2005) 17, doi: [10.1088/1475-7516/2005/04/017](https://doi.org/10.1088/1475-7516/2005/04/017), eprint: [astro-ph/0502150](https://arxiv.org/abs/astro-ph/0502150) (cit. on p. 48).
- [105] S. Horiuchi et al., “The Cosmic Core-collapse Supernova Rate Does Not Match the Massive-star Formation Rate,” *ApJ* 738, 154 (Sept. 2011) 154, doi: [10.1088/0004-637X/738/2/154](https://doi.org/10.1088/0004-637X/738/2/154), arXiv: [1102.1977](https://arxiv.org/abs/1102.1977) [[astro-ph.CO](https://arxiv.org/abs/astro-ph.CO)] (cit. on pp. 48, 49, 105, 106).

- [106] G. J. Mathews et al., “Supernova Relic Neutrinos and the Supernova Rate Problem: Analysis of Uncertainties and Detectability of ONeMg and Failed Supernovae,” *ApJ* 790, 115 (Aug. 2014) 115, doi: [10.1088/0004-637X/790/2/115](https://doi.org/10.1088/0004-637X/790/2/115), arXiv: [1405.0458](https://arxiv.org/abs/1405.0458) (cit. on pp. [48](#), [49](#), [84](#), [88](#)).
- [107] W. Li et al., “Nearby supernova rates from the Lick Observatory Supernova Search - III. The rate-size relation, and the rates as a function of galaxy Hubble type and colour,” *MNRAS* 412 (Apr. 2011) 1473–1507, doi: [10.1111/j.1365-2966.2011.18162.x](https://doi.org/10.1111/j.1365-2966.2011.18162.x), arXiv: [1006.4613](https://arxiv.org/abs/1006.4613) [[astro-ph.SR](#)] (cit. on pp. [48](#), [49](#), [105](#), [106](#), [140](#), [141](#), [146](#), [199](#), [201](#), [205](#)).
- [108] S. Ando, J. F. Beacom, and H. Yüksel, “Detection of Neutrinos from Supernovae in Nearby Galaxies,” *Physical Review Letters* 95.17, 171101 (Oct. 2005) 171101, doi: [10.1103/PhysRevLett.95.171101](https://doi.org/10.1103/PhysRevLett.95.171101), eprint: [astro-ph/0503321](https://arxiv.org/abs/astro-ph/0503321) (cit. on pp. [48](#), [49](#), [83](#), [84](#)).
- [109] S. Horiuchi et al., “Effects of Stellar Rotation on Star Formation Rates and Comparison to Core-collapse Supernova Rates,” *ApJ* 769, 113 (June 2013) 113, doi: [10.1088/0004-637X/769/2/113](https://doi.org/10.1088/0004-637X/769/2/113), arXiv: [1302.0287](https://arxiv.org/abs/1302.0287) [[astro-ph.SR](#)] (cit. on pp. [48](#), [105](#)).
- [110] K. Murase et al., “New class of high-energy transients from crashes of supernova ejecta with massive circumstellar material shells,” *Phys. Rev. D* 84.4, 043003 (Aug. 2011) 043003, doi: [10.1103/PhysRevD.84.043003](https://doi.org/10.1103/PhysRevD.84.043003), arXiv: [1012.2834](https://arxiv.org/abs/1012.2834) [[astro-ph.HE](#)] (cit. on pp. [49–51](#), [150](#), [151](#), [165](#)).
- [111] S. Razzaque, P. Mészáros, and E. Waxman, “TeV Neutrinos from Core Collapse Supernovae and Hypernovae,” *Physical Review Letters* 93.18, 181101 (Oct. 2004) 181101, doi: [10.1103/PhysRevLett.93.181101](https://doi.org/10.1103/PhysRevLett.93.181101), eprint: [astro-ph/0407064](https://arxiv.org/abs/astro-ph/0407064) (cit. on pp. [51](#), [52](#), [111](#)).
- [112] P. Mészáros, “Gamma-ray bursts,” *Reports on Progress in Physics* 69 (Aug. 2006) 2259–2321, doi: [10.1088/0034-4885/69/8/R01](https://doi.org/10.1088/0034-4885/69/8/R01), eprint: [astro-ph/0605208](https://arxiv.org/abs/astro-ph/0605208) (cit. on pp. [51](#), [55](#), [56](#), [111](#)).
- [113] S. Razzaque, P. Mészáros, and E. Waxman, “Erratum: TeV Neutrinos from Core Collapse Supernovae and Hypernovae [Phys. Rev. Lett. 93, 181101 (2004)],” *Physical Review Letters* 94.10, 109903 (Mar. 2005) 109903, doi: [10.1103/PhysRevLett.94.109903](https://doi.org/10.1103/PhysRevLett.94.109903) (cit. on p. [52](#)).
- [114] R. Salvaterra et al., “GRB090423 at a redshift of $z \sim 8.1$,” *Nature* 461 (Oct. 2009) 1258–1260, doi: [10.1038/nature08445](https://doi.org/10.1038/nature08445), arXiv: [0906.1578](https://arxiv.org/abs/0906.1578) (cit. on p. [55](#)).
- [115] I. Horváth et al., “Classification of Swift’s gamma-ray bursts,” *A&A* 489 (Oct. 2008) L1–L4, doi: [10.1051/0004-6361:200810269](https://doi.org/10.1051/0004-6361:200810269), arXiv: [0808.1067](https://arxiv.org/abs/0808.1067) (cit. on p. [55](#)).
- [116] N. Gehrels, E. Ramirez-Ruiz, and D. B. Fox, “Gamma-Ray Bursts in the Swift Era,” *ARA&A* 47 (Sept. 2009) 567–617, doi: [10.1146/annurev.astro.46.060407.145147](https://doi.org/10.1146/annurev.astro.46.060407.145147), arXiv: [0909.1531](https://arxiv.org/abs/0909.1531) [[astro-ph.HE](#)] (cit. on p. [55](#)).
- [117] P. Mészáros, “Gamma Ray Bursts as Neutrino Sources,” *ArXiv e-prints* (Nov. 2015), arXiv: [1511.01396](https://arxiv.org/abs/1511.01396) [[astro-ph.HE](#)] (cit. on p. [56](#)).

- [118] R. Abbasi et al.,
“An absence of neutrinos associated with cosmic-ray acceleration in γ -ray bursts,”
Nature 484 (Apr. 2012) 351–354, doi: [10.1038/nature11068](https://doi.org/10.1038/nature11068),
arXiv: [1204.4219](https://arxiv.org/abs/1204.4219) [[astro-ph.HE](#)] (cit. on p. 57).
- [119] IceCube-Gen2 Collaboration et al.,
“IceCube-Gen2: A Vision for the Future of Neutrino Astronomy in Antarctica,”
ArXiv e-prints (Dec. 2014), arXiv: [1412.5106](https://arxiv.org/abs/1412.5106) [[astro-ph.HE](#)] (cit. on p. 57).
- [120] The IceCube-PINGU Collaboration,
“Letter of Intent: The Precision IceCube Next Generation Upgrade (PINGU),”
ArXiv e-prints (Jan. 2014), arXiv: [1401.2046](https://arxiv.org/abs/1401.2046) [[physics.ins-det](#)] (cit. on pp. 57, 85, 107).
- [121] S. Fukuda et al., “The Super-Kamiokande detector,”
Nuclear Instruments and Methods in Physics Research A 501 (Apr. 2003) 418–462,
doi: [10.1016/S0168-9002\(03\)00425-X](https://doi.org/10.1016/S0168-9002(03)00425-X) (cit. on pp. 59, 60, 98).
- [122] Kamioka Observatory and ICRR (Institute for Cosmic Ray Research),
No.SK3-14, Completed mounting PMTs 5, The University of Tokyo, Mar. 17, 2010,
URL: <http://www-sk.icrr.u-tokyo.ac.jp/sk/gallery/index-e.html> (cit. on p. 60).
- [123] K. Abe et al., “Calibration of the Super-Kamiokande detector,”
Nuclear Instruments and Methods in Physics Research A 737 (Feb. 2014) 253–272,
doi: [10.1016/j.nima.2013.11.081](https://doi.org/10.1016/j.nima.2013.11.081), arXiv: [1307.0162](https://arxiv.org/abs/1307.0162) [[physics.ins-det](#)]
(cit. on pp. 59, 60).
- [124] T. Barszczak, *Images of Super-Kamiokande events from tscan*, University of California, Irvine,
Mar. 10, 1999, URL: <http://www.ps.uci.edu/~tomba/sk/tscan/pictures.html>
(cit. on p. 61).
- [125] V. Takhistov et al., “Search for Nucleon and Di-nucleon Decays with an Invisible Particle and a
Charged Lepton in the Final State at the Super-Kamiokande Experiment,”
ArXiv e-prints (Aug. 2015), arXiv: [1508.05530](https://arxiv.org/abs/1508.05530) [[hep-ex](#)] (cit. on p. 60).
- [126] M. Ikeda et al., “Search for Supernova Neutrino Bursts at Super-Kamiokande,”
ApJ 669 (Nov. 2007) 519–524, doi: [10.1086/521547](https://doi.org/10.1086/521547), arXiv: [0706.2283](https://arxiv.org/abs/0706.2283)
(cit. on pp. 60, 61, 83).
- [127] G. G. Raffelt, “Physics with supernovae,”
Nuclear Physics B Proceedings Supplements 110 (July 2002) 254–267,
doi: [10.1016/S0920-5632\(02\)01489-5](https://doi.org/10.1016/S0920-5632(02)01489-5), eprint: [hep-ph/0201099](https://arxiv.org/abs/hep-ph/0201099) (cit. on p. 60).
- [128] K. Bays et al., “Supernova relic neutrino search at super-Kamiokande,”
Phys. Rev. D 85.5, 052007 (Mar. 2012) 052007, doi: [10.1103/PhysRevD.85.052007](https://doi.org/10.1103/PhysRevD.85.052007),
arXiv: [1111.5031](https://arxiv.org/abs/1111.5031) [[hep-ex](#)] (cit. on pp. 60, 98, 107).
- [129] M. J. Aitken, “Archaeological dating using physical phenomena,”
Reports on Progress in Physics 62 (Sept. 1999) 1333–1376,
doi: [10.1088/0034-4885/62/9/202](https://doi.org/10.1088/0034-4885/62/9/202) (cit. on p. 61).
- [130] S. Abe et al.,
“Production of radioactive isotopes through cosmic muon spallation in KamLAND,”
Phys. Rev. C 81.2, 025807 (Feb. 2010) 025807, doi: [10.1103/PhysRevC.81.025807](https://doi.org/10.1103/PhysRevC.81.025807),
arXiv: [0907.0066](https://arxiv.org/abs/0907.0066) [[hep-ex](#)] (cit. on p. 62).

- [131] M. Malek et al., “Search for Supernova Relic Neutrinos at Super-Kamiokande,” *Physical Review Letters* 90.6, 061101 (Feb. 2003) 061101, doi: [10.1103/PhysRevLett.90.061101](https://doi.org/10.1103/PhysRevLett.90.061101), eprint: [hep-ex/0209028](https://arxiv.org/abs/hep-ex/0209028) (cit. on pp. 62, 98, 99, 107).
- [132] S. Ando, “Decaying neutrinos and implications from the supernova relic neutrino observation,” *Physics Letters B* 570 (Sept. 2003) 11–18, doi: [10.1016/j.physletb.2003.07.009](https://doi.org/10.1016/j.physletb.2003.07.009), eprint: [hep-ph/0307169](https://arxiv.org/abs/hep-ph/0307169) (cit. on p. 62).
- [133] J. F. Beacom and M. R. Vagins, “Antineutrino Spectroscopy with Large Water Čerenkov Detectors,” *Physical Review Letters* 93.17, 171101 (Oct. 2004) 171101, doi: [10.1103/PhysRevLett.93.171101](https://doi.org/10.1103/PhysRevLett.93.171101), eprint: [hep-ph/0309300](https://arxiv.org/abs/hep-ph/0309300) (cit. on p. 62).
- [134] M. Kowalski, “Status of High-Energy Neutrino Astronomy,” *ArXiv e-prints* (Nov. 2014), arXiv: [1411.4385](https://arxiv.org/abs/1411.4385) [[astro-ph.HE](https://arxiv.org/abs/1411.4385)] (cit. on pp. 62, 63).
- [135] A. Karle and for the IceCube Collaboration, “IceCube - status and recent results,” *ArXiv e-prints* (Jan. 2014), arXiv: [1401.4496](https://arxiv.org/abs/1401.4496) [[astro-ph.HE](https://arxiv.org/abs/1401.4496)] (cit. on pp. 62, 63, 85).
- [136] R. Abbasi et al., “The IceCube data acquisition system: Signal capture, digitization, and timestamping,” *Nuclear Instruments and Methods in Physics Research A* 601 (Apr. 2009) 294–316, doi: [10.1016/j.nima.2009.01.001](https://doi.org/10.1016/j.nima.2009.01.001), arXiv: [0810.4930](https://arxiv.org/abs/0810.4930) [[physics.ins-det](https://arxiv.org/abs/0810.4930)] (cit. on pp. 63, 64, 67, 68, 91).
- [137] M. G. Aartsen et al., “Improvement in fast particle track reconstruction with robust statistics,” *Nuclear Instruments and Methods in Physics Research A* 736 (Feb. 2014) 143–149, doi: [10.1016/j.nima.2013.10.074](https://doi.org/10.1016/j.nima.2013.10.074), arXiv: [1308.5501](https://arxiv.org/abs/1308.5501) [[astro-ph.IM](https://arxiv.org/abs/1308.5501)] (cit. on pp. 64, 71).
- [138] T. K. Gaisser and for the IceCube Collaboration, “IceCube at the Threshold,” *ArXiv e-prints* (July 2015), arXiv: [1507.07871](https://arxiv.org/abs/1507.07871) [[astro-ph.HE](https://arxiv.org/abs/1507.07871)] (cit. on p. 63).
- [139] IceCube Collaboration et al., “First year performance of the IceCube neutrino telescope,” *Astroparticle Physics* 26 (Oct. 2006) 155–173, doi: [10.1016/j.astropartphys.2006.06.007](https://doi.org/10.1016/j.astropartphys.2006.06.007), eprint: [astro-ph/0604450](https://arxiv.org/abs/astro-ph/0604450) (cit. on p. 63).
- [140] R. Abbasi et al., “The design and performance of IceCube DeepCore,” *Astroparticle Physics* 35 (May 2012) 615–624, doi: [10.1016/j.astropartphys.2012.01.004](https://doi.org/10.1016/j.astropartphys.2012.01.004), arXiv: [1109.6096](https://arxiv.org/abs/1109.6096) [[astro-ph.IM](https://arxiv.org/abs/1109.6096)] (cit. on p. 63).
- [141] S. Böser et al., “Detecting extra-galactic supernova neutrinos in the Antarctic ice,” *Astroparticle Physics* 62 (Mar. 2015) 54–65, doi: [10.1016/j.astropartphys.2014.07.010](https://doi.org/10.1016/j.astropartphys.2014.07.010), arXiv: [1304.2553](https://arxiv.org/abs/1304.2553) [[astro-ph.IM](https://arxiv.org/abs/1304.2553)] (cit. on pp. 63, 83).
- [142] M. G. Aartsen et al., “Measurement of South Pole ice transparency with the IceCube LED calibration system,” *Nuclear Instruments and Methods in Physics Research A* 711 (May 2013) 73–89, doi: [10.1016/j.nima.2013.01.054](https://doi.org/10.1016/j.nima.2013.01.054), arXiv: [1301.5361](https://arxiv.org/abs/1301.5361) [[astro-ph.IM](https://arxiv.org/abs/1301.5361)] (cit. on pp. 63, 65, 87, 90).

- [143] M. Ackermann et al., “Optical properties of deep glacial ice at the South Pole,” *Journal of Geophysical Research (Atmospheres)* 111, D13203 (July 2006) 13203, doi: [10.1029/2005JD006687](https://doi.org/10.1029/2005JD006687) (cit. on pp. 63, 77, 87, 90).
- [144] M. G. Aartsen et al., “Searches for Extended and Point-like Neutrino Sources with Four Years of IceCube Data,” *ApJ* 796, 109 (Dec. 2014) 109, doi: [10.1088/0004-637X/796/2/109](https://doi.org/10.1088/0004-637X/796/2/109), arXiv: [1406.6757](https://arxiv.org/abs/1406.6757) [astro-ph.HE] (cit. on pp. 66, 68).
- [145] M. G. Aartsen et al., “Energy reconstruction methods in the IceCube neutrino telescope,” *Journal of Instrumentation* 9, P03009 (Mar. 2014) 3009P, doi: [10.1088/1748-0221/9/03/P03009](https://doi.org/10.1088/1748-0221/9/03/P03009), arXiv: [1311.4767](https://arxiv.org/abs/1311.4767) [physics.ins-det] (cit. on pp. 66, 68, 69, 77, 78).
- [146] M. G. Aartsen et al., “Observation of High-Energy Astrophysical Neutrinos in Three Years of IceCube Data,” *Physical Review Letters* 113.10, 101101 (Sept. 2014) 101101, doi: [10.1103/PhysRevLett.113.101101](https://doi.org/10.1103/PhysRevLett.113.101101), arXiv: [1405.5303](https://arxiv.org/abs/1405.5303) [astro-ph.HE] (cit. on pp. 66, 109, 165).
- [147] J. Ahrens et al., “Muon track reconstruction and data selection techniques in AMANDA,” *Nuclear Instruments and Methods in Physics Research A* 524 (May 2004) 169–194, doi: [10.1016/j.nima.2004.01.065](https://doi.org/10.1016/j.nima.2004.01.065), eprint: [astro-ph/0407044](https://arxiv.org/abs/astro-ph/0407044) (cit. on p. 67).
- [148] J. van Santen, “Neutrino Interactions in IceCube above 1 TeV Constraints on Atmospheric Charmed-Meson Production and Investigation of the Astrophysical Neutrino Flux with 2 Years of IceCube Data taken 2010–2012,” English, Copyright - Copyright ProQuest, UMI Dissertations Publishing 2014; Last updated - 2015-08-26; First page - n/a, PhD thesis: University of Wisconsin–Madison, 2014 189, ISBN: 9781321369502, URL: <http://search.proquest.com/docview/1637727437?accountid=14618> (cit. on p. 68).
- [149] A. Franckowiak, “Searching for High-energy Neutrinos from Supernovae with IceCube and an Optical Follow-up Program,” PhD thesis: Universität Bonn, 2011, URL: <http://nbn-resolving.de/urn:nbn:de:hbz:5n-26728> (cit. on pp. 69, 79, 113, 115, 122, 140, 141, 145, 179).
- [150] J. Ahrens et al., “Muon track reconstruction and data selection techniques in AMANDA,” *Nuclear Instruments and Methods in Physics Research A* 524 (May 2004) 169–194, doi: [10.1016/j.nima.2004.01.065](https://doi.org/10.1016/j.nima.2004.01.065), eprint: [astro-ph/0407044](https://arxiv.org/abs/astro-ph/0407044) (cit. on pp. 70–73).
- [151] M. Soiron, “Untersuchungen zur Verbesserung der Myonspur-Rekonstruktion in IceCube,” ger, MA thesis: Rheinisch-Westfälische Technische Hochschule (RWTH) Aachen, 2012, URL: http://www.physik.rwth-aachen.de/fileadmin/user_upload/www_physik/Institute/Inst_3B/Forschung/IceCube/publications/thesis_MS.pdf (cit. on p. 72).
- [152] K. Schatto, “Stacked searches for high-energy neutrinos from blazars with IceCube,” eng, PhD thesis: Johannes Gutenberg-Universität Mainz, 2014, URL: <http://ubm.opus.hbz-nrw.de/volltexte/2014/3869/> (cit. on pp. 73, 74, 77, 78).

- [153] N. Whitehorn, J. van Santen, and S. Lafebre, “Penalized splines for smooth representation of high-dimensional Monte Carlo datasets,” *Computer Physics Communications* 184 (Sept. 2013) 2214–2220, doi: [10.1016/j.cpc.2013.04.008](https://doi.org/10.1016/j.cpc.2013.04.008), arXiv: [1301.2184](https://arxiv.org/abs/1301.2184) [[physics.data-an](#)] (cit. on p. 74).
- [154] T. Neunhoffer, “Estimating the angular resolution of tracks in neutrino telescopes based on a likelihood analysis,” *Astroparticle Physics* 25 (Apr. 2006) 220–225, doi: [10.1016/j.astropartphys.2006.01.002](https://doi.org/10.1016/j.astropartphys.2006.01.002), eprint: [astro-ph/0403367](https://arxiv.org/abs/astro-ph/0403367) (cit. on p. 75).
- [155] R. Abbasi et al., “Time-integrated Searches for Point-like Sources of Neutrinos with the 40-string IceCube Detector,” *ApJ* 732, 18 (May 2011) 18, doi: [10.1088/0004-637X/732/1/18](https://doi.org/10.1088/0004-637X/732/1/18), arXiv: [1012.2137](https://arxiv.org/abs/1012.2137) [[astro-ph.HE](#)] (cit. on p. 75).
- [156] J. Lünemann, “Suche nach Dunkler Materie in Galaxien und Galaxienhaufen mit dem Neutrino-teleskop IceCube,” ger, PhD thesis: Johannes Gutenberg-Universität Mainz, 2013, URL: <http://ubm.opus.hbz-nrw.de/volltexte/2014/3705/> (cit. on pp. 75, 76).
- [157] R. Abbasi et al., “An improved method for measuring muon energy using the truncated mean of dE/dx ,” *Nuclear Instruments and Methods in Physics Research A* 703 (Mar. 2013) 190–198, doi: [10.1016/j.nima.2012.11.081](https://doi.org/10.1016/j.nima.2012.11.081) (cit. on p. 77).
- [158] Dr. Ed Grayzeck, Dr. Edwin Bell, II, *NASA’s Tracking and Data Relay Satellites (TDRS)*, Aug. 2014, URL: <http://nssdc.gsfc.nasa.gov/multi/tdrs.html> (cit. on p. 80).
- [159] J. Teles, M. V. Samii, and C. E. Doll, “Overview of TDRSS,” *Advances in Space Research* 16 (1995) 67–76 (cit. on p. 80).
- [160] N. Gehrels et al., “The Swift Gamma-Ray Burst Mission,” *ApJ* 611 (Aug. 2004) 1005–1020, doi: [10.1086/422091](https://doi.org/10.1086/422091) (cit. on pp. 80, 112, 114).
- [161] Thuy Mai, *Tracking and Data Relay Satellite (TDRS)*, Aug. 2015, URL: http://www.nasa.gov/directorates/heo/scan/services/networks/txt_tdrs.html (cit. on p. 80).
- [162] M. Ageron et al., “ANTARES: The first undersea neutrino telescope,” *Nuclear Instruments and Methods in Physics Research A* 656 (Nov. 2011) 11–38, doi: [10.1016/j.nima.2011.06.103](https://doi.org/10.1016/j.nima.2011.06.103), arXiv: [1104.1607](https://arxiv.org/abs/1104.1607) [[astro-ph.IM](#)] (cit. on pp. 81, 85).
- [163] S. Adrián-Martínez et al., “Search for Cosmic Neutrino Point Sources with Four Years of Data from the ANTARES Telescope,” *ApJ* 760, 53 (Nov. 2012) 53, doi: [10.1088/0004-637X/760/1/53](https://doi.org/10.1088/0004-637X/760/1/53), arXiv: [1207.3105](https://arxiv.org/abs/1207.3105) [[hep-ex](#)] (cit. on p. 81).
- [164] R. Abbasi et al., “Calibration and characterization of the IceCube photomultiplier tube,” *Nuclear Instruments and Methods in Physics Research A* 618 (June 2010) 139–152, doi: [10.1016/j.nima.2010.03.102](https://doi.org/10.1016/j.nima.2010.03.102), arXiv: [1002.2442](https://arxiv.org/abs/1002.2442) [[astro-ph.IM](#)] (cit. on p. 81).
- [165] KM3NeT Collaboration, *KM3NeT: Astroparticle & Oscillations Research with Cosmics in the Abyss*, Oct. 2015, URL: <http://www.km3net.org/publications/2015/KM3NeT-Strategy.pdf> (cit. on p. 81).

- [166] I. A. Belolaptikov et al.,
“The Baikal underwater neutrino telescope: Design, performance, and first results,”
Astroparticle Physics 7 (Aug. 1997) 263–282, doi: [10.1016/S0927-6505\(97\)00022-4](https://doi.org/10.1016/S0927-6505(97)00022-4)
(cit. on p. 81).
- [167] A. D. Avrorin et al., “The prototyping/early construction phase of the BAIKAL-GVD project,”
Nuclear Instruments and Methods in Physics Research A 742 (Apr. 2014) 82–88,
doi: [10.1016/j.nima.2013.10.064](https://doi.org/10.1016/j.nima.2013.10.064), arXiv: [1308.1833](https://arxiv.org/abs/1308.1833) [[astro-ph.IM](#)] (cit. on p. 81).
- [168] A. Dighe, “Physics potential of future supernova neutrino observations,”
Journal of Physics Conference Series 136.2, 022041 (Nov. 2008) 022041,
doi: [10.1088/1742-6596/136/2/022041](https://doi.org/10.1088/1742-6596/136/2/022041), arXiv: [0809.2977](https://arxiv.org/abs/0809.2977) [[hep-ph](#)] (cit. on p. 83).
- [169] R. Abbasi et al., “IceCube sensitivity for low-energy neutrinos from nearby supernovae,”
A&A 535, A109 (Nov. 2011) A109, doi: [10.1051/0004-6361/201117810](https://doi.org/10.1051/0004-6361/201117810)
(cit. on pp. 83–85, 90, 91, 93).
- [170] G. G. Raffelt, “Supernova neutrino observations: What can we learn?”
Nuclear Physics B Proceedings Supplements 221 (Dec. 2011) 218–229,
doi: [10.1016/j.nuclphysbps.2011.09.006](https://doi.org/10.1016/j.nuclphysbps.2011.09.006), eprint: [astro-ph/0701677](https://arxiv.org/abs/astro-ph/0701677) (cit. on p. 83).
- [171] M. D. Kistler et al., “Core-collapse astrophysics with a five-megaton neutrino detector,”
Phys. Rev. D 83.12, 123008 (June 2011) 123008, doi: [10.1103/PhysRevD.83.123008](https://doi.org/10.1103/PhysRevD.83.123008),
arXiv: [0810.1959](https://arxiv.org/abs/0810.1959) (cit. on pp. 83–85, 140, 141).
- [172] L. Yang and C. Lunardini, “Revealing local failed supernovae with neutrino telescopes,”
Phys. Rev. D 84.6, 063002 (Sept. 2011) 063002, doi: [10.1103/PhysRevD.84.063002](https://doi.org/10.1103/PhysRevD.84.063002),
arXiv: [1103.4628](https://arxiv.org/abs/1103.4628) [[astro-ph.CO](#)] (cit. on pp. 84, 88–90).
- [173] R. M. Humphreys and K. Davidson, “The luminous blue variables: Astrophysical geysers,”
PASP 106 (Oct. 1994) 1025–1051, doi: [10.1086/133478](https://doi.org/10.1086/133478) (cit. on p. 84).
- [174] M. Modjaz et al., “From Shock Breakout to Peak and Beyond: Extensive Panchromatic
Observations of the Type Ib Supernova 2008D Associated with Swift X-ray Transient 080109,”
ApJ 702 (Sept. 2009) 226–248, doi: [10.1088/0004-637X/702/1/226](https://doi.org/10.1088/0004-637X/702/1/226), arXiv: [0805.2201](https://arxiv.org/abs/0805.2201)
(cit. on p. 84).
- [175] G. Pagliaroli, F. Rossi-Torres, and F. Vissani,
“Neutrino mass bound in the standard scenario for supernova electronic antineutrino emission,”
Astroparticle Physics 33 (June 2010) 287–291,
doi: [10.1016/j.astropartphys.2010.02.007](https://doi.org/10.1016/j.astropartphys.2010.02.007), arXiv: [1002.3349](https://arxiv.org/abs/1002.3349) [[hep-ph](#)]
(cit. on p. 84).
- [176] K. Nakamura, “Hyper-Kamiokande — A Next Generation Water Cherenkov Detector,”
International Journal of Modern Physics A 18 (2003) 4053–4063,
doi: [10.1142/S0217751X03017361](https://doi.org/10.1142/S0217751X03017361) (cit. on p. 85).
- [177] K. Abe et al., “Letter of Intent: The Hyper-Kamiokande Experiment — Detector Design and
Physics Potential —,” *ArXiv e-prints* (Sept. 2011), arXiv: [1109.3262](https://arxiv.org/abs/1109.3262) [[hep-ex](#)]
(cit. on p. 85).
- [178] C. K. Jung, “Feasibility of a next generation underground water Cherenkov detector: UNO,”
American Institute of Physics Conference Series, vol. 533,
American Institute of Physics Conference Series, Aug. 2000 29–34,
doi: [10.1063/1.1361721](https://doi.org/10.1063/1.1361721), eprint: [hep-ex/0005046](https://arxiv.org/abs/hep-ex/0005046) (cit. on p. 85).

- [179] M. Salathe, M. Ribordy, and L. Demirörs, “Novel technique for supernova detection with IceCube,” *Astroparticle Physics* 35 (Mar. 2012) 485–494, doi: [10.1016/j.astropartphys.2011.10.012](https://doi.org/10.1016/j.astropartphys.2011.10.012), arXiv: [1106.1937](https://arxiv.org/abs/1106.1937) [astro-ph.IM] (cit. on p. 85).
- [180] E. K. Akhmedov, S. Razzaque, and A. Y. Smirnov, “Mass hierarchy, 2-3 mixing and CP-phase with huge atmospheric neutrino detectors,” *Journal of High Energy Physics* 2, 82 (Feb. 2013) 82, doi: [10.1007/JHEP02\(2013\)082](https://doi.org/10.1007/JHEP02(2013)082), arXiv: [1205.7071](https://arxiv.org/abs/1205.7071) [hep-ph] (cit. on p. 85).
- [181] I. Bartos et al., “Detection Prospects for GeV Neutrinos from Collisionally Heated Gamma-ray Bursts with IceCube/DeepCore,” *Physical Review Letters* 110.24, 241101 (June 2013) 241101, doi: [10.1103/PhysRevLett.110.241101](https://doi.org/10.1103/PhysRevLett.110.241101), arXiv: [1301.4232](https://arxiv.org/abs/1301.4232) [astro-ph.HE] (cit. on p. 85).
- [182] K. Murase, K. Kashiyama, and P. Mészáros, “Subphotospheric Neutrinos from Gamma-Ray Bursts: The Role of Neutrons,” *Physical Review Letters* 111.13, 131102 (Sept. 2013) 131102, doi: [10.1103/PhysRevLett.111.131102](https://doi.org/10.1103/PhysRevLett.111.131102), arXiv: [1301.4236](https://arxiv.org/abs/1301.4236) [astro-ph.HE] (cit. on p. 85).
- [183] D. Lide, *CRC handbook of chemistry and physics*, Boca Raton: CRC Press, 2005, ISBN: 0-8493-0486-5 (cit. on p. 85).
- [184] J. B. Calvert, *Ice: Structure and Properties*, Aug. 7, 2003, URL: <http://mysite.du.edu/~jcalvert/phys/ice.htm> (visited on 08/24/2016) (cit. on p. 85).
- [185] J. Lundberg et al., “Light tracking through ice and water—Scattering and absorption in heterogeneous media with PHOTONICS,” *Nuclear Instruments and Methods in Physics Research A* 581 (Nov. 2007) 619–631, doi: [10.1016/j.nima.2007.07.143](https://doi.org/10.1016/j.nima.2007.07.143), eprint: [astro-ph/0702108](https://arxiv.org/abs/astro-ph/0702108) (cit. on pp. 87, 91).
- [186] K. Woschnagg, *Photonics Web Page*, URL: <http://icecube.berkeley.edu/kurt/photonics/> (visited on 01/15/2016) (cit. on p. 87).
- [187] A. Olivas, D. Chirkin, K. Hoshina, et al., *Photonics at sourceforge.net*, URL: <http://photonics.sourceforge.net> (visited on 01/15/2016) (cit. on p. 87).
- [188] F. S. Kitaura, H.-T. Janka, and W. Hillebrandt, “Explosions of O-Ne-Mg cores, the Crab supernova, and subluminous type II-P supernovae,” *A&A* 450 (Apr. 2006) 345–350, doi: [10.1051/0004-6361:20054703](https://doi.org/10.1051/0004-6361:20054703), eprint: [astro-ph/0512065](https://arxiv.org/abs/astro-ph/0512065) (cit. on p. 88).
- [189] B. Dasgupta et al., “Detecting the QCD phase transition in the next Galactic supernova neutrino burst,” *Phys. Rev. D* 81.10, 103005 (May 2010) 103005, doi: [10.1103/PhysRevD.81.103005](https://doi.org/10.1103/PhysRevD.81.103005), arXiv: [0912.2568](https://arxiv.org/abs/0912.2568) [astro-ph.HE] (cit. on p. 88).
- [190] K. Sumiyoshi, S. Yamada, and H. Suzuki, “Dynamics and Neutrino Signal of Black Hole Formation in Nonrotating Failed Supernovae. I. Equation of State Dependence,” *ApJ* 667 (Sept. 2007) 382–394, doi: [10.1086/520876](https://doi.org/10.1086/520876), arXiv: [0706.3762](https://arxiv.org/abs/0706.3762) (cit. on p. 88).

- [191] K. Nakamura et al., “Systematic features of axisymmetric neutrino-driven core-collapse supernova models in multiple progenitors,” *PASJ* (Oct. 2015), doi: [10.1093/pasj/psv073](https://doi.org/10.1093/pasj/psv073), arXiv: [1406.2415](https://arxiv.org/abs/1406.2415) [[astro-ph.HE](#)] (cit. on p. 88).
- [192] T. A. Thompson, A. Burrows, and P. A. Pinto, “Shock Breakout in Core-Collapse Supernovae and Its Neutrino Signature,” *ApJ* 592 (July 2003) 434–456, doi: [10.1086/375701](https://doi.org/10.1086/375701), eprint: [astro-ph/0211194](https://arxiv.org/abs/astro-ph/0211194) (cit. on pp. 88, 89).
- [193] K. Nakazato et al., “Oscillation and future detection of failed supernova neutrinos from a black-hole-forming collapse,” *Phys. Rev. D* 78.8, 083014 (Oct. 2008) 083014, doi: [10.1103/PhysRevD.78.083014](https://doi.org/10.1103/PhysRevD.78.083014), arXiv: [0810.3734](https://arxiv.org/abs/0810.3734) (cit. on p. 88).
- [194] K. Sumiyoshi et al., “Neutrino Signals from the Formation of a Black Hole: A Probe of the Equation of State of Dense Matter,” *Physical Review Letters* 97.9, 091101 (Sept. 2006) 091101, doi: [10.1103/PhysRevLett.97.091101](https://doi.org/10.1103/PhysRevLett.97.091101), eprint: [astro-ph/0608509](https://arxiv.org/abs/astro-ph/0608509) (cit. on p. 88).
- [195] R. Abbasi et al., “Calibration and characterization of the IceCube photomultiplier tube,” *Nuclear Instruments and Methods in Physics Research A* 618 (June 2010) 139–152, doi: [10.1016/j.nima.2010.03.102](https://doi.org/10.1016/j.nima.2010.03.102), arXiv: [1002.2442](https://arxiv.org/abs/1002.2442) [[astro-ph.IM](#)] (cit. on p. 91).
- [196] L. Schulte et al., “A large-area single photon sensor employing wavelength-shifting and light-guiding technology,” *ArXiv e-prints* (July 2013), arXiv: [1307.6713](https://arxiv.org/abs/1307.6713) [[astro-ph.IM](#)] (cit. on pp. 91, 93, 107).
- [197] D. Hebecker et al., “Progress on the Development of a Wavelength-shifting Optical Module,” (July 30–Aug. 6, 2015), The 34th International Cosmic Ray Conference, 2015, URL: <http://pos.sissa.it/cgi-bin/reader/conf.cgi?confid=236#session-2522> (visited on 01/18/2016) (cit. on p. 91).
- [198] J. Ahrens et al., “Sensitivity of the IceCube detector to astrophysical sources of high energy muon neutrinos,” *Astroparticle Physics* 20 (Feb. 2004) 507–532, doi: [10.1016/j.astropartphys.2003.09.003](https://doi.org/10.1016/j.astropartphys.2003.09.003), eprint: [astro-ph/0305196](https://arxiv.org/abs/astro-ph/0305196) (cit. on p. 94).
- [199] W. C. Haxton and R. G. H. Robertson, “Solar neutrino interactions with ^{18}O in the SuperKamiokande water Cerenkov detector,” *Phys. Rev. C* 59 (Jan. 1999) 515–519, doi: [10.1103/PhysRevC.59.515](https://doi.org/10.1103/PhysRevC.59.515), eprint: [nucl-th/9806081](https://arxiv.org/abs/nucl-th/9806081) (cit. on pp. 98–100).
- [200] J. N. Bahcall, A. M. Serenelli, and S. Basu, “New Solar Opacities, Abundances, Helioseismology, and Neutrino Fluxes,” *ApJ* 621 (Mar. 2005) L85–L88, doi: [10.1086/428929](https://doi.org/10.1086/428929), eprint: [astro-ph/0412440](https://arxiv.org/abs/astro-ph/0412440) (cit. on p. 98).
- [201] J. N. Bahcall et al., “Standard neutrino spectrum from ^8B decay,” *Phys. Rev. C* 54 (July 1996) 411–422, doi: [10.1103/PhysRevC.54.411](https://doi.org/10.1103/PhysRevC.54.411), eprint: [nucl-th/9601044](https://arxiv.org/abs/nucl-th/9601044) (cit. on pp. 98, 100).
- [202] B. Aharmim et al., “Low-energy-threshold analysis of the Phase I and Phase II data sets of the Sudbury Neutrino Observatory,” *Phys. Rev. C* 81.5, 055504 (May 2010) 055504, doi: [10.1103/PhysRevC.81.055504](https://doi.org/10.1103/PhysRevC.81.055504), arXiv: [0910.2984](https://arxiv.org/abs/0910.2984) [[nucl-ex](#)] (cit. on p. 98).

- [203] B. Aharmim et al., “Electron energy spectra, fluxes, and day-night asymmetries of ^8B solar neutrinos from measurements with NaCl dissolved in the heavy-water detector at the Sudbury Neutrino Observatory,” *Phys. Rev. C* 72.5, 055502 (Nov. 2005) 055502, doi: [10.1103/PhysRevC.72.055502](https://doi.org/10.1103/PhysRevC.72.055502), eprint: [nuc1-ex/0502021](https://arxiv.org/abs/nuc1-ex/0502021) (cit. on p. 98).
- [204] J. F. Beacom, “The Diffuse Supernova Neutrino Background,” *Annual Review of Nuclear and Particle Science* 60 (Nov. 2010) 439–462, doi: [10.1146/annurev.nucl.010909.083331](https://doi.org/10.1146/annurev.nucl.010909.083331), arXiv: [1004.3311](https://arxiv.org/abs/1004.3311) [[astro-ph.HE](https://arxiv.org/archive/hep)] (cit. on p. 99).
- [205] P. Askebjerg et al., “Optical properties of deep ice at the South Pole: absorption,” *Appl. Opt.* 36 (June 1997) 4168–4180, doi: [10.1364/AO.36.004168](https://doi.org/10.1364/AO.36.004168), eprint: [physics/9701025](https://arxiv.org/abs/physics/9701025) (cit. on p. 101).
- [206] F. Halzen and J. P. Rodrigues, “Detection of supernova explosions with IceCube,” *Classical and Quantum Gravity* 27.19, 194003 (Oct. 2010) 194003, doi: [10.1088/0264-9381/27/19/194003](https://doi.org/10.1088/0264-9381/27/19/194003) (cit. on p. 101).
- [207] N. L. Strotjohann,
A Megaton Neutrino Detector in Ice for the Detection of extragalactic Supernovae, English, Bachelor thesis, 2011 (cit. on pp. 102, 103, 105).
- [208] E. Cappellaro, R. Evans, and M. Turatto, “A new determination of supernova rates and a comparison with indicators for galactic star formation,” *A&A* 351 (Nov. 1999) 459–466, eprint: [astro-ph/9904225](https://arxiv.org/abs/astro-ph/9904225) (cit. on pp. 103, 104, 106).
- [209] D. J. White, E. J. Daw, and V. S. Dhillon, “A list of galaxies for gravitational wave searches,” *Classical and Quantum Gravity* 28.8, 085016 (Apr. 2011) 085016, doi: [10.1088/0264-9381/28/8/085016](https://doi.org/10.1088/0264-9381/28/8/085016), arXiv: [1103.0695](https://arxiv.org/abs/1103.0695) (cit. on pp. 103, 106).
- [210] J. Binney and M. Merrifield, *Galactic Astronomy*, 1998 (cit. on p. 105).
- [211] A. S. Dighe, M. T. Keil, and G. G. Raffelt,
“Detecting the neutrino mass hierarchy with a supernova at IceCube,”
J. Cosmology Astropart. Phys. 6, 005 (June 2003) 005,
doi: [10.1088/1475-7516/2003/06/005](https://doi.org/10.1088/1475-7516/2003/06/005), eprint: [hep-ph/0303210](https://arxiv.org/abs/hep-ph/0303210) (cit. on p. 107).
- [212] P. D. Serpico et al.,
“Probing the neutrino mass hierarchy with the rise time of a supernova burst,”
Phys. Rev. D 85.8, 085031 (Apr. 2012) 085031, doi: [10.1103/PhysRevD.85.085031](https://doi.org/10.1103/PhysRevD.85.085031),
arXiv: [1111.4483](https://arxiv.org/abs/1111.4483) [[astro-ph.SR](https://arxiv.org/archive/hep)] (cit. on p. 107).
- [213] O. Kavatsyuk et al., “Multi-PMT optical module for the KM3NeT neutrino telescope,” *Nuclear Instruments and Methods in Physics Research A* 695 (Dec. 2012) 338–341, doi: [10.1016/j.nima.2011.09.062](https://doi.org/10.1016/j.nima.2011.09.062) (cit. on p. 107).
- [214] M. G. Aartsen et al., “A Combined Maximum-likelihood Analysis of the High-energy Astrophysical Neutrino Flux Measured with IceCube,” *ApJ* 809, 98 (Aug. 2015) 98, doi: [10.1088/0004-637X/809/1/98](https://doi.org/10.1088/0004-637X/809/1/98), arXiv: [1507.03991](https://arxiv.org/abs/1507.03991) [[astro-ph.HE](https://arxiv.org/archive/hep)] (cit. on p. 111).
- [215] E. Waxman and J. Bahcall,
“High Energy Neutrinos from Cosmological Gamma-Ray Burst Fireballs,”
Physical Review Letters 78 (Mar. 1997) 2292–2295, doi: [10.1103/PhysRevLett.78.2292](https://doi.org/10.1103/PhysRevLett.78.2292),
eprint: [astro-ph/9701231](https://arxiv.org/abs/astro-ph/9701231) (cit. on p. 111).

- [216] B. Baret et al., “Bounding the time delay between high-energy neutrinos and gravitational-wave transients from gamma-ray bursts,” *Astroparticle Physics* 35 (Aug. 2011) 1–7, doi: [10.1016/j.astropartphys.2011.04.001](https://doi.org/10.1016/j.astropartphys.2011.04.001), arXiv: [1101.4669](https://arxiv.org/abs/1101.4669) [astro-ph.HE] (cit. on pp. [111](#), [232](#)).
- [217] IceCube Collaboration et al., “The IceCube Neutrino Observatory Part I: Point Source Searches,” *ArXiv e-prints* (Sept. 2013), arXiv: [1309.6979](https://arxiv.org/abs/1309.6979) [astro-ph.HE] (cit. on p. [112](#)).
- [218] R. Abbasi et al., “Searching for soft relativistic jets in core-collapse supernovae with the IceCube optical follow-up program,” *A&A* 539, A60 (Mar. 2012) A60, doi: [10.1051/0004-6361/201118071](https://doi.org/10.1051/0004-6361/201118071), arXiv: [1111.7030](https://arxiv.org/abs/1111.7030) [astro-ph.HE] (cit. on pp. [112](#), [113](#), [140](#)).
- [219] M. Kowalski and A. Mohr, “Detecting neutrino transients with optical follow-up observations,” *Astroparticle Physics* 27 (July 2007) 533–538, doi: [10.1016/j.astropartphys.2007.03.005](https://doi.org/10.1016/j.astropartphys.2007.03.005), eprint: [astro-ph/0701618](https://arxiv.org/abs/astro-ph/0701618) (cit. on p. [112](#)).
- [220] C. W. Akerlof et al., “The ROTSE-III Robotic Telescope System,” *PASP* 115 (Jan. 2003) 132–140, doi: [10.1086/345490](https://doi.org/10.1086/345490), eprint: [astro-ph/0210238](https://arxiv.org/abs/astro-ph/0210238) (cit. on p. [112](#)).
- [221] N. M. Law et al., “The Palomar Transient Factory: System Overview, Performance, and First Results,” *PASP* 121 (Dec. 2009) 1395–1408, doi: [10.1086/648598](https://doi.org/10.1086/648598), arXiv: [0906.5350](https://arxiv.org/abs/0906.5350) [astro-ph.IM] (cit. on pp. [112](#), [113](#), [145](#), [147](#), [152](#), [153](#), [192](#), [199](#)).
- [222] A. Rau et al., “Exploring the Optical Transient Sky with the Palomar Transient Factory,” *PASP* 121 (Dec. 2009) 1334–1351, doi: [10.1086/605911](https://doi.org/10.1086/605911), arXiv: [0906.5355](https://arxiv.org/abs/0906.5355) [astro-ph.CO] (cit. on pp. [112](#), [113](#)).
- [223] Aurore Simonnet, *Swift Rendering – A striking computer-generated drawing of the Swift satellite*, NASA E/PO, Sonoma State University, Apr. 2016, URL: <http://swift.sonoma.edu/resources/multimedia/images/> (cit. on p. [113](#)).
- [224] Caltech Optical Observatories, *Visiting Palomar Observatory*, California Institute of Technology, Mar. 2015, URL: <http://www.astro.caltech.edu/palomar/visitor/> (cit. on pp. [113](#), [219](#), [220](#)).
- [225] R. R. Laher et al., “IPAC Image Processing and Data Archiving for the Palomar Transient Factory,” *PASP* 126 (July 2014) 674–710, doi: [10.1086/677351](https://doi.org/10.1086/677351), arXiv: [1404.1953](https://arxiv.org/abs/1404.1953) [astro-ph.IM] (cit. on pp. [113](#), [181](#)).
- [226] E. O. Ofek et al., “The Palomar Transient Factory Photometric Calibration,” *PASP* 124 (Jan. 2012) 62–73, doi: [10.1086/664065](https://doi.org/10.1086/664065), arXiv: [1112.4851](https://arxiv.org/abs/1112.4851) [astro-ph.IM] (cit. on pp. [113](#), [154](#)).
- [227] Oschin Media/Palomar/Caltech, *48-inch (1.2-meter) Samuel Oschin Telescope Media*, Palomar Observatory/California Institute of Technology, Nov. 24, 2015, URL: <http://www.astro.caltech.edu/palomar/media/oschinmedia.html> (cit. on p. [114](#)).

- [228] A. Lien et al., “Probing the Cosmic Gamma-Ray Burst Rate with Trigger Simulations of the Swift Burst Alert Telescope,” *ApJ* 783, 24 (Mar. 2014) 24, doi: [10.1088/0004-637X/783/1/24](https://doi.org/10.1088/0004-637X/783/1/24), arXiv: [1311.4567](https://arxiv.org/abs/1311.4567) [[astro-ph.HE](#)] (cit. on p. [114](#)).
- [229] P. A. Evans et al., “Swift follow-up of IceCube triggers, and implications for the Advanced-LIGO era,” *MNRAS* 448 (Apr. 2015) 2210–2223, doi: [10.1093/mnras/stv136](https://doi.org/10.1093/mnras/stv136), arXiv: [1501.04435](https://arxiv.org/abs/1501.04435) [[astro-ph.HE](#)] (cit. on pp. [114](#), [135](#)).
- [230] R. Abbasi et al., “Neutrino Analysis of the 2010 September Crab Nebula Flare and Time-integrated Constraints on Neutrino Emission from the Crab Using IceCube,” *ApJ* 745, 45 (Jan. 2012) 45, doi: [10.1088/0004-637X/745/1/45](https://doi.org/10.1088/0004-637X/745/1/45), arXiv: [1106.3484](https://arxiv.org/abs/1106.3484) [[astro-ph.HE](#)] (cit. on p. [116](#)).
- [231] M. G. Aartsen et al., “Search for Prompt Neutrino Emission from Gamma-Ray Bursts with IceCube,” *ApJ* 805, L5 (May 2015) L5, doi: [10.1088/2041-8205/805/1/L5](https://doi.org/10.1088/2041-8205/805/1/L5), arXiv: [1412.6510](https://arxiv.org/abs/1412.6510) [[astro-ph.HE](#)] (cit. on p. [116](#)).
- [232] A. Hoecker et al., “TMVA - Toolkit for Multivariate Data Analysis,” *ArXiv Physics e-prints* (Mar. 2007), eprint: [physics/0703039](https://arxiv.org/abs/physics/0703039) (cit. on p. [125](#)).
- [233] M. Honda et al., “Calculation of atmospheric neutrino flux using the interaction model calibrated with atmospheric muon data,” *Phys. Rev. D* 75.4, 043006 (Feb. 2007) 043006, doi: [10.1103/PhysRevD.75.043006](https://doi.org/10.1103/PhysRevD.75.043006), eprint: [astro-ph/0611418](https://arxiv.org/abs/astro-ph/0611418) (cit. on p. [127](#)).
- [234] R. Enberg, M. H. Reno, and I. Sarcevic, “Prompt neutrino fluxes from atmospheric charm,” *Phys. Rev. D* 78.4, 043005 (Aug. 2008) 043005, doi: [10.1103/PhysRevD.78.043005](https://doi.org/10.1103/PhysRevD.78.043005), arXiv: [0806.0418](https://arxiv.org/abs/0806.0418) [[hep-ph](#)] (cit. on p. [127](#)).
- [235] G. D. Barr et al., “Three-dimensional calculation of atmospheric neutrinos,” *Phys. Rev. D* 70.2, 023006 (July 2004) 023006, doi: [10.1103/PhysRevD.70.023006](https://doi.org/10.1103/PhysRevD.70.023006), eprint: [astro-ph/0403630](https://arxiv.org/abs/astro-ph/0403630) (cit. on p. [127](#)).
- [236] David Bogen, *IceCube Teleport System Many-to-Many Communications Through Iridium’s SBD*, IceCube Project - University of Wisconsin-Madison, Apr. 24, 2008, URL: http://polarpower.org/PTC/2008_pdf/2008PTC_Bogen.pdf (cit. on p. [133](#)).
- [237] S. St. Laurent et al., *Programming Web Services with XML-RPC*, Beijing Cambridge Mass: O’Reilly Media, 2001, ISBN: 978-0-596-00119-3 (cit. on p. [134](#)).
- [238] W. D. Pence et al., “Definition of the Flexible Image Transport System (FITS), version 3.0,” *A&A* 524, A42 (Dec. 2010) A42, doi: [10.1051/0004-6361/201015362](https://doi.org/10.1051/0004-6361/201015362) (cit. on pp. [135](#), [220](#)).
- [239] J. Neyman, “Outline of a Theory of Statistical Estimation Based on the Classical Theory of Probability,” *RSPTA* 236 (Aug. 1937) 333–380, doi: [10.1098/rsta.1937.0005](https://doi.org/10.1098/rsta.1937.0005) (cit. on pp. [140](#), [150](#)).
- [240] J. Neyman, *A Selection of Early Statistical Papers of J. Neyman*, The Selected Papers of Jerzy Neyman and E. S. Pearson, University of California Press, 1967, ISBN: 9780520009929, URL: <http://books.google.de/books?id=269sQgAACAAJ> (cit. on pp. [140](#), [150](#)).

- [241] M. G. Aartsen et al.,
“The Search for Transient Astrophysical Neutrino Emission with IceCube-DeepCore,”
ApJ 816, 75 (Jan. 2016) 75, doi: [10.3847/0004-637X/816/2/75](https://doi.org/10.3847/0004-637X/816/2/75),
arXiv: [1509.05029](https://arxiv.org/abs/1509.05029) [[astro-ph.HE](#)] (cit. on p. 140).
- [242] M. G. Aartsen et al., “The Detection of a Type II_n Supernova in Optical Follow-up
Observations of IceCube Neutrino Events,” *ApJ* 811, 52 (Sept. 2015) 52,
doi: [10.1088/0004-637X/811/1/52](https://doi.org/10.1088/0004-637X/811/1/52), arXiv: [1506.03115](https://arxiv.org/abs/1506.03115) [[astro-ph.HE](#)]
(cit. on pp. 143, 150).
- [243] D. J. Eisenstein et al., “SDSS-III: Massive Spectroscopic Surveys of the Distant Universe, the
Milky Way, and Extra-Solar Planetary Systems,” *AJ* 142, 72 (Sept. 2011) 72,
doi: [10.1088/0004-6256/142/3/72](https://doi.org/10.1088/0004-6256/142/3/72), arXiv: [1101.1529](https://arxiv.org/abs/1101.1529) [[astro-ph.IM](#)]
(cit. on pp. 146, 153, 172).
- [244] J. E. Gunn et al., “The 2.5 m Telescope of the Sloan Digital Sky Survey,”
AJ 131 (Apr. 2006) 2332–2359, doi: [10.1086/500975](https://doi.org/10.1086/500975), eprint: [astro-ph/0602326](https://arxiv.org/abs/astro-ph/0602326)
(cit. on pp. 146, 153, 172).
- [245] C. P. Ahn et al., “The Tenth Data Release of the Sloan Digital Sky Survey: First Spectroscopic
Data from the SDSS-III Apache Point Observatory Galactic Evolution Experiment,”
ApJS 211, 17 (Apr. 2014) 17, doi: [10.1088/0067-0049/211/2/17](https://doi.org/10.1088/0067-0049/211/2/17),
arXiv: [1307.7735](https://arxiv.org/abs/1307.7735) [[astro-ph.IM](#)] (cit. on pp. 146, 153).
- [246] S. Alam et al., “The Eleventh and Twelfth Data Releases of the Sloan Digital Sky Survey: Final
Data from SDSS-III,” *ArXiv e-prints* (Jan. 2015), arXiv: [1501.00963](https://arxiv.org/abs/1501.00963) [[astro-ph.IM](#)]
(cit. on pp. 146, 153, 172).
- [247] J. Leaman et al., “Nearby supernova rates from the Lick Observatory Supernova Search - I.
The methods and data base,” *MNRAS* 412 (Apr. 2011) 1419–1440,
doi: [10.1111/j.1365-2966.2011.18158.x](https://doi.org/10.1111/j.1365-2966.2011.18158.x), arXiv: [1006.4611](https://arxiv.org/abs/1006.4611) [[astro-ph.SR](#)]
(cit. on pp. 147, 148, 192).
- [248] F. Zwicky, “On the Frequency of Supernovae. II.,” *ApJ* 96 (July 1942) 28,
doi: [10.1086/144430](https://doi.org/10.1086/144430) (cit. on p. 148).
- [249] W. Li et al., “Nearby supernova rates from the Lick Observatory Supernova Search - II. The
observed luminosity functions and fractions of supernovae in a complete sample,”
MNRAS 412 (Apr. 2011) 1441–1472, doi: [10.1111/j.1365-2966.2011.18160.x](https://doi.org/10.1111/j.1365-2966.2011.18160.x),
arXiv: [1006.4612](https://arxiv.org/abs/1006.4612) [[astro-ph.SR](#)] (cit. on pp. 148, 197, 200, 202, 205).
- [250] M. B. Brown,
“400: A Method for Combining Non-Independent, One-Sided Tests of Significance,” English,
Biometrics 31.4 (1975) pp. 987-992, issn: 0006341X,
url: <http://www.jstor.org/stable/2529826> (cit. on p. 149).
- [251] R. C. Littell and J. L. Folks,
“Asymptotic Optimality of Fisher’s Method of Combining Independent Tests,” English,
Journal of the American Statistical Association 66.336 (1971) pp. 802-806, issn: 01621459,
url: <http://www.jstor.org/stable/2284230> (cit. on p. 149).
- [252] R. Fisher, *Statistical Methods for Research Workers, Eleventh Edition, Revised*,
[Biological Monographs and Manuals. no. 5.] Edinburgh, London: Oliver and Boyd, 1950
99–101, url: https://books.google.de/books?id=_3b_MgEACAAJ (cit. on p. 149).

- [253] R. A. Fisher, *Statistical Methods, Experimental Design, and Scientific Inference: A Re-issue of Statistical Methods for Research Workers, The Design of Experiments, and Statistical Methods and Scientific Inference*, Oxford England New York: Oxford University Press, 1990, ISBN: 978-0198522294 (cit. on p. 149).
- [254] A. Stasik, “Search for Neutrino Emission from SNe IIn with the IceCube Detector,” English, MA thesis: Rheinische Friedrich-Wilhelms-Universität Bonn, 2013 (cit. on p. 150).
- [255] N. L. Strotjohann, “Constraints on Transient Neutrino Sources from the Search for Neutrino Multiplets with the IceCube Detector,” English, MA thesis: Rheinische Friedrich-Wilhelms-Universität Bonn, 2014, URL: http://internal.icecube.wisc.edu/reports/data/icecube/2014/09/001/icecube_201409001_v1.pdf (cit. on pp. 150, 153).
- [256] K. Murase, T. A. Thompson, and E. O. Ofek, “Probing cosmic ray ion acceleration with radio-submm and gamma-ray emission from interaction-powered supernovae,” *MNRAS* 440 (May 2014) 2528–2543, doi: [10.1093/mnras/stu384](https://doi.org/10.1093/mnras/stu384), arXiv: [1311.6778](https://arxiv.org/abs/1311.6778) [astro-ph.HE] (cit. on p. 151).
- [257] R. Margutti et al., “A Panchromatic View of the Restless SN 2009ip Reveals the Explosive Ejection of a Massive Star Envelope,” *ApJ* 780, 21 (Jan. 2014) 21, doi: [10.1088/0004-637X/780/1/21](https://doi.org/10.1088/0004-637X/780/1/21), arXiv: [1306.0038](https://arxiv.org/abs/1306.0038) [astro-ph.HE] (cit. on pp. 151, 158).
- [258] P. A. Evans et al., “1SXPS: A Deep Swift X-Ray Telescope Point Source Catalog with Light Curves and Spectra,” *ApJS* 210, 8 (Jan. 2014) 8, doi: [10.1088/0067-0049/210/1/8](https://doi.org/10.1088/0067-0049/210/1/8), arXiv: [1311.5368](https://arxiv.org/abs/1311.5368) [astro-ph.HE] (cit. on p. 151).
- [259] R. P. Kraft, D. N. Burrows, and J. A. Nousek, “Determination of confidence limits for experiments with low numbers of counts,” *ApJ* 374 (June 1991) 344–355, doi: [10.1086/170124](https://doi.org/10.1086/170124) (cit. on p. 151).
- [260] A. A. Miller et al., “SN 2008iy: an unusual Type IIn Supernova with an enduring 400-d rise time,” *MNRAS* 404 (May 2010) 305–317, doi: [10.1111/j.1365-2966.2010.16280.x](https://doi.org/10.1111/j.1365-2966.2010.16280.x), arXiv: [0911.4719](https://arxiv.org/abs/0911.4719) [astro-ph.HE] (cit. on pp. 152, 154, 155, 157, 161, 162, 164).
- [261] R. Willingale et al., “Calibration of X-ray absorption in our Galaxy,” *MNRAS* 431 (May 2013) 394–404, doi: [10.1093/mnras/stt175](https://doi.org/10.1093/mnras/stt175), arXiv: [1303.0843](https://arxiv.org/abs/1303.0843) [astro-ph.HE] (cit. on p. 152).
- [262] E. O. Ofek et al., “SN 2010jl: Optical to Hard X-Ray Observations Reveal an Explosion Embedded in a Ten Solar Mass Cocoon,” *ApJ* 781, 42 (Jan. 2014) 42, doi: [10.1088/0004-637X/781/1/42](https://doi.org/10.1088/0004-637X/781/1/42), arXiv: [1307.2247](https://arxiv.org/abs/1307.2247) [astro-ph.HE] (cit. on pp. 152, 158, 159, 161).
- [263] G. Svirski, E. Nakar, and R. Sari, “Optical to X-Ray Supernova Light Curves Following Shock Breakout through a Thick Wind,” *ApJ* 759, 108 (Nov. 2012) 108, doi: [10.1088/0004-637X/759/2/108](https://doi.org/10.1088/0004-637X/759/2/108), arXiv: [1202.3437](https://arxiv.org/abs/1202.3437) [astro-ph.HE] (cit. on pp. 152, 158).
- [264] T. M. Brown et al., “Las Cumbres Observatory Global Telescope Network,” *PASP* 125 (Sept. 2013) 1031–1055, doi: [10.1086/673168](https://doi.org/10.1086/673168), arXiv: [1305.2437](https://arxiv.org/abs/1305.2437) [astro-ph.IM] (cit. on p. 153).

- [265] I. M. Hook et al., “The Gemini-North Multi-Object Spectrograph: Performance in Imaging, Long-Slit, and Multi-Object Spectroscopic Modes,” *PASP* 116 (May 2004) 425–440, doi: [10.1086/383624](https://doi.org/10.1086/383624) (cit. on p. 153).
- [266] J. B. Oke et al., “The Keck Low-Resolution Imaging Spectrometer,” *PASP* 107 (Apr. 1995) 375, doi: [10.1086/133562](https://doi.org/10.1086/133562) (cit. on p. 153).
- [267] O. Yaron and A. Gal-Yam, “WiSeREP - An Interactive Supernova Data Repository,” *PASP* 124 (July 2012) 668–681, doi: [10.1086/666656](https://doi.org/10.1086/666656), arXiv: [1204.1891](https://arxiv.org/abs/1204.1891) [[astro-ph.IM](https://arxiv.org/abs/1204.1891)] (cit. on p. 153).
- [268] N. Kaiser, “Pan-STARRS: a wide-field optical survey telescope array,” *Ground-based Telescopes*, ed. by J. M. Oschmann Jr., vol. 5489, Proc. SPIE, Oct. 2004 11–22, doi: [10.1117/12.552472](https://doi.org/10.1117/12.552472) (cit. on p. 153).
- [269] E. A. Magnier et al., “The Pan-STARRS 1 Photometric Reference Ladder, Release 12.01,” *ApJS* 205, 20 (Apr. 2013) 20, doi: [10.1088/0067-0049/205/2/20](https://doi.org/10.1088/0067-0049/205/2/20), arXiv: [1303.3634](https://arxiv.org/abs/1303.3634) [[astro-ph.IM](https://arxiv.org/abs/1303.3634)] (cit. on p. 153).
- [270] E. Magnier, “The Pan-STARRS PS1 Image Processing Pipeline,” *The Advanced Maui Optical and Space Surveillance Technologies Conference*, 2006 50 (cit. on p. 153).
- [271] J. L. Tonry et al., “The Pan-STARRS1 Photometric System,” *ApJ* 750, 99 (May 2012) 99, doi: [10.1088/0004-637X/750/2/99](https://doi.org/10.1088/0004-637X/750/2/99), arXiv: [1203.0297](https://arxiv.org/abs/1203.0297) [[astro-ph.IM](https://arxiv.org/abs/1203.0297)] (cit. on p. 153).
- [272] Nasa High Energy Astrophysics Science Archive Research Center (Heasarc), *HEASoft: Unified Release of FTOOLS and XANADU*, Astrophysics Source Code Library, Aug. 2014, ascl: [1408.004](https://ascl.net/1408.004) (cit. on p. 153).
- [273] D. J. Schlegel, D. P. Finkbeiner, and M. Davis, “Maps of Dust Infrared Emission for Use in Estimation of Reddening and Cosmic Microwave Background Radiation Foregrounds,” *ApJ* 500 (June 1998) 525–553, doi: [10.1086/305772](https://doi.org/10.1086/305772), eprint: [astro-ph/9710327](https://arxiv.org/abs/astro-ph/9710327) (cit. on pp. 153, 194).
- [274] J. A. Cardelli, G. C. Clayton, and J. S. Mathis, “The relationship between infrared, optical, and ultraviolet extinction,” *ApJ* 345 (Oct. 1989) 245–256, doi: [10.1086/167900](https://doi.org/10.1086/167900) (cit. on pp. 153, 194).
- [275] E. O. Ofek et al., “SN 2006gy: An Extremely Luminous Supernova in the Galaxy NGC 1260,” *ApJ* 659 (Apr. 2007) L13–L16, doi: [10.1086/516749](https://doi.org/10.1086/516749), eprint: [astro-ph/0612408](https://arxiv.org/abs/astro-ph/0612408) (cit. on p. 155).
- [276] N. Smith and R. McCray, “Shell-shocked Diffusion Model for the Light Curve of SN 2006gy,” *ApJ* 671 (Dec. 2007) L17–L20, doi: [10.1086/524681](https://doi.org/10.1086/524681), arXiv: [0710.3428](https://arxiv.org/abs/0710.3428) (cit. on p. 155).
- [277] I. Agnoletto et al., “SN 2006gy: Was it Really Extraordinary?” *ApJ* 691 (Feb. 2009) 1348–1359, doi: [10.1088/0004-637X/691/2/1348](https://doi.org/10.1088/0004-637X/691/2/1348), arXiv: [0810.0635](https://arxiv.org/abs/0810.0635) (cit. on p. 155).
- [278] K. S. Kawabata et al., “Extremely Luminous Supernova 2006gy at Late Phase: Detection of Optical Emission from Supernova,” *ApJ* 697 (May 2009) 747–757, doi: [10.1088/0004-637X/697/1/747](https://doi.org/10.1088/0004-637X/697/1/747), arXiv: [0902.1440](https://arxiv.org/abs/0902.1440) [[astro-ph.SR](https://arxiv.org/abs/0902.1440)] (cit. on p. 155).

- [279] A. A. Miller et al.,
“New Observations of the Very Luminous Supernova 2006gy: Evidence for Echoes,”
AJ 139 (June 2010) 2218–2229, doi: [10.1088/0004-6256/139/6/2218](https://doi.org/10.1088/0004-6256/139/6/2218), arXiv: [0906.2201](https://arxiv.org/abs/0906.2201)
(cit. on p. 155).
- [280] R. Stoll et al.,
“SN 2010jl in UGC 5189: Yet Another Luminous Type II_n Supernova in a Metal-poor Galaxy,”
ApJ 730, 34 (Mar. 2011) 34, doi: [10.1088/0004-637X/730/1/34](https://doi.org/10.1088/0004-637X/730/1/34), arXiv: [1012.3461](https://arxiv.org/abs/1012.3461)
(cit. on pp. 155, 164).
- [281] T. Zhang et al.,
“Type II_n Supernova SN 2010jl: Optical Observations for over 500 Days after Explosion,”
AJ 144, 131 (Nov. 2012) 131, doi: [10.1088/0004-6256/144/5/131](https://doi.org/10.1088/0004-6256/144/5/131),
arXiv: [1208.6078](https://arxiv.org/abs/1208.6078) [[astro-ph.SR](https://arxiv.org/abs/1208.6078)] (cit. on pp. 155, 161).
- [282] E. O. Ofek et al., “X-Ray Emission from Supernovae in Dense Circumstellar Matter
Environments: A Search for Collisionless Shocks,” *ApJ* 763, 42 (Jan. 2013) 42,
doi: [10.1088/0004-637X/763/1/42](https://doi.org/10.1088/0004-637X/763/1/42), arXiv: [1206.0748](https://arxiv.org/abs/1206.0748) [[astro-ph.HE](https://arxiv.org/abs/1206.0748)] (cit. on p. 155).
- [283] A. J. Drake et al., “Discovery of the Extremely Energetic Supernova 2008fz,”
ApJ 718 (Aug. 2010) L127–L131, doi: [10.1088/2041-8205/718/2/L127](https://doi.org/10.1088/2041-8205/718/2/L127),
arXiv: [0908.1990](https://arxiv.org/abs/0908.1990) [[astro-ph.HE](https://arxiv.org/abs/0908.1990)] (cit. on p. 155).
- [284] M. Turatto et al., “The Type II supernova 1988Z in MCG + 03-28-022 - Increasing evidence of
interaction of supernova ejecta with a circumstellar wind,” *MNRAS* 262 (May 1993) 128–140
(cit. on pp. 155, 162).
- [285] S. R. Kulkarni, “Modeling Supernova-like Explosions Associated with Gamma-ray Bursts with
Short Durations,” *ArXiv Astrophysics e-prints* (Oct. 2005), eprint: [astro-ph/0510256](https://arxiv.org/abs/astro-ph/0510256)
(cit. on pp. 157, 158, 174).
- [286] M. Wang et al., “The Ame2012 atomic mass evaluation,”
Chinese Physics C 36.12 (Dec. 2012) 1603, doi: [10.1088/1674-1137/36/12/003](https://doi.org/10.1088/1674-1137/36/12/003),
URL: <http://stacks.iop.org/1674-1137/36/i=12/a=003> (cit. on p. 158).
- [287] H. Junde, H. Su, and Y. Dong, “Nuclear Data Sheets for A = 56,”
Nuclear Data Sheets 112 (June 2011) 1513–1645, doi: [10.1016/j.nds.2011.04.004](https://doi.org/10.1016/j.nds.2011.04.004)
(cit. on p. 158).
- [288] O. Pejcha and T. A. Thompson,
“The Landscape of the Neutrino Mechanism of Core-collapse Supernovae: Neutron Star and
Black Hole Mass Functions, Explosion Energies, and Nickel Yields,”
ApJ 801, 90 (Mar. 2015) 90, doi: [10.1088/0004-637X/801/2/90](https://doi.org/10.1088/0004-637X/801/2/90),
arXiv: [1409.0540](https://arxiv.org/abs/1409.0540) [[astro-ph.HE](https://arxiv.org/abs/1409.0540)] (cit. on p. 158).
- [289] A. Gal-Yam, “Luminous Supernovae,” *Science* 337 (Aug. 2012) 927–,
doi: [10.1126/science.1203601](https://doi.org/10.1126/science.1203601), arXiv: [1208.3217](https://arxiv.org/abs/1208.3217) [[astro-ph.CO](https://arxiv.org/abs/1208.3217)] (cit. on p. 158).
- [290] T. J. Moriya et al., “An analytic bolometric light curve model of interaction-powered
supernovae and its application to Type II_n supernovae,” *MNRAS* 435 (Oct. 2013) 1520–1535,
doi: [10.1093/mnras/stt1392](https://doi.org/10.1093/mnras/stt1392), arXiv: [1307.2644](https://arxiv.org/abs/1307.2644) [[astro-ph.HE](https://arxiv.org/abs/1307.2644)] (cit. on p. 158).
- [291] N. N. Chugai and I. J. Danziger,
“Supernova 1988Z - Low-Mass Ejecta Colliding with the Clumpy Wind,”
MNRAS 268 (May 1994) 173, doi: [10.1093/mnras/268.1.173](https://doi.org/10.1093/mnras/268.1.173) (cit. on pp. 158, 162).

- [292] E. Chatzopoulos, J. C. Wheeler, and J. Vinko, “Generalized Semi-analytical Models of Supernova Light Curves,” *ApJ* 746, 121 (Feb. 2012) 121, doi: [10.1088/0004-637X/746/2/121](https://doi.org/10.1088/0004-637X/746/2/121), arXiv: [1111.5237](https://arxiv.org/abs/1111.5237) [astro-ph.HE] (cit. on p. 158).
- [293] R. A. Chevalier, “The radio and X-ray emission from type II supernovae,” *ApJ* 259 (Aug. 1982) 302–310, doi: [10.1086/160167](https://doi.org/10.1086/160167) (cit. on p. 159).
- [294] M. Fukugita et al., “The Sloan Digital Sky Survey Photometric System,” *AJ* 111 (Apr. 1996) 1748, doi: [10.1086/117915](https://doi.org/10.1086/117915) (cit. on pp. 160, 210).
- [295] N. Smith et al., “Systematic Blueshift of Line Profiles in the Type II_n Supernova 2010jl: Evidence for Post-shock Dust Formation?” *AJ* 143, 17 (Jan. 2012) 17, doi: [10.1088/0004-6256/143/1/17](https://doi.org/10.1088/0004-6256/143/1/17), arXiv: [1108.2869](https://arxiv.org/abs/1108.2869) [astro-ph.HE] (cit. on pp. 162, 163).
- [296] C. Gall et al., “Rapid formation of large dust grains in the luminous supernova 2010jl,” *Nature* 511 (July 2014) 326–329, doi: [10.1038/nature13558](https://doi.org/10.1038/nature13558), arXiv: [1407.4447](https://arxiv.org/abs/1407.4447) [astro-ph.SR] (cit. on p. 162).
- [297] C. Fransson et al., “High-density Circumstellar Interaction in the Luminous Type II_n SN 2010jl: The First 1100 Days,” *ApJ* 797, 118 (Dec. 2014) 118, doi: [10.1088/0004-637X/797/2/118](https://doi.org/10.1088/0004-637X/797/2/118), arXiv: [1312.6617](https://arxiv.org/abs/1312.6617) [astro-ph.HE] (cit. on p. 163).
- [298] A. H. Harutyunyan et al., “ESC supernova spectroscopy of non-ESC targets,” *A&A* 488 (Sept. 2008) 383–399, doi: [10.1051/0004-6361:20078859](https://doi.org/10.1051/0004-6361:20078859), arXiv: [0804.1939](https://arxiv.org/abs/0804.1939) (cit. on pp. 163, 164).
- [299] H. Lee et al., “On Extending the Mass-Metallicity Relation of Galaxies by 2.5 Decades in Stellar Mass,” *ApJ* 647 (Aug. 2006) 970–983, doi: [10.1086/505573](https://doi.org/10.1086/505573), eprint: [astro-ph/0605036](https://arxiv.org/abs/astro-ph/0605036) (cit. on p. 164).
- [300] B. Katz, N. Sapir, and E. Waxman, “X-rays, γ -rays and neutrinos from collisionless shocks in supernova wind breakouts,” *Death of Massive Stars: Supernovae and Gamma-Ray Bursts*, vol. 279, IAU Symposium, Sept. 2012 274–281, doi: [10.1017/S174392131201304X](https://doi.org/10.1017/S174392131201304X) (cit. on p. 165).
- [301] H. Falcke and L. Rezzolla, “Fast radio bursts: the last sign of supramassive neutron stars,” *A&A* 562 (2014) A137, doi: [10.1051/0004-6361/201321996](https://doi.org/10.1051/0004-6361/201321996), arXiv: [1307.1409](https://arxiv.org/abs/1307.1409) [astro-ph.HE] (cit. on pp. 165, 166).
- [302] D. R. Lorimer et al., “A Bright Millisecond Radio Burst of Extragalactic Origin,” *Science* 318 (Nov. 2007) 777, doi: [10.1126/science.1147532](https://doi.org/10.1126/science.1147532), arXiv: [0709.4301](https://arxiv.org/abs/0709.4301) (cit. on p. 166).
- [303] E. Bertin and S. Arnouts, “SExtractor: Software for source extraction,” *A&AS* 117 (June 1996) 393–404, doi: [10.1051/aas:1996164](https://doi.org/10.1051/aas:1996164) (cit. on p. 169).
- [304] E. Bertin, *SExtractor v2.13 — User’s manual*, Institut d’Astrophysique & Observatoire de Paris, URL: <https://www.astromatic.net/pubsvn/software/sextractor/trunk/doc/sextractor.pdf> (visited on 04/26/2016) (cit. on pp. 169, 229, 230).

- [305] E. Bertin, “Automatic Astrometric and Photometric Calibration with SCAMP,” *Astronomical Data Analysis Software and Systems XV*, ed. by C. Gabriel et al., vol. 351, Astronomical Society of the Pacific Conference Series, July 2006 112 (cit. on p. 169).
- [306] E. Bertin, *SCAMP v1.20 — User’s guide*, Institut d’Astrophysique de Paris, Feb. 19, 2014, URL: <https://www.astromatic.net/pubsvn/software/scamp/trunk/doc/scamp.pdf> (visited on 04/26/2016) (cit. on pp. 169, 227).
- [307] E. Bertin et al., “The TERAPIX Pipeline,” *Astronomical Data Analysis Software and Systems XI*, ed. by D. A. Bohlender, D. Durand, and T. H. Handley, vol. 281, Astronomical Society of the Pacific Conference Series, 2002 228 (cit. on p. 169).
- [308] E. Bertin, *SWarp v2.21 — User’s guide*, Institut d’Astrophysique de Paris, Dec. 17, 2010, URL: <https://www.astromatic.net/pubsvn/software/swarp/trunk/doc/swarp.pdf> (visited on 04/26/2016) (cit. on pp. 169, 227).
- [309] A. Becker, *High Order Transform of PSF ANd Template Subtraction*, Department of Astronomy, University of Washington, Dec. 21, 2012, URL: <http://www.astro.washington.edu/users/becker/v2.0/hotpants.html> (visited on 05/09/2016) (cit. on pp. 170, 228, 229).
- [310] J. S. Bloom et al., “Automating Discovery and Classification of Transients and Variable Stars in the Synoptic Survey Era,” *PASP* 124 (Nov. 2012) 1175–1196, doi: 10.1086/668468, arXiv: 1106.5491 [astro-ph.IM] (cit. on pp. 170, 176, 205).
- [311] L. Breiman, “Random Forests,” *Machine Learning* 45.1 (2001) 5–32, ISSN: 1573-0565, doi: 10.1023/A:1010933404324, URL: <http://dx.doi.org/10.1023/A:1010933404324> (cit. on p. 170).
- [312] M. Hall et al., “The WEKA Data Mining Software: An Update,” *SIGKDD Explorations* 11 (1 2009) (cit. on p. 170).
- [313] *Weka 3: Data Mining Software in Java*, Machine Learning Group at the University of Waikato, URL: <http://www.cs.waikato.ac.nz/ml/weka/index.html> (visited on 05/11/2016) (cit. on p. 170).
- [314] C. Stoughton et al., “Sloan Digital Sky Survey: Early Data Release,” *AJ* 123 (Jan. 2002) 485–548, doi: 10.1086/324741 (cit. on pp. 172, 187).
- [315] *SDSS Data Release 12 Scope — Imaging statistics*, Astrophysical Research Consortium (ARC) and The Sloan Digital Sky Survey (SDSS) Collaboration, 2016, URL: <http://www.sdss.org/dr12/scope/#Imagingstatistics> (visited on 05/16/2016) (cit. on p. 172).
- [316] M. F. Skrutskie et al., “The Two Micron All Sky Survey (2MASS),” *AJ* 131 (Feb. 2006) 1163–1183, doi: 10.1086/498708 (cit. on p. 172).
- [317] G. Kauffmann et al., “The host galaxies of active galactic nuclei,” *MNRAS* 346 (Dec. 2003) 1055–1077, doi: 10.1111/j.1365-2966.2003.07154.x, eprint: astro-ph/0304239 (cit. on p. 172).
- [318] G. Kauffmann, *AGN Catalogue*, Max-Planck-Institut für Astrophysik, URL: <http://wwwmpa.mpa-garching.mpg.de/SDSS/DR4/Data/agncatalogue.html> (visited on 05/07/2015) (cit. on p. 172).

- [319] M. Taylor et al., “The Core Collapse Supernova Rate from the SDSS-II Supernova Survey,” *ApJ* 792, 135 (Sept. 2014) 135, doi: [10.1088/0004-637X/792/2/135](https://doi.org/10.1088/0004-637X/792/2/135), arXiv: [1407.0999](https://arxiv.org/abs/1407.0999) [astro-ph.SR] (cit. on pp. 173, 202).
- [320] J. M. Silverman et al., “Berkeley Supernova Ia Program - I. Observations, data reduction and spectroscopic sample of 582 low-redshift Type Ia supernovae,” *MNRAS* 425 (Sept. 2012) 1789–1818, doi: [10.1111/j.1365-2966.2012.21270.x](https://doi.org/10.1111/j.1365-2966.2012.21270.x), arXiv: [1202.2128](https://arxiv.org/abs/1202.2128) (cit. on pp. 173–175).
- [321] D. F. Cowen, A. Franckowiak, and M. Kowalski, “Estimating the explosion time of core-collapse supernovae from their optical light curves,” *Astroparticle Physics* 33 (Feb. 2010) 19–23, doi: [10.1016/j.astropartphys.2009.10.007](https://doi.org/10.1016/j.astropartphys.2009.10.007), arXiv: [0901.4877](https://arxiv.org/abs/0901.4877) [astro-ph.HE] (cit. on p. 173).
- [322] E. Waxman, P. Mészáros, and S. Campana, “GRB 060218: A Relativistic Supernova Shock Breakout,” *ApJ* 667 (Sept. 2007) 351–357, doi: [10.1086/520715](https://doi.org/10.1086/520715), eprint: [astro-ph/0702450](https://arxiv.org/abs/astro-ph/0702450) (cit. on pp. 173, 174).
- [323] M. S. Bessell, “UBVRI passbands,” *PASP* 102 (Oct. 1990) 1181–1199, doi: [10.1086/132749](https://doi.org/10.1086/132749) (cit. on p. 175).
- [324] M. R. Blanton et al., “The Broadband Optical Properties of Galaxies with Redshifts $0.02 < z < 0.22$,” *ApJ* 594 (Sept. 2003) 186–207, doi: [10.1086/375528](https://doi.org/10.1086/375528), eprint: [astro-ph/0209479](https://arxiv.org/abs/astro-ph/0209479) (cit. on p. 187).
- [325] D. Scott, *Multivariate density estimation : theory, practice, and visualization*, New York: Wiley, 1992, ISBN: 0471547700 (cit. on p. 197).
- [326] E. Bellm, “The Zwicky Transient Facility,” *The Third Hot-wiring the Transient Universe Workshop*, ed. by P. R. Wozniak et al., 2014 27–33, arXiv: [1410.8185](https://arxiv.org/abs/1410.8185) [astro-ph.IM] (cit. on p. 205).
- [327] R. M. Smith et al., “The Zwicky transient facility observing system,” *Ground-based and Airborne Instrumentation for Astronomy V*, vol. 9147, Proc. SPIE, July 2014 914779, doi: [10.1117/12.2070014](https://doi.org/10.1117/12.2070014) (cit. on p. 205).
- [328] J. B. Oke and J. E. Gunn, “Secondary standard stars for absolute spectrophotometry,” *ApJ* 266 (Mar. 1983) 713–717, doi: [10.1086/160817](https://doi.org/10.1086/160817) (cit. on p. 210).
- [329] J. Neyman and E. S. Pearson, “On the Problem of the Most Efficient Tests of Statistical Hypotheses,” *Royal Society of London Philosophical Transactions Series A* 231 (1933) 289–337, doi: [10.1098/rsta.1933.0009](https://doi.org/10.1098/rsta.1933.0009) (cit. on p. 215).
- [330] J. Braun et al., “Methods for point source analysis in high energy neutrino telescopes,” *Astroparticle Physics* 29 (May 2008) 299–305, doi: [10.1016/j.astropartphys.2008.02.007](https://doi.org/10.1016/j.astropartphys.2008.02.007), arXiv: [0801.1604](https://arxiv.org/abs/0801.1604) (cit. on p. 215).
- [331] J. Braun et al., “Time-dependent point source search methods in high energy neutrino astronomy,” *Astroparticle Physics* 33 (Apr. 2010) 175–181, doi: [10.1016/j.astropartphys.2010.01.005](https://doi.org/10.1016/j.astropartphys.2010.01.005), arXiv: [0912.1572](https://arxiv.org/abs/0912.1572) [astro-ph.IM] (cit. on pp. 215, 216).

-
- [332] F. Kasten and A. T. Young, “Revised optical air mass tables and approximation formula,” *Appl. Opt.* 28 (Nov. 1989) 4735–4738, doi: [10.1364/AO.28.004735](https://doi.org/10.1364/AO.28.004735) (cit. on p. 219).
- [333] *Meteorological service for international air navigation. Annex 3, Convention on International Civil Aviation*, International Civil Aviation Organization, 2013,
URL: http://www.wmo.int/pages/prog/www/ISS/Meetings/CT-MTDCF-ET-DRC_Geneva2008/Annex3_16ed.pdf (cit. on p. 219).
- [334] *METAR Tutorial*, College of DuPage Meteorology,
URL: <https://www.wunderground.com/metarFAQ.asp> (visited on 05/07/2015)
(cit. on p. 219).
- [335] *Meteorological Station Information Lookup for KRNM*, National Oceanic and Atmospheric Administration, Dec. 11, 2003,
URL: http://weather.noaa.gov/cgi-bin/nsd_lookup.pl?station=KRNM
(cit. on p. 220).
- [336] C. Alard, “Image subtraction using a space-varying kernel,” *A&AS* 144 (June 2000) 363–370,
doi: [10.1051/aas:2000214](https://doi.org/10.1051/aas:2000214) (cit. on pp. 228, 229).
- [337] B. W. Holwerda, *Source Extractor for Dummies*, Space Telescope Science Institute,
URL: <https://www.astromatic.net/pubsvn/software/sextractor/trunk/doc/sextractor.pdf>
(visited on 04/26/2016) (cit. on p. 229).

Acknowledgements

I would like to thank everyone who helped me on this long and not always easy journey. First and foremost, my supervisor Marek Kowalski for continued support, guidance, excellent ideas, and incredibly powerful sense of understanding and intuition. Apart from that: Marek, thank you for being so generous, funny, and good at heart.

Special thanks go to the PTF collaboration and in particular Peter Nugent, who provided much code, help, inspiration, and feedback, without which this thesis would have been impossible. Thanks also go to Eran Ofek, Mansi Kasliwal, Yi Cao and everyone else who contributed in carrying out the IceCube follow-up at PTF and provided data on the supernova PTF12csy. Another big thanks goes to Chris Frohmaier, who shared invaluable fake supernova simulation data, without which the Monte Carlo simulation of the SN detection algorithm would have been entirely impossible. Also, big kudos go to the IceCube collaboration for building and operating such an excellent neutrino detector in an extreme environment. Since I cannot mention everyone, I subjectively drop the names of Erik Blaufuss (for friendly and uncomplicated support at the low-level side of the follow-up), Torsten Schmidt (for pulling strings in the background), Jan Lünemann (for development of the Cramér-Rao directional uncertainty estimator), Chad Finley (for benevolent support concerning point source analyses, and just being a great guy), and Julia Tjus and Naoko Kurahashi-Neilson (for their help with the PTF12csy paper). I also thank Phil Evans for friendly and fruitful cooperation on the Swift X-ray follow-up and contributing X-ray data on PTF12csy.

Of course, I also owe big thank yous to my more direct colleagues in Bonn and later Berlin/Zeuthen: Andreas Homeier (I miss working with you, you were such a nice office mate!), Lukas Schulte (thanks for generously proof-reading a large part of my thesis!), Nora Linn Strotjohann (it was always nice with you!), Alexander Stasik (I enjoyed “pair-programming” with you!), Anna Franckowiak (you are the nicest colleague I can imagine, and you left such an immense footprint in the optical follow-up!), Sebastian Böser (you were arguably the coolest supervisor I ever had, at the same time extremely creative and just a good friend!), and Dustin Hebecker (thanks for your Linux distro tips). Also thanks to my friends from the cosmology side: Uli Feindt, Simona Lombardo, Matthias Kerschhaggl, Clément Buton, Amir Moqanaki (OK, he’s into photonics now), Jakob Nordin, Mickael Rigault, and Daniel Küsters. Thanks also to those I forgot to mention here.

And, last but not least, for never stopping to believe in me, I’d like to thank my dear wife Ann-Kathrin.